

Quench sensitivity of aluminium alloys: Analysis of the kinetics and nature of quench-induced precipitation

Cumulative habilitation thesis to achieve
the academic degree **Dr.-Ing. habil.**
submitted to the Faculty for Mechanical Engineering and
Marine Technology, University of Rostock

*Submitted by Dr.-Ing. Benjamin Milkereit
born on 16th of August 1980 in Teterow, Germany*

Referees:

Prof. Dr.-Ing. habil. Olaf Keßler

University of Rostock, Germany
Faculty for Mechanical Engineering and Marine Technology,
Chair of Materials Science

Prof. Dr. rer. nat. habil. Christoph Schick

University of Rostock, Germany
Faculty of Mathematics and Natural Sciences
Institute of Physics, Group of Polymer Physics

Prof. Alexis Deschamps, PhD

Grenoble Institute of Technology, Grenoble, France

Date of submission: 02.10.2019



Dieses Werk ist lizenziert unter einer
Creative Commons Namensnennung 4.0 International Lizenz.

Plus et en vous
et
Navigare necesse est

Abstract

After steels, aluminium alloys are the second most important group of technological usable metallic alloys. The global production of aluminium has amounted to about 60 % of the global tonnage of all non-ferrous alloys in recent years. In addition, the global demand for aluminium has doubled within the last ten years, reaching about 60 Mt in 2017. To promote the usage of iron or aluminium as construction materials, their strength must be increased, and the mechanical properties of metallic alloys are frequently adjusted by thermal and thermo-mechanical treatments. These treatments frequently utilise solid-solid phase transformations, for instance precipitation and its hardening effects. In aluminium alloys, precipitation strengthening is controlled by age-hardening heat treatments, including solution treatment, quenching, and ageing. In terms of technological applications, quenching is considered a critical step, because detrimental quench-induced precipitation must be avoided to exploit the full age-hardening potential of the alloy. The alloy therefore needs to be quenched faster than a critical cooling rate, but slow enough to avoid undesired distortion and residual stresses. These contrary requirements for quenching can only be aligned based on detailed knowledge of the kinetics of quench-induced precipitation. The solution treatment sets the structural starting condition for the quenching process, and thus also has great importance. Until the beginning of the 21st century, the kinetics of relevant solid-solid phase transformations during cooling of aluminium alloys could only be estimated by ex-situ testing of different properties, as no metrological methods were available for their in situ measurement. Over the past ten years, significant progress has been achieved in this field of materials science. The main progress in understanding solid-solid phase transformation kinetics was enabled by the development of highly sensitive calorimetric measurement techniques, based on the application of differential scanning calorimetry (DSC) and the chip-sensor-based differential fast scanning calorimetry (DFSC). A combination of DSC and DFSC methods now enables the kinetics of solid-solid phase transformations to be analysed over the full range of technologically and physically relevant heating and cooling rates. The progress made thus far has been reported in several original papers, which mostly cover single alloys or groups of alloys from the same alloy family. This thesis presents a comprehensive report on this progress for the first time, by covering research conducted on the nature and kinetics of solid-solid phase transformations of 27 aluminium alloys. The key features of the calorimetric techniques and their applicability to other age-hardening metallic alloy systems are discussed. The insights into the solid-solid phase transformation kinetics in Al alloys cover precipitation and dissolution reactions during heating from different initial states, dissolution during solution annealing and to a vast extent quench-induced precipitation during continuous cooling over a dynamic cooling rate range of ten orders of magnitude. The insights from kinetic analysis into quench-induced precipitation are complemented by sophisticated micro- and nano-structural analyses and continuous cooling precipitation (CCP) diagrams are derived. The measurement of enthalpies released by quench-induced precipitation as a function of the cooling rate also enables predictions of the quench sensitivities of Al alloys using physically-based models. The various types of alloys are compared, and general aspects of quench-induced precipitation in Al alloys are derived. This particularly includes general statements on quench-induced phases which precipitate at certain temperatures and times, as well as their common nucleation mechanisms. Based on these aspects, options for adjusting/controlling the quench sensitivity of age-hardening Al alloys are derived.

Kurzfassung

Nach Stählen sind Aluminium-Legierungen die zweitwichtigste Gruppe von technologisch nutzbaren Metallen. In den vergangenen Jahren betrug die globale Produktion von Aluminium etwa 60 % aller Nichteisen-Metalle, wobei sich der weltweite Absatz von Aluminium in den vergangenen 10 Jahren auf ca. 60 Mt im Jahr 2017 verdoppelt hat. Um die Verwendung von Eisen oder Aluminium als Konstruktionswerkstoff zu ermöglichen, muss deren Festigkeit gesteigert werden. Die mechanischen Eigenschaften von metallischen Legierungen werden häufig durch thermomechanische Behandlungen eingestellt, wobei oft Phasenumwandlungen im festen Zustand, wie z. B. Ausscheidungen und deren verfestigender Effekt ausgenutzt werden. In Aluminium-Legierungen wird die Ausscheidungsverfestigung durch die Wärmebehandlung Ausscheidungshärten kontrolliert, welche die Prozessschritte Lösungsglühen, Abschrecken und Auslagern umfasst. Aus Sicht der technologischen Umsetzung ist das Abschrecken kritisch: Zum einen müssen unerwünschte abschreckinduzierte Ausscheidungen verhindert werden, um das volle Aushärtungspotenzial nutzen zu können; dies erfordert rasches Abschrecken. Gleichzeitig sollen in vielen Fällen Verzug und Eigenspannungen klein gehalten werden, was langsames Abkühlen erfordert. Um diese gegensätzlichen Anforderungen in Einklang zu bringen, muss die Kinetik abschreckinduzierter Ausscheidungen bekannt und die Legierung mit einer legierungsspezifischen kritischen Abschreckgeschwindigkeit abgeschreckt werden. Das Lösungsglühen erzeugt die strukturellen Startbedingungen und hat damit auch eine große Bedeutung. Bis zum Beginn des 21ten Jahrhunderts konnte die Kinetik relevanter Festphasenumwandlungen beim Abkühlen von Aluminiumlegierungen nur anhand von ex-situ Messungen verschiedener Eigenschaften abgeschätzt werden, da es keine Messtechnik gab, die eine in-situ Messung ermöglichte. An dieser Stelle der Werkstoffwissenschaften ist in den vergangenen 10 Jahren ein erheblicher Fortschritt erzielt worden, indem hoch sensitive kalorimetrische Messmethoden entwickelt wurden, die auf der dynamischen Differenz-Kalorimetrie (DSC) und der Chip-Sensor basierten schnellen dynamischen Differenz-Kalorimetrie (DFSC) basieren. Die Kombination von DSC und DFSC ermöglicht es heute, dass die Zeitabhängigkeit der Festphasenumwandlungen im gesamten technisch und physikalisch relevanten Erwärm- und Kühlgeschwindigkeitsbereich analysiert werden kann. Der erzielte Fortschritt wurde bereits in etlichen Journal-Artikeln veröffentlicht, welche häufig eine Legierung oder Gruppen von Legierungen desselben Systems betrachten. Diese Arbeit gibt erstmals einen umfassenden Überblick über die Ergebnisse von 27 Aluminium-Legierungen. Die Schlüsselaspekte der kalorimetrischen Messmethoden und deren Anwendbarkeit auf andere Legierungssysteme werden diskutiert. Die Erkenntnisse zur Festphasenumwandlungskinetik von Aluminiumlegierungen umfassen Ausscheidungs- und Auflösungsreaktionen beim Erwärmen verschiedener Ausgangszustände, Auflösung während des Lösungsglühens und größtenteils abschreckinduzierte Ausscheidung während der Abkühlung über eine Kühlgeschwindigkeitsbandbreite von 10 Größenordnungen. Die Erkenntnisse zur Kinetik werden durch Untersuchungen zur Mikro- und Nanostruktur ergänzt und kontinuierliche Zeit-Temperatur-Ausscheidungsdiagramme wurden erstellt. Die Modellierung der von den abschreckinduzierten Ausscheidungen freigesetzten Enthalpie als Funktion der Kühlgeschwindigkeit ermöglicht Vorhersagen zur Abschreckempfindlichkeit von Aluminiumlegierungen. Die verschiedenen Al-Legierungssysteme werden verglichen, wovon allgemeine Aspekte abschreckinduzierter Ausscheidung abgeleitet werden. Dies umfasst insbesondere Aussagen zu den abschreckinduzierten Phasen, welche bei bestimmten Temperaturen und Zeiten ausscheiden, sowie deren übliche Keimbildungsmechanismen. Basierend auf den gesammelten Ergebnissen werden Möglichkeiten aufgezeigt, die Abschreckempfindlichkeit von Aluminiumlegierungen gezielt einzustellen.

1	Introduction	1
2	Measuring techniques and methods for the analysis of solid-solid phase transformations	9
2.1	Methods for in situ kinetic analysis of solid-solid phase transformations in metals.....	9
2.2	Methodology and systematics of state-of-the-art kinetic DSC analysis.....	12
2.2.1	Basic concepts of DSC measurements	12
2.2.2	Key features for in situ quantification of enthalpy changes of solid-solid phase transformation as a function of the scanning rate or time	13
2.3	Construction scheme for continuous cooling precipitation diagrams	21
2.4	Methods and systematics for complementary micro- and nano-structure analysis.....	23
2.5	Analysis of resulting mechanical properties	24
2.6	General illustration of results and reading guidelines for CCP diagrams.....	24
3	Solid-solid phase transformations in Al alloys over a wide dynamic range	27
3.1	Heating to solution treatment and isothermal soaking	27
3.1.1	Capabilities and limitations of DSC heating curve analysis and interpretation	27
3.1.2	Achieving a complete solid solution.....	31
3.1.3	Extending the scanning rate by reheating experiments.....	31
3.2	Quench-induced precipitation during cooling from solution treatment	34
3.2.1	AlSi binary wrought alloys.....	34
3.2.2	6xxx AlMgSi wrought alloys	38
3.2.3	7xxx AlZnMg(Cu) wrought alloys	51
3.2.4	2xxx AlCu(Mg) wrought alloys	61
3.2.5	AlSiMg cast alloys.....	63
4	General aspects of quench-induced precipitation in Al alloys	69
5	Application of the derived DSC methods to other alloy systems	73
6	Conclusions	77
6.1	In situ DSC analysis of solid-solid phase transformations in precipitation hardening alloys ..	77
6.2	Continuous heating and solution annealing.....	78
6.3	Continuous cooling and analysis of quench-induced precipitation.....	78
7	References	81
7.1	References underpinning the habilitation thesis.....	81
7.2	Further references by the author and external references	82

8	Manuscripts of publications forming the basis of the cumulative habilitation thesis;.....	91
[BM1]	Milkereit B, Kessler O, Schick C: <i>Recording of continuous cooling precipitation diagrams of aluminium alloys</i> . Thermochemica Acta 492 (2009): 73–78.....	93
[BM2]	Milkereit B, Wanderka N, Schick C, Kessler O: <i>Continuous cooling precipitation diagrams of Al-Mg-Si alloys</i> . Materials Science Engineering A 550 (2012): 87–96.....	113
[BM3]	Zhang Y, Milkereit B, Kessler O, Schick C, Rometsch PA: <i>Development of continuous cooling precipitation diagrams for aluminium alloys AA7150 and AA7020</i> . Journal of Alloys and Compounds 584 (2014): 581–589.....	141
[BM4]	Schumacher P, Pogatscher S, Starink MJ, Schick C, Mohles V, Milkereit B: <i>Quench-induced precipitates in Al–Si alloys: Calorimetric determination of solute content and characterisation of microstructure</i> . Thermochemica Acta 602 (2015): 63–73.	159
[BM5]	Osten J, Milkereit B, Schick C, Kessler O: <i>Dissolution and precipitation behaviour during continuous heating of Al-Mg-Si alloys in a wide range of heating rates</i> . Materials 8-5 (2015): 2830–2848.....	185
[BM6]	Milkereit B, Starink MJ: <i>Quench sensitivity of Al-Mg-Si alloys: A model for linear cooling and strengthening</i> . Materials & Design 76 (2015) 117–129.....	205
[BM7]	Starink MJ, Milkereit B, Zhang Y, Rometsch PA: <i>Predicting the quench sensitivity of Al-Zn-Mg-Cu alloys: A model for linear cooling and strengthening</i> . Materials & Design 88 (2015): 958–971.....	237
[BM8]	Zhang Y, Weyland M, Milkereit B, Reich M, Rometsch PA: <i>Precipitation of a new platelet phase during the quenching of an Al-Zn-Mg-Cu alloy</i> . Scientific Reports 6 (2016): 23109.....	277
[BM9]	Yang B, Milkereit B, Zhang Y, Rometsch PA, Kessler O, Schick C: <i>Continuous cooling precipitation diagram of aluminium alloy AA7150 based on a new fast scanning calorimetry and interrupted quenching method</i> . Materials Characterization 120 (2016): 30–37.....	287
[BM10]	Fröck H, Milkereit B, Wiechmann P, Springer A, Sander M, Kessler O, Reich M: <i>Influence of Solution-Annealing Parameters on the Continuous Cooling Precipitation of Aluminum Alloy 6082</i> . Metals 8-265 (2018): 1–16.....	313
9	Appendix	330

1 Introduction

Aluminium alloys are the second most important metallic materials. In 2014, the global production of steel (about 1,670 Mt) amounted to about 90 % of global metal production [1, 2]. Of the remaining metals, aluminium represents the majority, and in 2013 and 2014, aluminium amounted to about 60 % of the total tonnage of the global production of non-ferrous metals [2]. In terms of castings, Fe-based castings represented about 80 % of the global production tonnage in 2016, while Al-based castings amounted to about 17 %, with Cu less than 2 % [3] and other metals below 1 % in total. Thus, considering non-ferrous metal castings, aluminium amounted to about 85 % of the global production. The importance of aluminium and its products can also be seen from the fact that the global demand for aluminium has doubled during the last ten years, reaching more than 60 Mt in 2017 [4].

However, pure aluminium has poor strength, and its application is largely limited to packaging and foil, electronic conductors, chemical process equipment and lithographic plates [5]. In order to make use of aluminium as a construction material or in applications as an engineering material for lightweight constructions, for instance aeroplanes, the strength of Al-based materials must be increased [5–7]. This strength increase, i.e. an increase in the resistance against plastic deformation, can be achieved by four physical mechanisms: (i) grain-boundaries; (ii) dislocations (work hardening); (iii) alloying elements in solid solution; and (iv) alloying elements precipitated in nano-sized particles [6–8]. To understand these mechanisms, it is essential to know that plastic deformation (at temperatures below 0.4 times the melting temperature in K, for aluminium below about 100 °C) involves the gliding of dislocations on certain lattice plains of the metallic matrix crystal. All four mechanisms that can increase the strength are therefore based on the effect of hindering dislocations from gliding. The mechanism of precipitation strengthening is typically used to achieve the highest strengths in Al-based products [5, 9].

As seen from the above—and which is true for every engineering material—the structure of the material at micro- and nanoscales affects its properties. Thus, for several metallic alloys, changes in the inner structure due to solid-solid phase transformations control the properties. This includes not only mechanical properties such as strength, ductility and toughness, but also corrosion properties and others. The precipitation of secondary phase particles from a solid solution represents a solid-solid phase transformation. In technological applications, solid-solid phase transformations are typically adjusted by controlled heat treatments. Figure 1 shows a schematic diagram of the time-temperature profiles of some heat treatments

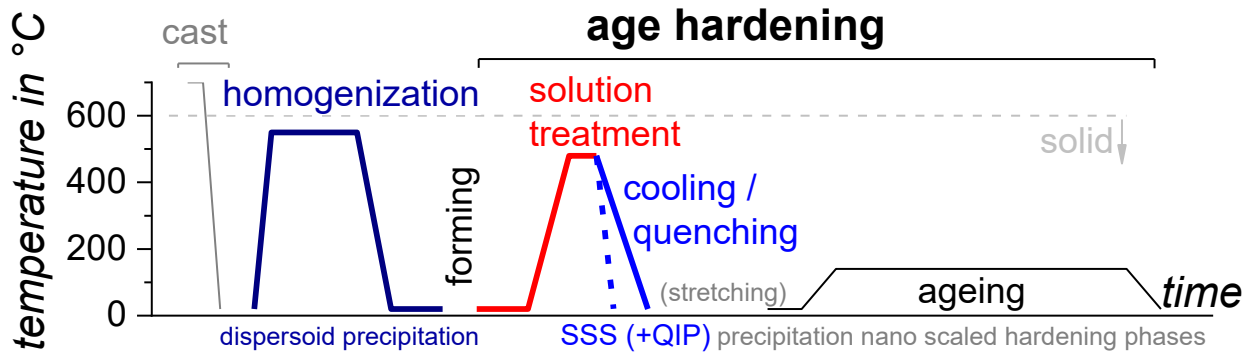


Figure 1: Simplified temperature-time profile of heat treatments within the production of structural Al products (SSS supersaturated solid solution, QIP quench-induced precipitates).

that are relevant to the production of Al alloys. In addition to heat treatments, the production may incorporate several forming operations such as rolling or extrusion (at ambient or elevated temperatures), which substantially influence the microstructure. In addition, rolled or extruded products with relatively simple cross sections may experience a stretching treatment subsequent to the quenching process within the age-hardening treatment (prior ageing). This stretching causes relief of residual stresses induced by quenching, straightens the products and increases the dislocation density and thereby the nucleation site density for nanoscale precipitation during the final ageing.

For Al alloys, the most relevant heat treatment that influences strength is age-hardening [5]. To allow age-hardening in the first instance, alloying element atoms need to be added to the Al base material. This is mostly done in the liquid phase during casting. Age-hardening makes use of the decreasing solubility of aluminium with respect to the major alloying elements (see Figure 2). The heat treatment process of age-hardening consists of three major steps: solution treatment, quenching and ageing. The solution treatment aims to achieve a solid solution. A certain duration of soaking at solution temperature is often used to finalise the dissolution processes and/or to obtain a homogeneous distribution of the dissolved alloying element atoms within the matrix. The amount of dissolved major alloying elements typically substantially exceeds the solubility at room temperature. However, during cooling or quenching, the alloying elements need to be kept in solid solution, resulting in supersaturation of the base material. This condition is far from the thermodynamic equilibrium and is thus unstable (this is often referred to as meta-stable since the stability is relative within the timescales considered). From this unstable supersaturated solid-solution during the final ageing treatment, a high particle number density of nano-scale precipitates grows, which hinder the dislocation movement and thereby increase the strength.

The cooling step (quenching) is the most critical step in the age-hardening heat treatment process with regard to technological applications. This is because some alloys require very fast cooling to achieve a completely supersaturated solid solution, and in several cases, it is hard to achieve these fast cooling rates in technological applications. Thicker products may also give variations in the material properties across the thickness, due to varying cooling rates. The tendency towards quench-induced precipitation and variation in properties across the thickness are often referred to as quench sensitivity. If cooling takes place at less than a certain critical cooling rate, detrimental quench-induced precipitates grow during cooling. These undesired precipitates are coarse compared to precipitates originating from ageing, and thus lower the amount of solutes available for ageing. Due to the combined effect of coarse quench-induced

precipitates and a lowered solute concentration, and thus a reduced fraction of the strength-increasing nano precipitates, several properties are affected and mostly degraded; for instance, the strength improvement, which is often important, is reduced. In many applications, other properties are even more important, such as toughness, fatigue resistance and stress corrosion cracking (SCC). Moreover, quench-induced precipitation also affects the presence and width of precipitation-free zones (after ageing) as well as the kinetics of natural and artificial ageing.

The quench sensitivity of Al alloys has been researched for about 70 years (e.g. [10–30]). Within the existing substantial body of work, the definitions of the term “quench sensitivity” differ, and this term generally refers to a reduction in the final properties (e.g. strength; ductility/toughness; corrosion-resistance) in the as-quenched state [21] or after ageing, generally as a result of reduced cooling rates [15, 19, 27]. The reason for this reduction, for instance in the hardness or yield strength, is the coarse precipitates which grow during cooling [25, 31, 32]. Although these coarse quench-induced precipitates have very little hardening effect in themselves [33], the atomic fraction of alloying elements that is bound in quench-induced precipitates reduces the amount of solutes available for the formation of strengthening precipitates during ageing. The degree of solute reduction obviously depends on the fraction of quench-induced precipitates that is formed. Another aspect relating to quench sensitivity is the loss of properties across the thickness of a thicker product, which is related to a reduced cooling rate in the core of the material [34, 35]. However, the definition of quench sensitivity is refined here, and the tendency of an age-hardening alloy to “lose” solute atoms to coarse (some 100 nm to μm sized), undesired quench-induced precipitates is called quench sensitivity. As will be demonstrated below, the quench sensitivity can be characterised by two major attributes: firstly by the minimum cooling rate, which is required to obtain a fully supersaturated solid solution (which after ageing can produce the highest strength), i.e. the so-called upper critical cooling rate (UCCR), and secondly by the slope of property loss as a function of the reducing cooling rate.

With respect to the technological applications, there is another important aspect related to quenching. Rapid quenching can cause severe thermal stresses which may lead to severe distortion [36–43]. This can create important additional costs due to the extra work required for stress-relief or straightening operations. In several cases, the quenching process is therefore confronted with two opposite requirements: cooling as rapidly as needed (to achieve maximum strength), and cooling as slowly as possible (to avoid residual stresses and distortion). Faster quenching may not be detrimental in all cases, since for example some

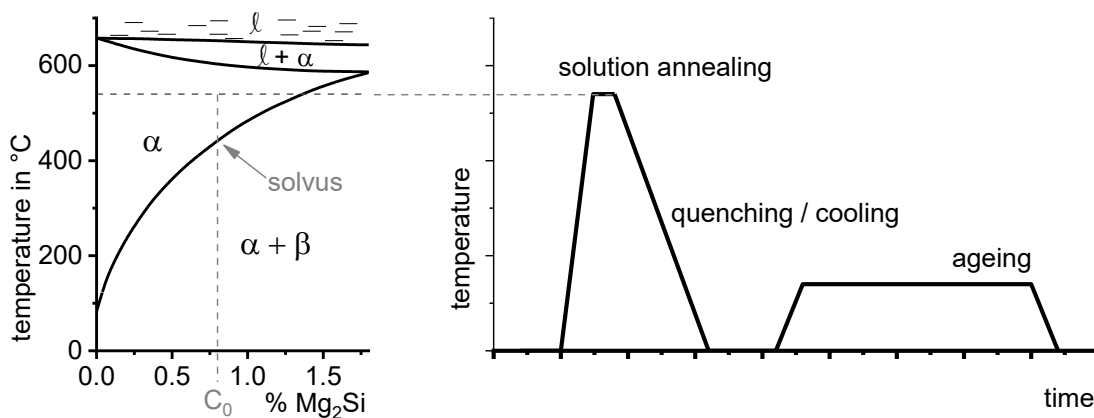


Figure 2: Pseudo-binary phase diagram for Al-Mg₂Si (adapted from [5]) and schematic temperature-time profile of an age-hardening procedure.

extruded and rolled products are subsequently stretched anyway. Thus, in terms of detrimentally fast quenching, there is a difference between wrought products with simple shapes and cast and other net-shaped products. The alignment of these opposing demands on quenching is therefore a more important issue in the latter type. However, the alloy-specific UCCR typically represents the optimum cooling rate. The maximum achievable quench rates in the heat treatment shop for different types of products (e.g. thick vs. thin gauge) may therefore determine the alloy of choice and thus the strength level achievable.

In order to obtain a comprehensive understanding of the quench sensitivity of age-hardening alloys, the kinetics and nature of quench-induced precipitation must be analysed. Since there were limited options for in situ analysis prior to the major work reviewed here, most of the earlier experimental work was based on ex situ experiments. In 2010 Shuey and Tiryakioglu published a reviewing chapter on “quenching of aluminium alloys” including experimental results on a broad range of alloys as well as theoretical options for their evaluation [44]. Different quenching paths have therefore been frequently used for samples, for instance by using different quenching media [45–49] or by applying Jominy end-quench tests [50–53]. Subsequent post-quench analysis of certain properties has led to the assessment of the quench sensitivity. Besides continuous cooling, quenching to various isothermal soaking temperatures has also been frequently applied, again in combination with a subsequent property analysis, which allows isothermal time-temperature property diagrams to be derived, for instance [10, 18, 23, 54]. In order to allow evaluation of continuous cooling basing on isothermal experiments, the quench factor analysis method was developed [20] and refined [47, 48, 52, 55–58].

In contrast to the martensitic hardening of steels, the relevant quench-induced precipitation only amounts to a small percentage of the total atoms. However, this fraction is only transformed in equilibrium conditions. Under technologically relevant cooling conditions, quench-induced precipitation is already suppressed to a wide extent, and this is the reason why very small amounts of precipitation need to be detected under certain relevant conditions. This means that a very sensitive measurement setup is required for detection of this unwanted precipitation, which covers the entire relevant dynamic range. There are few physical effects that allow for the in situ detection of changes within the solid-solid phase transformation status. Solid-solid phase transformations can rarely be detected directly, although this might be possible to a certain extent using in situ TEM, requiring very high effort. Hence, the in-situ detection and analysis of quench-induced precipitation typically requires the in situ measurement of changes in certain material properties. For this purpose, properties that change with the phase transition of interest are suitable. This may be the electrical conductivity or resistivity [59–63], the associated changes in volume (measured by dilatometry) [64, 65], or the crystallographic features (for instance measured by in situ X-ray scattering experiments [66–71]). Since the relevant solid-solid phase transformations all show a heat effect (e.g. precipitation = exothermic; dissolution = endothermic), one valuable measurement technique for analysing a solid-solid phase transformation in situ is calorimetry, and particularly differential scanning calorimetry (DSC). The reason for the importance of DSC is that it allows us to measure the enthalpy changes associated with precipitation. Moreover, this precipitation enthalpy is often directly proportional to the atomic fraction of the precipitates formed. However, previous DSC analysis of in situ solid-solid phase transformations is mostly restricted to works that concern heating, and which often carry out only a qualitative evaluation. Additionally, these earlier works commonly lack a sufficient dynamic range, and primarily consider heating rates of about 0.1 to 1 K/s (five to a few tens of K/min) (e.g. [72–77]). Until the

early 2000s, no DSC analyses involving cooling experiments on quench-induced precipitation in Al alloys were reported; the first works on this topic were published by Kessler et al. [78–80] between 2002 and 2007, and Deschamps et al. [31] in 2009. However, due to the use of only a single DSC device in all cases, these works are still restricted to a relatively limited range of cooling rates. There are a few more recent works that have published cooling DSC curves for AlZnMgCu alloys, using only one cooling rate [34, 60].

All of the mentioned heat treatment steps make use of or are directly related to diffusion-controlled solid-solid phase transformations. In particular, in the heating and cooling steps of the heat treatment, solid-solid phase transformations take place under continuously changing temperatures. In practical applications, these dynamic changes in temperature generally depend on the quenching media used and the dimensions of the components and/or the batch (see for instance Fig. 3.64 in Ref. [81], page 613). Since diffusion is strongly dependent on temperature and time, a wide range of relevant heating and cooling rates needs to be assessed. This means that diffusion-controlled processes like precipitation in Al alloys need to be considered on logarithmic time scales. This can be derived from a theoretical description of diffusion, for instance, and is illustrated by an example in Figure 3. Diffusion-controlled precipitation reactions can be described by a Starink-model based on the extended volume α_{ext} concept [82]. Figure 3 for an isothermal precipitation plots the fraction transformed as a function of time, on a linear time scale (Figure 3 A) and on a logarithmic time scale (Figure 3 B). It can be seen from Figure 3 that only by using a logarithmic time scale can we analyse this diffusion process in its entirety. Thus, cooling DSC analysis on quench induced precipitation should also cover a cooling rate range spanning several orders of magnitude, and the results should be displayed on logarithmic time scales.

The major progress that has been made relates to an extension of the dynamic range that is accessible for quantitative DSC analysis of solid-solid phase transformations under non-isothermal conditions. That is, conventional in situ DSC on heating and cooling is now possible over a dynamic range of $\approx 3 \times 10^{-4}$ to 3 K/s. When complemented by indirect DSC and indirect DFSC, a total range of 10^{-5} to 10^5 K/s can be covered. The metrological methods required to achieve this dynamic range have been developed, and currently allow for quantitative evaluation covering the whole range of heating and cooling rates of technological and physical relevance. The consideration of this very broad dynamic width is associated with a large range of associated micro- and nano-structural features, i.e. the dimensions of quench-induced precipitates can range from several tens of μm to just a few nm. Several microstructure observation techniques including optical, scanning-electron- and transmission-electron-microscopy (as well as other techniques) therefore

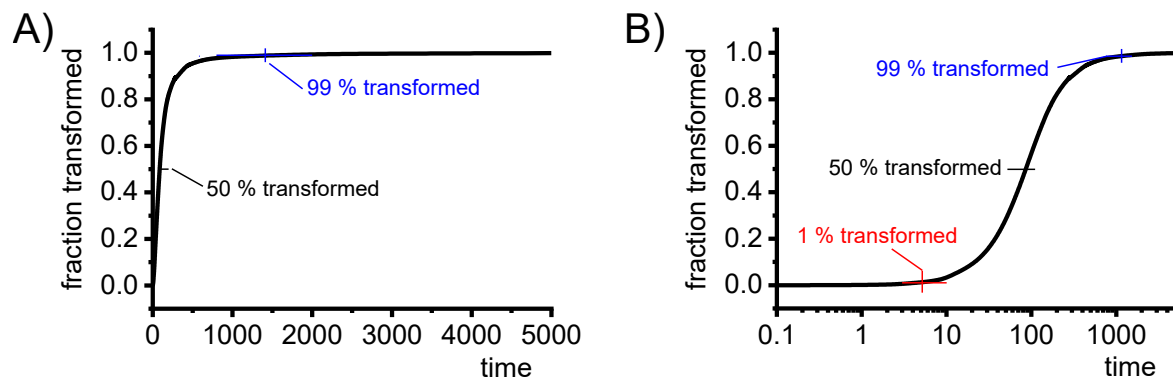


Figure 3: Example of a model for diffusion-controlled precipitation reactions [82]: (A) plotted on a linear time scale; (B) plotted on a logarithmic time scale.

Table 1 Primary scientific publications* with significant contributions from Dr.-Ing. Benjamin Milkereit as the basis of the cumulative habilitation thesis.

Reference and current 5-year journal impact factors**			Main content	Al-alloys
[BM1]	Thermochimica Acta 492 (2009) 73-87	2.41	Basic DSC cooling method	6005A
[BM2]	Materials Science and Engineering A 550 (2012) 87-69	4.01	DSC cooling, SEM & TEM, CCP diagrams	6005A, 6060, 6063, 6082
[BM3]	Journal of Alloys and Compounds (2014) 581-589	3.62	DSC cooling, SEM, CCP diagrams	7020, 7150
[BM4]	Thermochimica Acta 602 (2015) 63-73	2.41	Indirect DSC slow cooling rates, kinetic modelling	Al0.26Si, Al0.72Si
[BM5]	Materials 8 (2015) 2830-2848	3.53	Heating DSC, continuous heating dissolution diagrams	6005A, 6082, 6016, 6181
[BM6]	Materials and Design 75 (2015) 117-129	5.8	Modelling of quench-induced precipitation in AlMgSi alloys	6005A, 6063, 6082 _I , 6082 _V
[BM7]	Materials and Design 88 (2015) 958-971	5.8	Modelling of quench-induced precipitation in AlZnMg(Cu) alloys	7055, 7150, 7055, 7085, 7049A
[BM8]	Scientific Reports 6 (2016) art. No. 23109	4.53	HR-TEM Y-phase	7150
[BM9]	Materials Characterization 120 (2016) 30-37	3.46	Indirect DSC fast cooling rates	7150
[BM10]	Metals 8-265 (2018) 1-16	2.37	Effects of incomplete dissolution on quench sensitivity	6082 _{III}

*basing on data retrieval from the database Scopus on Sept. 19th, 2019, these 10 publications in total received 336 citations

** retrieval of the data from the journals web-pages on Sept. 12th, 2019

need to be applied to comprehensively analyse quench-induced precipitates. To complete the analysis, the obtained quantitative DSC enthalpy data are assessed using physically-based models. The models consider the alloy composition and formation of the phases that are most relevant for quench-induced precipitates, as revealed by experiment.

The scientific publications considered for this cumulative habilitation thesis is summarised in Table 1. The experimental methods derived here can generally be applied to nearly any metallic precipitation-hardening alloy system. Since most of the metrological aspects have been published in great detail in two book chapters [83, 84], the experimental aspects are condensed to their key features in this thesis. The materials science aspects are summarised in this work, involving a substantial number of alloys and thousands of individual experiments. The kinetics and nature of quench-induced precipitation are analysed for a total of

27 alloys, comprising 24 wrought alloys (two AlSi binary alloys, 10 AlMgSi alloys, 10 variants of AlZnMg(Cu) alloys and two AlCu(Mg) alloys) and three AlSiMg cast alloys. The enthalpy changes from quench-induced precipitation are quantified, and the drop in hardness is evaluated in terms quench-induced precipitation. Other properties are not focused on, because the small size of DSC samples does not permit materials tests that require large volumes. In some cases, larger samples with similar temperature/time paths as DSC samples are prepared and mechanically tested.

Based on this work, general conclusions on the nature and kinetics of quench-induced precipitation in Al alloys are drawn.

2 Measuring techniques and methods for the analysis of solid-solid phase transformations

2.1 Methods for in situ kinetic analysis of solid-solid phase transformations in metals

In metals which allow precipitation hardening, the relevant solid-solid phase transformations typically only amount to a small percentage of the total atomic fraction (excluding Ni-based super-alloys), and thus their detection requires very sensitive measurement setups. As mentioned in the introduction, the in-situ analysis of solid-solid phase transformations typically requires continuous analysis of the property of a particular material that changes with the phase transformation.

In view of this, suitable signals for in situ measurement include:

- changes in the electric conductivity or resistivity;
- changes in the volume;
- changes occurring in the crystal structure and related scattering effects; and
- changes in the enthalpy due to the endothermic nature of dissolution reactions or the exothermic nature of precipitation reactions.

One additional requirement that allows the analysis of quench-induced precipitation, of course, is the need for controlled cooling covering a wide range of cooling rates. This aspect of the metrological implementation might be difficult in several cases. All of the abovementioned methods also have certain advantages and some drawbacks, and these will be briefly reviewed with respect to their capabilities and limitations for the analysis of quench-induced precipitation.

Hong-Ying Li et al. demonstrated that continuous measurements of the electrical resistivity can be applied for the determination of continuous cooling transformation or precipitation diagrams [59, 60, 85–87]. However, it appears that the problem of control over the sample temperature has still not been fully solved, as this group applied several different approaches to achieve continuous cooling, including a self-made temperature control system [59]. They also later quenched samples in different media [60, 88], and thereby achieved a considerable range of cooling rates. To the best knowledge of the authors, no commercial device is currently available that allows for the continuous measurement of electrical properties over a wide

range of temperatures whilst achieving controlled cooling. In addition, the electrical conductivity is affected by several factors, making interpretations of precipitation difficult. For example, alloying elements in solution reduces the electrical conductivity [89], and precipitates may also have a negative influence on the conductivity [90]. The latter is generally lower compared to elements in solution, although the exact value depends on the size and strain field caused by the precipitates [90, 91]. Furthermore, the different alloying elements in solid solution impact the electrical properties by substantially different factors [89]. For these reasons, the measured changes in the electrical resistance or conductivity are not directly related to precipitation or the volume fraction of precipitates, and potential changes in the superimposed influencing factors cannot be directly assigned to precipitation.

Similar problems occur in the dilatometric measurement of quench-induced precipitation. Modern dilatometers have a very high resolution for length changes, which even allow the detection of early cluster formation in age-hardening Al alloys [64, 65, 92]. It has been shown that dilatometry is also able to detect quench-induced precipitation in Al alloys over a wide range of cooling rates [93, 94]. Nevertheless, the changes in the volume of a sample during cluster formation and precipitation are affected by the complex interplay between the volume changes in the matrix crystals and the volume changes due to the precipitated phase. That is, in some cases, precipitation can cause volumetric expansion of the sample, while precipitation of another phase can cause volumetric contraction [64, 84, 94]. The latter aspect complicates the evaluation of dilatometric measurements of quench-induced precipitation, as different phases that precipitate during cooling can cause opposite changes in length.

Positron lifetime spectroscopy [95, 96] can be utilised to investigate the precipitation processes in age-hardening Al alloys [96–101]. However, since the recording of single data points takes at least a few minutes (and up to some hours if the spectra are to be decomposed), this technique would be very slow for in situ cooling experiments [102]. This is probably one reason why no in situ cooling experiments have been published, to the knowledge of the authors.

Another option for the detection of quench-induced precipitates is through the scattering effects of X-rays, i.e. by applying small angle X-ray scattering (SAXS) measurements during cooling of relevant alloys [103–105]. In addition to X-ray scattering, small-angle neutron scattering (SANS) can also in principle be used for the detection of precipitation processes [70, 106], although the “neutron fluxes are lower and the interaction is also lower, therefore the counting times are usually higher (i.e. hours) in SANS which is a limitation for in situ measurements” [107]. The detection limit in terms of particle size depends on the small angle resolution, and is therefore dependent on the distance between the detector and the sample [107]. These small-angle scattering techniques are typically restricted to the detection of very small precipitates, with dimensions below about 100 nm [71, 106, 108]. This is a severe limitation for the detection of quench-induced precipitation, as several of the quench-induced particles are much larger. In addition, wide-angle X-ray scattering (WAXS) can be applied for the detection of precipitation processes [109, 110]. A specifically adapted Baehr 805 quenching dilatometer has been installed to allow in situ detection of WAXS and SAXS signals within the high-energy materials science beamline “P07” at PETRA III within the *Deutsches Elektronen Synchrotron* (DESY). This setup allows the in situ detection of phase formation during cooling of metallic alloys [111]. The applied high energy of this beamline results in a sufficient time resolution for in situ experiments, and the capability of this setup for in situ analysis of quench-induced precipitation in AlZnMgCu alloys has been demonstrated very recently [112]. Using the abovementioned scattering

techniques, information on the presence of certain crystal structures and therefore phases can be gained (WAXS), and conclusions on the particle size and volume fractions can be drawn (SAXS, SANS). For details on these techniques and their theory, the reader is referred e.g. to Ref. [113].

Since precipitation is an exothermic process, and dissolution an endothermic one, they can be detected by thermal analysis. Cavazos and Colas used direct thermal analysis of Jominy-like end-quench samples, i.e. they evaluated the changes in slope of the measured temperature development at different positions in the sample [25]. A more precise analysis of the thermal effects of solid-solid phase transformations is possible using calorimetry. DSC, in particular, allows for the detection of quench-induced precipitation in age-hardening metals [31, 78–80]. Amongst the potential methods for the in situ detection of quench-induced precipitation in aluminium alloys, DSC is the most effective approach, as it has significant advantages. These in brief are:

- DSC allows for controlled linear heating and cooling by providing the largest accessible dynamic scanning rate range, which now covers the whole cooling rate range of technological and physical relevance. By using a combination of different DSC devices, rates of about 10^{-5} to 10^5 K/s [83, 84] can be achieved.
- DSC samples are typically in the mm range, which in most cases allows further analysis after the DSC experiment, for instance for hardness testing or microstructural investigations [83, 84, 114].
- In addition to linear cooling, nonlinear Newtonian heating and cooling can also be investigated using DSC [115].
- With regard to the abovementioned detection limits, DSC offers the highest sensitivity of all techniques over the whole dynamic range. In particular, precipitation of any precipitate size and very small volume fractions of precipitation can be detected by DSC, and even cluster formation can be recorded [100, 116].
- If properly conducted, DSC allows for quantitative evaluation of the enthalpy changes related to precipitation. Since these enthalpy changes are directly proportional to the atomic fraction transformed, analysis of the volume fraction of precipitates is possible [117, BM4, BM6, BM7].

However, DSC also has certain disadvantages and limitations. In particular, DSC detects the heat effects of all occurring reactions in sum. Since different reactions occur simultaneously in several cases, it can be hard to distinguish the different parts of the signal that belong to specific reactions. This makes the interpretation of DSC heating experiments particularly complicated, as opposite heat effects from endothermic dissolution and exothermic precipitation can occur during heating [BM5]. Since only precipitation will take place during cooling, DSC still is the most promising method for comprehensive analysis of the kinetic behaviour of quench-induced precipitation.

2.2 Methodology and systematics of state-of-the-art kinetic DSC analysis

2.2.1 Basic concepts of DSC measurements

DSC allows us to measure heat release or consumption, or in other words the amounts of enthalpy that are exchanged by samples, for instance due to phase transitions. In order to enhance the sensitivity compared to a classical calorimeter and to allow non-isothermal operation in a differential calorimeter, the signals of two calorimetric sensors are compared [114]. Operation under non-isothermal conditions is possible, as both sensors are located symmetrically in surroundings at the same temperature (see the schematic example of power-compensated DSC sensors in Figure 4). A differential scanning calorimeter is generally operated in scanning mode rather than under isothermal conditions, i.e. the temperature typically changes at a constant heating or cooling rate. DSC uses two symmetric (ideally identical) sensors, one of which measures the sample to be investigated, while the other measures an inert reference sample. There are two different types of signals that can be measured: either the temperature difference between the two sensors, or the difference in heating power. In the first case, the device is called a heat flux differential scanning calorimeter, and both sensors are located in one furnace, which is used for the general temperature-time program providing the same surrounding temperature for both sensors. In the second case, both sensors are located separately, in surroundings of constant temperature (a cooled block), and both are equipped with a micro furnace that incorporates a temperature sensor, i.e. the sensor is both a furnace and a sensor at the same time. This version of DSC is called power-compensated DSC (see Figure 4). Nevertheless, both types of DSC devices can be used in a very similar way, and the setup of the experiments and the data evaluation are very alike, as in both cases the (electronic) signal is converted to the value of heat flow by calibration. For more details on specific setups and the peculiarities of the different types and operation modes of DSC devices, the reader is referred to Ref. [114].

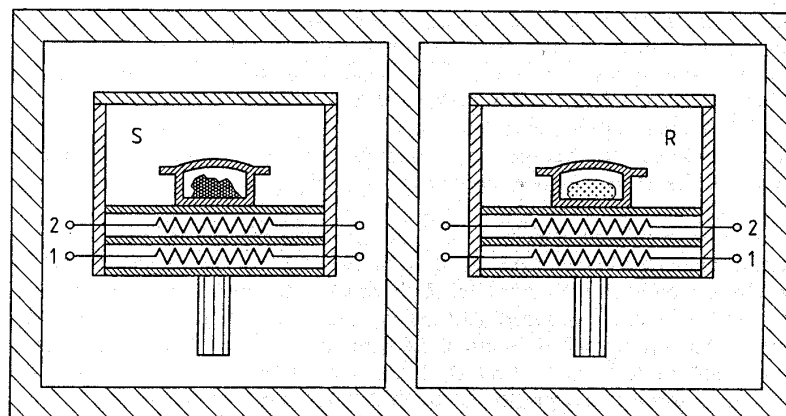


Figure 4: Construction scheme of a power-compensated scanning calorimeter (PerkinElmer Instruments). S: Sample furnace with sample in crucible; R: reference-furnace (analogous to sample-furnace); 1: heating wire; 2 resistance thermometer. Both sensors are separated from each other and located in surroundings at constant temperature (cold block) [114].

In this thesis, each temperature-time profile of a DSC measurement starts and ends with an isothermal section (see Figure 5). This is needed for heat capacity calculation employing two or three curve methods (for details see [112]).

In general, an accurate DSC analysis of the sample requires at least two measurements: a measurement of a sample versus a reference, and a baseline measurement (inert reference samples on both sensors). The heat flow signal of the baseline measurement is subtracted from the heat flow signal of the sample measurement, and the resulting heat flow signal is corrected for small device-specific asymmetries which, although minimised in the design, can still influence the accuracy when low-heat-flow, high-accuracy measurements are required. Examples of such small asymmetries include slight differences in sensor positions and differences in the sensors themselves.

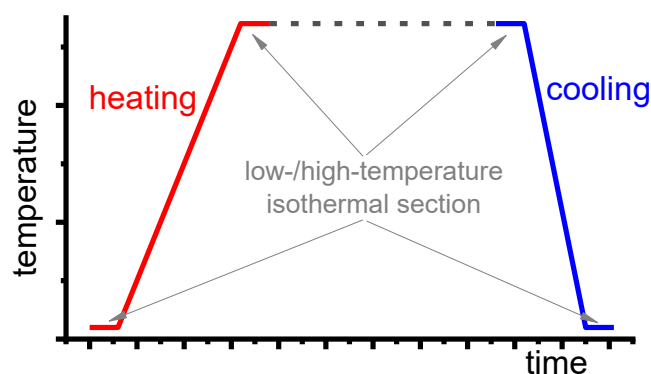


Figure 5: Basic time-temperature profile of DSC experiments.

2.2.2 Key features for in situ quantification of enthalpy changes of solid-solid phase transformation as a function of the scanning rate or time

Excess specific heat capacity

To allow for quantitative analysis of solid-solid phase transitions, very sensitive measurement setups are required. To obtain the best possible DSC sensitivity for this particular purpose, and to allow a purposeful comparison of different heating rates and sample masses, the experimental setup needs to allow for conversion of the measured signals to the specific excess heat capacity of the sample. When studying precipitation reactions, the contribution of the heat capacity can be subtracted during the measurement by using inert reference samples [BM1]. In the following, the apparent heat capacity due to precipitation (latent heat) in addition to the heat capacity of the matrix is called excess heat capacity. Figure 6 clarifies the difference between a conventional measurement of sample heat capacity (Figure 6A) and a measurement of the specific excess heat capacity (Figure 6B). The heat capacity (measurement setup sample versus an empty reference sensor) can be considered as the sum of the heat capacity that increases with temperature

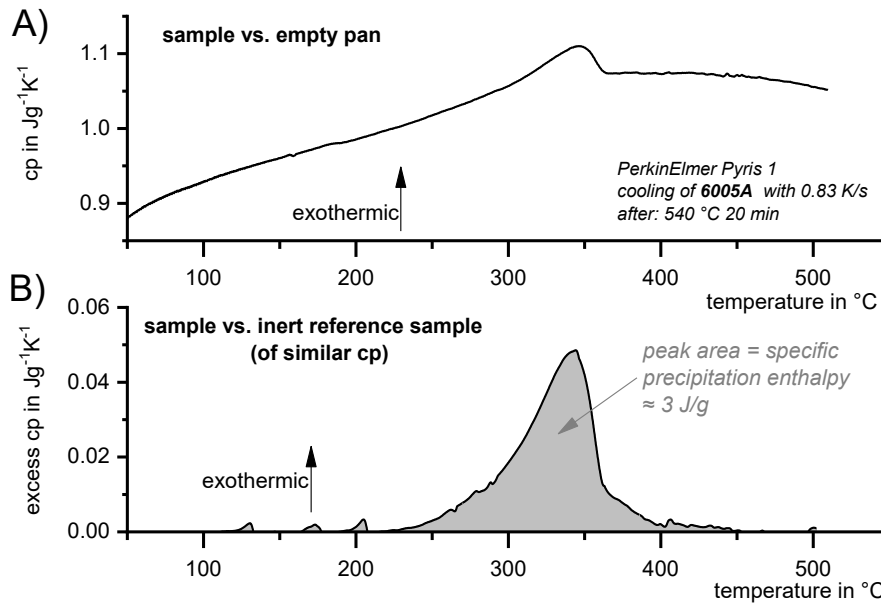


Figure 6: Comparison of two basic measurement set-ups: (A) a sample versus an empty reference sensor, acquiring the specific heat capacity of the sample; (B) a sample versus an inert reference sample of similar heat capacity, acquiring the specific excess heat capacity of the sample compared to the reference.

and the apparent heat capacity caused by the latent heat effects due to precipitation¹. The latter, of course, has a dependence on temperature and time.

The specific excess heat capacity is obtained here by measuring an alloyed sample versus a reference sample with similar heat capacity. The specific excess heat capacity is then defined to be the difference between the specific heat capacity of the alloyed sample and that of an inert reference sample. In an ideal situation, the reference and the alloy sample have highly similar absolute heat capacities over the entire temperature range of interest. Another requirement for the reference sample is that it must be inert with respect to thermal reactions within the temperature range of interest. It may be difficult to find appropriate reference material, but in the case of Al alloys, pure Al has proven to be very well suited [BM1, BM5]. Pure Al reference samples are preferably used in a pre-oxidised condition, i.e. heated once before the actual measurement; however, there are various strategies for obtaining a suitable reference sample [118], and changes in the sample mass to adjust the total heat capacities of the sample and reference sample may further improve the signal quality [118, 119].

To acquire the excess specific heat capacity (excess c_p), the alloyed sample is placed in the sample sensor, while the reference sample is placed in the reference sensor. Since both sample and reference have very similar absolute heat capacities, this setup retains the symmetry within the differential scanning calorimeter and its entire measurement setup. This supports the basic idea of DSC, which is a steady comparison of two equal measuring systems. In an ideal system, the only remaining differences—and therefore the only remaining thermal asymmetries—are thermal effects related to reactions within the sample. The resulting signal can therefore be directly and solely related to the phase transformation of interest.

As described above, in the first instance the measured signal is a heat flow signal. The DSC heat flow signal depends on the amount of sample used (expressed as a mass or in moles) and the scanning rate

¹ In the case of an alloy that shows any kind of phase transformation, the measured apparent heat capacity is a sum of the heat capacity and the effects due to heat or enthalpy release/consumption by the occurring phase transition.

applied. To allow for a quantitative comparison of measurements with different scanning rates and sample masses, the heat flow signal \dot{Q} must be normalised by the sample mass (or the number of atoms) and the scanning rate β , resulting in the unit of specific heat capacity (per g or per mole):

$$\text{excess } c_p = \frac{\dot{Q}_{\text{sample}} - \dot{Q}_{\text{baseline}}}{\text{sample mass} \times \text{scanning rate}}$$

$$[\text{excess } c_p] = 1 \frac{mW - mW}{mg \times \frac{K}{s}} = 1 \frac{Ws}{g \times K} = 1 \frac{J}{gK} \quad (1)$$

The excess c_p thus represents only the changes in specific heat capacity that are caused by a reaction inside the sample. Integration of the excess c_p peak versus temperature (bounded by the zero level) determines the specific precipitation heat, or more generally, the enthalpy changes caused by the occurring phase transformation.

Zero-level accuracy

In terms of the intended evaluation of solid-solid phase transitions, the zero level of the considered DSC measurement is of outstanding importance, particularly when the enthalpy changes are to be determined quantitatively. The measured signal of excess c_p can still be curved, and may particularly deviate from zero in temperature regions in which no reactions are occurring (the excess c_p should be zero here). This zero-level curvature can have multiple reasons. To ensure a reliable and straight signal close to zero level, only adequately calibrated calorimeters should be used (for calibration details, see [114, 120]). It is also reasonable to check each DSC run and its corresponding baseline measurement using the following quality attributes: (i) the heat flow difference between the high- and low-temperature isothermal section (Figure 7A); and (ii) the heat flow difference between the heat flow values of the sample and baseline measurements of the high-temperature isothermal section (Figure 7B). The acceptable values of the heat flow difference depend on both the specific device and their continuity with time; for instance, the heat flow difference between the isothermal sections at high and low temperatures depends mostly on the symmetry and adjustment of the device. More important than the absolute values of these differences is the

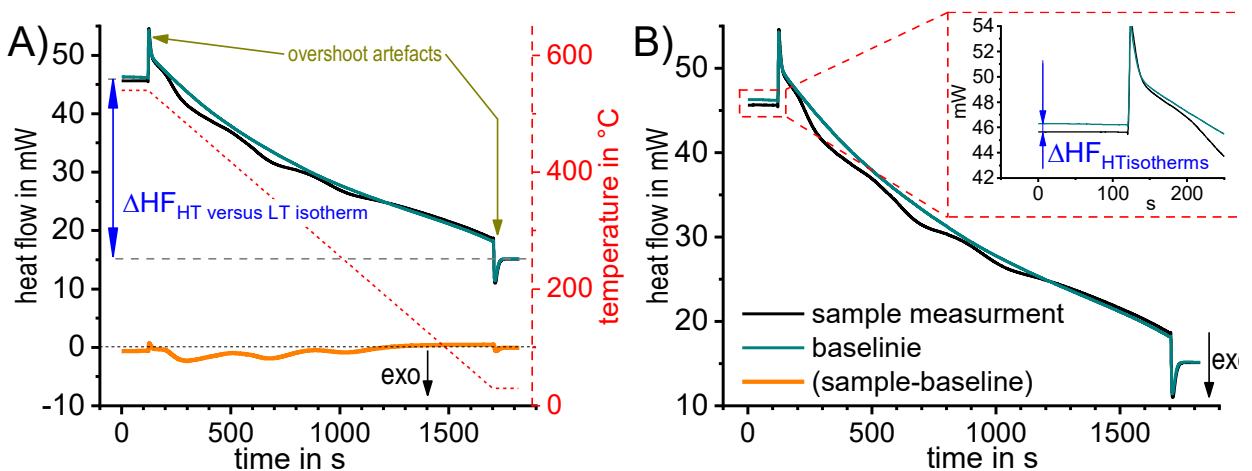


Figure 7: Quality attributes of DSC raw data. A & B show the same raw data, measured by cooling an AlCuMg alloy with 0.3 K/s in a PerkinElmer Pyris 1 DSC. (A) Overshoot artefacts and the quality attribute of the heat flow difference between the high- and low-temperature isotherm, are highlighted; (B) the quality attribute of heat flow difference between sample and baseline measurements in the isothermal section at high-temperatures is highlighted.

reproducibility. An unfavourable value may be acceptable as long as it is constant with time [83], but for highest accuracy, the values of heat flow differences should be small, i.e. in case (i) within the range of few tenths of mW, and in case (ii) within the range of a few mW for the PerkinElmer power-compensated differential scanning calorimeter.

To obtain good zero-level accuracy, it is important to ensure that symmetry is maintained within the experimental setup. This includes sample and reference heat capacities [118, 119], crucible or pan masses/heat capacities, and of course sample positioning and potentially sensor cover placement [121].

In any case, the sample must be packed properly, for instance using high-purity aluminium pans. If this aspect is disregarded, an incorrect measurement might result (see Figure 8). The reason for this is that the colour of the sample surface, which influences the heat exchange by radiation between sample and furnace, needs to be kept constant [BM1]. A purge with inert gas is also required to prevent oxidation and keep heat transfer conditions constant. Nitrogen gas is therefore preferable to helium, as nitrogen purging results in the best baseline stability of the DSC instrument. Helium may be suitable for increasing the achievable cooling rates [78].

For each individual sample measurement, a corresponding baseline measurement needs to be performed [BM1, 75, 114], and this measurement should be made promptly. This is particularly true for power-compensated devices, as their baseline behaviour drifts more strongly with time [122] than that of heat flow calorimeters.

In terms of statistical validation, a sufficient number of experiments is required, and the exact number depends on the sample and the considered effect. Of course, the number of experiments is always a compromise between statistical validation and time effort, and this especially holds for slow, long-lasting measurements. For these, two to four experiments and one or two baseline runs are typically done, while for the faster experiments at least six samples and three baselines are generally measured.

Even if all of the abovementioned aspects are ensured, the zero level of the resulting specific excess heat capacity may still show a slight curvature, and this is slightly different for each experiment [75]. This may be caused by slight differences in the sample position for each individual measurement, for instance [121].

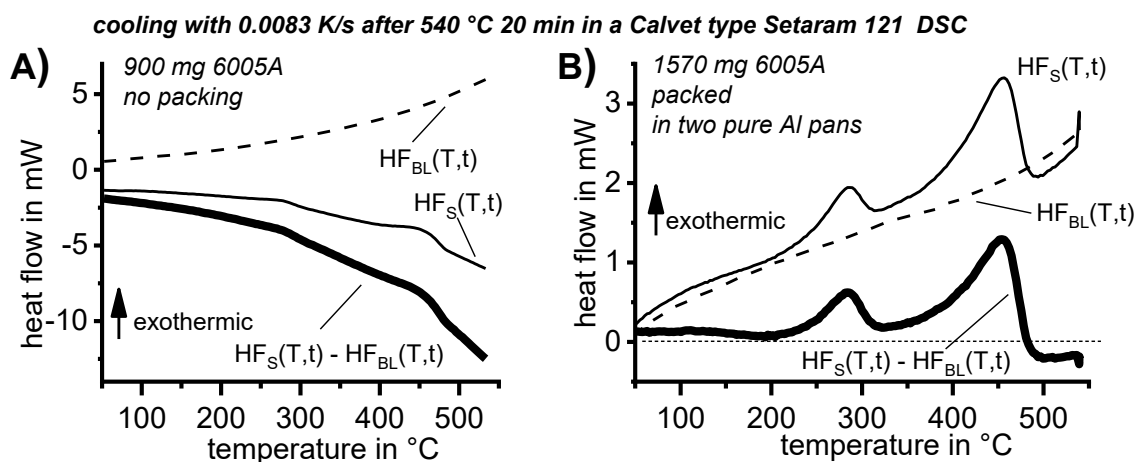


Figure 8: Effects of inadequate or adequate sample packing in a CALVET-type heat flux differential scanning calorimeter under otherwise very similar experimental conditions: (A) heat flow of sample (HF_S) and baseline (HF_{BL}) measurements without sample packing showing substantially different heat flow in regions without phase transformations; (B) if the samples are packed properly HF_S and HF_{BL} are very similar in reaction-free temperature regions, i.e. subtracting HF_{BL} from HF_S results in a nearly straight zero-level.

Thus, the raw DSC data must undergo a sophisticated data treatment prior to evaluation, including baseline subtraction in each case, and possibly also the elimination of the remaining zero-level curvature [BM5] or a mean value curve calculation [118, 119, 123]. If efforts are made to ensure the best zero level quality, a result that is straight and close to zero can be achieved. In heating experiments, this allows us to judge whether exo- or endothermic reactions predominate at a certain temperature or time [75, BM5]. In addition, the zero level can act as an integration reference for enthalpy calculations [75, BM1, BM5].

Large dynamic range

A large dynamic range (of time or heating/cooling rates) allows us to comprehensively analyse the kinetic development of single reactions. Any relevant solid-solid phase transition is related to diffusion, and as described above, diffusion is dependent on logarithmic time scales, implying the need for a large dynamic range. However, this need for a large dynamic range can be considered from two perspectives: (i) the specific physical and alloy requirements and (ii) metrological aspects.

Specific physical requirements for the alloy over the considered dynamic range

To enable a full physical understanding of solid-solid phase transformations, the required high dynamic range is bounded on the one hand by very slow transformations close to equilibrium conditions, and on the other hand by relatively fast cooling beyond the critical cooling rates of the relevant transitions. For instance, for aluminium alloys, the adjustment of maximum strength values requires the complete suppression of any precipitation reaction upon cooling from solution annealing. The slowest cooling rate that just retains all alloying elements in solid solution is the UCCR [BM2]. For highly alloyed Al-Zn-Mg-Cu wrought alloys or Al-Si-Mg cast alloys, the UCCR can easily reach several hundreds of K/s [BM9, 124, 125]. The lower critical cooling rate defines the fastest cooling rate at which all the alloying elements (compared to the equilibrium solubility) precipitate during cooling from solution annealing, yielding enthalpy changes on a saturation level. For an Al-0.72Si alloy, this lower critical cooling rate is about 3×10^{-5} K/s [BM4, 126]. To identify both critical cooling rates, they must be experimentally exceeded by at least one order of magnitude in terms of both slower and faster cooling, which requires a dynamic range of about 10^{-5} K/s to 10^3 K/s. This wide dynamic range is now available, even for cooling, in scanning calorimetry using multiple devices.

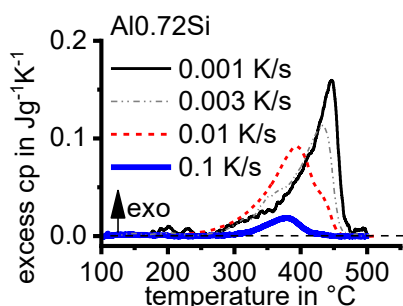


Figure 9: DSC cooling curves of a pure binary Al-Si alloy covering a wide range of cooling rates. It can be seen that exothermic precipitation reactions at higher temperatures are only detected at slower cooling rates. Original data from [BM4].

Aside from the determination of the critical cooling rates, a further aspect can only be understood if almost the full range of cooling rates is considered. As discussed later, it has been shown that for any age-hardening alloy, quench-induced precipitation during slow cooling predominantly occurs at alloy-specific high temperatures (compare e.g. [BM1, BM4, BM3]). At faster rates, the high-temperature reactions will be suppressed to a certain extent, and maybe even suppressed completely, and quench-induced precipitation will then probably take place via a medium- or low-temperature reaction [BM3, BM7]. An example is shown in Figure 9 for the pure binary alloy Al_{0.72}Si. At a “high” cooling rate of 0.1 K/s (which may be a relatively slow cooling rate for higher

concentrated alloys), quench-induced precipitation only occurs in a “low-temperature reaction” ($\approx 400\text{--}300^\circ\text{C}$). In contrast, during slow cooling at 0.001 K/s , the vast majority of quench-induced precipitation occurs at high temperatures ($\approx 470\text{--}350^\circ\text{C}$). At medium rates, both types of reactions overlap.

Thus, if only the faster rates are considered in the analysis of quench-induced precipitation, the high-temperature reactions may be disregarded [BM1]. By inversion of the above argument, it can be seen that all relevant precipitation reactions can be detected only if the full range of physically relevant cooling rates is analysed.

Metrological aspects of a large dynamic range

Obtaining a large dynamic range is a much bigger challenge in cooling experiments than in heating experiments. Each DSC device has its own spectrum of heating/cooling rates, which also depends on the particular setup of the device (see Ref. [83] for more details). The scanning rate spectrum is typically analysed by measuring a performance diagram (see the example in Figure 10). It can be seen that during heating, a scanning rate of 5 K/s is reached after a short period, and can be controlled over nearly the entire temperature range, which was 0 to 600°C in this case. However, during cooling, control over the scanning rate is lost at a certain temperature, and this takes place earlier at increasing cooling rates. The loss of cooling control is accompanied by the loss of an evaluable DSC signal, which is typically more severe for power-compensated calorimeters. In the example given in Figure 10, the critical temperature during cooling at 5 K/s is about 350°C . This is clearly a limiting factor, since relevant reactions might occur at lower temperatures, and these cannot be therefore analysed with this particular DSC device at this cooling rate.

To obtain a dynamic range that covers cooling rates of several orders of magnitude and also allows us to analyse the full temperature range, it is essential to combine several types of DSC device [83]. In this work, a total of five different DSC devices were used: two relatively slow CALVET-type heat-flux differential scanning calorimeters, a disc-sensor type heat-flux differential scanning calorimeter, a power-compensated differential scanning calorimeter and a chip-sensor-based differential fast scanning calorimeter (DFSC, [127]). These devices and their ranges of scanning rates can be seen in Figure 11A. As is obvious from

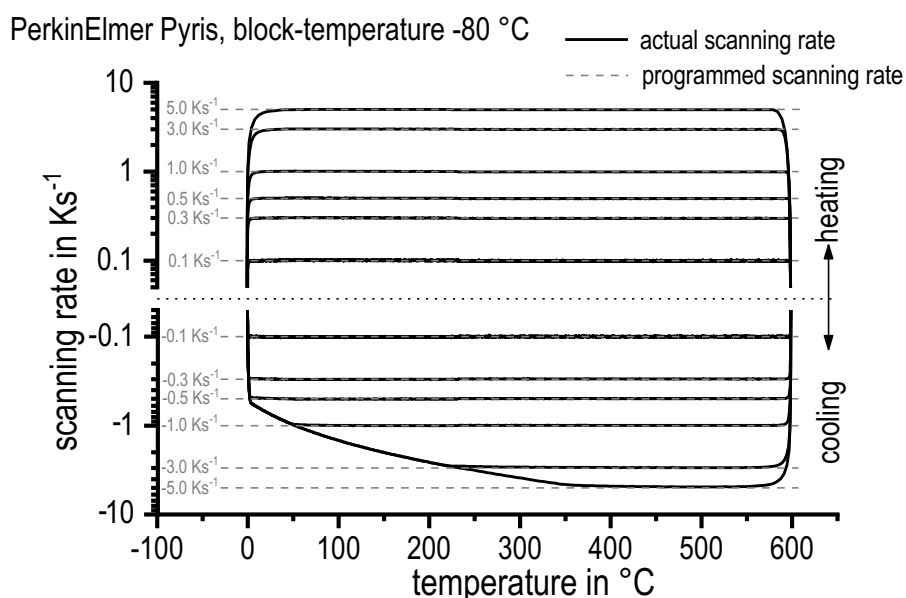


Figure 10: Typical performance diagram of a PerkinElmer Pyris diamond DSC.

Figure 11B, the large variation in cooling rates also causes a strong variation in the sample mass. Large sample masses are crucial for slow scans, since the heat flow signal is proportional to the scanning rate and sample mass. This means that if the scanning rate is very small, the signal can only become strong enough for detection if the sample mass is large. On the other side of the spectrum, small sample masses are essential to allow for fast cooling [127]. The cooling rate range can be extended in either direction (slower and faster cooling) by indirect measurements [BM4, BM9]. The basic concept of these extending experiments is the same in either direction, and will be explained in Section 3.1.1.

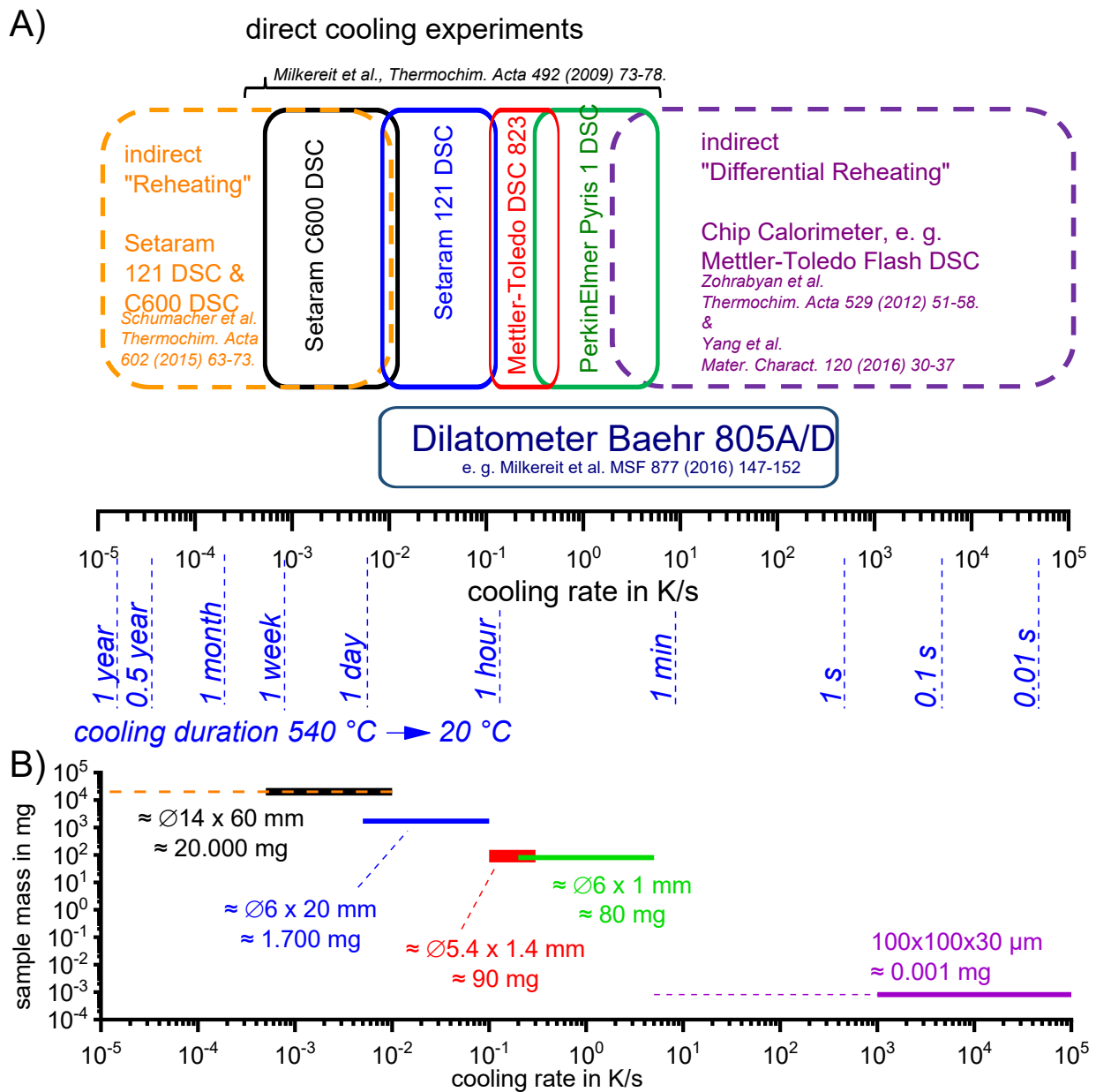


Figure 11: (A) Scanning rate ranges of different DSC devices and the quenching dilatometer; (B) related sample dimensions and masses (in the case of Al samples). In order to make the broad dynamic range easier knowable the cooling rate axis is complemented by the durations of cooling, which are needed to cover the temperature range of 540 to 20°C (typical for the age-hardening of Al alloys).

Another aspect is that in general, if cooling becomes faster, precipitation is increasingly suppressed, and the amount of heat released decreases with increasing cooling rate when approaching the UCCR. This is because precipitation reactions are diffusion-controlled, and diffusion is increasingly suppressed if the time available shortens. One very important aim of these studies from a technological point of view is the detection of the UCCR at which precipitation during cooling is completely suppressed, i.e. at which all alloying elements dissolved during solution annealing remain in a supersaturated solid solution. The UCCR is very relevant in technological applications, and it is shown below that the maximum age-hardening potential can be exploited only if the alloy is cooled at the UCCR or faster. However, faster cooling may result in undesired residual stresses and distortion of age-hardened aluminium components [38, 41–43, 105, 128–130]. Although this is of lower importance for extrusions or rolled products, which are stretched after quenching, residual stresses and distortion are very important for complex cross-section extrusions and net-shaped cast and forged products.

In the DSC analysis, the measure of the fraction of precipitates is the specific precipitation heat (or enthalpy) released by the precipitation. On reaching the UCCR, the enthalpy change by precipitation is obviously zero. This leads to a metrological problem: in a range of cooling rates close to the UCCR, we need to determine whether no precipitation heat is detectable in the measured curves. Thus, the challenge is to decide when a precipitation signal is above the device-specific noise level.

An objective criterion is therefore needed. The detection limit was defined in Ref. [BM1] in the following way:

- The reaction is detectable in at least three repeated experiments;
- The reaction is also detectable at the next slower cooling rate;
- The specific precipitation heat is at least 0.1 J/g; and
- Peak temperatures are in the same region as for the next slower rate.

The detection limit of 0.1 J/g for instance in the Al-Mg-Si system corresponds to a Mg_2Si precipitation volume fraction of about 0.01 % [117]. For comparison, the maximum precipitation heat measured by DSC of 6005A alloys amounts to 12 J/g, and the related $\beta\text{-Mg}_2\text{Si}$ precipitate volume fraction amounts to 1.15 %.

For correct curve interpretation, evaluation must be done from the slowest to faster cooling. Other features of DSC cooling experiments can be found in Refs. [83, 84].

The required wide range of cooling rates is accompanied by another metrological challenge, in that the dimensions of the quench-induced precipitates vary substantially within the cooling rate range. This aspect is illustrated in Figure 12. It can be seen that the dimensions of quench-induced precipitates vary between several tens of μm down to thicknesses of a few atomic layers ($\approx \text{nm}$), i.e. the dimensions vary by a factor of $>10,000$. Comprehensive imaging of quench-induced precipitates over the entire relevant dynamic range (of cooling rates and duration) requires the application of three different types of microscopy: optical microscopy (OM), scanning electron microscopy (SEM) and transmission electron microscopy (TEM). Of course, the application of additional analytical methods can provide further detailed information on quench-induced precipitation, and these will be briefly introduced in Section 2.4

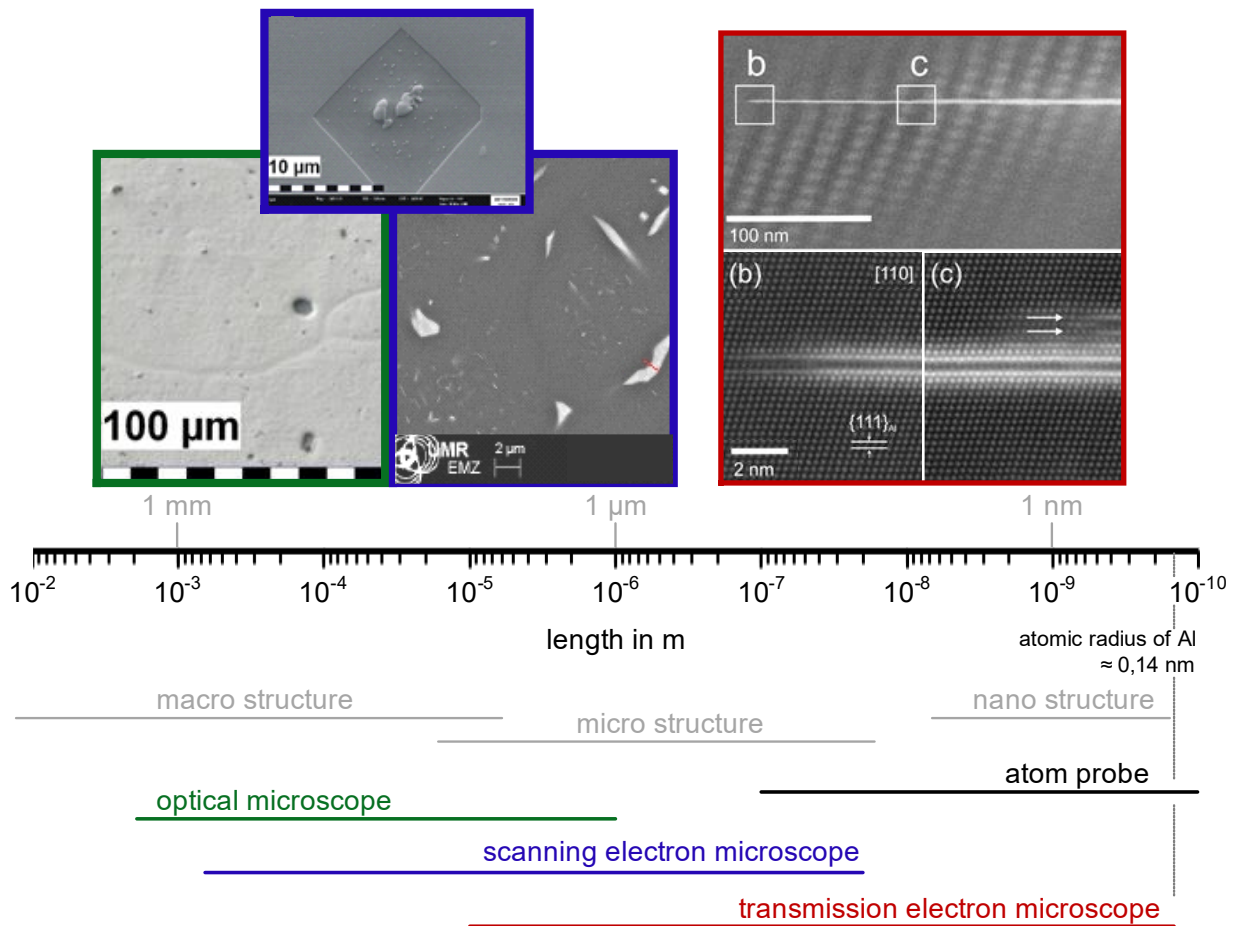


Figure 12: Dimensions of quench-induced precipitation illustrated by micrographs from optical, scanning electron and transmission electron microscopy from an AlMgSi and an AlZnMgCu alloy.

2.3 Construction scheme for continuous cooling precipitation diagrams

A substantial compression of the information generated for quench-induced precipitation is plotted in continuous cooling precipitation (CCP) diagrams, which correspond to the well-established continuous cooling transformation (CCT) diagrams for steels. CCP diagrams allow us to choose suitable heat treatment parameters for a certain alloy in the heat treatment shop, and thus allow for the practical application of the findings on the quench sensitivity of Al alloys. Furthermore, they are important input data for heat treatment simulations.

Since a CCP diagram involves the kinetic behaviour of precipitation during cooling from solution treatment, the time-temperature profiles of the varied linear (i.e. constant) cooling rates form the basis of the diagram. These are plotted on a temperature-time diagram with logarithmic scaling of the time axis. To allow construction of a CCP diagram for a specific alloy, three distinct aspects of quench-induced precipitation need to be analysed for each specific alloy using different experimental methods, as schematically illustrated in Figure 13.

In the first step, the temperature and times at which a distinct precipitation reaction starts and finishes need to be determined. This can be measured by DSC: the onset or end temperature of the reaction can be read directly from the DSC curves, and the associated time values are derived from the cooling rates applied.

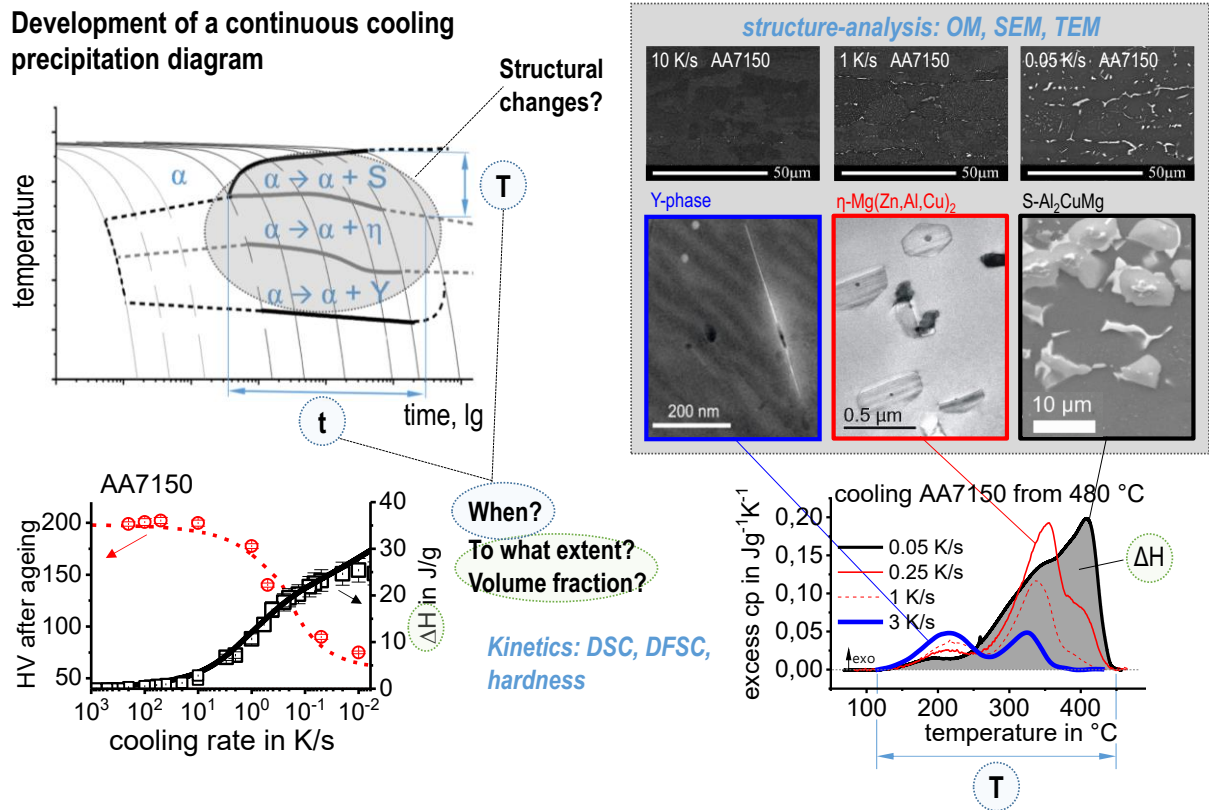


Figure 13: Scheme of the different analyses required for construction of a complete continuous cooling precipitation diagram, illustrated here for alloy 7150.

The obtained values for the onset or end temperatures and times of the reaction are inserted into the related cooling rates. In this way, the single values for any relevant cooling rate can be graphically connected by splines, to illustrate the regions of the specific precipitation reactions. In the second step, the intensity of the distinct precipitation reactions (or at least the total overall precipitation) at this cooling rate needs to be determined. This relates to the amount of the fraction transformed, i.e. the atomic or volume fraction of precipitation. Although this question might be hard to answer in detail, the specific precipitation enthalpy measured by DSC at least gives a value that is directly proportional to the fractions transformed. In the third and final step, the nature of the micro- and nano-structural changes related to the different DSC peaks needs to be determined, i.e. we need to determine which phases are precipitating. This involves several additional scientific aspects, for instance the chemical composition, crystal structure, particle morphology, active nucleation mechanism, particle size distributions and particle densities depending on the cooling rate. In some cases, several of these aspects cannot be revealed with high accuracy; however, any information generated in this respect helps to complete the CCP diagrams.

2.4 Methods and systematics for complementary micro- and nano-structure analysis

As described above, a comprehensive understanding of the microstructural changes in the alloys caused by cooling is crucial. As shown in Figure 12, the dimensions of quench-induced precipitates vary substantially and cover about five orders of magnitude. Thus, the use of a range of microscopes is required for imaging of the relevant precipitates. Coarse quench-induced precipitates originating from high temperatures and slow cooling rates can be imaged by OM [113, 117, 131]. OM images also allow us to evaluate the volume fractions of coarse quench-induced precipitation [117, 131, 132, BM6, BM7]. SEM (e.g. [133]) allows imaging of coarser quench-induced precipitates. Imaging is typically done with either secondary electrons (SEs) or backscattered electrons (BSEs), the latter of which give better contrast for different atom masses. Analytical techniques integrated into SEM allow further valuable information to be acquired; for example, energy-dispersive X-ray spectroscopy (EDS) enables the determination of the chemical composition of precipitates [113, 131], while electron backscatter diffraction (EBSD) can reveal the crystal structure of coarse precipitates [131]. EDS always involves a compromise between spatial resolution and element-specific stimulation. A sufficient acceleration voltage is required for the EDS detection of alloying elements with heavier atomic masses; for example, the EDS detection of Zn typically requires an acceleration voltage of 25 kV [113]. However, this enlarges the interaction volume, and may make it larger than the particle of interest. Thus, in most cases, it is rarely possible to obtain EDS signals solely from the precipitate, and part of the stimulated and measured X-rays generally originates from the matrix [131].

The presence of crystal structures with volume fractions of above $\approx 1\%$ and large precipitates can be detected by common X-ray diffraction (XRD) [113, 131]. Hence, this technique is again limited to relatively slow cooling rates, which produce corresponding volume fractions and particle dimensions of the phase of interest. In addition, the wide and small-angle X-ray scattering techniques briefly discussed above can generate information on quench-induced precipitation [103–105, 112].

Imaging of precipitates of dimensions below about $1\ \mu\text{m}$ is commonly done by TEM (e.g. [134]) [113, 135, BM2, BM6–BM8]. In this work, bright-field TEM images and high angle annular dark field (HAADF) images from (scanning) TEM are used. In TEM, additional analysis with EDS allows conclusions to be drawn on the elemental composition of certain relevant particles, down to precipitate structures composed of just a few layers of atoms [BM8]. The chemical analysis of the latter can potentially be supplemented or even improved by the application of electron energy loss spectroscopy (EELS) [BM8]. When using TEM, information on local crystal structures can be generated by selected area electron diffraction (SAED) or nanobeam diffraction (NBD).

To improve the meaningfulness of the structure analysis, it is helpful to investigate samples using systematically varied heat treatments. Two major heat treatment routes were therefore examined (see Figure 14). Firstly, the development of quench-induced precipitation during linear cooling with varying rates down to room temperature is analysed. The formation of quench-induced precipitates at a certain cooling rate is also analysed via cooling to a specific temperature followed by rapid overcritical quenching, which allows us to match certain quench-induced phases to specific peaks found in the DSC curves.

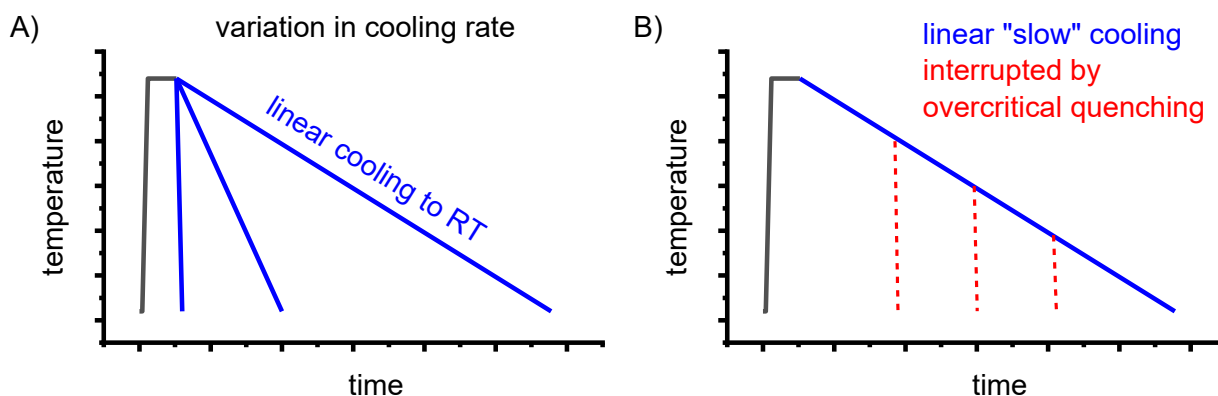


Figure 14: Schematic presentation of heat treatments applied to alloys in this work (introduced in [BM2]): (A) variation in cooling rate; (B) interrupted cooling.

2.5 Analysis of resulting mechanical properties

The small dimensions of the DSC samples only allow hardness testing to be done directly on the DSC sample. Hardness testing (commonly Vickers hardness HV1 or HV5) was done regularly after cooling at various rates and subsequent (mostly artificial) ageing.

However, hardness is only loosely related to strength. Thus, in some cases, additional compression or tensile tests were performed on samples cooled at controlled rates to certain temperatures. Details of these tests can be found in Refs. [37, 126, BM4]. In general, thermo-mechanical-analysis (TMA) is performed with a quenching and deformation dilatometer to obtain mechanical properties from tensile [136] and compression tests [36, 37, 126, 137].

2.6 General illustration of results and reading guidelines for CCP diagrams

In the following sections, a large number of similar plots are presented. In particular, three types of plots occur several times. To ensure a full understanding, their general layout is explained here.

DSC curves are generally presented in terms of the specific excess heat capacity as a function of temperature. The associated zero level of the DSC curve is plotted as a dashed straight line. In the case of DSC heating experiments, the zero level allows us to assess whether exo- or endothermic reactions predominate, while endothermic reactions are plotted in the upward direction. For cooling DSC curves, only precipitation reactions can occur. For cooling experiments, by definition, exothermic precipitation reactions are plotted in the upward direction. In plots with multiple cooling DSC curves at various scanning rates, the zero levels are in most cases shifted by a fixed offset, with the DSC curve with the slowest scanning rate on top. The specific solution treatment applied prior to the DSC cooling experiments is stated in plots of this type.

In another frequently used plot, the specific precipitation enthalpy is plotted as a function of the cooling rate. A third type plots the hardness after cooling at various rates and subsequent (mostly artificial) ageing. In

several cases, the latter two diagrams are combined into one plot with two ordinate axes. To allow interpretation and comparison with the timescale of CCP diagrams, the cooling rate axis is scaled in descending logarithmic order, i.e. proportional to the duration of cooling.

As the most compressed illustration of information on quench-induced precipitation in Al alloys, CCP diagrams describe the precipitation behaviour of aluminium alloys during continuous cooling from solution annealing, as a function of temperature and time. Since a very broad time (cooling rate) range is physically and technologically relevant, the time axis is scaled logarithmically. We define the time axis as ranging from 0.1 s to 1,000,000 s in each case, while the plotted temperature range is fixed at 550 °C to 0 °C. This allows us to cover the relevant time and temperature scales for most alloys.

CCP diagrams can only be read along the continuous cooling curves, and isothermal readings are not possible from these diagrams. Moreover, CCP diagrams are only valid for the particular alloy composition investigated and the specific solution treatment applied, which both have a great impact on the quench sensitivity of the alloy. The solution treatment and the mass fractions of alloying elements are therefore given at the top of each diagram. This also holds for the initial microstructure, i.e. the grain size or secondary dendrite arm or cell spacing. The reader should be aware that different batches with similar chemical composition may therefore still behave differently.

The start and finish temperatures of precipitation, depending on quenching rate, are shown by bold lines. In almost all cases, several precipitation reactions occur sequentially during cooling and there is often some overlap. The onset of precipitation in the first reaction and the end of precipitation in the last reaction can be determined exactly, and are shown in continuous black lines. Overlapping reactions are hard to separate by DSC, and intermediate start and finish precipitation temperatures have been estimated using the procedure outlined in Ref. [115, BM6] and are shown in continuous grey lines. In some cases, precipitation start and finish temperatures have been extrapolated for readability by dashed black lines.

To provide information about precipitation intensity, the total cooling rate specific precipitation enthalpy Δh_{total} is plotted below certain cooling paths in rectangles. The specific precipitation enthalpy is proportional to the volume fraction of precipitates formed during cooling. The Vickers hardness HV1 (HV5 for some 7xxx alloys) after cooling and additional ageing is shown by ovals. The precipitation enthalpy is high for slow cooling, whereas hardness after ageing is high for rapid quenching. Strong precipitation during cooling causes a loss of availability of alloying elements for subsequent ageing.

The slowest cooling rate at which a certain precipitation reaction is completely suppressed during cooling is defined as the UCCR. These values are provided in the lower left-hand corner of the diagrams. In cases where (in situ) DSC measurements were not possible up to cooling rates above the UCCR, the latter is estimated based on the hardness results.

An example of a CCP diagram in the format described above is shown in Figure 15. In Ref. [138], we published CCP diagrams in this format for 11 Al wrought alloys and one Al cast alloy. A range of additional CCP diagrams is found in the appendix of this publication.

6063

linear cooling from solution annealing: 540 °C 20 min

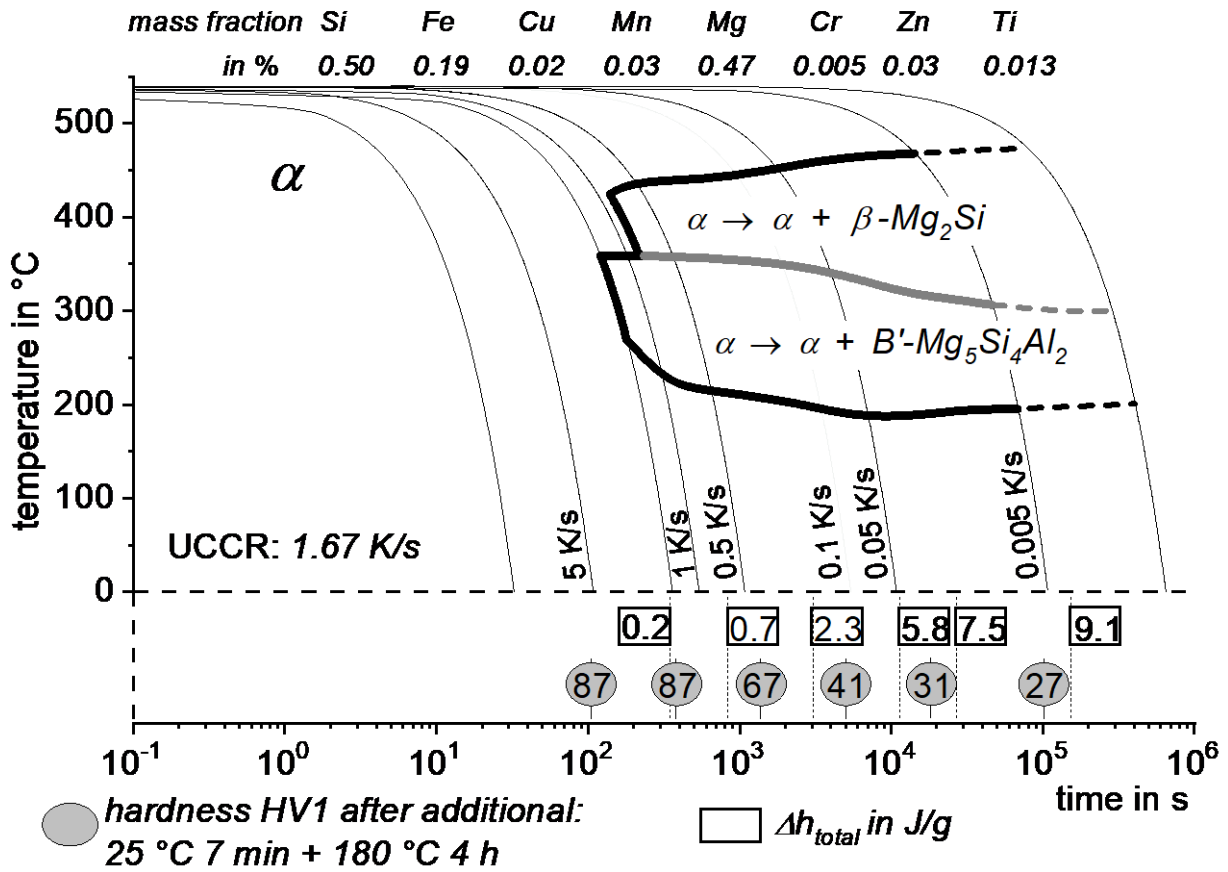


Figure 15: Continuous cooling precipitation diagram of 6063, as published in Ref. [138].

3 Solid-solid phase transformations in Al alloys over a wide dynamic range

This chapter provides assessments of the kinetics of solid-solid phase transformation, and particularly the kinetics of quench-induced precipitation for two AlSi binary wrought alloys, two high purity AlMgSi ternary wrought alloys, and a range of 20 wrought alloys from the heat treatable alloy systems AlMgSi (eight variants), AlZnMg(Cu) (10 variants) and AlCuMg (two variants). Some of the aforementioned alloys are laboratory alloys, and some were produced commercially; however, all contain amounts of trace elements and impurities typical of commercial production. Three AlSiMg cast alloys are also considered. Table 4 in the Appendix gives alloy compositions and some details of their original processing.

3.1 Heating to solution treatment and isothermal soaking

3.1.1 Capabilities and limitations of DSC heating curve analysis and interpretation

The vast majority of published DSC work on Al alloys involves heating experiments. This is likely to be due to the fact that DSC was originally intended for use during heating, and DSC heating experiments are easier in terms of scanning rate control (see Figure 10). However, the interpretation of heating DSC curves for age-hardening Al alloys is complicated by severely overlapping endo- and exothermic reactions i.e. dissolution and precipitation reactions [BM5]. Unfortunately, the superposition of different reactions is rarely verifiable and thus is too often disregarded. As will be shown later, the consideration of DSC heating curves over a wide range of heating rates can help to identify superposition issues. In DSC heating experiments, it is reasonable to choose the maximum temperature to be as high as possible while keeping the sample in the solid state and avoiding incipient melting. This is because the dissolution of the major alloying elements is typically of particular interest for heating experiments. Since the heating rate specific solvus temperature rises with increasing heating rate, high maximum temperatures are preferable. A quantitative analysis of the total enthalpy changes during heating can only be carried out if the heating rate specific solvus temperature is exceeded (see below).

Why are overlapping microstructural reactions a problem in the interpretation of the DSC heating curve? DSC detects (only) the sum of any heat that is released or consumed by the reactions inside the sample. In a theoretical case, a precipitation and a dissolution reaction with equal quantities of enthalpy but opposite algebraic signs may occur, and in this case, the resulting DSC signal would be zero. Thus, a heat flow signal of zero during heating does not necessarily mean that no reactions are taking place. In addition, the peak temperature of a certain heating DSC peak is not necessarily equal to the intensity maximum of the related microstructural reaction [BM5]. The above-discussed aspects imply that kinetic evaluation methods that focus on single heating DSC peaks, for instance the Kissinger method [139], are problematic for the precipitation hardening of Al alloys. The issue of superimposed reactions can be exemplified by Figure 16, which plots DSC heating curves of 6082_{III} in the initial state T651. During slow heating with 0.01 K/s, there are two smaller dissolution peaks B and F at about 200 °C and 330 °C, respectively. In addition to the fact that the peaks shift towards higher temperatures at higher heating rates, the peak areas also substantially increase. It is very unlikely that a diffusion-controlled dissolution reaction increases its transformed fraction if the time available for that reaction is substantially shortened. The phenomenon of increasing peak area can only be explained by a significant variation in the superposition of different reactions. This may be caused by a more severe suppression of the overlapping exothermic precipitation reaction.

Similar cases with increasing areas of the dissolution peaks at higher heating rates can be found in multiple cases of different age-hardening Al alloys and different initial heat treatment states [BM5, 123, 136, 140]. One likely reason for the more severe suppression of precipitation compared to dissolution is the different

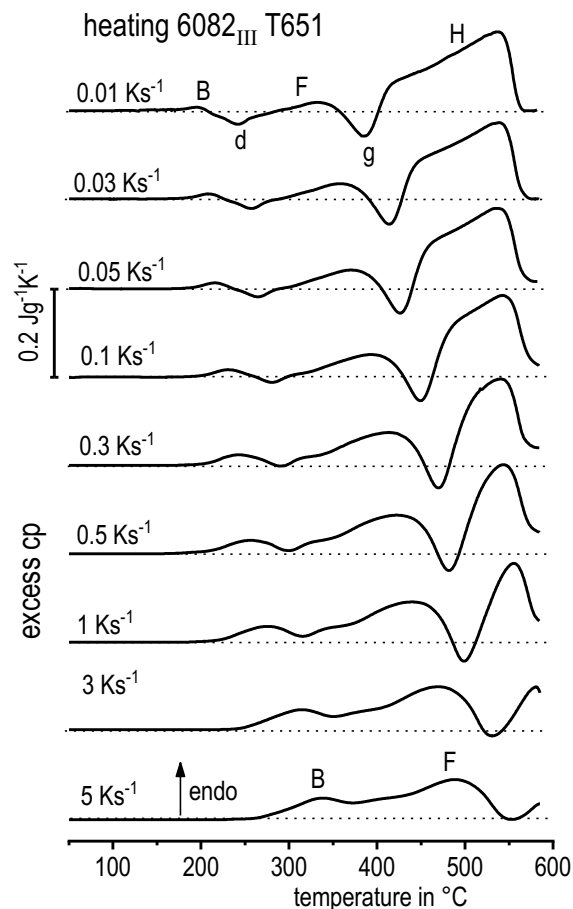


Figure 16: Heating DSC curves of 6082_{III} in initial state T651 [BM10].

diffusion distances of these reactions. This can be seen in Figure 17, which schematically shows the development of these reactions over time in similarly large microstructure areas. In Figure 17A, showing precipitation from a homogeneously distributed solid solution, the alloying element atoms have to diffuse a certain distance in order to consolidate with one precipitate particle, forming its own crystal structure. This effectively causes the exothermic heat effect of precipitation. In Figure 17B, the dissolution of an existing precipitate only requires the crystal structure of the precipitate to be dissolved in order to provoke the endothermic heat effect. This dissolution of the previously existing precipitate structure requires the alloying elements to diffuse over a much shorter distance; this requires a shorter duration to complete the reaction. Thus, if the time available for the reaction is shortened and we assume that both the dissolution and precipitation of similar phases proceed at very similar or equal diffusion rates, it must be concluded that the kinetic suppression of both types of reactions is similar. However, since the diffusion distances are different, a similar shortening

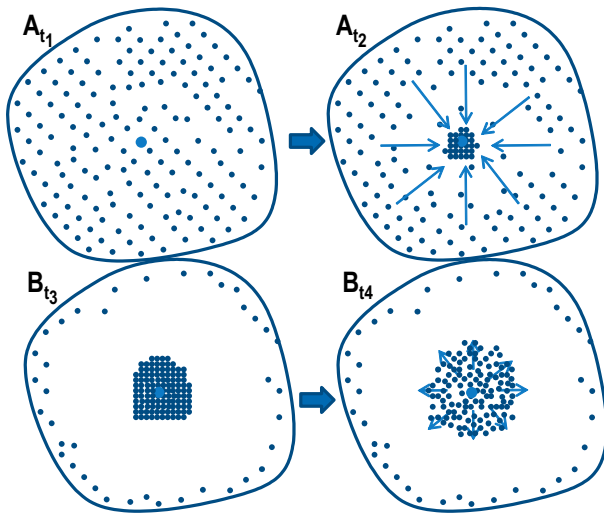


Figure 17: Schemes for (A) a precipitation process from a homogeneously distributed solid solution covering time steps t_1 to t_2 ; (B) dissolution of a precipitate covering the time steps t_3 to t_4 , $t_4-t_3 < t_2-t_1$.

of the reaction time causes a more severe suppression of the precipitation reactions. As a side effect, due to the increased heating or cooling rates (and hence a shortened diffusion time), precipitates tend to become smaller, and this also arises from the reduced diffusion pathways. However, dissolution reactions are also increasingly suppressed with rising heating rates.

It should be stated that new methods need to be developed in the future to evaluate the kinetic data from DSC heating curves. All of the existing methods are based on the assumption that the transformed fraction of alloying elements is independent of the varying heating rates [75, 141, 142]. This basic assumption obviously does not hold, and this is particularly the case for heating rate variations over

a wide dynamic range. This leads to the need for developing new methods in the future for the evaluation of kinetic parameters, a problem which could be solved by kinetic modelling. Some available models even use a combination of both precipitation and dissolution to model the whole DSC heating curve from room temperature up to the solvus temperature (e.g. [143–147]). In the future, these models will need to implement the kinetic suppression of diffusion-controlled reactions.

Despite the abovementioned issues with the analysis of DSC heating curves, there are some aspects that can still be derived from DSC heating curves, such as the following:

- The course of the DSC heating curve strongly depends on the initial state of the sample and the heating rate, e.g. Ref. [75, 123, 136, 148–151, BM4, BM5]. The differences from the initial state are therefore mostly relevant at temperatures below about 300 °C (see Figure 18, which shows heating DSC curves for three AlMgSi alloys in different initial heat treatment states). Above 300 °C, the differences between the DSC curves resulting from different initial precipitation states are mostly equalised, and thus the heating DSC curves are very similar at high temperatures.

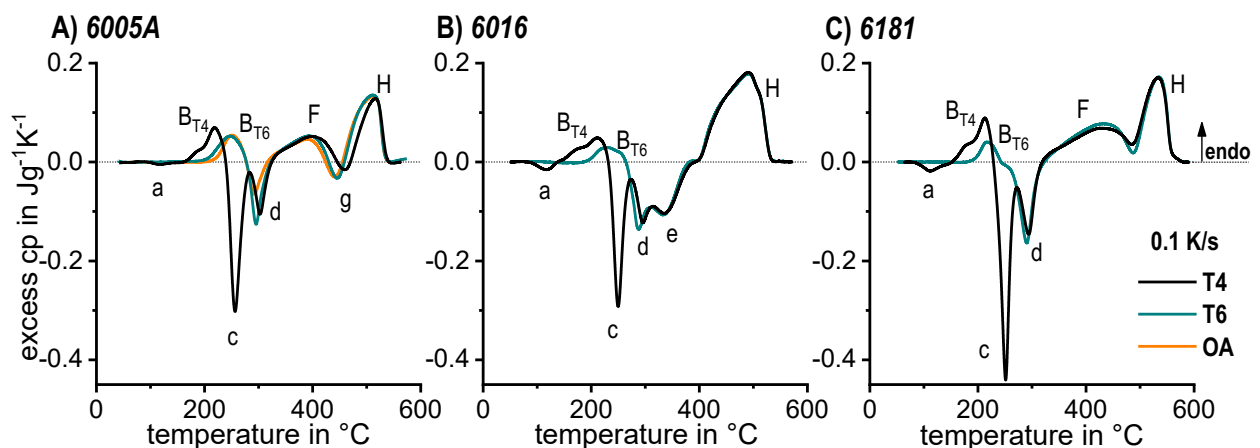


Figure 18: DSC heating at 0.1 K/s for the alloys (a) 6005A; (b) 6016; and (c) 6181 with the initial conditions T4 and T6, and in case of 6005A overaged (solution treated, over-critically quenched and aged at 200 °C for 10 h) [BM5].

- If the maximum temperature of the heating program is chosen to be high enough, and if the alloy happens to allow the complete dissolution of the major alloying elements, the heating rate-dependent solvus temperature can be determined by heating DSC. In Figure 18, this characteristic temperature relates to the end of peak H, where the DSC signal finally drops back towards zero. This aspect has high technological relevance, as determination of the solvus temperature allows us to choose a proper solution treatment temperature. Choosing a solution temperature well above the solvus is crucial in cases where a short soaking is necessarily related to the technological process, for instance in continuous annealing processes during sheet production [BM10].
- If the abovementioned condition is fulfilled and the DSC heating curves exceed the scanning-rate-specific solvus temperature, the total integral of the DSC heating curve $\int_{T_{min}}^{T_{max}} excess\ cp(T)$ gives the enthalpy level Δh of the initial state. This enthalpy level is an indicator of the thermal and kinetic stability of the initial state. That is, a more stable precipitation state has a larger enthalpy level (6005A: $\Delta h_{T4} = 6\text{ J/g} < \Delta h_{T6} = 10\text{ J/g} < \Delta h_{oa} = 12\text{ J/g}$, see Figure 19, [BM5]). In the case of a soft annealed 6005A (Figure 19E), the precondition for complete dissolution during heating to T_{max} does not hold. The determination of the enthalpy level of the initial state can be useful in two different ways: firstly, the heat treatment state of an unknown delivery condition of an alloy can be estimated; and secondly, the determination of the enthalpy level by a reheating experiment allows us to determine the enthalpy changes caused by preceding heat treatments, which is very valuable in order to extend the DSC scanning rate range by indirect experiments, for instance.

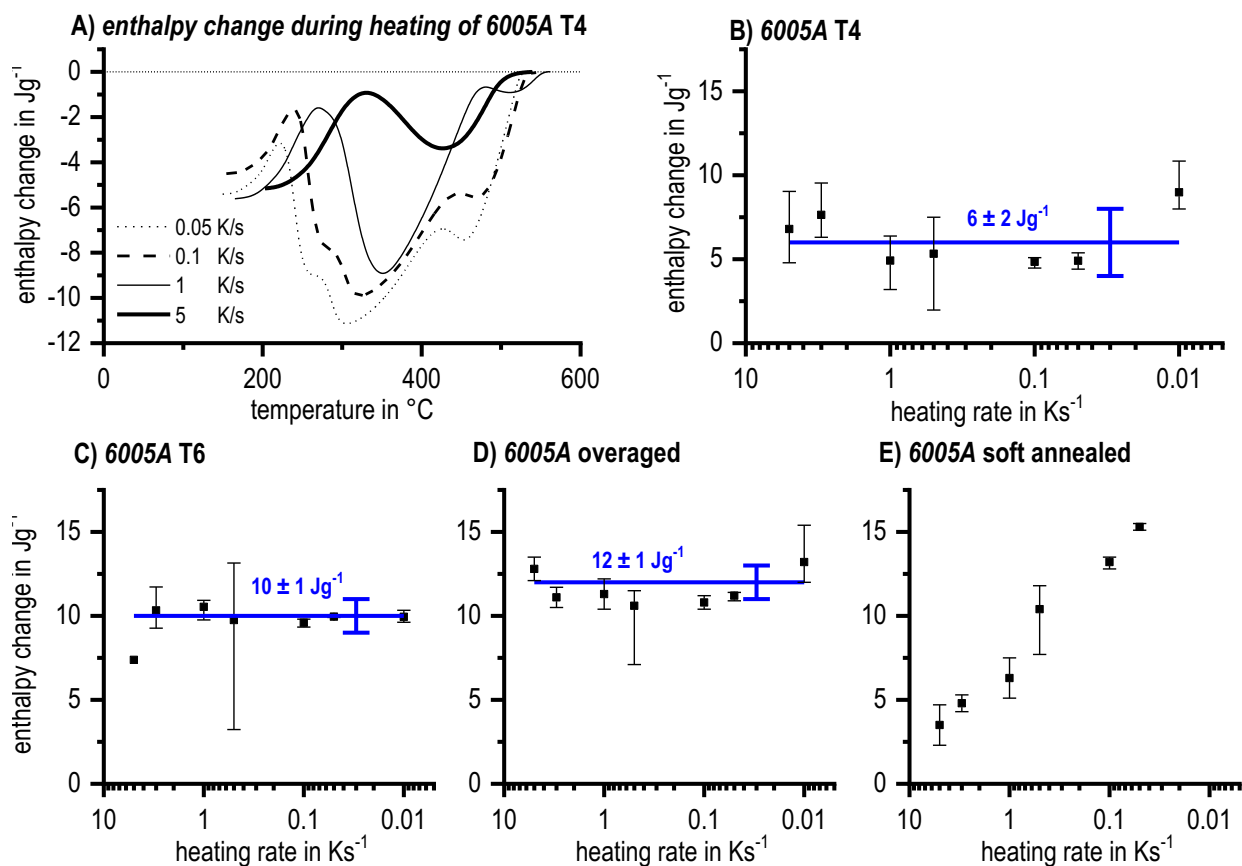


Figure 19: (A) Enthalpy change of 6005A T4 during heating to 580 $^{\circ}\text{C}$; (B)–(E) enthalpy levels of 6005A for initial conditions T4 and T6, over-aged and soft annealed, respectively, covering the heating rate range 0.01 to 5 K/s [BM5].

3.1.2 Achieving a complete solid solution

Producing a complete solid solution in terms of the dissolution of the major alloying elements of wrought Al alloys has major importance in terms of utilising the full age-hardening potential. In addition, incomplete dissolution will increase the quench sensitivity of an alloy [BM10]. This is because quench-induced precipitation is accelerated by the higher number of available nucleation sites that are present in the form of undissolved secondary phase particles (of the same or a highly similar phase, which precipitates during cooling). More precisely, if undissolved particles remain, nucleation is not necessary and instantaneous growth can take place. In such cases, the hardness after ageing (the age-hardening potential) can be substantially reduced [BM10].

DSC analysis can help to identify proper solution treatment parameters. In the first instance, the solvus temperature can be estimated from DSC heating experiments, as discussed above. In this case, the solution temperature is ideally chosen to be a few tens of K above the solvus temperature. If the overheating above the solvus must be kept small, or if very coarse precipitates are to be dissolved, and if the homogeneity of the elemental distribution is also a consideration, a particular soaking duration is required at the solution temperature. In Ref. [152], we showed that the heat-flow development during isothermal soaking in a differential scanning calorimeter at the solution treatment temperature can be used to estimate the duration of the dissolution processes. Based on this, suitable solution treatment parameters can be derived.

3.1.3 Extending the scanning rate by reheating experiments

The determination of the enthalpy level of any initial state can be utilised in indirect DSC reheating experiments. The basic idea is to perform systematic variations of the initial state via defined heat treatments and the subsequent determination of the enthalpy level by a DSC reheating experiment [BM9, BM4, 124]. One prerequisite for this approach is that the alloy allows the formation of a complete solution at the solution treatment temperature. The complete solid solution is an equilibrium state, and its enthalpy level h_0 can be defined as zero. A second prerequisite is that this equilibrium enthalpy state $h_0=0$ must be reached again during reheating.

Figure 20 schematically illustrates some potential applications of this basic idea. In Figure 20A, an enthalpy change Δh_{sc} due to quench-induced precipitation during slow cooling is assumed. Since the reheating step ends in an enthalpy state $h_0=0$, the same magnitude of enthalpy change (with an opposite algebraic sign compared to cooling) must be exchanged during reheating. Reheating can therefore reveal the enthalpy change caused by precipitation during slow cooling. Reheating experiments after variations of the “slow” cooling rate thus allow for the determination of precipitation enthalpy as a function of the cooling rate [BM4, 124]. Since “slow” cooling in this case refers to the capability of the calorimeter used, reheating can be applied to extend the cooling rate range in both directions, i.e. both slower and faster experiments. In both cases, quantitative statements of the enthalpy changes are possible [BM4, BM9]. We performed slow cooling in a controlled air furnace with rates down to 3×10^{-5} K/s, corresponding to a cooling duration (540 to 20 °C) of more than half a year [126]. On the other side of the spectrum, using the chip-sensor based DFSC, “slow” cooling may be as fast as several hundreds of K/s [BM9, 124]. These DFSC devices

commonly require scanning rates above 1,000 K/s to obtain a sufficient signal to noise ratio [127]. Thus, reheating in a DFSC is typically carried out at rates above 1,000 K/s [124, 153, BM9]. The reheating approach can be extended to a temperature-dependent determination of the precipitation enthalpy by interrupting the precipitation process during “slow” cooling at a certain temperature T_i (see Figure 20C) [BM9].

Another form of this idea involves the systematic variation of a particular heat treatment, for instance an ageing treatment, prior to reheating (see Figure 20B). If cooling from solution treatment is carried out faster than the UCCR, the subsequent reheating step will give a total enthalpy change of zero [BM4, 124] (see Figure 20D). This fact can be utilised as a baseline correction for the preceding reheating experiment [BM9, 124]. Based on this idea, the differential reheating method (DRM) was introduced in Refs. [124, 153], an approach that allows the application of chip-sensor-based DFSC for the analysis of the kinetics of quench-induced precipitation in Al alloys. In particular, the specific precipitation enthalpy can be obtained as a function of the cooling rate, allowing us to determine the UCCR of the alloy. In Ref. [BM9], the DRM was developed further towards the obtainment of the specific enthalpy changes depending on the temperature. The latter allowed assessment of the start and end temperatures of certain precipitation reactions, which helps in completing the CCP diagrams for highly concentrated alloys with high UCCRs [BM9].

The above considerations lead to the postulation of two critical heating rates for the dissolution of a specific initial heat treatment state, as illustrated in Figure 21. The first of these is the lower critical heating rate (LCHR), and the second is the upper critical heating rate (UCHR). The LCHR is postulated to be the fastest

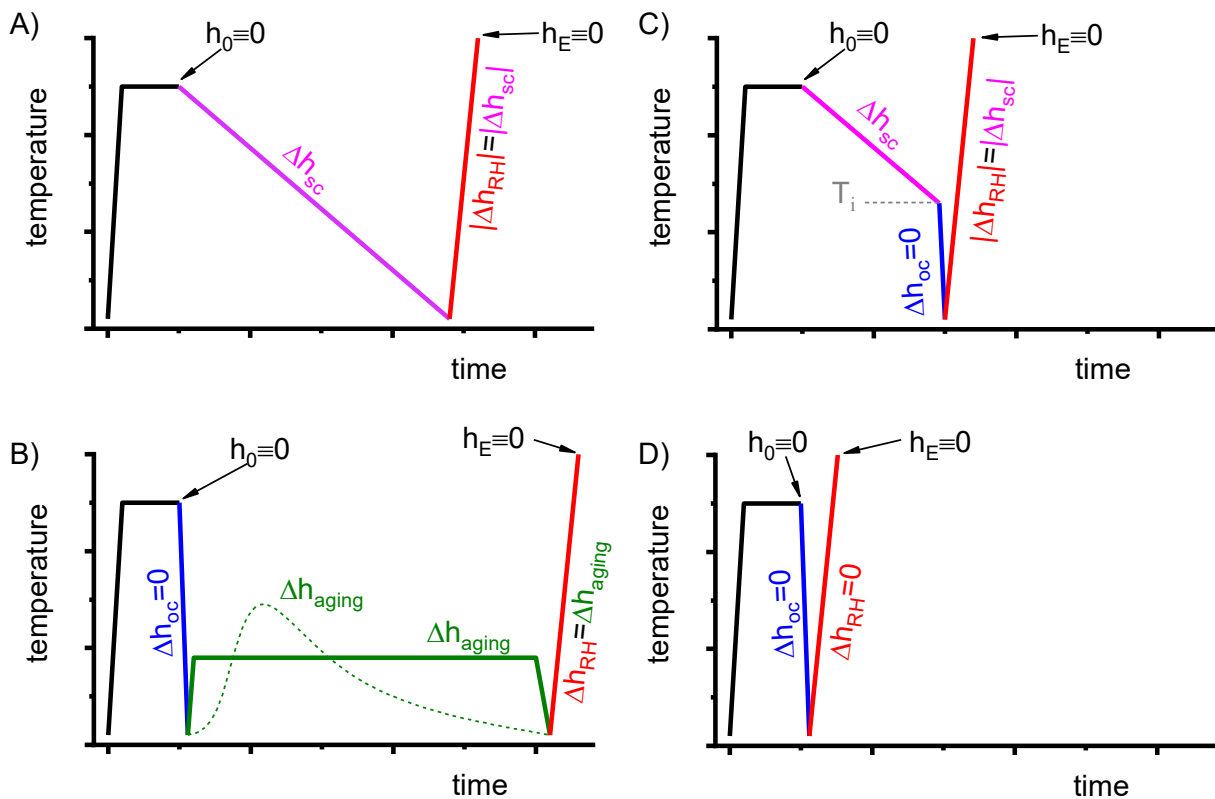


Figure 20: Schematic development of the enthalpy level Δh for different temperature-time profiles with final reheating (RH). (A) Slow cooling (sc) from solution treatment to room temperature; (B) slow cooling from solution treatment to a certain temperature and interruption by overcritical cooling; (C) arbitrary types of aging after overcritical cooling from solution treatment; and (D) overcritical cooling (oc) from solution treatment.

heating rate at which the particular initial state can be dissolved completely during heating to a certain maximum temperature T_{\max} (which must be above the solvus temperature of the alloy). A potential further increase in this temperature in the solid state will reduce the LCHR. If heating is carried out to T_{\max} at a rate slower than the LCHR, a complete solid solution will be obtained during heating. The LCHR therefore has high technological importance. For a soft annealed state of 6005A, we found indications that the LCHR is on the order of 0.01 K/s, although there is no extensive experimental proof of this. The UCHR is theoretically defined as a fast heating rate at which diffusion is prevented completely and no dissolution takes place. Currently, for the soft annealed 6005A, a UCHR can only be estimated as about 10 to 20 K/s (compare Figure 19E with Figure 21).

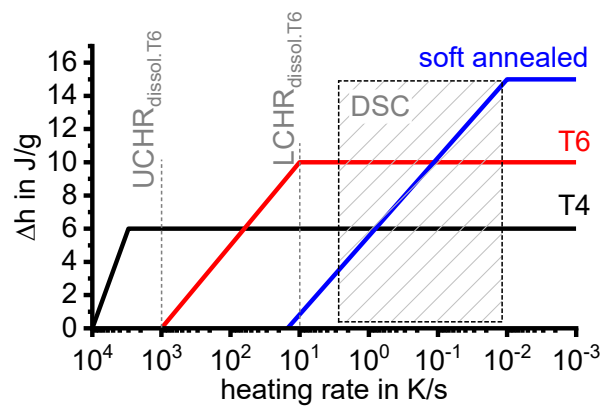


Figure 21: Schematic development of the enthalpy levels of three different heat treatment states in a medium-strength AlMgSi alloy obtainable by reheating to a certain maximum temperature. Values are based on those of 6005A in [BM5]. The shaded area signifies the heating rate range covered by DSC in Ref. [BM5].

3.2 Quench-induced precipitation during cooling from solution treatment

3.2.1 AlSi binary wrought alloys

Figure 22A and B show direct cooling curves for alloys Al0.26Si and Al0.72Si, while Figure 22C displays DSC reheating curves for Al0.26Si after various extremely slow cooling rates were applied. The specific precipitation enthalpy values are given in Figure 24.

From Figure 22A and B and Figure 24, it can be seen that even in lean pure binary Al-Si alloys, quench-induced precipitation is separated into high-temperature (HTR) and low-temperature (LTR) reactions. For Al0.26Si, the HTR is detected only after extremely slow cooling at 3×10^{-5} K/s (seen as a two stage dissolution reaction during reheating in Figure 22C). The UCCR of Al0.72Si was found to be 1 K/s [126, BM4], while for Al0.26Si this is only 3×10^{-2} K/s [126].

Analysis using SEM and HR-TEM with EDS and SAED/NBD [126] showed that both reactions were caused by the precipitation of the same phase, i.e. the Si phase with diamond cubic crystal structure, but that the morphologies and dimensions were different: during HTRs, polygonal particles with a low aspect ratio grew (up to several tens of μm in diameter), while during LTRs, plate-like particles with a high aspect ratio were formed (up to several μm in length but only several hundreds of nm or less in thickness) [126, BM4].

From Figure 22D, it can be seen that the precipitation enthalpy obtained directly from in situ cooling DSC and the values from indirect DSC measurements fit together very well, thus providing additional confirmation of the validity of these approaches. In Ref. [BM4], it is demonstrated that the specific

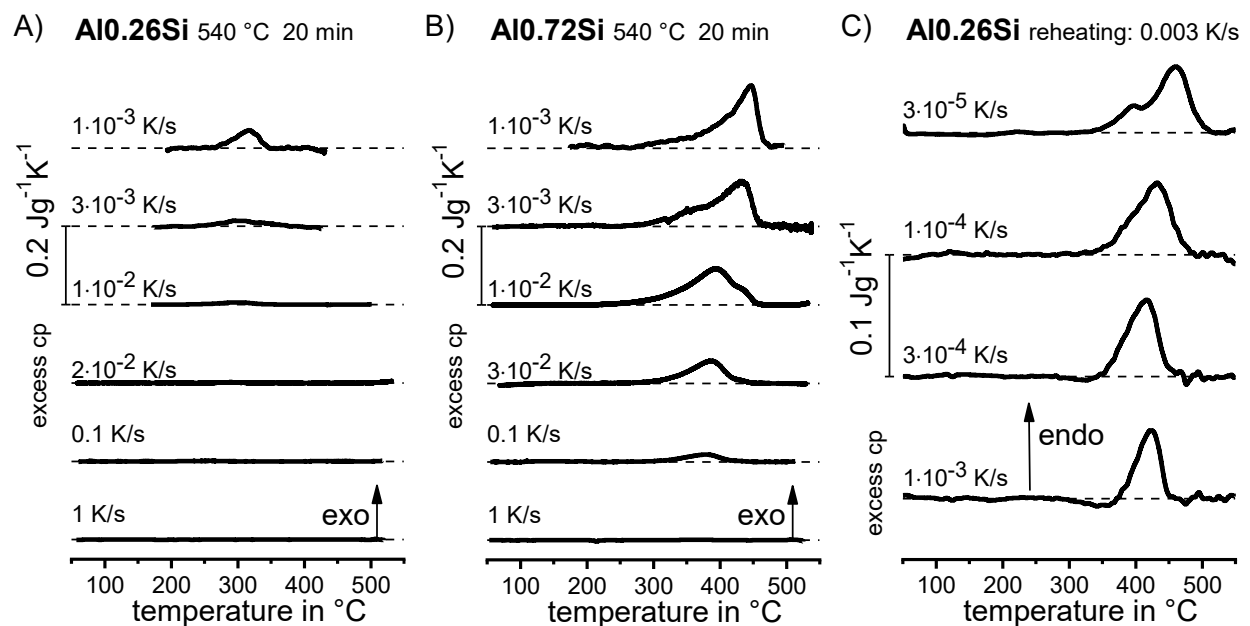


Figure 22: Direct cooling DSC curves of (A) Al0.26Si and (B) Al0.72Si in a range of cooling rates from 1 to 10^{-3} K/s; (C) DSC reheating curves of Al0.26Si after cooling at rates down to 3×10^{-5} K/s.

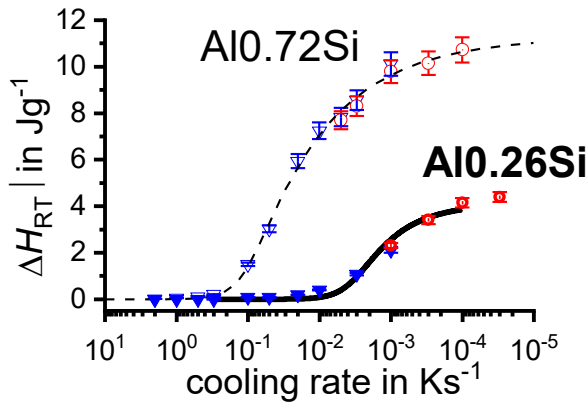


Figure 24: Enthalpy development by quench-induced precipitation. Combination of directly (blue triangles) and indirectly (red circles) measured results. Predictions obtained from model in Ref. [BM4].

precipitation enthalpy shown in Figure 24 is directly proportional to the volume fraction of quench-induced Si precipitation. The continuous lines plotted in Figure 24 in addition to the measured data points are the results of a model (for details, see [BM4, 126]). This model allows us to accurately calculate the volume fraction of quench-induced Si precipitation as well as the fraction of Si left in the solid solution for various temperatures and cooling rates.

Figure 23 and Figure 25 display microstructural images depending on the cooling rate in Al0.72Si. Optical microscopy after very slow cooling with 10^{-4} K/s (Figure 23) reveals polygonal-shaped Si particles. If cooling is carried out ten times faster, at 10^{-3} K/s, the number of quench-induced particles is substantially increased (Figure 23B), while their particle size is reduced. From Figure 22D, it can be seen that the volume fraction of quench-induced precipitation is similar for these two very slow cooling rates. In Ref. [BM4, 126] we demonstrated that these polygonal-shaped precipitates originate from the HTRs seen in cooling DSC. At a cooling rate of 10^{-2} K/s, quench-induced particles are further reduced in size. A detailed analysis of the OM images reveals that next to the

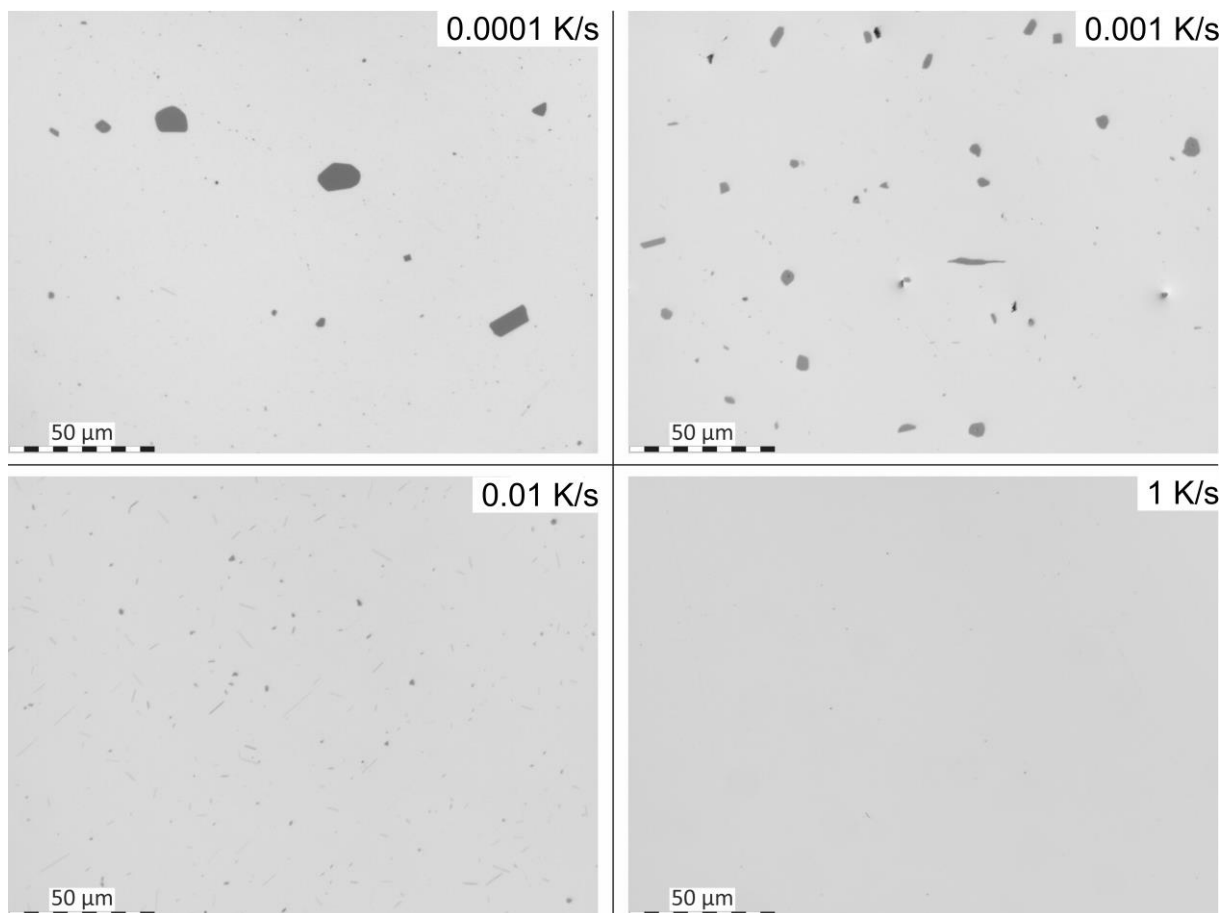


Figure 23: OM images of “quench-induced” precipitation in Al0.72Si after cooling at different rates.

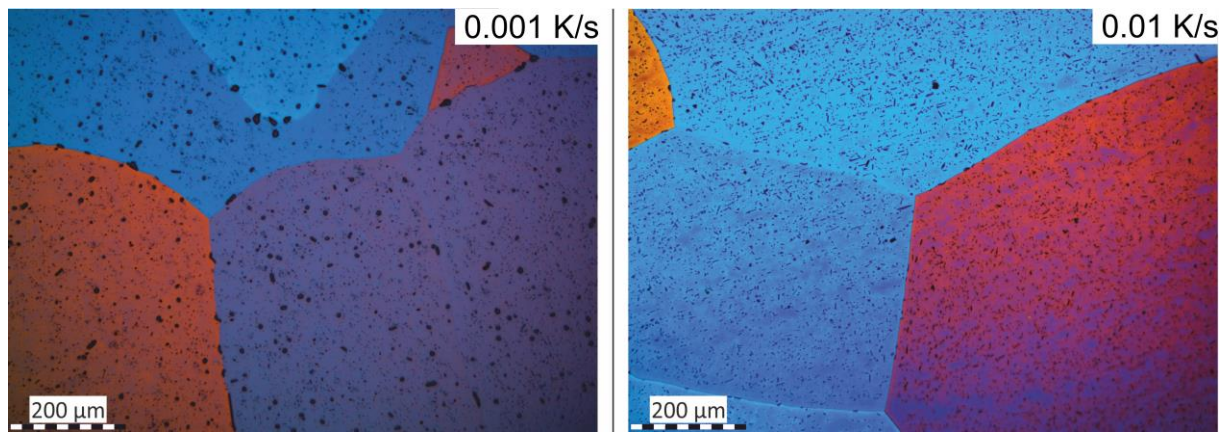


Figure 25: OM images of Barkers-etched Al_{0.72}Si samples after two different cooling rates, revealing that the vast majority of quench-induced precipitation occurs inside the grains.

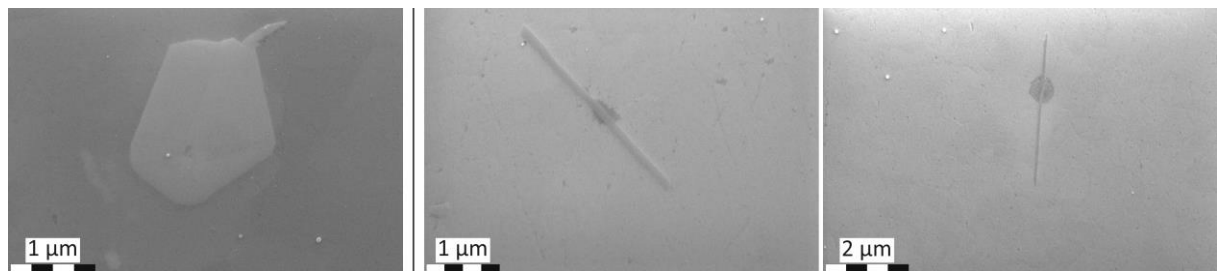


Figure 26: SEM-SE images of quench-induced precipitates in Al_{0.72}Si after cooling at 0.01 K/s. Left: Polygonal particle originating from the HTR; middle and right: needle-/plate-shaped particles from the LTR [126].

polygonal-shaped particles, further plate-like particles (appearance: needle or rod-shaped) with distinct orientations appear (see also Figure 26). It has been proven that these plate-shaped particles originate from the LTRs [BM4, 126]. After cooling at 1 K/s, no quench-induced precipitates can be seen in OM. Figure 25 demonstrates that the vast majority of quench-induced precipitates form inside the grains. In high-purity alloys such as this one, grains are generally coarse. The OM results are consistent with the DSC results in Figure 22, indicating that at 0.01 K/s, the HTR has already been suppressed to a great extent. However, at this cooling rate, and for even faster cooling at 0.1 K/s, TEM unambiguously shows that some precipitates form during the quench (see Figure 27 and Figure 28).

In Figure 26, the individual particles that form in the HTR and LTR are compared using SEM. SEM-EDS and TEM-EDS reveal that both the needle-/plate-shaped and polygonal particle types are nearly pure Si. Selected area electron diffraction (SAED) in TEM additionally reveals that both particle types have the same diamond cubic lattice structure. Figure 27 shows a BF-STEM image of a quench-induced Si plate-shaped precipitate (formed during the LTR) after cooling at 0.1 K/s. Under this cooling condition, these Si plates have thicknesses of about 50 nm, with an edge length of 5–20 μm. Via TEM experiments employing sample rotation (see Figure 28), it was confirmed that particles such as those shown in Figure 26 (middle and right) and Figure 27 are indeed plate-shaped.

At first impression, it may seem odd that pure binary AlSi shows two quench-induced precipitation reactions in which the same phase is formed. However, it has been reported earlier that Si particles in Al can precipitate either as equiaxed particles (here, polygonal particles) or as hexagonal plates [154, 155].

During cooling, competing effects occur, as the increasing supersaturation with decreasing temperature leads to an increasing driving force for precipitation, while the precipitation itself depletes the matrix, leading

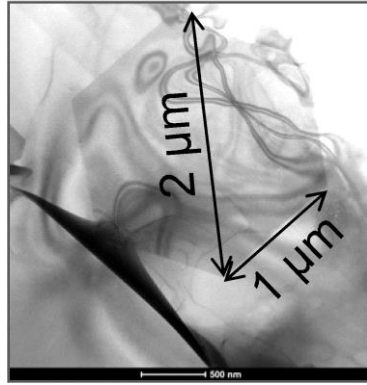


Figure 27: BF-STEM images of hexagonal Si plate in $\text{Al}_{0.72}\text{Si}$ after cooling at 0.1 K/s, zone axis $[001]_{\text{Al}}$ [126].

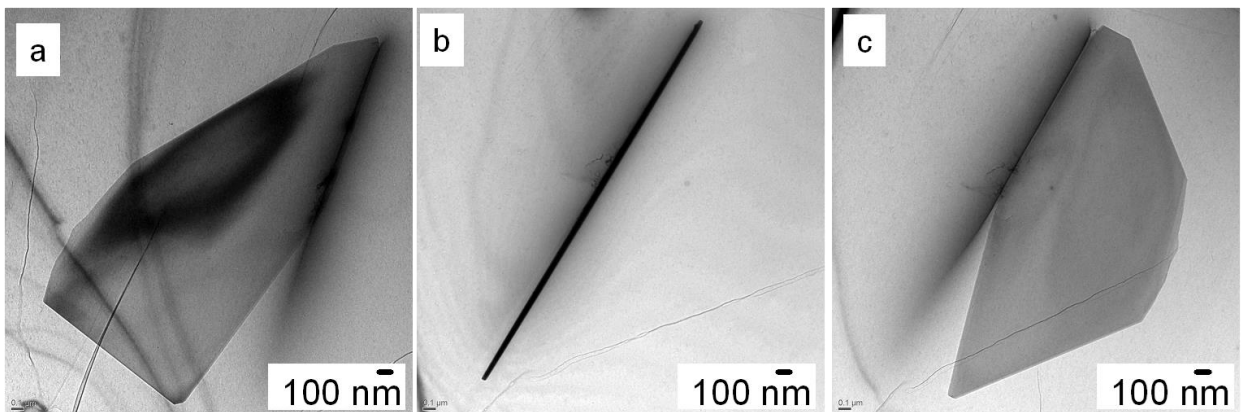


Figure 28: BF-STEM images of a thin plate formed from cooling at 0.1 K/s (pure Si, diamond cubic), standing out from the Al matrix in three different rotations: (A) -40° ; (B) 0° (zone axis $[001]_{\text{Al}}$); and (C) 40° [126].

to a slowed reaction. In addition, the diffusion rate is steadily reduced as cooling progresses, and the lattice misfit between precipitate and matrix changes due to the differing thermal contraction of Al and Si. Indeed, the thermal expansion coefficient of Si is much lower than that of Al, with the difference being higher than most other light-alloy–precipitate combinations. These effects can combine to cause the same phase to form in two morphologies, as also shown for Ni-based superalloys, for instance [156–159].

During cooling of the binary AlSi alloys, high and low-temperature precipitation compete for the same alloying element (i.e. Si). If cooling is carried out very slowly, precipitation will primarily result in coarse, polygonal-shaped particles being formed during the HTR. As the majority of those particles are precipitated inside the grain, homogeneous nucleation can be expected, particularly since this is promoted by the vacancies that are expected to be present at higher temperatures [126]. If precipitation at high temperatures is suppressed to a certain extent, a fraction of the solved Si will be precipitated at lower temperatures. From the classical theory of nucleation and growth, it is known that the morphology of precipitates is dependent on the formation temperature [160]. At high temperatures, the phase transition is mainly inhibited by the formation of new interfaces. Since polygonal-shaped particles have a lower surface-to-volume ratio, precipitation of these particles is preferred at high temperatures [126]. At lower temperatures, the lattice distortion mainly inhibits the precipitation, and this is why high aspect ratio particles preferentially precipitate at lower temperatures [126].

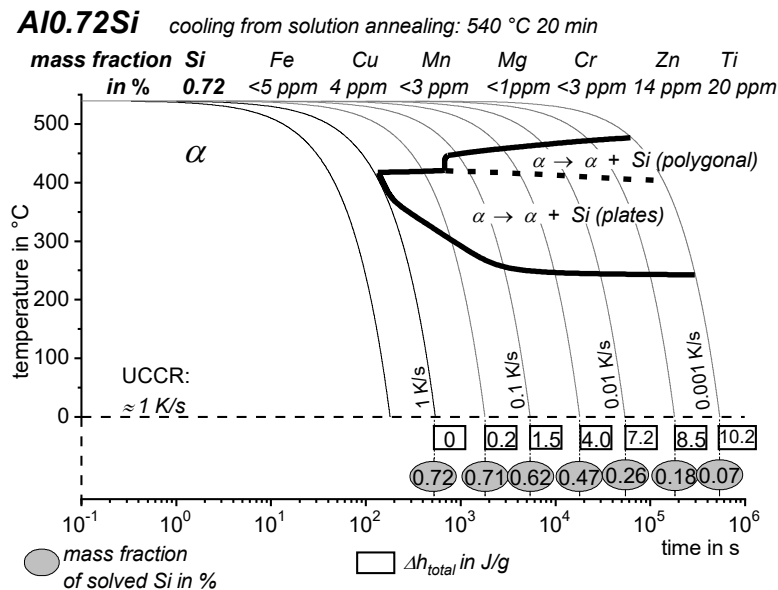


Figure 29: CCP diagram of Al0.72Si. Instead of hardness values, the mass fraction of Si supersaturation is stated.

The nucleation mechanism of the low-temperature plate particle precipitation is not yet fully resolved. Figure 26 (middle and right image) show that plate-shaped Si particles with a length of several μm have nucleated on an equiaxed particle of about 200 nm diameter. It therefore appears that at a cooling rate close to the critical cooling rate, some of the plate-shaped particles forming in the LTR can nucleate on fine Si particles formed in the HTR. However, this is only possible if there is a sufficient driving force for precipitation during the LTR in the vicinity of the equiaxed particle, i.e. if the HTR reaction is incomplete and leaves a substantial supersaturation of Si in the Al-rich phase near the small equiaxed particle. This explains why this type of nucleation of plate-shaped particles is only seen for cooling rates close to the critical cooling rate.

The results obtained for quench-induced precipitation of the binary Al0.72Si alloy are summarised in the CCP diagram shown in Figure 29. As this binary Al-Si alloy is not an age-hardening alloy, no hardness values are shown. Instead, the measured mass fraction of Si remaining in (supersaturated) solid solution after cooling is stated.

3.2.2 6xxx AlMgSi wrought alloys

In this work, a total of 10 different AlMgSi wrought alloys are investigated, none of which contain substantial amounts of Cu. The set of AlMgSi alloys includes two high-purity ternary alloys and eight commercial variants, which also contain further alloying additions and impurities besides Mg and Si, such as Mn, Fe and Cr.

Figure 30A presents DSC cooling curves for 6005A, showing effects that are typical for AlMgSi alloys. Two dominating reaction regions are seen, namely the HTRs and LTRs [BM2, BM6, 131]. A comparison of the DSC cooling curves of the 10 AlMgSi alloys in Figure A1 in the Appendix (partly published in Refs. [BM2, BM6, 131]) reveals that these two reaction regions dominate during cooling of all AlMgSi alloys. However, as will be discussed later, several additional and superimposed reactions are also seen.

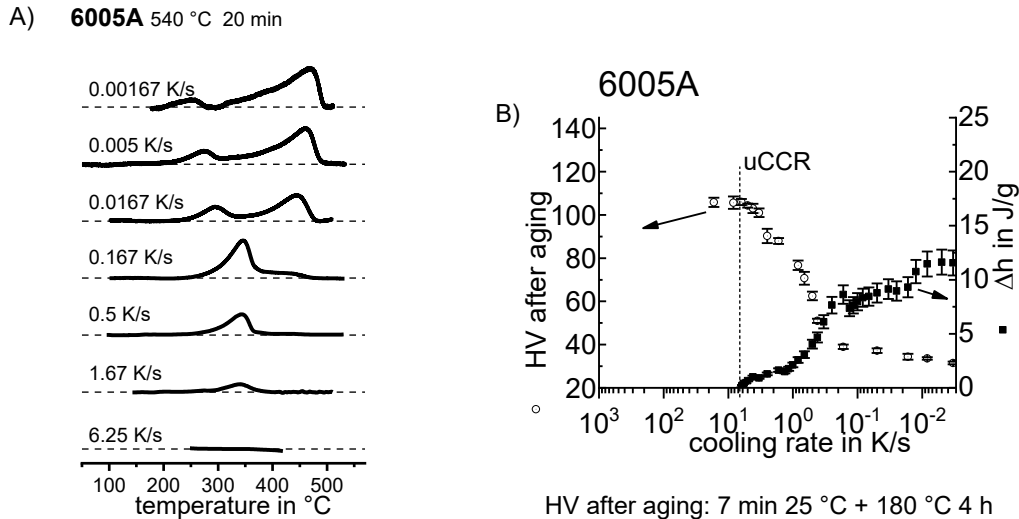


Figure 30: (A) Cooling DSC curves for 6005A; and (B) related specific precipitation enthalpy after cooling and hardness after subsequent ageing.

HTRs are the dominating heat effects during slow cooling, and are increasingly suppressed at increasing cooling rates. At cooling rates where the HTRs are substantially suppressed, the LTRs of the eight commercial alloys studied become more dominant, and the peaks shift towards higher temperatures. These two effects can be explained by the higher concentration of alloying elements that is left in solution prior to the LTR. The high-purity alloys behave differently in this respect from the commercial alloys, and one major reason for this is the difference in the nucleation mechanism of the LTR (shown below in more detail). At even higher rates, the LTRs also experience increasing suppression. For 6005A, a complete suppression of precipitation during cooling was achieved at about 6 K/s. From Figure 30B, it can be seen that the total specific precipitation enthalpy Δh measured by DSC drops to zero at the UCCR. It can also be observed that at higher cooling rates, the hardness after ageing reached a saturation level.

As can be seen from the comparative plot of hardness after ageing and specific precipitation enthalpy during cooling for all considered AlMgSi alloys in Figure A2 in the Appendix, a correlation between precipitation enthalpy and hardness after ageing is shown for all AlMgSi alloys for which DSC was able to achieve sufficiently fast cooling. Thus, in cases where DSC is not fast enough, the hardness data after ageing can provide a good approximation of the UCCR. Figure 31 shows the values of the UCCR on a logarithmic scale for nine different AlMgSi alloys as a function of the summarised Mg+Si content. This figure shows that the UCCR increases substantially with increasing alloying element concentration. Figure 31 also includes four different alloys within the chemical specification of 6082 (which is very broad), and it is interesting to note that their UCCRs can vary by a factor of up to 10. A strong batch influence can therefore be expected in terms of the quench sensitivity of Al alloys with a broad specification range for their composition.

The obtained UCCRs for 6082₁ and 6063 correspond well with the results obtained in Ref. [23]. In [23], an UCCR of 1 K/s for 6063 is reported, which is the same as that found in this work for a slightly higher concentrated version of 6063 [BM2]. For 6082, Ref. [23] reports an UCCR of above 10 K/s. The amounts of Mg and Si in the 6082 variant considered in [23] is close to those of the 6082₁ in this work, for which we obtained an UCCR of ≈ 17 K/s.

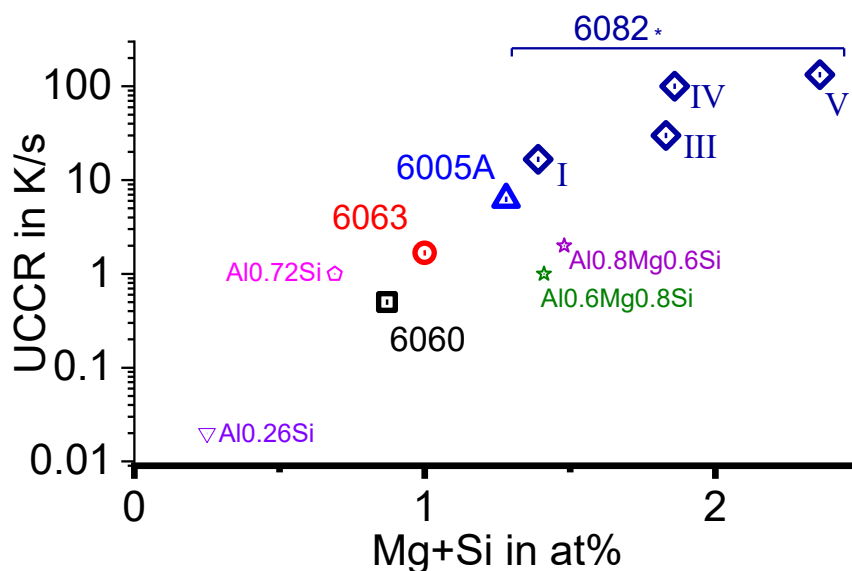


Figure 31: Upper critical cooling rates for nine different AlMgSi alloys and two binary AlSi alloys as a function of their total Mg+Si content.

Cavazos and Colás obtained a CCP diagram for 6063 from Jominy-like bar-end-quench tests [25]. They measured the actual cooling rates achieved at different distances of the quench bar end (see the example in Figure 32A for a distance of 5.5 cm). The characteristic transformation temperatures were evaluated from the inflection points of the cooling rate curve shown in Figure 32B. Using this approach, these authors were able to construct a CCP diagram. The 6063 variant considered in Ref. [25] contained mass fractions of 0.50 % Si, 0.52 % Mg, 0.21 % Fe and 0.022 % Cu, i.e. very similar to our 6063 variant [BM2]. The CCP diagrams obtained in Refs. [25] and [BM2] are compared in Figure 33. Although the 6063 variant in [25] showed slightly faster quench-induced precipitation, it can be seen that the nose temperature is very similar. Considering the sequence of HTR and LTR, it can be concluded that the DSC data are much more detailed, and cover a substantially wider cooling rate range. The authors of Ref. [25] found the UCCR of 6063 to be ≈ 10 K/s [25], while in Ref. [BM2] an UCCR of only 1 K/s was found. The higher UCCR of the 6063 variant analysed in Ref. [25] compared to that of Ref. [BM2] again shows that the quench sensitivity of different batches of alloys that are nominally the same may be substantially different.

As can be seen from Figure 31, the two laboratory alloys Al0.6Mg0.8Si and Al0.8Mg0.6Si form an exception in terms of their UCCR: they have much lower values compared to commercial alloys with comparable Mg and Si contents. This is due to the substantially lower concentration of nucleation sites for quench-induced precipitation, as demonstrated below.

For several AlMgSi alloys, DSC indicates the superposition of several microstructural reactions beneath the HTRs and LTRs. This is exemplified by Figure 34 for 6063, and can be also seen for instance in Figure A1F and G, and Figs. 40-41 in Ref. [117].

To identify these overlapping microstructural reactions, a relatively large body of work is available, e.g. [23, 117, 131, 161–164, BM6, BM2]. Figure 35 illustrates the authors' own work on quench-induced precipitation in 6005A at different cooling rates, showing optical micrographs (A), SEM secondary electron images (B) and TEM bright-field images (C) after cooling from solution treatment to the ambient temperature at different rates. It can clearly be seen from Figure 35A and B that precipitates with lower aspect ratio (appearing dark) become substantially smaller as the cooling rate rises. These HTR-quench-induced precipitates are

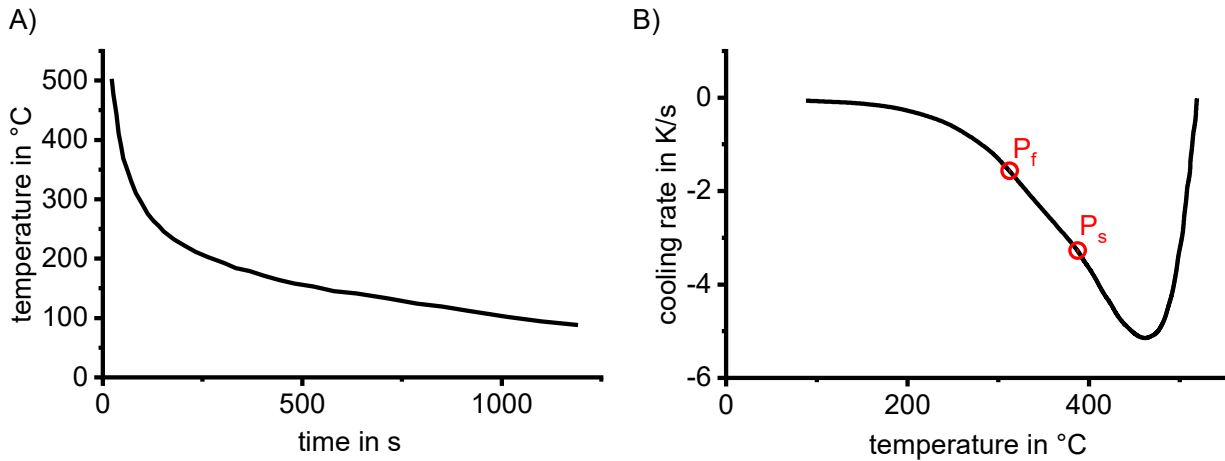


Figure 32: (A) Cooling resulting from placing one end of the experimental bar in water, measured at a distance of 5.5 cm from the bar end; (B) “instantaneous cooling rate as a function of temperature (as given in A). The points indicate the start (Ps) and end (Pf) of precipitation [25].” Digitized data from Ref. [25].

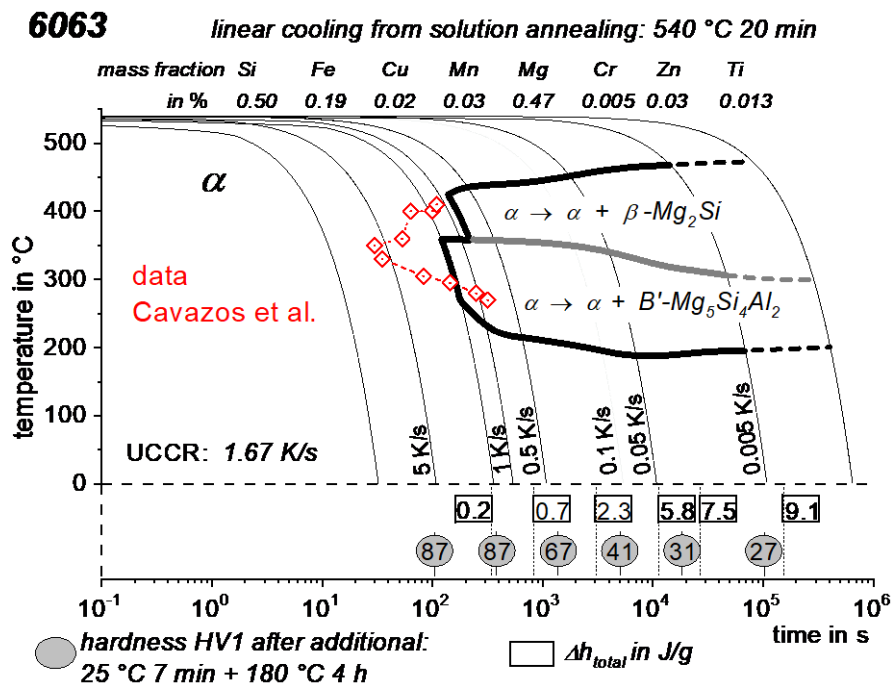


Figure 33: CCP diagram for 6063 obtained by DSC [BM2] comparing the data points (red) of Ref. [25].

β-Mg₂Si phase particles, which partially precipitate at grain boundaries and mainly precipitate inside the grains (see Figure 35A and B). The fcc structure of β-Mg₂Si has been proven by electron backscatter diffraction (EBSD) and X-ray diffraction (XRD) analysis [117, 131]. At a cooling rate of 0.16 K/s, hardly any quench-induced precipitation is seen in OM and SEM; however, at this cooling rate, a large number of rod-like quench-induced precipitates with much higher aspect ratios is found in TEM (Figure 35C). The lengths of these rod- and lath-shaped secondary precipitates were observed to decrease from about 600 nm after cooling at 0.16 K/s to about 300 nm at a cooling rate of 1.6 K/s.

Figure 36A shows BSE-SEM images of the microstructural development of 6005A observed at a constant cooling rate of 0.0016 K/s down to different temperatures (Figure 14). At 500 °C, only primary precipitates are visible. The first Mg₂Si particles were detected at 475 °C, immediately before the intensity maximum of the HTR was reached, as shown in Figure 30A. A high fraction of Mg₂Si precipitates was observed by SEM

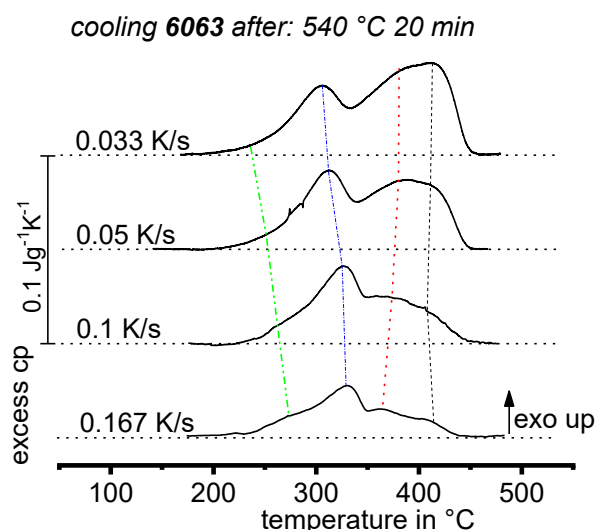


Figure 34: Cooling DSC curves for 6063 in a narrow range of cooling rates at higher excess cp magnification, indicating at least four separate peaks below the two major reaction regions.

at 450 °C after passing the peak of the HTRs. As revealed by SEM, the microstructure did not change significantly with a further decrease in temperature. It was therefore concluded that the Mg₂Si precipitation originates from the HTRs. During faster cooling of 6005A at 0.16 K/s, where the LTR dominates (Figure 30A and Figure 40 on page 47), rod-/lath-shaped precipitates could be detected for the first time at 325 °C. At temperatures below 325 °C, the rod-/lath-shaped precipitates grew only slightly, as illustrated in the TEM micrographs in Figure 36B. Hence, it was concluded that the precipitation of rod-/lath-shaped precipitates corresponds to the LTR.

Figure 37 shows a TEM bright-field micrograph of a rod-shaped precipitate embedded in an Al matrix. The corresponding SAED pattern of the [001] Al zone axis is shown in the inset. Additional superlattice reflections initiated from the rod precipitate in the SAED pattern are visible. Rod- and lath-shaped precipitates show similar diffraction patterns in the [001] Al zone axis. Since parts of the diffraction pattern initiated from the rod-/lath-shaped precipitates are located at the <100> positions of the aluminium matrix, these precipitates are coherent with the Al matrix along this direction. The diffraction pattern of the [001] zone axis of Al indicates superlattice reflections (Figure 37) that are very similar to those reported in the literature for the same kind of precipitates [165–170]. However, the interpretation of these results differs significantly between authors. While the authors of Refs. [165, 167–169] suggest a hexagonal structure based on the TEM diffraction pattern, the authors of Refs. [170] report a monoclinic structure determined from similar diffraction images. Furthermore, it has been found that both the hexagonal and the monoclinic crystal structure of these precipitates build upon the same Si-based network structure [170]. Due to the coherence of the rod- and lath-shaped precipitates observed along the <100> direction of the aluminium matrix, at least one lattice parameter is known (0.405 nm), which is in agreement with the reported values of the hexagonal structure for β' ($a = 0.705$ nm, $c = 0.405$ nm) and B' ($a = 1.03$ nm, $c = 0.405$ nm) [168, 167, 166, 165]. According to [5], both types of precipitates, β' and B' , can exist concurrently, although B' occurs particularly at high Si:Mg ratios. Hence, it can be assumed that the low-temperature precipitates are β' and/or B' . A recent work [171] confirms the quench-induced precipitation of the hexagonal β' phase during the LTR due to a combination of cooling DSC, TEM, EDS and SAED in an Mn-rich dispersoid-containing model alloy with a composition of Al-0.67Si-0.84Mg-0.35Mn-0.25Fe (mass fraction in %).

Figure 30 shows that at cooling rates faster than 0.5 K/s, the start of the LTR for 6005 is about 400 ± 10 °C, and the peaks of this reaction for all cooling rates faster than 0.16 K/s are located at about 320–340 °C. According to the solvi temperatures determined from first principles modelling in [172], this onset temperature is about 90 K below the solvus of the β' -phase. Hence this reaction is unlikely, due to formation of the β' -phase. Instead, the start temperature corresponds closely (within 10 K) to the solvi temperatures of the hexagonal Al₂MgSi₂ phase, the hexagonal Al₄Mg₈Si₇ phase and the orthorhombic Al–Mg–Si phase

[172]. It has been shown that the Mg:Si ratio in the hexagonal precipitate formed at these temperatures [167, 173] is close to 1.15 [167], and hence the dominant reaction is thought to be the formation of this $\text{Al}_4\text{Mg}_8\text{Si}_7$ phase, which is termed B' (for further discussion, see [BM6]). The length of LTR B' particles is on the order of several hundreds of nm, while their aspect ratio is about 10 [117]. The chemical composition of the rod-/lath-shaped precipitates consists of Al, Si and Mg, and sometimes Cu, as measured by TEM-EDS [BM2]. In most cases, more Si than Mg was detected; however, the chemical composition varied between the individual precipitates.

In addition to the formation of $\beta\text{-Mg}_2\text{Si}$ and B' precipitates, pure Si particles were found after relatively slow cooling, as shown by the particle in Figure 38 for which EDS analysis revealed nearly pure Si (EDS results not shown here). Regarding the precipitation of pure Si in an AlMgSi alloy with excess Si relative to the stoichiometric composition of Mg_2Si , it is reasonable to compare the DSC cooling curves of AlMgSi alloys with those of pure binary AlSi alloys. For the latter, it can be seen that both the HTR and the LTR occur within a temperature range of $\approx 460\text{--}300\text{ }^\circ\text{C}$ at 0.01 K/s. When the same cooling rate for 6005 is compared in the same temperature range, only the HTR peak is seen. In terms of the overlapping reactions beneath the HTRs and LTRs, it can be assumed that the precipitation of Si adds a certain heat effect to the HTRs.

Figure 39 shows detailed images of quench-induced $\beta\text{-Mg}_2\text{Si}$ particles. If precipitated inside a grain, square plate particles with a thickness of about one third of their edge length (i.e. an aspect ratio of 1/3) are common. This can be seen from Figure 39A and B, as the particle in Figure 39A is in a perpendicular plane compared to that of Figure 39B. Stepwise polishing of a metallographic sample revealed this aspect ratio for several particles [131]. For alloys with small grain size close to the size of potential quench-induced $\beta\text{-Mg}_2\text{Si}$ precipitates, the precipitation of $\beta\text{-Mg}_2\text{Si}$ seems to occur only at grain boundaries [BM6]. The $\beta\text{-Mg}_2\text{Si}$ particles at grain boundaries have irregular and variable particle shapes (Figure 39C). At either location, the nucleation of quench-induced $\beta\text{-Mg}_2\text{Si}$ particles appears to occur on coarse (μm range) primary precipitates typically enriched in Fe, Si and Mn (see Figure 39A-C and [131, BM2, BM6]). As exemplified by Figure 39D, nucleation of the LTR B'-phase particles takes place on dispersoids (see also [17, 164, 171, BM6]).

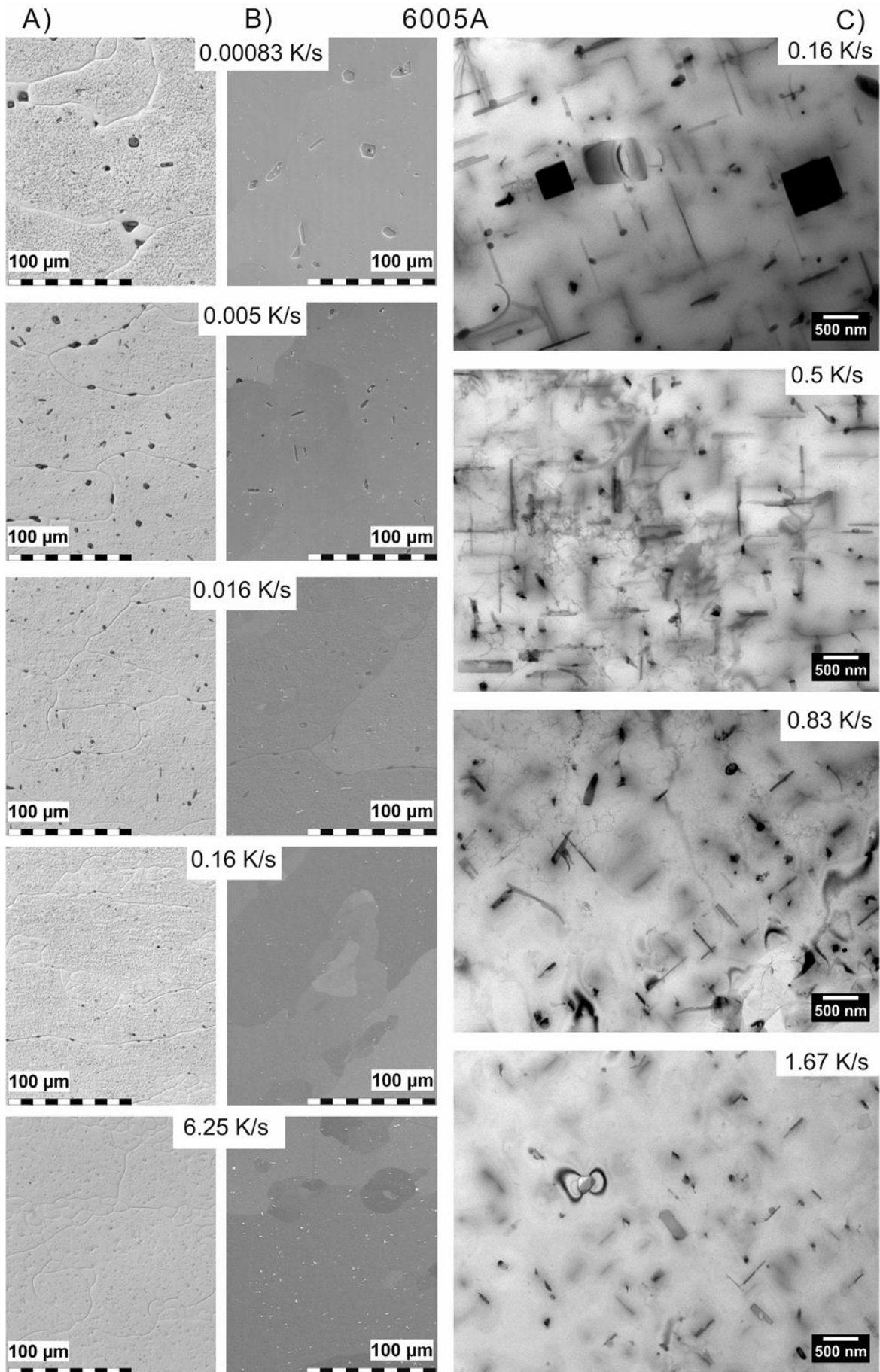


Figure 35: Quench-induced precipitation in 6005A after different cooling rates [BM2]: (A) OM and (B) SEM secondary electron micrographs of quench-induced β -Mg₂Si particles originating from the HTRs; (C) TEM images of quench-induced rod-shaped B' or β' particles. In each case, the particle dimensions are substantially reduced with increasing cooling rate.

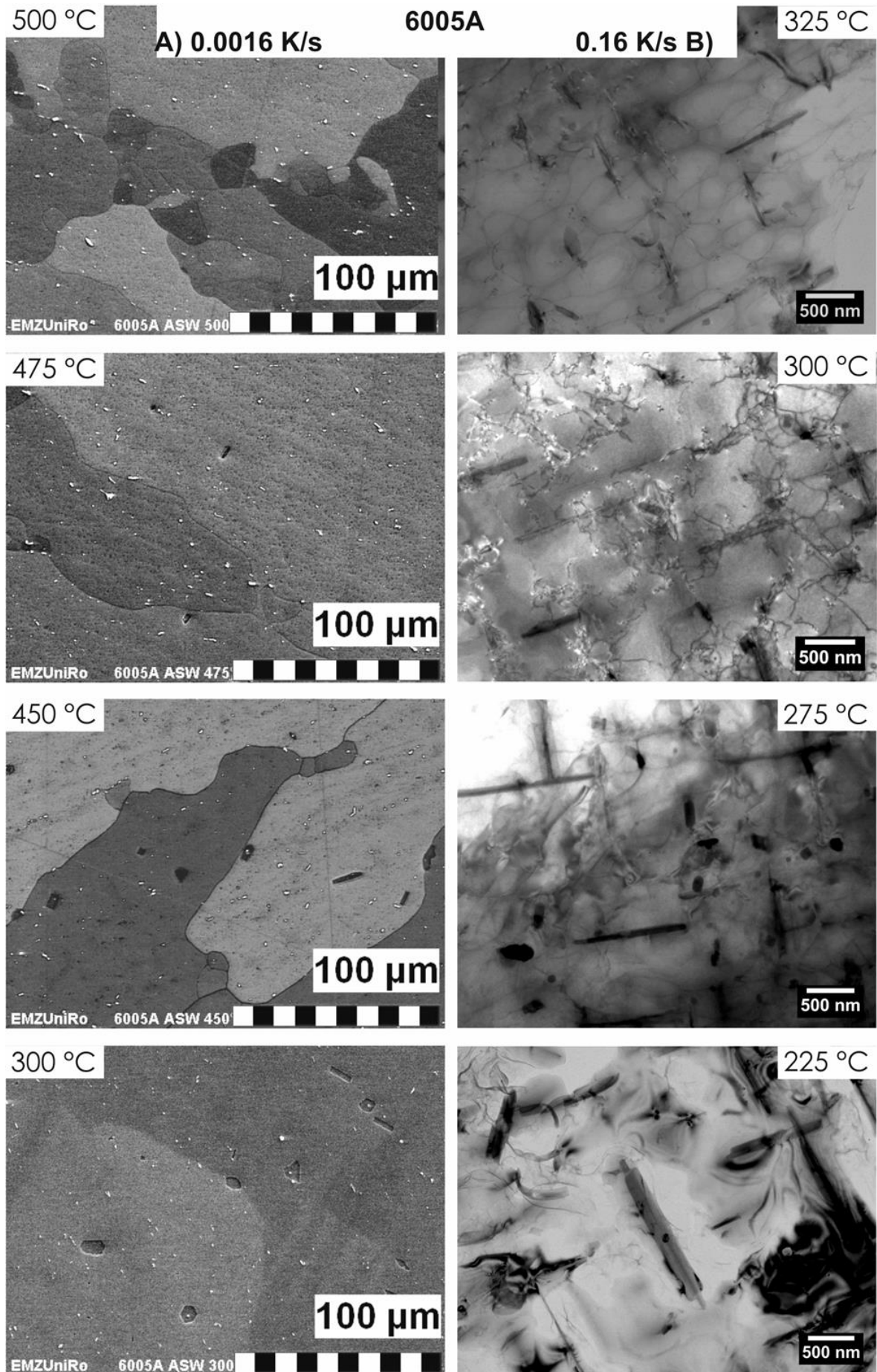


Figure 36: Microstructure of 6005A alloy samples investigated at different temperatures: (A) using SEM backscattered electron images at a cooling rate of 0.0016 K/s; and (B) using bright-field TEM at a cooling rate of 0.16 K/s [BM2].

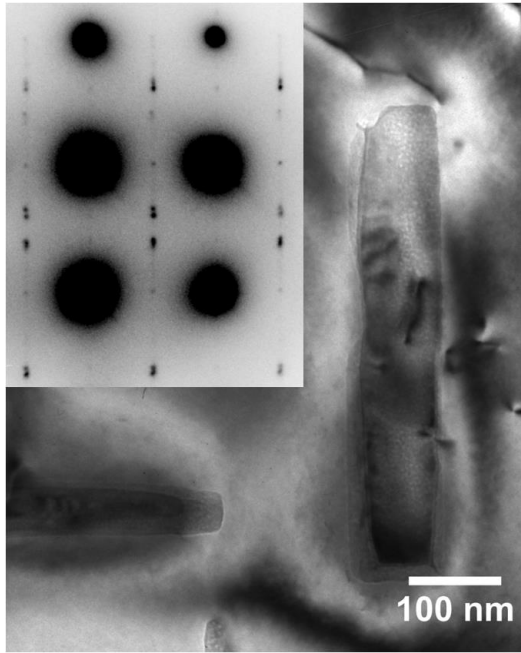


Figure 37: Bright-field TEM micrograph of a 6005A specimen after cooling at 0.16 K/s [BM2].

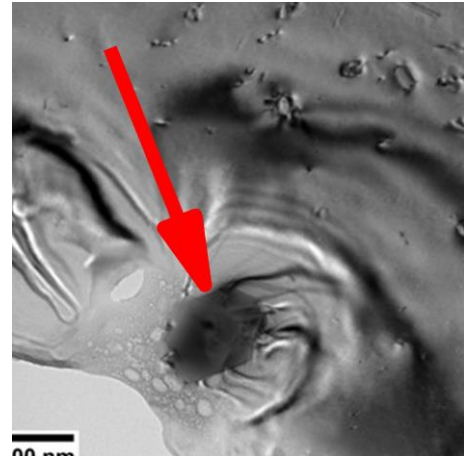


Figure 38: BF-TEM images of a quench-induced hexagonal Si plate particle, precipitated in 6005A cooled from 540 °C 20 in at 0.167 K/s to 375 °C.

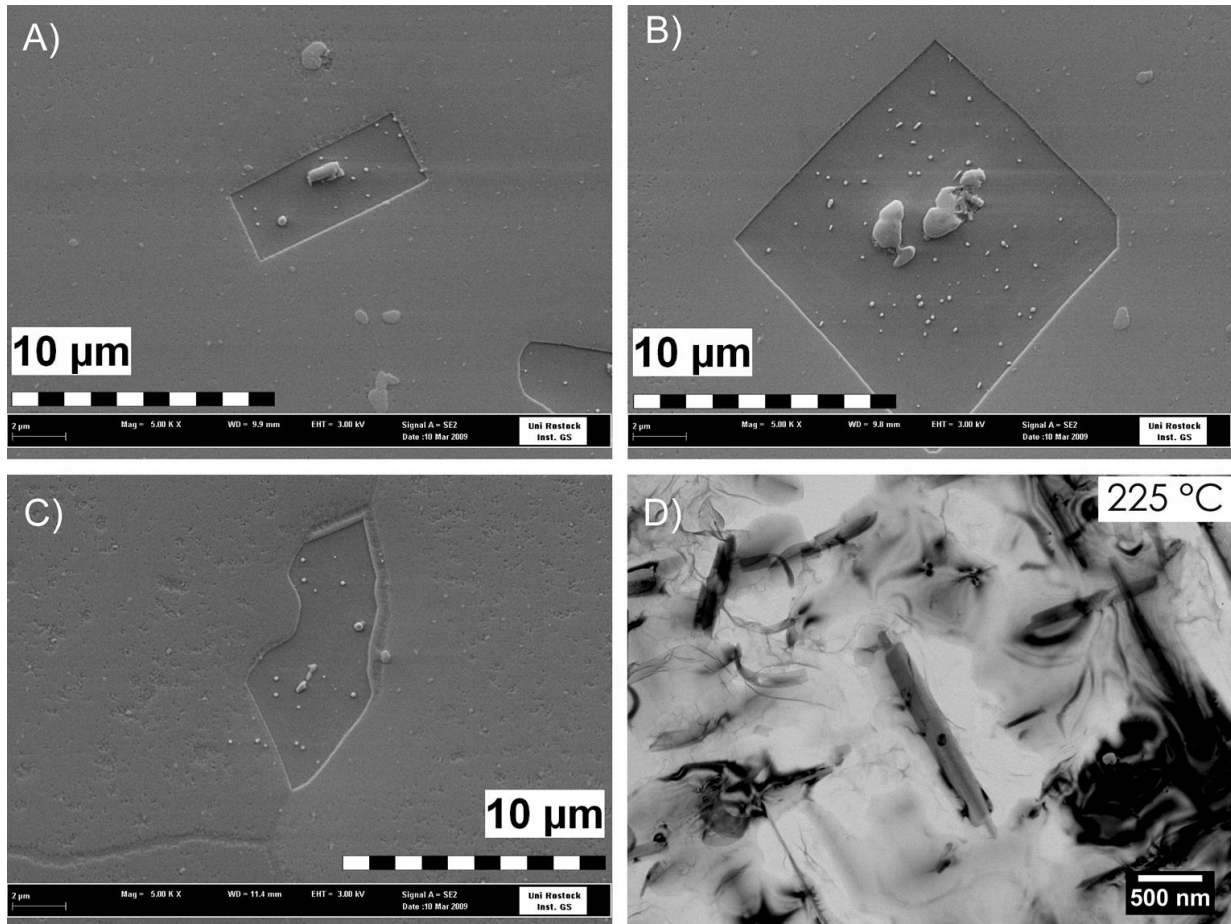


Figure 39: Microstructural details of 6005A: (A)-(C) SEM secondary electron images of Mg_2Si particles after very slow cooling (0.00083 K/s), which all seem to be nucleated on coarse primary Fe-rich particles [131, BM2]. (A), (B) Intragranular precipitated Mg_2Si plates in two perpendicular alignments; (C) Mg_2Si precipitate on the grain boundary; (D) TEM-BF image of rod-shaped precipitate from LTR during cooling with 0.16 K/s to 225 °C (β' / B' [BM6, BM2]). Nucleation seems to take place on an Mn-rich dispersoid particle [BM2].

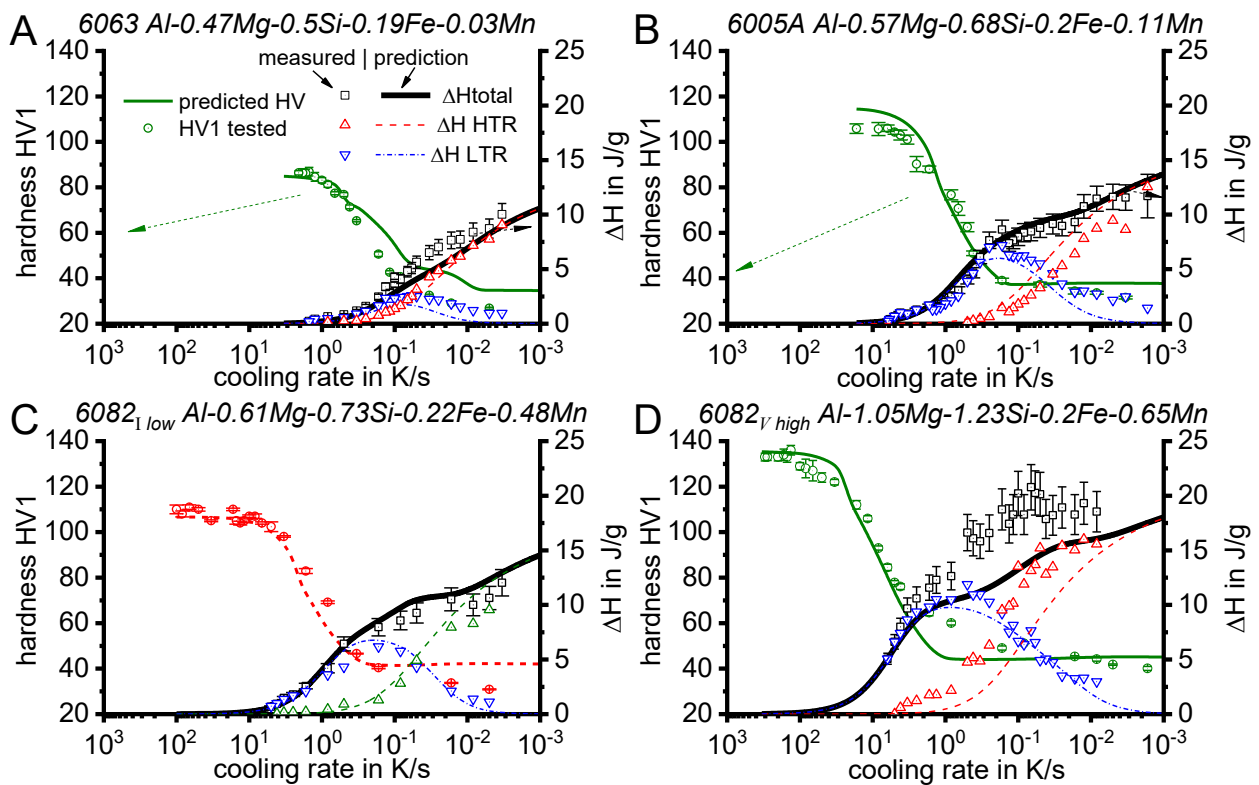


Figure 40: Comparison of measured and predicted values for the specific precipitation enthalpies and hardness after artificial ageing as a function of cooling rate for four AlMgSi alloys. The specific precipitation enthalpy values are plotted for total reactions (black squares), high-temperature reactions (red triangle, tip upwards) and low-temperature reactions (blue triangle, tip downwards). (A) 6063; (B) 6005A; (C) 6082_{low}; and (D) 6082_{high} [BM6].

Figure 40 compares the measured and predicted values of the specific precipitation enthalpy and hardness after ageing for four commercial AlMgSi wrought alloys. The prediction results are drawn from the model derived in Ref. [BM6]. As already seen for 6005A in Figure 30B, the specific precipitation enthalpy generally drops to zero at a certain cooling rate. For higher cooling rates, the hardness typically reaches a saturation level. In general, these model predictions are accurate, and a more detailed discussion is provided in [BM6]. The model considers precipitation of the phases β -Mg₂Si and B'-Mg₅Si₄Al₂. It is also notable that the predicted values for these separate phases show close agreement with the measured enthalpies of the HTR and LTR. This is particularly true for the LTR-quench-induced precipitates of B'-Mg₅Si₄Al₂ and industrially relevant cooling rates.

Figure 41 shows a comparison of the predicted hardness values as a function of cooling rate for 6063 and two variants of 6082. This comparison is especially remarkable in terms of the technological application of age-hardening and the design of the applied heat treatment processes. It can be seen that the highest maximum hardness is achieved for the alloy with the highest alloying element concentration (6082_v) after very rapid quenching. Thus, if the main objective is to obtain maximum hardness and strength, a highly concentrated alloy is required, although it is also necessary to ensure sufficiently fast cooling via the technologically applied cooling process. It may be difficult, if not impossible, to achieve >100 K/s as an average cooling rate in the relevant temperature range (\approx 500–200 °C) for thick sections and large batches/loads. In such conditions, it might be more appropriate to choose a leaner alloy. As can be seen from Figure 41, in a certain range of slower cooling rates, the maximum hardness is achieved with the leanest alloy in this comparison. Slower cooling rates may be of interest, for instance due to requirements

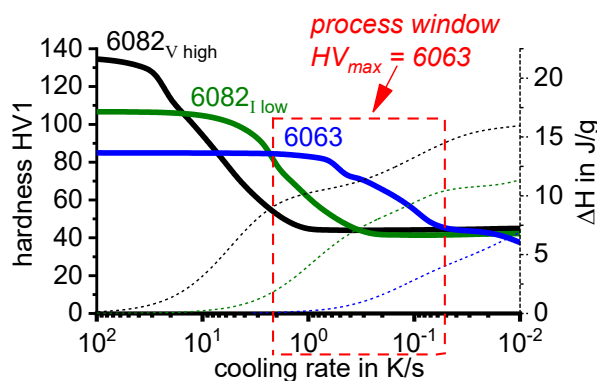


Figure 41: Comparison of hardness after ageing and total precipitation enthalpy predicted by the model from Ref. [BM6] for alloys 6063, 6082_I, and 6082_v.

for distortion control or reduction. The results obtained in this work allow us to choose either a suitable process for a specific alloy or a suitable alloy for a certain fixed process.

In Ref. [BM10], it was shown for 6082_{III} that β -Mg₂Si particles, which are not fully dissolved during (insufficient) solution treatment, strongly influence the mechanism of nucleation and growth of quench-induced precipitates. Partly dissolved β -Mg₂Si particles may occur for instance when a solution temperature below the solvus is chosen, or a solution temperature very close to the solvus temperature with short soaking durations. In the presence of undissolved β -Mg₂Si at the end of the solution treatment, no additional nucleation is required with the onset of cooling, and these undissolved β -Mg₂Si particles instantaneously start to grow. This effect considerably increases the quench sensitivity of the alloy. In this way, the critical cooling rate can be increased by a factor of three, and the hardness after ageing can be reduced by about 30 % for medium cooling rates [BM10]. As an additional effect in such cases, the HTR dominates over the entire cooling rate range (Figure A1 H).

Furthermore, the alloying elements Fe and Mn are of primary importance for the nucleation of quench-induced precipitation, as these elements are typically found in either coarse primary particles, which act as nucleation sites for HT-Mg₂Si particles, or in dispersoids, which are the preferred nucleation sites of the rod-shaped LT particles [17, 23, 48, 161, 171, 174]. Nevertheless, the influence of these minor element additions has not yet been fully quantified. One attempt to quantify the influence of dispersoid forming elements is presented in Figure 42, which shows a comparison of the commercially produced 6082_I and a pure ternary Al_{0.6}Mg_{0.8}Si alloy. Both alloys have a highly similar content of the main alloying elements, Mg and Si. The major difference between them is the additional mass fraction of 0.2 % Fe and 0.5 % Mn in 6082_I (atomic fractions: 0.11 % Fe; 0.24 % Mn). Figure 42A and B show the DSC cooling curves of both alloys, while Figure 42C and D compare the specific precipitation enthalpy after cooling and the hardness after additional ageing, respectively.

In Al_{0.6}Mg_{0.8}Si, the HTRs are dominant over the entire range of cooling rates, and it can be concluded that the equilibrium phase β -Mg₂Si is primarily precipitated. Compared to the commercial variant, substantially reduced LTRs are seen for the pure alloy, and this is probably due to the reduced number of nucleation sites. A direct comparison at about 0.1 K/s shows that for the commercial 6082_I, quench-induced precipitation is clearly dominated by the LTR, while quench-induced precipitation for Al_{0.6}Mg_{0.8}Si is dominated by the HTR. For cooling rates higher than 0.5 K/s in Al_{0.6}Mg_{0.8}Si, barely any reaction can be seen in DSC, whereas for 6082_I the LTRs are still well above the DSC detection limit and the total specific

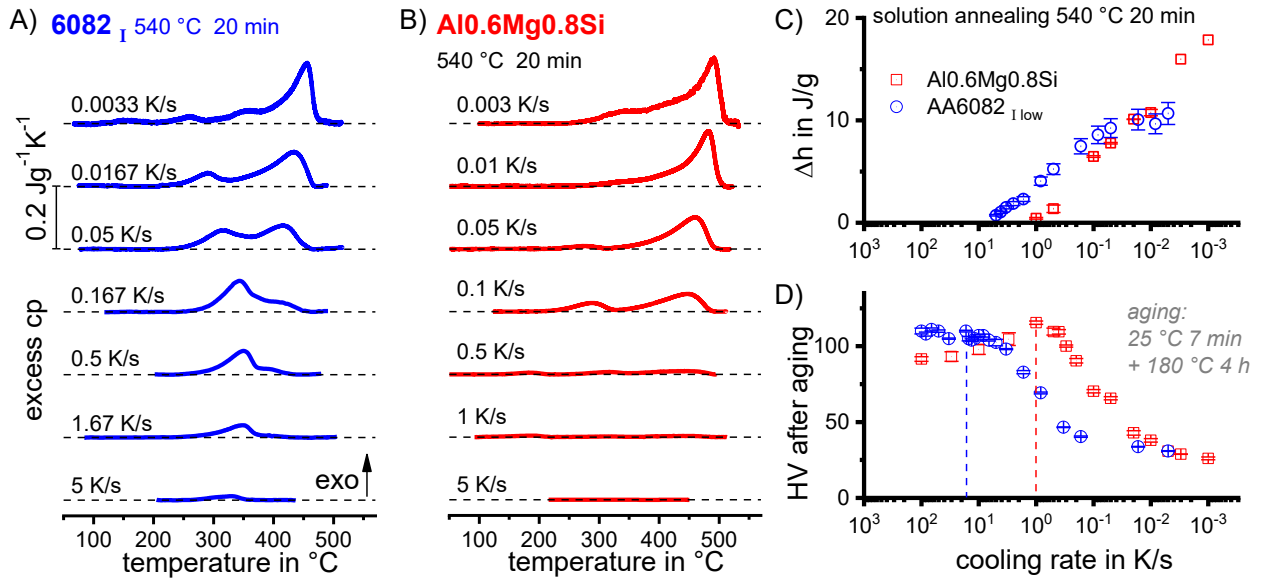


Figure 42: DSC cooling curves for (A) 6082 I and (B) Al_{0.6}Mg_{0.8}Si; (C) total specific precipitation enthalpies; and (D) hardness after ageing of both alloys as functions of cooling rate.

precipitation enthalpy still amounts to about 5 J/g for 0.5 K/s (see Figure 42C). Although both alloys can achieve the same maximum hardness, this maximum is reached at substantially different cooling rates. A comparison of Figure 42C and D shows that the UCCRs of these two alloys differ by a factor of ≈ 20 , which quantifies the influence of an addition of an atomic fraction of $\approx 0.35\%$ Fe+Mn to a medium AlMgSi alloy. This factor may of course also depend in detail on the particular distribution size of the dispersoid particles and therefore on the homogenisation treatment [48]. It is also interesting to note from Figure 42 that the solvus temperature of these two alloys differs. For cooling at a rate of 0.003 K/s, the onset of quench-induced precipitation for Al_{0.6}Mg_{0.8}Si is about 510 °C, while for 6082_I it is about 475 °C. It can be assumed that Si is partially bound in the eutectic primary phases and dispersoids, thus reducing the Si solute concentration at the end of the solution treatment and thereby the solvus temperature. This assumption is supported by the total specific precipitation enthalpy, for which $\Delta h_{\text{Al}_{0.6}\text{Mg}_{0.8}\text{Si}} > \Delta h_{\text{6082I}}$ holds during very slow cooling. The abovementioned differences in the nucleation of the equilibrium β -Mg₂Si phase (commercial alloy: coarse primary particles enriched in Fe, Mn, Si; lab alloys: unclear) suggest that the HTR-quench-induced precipitates nucleate more easily in commercial alloys. However, the higher precipitation onset temperature for Al_{0.6}Mg_{0.8}Si hints at the dominating influence of a higher amount of solved alloying elements, particularly Si, on precipitation onset in the stable phases. The opposite behaviour is seen for the LTR, which is obviously much more strongly influenced by nucleation promoted in the presence of dispersoids.

Another interesting aspect can be seen in Figure 42D, in which the hardness after cooling and ageing for pure Al_{0.6}Mg_{0.8}Si shows a maximum at the UCCR determined by DSC, and unlike all other alloys studied in this work, the hardness drops with faster cooling rates. Similar results have been reported for high-purity AlZnMg alloys [175]. It is possible that small quench-induced precipitates forming around the UCCR contribute a hardening effect.

The information revealed on the nature of quench-induced precipitates for AlMgSi alloys is summarised in Table 2.

Table 2 Quench-induced phases in AlMgSi alloys

	Quench-induced phases	Alloy	Precipitation temperature range from DSC	Particle morphology and (aspect ratio: length/thickness)	Nucleation on	Reference
Stable phases	β -Mg ₂ Si, fcc	6005A	HTR	Plates (3)	Coarse primary Fe, Si, Mn-rich particles (inside the grain and on grain boundaries) or on undissolved Mg ₂ Si [BM10]	[BM2, 131]
		Al0.6Mg0.8Si	HTR & LTR	Plates (?) and needles? (100)	?	This work
	Si, diamond cubic	6005A	HTR (LTR?)	Polygonal particles (close to 1) Potentially plates	?	This work
Metastable phases	β' -Mg ₉ Si ₅ , hexagonal	6005A	LTR	Rods (19)	Dispersoids	[BM6]
		Al0.67Si0.84 Mg0.35Mn0.2 5Fe (mass %)				[171]
		Al0.6Mg0.8Si Al0.8Mg0.6Si	LTR	Rods/plates?	?	This work
	B'-Mg ₅ Si ₄ Al ₂ , hexagonal	6005A 6082	LTR	Rods (10)	Dispersoids (potentially on grain boundaries)	[BM2, BM6]

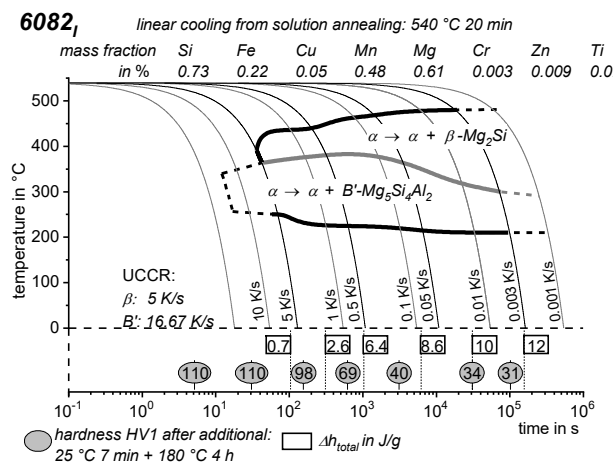


Figure 43: CCP diagram for 6082₁ [138, BM2]

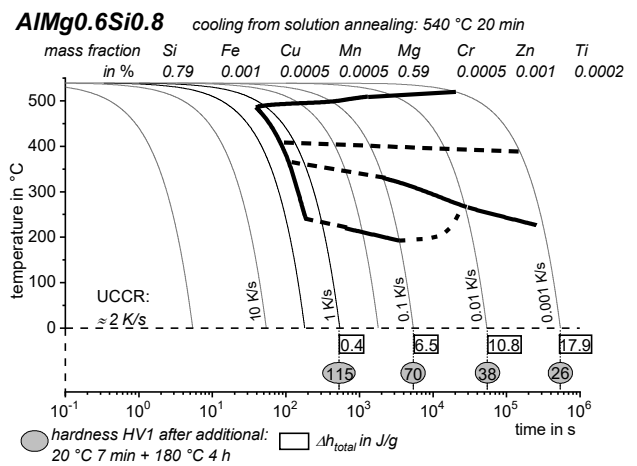


Figure 44: CCP diagram for Al0.6Mg0.8Si

The CCP diagrams for 6082₁ and Al0.6Mg0.8Si are compared in Figure 43 and Figure 44, respectively. Here, we can see a considerable difference between these alloys, which is caused by the different numbers of nucleation sites and thus different nucleation mechanisms for quench-induced precipitates. A comparison with a CCP diagram for a 6082 alloy obtained from in situ electrical resistivity curves is possible by considering Ref. [85]. In Ref. [85], over a cooling rate range of ≈16–0.03 K/s, the precipitation start temperature was found to be about 375 °C, which is close to the start of the LTR determined by DSC

(compare Figure 43). In Ref. [85], the end-temperature of precipitation was evaluated to be about 225–300 °C, which is comparable to the end of the LTR identified by DSC. From this, it can be concluded that the in situ electrical resistivity measurements were able to detect the LTR in 6082. It seems likely that the HTRs were not identified by this method; however, the UCCR was determined within a range of ≈ 16 to 30 K/s [85], which is very similar to that identified for 6082, [BM2].

3.2.3 7xxx AlZnMg(Cu) wrought alloys

Ten variants of the alloying system AlZnMg(Cu) are considered in this work. Due to the multiple potential combinations of alloying elements, the 7xxx alloying system can be considered a very complex system in terms of precipitation. It is often a quaternary system, as in addition to Al, Zn and Mg, Cu and other elements such as Si are often incorporated. Cu and Si may add additional precipitation sequences, for instance those of δ -Al₂CuMg and/or β -Mg₂Si [35, 176]. Moreover, the Zn- and Mg-containing phases do not have a fixed composition, and isostructure variants are known for the η -Mg(Zn,Al,Cu)₂ phase [177, 178]. For most of the 10 AlZnMg(Cu) alloys analysed here, DSC indicates the presence of three or four different main reaction intervals during cooling. DSC cooling curves for 7020 (an AlZnMgSi alloy) and 7150 (an AlZnMgCu alloy) can be seen in Figure 45 and Figure 46, respectively. Although these two alloys have substantially different alloy compositions, they both show at least three main reaction intervals, which are

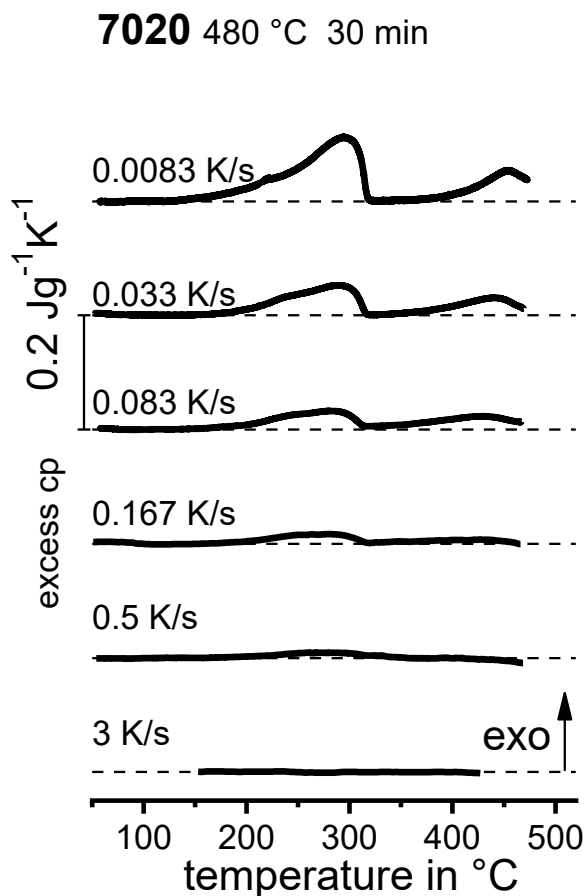


Figure 45: Cooling DSC curves for 7020.

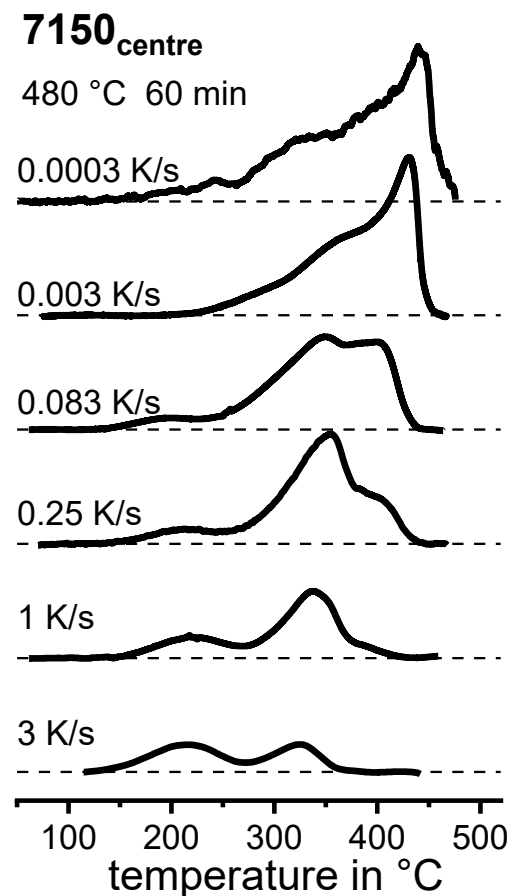


Figure 46: Cooling DSC curves for 7150.

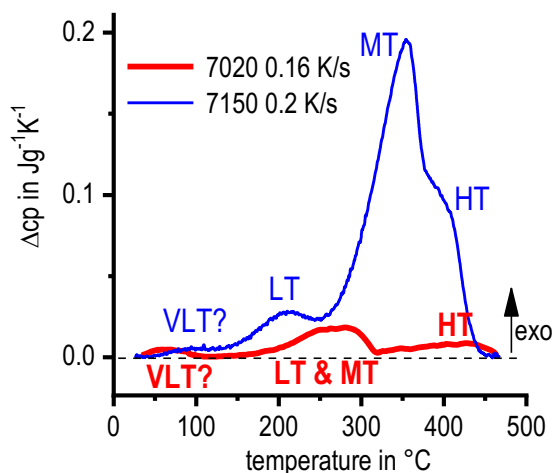


Figure 47: Cooling DSC curves for 7150 and 7020, showing hints of a precipitation reaction at very low temperatures (150 to 50 °C) [BM3].

HTRs (typically $\approx 450\text{--}350\text{ }^{\circ}\text{C}$), medium-temperature-reactions (MTRs, $\approx 350\text{--}250\text{ }^{\circ}\text{C}$) and LTRs, ($\approx 250\text{--}150\text{ }^{\circ}\text{C}$). This holds for the majority of the 10 AlZnMg(Cu) alloys investigated, as can be seen from Figure A3 in the appendix. In some cases, a fourth reaction was detected at an even lower temperature of about $150\text{--}50\text{ }^{\circ}\text{C}$, as shown in Figure 47. For the 7xxx alloys with highest concentration of alloying elements such as 7075, 7049A (Figure A3 in the Appendix and Refs. [153, 152]) and 7068 [179], cooling DSC appears to show only one very broad peak, which ranges from about 450 to $150\text{ }^{\circ}\text{C}$. It can be assumed that this very broad heat effect is caused by the sum of numerous reactions.

The in situ cooling DSC experiments shown in Figure 46 cover four orders of magnitude and thereby an extreme dynamic DSC. The slowest cooling at 0.0003 K/s requires a cooling duration of >17 days, while the fastest cooling 3 K/s is completed within 2.5 min. Furthermore, DFSC was performed for this alloy, extending the investigated scanning rate range to some hundreds of K/s. Thus, the fastest cooling was achieved in times of less than 1 s.

Similarly to the AlSi and AlMgSi alloys, the reactions are in total increasingly suppressed with increasing cooling rates. Thus, in most cases, the reactions at higher temperatures are first suppressed, while the reactions at lower temperatures first show an increase in the fraction transformed. The latter is due to the increased concentration of alloying elements left in solution after the suppressed HTR is complete.

The type and nature of quench-induced precipitation in 7xxx alloys has been widely investigated [31, 35, 104, 105, 176, 180–183, BM3, BM8]. In general, it can be stated that in presence of Cu, the S-Al₂CuMg phase is precipitated, and in the presence of Si, the β -Mg₂Si phase is precipitated during the HTRs [176, 184, BM3, BM7]. Nucleation of these two phases appears to take place on coarse intermetallic particles. In almost every AlZnMg alloy, the MTRs seem to be dominated by the precipitation of isostructure variants of the η -Mg(Zn,Al,Cu)₂ phase [BM7]. Examples of this quench-induced phase are seen in Figure 48. Nucleation of quench-induced η -Mg(Zn,Al,Cu)₂ apparently occurs on dispersoids [31, 35, 176, 181–183, BM7]. In cold-rolled sheet material, dispersoids are heterogeneously aligned in lines, resulting in bands of quenched-induced precipitates [183]. As a result, fine precipitates originating from ageing can only be found heterogeneously distributed between the bands of quench-induced precipitates [182].

In AlZnMg(Cu) alloys, quench-induced precipitates of the η -Mg(Zn,Al,Cu)₂ phase can be considered the most detrimental precipitation in terms of quench sensitivity, since this phase forms at relatively fast cooling rates while its precipitates barely have a hardening effect. Quench-induced phases at even lower temperatures, namely thin Y-phase platelets [185, BM7, BM8] and clusters [103–105], may form during even faster cooling. These quench-induced precipitates are small enough to cause a significant hardening effect [BM8].

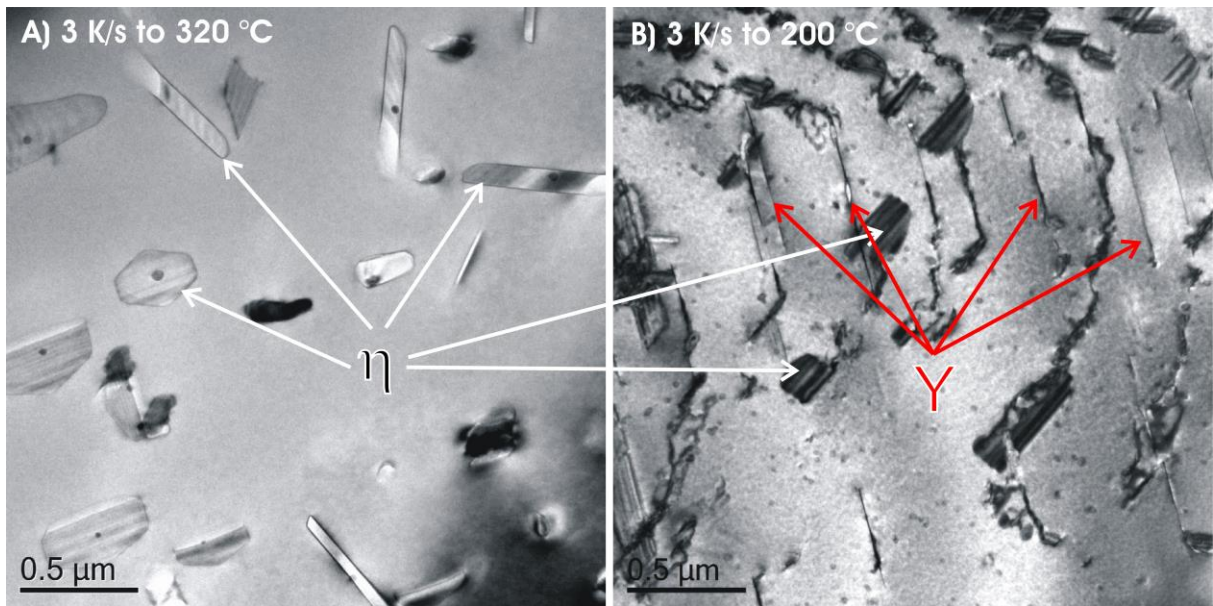


Figure 48: Quench-induced precipitation in 7150 during cooling at 3 K/s [BM9].

As outlined in several prior works [31, 35, 86, 176, 181, 186–191], nucleation of quench-induced η -Mg(Zn,Al,Cu)₂ takes place on dispersoids. At least for Al₃Zr dispersoids, it has also been shown that their nucleation activity for quench-induced η -Mg(Zn,Al,Cu)₂ is dependent on the interface relation of the dispersoid to the matrix [176, 181], and only incoherent Al₃Zr dispersoid particles appear to be active nucleation sites for η -Mg(Zn,Al,Cu)₂. Al₃Zr dispersoids are typically coherent with the Al matrix, although after thermo-mechanical processing, recrystallisation can occur. This recrystallisation in the Al matrix can change the interface of the dispersoid towards incoherence. An example of this phenomenon is seen in Figure 49, which shows a TEM image of hot-rolled 7150 [176, 181]. Subgrains and recrystallised grains were distinguished by the lattice orientation, as revealed by SEM-EBSD (see Refs. [181, 176] for details). Quench-induced η -Mg(Zn,Al,Cu)₂ particles are found at subgrain-boundaries and in the recrystallised grain shown on the left, nucleated on incoherent Al₃Zr dispersoids. However, in the non-recrystallised subgrains, the coherent Al₃Zr dispersoids do not have quench-induced precipitates attached.

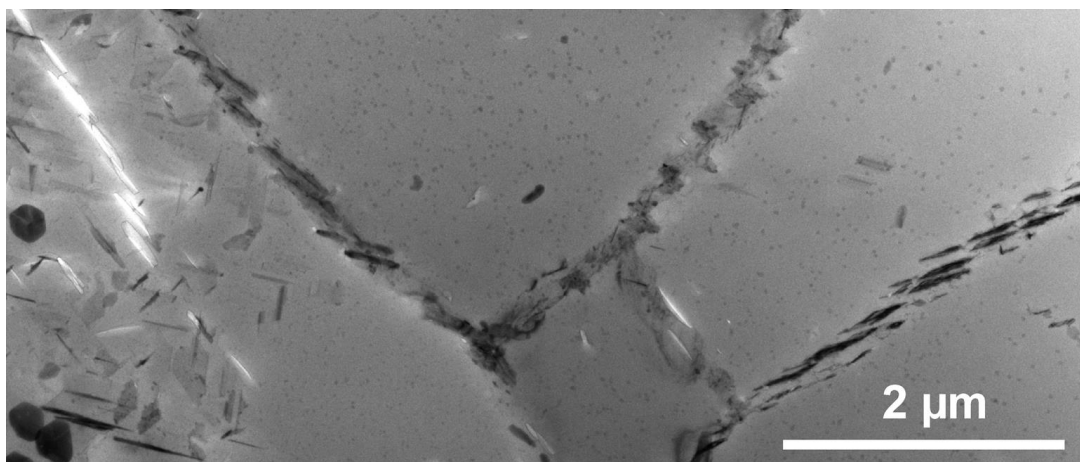


Figure 49: TEM image of an air-cooled 7150 sample (average cooling rate 1 K/s) showing a recrystallised grain on the left-hand side and several subgrains on the right. It can be seen that the quench-induced η -Mg(Zn,Al,Cu)₂ precipitates preferentially nucleate at grain/subgrain boundaries and also appear inside the recrystallised grain, nucleating at Al₃Zr dispersoids [BM7].

The LTR in 7150 has been shown to relate to a previously unknown thin plate phase that is enriched in Zn and Cu, and it was labelled as the Y-phase [BM8]. Y-phase platelets have been confirmed to form during cooling by others too [185]. An example of a Y-phase platelet can be seen in the high angle annular dark field (HAADF)-STEM images in Figure 50. Based on the interrupted quenching method, we conclude that the LTR in a temperature range of about 250–150 °C is dominated by the precipitation of the Zn–Cu-rich thin plate Y-phase (compare Figure 48 with the DSC curve of 3 K/s in Figure 46). The Y-phase features strong structural similarities to the T1 phase in Al-Li alloys, with a hexagonal symmetry ($a = 0.429$ nm, $c = 1.385$ nm). The authors of Ref. [88] assume the low-temperature precipitation to refer to the η' -phase.

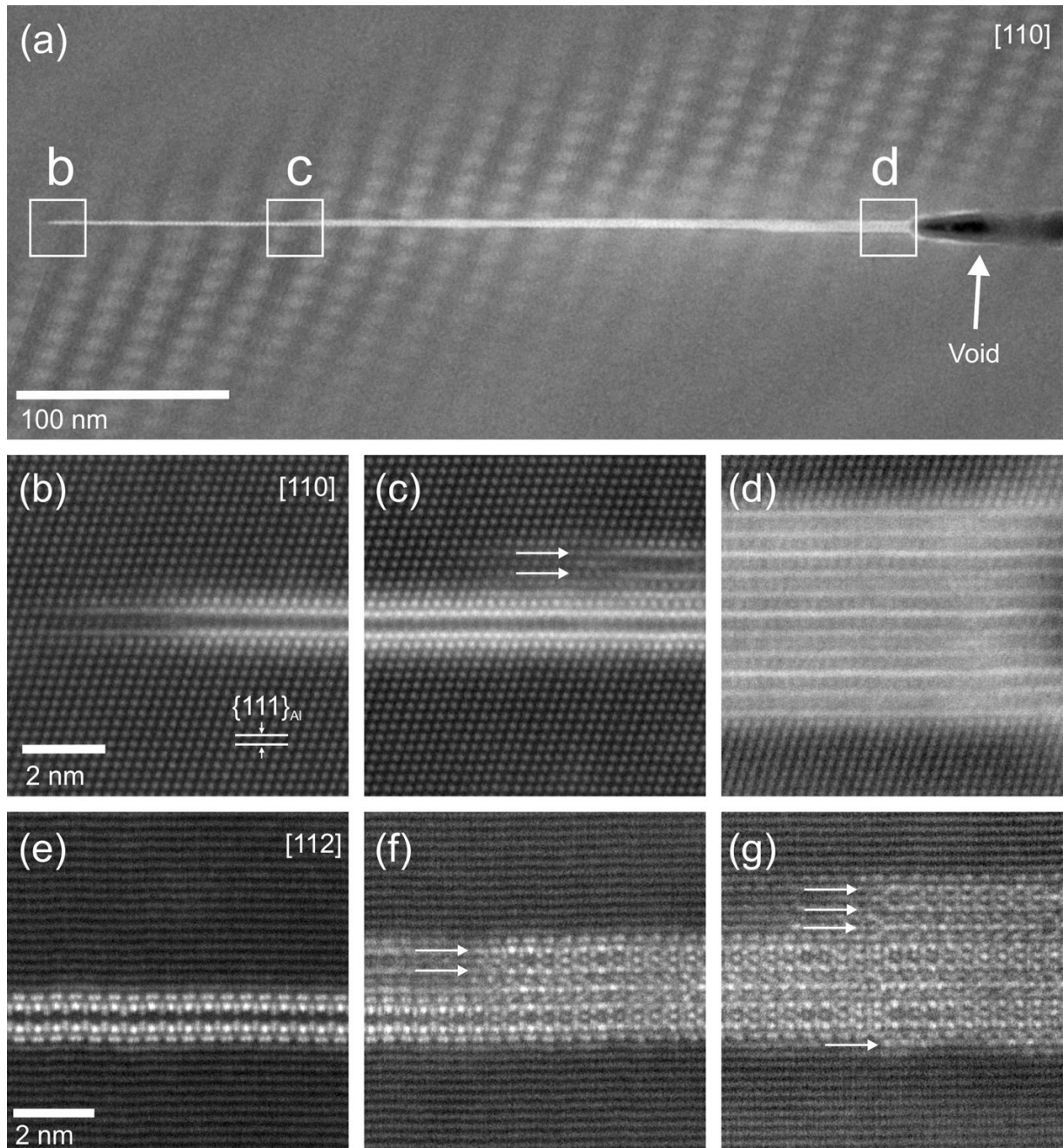


Figure 50: HAADF-STEM images of Y-phase platelets enriched in Zn and Cu after cooling of 7150 at 10 K/s, viewed from the $[110]_{\alpha}$ direction, showing that the thickness varies along its length, with growth ledges indicated by arrows in (C). The regular pattern in the matrix on either side of the plate in (A) is an artefact caused by Moiré fringing between the lattice and scan frame. This plate appears to be nucleating from an attached void. Similar images in (E–G) from a second plate, but viewed from the $[112]_{\alpha}$ direction, show variations in thickness and stacking order along the length of the precipitate [BM8].

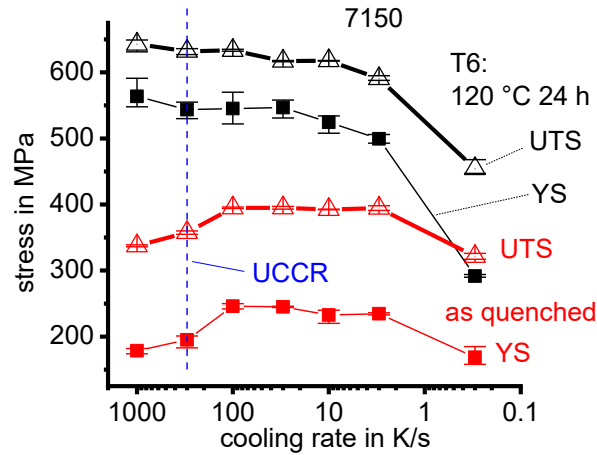


Figure 51: Ultimate tensile strength and yield strength of 7150 in the as-quenched and artificially aged conditions [BM8].

At even lower temperatures of about 150 to 50 °C (see VLT peak in the DSC curves in Figure 47), co-clusters may precipitate during quenching, as shown in SAXS experiments involving continuous cooling of 7449 to below 100 °C in Refs. [104, 105]. The small Y-phase platelets and clusters cause a direct hardening effect, which is seen in the peaks in the as-quenched hardness, yield strength and ultimate tensile strength for cooling rates of about one to two orders of magnitude slower than the UCCR [BM8]. Tensile testing indicates that this Y-phase appears to contribute up to ≈ 50 MPa to the as-quenched strength in the investigated alloy 7150 (see Figure 51, [BM8]).

The findings on quench-induced precipitation in AlZnMg(Cu) alloys are summarised in Table 3.

In Figure 52, the experimentally obtained values for the total specific precipitation enthalpy after cooling and the hardness after artificial ageing of six different AlZnMg(Cu) alloys are compared to the predictions of the model derived in Ref. [BM7]. A general chart of these values as a function of cooling rate for each 7xxx Al alloy investigated is given in the appendix, in Figure A4. As can be seen from Figure 52, the model

Table 3: Quench-induced phases in AlZnMg(Cu) alloys

	Quench-induced phases	Alloy	Precipitation temperature range from DSC	Particle morphology (Aspect ratio)	Nucleation	Reference
Stable phases	S-Al ₂ CuMg	7150	HTR	(<5?)	On coarse primary Al ₇ CuFe and grain boundaries	[176, BM3, BM7]
	β -Mg ₂ Si	7020	HTR	Plates (?)	(?)	
	η -Mg(Zn,Al,Cu) ₂	7150	MTR	Polygonal plates (<10)	On dispersoids [31, 181] and grain boundaries [176, BM7]	
		7020	MTR	Plates (?)	(?)	
Metastable phases	Y-phase (enriched in Zn, Cu)	7150	LTR	Thin plates (≈ 100)	Presumably on vacancy clusters or dislocations	[BM7, BM8]
	Cluster	7449	vLTR			[105, 104]

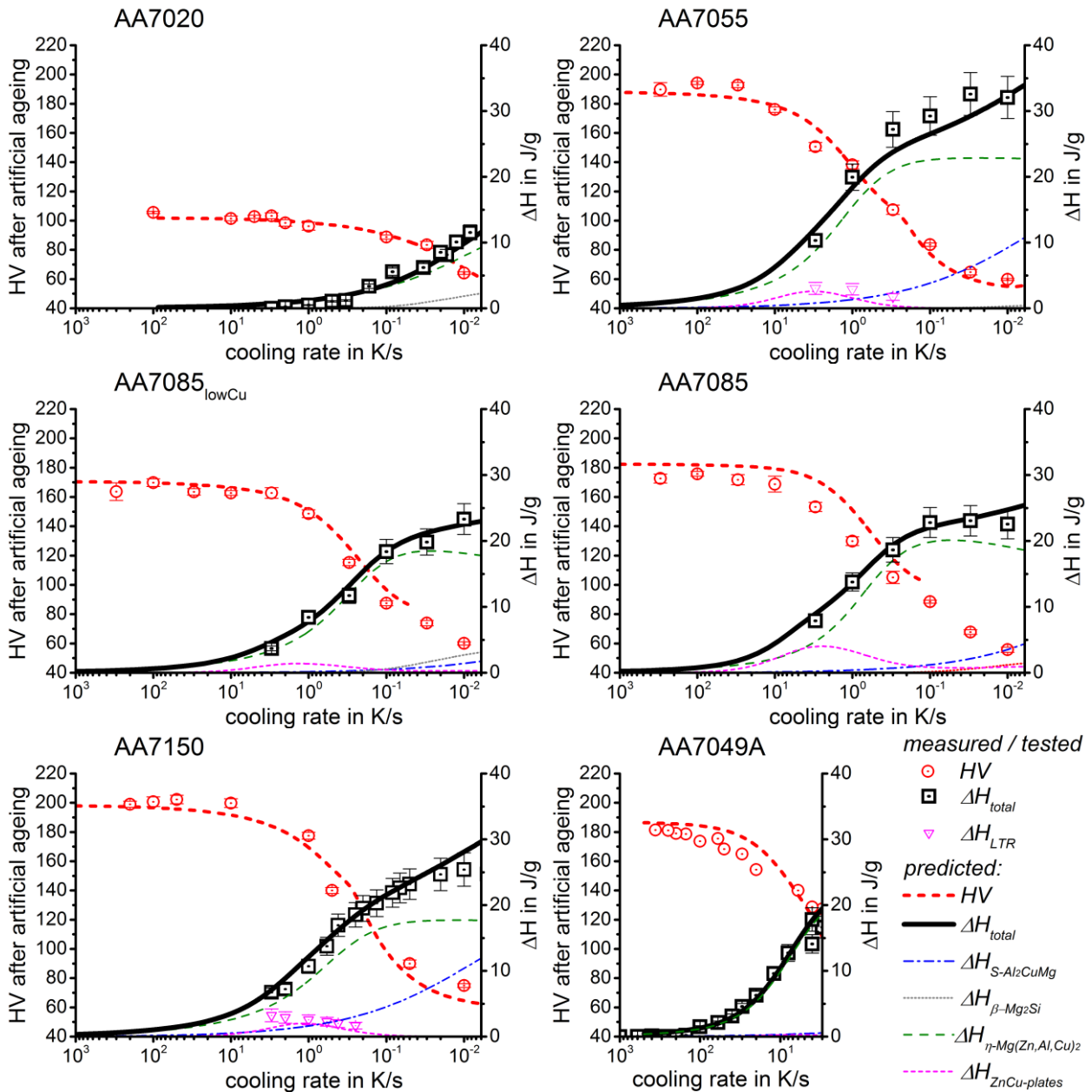


Figure 52: Measured values and model predictions for hardness after ageing and specific precipitation enthalpies of six AlZnMg(Cu) alloys [BM7]. Values for the total specific precipitation enthalpy were obtained by in situ cooling DSC as outlined above. For 7049A, chip-sensor based differential fast scanning calorimetry was applied [124, 153].

predictions are found to be very accurate to a wide range of AlZnMg(Cu) alloys and the total specific precipitation enthalpy generally decreases with increasing cooling rate for all alloys. A high level of similarity to the AlMgSi alloys is found for the general kinetic behaviour. However, the specific enthalpy values, as well as the obtainable hardness values, are generally higher for the 7xxx alloys. This is reasonable, as the latter contain higher concentrations of alloying elements. As for the 6xxx alloys, the hardness after ageing reaches a saturation level for cooling rates above the UCCR ranging from about 3 K/s for 7020 to about 300 K/s for highly concentrated alloys such as 7150 or 7049A.

As discussed for AlMgSi alloys, it also holds for AlZnMgCu alloys that a lower concentrated AlZnMgCu alloy can achieve higher hardness values if cooling is restricted to medium cooling rates. Figure 53 compares 7075₁, 7085 and 7085_{lowCu}. Of these three variants, 7085_{lowCu}, has the lowest Mg content, despite its low Cu content. The age-hardening potential of 7085_{lowCu} that remains after cooling at 1 K/s results in a hardness

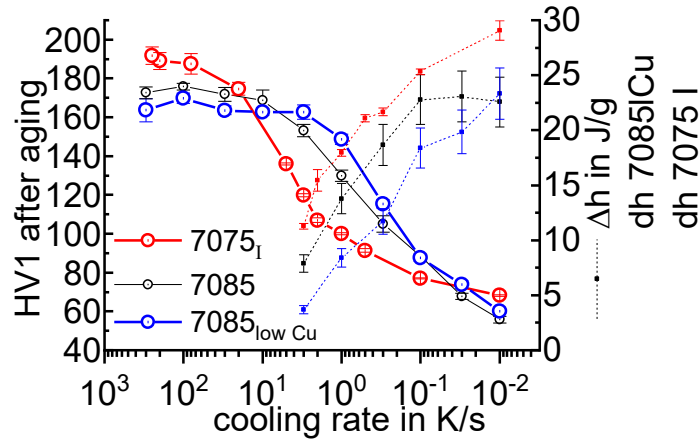


Figure 53: Comparison of experimentally obtained specific precipitation enthalpies after cooling and hardness after additional ageing for three differently concentrated AlZnMgCu alloys.

of almost 150 HV1. At this cooling rate, the age-hardening potential of 7075_I has already dropped to just 100 HV1. Under these conditions, the lower concentrated alloy would achieve $\approx 150\%$ of the strength of the highly concentrated alloy (i.e. 7085_{low Cu} is less quench sensitive than both 7075_I and 7085). Considering the concentrations of alloying elements, it can be assumed that the concentration of Mg predominantly drives the precipitation kinetics. This fits with the finding in [BM7] that the main quench-induced precipitate phase that causes quench sensitivity is $\eta\text{-Mg}(\text{Zn,Cu,Al})_2$ for these types of alloys.

In general, it is found that the AlZnMgCu series should be considered very quench sensitive. This is reasonable, as these alloys typically contain the highest concentration of alloying elements amongst the age-hardening Al alloys. However, there are indications that small additions of Ge and Ag might reduce the quench sensitivity of 7xxx alloys [192].

From Figure 52 and Figure 53, it also becomes obvious that in several cases, a substantial amount of enthalpy change caused by quench-induced precipitates is detected. Figure 52 includes experimental findings from DFSC obtained on 7049A in a range of cooling rates up to some hundreds of K/s [124, 153]. As outlined in Section 3.1.3, DFSC allows us to obtain the specific precipitation enthalpies of highly concentrated alloys via a differential reheating measurement [124, 153, BM9]. This is demonstrated in Figure 54A, which shows raw DFSC data for the first reheating (after relatively “slow” cooling with 10 K/s) and a second reheating after overcritical fast cooling (100,000 K/s, baseline). During the first reheating at 1000 K/s, endothermic dissolution reactions of phases precipitated during the preceding “slow” cooling are clearly seen. Figure 54B shows DFSC data for cooling rates of up to 500 K/s. Normalisation by sample mass and scanning rate and subsequent integration of the curves, as shown in Figure 54B, allows us to obtain the specific precipitation enthalpies as a function of cooling rate [BM9]. Figure 55A shows precipitation enthalpies for six samples of 7150 [BM9]. In Figure 55B, the averaged DFSC values from [BM9] and data from DSC [BM3] are plotted, and these fit together smoothly. The UCCR of 7150 was determined to be about 300 K/s for 7150 [BM9]. In Figure 55, the solid lines for the specific precipitation enthalpy Δh and for the hardness after ageing are the model predictions from [BM7]. The model predictions were created without knowledge of the DFSC data, as the DFSC experiments had not yet been done. Very good agreement between the measured and predicted values is seen, and this further confirms the high accuracy of the derived model for quench-induced precipitation of AlZnMg(Cu) alloys.

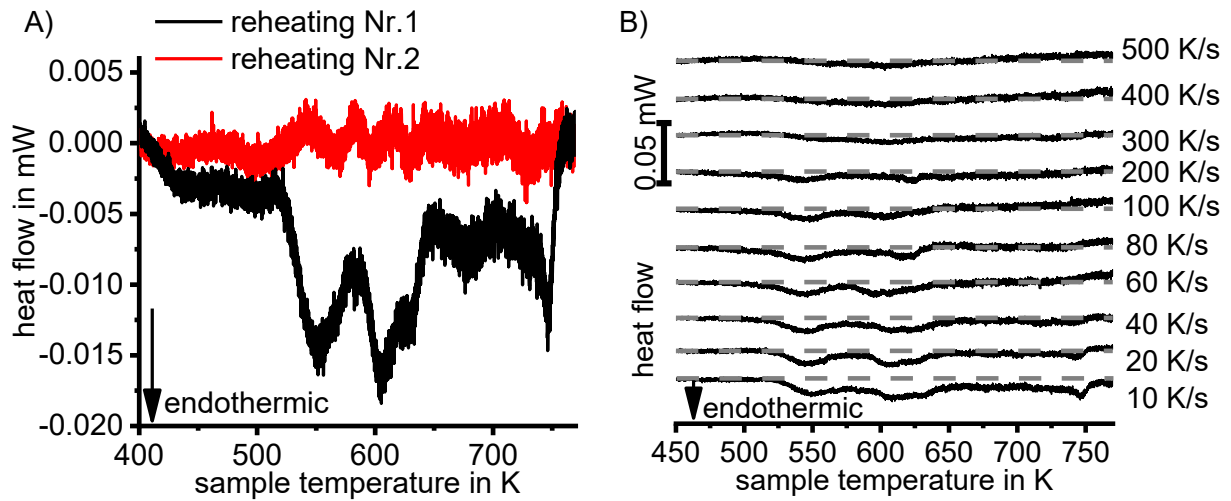


Figure 54: (A) Raw 1000 K/s reheating curves for states previously cooled at rates of 10 K/s (first reheating) and 10^5 K/s (second reheating = baseline measurement). (B) Subtracted measurement curves, i.e. curves measured for the first reheating minus the curves measured for the second reheating, for various cooling rates. The baselines for integration are indicated by dashed lines [BM9].

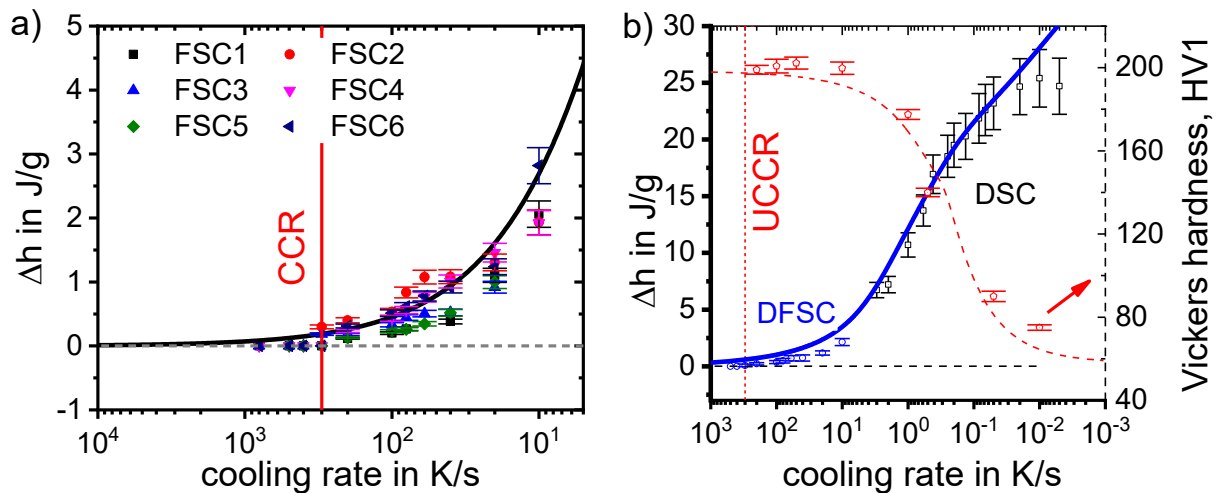


Figure 55: (A) Specific precipitation enthalpy after cooling from solution annealing of alloy 7150, as a function of cooling rate measured by DFSC. (B) Specific precipitation enthalpy after cooling from solution annealing and Vickers hardness after subsequent ageing (120 °C 24 h) of alloy 7150, as a function of cooling rate. The enthalpy values obtained by DFSC are shown as average values and standard deviation for six samples. The solid lines are model predictions from Ref. [BM7]. The DSC and hardness data tested on large samples were published in Ref. [BM3]. Hardness was tested for samples at the millimetre scale at the same cooling rates, obtained using a quenching dilatometer [BM9].

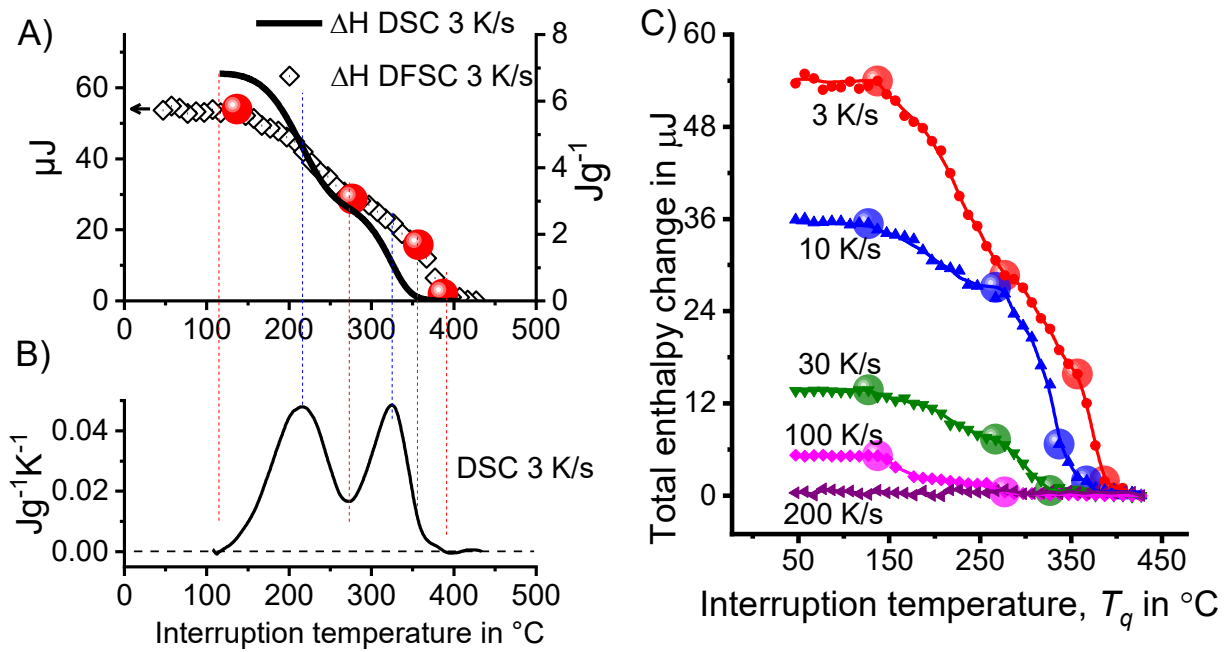


Figure 56: Results for 7150, showing (A) the total enthalpy change at a cooling rate of 3 K/s measured by DFSC and DSC; (B) the DSC curve at a cooling rate of 3 K/s, shown for comparison. The vertical red dashed lines indicate the precipitation start and end temperatures. (C) Total enthalpy change at different interruption temperatures and different cooling rates. The enlarged dots indicate the transition temperatures for the various precipitation reactions [BM9].

As demonstrated above, the DFSC-DRM is very helpful in assessing the kinetics of quench-induced precipitation as a function of cooling rate. However, no precipitation start and finish temperatures, which are crucial for the completion of a CCP diagram, are evaluable from the measurements shown above. In Ref. [BM9], the DRM was developed further to allow a temperature-dependent recording of the precipitation enthalpy values (Figure 20C). The results are summarised in Figure 56. The transition temperatures evaluated in Figure 56C allow completion of the CCP diagram with respect to the characteristic start and end temperatures of quench-induced precipitates.

Figure 57 shows the CCP diagram for 7020, and this can be compared to Figure 58, which shows the complete CCP diagram for 7150. The latter covers an extreme range of seven orders of magnitude of analysed cooling rates. The CCP diagram in Figure 58 incorporates quantitative data from five different types of DSC device, as outlined in Section 2.2.2, and results from hardness testing over the entire cooling rate range, allowing for a profound knowledge of the kinetics quench-induced precipitation.

For comparison, Figure 59 illustrates in situ electrical resistivity measurements and Figure 60 the obtained CCP diagram for alloy 7050 taken from Ref. [88]. A comparison of the evaluation in Figure 59 with the DSC cooling results seen in Figure 46 indicates that DSC generates much more convincing results, particularly in terms of reaction identification. However, highly similar results were obtained in Ref. [88] for 7050 as for 7150, which has a similar chemical composition. Using electrical resistivity measurements, the authors of Ref. [88] identified three distinct reactions at high, medium and low temperatures. The temperature ranges were relatively similar, and complete suppression of the HTR was identified within a similar range of cooling rates as in the CCP diagram for 7150 in Figure 58. The in situ electrical resistivity measurements were obtained during nonlinear cooling, which might be an advantage in terms of comparability with technological applications. The cooling time range covered is relatively large, although it is still narrower than that of the DSC work.

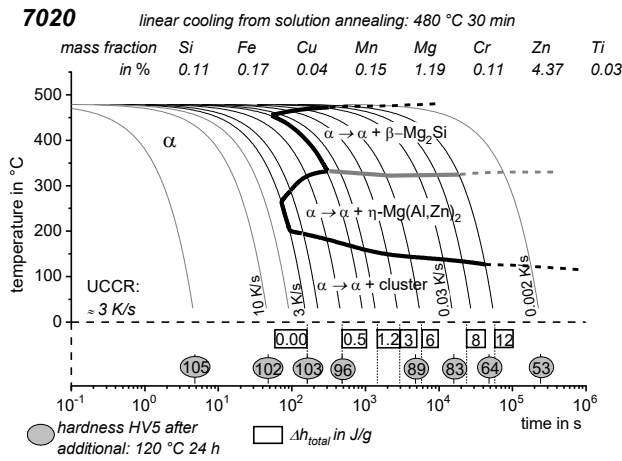


Figure 57: Continuous cooling precipitation diagram for 7020 [138].

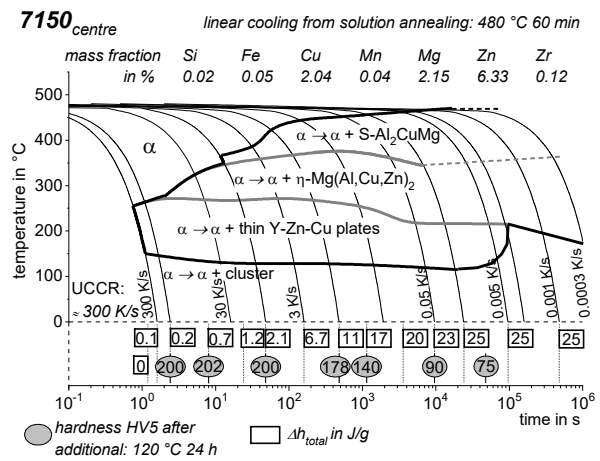


Figure 58: Complete continuous cooling precipitation diagram for 7150, covering seven orders of magnitude of cooling rates/cooling duration.

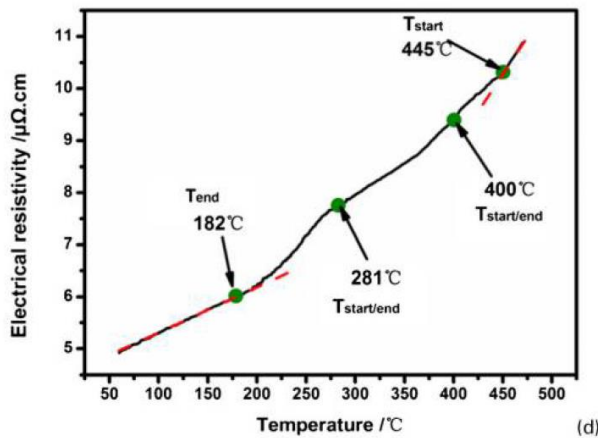


Figure 59: Evaluation of the characteristic transformation start and end temperatures applied in Ref. [88], using in situ measurements of the electrical resistivity. Example of an average cooling rate of 0.7 K/s.

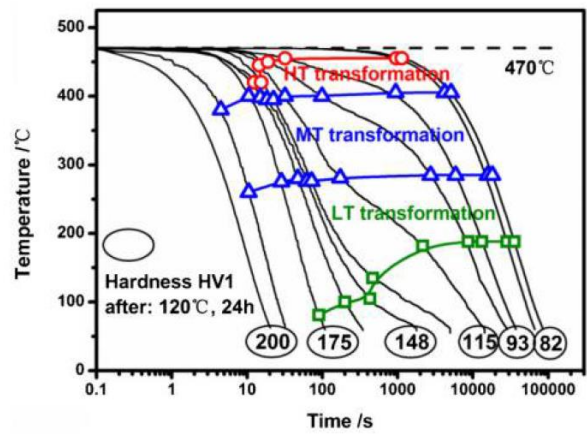


Figure 60: CCP diagram for 7050 obtained by in situ electrical resistivity measurements in Ref. [88]. Mass fractions of major alloying elements in %: 6.1 Zn, 2.15 Mg; 2.37 Cu.

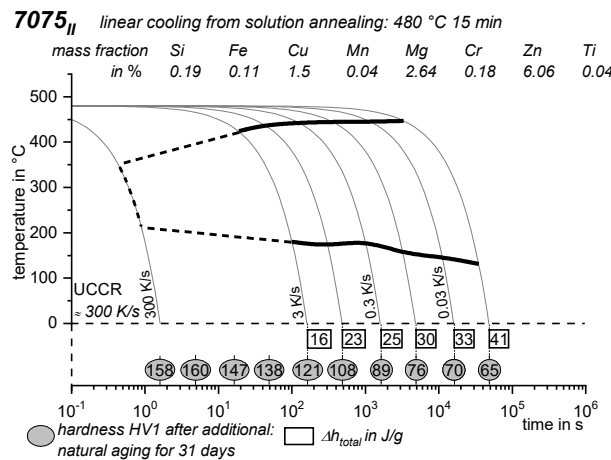


Figure 61: CCP diagram for 7075_{II} [152].

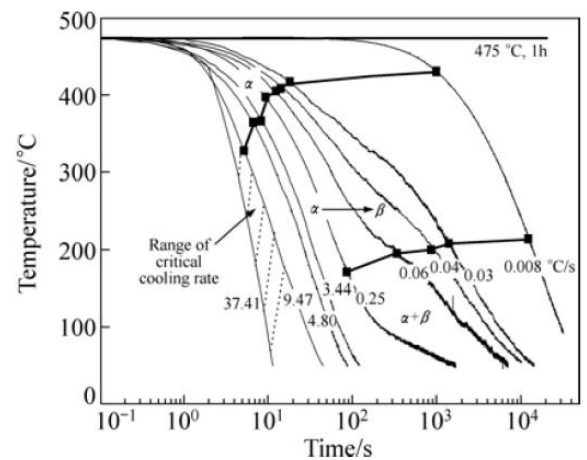


Figure 62: CCP diagram for alloy 7075 from Ref. [60] obtained by in situ voltage measurements. Mass fractions of major alloying elements in %: 5.44 Zn; 2.55 Mg; 1.37 Cu.

Another set of CCP diagrams for two variants of 7075 is compared in Figure 61 and Figure 62. The diagram in Figure 61 was recorded by DSC and hardness testing after natural ageing [152], while the second was established based on in situ electrical resistivity measurements in Ref. [60]. Both variants of 7075 considered here have comparable chemical compositions, although the variant from Ref. [152] is slightly more highly concentrated. For 7075, both methods obtained similar results in terms of the temperature ranges evaluated for the start and end of precipitation. However, the UCCRs are significantly different. While a combination of DSC and hardness testing after controlled linear cooling gave a rate of 300 K/s, the in situ electrical resistivity measurements suggested a UCCR range of ≈ 10 to 40 K/s [88]. This difference may result from a significant batch sensitivity in terms of the quench sensitivity of precipitation hardening Al alloys or from the abovementioned difficulties in evaluating in situ electrical resistivity measurements.

3.2.4 2xxx AlCu(Mg) wrought alloys

The kinetic behaviour of quench-induced precipitation in AlCu(Mg) alloys is shown in Figure 63 based on DSC cooling data for 2024 and 2219. The total precipitation enthalpy (Figure 63C) and the hardness after ageing (Figure 65D, 2024 natural ageing, 2219 artificial ageing) are also shown. As seen for the other alloy systems, multiple precipitation reactions occur. During slow cooling of 2219, two major reaction areas can be detected within the considered cooling rate range, while for 2024, three distinct reaction intervals can clearly be seen. For 2219, significant superposition of the two reaction peaks occurs, meaning that the second peak is seen only as a shoulder at ≈ 400 °C during slow cooling. During slow cooling of 2024, only two main reaction peaks are seen, a HTR and a medium temperature reaction (MTR). The HTR is increasingly suppressed with increasing cooling rate. At the same time, the MTR increases in intensity up to a cooling rate of about 0.3 K/s. If the suppression of the HTRs is almost complete, an additional LTR (≈ 250 – 150 °C) is seen. 2219 has only Cu as its main alloying element, but 2024 contains a considerable amount of Mg in addition to Cu. This obviously adds an additional reaction to the quench-induced precipitation.

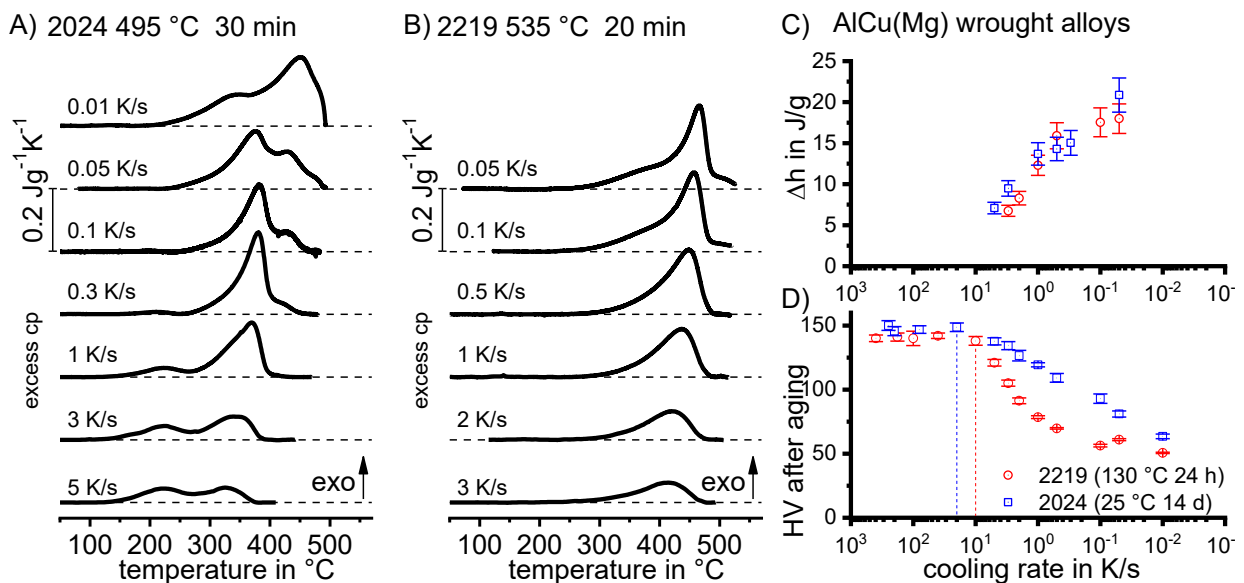


Figure 63: Comparison of two AlCu(Mg) alloys: (A) DSC cooling curves of 2024; (B) DSC cooling curves for 2219; (C) total specific precipitation enthalpies after cooling; and (D) hardness after additional ageing for both alloys.

As can be seen from the specific precipitation enthalpies in Figure 63C, the total precipitation process is increasingly suppressed with rising cooling rate. The specific precipitation enthalpies of both alloys are relatively similar. For the two AlCu(Mg) alloy variants considered here, the UCCR could not be determined by in situ cooling DSC. At the fast rates measured with DSC (3 and 5 K/s, respectively), relatively high specific precipitation enthalpies of about 7 J/g are still detected. Supplemental hardness testing after various cooling rates and subsequent ageing shows hardness saturation levels at cooling rates of above 10 K/s for 2219 and 20 K/s for 2024. These rates can therefore be considered the UCCRs for these alloys for the purposes of technological applications. It is noteworthy that although the UCCRs for the two alloys are similar, the loss in hardening potential (due to quench-induced precipitates) is more severe for 2219. Hence, the achievement of high hardness values over the whole thickness of a thick plate is restricted to a reduced maximum thickness compared to 2024.

In Ref. [193], quench-induced precipitation in an AlCuMg alloy 2618 was investigated. Cooling DSC was conducted over a cooling rate range of about 0.02 to 1 K/s. The DSC results for 2618 obtained in Ref. [193] are highly similar to those for 2024 in this work, and comparable precipitation enthalpies have been determined. However, since very slow cooling was not possible in the DSC device used in [193], the authors could not identify the HTR seen in 2024 (Figure 63).

The authors of Ref. [193] ascribe precipitation in an AlCuMg alloy at high temperatures to the formation of S-Al₂CuMg or S'-phase. In Ref. [103], the S-phase was also revealed by SAXS for cooling rates lower than 0.5 K/s. As the HTR in Figure 63A is substantially suppressed at rates higher than 0.5 K/s, it can be concluded that the HTRs revealed by DSC refer to the formation of S-Al₂CuMg. In addition, also isothermal experiments on a 2024 type alloys suggest the formation of the S-Al₂CuMg phase [58, 194, 195] at high temperatures occurring on grain boundaries [58, 194] and for medium temperatures precipitation of the S-Al₂CuMg as well as the θ -Al₂Cu phase, both nucleating on dispersoids [58, 194]. The quench-induced formation of the θ -Al₂Cu phase in AlCuMg alloys is also supported by Refs. [196, 197]. In Ref. [198], indications of quench-induced precipitation of the T-Al₂₀Cu₂Mn₃ phase were found in a Jominy end quench sample of another AlCuMg alloy. Continuous cooling SAXS measurements in Ref. [103] revealed the precipitation of Cu-Mg co-clusters below 250 °C. This shows good agreement with the low-temperature DSC peak for 2618 and 2024.

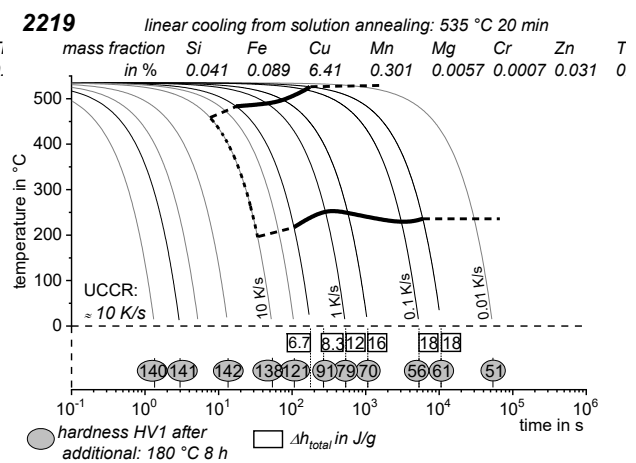
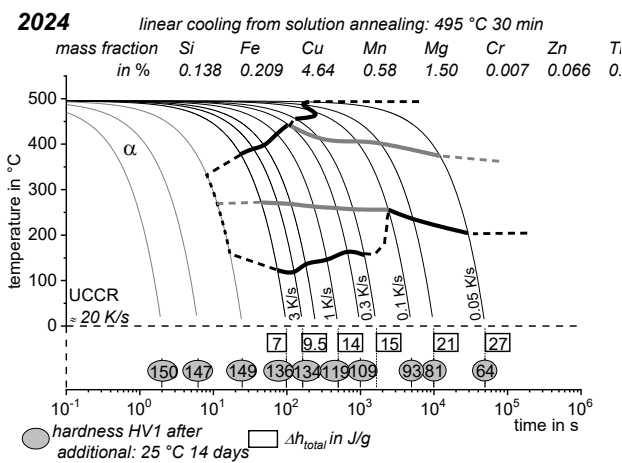


Figure 64: CCP diagram for 2024 [138], revised version. Hardness values obtained after cooling and natural ageing. **Figure 65: CCP diagram for 2019 [138]. Hardness values obtained after cooling and artificial ageing.**

For 2219, it seems highly likely that quench-induced precipitates will be dominated by θ -Al₂Cu and potentially θ' -precipitates. This is supported by findings from isothermal experiments in Refs. [196, 197, 199, 200].

The CCP diagrams for 2024 and 2219 are plotted in Figure 64 and Figure 65, respectively. As the overlap of the reactions is severe in 2219, no distinction of these reactions can be made.

3.2.5 AlSiMg cast alloys

The quench sensitivity of AlSiMg cast alloys has been investigated by a range of researchers, and ex situ methods have generally been used to analyse quench-induced precipitation or its detrimental effects on the resulting properties e.g. [45, 47, 49, 53, 56]. None of these previous reports used in situ cooling DSC analysis.

In this work, three variants of AlSiMg cast alloys are assessed, namely permanent mould-cast Al7Si0.3Mg [201], high-pressure die-cast Al10Si0.3Mg [125] and additively manufactured (laser-beam melted, LBM) Al10Si0.3Mg [125]. Figure 66 compares these three cast alloy variants in terms of their DSC cooling curves (A, B) and the resulting precipitation enthalpies and hardness after ageing (C, D). In the same way as for AlMgSi wrought alloys, two main reaction intervals are observed that are strongly overlapped. A broad HTR stretching over more than 100 K with a peak around 450 to 510 °C dominates over the entire cooling rate range considered. It can also be seen that DSC detects a nearly instantaneous onset of precipitation with the start of cooling i.e. nearly no undercooling is required for the reaction to start. Although a detailed experimental analysis of the nature of quench-induced precipitates has not been performed for these cast alloys, it can be assumed that precipitation of Si is important [47], i.e. during relatively slow cooling, part of the dissolved Si will diffuse to the existing eutectic Si [47]. This explains the instantaneous start of precipitation with the onset of cooling, as no separate nucleation is required: Si phase formation can proceed via growth of the existing Si particles. The latter assumption fits perfectly with the findings of instantaneous growth of undissolved β -Mg₂Si in AlMgSi alloys [BM10]. In addition to Si, the formation of β -Mg₂Si is also likely to occur at high temperatures during slow cooling of AlSiMg cast alloys. Ref. [47] reports on the nucleation of β -Mg₂Si phase particles on eutectic Si particles at slower rates, and the formation of β -Mg₂Si phase particles within the Al matrix at slightly faster cooling rates. It is likely that the formation of both Si and β -Mg₂Si contributes to the HTRs. β' -phase particles have also been assumed to precipitate during cooling [47, 49]. It is likely that these semi-coherent precursor precipitates form during the LTRs, which have a peak at about 350 °C in the cast alloy variants.

By comparing the two variants of Al10Si0.3Mg, it can be seen that the die-cast alloy has a higher concentration of Si, while the concentration of Mg is slightly higher in the LBM version, see Table 4 in the appendix. A further difference is that the LBM version contains almost no Mn, while the die-cast variant contains a mass fraction of ≈ 0.4 %. It is found that the LBM variant of Al10Si0.3Mg generally produces higher values of specific precipitation enthalpy, and that the loss in hardness potential (i.e. the quench sensitivity) is also higher in this alloy. Since the laser-beam-melting process involves extremely fast cooling rates for solidification, the eutectic like structure of the LBM material is much finer compared to that of the die-cast eutectic (see Figure 67). This much finer eutectic structure is considered to increase the number

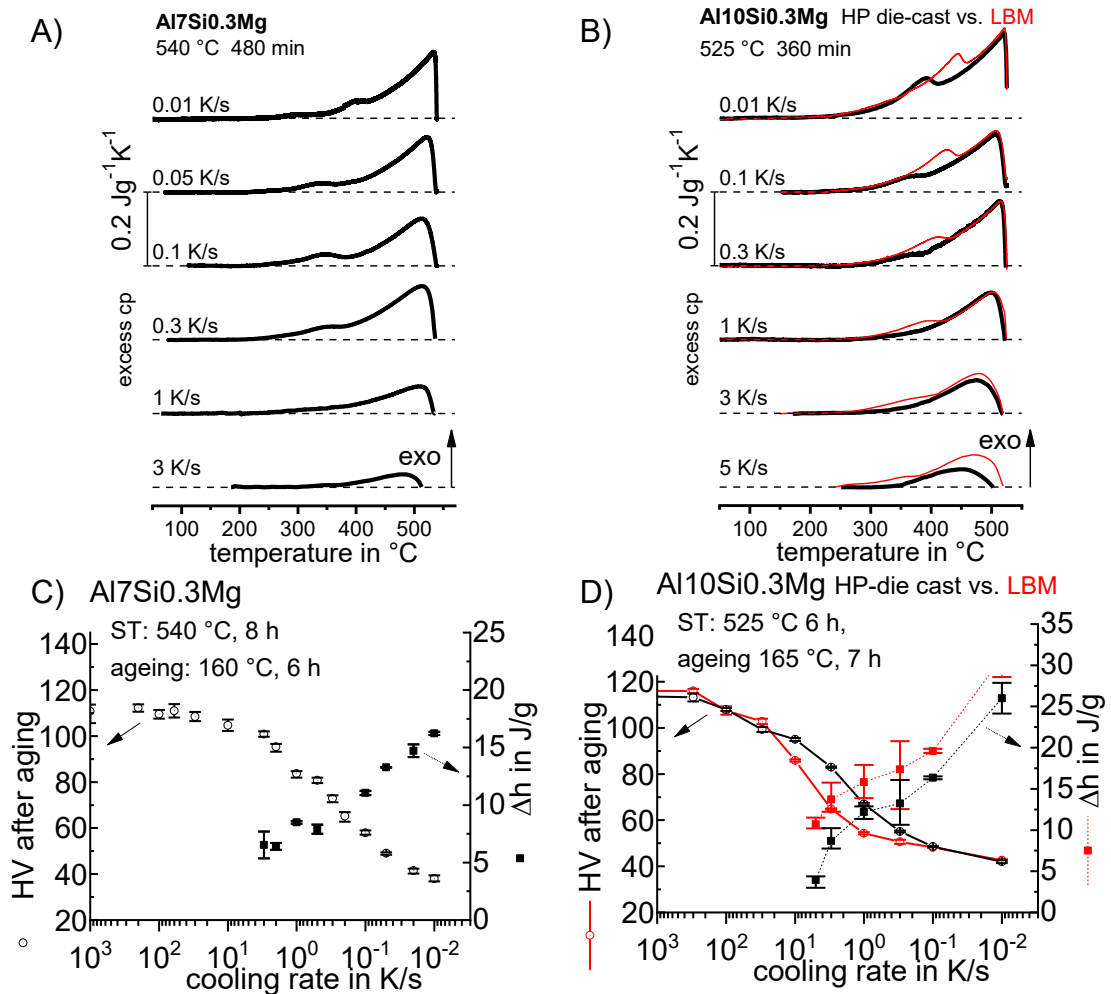


Figure 66: Comparison of three different AlSiMg cast alloys: (A) cooling DSC curves for permanent mould-cast Al7Si0.3Mg , [201]; (B) cooling DSC curves for two variants of Al10Si0.3Mg – one of the variants was produced by high-pressure die-casting, the second by laser beam melting, [202, 125]; (C) and (D) values of specific precipitation enthalpy and hardness after aging for the three cast alloys.

of available nucleation sites, thus promoting quench-induced precipitation. In line with this, the peak temperature of the LRT is shifted to higher temperatures in the LBM alloy.

No systematic study of the interacting influences of prior solidification rate, solution treatment and alloying element concentration on quench-induced precipitation is currently available for cast alloys. However, there are differences of several orders of magnitude in the solidification rates for the three alloys considered here. These solidification rates are estimated to be around 10^5 K/s for LBM [203, 204], 10^3 K/s for die casting and 10^1 K/s for conventional casting [205]. Further, the solidification structure is greatly changed by prolonged soaking at solution temperature. For the AlSiMg cast alloys, it appears that both the alloy composition and the microstructure prior to quenching have an influence on the kinetics of quench-induced precipitation. The microstructure at the end of the solution treatment is a result of the structure after casting (or LBM) and the coarsening caused by the solution treatment. The latter can be seen in Figure 68, which compares the microstructure of the two Al10Si0.3Mg variants in the initial condition and after different soaking durations at solution temperature. This figure shows that the initial difference in the microstructure virtually disappears after six hours of soaking at 525 °C, and similar coarse microstructures are seen for both materials.

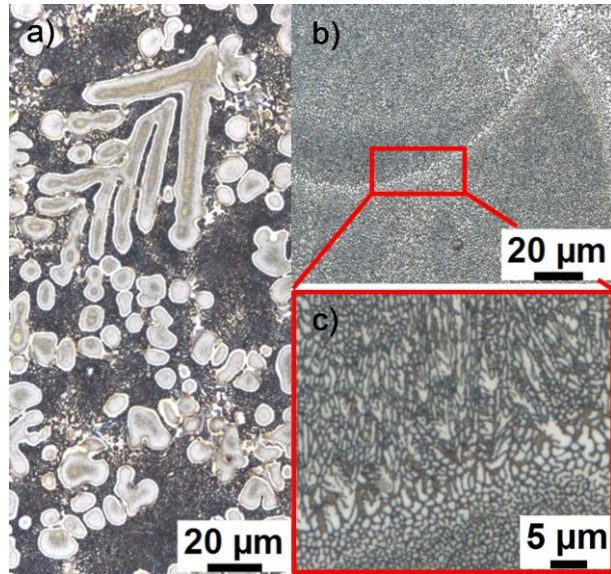


Figure 67: Comparison of the initial microstructures of (A) as-cast and (B), (c) as-LBM Al₁₀Si_{0.3}Mg [202].

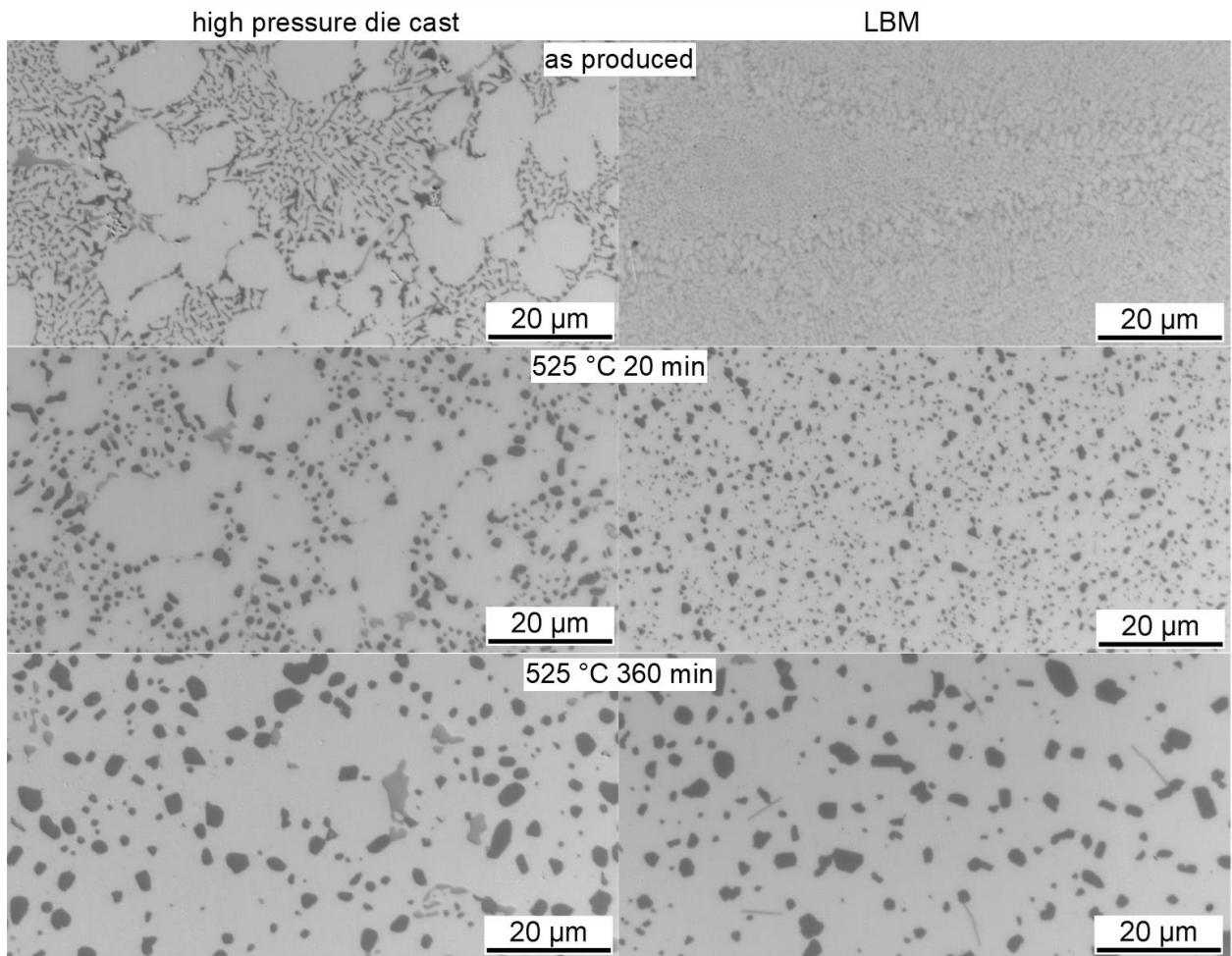


Figure 68: Eutectic structure of Al₁₀Si_{0.3}Mg produced by high-pressure die-cast and LBM, for different soaking times at 525 °C.

Figure 69 shows a substantial acceleration of quench-induced precipitation and the drop in hardness is shifted to faster cooling rates for a shorter solution treatment in the case of a much finer initial microstructure prior to cooling (compare Figure 68). The UCCR of the finer eutectic structure (after 20 min soaking at 525 °C) appears to be above 1000 K/s. For this reason, the difference in the solution treatments between Al7Si0.3Mg and Al10Si0.3 should be kept in mind when considering Figure 70.

Figure 70 shows that the maximum hardness achievable for the three alloys is very similar (111 to 116 HV1), and this hardness is achieved using high cooling rates in excess of ≈ 100 K/s [125, 201]. This result perfectly fits with those of Ref. [49], in which the maximum hardness after ageing was found to occur after cooling at 110 K/s and above (average cooling rates between 450 and 200 °C). If cooling is performed at lower rates, the age-hardening potential drops significantly for the different alloys, and drops much more quickly for the fast solidified variant (with finer structure) and/or higher concentrated alloys. For instance, at a cooling rate of 2 K/s, which is a typical value for gas cooling, Al7SiMg0.3 still reaches 95 HV after ageing, while the hardness of the LBM variant of Al10Si0.3Mg drops to only around 60 HV1. Dimensional and shape distortion after quenching is very relevant for net-shaped cast products, and quenching rates are therefore often restricted to lower rates. In this case, a permanent mould cast (and less concentrated) alloy could achieve ≈ 150 % of the strength of the LBM alloy. This finding correlates well with the discussion of the AlMgSi and AlZnMgCu wrought alloys (Figure 41 and Figure 53, respectively).

CCP diagrams for the cast alloys are given in Figure 71, Figure 72 and Figure 73. As precipitation starts instantaneously with the onset of cooling for all the cast alloys, these CCP diagrams show that the onset of precipitation is the same for any cooling rate. The start of high-temperature precipitation is therefore plotted as a straight line starting at the solution treatment temperature. The reactions that are most likely to be occurring are labelled.

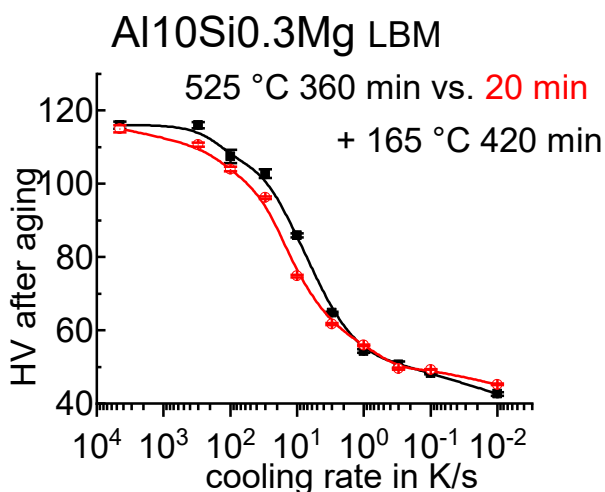


Figure 69: Comparison of hardness after cooling and subsequent ageing for LBM Al10Si0.3Mg.

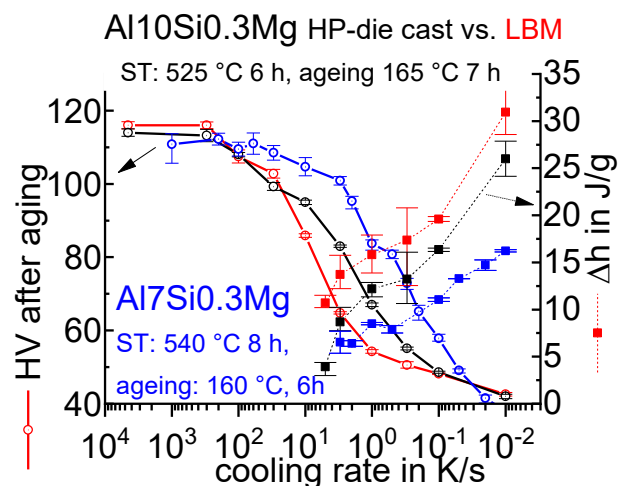


Figure 70: Comparison of specific precipitation enthalpies after cooling and hardness after subsequent ageing for the three AlSiMg cast alloys.

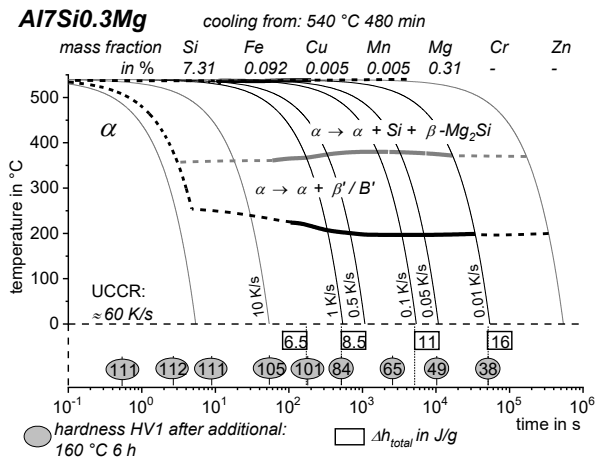


Figure 71: CCP diagram for Al7Si0.3.

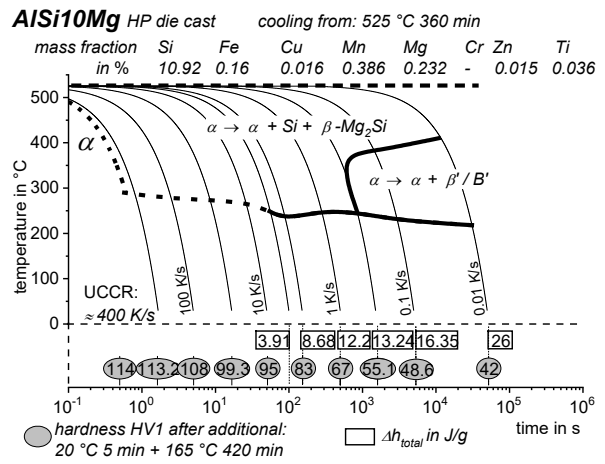


Figure 72: CCP diagram for high-pressure die-cast Al10Si0.3.

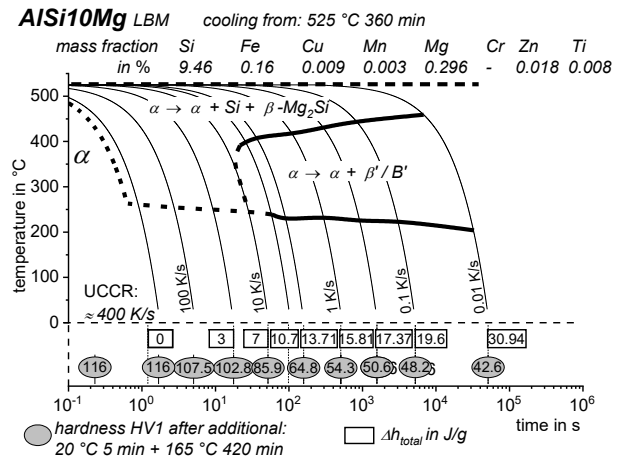


Figure 73: CCP diagram of LBM Al10Si0.3.

4 General aspects of quench-induced precipitation in Al alloys

As demonstrated in Figure 74, quench-induced precipitation in all the Al alloys investigated here generally falls into different temperature and time (cooling rate) intervals. For most alloys, two or three main reaction intervals can be identified. However, there are several hints of the superposition of multiple reactions beneath the main reaction intervals. In addition, a cooling rate that is fast in terms of precipitation for a certain lean alloy may be relatively slow in terms of precipitation for an alloy of higher concentration, and the same holds for the temperature ranges. For instance, the LTR for Al0.72Si (Figure 74A) occurs at a temperature range of about 420 to 300 °C, which is almost the same temperature range as for the MTRs of 7150 and 2024 (at least at certain cooling rates).

In a comparison of DSC cooling curves for the four substantially different aluminium alloys shown in Figure 74, it is notable that the precipitation behaviour is to a large extent similar. This is particularly true for a comparison of the alloys 7150 and 2024, which are substantially different in composition but which show highly similar dynamic behaviour of quench-induced precipitation.

For all of the precipitation hardening Al alloys investigated, it holds that if the alloy is cooled sufficiently slowly, quench-induced precipitation occurs at relatively high temperatures. During the HTRs, essentially stable equilibrium phases of the alloying system are precipitated in relatively coarse particles with a low aspect ratio, and their dimensions can reach more than 10 μm . If the grain size of the alloy is considerably larger than this, precipitation will predominantly occur inside the grains. However, quench-induced precipitation also occurs on the grain boundaries. In commercial wrought alloys, nucleation of these

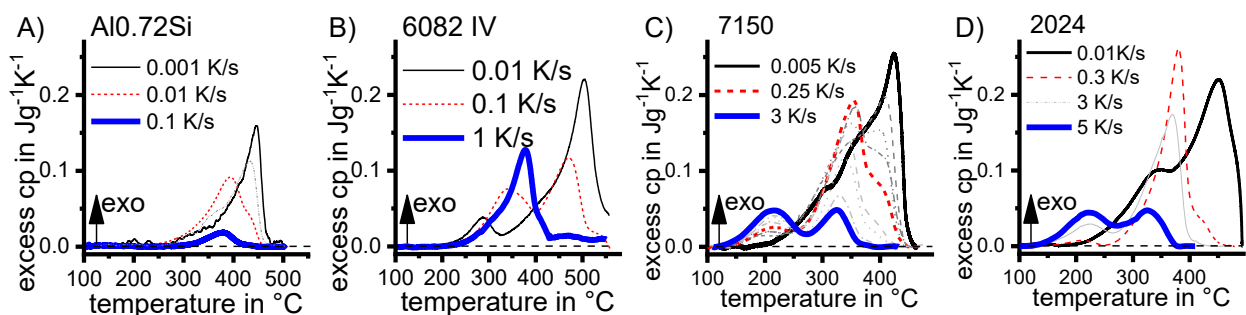


Figure 74: Dynamic behaviour of quench-induced precipitation in four substantially different Al-based alloys.

equilibrium phase particles at high temperatures takes place on relatively coarse primary particles comprised of elements such as Fe, Mn and Si. In addition, pre-existing particles from the same phase that were not dissolved during the solution treatment can also act as nucleation sites. These undissolved particles start to grow instantly with the onset of cooling. This is obvious from Figure 75, which compares DSC cooling curves for aluminium alloys after incomplete dissolution with those after full dissolution. A comparison of Figure 75D and F is most impressive, as these show DSC cooling curves for the same alloy and the same cooling rate. The obvious difference in the precipitation behaviour during cooling is attributed to incomplete dissolution of β -Mg₂Si after solution treatment at 540 °C for 20 min, while a full solution was achieved in Figure 78F at 560 °C. In Ref. [BM10], we showed that this incomplete dissolution increases the quench sensitivity and that the UCCR is increased by about a factor of three.

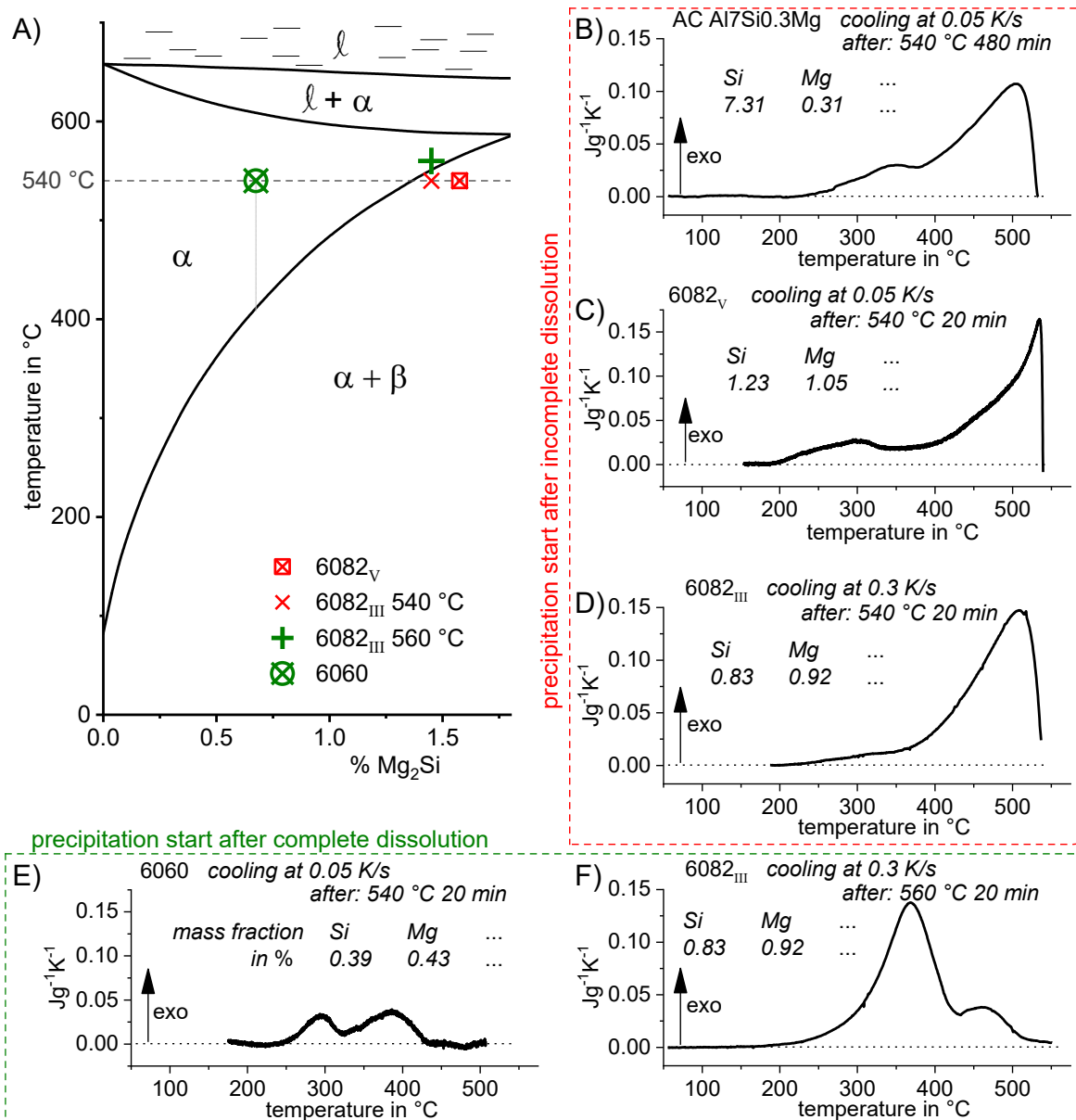


Figure 75: (A) Quasi-binary phase diagram for Al-Mg₂Si (adapted from [5]). (B), (C), (D) DSC cooling curves for three different alloys for which the applied solution treatment resulted in an incomplete dissolution. (E), (F) DSC cooling curves for two different alloys for which the applied solution treatment resulted in complete dissolution. In (D) and (F), the same alloy is considered, although cooling started from two different temperatures: 540 °C and 560 °C. The mass fractions of Mg and Si for the different alloys are stated.

If the reactions at higher temperatures are suppressed to a certain extent by higher cooling rates, another reaction (or multiple reactions) occur(s) at lower temperatures. The quench-induced MTRs and LTRs of precipitation hardening Al alloys may therefore initially give an increase in the fraction transformed with increasing cooling rates (see the enthalpy change of the LTR in Figure 40). This is also typically related to an increase in the reaction temperatures. The reason for this behaviour is increasing supersaturation (due to the increasing suppression of the HTRs). This increases the driving force for precipitation of the related phases (which typically competes for the same alloying element atoms, like the HTRs).

In general, it can be stated that at lower temperatures, metastable precursor phases are precipitated. These particles have much larger aspect ratios compared to high-temperature particles, but are still relatively coarse. Their dimensions can reach several hundreds of nm, and thus contribute little to direct hardening. Nucleation of these quench-induced lower temperature precursor phases takes place mostly on incoherent dispersoids (and on grain boundaries; see for instance Figure 49). The dispersoid particle number density therefore substantially influences quench-induced precipitation and quench sensitivity.

For some alloys, quench-induced precipitation at relatively high cooling rates is shown to proceed at relatively low temperatures. Particularly for AlZnMgCu alloys, it has been found that a thin platelet phase can precipitate at temperatures between 250 and 150 °C [BM7, BM8, 185]. At even lower temperatures of down to ≈50 °C, cluster formation has been identified [103–105]. Although the latter two particle types already provide a considerable direct hardening effect, since the volume fractions generated for these quench-induced particles are small, the total hardening effect is still relatively low.

For pure laboratory alloys in the AlSi system, it was shown that one phase can contribute both to the HTR with low aspect ratio precipitates and also to the reactions at lower temperatures with high aspect ratio precipitates. It was demonstrated that additions of further alloying elements can cause an additional sequence of potential quench-induced precipitates.

In general, the UCCRs of commercial precipitation-hardening Al alloys range between about 0.5 K/s (6060, [BM2]) and about 300 K/s for highly concentrated AlZnMgCu alloys [BM9, BM7, 124, 153].

The kinetics of quench-induced reactions are accelerated by an increased concentration of alloying elements. At medium cooling rates, which are particularly relevant for gas cooling, for instance, more highly concentrated alloys may lose a large amount of their age-hardening potential by quench-induced precipitation. Applying the same gas cooling rates to leaner alloys might still achieve sufficient supersaturation, allowing these alloys to exploit nearly their full age-hardening potential. Leaner alloys might therefore achieve higher hardness and strength after medium-slow cooling, as compared to more highly concentrated alloys. This aspect was demonstrated for AlMgSi and AlZnMgCu wrought and AlSiMg cast alloys (compare Figure 41, Figure 53 and Figure 70, respectively). Particularly for the latter, the applied solution treatment makes a substantial impact, since the coarsening of the eutectic, which increases with soaking duration, influences the density of nucleation sites. In all cases, the lower concentrated alloy after medium-slow cooling at approximately 1 K/s and additional ageing achieved a hardness of about 150 % of the highest alloy concentration considered. This aspect has particular technological relevance if the aim is to retain high dimensional stability of the quenched parts, or to limit their residual stresses, which is often associated with reduced cooling rates. The knowledge obtained of the kinetics of quench-induced precipitation now allows us to choose either an appropriate cooling process for a certain fixed alloy and/or an appropriate alloy for a certain fixed cooling process.

5 Application of the derived DSC methods to other alloy systems

The methodology for heating and cooling DSC described in Section 2 has been applied to analyse a range of solid-solid phase transformations in other metallic alloy systems. For instance, quench-induced precipitation in magnesium alloys [119] and the tempering of steels have been analysed [206, 207]. Recently, our DSC method for the analysis of solid-solid phase transformation kinetics was successfully adapted for use with high-temperature alloys up to 1100 °C [118]. The in situ analysis of quench-induced precipitation in precipitation hardening martensitic steels [118, 125, 202], and Ni-based alloys [118] has successfully been demonstrated.

The strength of a range of magnesium alloys is increased by precipitate strengthening, achieved through post-quench ageing [5]. The age-hardening potential of precipitation-hardening Mg alloys can be lowered by quench-induced precipitation. Until recently, the analysis of precipitation reactions by DSC was restricted to temperatures well below the solution temperature, mainly due to the low eutectic melting temperature in the system Mg-Al, occurring between Mg samples and Al crucibles. To solve this limitation we recently adapted our DSC methods by using graphite crucibles to allow the kinetic analysis of precipitation and dissolution reactions in Mg alloys up to solution annealing temperatures [119]. An example of DSC cooling curves for the WE43 Mg-Y-Re alloy from solution treatment temperature is shown in Figure 76, and these DSC curves show a high similarity to the DSC cooling curves for Al alloys. DSC has been shown in our recent work to allow the derivation of a continuous cooling precipitation diagram for Mg alloys [119]. The CCP diagram for the WE43 Mg-Y-RE alloy is presented in Figure 77. The UCCR of this alloys is in the range of 10 to 100 K/s [119].

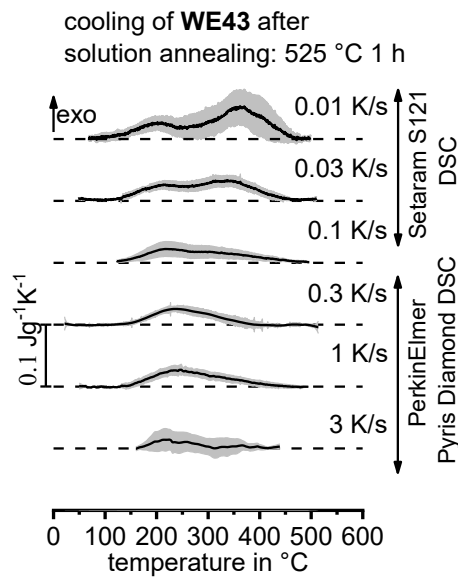


Figure 76: DSC cooling curves for age-hardening Mg alloy WE43 [119].

In the martensitic precipitation hardening of steels such as X5CrNiCuNb16-4, strengthening is caused by the precipitation of fine Cu-rich particles [208–211]. In terms of cooling from solution treatment, the quench-induced precipitation of Cu-rich phases has thus far been disregarded, since the available continuous time-temperature transformation diagrams for precipitation hardening steels were recorded by dilatometry. The available continuous time-temperature-transformation diagrams therefore neglect precipitation, and only the martensitic transformation has been analysed in work using dilatometry [212]. Recently published work by the present author [118, 125] covering cooling DSC on X5CrNiCuNb16-4 clearly reveals quench-induced precipitation and its negative effect on the hardness after ageing (see Figure 78). In a similar way to aluminium alloys, precipitation occurs in two different temperature regimes and the UCCR for this steel is about 30 K/s.

Ni-based alloys can also benefit from precipitation strengthening. We recently investigated the precipitation behaviour of Inconel 718 (a Ni-17Cr-17Fe-5Nb-3Mo alloy) during cooling from solution treatment [118]. Figure 79(a) shows continuous DSC cooling curves for this alloy after solution annealing at 980 °C for 60 min, and Figure 79(b) illustrates the hardness and the specific precipitation heat, which depend upon the cooling rate. Linear cooling (e.g. cooling in the DSC) involves a two-stage precipitation process that is kinetically suppressed by an increase in the cooling rate. It can be seen from Figure 79B that there is a substantial direct hardening effect of quenched induced precipitates. This effect is known to occur in Ni-based alloys in an extend allowing technological application for strengthening [213–215]. Compared to Al alloys, this effect is much stronger due to the substantially larger fractions of alloying elements. The UCCR in terms of hardness after ageing is in the range of just 0.1 K/s.

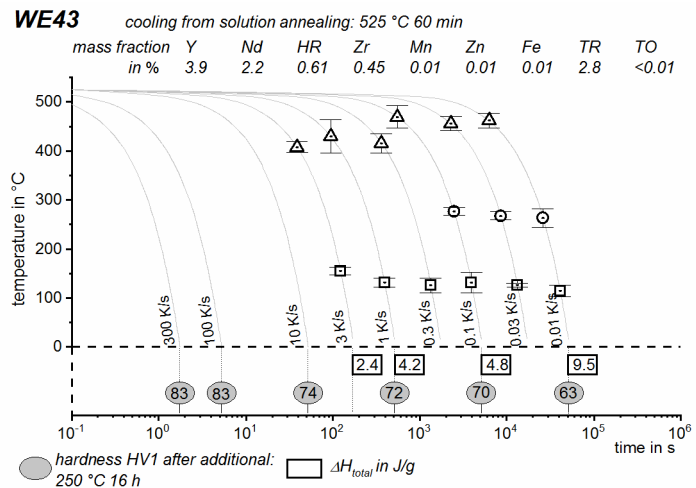


Figure 77: Continuous cooling precipitation diagram of age-hardening Mg alloy WE43 [119].

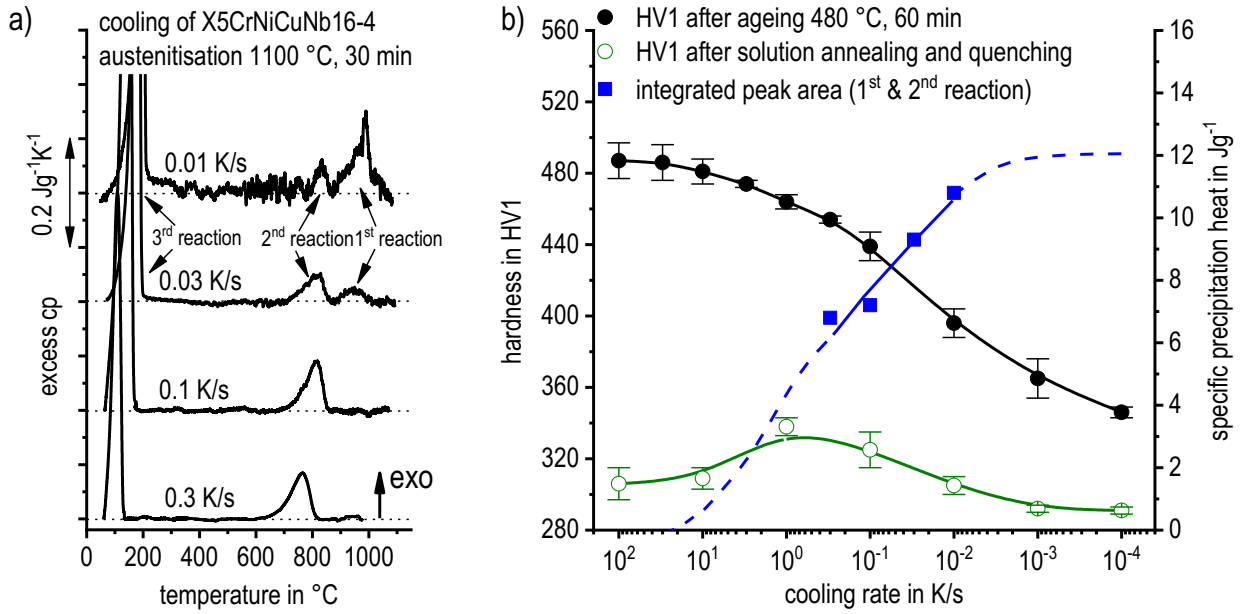


Figure 78: X5CrNiCuNb16-4 (A) Selected DSC cooling curves of X5CrNiCuNb16-4 after austenitisation at 1100 °C, 30 min. The DSC peaks between about 1000 °C and 600 °C indicate the quench-induced precipitation of Cu-rich particles, while the strong peak below about 200 °C corresponds to the martensitic transformation. (B) Hardness as a function of the cooling rate in the quenched and in the quenched and aged conditions, adapted from [118].

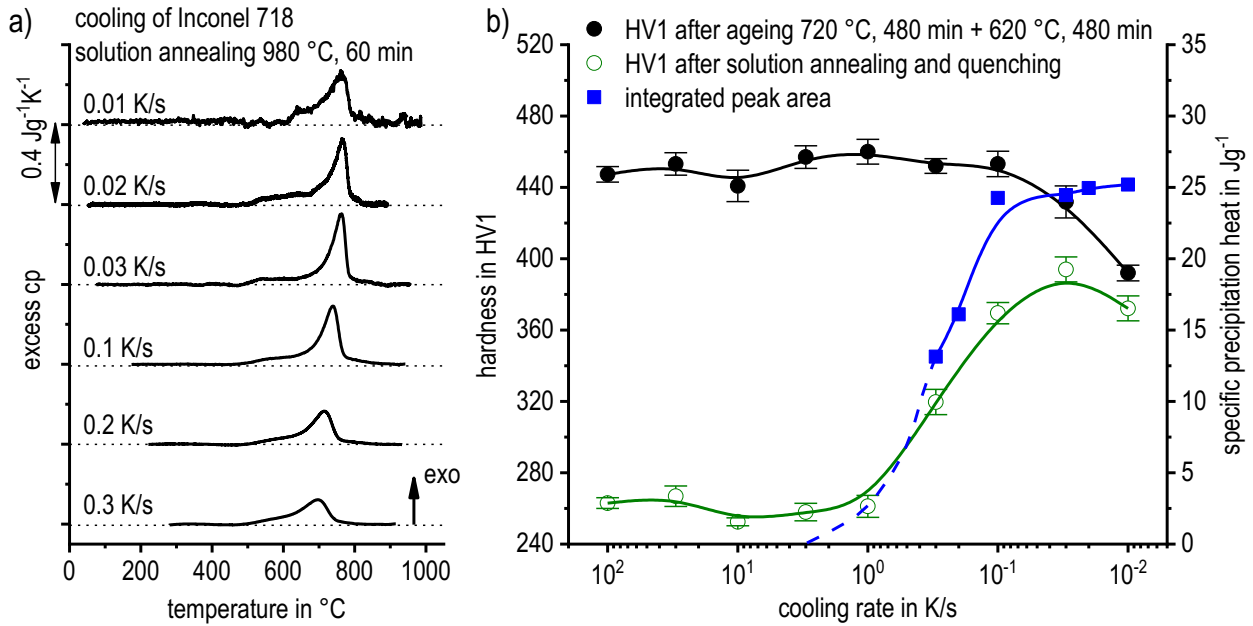


Figure 79: (A) Continuous DSC cooling curves of Inconel 718; (B) hardness profile and specific precipitation heat depending on the cooling rate [118].

6 Conclusions

6.1 In situ DSC analysis of solid-solid phase transformations in precipitation hardening alloys

- Compared to the state of the art prior to the work carried out here, the dynamic range of in situ DSC on age-hardening alloys has been substantially extended, particularly in terms of continuous cooling experiments. A range of cooling rates from about 3×10^{-4} to 3 K/s can now be applied in a reliable analysis method using direct, in situ DSC experiments. Based on a typical temperature interval for the cooling of light metal alloys from solution treatment, this is equivalent to cooling durations ranging from several weeks up to a few minutes.
- By combining direct, in situ DSC measurements with indirect DSC measurements where no direct measurement is possible, the accessible cooling rate range is extended to 10 orders of magnitude, from about 10^{-5} to 10^5 K/s. When applied to the cooling of aluminium alloys from solution annealing, this corresponds to cooling over several months down to cooling within several hundredths of a second.
- The key features which make these in situ DSC analyses of solid-solid phase transformation possible are as follows:
 - Measurement and evaluation of the specific excess heat capacity;
 - Taking great care with the accuracy of the DSC zero level; and
 - Consideration of a large dynamic range of heating or cooling rates as well as the analysed scales of microstructural changes.
- DSC can help a great deal in choosing appropriate heat treatment parameters for age-hardening alloys based on in situ experiments. This holds for the solution treatment (heating rates, solution temperature and soaking duration) and particularly for quenching.
- The obtained DSC methods have also been successfully adapted and applied to the analysis of solid-solid phase transformations in other precipitation hardening alloy systems, including Mg alloys, precipitation-hardening martensitic steels and Ni-based alloys.

6.2 Continuous heating and solution annealing

- DSC heating curves of precipitation hardening alloys for a specific initial condition allow us to judge whether dissolution or precipitation reactions are predominant at certain times and temperatures.
- Interpretations of DSC heating curves for precipitation-hardening alloys are often found to be challenging. The strong superposition of opposite endo- and exothermic reactions (dissolution/precipitation) make exact interpretations difficult; that is, single DSC peaks, their peak positions and peak areas are not necessarily equal to the maximum intensity of the underlying microstructural reaction.
- Nevertheless, as a general rule, it can be derived that:
 - Any diffusion-controlled reaction is increasingly suppressed with increasing heating rate. Suppression of precipitation reactions seems to be easier than suppression of dissolution reactions. Consequently, at sufficiently high heating rates, only dissolution reactions will occur.
 - Any diffusion-controlled reaction shifts to higher temperatures with increasing heating rate. Increasing the heating rate by a factor of 100 typically causes shifts on the order of more than 100 K.
- If the alloy and heating rate specific solvus temperature is exceeded, the total integral of the DSC heating curve reveals the enthalpy level of the initial alloy state. This enthalpy level provides information about the thermal stability of the initial condition, and is higher for more stable conditions.
- For aluminium alloys undergoing different initial heat treatment states such as “as quenched”, T4, T6 or T7, DSC heating curves show severe differences at temperatures below about 300 °C. Above this temperature, the differences are typically small.
- DSC heating is able to identify appropriate temperature ranges for solution treatment, particularly at slow heating rates, since for slower heating the alloy- and heating-rate-specific solvus temperature can be identified. At very slow heating rates, the latter will be close to the equilibrium solvus temperature. Additional experiments can be performed to check whether a complete dissolution of the major alloying elements has been achieved. These additional experiments include isothermal DSC during soaking within the previously identified temperature range.

6.3 Continuous cooling and analysis of quench-induced precipitation

- During cooling, only exothermic precipitation occurs, making interpretation of DSC cooling curves easier than for DSC heating curves. However, in most cases, several different reactions overlap, and their deconvolution may be challenging. Multiple reactions occurring sequentially were detected for all alloys investigated.
- The nature and kinetics of quench-induced precipitates in age-hardening Al-alloys were analysed for 27 different alloys, and both differences and similarities were identified between different alloying systems:

- Quench-induced precipitation occurs at both, grain boundaries and predominantly inside grains. The latter particularly holds for grain sizes above several tens of μm .
- Nucleation of quench-induced precipitation generally occurs on existing crystal defects such as grain boundaries, primary precipitates and dispersoids.
- At high temperatures ($\approx 500\text{--}350\text{ }^\circ\text{C}$), the stable equilibrium phases of the alloy system precipitate as coarse particles with a low aspect ratio (aspect ratios = length/ (thickness or diameter) is about 1 to 5), and nucleation occurs on coarse primary particles.
- At medium temperatures ($\approx 350\text{--}200\text{ }^\circ\text{C}$) in the AlMgSi system, precipitation of MgSi precursor phases occurs as rods with aspect ratios of about 10. In the AlZnMg(Cu) system, precipitation of the $\eta\text{-Mg}(\text{Zn},\text{Al},\text{Cu})_2$ phase occurs as plates with aspect ratios of up to 10. In both alloy systems, quench-induced precipitation at medium temperatures nucleates on dispersoids.
- At low temperatures ($\approx 250\text{--}150\text{ }^\circ\text{C}$) in the AlZnMg(Cu) system, thin plates enriched with Cu and Zn were detected as quench-induced precipitation. At very low temperatures ($\approx 150\text{--}50\text{ }^\circ\text{C}$) in the AlZnMg(Cu) and AlMg(Cu) systems, quench-induced precipitation of clusters was revealed.
- The major aspects influencing the quench sensitivity are:
 - The concentrations of the main and dispersoid-forming alloying elements;
 - The density of nucleation sites (coarse primary particles, particularly dispersoids, grain boundaries, undissolved secondary phases, eutectic structure), i.e. the initial microstructure initial prior to the start of cooling;
 - Concentrations and nucleation sites form the major reason for the significant alloy batch sensitivity in terms of the kinetics of quench-induced precipitation. For instance, for different batches of 6082, the upper critical cooling rate (UCCR) might vary by up to a factor of 10;
 - Moreover, the result of the solution treatment in terms of complete or incomplete dissolution influences the quench sensitivity; incompletely dissolved remaining particles can instantly start to grow with the onset of cooling (with no nucleation required, and no undercooling). This can increase the UCCR by a factor of three.
- The most highly concentrated Al alloys have a UCCR in the range of several hundreds of K/s. Lean commercial alloys such as 6060 may have a UCCR as low as 0.5 K/s, and for pure laboratory alloys (with a substantially reduced number of nucleation sites), this may be even lower (e.g. pure binary Al0.26Si about 0.02 K/s).
- A systematic methodology for the analysis, evaluation and construction of continuous cooling precipitation diagrams for precipitation hardening alloys and guidelines for reading these were derived. This significantly advances the state of the art in the heat treatment of aluminium alloys.
- It was shown that the highest alloying element contents are able to obtain the highest hardness if the necessary high upper critical cooling rate is reached. However, if the technological application requires slower cooling (for instance due to thick products or to keep distortion low), a lower concentration of alloying elements can lead to higher hardness due to quench-induced precipitation kinetics and the related loss of age-hardening potential.

7 References

7.1 References underpinning the habilitation thesis

- BM1. Milkereit B, Kessler O, Schick C: Recording of continuous cooling precipitation diagrams of aluminium alloys. *Thermochim Acta* 492 (2009): 73–78.
- BM2. Milkereit B, Wanderka N, Schick C, Kessler O: Continuous cooling precipitation diagrams of Al-Mg-Si alloys. *Mater Sci Eng A* 550 (2012): 87–96.
- BM3. Zhang Y, Milkereit B, Kessler O, Schick C, Rometsch PA: Development of continuous cooling precipitation diagrams for aluminium alloys AA7150 and AA7020. *J Alloys Compd* 584 (2014): 581–589.
- BM4. Schumacher P, Pogatscher S, Starink MJ, Schick C, Mohles V, Milkereit B: Quench-induced precipitates in Al–Si alloys: Calorimetric determination of solute content and characterisation of microstructure. *Thermochim Acta* 602 (2015): 63–73.
- BM5. Osten J, Milkereit B, Schick C, Kessler O: Dissolution and precipitation behaviour during continuous heating of Al-Mg-Si alloys in a wide range of heating rates. *Mater* 8-5 (2015): 2830–2848.
- BM6. Milkereit B, Starink MJ: Quench sensitivity of Al-Mg-Si alloys: A model for linear cooling and strengthening. *Mater Des* 76 (2015): 117–129.
- BM7. Starink MJ, Milkereit B, Zhang Y, Rometsch PA: Predicting the quench sensitivity of Al-Zn-Mg-Cu alloys: A model for linear cooling and strengthening. *Materials & Design* 88 (2015): 958–971.
- BM8. Zhang Y, Weyland M, Milkereit B, Reich M, Rometsch PA: Precipitation of a new platelet phase during the quenching of an Al-Zn-Mg-Cu alloy. *Scientific Reports* 6 (2016): 23109.
- BM9. Yang B, Milkereit B, Zhang Y, Rometsch PA, Kessler O, Schick C: Continuous cooling precipitation diagram of aluminium alloy AA7150 based on a new fast scanning calorimetry and interrupted quenching method. *Mater Charact* 120 (2016): 30–37.
- BM10. Fröck H, Milkereit B, Wiechmann P, Springer A, Sander M, Kessler O, Reich M: Influence of Solution-Annealing Parameters on the Continuous Cooling Precipitation of Aluminum Alloy 6082. *Metals* 8-265 (2018): 1–16

7.2 Further references by the author and external references

1. statista: Global raw-steel production from 2002 to 2017: id153008, Recource: World Steel Association. <https://de.statista.com/statistik/daten/studie/153008/umfrage/welt-rohstahlerzeugung-seit-2008/>; retrieval on 11.07.2018.
2. statista: Global Production Amount of Major non-ferrus Metals in 2013 and 2014: 323132 Resource: World Bureau of Metal Statistics. <https://de.statista.com/statistik/daten/studie/323132/umfrage/produktion-der-wichtigsten-ne-metalle-weltweit/>; retrieval on 11.07.2018.
3. statista: Global production of castings from various metals in 2016: Ressources: European Foundry Association; American Foundry Society. <https://de.statista.com/statistik/daten/studie/421534/umfrage/produktion-von-guss-weltweit-nach-metall/>; retrieval on 11.07.2018.
4. statista: Global demand for Aluminum from 2006 to 2019: id156039. <https://de.statista.com/statistik/daten/studie/156039/umfrage/weltweite-aluminiumnachfrage-seit-2006/>; retrieval on 11.07.2018.
5. Polmear IJ: Light alloys: From traditional alloys to nanocrystals. 4th ed. Amsterdam: Elsevier Butterworth-Heinemann 2006.
6. Hornbogen E: Hundred years of precipitation hardening. *Journal of Light Metals* 1 (2001): 127–132.
7. Hornbogen E: Precipitation hardening - The oldest nanotechnology. *Metall* 55 (2001): 522–526.
8. Gottstein G: *Physikalische Grundlagen der Materialkunde: Mit 28 Tabellen*. 3rd ed. Berlin, Heidelberg, New York: Springer-Verlag 2007.
9. Kammer C: *Aluminium-Taschenbuch: CD-ROM*. Bd. 1-3. 2nd ed. Düsseldorf: Alu Media GmbH 2011.
10. Fink WL, Willey LA: Quenching of 75s-aluminum alloy. *Transactions of the American Institute of Mining and Metallurgical Engineers* 175 (1948): 414–427.
11. Bryant AJ: Effect of composition on quench-sensitivity of some Al-Zn-Mg alloys. *Journal of the Institute of Metals* 94 (1966): 94.
12. Holl HA: Investigations into possibility of reducing quench-sensitivity in high-strength Al-Zn-Mg-Cu alloys. *Journal of the Institute of Metals* 97 (1969): 200.
13. Conserva M, Russo E, Caloni O: Comparison of the influence of chromium and zirconium on the quench sensitivity of Al-Zn-Mg-Cu alloys. *Metallurgical transactions A: Physical metallurgy and materials science* 2 (1971): 1227–1232.
14. Zoller H, Ried A: Metallurgical aspects in developement of AlMgSi alloys with a low sensitivity to quenching. *Zeitschrift fuer Metallkunde/Materials Research and Advanced Techniques* 62 (1971): 354–358.
15. Thompson DS, Subramanya BS, Levy SA: Quench rate effects in Al-Zn-Mg-Cu alloys. *Metallurgical transactions A: Physical metallurgy and materials science* 2 (1971): 1149–1160.
16. Conserva M, Fiorini P: Interpretation of quench-sensitivity in Al-Zn-Mg-Cu alloys. *Metallurgical transactions A: Physical metallurgy and materials science* 4 (1973): 857–862.
17. Lohne O, Dons AL: Quench sensitivity in AlMgSi alloys containing Mn or Cr. *Scandinavian Journal of Metallurgy* 12 (1983): 34–36.
18. Evancho JW, Staley JT: Kinetics of precipitation in aluminum alloys during continuous cooling. *Metallurgical transactions A: Physical metallurgy and materials science* 1974: 43–47.
19. Dons AL, Lohne O: Quench Sensitivity of AlMgSi-Alloys Containing Mn or Cr. *Materials Research Society Symposia Proceedings* (1984): 723–728.
20. Staley JT: Quench factor analysis of aluminium alloys. *Materials Science and Technology* 3 (1987): 923–935.
21. Thomas MP, King JE: Quench sensitivity of 2124 Al alloy and Al/SiCp metal matrix composite. *Scripta Metallurgica et Materialia* 31 (1994): 209–214.
22. Cavazos JL, Colás R: Aging of an aluminum alloy resulting from variations in the cooling rate. *Journal of Materials Engineering and Performance* 8 (1999): 509–512.
23. Zajac S, Bengtsson B, Jönsson C, Isaksson A: Quench sensitivity of 6063 and 6082 aluminium alloys. In: *7th International Aluminum Extrusion Technology Seminar, Chicago, 2000*; 73–82.
24. Cavazos JL, Colás R: Precipitation in a heat-treatable aluminum alloy cooled at different rates. *Materials Characterization* 47 (2001): 175–179.

25. Cavazos JL, Colás R: Quench sensitivity of a heat treatable aluminum alloy. *Materials Science and Engineering A* 363 (2003): 171–178.
26. Lim ST, Yun SJ, Nam SW: Improved quench sensitivity in modified aluminum alloy 7175 for thick forging applications. *Materials Science and Engineering A* 371 (2004): 82–90.
27. Strobel K, Easton MA, Sweet L, Couper MJ, Nie JF: Relating quench sensitivity to microstructure in 6000 series aluminium alloys. *Materials Transactions* 52 (2011): 914–919.
28. Strobel K, Lay MDH, Easton MA, Sweet L, Zhu S, Parson NC, Hill AJ: Effects of quench rate and natural ageing on the age hardening behaviour of aluminium alloy AA6060. *Materials Characterization* 111 (2016): 43–52.
29. Yoshida H, Watanabe T, Hatta H: Effect of quenching rate on age hardening in an Al–Zn–Mg alloy sheet. *Journal of Japan Institute of Light Metals* 67 (2017): 41–48.
30. Hirano S, Yoshida H, Uno T: Quench Sensitivity in Al–Li based alloys. In: Sanders TH, Starke EA, Pitts D (eds): *Proceedings of the Fifth International Aluminum-Lithium Conference*. Birmingham, UK 1989; 335–44.
31. Deschamps A, Texier G, Ringeval S, Delfaut-Durut L: Influence of cooling rate on the precipitation microstructure in a medium strength Al–Zn–Mg alloy. *Materials Science and Engineering A* 501 (2009): 133–139.
32. Martin JW: *Micromechanisms in particle-hardened alloys*. Cambridge, UK: Cambridge University Press 1980.
33. Schumacher P, Pogatscher S, Starink MJ, Kessler O, Schick C, Mohles V, Milkereit B: Control of phase transformation during heat treatments based on DSC experiments. In: Militzer M, Botton G, Chen L-Q, Howe JM, Sinclair CW, Zurob H (eds): *Proceedings of the International Conference on Solid-Solid Phase Transformations in Inorganic Materials 2015* 2015; 699–706.
34. Deng YL, Wan L, Zhang YY, Zhang XM: Influence of Mg content on quench sensitivity of Al–Zn–Mg–Cu aluminum alloys. *Journal of Alloys and Compounds* 509 (2011): 4636–4642.
35. Rometsch PA, Zhang Y, Knight S: Heat treatment of 7xxx series aluminium alloys - Some recent developments. *Transactions of Nonferrous Metals Society of China* 24 (2014): 2003–2017.
36. Reich M: *Mechanische Eigenschaften unterkühlter Aluminiumlegierungen und deren Implementierung in die Wärmebehandlungssimulation*. Aachen: Shaker Verlag 2013.
37. Reich M, Kessler O: Mechanical properties of undercooled aluminium alloys and their implementation in quenching simulation. *Materials Science and Technology* 28 (2012): 769–772.
38. Reich M, Kessler O: Numerical and experimental analysis of residual stresses and distortion in different quenching processes of aluminum alloy profiles. In: MacKenzie DS (ed): *Quenching Control and Distortion 2012 - Proceedings of the 6th International Quenching and Control of Distortion Conference*. (September 9-13, 2012, Chicago, IL, USA): ASM International 2012; 563–74.
39. Chobaut N: *Measurements and modelling of residual stresses during quenching of thick heat treatable aluminium components in relation to their precipitation state*. PhD thesis. EPFL Lausanne 2015.
40. Chobaut N, Carron D, Drezet JM: Monitoring precipitation kinetics in heat treatable aluminium alloys using in-situ resistivity in gleeble thermomechanical simulator. *Materials Science Forum* 794-796 (2014): 921–925.
41. MacKenzie DS (ed): *Quenching Control and Distortion 2012 - Proceedings of the 6th International Quenching and Control of Distortion Conference*. (September 9-13, 2012, Chicago, IL, USA): ASM International 2012.
42. Hoffmann F, Kessler O, Lübben T, Mayr P: *Distortion Engineering - Verzugsbeherrschung in der Fertigung*. *HTM Journal of Heat Treatment and Materials* 57 (2002): 213–217.
43. Hoffmann F, Kessler O, Lübben T, Mayr P: "Distortion Engineering" - Distortion control during the production process. *Heat Treatment of Metals* 31 (2004): 27–30.
44. Shuey RT, Tiryakioğlu M: *Quenching of Aluminum Alloys*. In: *Quenching Theory and Technology*, CRC Press, 2nd edition, 2011.
45. Sjölander E, Seifeddine S, Fracasso F: Influence of quench rate on the artificial ageing response of an Al–8Si–0.4Mg cast alloy. *Materials Science Forum* (2015).
46. Saikawa S, Morioka R, Matsuda K, Ikeno S, Yanagihara E, Orii S: Age-hardening behavior of Al–10%Si–0.3%Mg alloy with water quenching and direct quenching after solution treatment. *J Jpn Inst Light Met (Journal of Japan Institute of Light Metals)* 65 (2015): 218–223.
47. Tiryakioğlu M, Shuey RT: Quench sensitivity of an Al–7 pct Si–0.6 pct Mg alloy: Characterization and modeling. *Metallurgical and Materials Transactions B: Process Metallurgy and Materials Processing Science* 38 (2007): 575–582.
48. Rometsch PA, Wang SC, Harriss A, Gregson PJ, Starink MJ: The effect of homogenizing on the quench sensitivity of 6082. In: *Proceedings of the 8th International Conference Aluminium Alloys. Their Physical and Mechanical Properties (ICAA8, Oxford, UK)* 396–402 (2002).

49. Zhang DL, Zheng L: The quench sensitivity of cast Al-7 Wt pct Si-0.4 Wt pct Mg alloy. *Metallurgical and Materials Transactions A: Physical Metallurgy and Materials Science* 27 (1996): 3983–3991.
50. Chaudhury SK, Apelian D: Effects of Mg and Cu content on quench sensitivity of Al-Si-Mg alloy. *International Journal of Metalcasting* 10 (2016): 138–146.
51. Tzeng YC, Wu CT, Lee SL: The effect of trace Sc on the quench sensitivity of Al-7Si-0.6 Mg alloys. *Materials Letters* 161 (2015): 340–342.
52. Sisson Jr. RD, Ma S: Predicting quench rate effect on cast Al alloy mechanical properties. *Heat Treating Progress* 6 (2006): 24.
53. Newkirk JW, Mehta S: Studying the Quench Sensitivity of Cast Al Alloys. In: Funatani K, Totten GE (eds): *Heat Treating: Proceedings of the 20th Conference*; St. Louis, MO, USA 2000; 1094–1100.
54. Dorward RC: A dynamic quench model for strength predictions in heat-treatable aluminum alloys. *Journal of Materials Processing Technology* 66 (1997): 25–29.
55. Ma S, Maniruzzaman MD, MacKenzie DS, Sisson RD: A methodology to predict the effects of quench rates on mechanical properties of cast aluminum alloys. *Metallurgical and Materials Transactions B: Process Metallurgy and Materials Processing Science* 38 (2007): 583–589.
56. Rometsch PA, Schaffer GB: Quench modelling of Al-7Si-Mg casting alloys. *International Journal of Cast Metals Research* 12 (2000): 431–439.
57. Rometsch PA, Starink MJ, Gregson PJ: Improvements in quench factor modelling. *Materials Science and Engineering A* 339 (2003): 255–264.
58. Tiryakioğlu M, Shuey RT: Modeling quench sensitivity of aluminum alloys for multiple tempers and properties: Application to AA2024. *Metallurgical and Materials Transactions A: Physical Metallurgy and Materials Science* 41 (2010): 2984–2991.
59. Li H-Y, Geng JF, Zheng ZQ, Wang JQ, Su Y, Hu B: Continuous cooling transformation curve of a novel Al-Cu-Li alloy. *Transactions of Nonferrous Metals Society of China* 16 (2006): 1110–1115.
60. Li H-Y, Bin J, Zhao Y-k, WANG XF: Establishment of continuous cooling transformation diagrams of aluminum alloys using in situ voltage measurement. *Transactions of Nonferrous Metals Society of China* 21 (2011): 1944–1949.
61. Li H-Y, Bin J, Wang XF, Tang Y: Continuous cooling transformation of 2A12 aluminum alloy studied by using in-situ electrical resistivity measurement. *Zhongguo Youse Jinshu Xuebao/Chinese Journal of Nonferrous Metals* 21 (2011): 2068–2074.
62. Li H-Y, ZENG C-t, Has M-S, Liu J-j, LU X-c: Time–temperature–property curves for quench sensitivity of 6063 aluminum alloy. *Transactions of Nonferrous Metals Society of China* 23 (2013): 38–45.
63. Li H-Y, Zhao YK, Tang Y, Wang XF, Deng YZ: Continuous cooling transformation curve for 2A14 aluminum alloy and its application. *Zhongguo Youse Jinshu Xuebao/Chinese Journal of Nonferrous Metals* 21 (2011): 968–974.
64. Hengge E, Enzinger R, Luckabauer M, Sprengel W, Würschum R: Quantitative volumetric identification of precipitates in dilute alloys using high-precision isothermal dilatometry. *Philosophical Magazine Letters* 98 (2018): 301–309.
65. Luckabauer M, Hengge E, Klinser G, Sprengel W, Würschum R: In Situ Real-Time Monitoring of Aging Processes in an Aluminum Alloy by High-Precision Dilatometry. In: Solanki K., Orlov D., Singh A., Neelameggham N. (eds) *Magnesium Technology 2017. The Minerals, Metals & Materials Series*. Springer, Cham (2017): 669–674.
66. Tsao C-S, Huang E-W, Wen M-H, Kuo T-Y, Jeng S-L, Jeng U-S, Sun Y-S: Phase transformation and precipitation of an Al-Cu alloy during non-isothermal heating studied by in situ small-angle and wide-angle scattering. *Journal of Alloys and Compounds* 579 (2013): 138–146.
67. Huang E-W, Tsao C-S, Wen M-H, Kuo T-Y, Tu S-Y, Wu B-W, Su C-J, Jeng U-S: Resolution of structural transformation of intermediates in Al-Cu alloys during non-isothermal precipitation. *Journal of Materials Research* 29 (2014): 874–879.
68. De Geuser F, Styles MJ, Hutchinson CR, Deschamps A: High-throughput in-situ characterization and modeling of precipitation kinetics in compositionally graded alloys. *Acta Materialia* 101 (2015): 1–9.
69. Zhang F, Levine LE, Allen AJ, Campbell CE, Creuziger AA, Kazantseva N, Ilavsky J: In situ structural characterization of ageing kinetics in aluminum alloy 2024 across angstrom-to-micrometer length scales. *Acta Materialia* 111 (2016): 385–398.
70. Ivanov R, Deschamps A, De Geuser F: A combined characterization of clusters in naturally aged Al-Cu-(Li, Mg) alloys using small-angle neutron and X-ray scattering and atom probe tomography. *Journal of Applied Crystallography* 50 (2017): 1725–1734.
71. Ivanov R, Deschamps A, De Geuser F: Clustering kinetics during natural ageing of Al-Cu based alloys with (Mg, Li) additions. *Acta Materialia* 157 (2018): 186–195.
72. Biroli G, Caglioti G, Martini L, Riontino G: Precipitation kinetics of AA4032 and AA6082: A comparison based on DSC and TEM. *Scripta Materialia* 39 (1998): 197–203.

73. Li XM, Starink MJ: Analysis of Precipitation and Dissolution in Overaged 7xxx Aluminium Alloys using DSC. *Materials Science Forum* 331-337 (2000): 1071–1076.
74. Starink MJ: Heating rate dependence of precipitation in an Al-1%Si alloy. *Journal of Materials Science Letters* 15 (1996): 1749–1751.
75. Starink MJ: Analysis of aluminium based alloys by calorimetry: Quantitative analysis of reactions and reaction kinetics. *International Materials Reviews* 49 (2004): 191–226.
76. Birol Y: DSC analysis of the precipitation reaction in AA6005 alloy. *Journal of Thermal Analysis and Calorimetry* 93 (2008): 977–981.
77. Birol Y: DSC Analysis of the precipitation reactions in the alloy AA6082. *Journal of Thermal Analysis and Calorimetry* 83 (2006): 219–222.
78. Herding T, Kessler O, Hoffmann F, Mayr P: An Approach for Continuous Cooling Transformation (CCT) Diagrams of Aluminium Alloys. *Materials Science Forum* 396-402 (2002): 869–874.
79. Kessler O, Bargaen R von, Hoffmann F, Zoch HW: Continuous cooling transformation (CCT) diagram of aluminum alloy Al-4.5Zn-1Mg. In: Poole WJ, Wells MA, Lloyd DJ (eds): 10 th International Conference on Aluminium Alloys 2006, Pts 1 and 2: Trans Tech Publications 2006; 1467–72.
80. Bargaen R von, Kessler O, Zoch HW: Kontinuierliche Zeit- Temperatur- Ausscheidungsdiagramme der Aluminiumlegierungen 7020 und 7050. *HTM Journal of Heat Treatment and Materials* 62 (2007): 8.
81. Ostermann F: *Anwendungstechnologie Aluminium*. 3rd ed. Berlin, Heidelberg: Springer-Verlag 2014.
82. Starink MJ: A new model for diffusion-controlled precipitation reactions using the extended volume concept. *Thermochimica Acta* 596 (2014): 109–119.
83. Milkereit B, Kessler O, Schick C: Precipitation and Dissolution Kinetics in Metallic Alloys with Focus on Aluminium Alloys by Calorimetry in a Wide Scanning Rate Range. In: Schick C, Mathot V (eds): *Fast Scanning Calorimetry*. Cham: Springer International Publishing 2016; 723–73.
84. Milkereit B, Kessler O, Schick C: Recent Advances in Thermal Analysis and Calorimetry of Aluminum Alloys. In: Vyazovkin S, Koga N, Schick C (eds): *Handbook of Thermal Analysis and Calorimetry: Recent Advances, Techniques and Applications*, 6th ed. New York: Elsevier Ltd; Elsevier Science 2018.
85. Li H-Y, Zhao YK, Tang Y, Wang XF: Determination and application of CCT diagram for 6082 aluminum alloy. *Acta Metallurgica Sinica* 46 (2010): 1237–1243.
86. Li PY, Xiong BQ, Zhang YA, Li ZH, Zhu BH, Wang F, Liu HW: Quench sensitivity and microstructure character of high strength AA7050. *Transactions of Nonferrous Metals Society of China* 22 (2012): 268–274.
87. Li SL, Huang ZQ, Chen WP, Liu ZM, Qi WJ: Quench sensitivity of 6351 aluminum alloy. *Transactions of Nonferrous Metals Society of China* 23 (2013): 46–52.
88. Li H-Y, Liu JJ, Yu WC, Li DW: Development of non-linear continuous cooling precipitation diagram for Al-Zn-Mg-Cu alloy. *Materials Science and Technology* 31 (2015): 1443–1451.
89. Ólafsson P, Sandström R, Karlsson Å: Comparison of experimental, calculated and observed values for electrical and thermal conductivity of aluminium alloys. *Journal of Materials Science* 32 (1997): 4383–4390.
90. Esmaeili S, Vaumousse D, Zandbergen MW, Poole WJ, Cerezo A, Lloyd DJ: A study on the early-stage decomposition in the Al-Mg-Si-Cu alloy AA6111 by electrical resistivity and three-dimensional atom probe. *Philosophical Magazine* 87 (2007): 3797–3816.
91. Rometsch PA, Xu Z, Zhong H, Yang H, Ju L, Wu XH: Strength and Electrical Conductivity Relationships in Al-Mg-Si and Al-Sc Alloys. *Materials Science Forum* 794-796 (2014): 827–832.
92. Luckabauer M, Sprengel W, Würschum R: A high-stability non-contact dilatometer for low-amplitude temperature-modulated measurements. *Review of Scientific Instruments* 87 (2016).
93. Kövér M, Sláma P: Aluminium Alloys Measurement in Quenching Dilatometer and Application of the Data. *Advanced Materials Research* 1127 (2015): 73–77.
94. Milkereit B, Reich M, Kessler O: Detection of Quench Induced Precipitation in Al Alloys by Dilatometry. *Materials Science Forum* 877 (2016): 147–152.
95. Krause-Rehberg R, Leipner HS: *Positron annihilation in semiconductors: Defect studies ; with 20 tables*. Berlin: Springer 2003.
96. Dlubek G, Krause R, Brümmer O, Plazaola F: Study of formation and reversion of Guinier-Preston zones in Al-4.5 at%Zn-x at%Mg alloys by positrons. *Journal of Materials Science* 21 (1986): 853–858.
97. Banhart J, Liu M, Yong Y, Liang Z, Chang CST, Elsayed M, Lay MDH: Study of ageing in Al-Mg-Si alloys by positron annihilation spectroscopy. *Physica B: Condensed Matter* 407 (2012): 2689–2696.

98. Banhart J, Lay MDH, Chang CST, Hill AJ: Kinetics of natural aging in Al-Mg-Si alloys studied by positron annihilation lifetime spectroscopy. *Physical Review B - Condensed Matter and Materials Physics* 83 (2011): <https://doi.org/10.1103/PhysRevB.83.014101>.
99. Banhart J, Lay MDH, Chang CST, Hill AJ: Kinetics of natural aging in Al-Mg-Si alloys studied by positron annihilation lifetime spectroscopy. *Physical Review B - Condensed Matter and Materials Physics* 83 (2011).
100. Banhart J, Chang CST, Liang Z, Wanderka N, Lay MDH, Hill AJ: Natural Aging in Al-Mg-Si Alloys - A Process of Unexpected Complexity. *Advanced Engineering Materials* 12 (2010): 559–571.
101. Liu M, Klobes B, Banhart J: Positron lifetime study of the formation of vacancy clusters and dislocations in quenched Al, Al-Mg and Al-Si alloys. *Journal of Materials Science* 51 (2016): 7754–7767.
102. John Banhart: Suitability of PALS for in situ experiments. e-mail. Berlin, Rostock 2019.
103. Schloth P, Menzel A, Fife JL, Wagner JN, van Swygenhoven H, Drezet J-M: Early cluster formation during rapid cooling of an Al-Cu-Mg alloy: In situ small-angle X-ray scattering. *Scripta Materialia* 108 (2015): 56–59.
104. Schloth P, Wagner JN, Fife JL, Menzel A, Drezet JM, van Swygenhoven H: Early precipitation during cooling of an Al-Zn-Mg-Cu alloy revealed by in situ small angle X-ray scattering. *Applied Physics Letters* 105-101908 (2014): 1–4.
105. Schloth P: Precipitation in the high strength AA7449 aluminium alloy: implications on internal stresses on different length scales. PhD thesis. EPFL Lausanne 2015.
106. De Geuser F, Deschamps A: Precipitate characterisation in metallic systems by small-angle X-ray or neutron scattering. *Comptes Rendus Physique* 13 (2012): 246–256.
107. Frédéric de Geuser: detection limits of SAXS and SANS. e-mail correspondence 2019.
108. Briggs SA, Edmondson PD, Littrell KC, Yamamoto Y, Howard RH, Daily CR, Terrani KA, Sridharan K, Field KG: A combined APT and SANS investigation of α' phase precipitation in neutron-irradiated model FeCrAl alloys. *Acta Materialia* 129 (2017): 217–228.
109. Andrews RN, Serio J, Muralidharan G, Ilavsky J: An in situ USAXS-SAXS-WAXS study of precipitate size distribution evolution in a model Ni-based alloy. *Journal of Applied Crystallography* 50 (2017): 734–740.
110. Haas S, Andersson J, Fisk M, Park J-S, Lienert U: Correlation of precipitate evolution with Vickers hardness in Haynes® 282® superalloy: In-situ high-energy SAXS/WAXS investigation. *Materials Science and Engineering A* 711 (2018): 250–258.
111. Tolnai D, Mendis CL, Stark A, Szakács G, Wiese B, Kainer KU, Hort N: In situ synchrotron diffraction of the solidification of Mg₄Y₃Nd. *Materials Letters* 102-103 (2013): 62–64.
112. B. Milkereit, C. Rowolt, H. Fröck, et al.: In-Situ X-Ray Diffraction During Quenching of Aluminum Alloy 7150. Lecture at 16th International Conference on Aluminium Alloys, Montreal, Canada 2018.
113. Hunger H-J (ed): *Werkstoffanalytische Verfahren: Eine Auswahl ; mit 39 Tabellen*. 1st ed. Leipzig: Dt. Verl. für Grundstoffindustrie 1995.
114. Höhne, G. W. H., Hemminger WF, Flammersheim HJ: *Differential Scanning Calorimetry*. 2nd ed. Berlin, Heidelberg: Springer-Verlag 2003.
115. Milkereit B, Beck M, Reich M, Kessler O, Schick C: Precipitation kinetics of an aluminium alloy during Newtonian cooling simulated in a differential scanning calorimeter. *Thermochimica Acta* 522 (2011): 86–95.
116. Chang CST, Banhart J: Low-temperature differential scanning calorimetry of an Al-Mg-Si Alloy. *Metallurgical and Materials Transactions A: Physical Metallurgy and Materials Science* 42 (2011): 1960–1964.
117. Milkereit B: *Kontinuierliche Zeit-Temperatur-Ausscheidungs-Diagramme von Al-Mg-Si-Legierungen*. Dissertation. Rostock, PhD-Thesis, University of Rostock, Shaker Verlag, Aachen, DOI: 10.2370/9783832299934 2011.
118. Rowolt C, Milkereit B, Andreatza P, Kessler O: Quantitative High Temperature Calorimetry on Precipitation in Steel and Nickel Alloys. *Thermochimica Acta* 677 (2019): 169–179.
119. Milkereit B, Burschat L, Kemsies RH, Springer A, Schick C, Kessler O: In situ differential scanning calorimetry analysis of dissolution and precipitation kinetics in Mg-Y-RE alloy WE43. *Journal of Magnesium and Alloys* 7 (2019): 1–14.
120. Sarge SM, Hemminger WF, Gmelin E, Höhne, G. W. H., Cammenga HK, Eysel W: Metrologically based procedures for the temperature, heat and heat flow rate calibration of DSC. *Journal of Thermal Analysis and Calorimetry* 49 (1997): 1125–1134.
121. Höhne, G. W. H., Glöggl E: Some peculiarities of the DSC-2/-7 (Perkin-Elmer) and their influence on accuracy and precision of the measurements. *Thermochimica Acta* 151 (1989): 295–304.
122. Zahra CY, Zahra A-M: The Perkin-Elmer 1020 series thermal analysis system. *Thermochimica Acta* 276 (1996): 161–174.
123. Kemsies RH, Milkereit B, Wenner S, Holmestad R, Kessler O: In situ DSC investigation into the kinetics and microstructure of dispersoid formation in Al-Mn-Fe-Si(-Mg) alloys. *Materials & Design* 146 (2018): 96–107.

124. Zohrabyan D, Milkereit B, Kessler O, Schick C: Precipitation enthalpy during cooling of aluminum alloys obtained from calorimetric reheating experiments. *Thermochimica Acta* 529 (2012): 51–58.
125. Rowolt C, Milkereit B, Gebauer M, Seidel C, Müller B, Kessler O: In-Situ Phase Transition Analysis of Conventional and Laser Beam Melted AlSi10Mg and X5CrNiCuNb16-4 Alloys. *HTM - Journal of Heat Treatment and Materials* 73 (2018): 317–334.
126. Schumacher P: Plastisches Verformungsverhalten unterkühlter Aluminiumlegierungen im System Al-Mg-Si: PhD thesis, Universität Rostock 2018.
127. Zhuravlev E, Schick C: Fast scanning power compensated differential scanning nano-calorimeter: 1. The device. *Thermochimica Acta* 50 (2010): 1–13.
128. Reich M, Kessler O: Quenching Simulation of Aluminum Alloys Including Mechanical Properties of the Undercooled States. *Materials Performance and Characterization* 1 (2012): 104632.
129. Chobaut N, Carron D, Arsène S, Schloth P, Drezet JM: Quench induced residual stress prediction in heat treatable 7xxx aluminium alloy thick plates using Gleeble interrupted quench tests. *Journal of Materials Processing Technology* 222 (2015): 373–380.
130. Drezet JM, Chobaut N, Schloth P, van Swygenhoven H: Internal stress generation during quenching of thick heat treatable aluminium alloys. In: TMS 2013 Annual Meeting and Exhibition. San Antonio, TX 2013.
131. Milkereit B, Jonas L, Schick C, Kessler O: The continuous cooling precipitation diagram of an aluminum alloy en AW-6005A. *HTM Journal of Heat Treatment and Materials* 65 (2010): 159–171.
132. Schumann H: Metallographie: mit einer Einführung in die Keramografie. 15th ed.: Wiley-VCH Verlag 2011.
133. Goldstein JI, Newbury DE, Michael JR, Ritchie NWM, Scott JHJ, Joy DC: Scanning Electron Microscopy and X-Ray Microanalysis. New York, NY: Springer New York 2018.
134. Brydson R: Aberration-Corrected Analytical Transmission Electron Microscopy. Chichester, UK: John Wiley & Sons, Ltd 2011.
135. Hornbogen E, Skrotzki B: Mikro- und Nanoskopie der Werkstoffe. 3rd ed. Berlin, Heidelberg: Springer-Verlag 2009.
136. Osten J: Werkstoffstrukturen und Eigenschaften beim laserunterstützten Clinchen von hochfesten Stahl/Aluminium-Mischverbindungen. PhD thesis. University of Rostock 2018.
137. Schumacher P, Reich M, Mohles V, Pogatscher S, Uggowitzer PJ, Milkereit B: Correlation between supersaturation of solid solution and mechanical behaviour of two binary Al-Si-alloys. *Materials Science Forum* 794-796 (2014): 508–514.
138. Milkereit B, Kessler O: Continuous-Cooling Precipitation Diagrams. In: George E. Totten (ed): ASM Handbook Volume 4E: Heat Treating of Nonferrous Alloys. Materials Park, Ohio: ASM International 2016; 191–7.
139. Kissinger HE: Reaction Kinetics in Differential Thermal Analysis. *Analytical Chemistry* 29 (1957): 1702–1706.
140. Fröck H, Graser M, Reich M, Lechner M, Merklein M, Kessler O: Influence of short-term heat treatment on the microstructure and mechanical properties of EN AW-6060 T4 extrusion profiles: Part A. *Production Engineering* 10 (2016): 383–389.
141. Starink MJ: The determination of activation energy from linear heating rate experiments: A comparison of the accuracy of isoconversion methods. *Thermochimica Acta* 404 (2003): 163–176.
142. Starink MJ: Activation energy determination for linear heating experiments: Deviations due to neglecting the low temperature end of the temperature integral. *Journal of Materials Science* 42 (2007): 483–489.
143. Lang P, Povoden-Karadeniz E, Falahati A, Kozeschnik E: Simulation of the effect of composition on the precipitation in 6xxx Al alloys during continuous-heating DSC. *Journal of Alloys and Compounds* 612 (2014): 443–449.
144. Falahati A, Wu J, Lang P, Ahmadi MR, Povoden-Karadeniz E, Kozeschnik E: Assessment of parameters for precipitation simulation of heat treatable aluminum alloys using differential scanning calorimetry. *Transactions of Nonferrous Metals Society of China* 24 (2014): 2157–2167.
145. Falahati A, Povoden-Karadeniz E, Lang P, Warczok P, Kozeschnik E: Thermo-kinetic computer simulation of differential scanning calorimetry curves of AlMgSi alloys. *International Journal of Materials Research* 101 (2010): 1089–1096.
146. Hersent E, Driver JH, Piot D: Modelling differential scanning calorimetry curves of precipitation in Al–Cu–Mg. *Scripta Materialia* 62 (2010): 455–457.
147. Khan IN, Starink MJ: Microstructure and strength modelling of Al-Cu-Mg alloys during non-isothermal treatments Part 1 - Controlled heating and cooling. *Materials Science and Technology* 24 (2008): 1403–1410.
148. Birol Y: A calorimetric analysis of the precipitation reactions in AlSi1MgMn alloy with Cu additions. *Thermochimica Acta* 650 (2017): 39–43.
149. Starink MJ, Zahra AM: β' and β precipitation in an Al-Mg alloy studied by DSC and TEM. *Acta Materialia* 46 (1998): 3381–3397.

150. Kim SN, Kim JH, Tezuka H, Kobayashi E, Sato T: Formation Behavior of Nanoclusters in Al–Mg–Si Alloys with Different Mg and Si Concentration. *Materials Transactions* 54 (2013): 297–303.
151. Papazian JM: A calorimetric study of precipitation in aluminum alloy 2219. *Metallurgical transactions A: Physical metallurgy and materials science* 12 (1981): 269–280.
152. Milkereit B, Österreich M, Schuster P, Kirov G, Mukeli E, Kessler O: Dissolution and Precipitation Behavior for Hot Forming of 7021 and 7075 Aluminum Alloys. *Metals* 8 (2018).
153. Zohrabyan D, Milkereit B, Schick C, Kessler O: Continuous cooling precipitation diagram of high alloyed Al-Zn-Mg-Cu 7049A alloy. *Transactions of Nonferrous Metals Society of China* 24 (2014): 2018–2024.
154. Lasagni FA, Mingler B, Dumont M, Degischer HP: Precipitation kinetics of Si in aluminium alloys. *Materials Science and Engineering A* 480 (2008): 383–391.
155. Rosenbaum HS, Turnbull D: Metallographic investigation of precipitation of silicon from aluminum. *Acta Metallurgica* 7 (1959): 664–674.
156. Zhang W, Liu L, Huang T, Zhao X, Yu Z, Fu H: Effect of cooling rate on γ' precipitate of DZ4125 alloy under high thermal gradient directional solidification. *Jinshu Xuebao/ Acta Metallurgica Sinica* 45 (2009): 592–596.
157. Mallikarjuna HT, Caley WF, Richards NL: The effect of cooling rate on the γ' composition, morphology and corrosion behaviour of IN738LC. *Corrosion Science* 149 (2019): 37–44.
158. Rakoczy Ł, Cempura G, Kruk A, Czyrska-Filemonowicz A, Zielińska-Lipiec A: Evolution of γ' morphology a γ/γ' lattice parameter misfit in a nickel-based superalloy during non-equilibrium cooling. *International Journal of Materials Research* 110 (2019): 66–69.
159. Hisazawa H, Terada Y, Takeyama M: Morphology evolution of γ' precipitates during isothermal exposure in wrought Ni-based superalloy Inconel X-750. *Materials Transactions* 58 (2017): 817–824.
160. Porter DA, Easterling KE: *Phase transformations in metals and alloys*. 2nd ed. London, New York: Chapman & Hall 1992.
161. Ives LK, Swartzendruber LJ, Boettinger WJ, et al.: *Processing/microstructure/property relationships in 2024 aluminum alloy plates*; National Bureau of Standards Report 83-2669. Washington DC: 270 1983.
162. Zajac S, Bengtsson B, Jönsson C: Influence of Cooling after Homogenisation and Reheating to Extrusion on Extrudability and Final Properties of AA 6063 and AA6082 Alloys. *Materials Science Forum* 396-402 (2002): 399–404.
163. Zajac S, Bengtsson B, Johansson A, Gullman LO: Optimisation of Mg₂Si phase for extrudability of AA 6063 and AA 6005 alloys. *Materials Science Forum* 217-222 (1996): 397–402.
164. Birol Y: Effect of cooling rate on precipitation during homogenization cooling in an excess silicon AlMgSi alloy. *Materials Characterization* 73 (2012): 37–42.
165. Morgeneyer TF, Starink MJ, Wang SC, Sinclair I: Quench sensitivity of toughness in an Al alloy: Direct observation and analysis of failure initiation at the precipitate-free zone. *Acta Materialia* 56 (2008): 2872–2884.
166. Jacobs MH: The structure of metastable precipitates formed during aging of an Al-Mg-Si alloy. *Philosophical Magazine* 26 (1972): 1–13.
167. Sagalowicz L, Lapasset G, Hug G: Transmission electron microscopy study of a precipitate which forms in the Al-Mg-Si system. *Philosophical Magazine Letters* 74 (1996): 57–66.
168. Edwards GA, Stiller K, Dunlop GL, Couper MJ: The precipitation sequence in Al-Mg-Si alloys. *Acta Materialia* 46 (1998): 3893–3904.
169. Cayron C, Sagalowicz L, Beffort O, Buffat PA: Structural phase transition in Al-Cu-Mg-Si alloys by transmission electron microscopy study on an Al-4 wt% Cu-1 wt% Mg-Ag alloy reinforced by SiC particles. *Philosophical Magazine a-Physics of Condensed Matter Structure Defects and Mechanical Properties* 79 (1999): 2833–2851.
170. Cayron C, Buffat PA: Transmission electron microscopy study of the β' phase (Al-Mg-Si alloys) and QC phase (Al-Cu-Mg-Si alloys): Ordering mechanism and crystallographic structure. *Acta Materialia* 48 (2000): 2639–2653.
171. Marioara CD, Andersen SJ, Stene TN, Hasting H, Walmsley J, Van Helvoort ATJ, Holmestad R: The effect of Cu on precipitation in Al-Mg-Si alloys. *Philosophical Magazine* 87 (2007): 3385–3413.
172. Strobel K, Easton MA, Lay MDH, Rometsch PA, Zhu S, Sweet L, Parson NC, Hill AJ: Quench Sensitivity in a Dispersoid-Containing Al-Mg-Si Alloy. *Metallurgical and Materials Transactions A* (2019).
173. Povoden-Karadeniz E, Lang P, Warczok P, Falahati A, Jun W, Kozeschnik E: CALPHAD modeling of metastable phases in the Al-Mg-Si system. *Computer Coupling of Phase Diagrams and Thermochemistry* 43 (2013): 94–104.
174. Dumolt SD, Laughlin DE, Williams JC: Formation of a modified β' -phase in aluminum alloy 6061. *Scripta Metallurgica* 18 (1984): 1347–1350.
175. Bratland DH, Grong Ø, Shercliff H, Myhr OR, Tjøtta S: Modelling of precipitation reactions in industrial processing. *Acta Materialia* 45 (1997): 1–22.

176. H. Yoshida, T. Watanabe, H. Hatta: Effect of quenching rate on age hardening in an Al-Zn-Mg alloy sheet. In: Mary Wells MB (ed): 16th International Conference on Aluminium Alloys, Montreal, Canada: METSOC.org 2018; paper 393778.
177. Yong Zhang: Quench Sensitivity of 7xxx Series Aluminium Alloys. PhD thesis. Monash University, Melbourne, Australia 2014.
178. Fang X, Song M, Li K, Du Y, Zhao D, Jiang C, Zhang H: Effects of Cu and Al on the crystal structure and composition of η (MgZn₂) phase in over-aged Al-Zn-Mg-Cu alloys. *Journal of Materials Science* 47 (2012): 5419–5427.
179. Andrae D, Paulus B, Wedig U, Jansen M: A first-principles study of electronic structure of the laves phase MgZn₂. *Zeitschrift für Anorganische und Allgemeine Chemie* 639 (2013): 1963–1967.
180. Osten J, Reich M, Milkereit B, Kessler O: Adapting age hardening parameters of high-alloyed 7xxx aluminium alloys through thermal analysis. Lecture at 16th International Conference on Aluminium Alloys, Montreal, Canada 2018.
181. Zhang Y, Pelliccia D, Milkereit B, Kirby N, Starink MJ, Rometsch PA: Analysis of age hardening precipitates of Al-Zn-Mg-Cu alloys in a wide range of quenching rates using small angle X-ray scattering. *Materials and Design* 142 (2018): 259–267.
182. Zhang Y, Bettles C, Rometsch PA: Effect of recrystallisation on Al₃Zr dispersoid behaviour in thick plates of aluminium alloy AA7150. *Journal of Materials Science* 49 (2014): 1709–1715.
183. Deschamps A, Bréchet Y: Nature and distribution of quench-induced precipitation in an Al-Zn-Mg-Cu alloy. *Scripta Materialia* 39 (1998): 1517–1522.
184. Deschamps A, Bréchet Y: Influence of quench and heating rates on the ageing response of an Al-Zn-Mg-(Zr) alloy. *Materials Science and Engineering A* 251 (1998): 200–207.
185. Lervik A, Marioara CD, Kadanik M, Walmsley JC, Milkereit B, Holmestad R: Precipitation in an extruded AA7003 aluminium alloy: observations of 6xxx-type hardening phases. *Materials and Design* (2019, in press).
186. Liu S, Li Q, Lin H, Sun L, Long T, Ye L, Deng Y: Effect of quench-induced precipitation on microstructure and mechanical properties of 7085 aluminum alloy. *Materials and Design* 132 (2017): 119–128.
187. Godard D, Archambault P, Aeby-Gautier E, Lapasset G: Precipitation sequences during quenching of the AA 7010 alloy. *Acta Materialia* 50 (2002): 2319–2329.
188. Suzuki H, Kanno M, SAITOH H, Itoi K: Effects of zirconium addition on quench-sensitivity of Al-Zn-Mg-Cu alloys. *Journal of Japan Institute of Light Metals* 33 (1983): 29–37.
189. Zhang X, Liu W, Liu S, Zhou M: Effect of processing parameters on quench sensitivity of an AA7050 sheet. *Materials Science and Engineering A* 528 (2011): 795–802.
190. Liu S, Zhong Q, Zhang Y, Liu W, Zhang X, Deng Y: Investigation of quench sensitivity of high strength Al-Zn-Mg-Cu alloys by time-temperature-properties diagrams. *Materials and Design* 31 (2010): 3116–3120.
191. Baba Y: Influence of Additional Elements on the Quench-Sensitivity and Nucleation of Precipitates in Al-Zn-Mg Alloys. *Nippon Kinzoku Gakkaishi/Journal of the Japan Institute of Metals* 31 (1967): 910–915.
192. Baba Y: Quench-Sensitivity and Age-Hardening of Al-Zn-Mg Alloys Containing Trace Elements. *Transactions of the Japan Institute of Metals* S 9 (1968): 356.
193. Lin L, Liu Z, Bai S, Zhou Y, Liu W, Lv Q: Effects of Ge and Ag additions on quench sensitivity and mechanical properties of an Al-Zn-Mg-Cu alloy. *Materials Science and Engineering A* 682 (2017): 640–647.
194. Chobaut N, Carron D, Drezet JM: Characterisation of precipitation upon cooling of an AA2618 Al-Cu-Mg alloy. *Journal of Alloys and Compounds* 654 (2016): 56–62.
195. Ber LB: Accelerated artificial ageing regimes of commercial aluminum alloys. I. Al-Cu-Mg alloys. *Materials Science and Engineering A* 280 (2000): 83–90.
196. Zhang Y, Yi Y, Huang S, Dong F, Wang H: Investigation of the quenching sensitivity of forged 2A14 aluminum alloy by time-temperature-tensile properties diagrams. *Journal of Alloys and Compounds* 728 (2017): 1239–1247.
197. Tiryakioğlu M, Shuey RT: Quench sensitivity of 2219-T87 aluminum alloy plate. *Materials Science and Engineering A* 527 (2010): 5033–5037.
198. Yin Y, Luo BH, Jing HB, Bai ZH, Gao Y: Influences of Quench Cooling Rate on Microstructure and Corrosion Resistance of Al-Cu-Mg Alloy Based on the End-Quenching Test. *Metallurgical and Materials Transactions B: Process Metallurgy and Materials Processing Science* 49 (2018): 2241–2251.
199. Wang H, Yi Y, Huang S: Investigation of quench sensitivity of high strength 2219 aluminum alloy by TTP and TTT diagrams. *Journal of Alloys and Compounds* 690 (2017): 446–452.
200. Ber LB: Accelerated artificial ageing regimes of commercial aluminium alloys. II: Al-Cu, Al-Zn-Mg-(Cu), Al-Mg-Si-(Cu) alloys. *Materials Science and Engineering A* 280 (2000): 91–96.
201. Milkereit B, Fröck H, Schick C, Kessler O: Continuous cooling precipitation diagram of cast aluminium alloy Al-7Si-0.3Mg. *Transactions of Nonferrous Metals Society of China* 24 (2014): 2025–2033.

202. Rowolt C, Gebauer M, Seidel C, Müller B, Milkereit B, Kessler O: Influence of heat treatment on the material properties of laser-melted components made of AlSi10Mg and X5CrNiCuNb16-4. *Schweissen und Schneiden* 70 (2018): 634–641.
203. Li Y, Gu D: Parametric analysis of thermal behavior during selective laser melting additive manufacturing of aluminum alloy powder. *Materials and Design* 63 (2014): 856–867.
204. Doubenskaia MA, Zhirnov IV, Teleshevskiy VI, Bertrand P, Smurov IY: Determination of true temperature in selective laser melting of metal powder using infrared camera: Trans Tech Publications Ltd 2015.
205. Campbell J: Complete casting handbook: Metal casting processes, metallurgy, techniques and design. 1st ed. Oxford: Butterworth-Heinemann 2011.
206. Reich M, Osten J, Milkereit B, Kalich J, Füssel U, Kessler O: Short-time Heat Treatment of Press Hardened Steel for Laser-assisted Clinching. *Materials Science and Technology* 30 (2013): 1287–1296.
207. Reich M, Milkereit B, Bader M, Oehmingen HG, Kessler O: Kalorimetrische und dilatometrische Analyse des Anlassverhaltens in der Wärmeeinflusszone von Schweißnähten des Stahls T24. *HTM Journal of Heat Treatment and Materials* 68 (2013): 274–282.
208. Antony KC: Aging reactions in precipitation hardenable stainless steel. *Journal of metals* 15 (1963): 922–927.
209. Hsiao CN, Chiou CS, Yang JR: Aging reactions in a 17-4 PH stainless steel. *Materials Chemistry and Physics* 74 (2002): 134–142.
210. Goller GN, Clarke WC: New Precipitation-Hardening Stainless Steel. *Iron Age* 165 (1950): 86-89 & 79-83.
211. Viswanathan UK, Banerjee S, Krishnan R: Effects of aging on the microstructure of 17-4 PH stainless steel. *Materials Science and Engineering A* 104 (1988): 181–189.
212. Brezina P, Sonderegger B: Wärmebehandlung, Gefüge und Eigenschaften des korrosionsträgen, martensitaushärtbaren Stahles X5CrNiMoCuNb14-5 (14-5 PH). *HTM Journal of Heat Treatment and Materials* 33 (1978): 1–12.
213. Bürgel R, Maier HJ, Niendorf T: Handbuch Hochtemperatur- Werkstofftechnik. Wiesbaden: Vieweg+Teubner Verlag 2011.
214. Renhof L: Mikrostruktur und mechanische Eigenschaften der Nickellegierung IN 718. PhD thesis, Technical University Munich, 2007. <http://mediatum2.ub.tum.de/doc/622870/document.pdf>.
215. Jackson MP, Starink MJ, Reed RC: Determination of the precipitation kinetics of Ni₃Al in the Ni-Al system using differential scanning calorimetry. *Materials Science and Engineering A* 264 (1999): 26–38.

8 Manuscripts of publications forming the basis of the cumulative habilitation thesis; including a short description of Benjamin Milkereit's contributions

[BM1] Milkereit B, Kessler O, Schick C:
Recording of continuous cooling precipitation diagrams of
aluminium alloys.
Thermochimica Acta 492 (2009): 73–78.

Benjamin's contributions: I did the DSC measurements, their evaluation and plotting of the data. In addition, I wrote the original draft of the manuscript.

Published in: Thermochemica Acta 492, 2009 (Special Issue "Calorimetry on a Nano-scale"), 73-78

Recording of Continuous Cooling Precipitation Diagrams of Aluminium Alloys

Benjamin Milkereit*¹, Olaf Kessler:

University of Rostock

Faculty of Mechanical Engineering and Marine Technology

18051 Rostock - Germany

Christoph Schick:

University of Rostock

Inst. of Physics

18051 Rostock – Germany

¹ benjamin.milkereit@uni-rostock.de

Abstract

The purpose of this report is to present a methodology to record Continuous Cooling Precipitation (CCP) diagrams over the complete range of technical interesting cooling rates for some aluminium wrought alloys. With the information out of CCP-diagrams, the quenching step of the heat-treatment process "Age Hardening" can be optimized. The nanosized precipitations were detected via Differential Scanning Calorimetry (DSC) by identifying their exothermal heat. Aluminium wrought alloy EN AW-6005A was age hardened in three different DSCs whereby cooling rate-range varies over 3 orders of magnitude. With increasing cooling rate, the precipitation heat is decreasing. The CCP-diagram covers cooling rates from close to equilibrium conditions at 0.1 K/min up to the critical cooling rate at 375 K/min where the precipitation reaction is suppressed completely. The DSC delivers a very useful method to record full range CCP-diagrams of aluminium alloys. Opposite to other possible methods, it also delivers a measure for the amount of the nanosized precipitates by the amount of released heat. A strategy is presented for the deconvolution of overlapping DSC-peaks.

Keywords: Differential Scanning Calorimetry (DSC); hyperDSC; aluminium; alloy 6005A; age hardening; continuous cooling precipitation (CCP) diagrams

Introduction

For the strengthening of suitable aluminium alloys a heat-treatment, which is called age hardening is performed. Thereby strength is increased by the mechanism of particle strengthening. The particles, which cause the strengthening, have a typical size in the nanometre-scale. Age hardening contains out of three steps: solution annealing, quenching and aging. During the solution annealing, the relevant alloying elements are dissolved in a solid solution. This state is frozen by quenching and a supersaturated solid solution (SSS) results. In a third step the material is aged, naturally (at room temperature) or artificially (temperatures usually up to 200 °C), for a certain time to get a controlled precipitation of strengthening particles. The precipitation process follows an alloy specific sequence. Maximum strength is reached, when precipitate size and structure hinder dislocation movement most efficiently. These strengthening particles are very small compared to the incoherent equilibrium-phase particles [1].

When an age hardening aluminium alloy is solution annealed and afterwards cooled too slowly, a precipitation reaction occurs already during cooling. This reaction must be eliminated completely to reach maximum strength during the following aging. Therefore cooling must be done as fast as needed to suppress precipitation. On the other hand cooling should be done as slow as possible to avoid extensive residual stresses and distortions. In order to fit those opposite requirements cooling should be done just above the critical cooling rate, which is the slowest cooling rate where no precipitation reaction occurs. The influence of the cooling rate on the precipitation behaviour is described by Continuous Cooling Precipitation (CCP) diagrams. This information can be used to optimize the quenching step of the age hardening process. Furthermore, simulation of precipitation during the cooling step out of the age hardening process is impossible without CCP-diagrams. However, for aluminium alloys only very few CCP-diagrams exist because common procedures to record such diagrams for steels, like dilatometry, are not usable for aluminium alloys. One significant difference between steel and aluminium alloys is that during the comparable heat treatment of steels usually phase transformations with large volume changes take place. For aluminium alloys the matrix phase is constant and only alloying elements (which is typically only few wt.- percent) precipitate out of the matrix. Hence, the volume effects are much smaller at aluminium alloys.

The precipitation reactions during cooling of solution annealed heat-treatable aluminium alloys are exothermic. Recently it was reported that this precipitation reaction can be detected by Differential Scanning Calorimetry (DSC) in a cooling rate range from 5 to 475 K/min. It was found that with increasing cooling rate the precipitation heat decreases. Consequently, the released heat has been established as a measure for the amount of precipitated particles [2-5].

Cavazos et al. [6] also used the fact that the precipitation is exothermic. They measured precipitation during cooling with a special (Jominy) end-quench test by which several additional thermocouples were placed at the middle axis of the cylindrical sample. This method could implement many sources of error like that this is not a closed system. Additionally the end-quench causes non-linear cooling. The presented CCP-diagram of aluminium alloy 6063 covers a cooling rate range of approximately 2100 K/min to 35 K/min. Moreover, no direct measure for the amount of precipitates was reported. Li et al. [7] measured continuous cooling precipitation curves of an Al-

Cu-Li alloy. Amongst other methods they used the change of electric resistance to follow precipitation during cooling. This method also delivers a large range of cooling rates from approximately 70 to 1000 K/min. However, no direct measure for the amount of precipitation was reported.

As shown above it is possible to record CCP-diagrams with different methods in different ranges of cooling rates. Until today, no complete CCP-diagrams for aluminium alloys have been published. In order to record complete CCP-diagrams of aluminium alloys the DSC method seems to be most informative because it supplies a measure for the amount of precipitates via the amount of released heat in dependence of cooling rate. However, the mentioned DSC-studies cover only a small range of cooling rates. Nevertheless nowadays scanning calorimetry is possible in a very wide range of cooling rates. Very slow scanning to follow near equilibrium phase changes can be done, beside others, with Heat-Flow-DSCs of the CALVET-type [8]. Ultra fast scanning calorimetry up to 1 MK/s cooling rate is possible with thin film chip calorimeters [9, 10]. With the device used by Gao et al. [11] the previously existing gap in heating and cooling rates between ultrafast and conventional DSC is closed now. Even such calorimeters are available, they were not applied to aluminium samples yet because they have to be adjusted to the specific problem. Further the DSC technique is an established method for the investigation of the precipitation sequence during reheating of samples, which are solution annealed and typically quenched in water [12-15]. A review of DSC-work done on aluminium based alloys from 1994 to 2004 is given by Starink [16].

The purpose of this report is to present a method for recording full range CCP-diagrams for low to middle quench sensitive aluminium alloys in the range from very slow cooling near equilibrium (0.1 K/min) to some hundred K/min. The challenges here are relative high temperatures, a wide range of cooling rates and as the most difficult task the detection of the disappearance of the precipitation reaction near the critical cooling rate. To detect the alloy specific critical cooling rate the DSC reaches its limits because of zero released heat when the supersaturated solid solution is obtained completely. The challenge here is to distinguish objectively between a tiny reaction and instrumental noise. An additional problem is the deconvolution of overlapping reaction peaks. Despite the relative big samples, signal smearing is no problem, due to the good thermal conductivity of aluminium. Compared to the research published so far in

this field, the developed evaluation method is more objective. It also enables evaluation of the characteristic data in case of overlapping reactions.

Materials and Methods

The presented investigation was performed with the age hardening aluminium-magnesium-silicon wrought alloy EN AW- 6005A. This is an often-used alloy with middle alloying content. Therefore, a relatively low critical cooling rate was expected. Cylindrical samples were turned from an extruded profile. Samples were turned cylinders with sample masses from 32 mg to 1550 mg with dimensions from 4 to 6.5 mm in diameter and from 1 to 22 mm in length adapted to cooling rate and calorimeter used. As an inert reference material for the DSC measurements EN AW-1050, pure aluminium with an Al-content of over 99.5 wt.-%, was used. The reference samples were turned out of a cast block. The detailed amounts of alloying elements of both materials are shown in Table 1.

Table 1: Alloying elements of the investigated aluminium basis-material: EN AW-6005A and EN AW-1050 (inert reference material)

wt.-%	Si	Fe	Cu	Mn	Mg	Cr	Zn	Ti
EN AW-1050	0.09	0.32	0.002	0.004	0.001	0.001	0.01	0.004
EN AW-6005A	0.68	0.20	0.01	0.11	0.57	0.040	0.01	0.018

The samples were solution annealed and cooled in three different types of DSC devices. An EN AW-1050 reference sample was placed in the reference furnace. Cooling rate varies from very slow cooling (0.1 K/min – equilibrium is expected) in discrete intervals up to critical cooling rate whereby the precipitation is completely suppressed. Selected samples have been artificially aged afterwards. Following hardness testing and metallographic investigations have been performed to confirm the DSC results.

Some conditions were constant for all DSC-experiments:

- Solution annealing temperature and time were 540 °C, 20 min, respectively

- Excess specific heat capacity was determined from all measurements. That means the difference in specific heat capacity between alloy EN AW-6005A and EN AW-1050. Therefore, a baseline-measurement was done for each cooling rate with EN AW-1050 samples in reference and sample furnaces.
- Measurements were done at ambient pressure
- Artificially aging was done at 25 °C for 7 min followed by 180 °C for 4 h

In the cooling rate region above 30 K/min at least three experiments with the same conditions were performed. In the following the average values are shown. At slower cooling fewer experiments were performed because of their long duration.

For each DSC-device, different conditions have been identified to reach optimal results:

The slowest experiments were done with a Heat-Flow-DSC of CALVET- Type (Setaram DSC 121). The optimal samples have dimensions of about 5.7 mm in diameter and 21.7 mm in length, which results in a sample mass of approximately 1570 mg. The samples were covered by two standard 300 µl aluminium crucibles with a mass of about 360 mg. Heating was carried out at 5 K/min. The block-temperature was set to 15 °C, but rises up to 30°C when the furnace reaches the maximum temperature of 540 °C. Cooling power of the circulating bath was not high enough to keep cooling jacket temperature at 15 °C but this is not important for this type of instrument. Cooling rate ranges from 0.05 K/min to 8 K/min.

Cooling rates in the intermediate range from 10 K/min to 30 K/min were performed employing the heat flow type Mettler DSC 823. The optimal samples for these rates and this device have dimensions of about 5.4 mm in diameter and 1.4 mm in height, which results in a sample mass of approximately 92 mg. The samples were placed in standard aluminium crucibles (49 mg). These crucibles have a positioning pin for exact and equal positioning on the sensing area. The crucibles were tightly closed by a press. Hence, a small hole is to place in the lid in order to avoid buckling of the crucible. Buckling would result from air expansion caused by the large temperature-range. Buckling would disturb the heat flow between sample and sensor. Heating was performed with 30 K/min. A pure nitrogen purge was used. Cooling was realized by a double-stage mechanical cooler.

The fastest used DSC was a Perkin-Elmer Pyris 1, which is a power-compensated DSC. The samples were about 4 mm in diameter and 1 mm in height, which results in a sample mass of about 32 mg. The samples were placed on a plate of pure aluminium foil (5 mg) to prevent the micro furnace from element-diffusion. A double-stage mechanical cooler (Intracooler II) and pure nitrogen as purge gas were used. To reach maximum cooling rates massive metal guard-ring inserts were attached (instead of the star shaped guard-ring inserts) to improve heat exchange between the ovens and the cold block. The block-temperature is -80°C . The DSC is covered by a Glove-Box. This box was under slight over-pressure of dry air. Because of the dry-condition under the glove-box icing was reduced to a minimum. To avoid baseline drift problems sample- and baseline-measurements were done directly after each other.

Radiation losses play an important role for baseline stability in all DSCs. During the measurement, the alloyed samples are changing their surface colour from bright to grey due to surface reactions. The change of surface colour is much stronger for the alloyed samples than for the pure aluminium reference samples. Due to this surface-effect, the radiation behaviour is changing. Thereby the DSC-curves are bending. This bending can be strongly reduced by packing the samples in pure aluminium crucibles. At least in the heat-flow-DSCs crucibles are necessary to get a good accordance of sample- and baseline-measurement (Fig. 1).

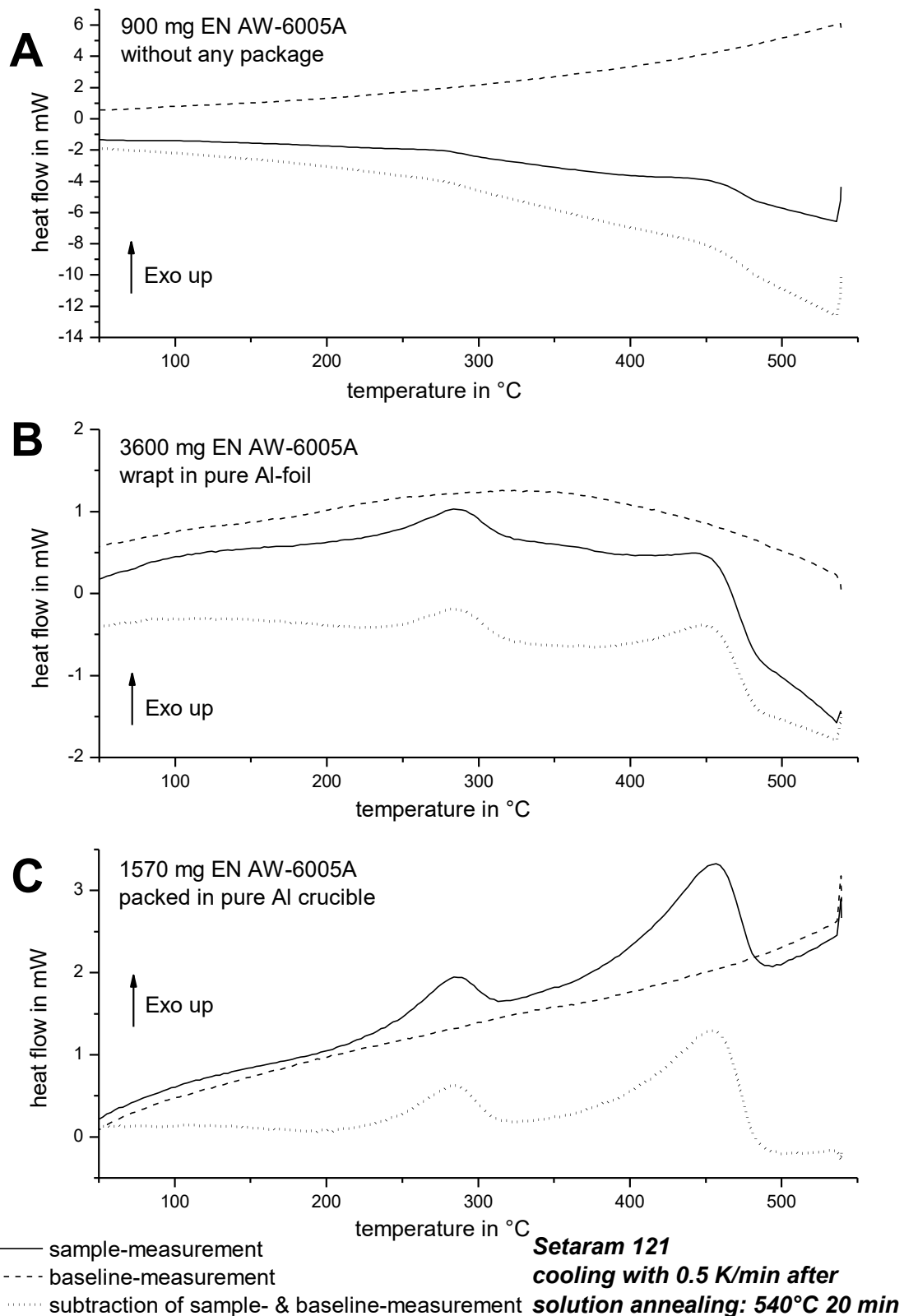


Fig. 1: Comparison of different sample-packing in the Heat-Flow DSC of CALVET-Type (Setaram 121); A: no packing, B: 40 mg pure Al-foil, C: 360 mg pure Al-crucible

However, also for the power compensated DSC the curves are better reproduced with complete covering of the sample avoiding colour changes of the heat exchanging

surfaces of the sample. The influence of colour changes on the measured heat flow rates even for the nearly perfect three dimensional heat flow rate sensor in a Calvet type DSC is shown in Fig. 1.

As mentioned above evaluation was done on the excess specific heat capacity curves. To get these curves the heat-flow curves of a baseline-measurement (pure Al as sample and reference) was subtracted from the heat-flow curve of the appropriate sample-measurement and the start- and end-isotherms were aligned. The resulting curve was divided by sample mass and cooling rate as common to obtain excess specific heat capacity [17]. This was found by preliminary investigations to be the best way to resolve the precipitation reaction in the DSC signal on cooling.

Although it was tried to ensure optimal measurement conditions most curves were slightly bended. The curve bending changes continuously with changing cooling rate. Especially at high cooling rates, due to the tiny reactions, a highly scaled-up view of the DSC-curves was used for evaluation. Thereby the influence of curve bending on the relative evaluation error is increasing with increasing cooling rate. The commonly observed problems with curve bending at lower rates due to decreasing signal were avoided by choosing large sample masses and the appropriate calorimeter. The curve bending can be corrected with a polynomial curve of second-order (Fig. 2). In doing so, the error in integrating the peak-area was kept as small as possible.

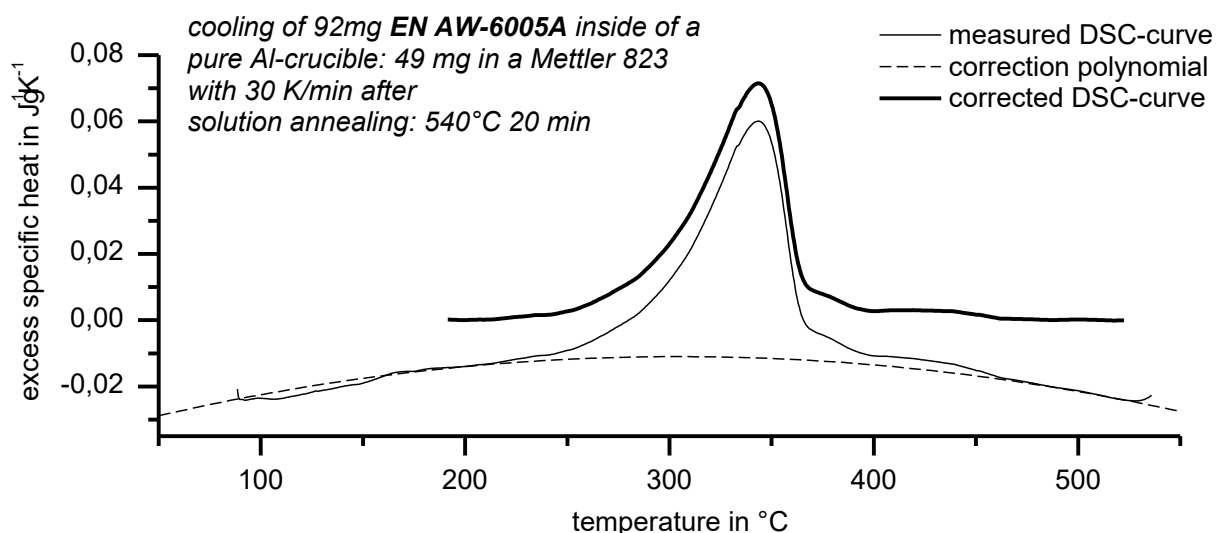


Fig. 2: Bending-correction with polynomial-function

The curves were evaluated for the characteristic temperatures of the reaction: start- and end-temperature but also for peak-area. The area under the peak(s) gives

information about the released specific heat, which precisely is called “specific precipitation heat”. This value is a measure for the amount of precipitates. With decreasing cooling rate the released specific precipitation heat approaches a limit: the equilibrium state. Under equilibrium or quasi static conditions the alloying elements are precipitated according to the corresponding phase diagram. This limiting specific precipitation heat can be used to estimate the amount of precipitates at higher rates as percentage of the quasi static value. Under quasi static conditions the precipitates are micron sized while at higher cooling rates they are mainly nanosized, see Fig. 8 below. Therefore size effects, e.g. surface energies, have to be taken into account for a correct determination of the amount of precipitates, which was not the aim of this study.

In some experiments at least two reactions overlap. The total precipitation heat measured is the sum of both released heats. For complete continuous cooling precipitation diagrams, a separation of the reactions is needed. Therefore, it was assumed that a single reaction causes a heat-peak that is shaped like a Gaussian distribution curve. The measured excess specific heat capacity curves $c_p(T)$, were then approximated as a sum of two Gaussian peaks (Fig. 3).

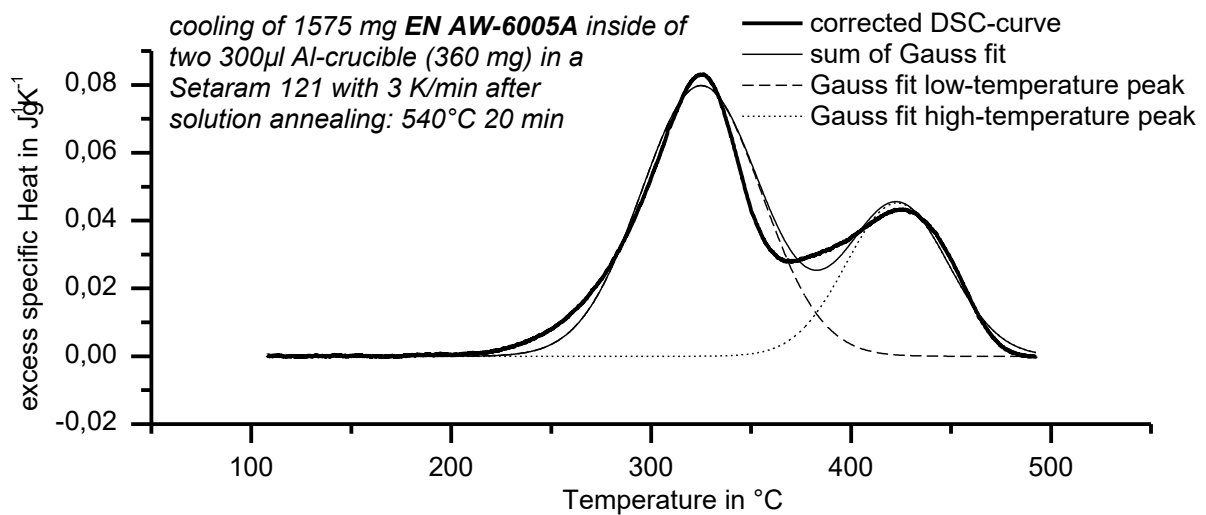


Fig. 3: Fit of the corrected excess specific heat capacity with two Gaussian curves

For the evaluation of start- and end-temperatures defined points of the Gauss-curve were used:

$$c_p(T) = \left(\frac{\Delta h_1}{w_1 \sqrt{\pi/2}} \right) e^{-2 \left(\frac{T - T_{peak\ 1}}{w_1} \right)^2} + \left(\frac{\Delta h_2}{w_2 \sqrt{\pi/2}} \right) e^{-2 \left(\frac{T - T_{peak\ 2}}{w_2} \right)^2}$$

with the two sets of fit parameters T_{peak} - peak-temperature, Δh - specific precipitation heat (peak-area) and w - width of the Gauss-curve.

Start- and end-temperatures of the peaks were defined as $T_{peak} \pm w$ respectively. They correspond to the points where the peak deviates for about 15 % of the peak height from the baseline. Even though the so calculated start- and end-temperatures of the reaction are not the real reaction start- and end-temperatures, this method offers an objective evaluation of the characteristic temperatures also in the region of overlapping peaks.

The amount of released heat decreases with increasing cooling rate. One aim of this study is the detection of the critical cooling rate at which the precipitation does not occur anymore. Therefore, an objective criterion is needed when no precipitation heat is detectable in the measured curves. The challenge is to decide when a precipitation peak is above the noise level. The detection limit was defined by the following criteria:

- the reaction is detectable in at least three repeated experiments
- the reaction is detectable also at the next slower cooling rate
- specific precipitation heat is at least 0.1 J/g
- peak-temperatures are in the same region as for next slower rate

One example of a curve evaluation near the detection limit is shown in Fig. 4. For correct curve interpretation, the evaluation must be done from slowest to faster cooling. Fig. 5 gives an overview over all cooling rates and thereby information about the peak-development. Additionally only with a general overview the curve bending can be corrected.

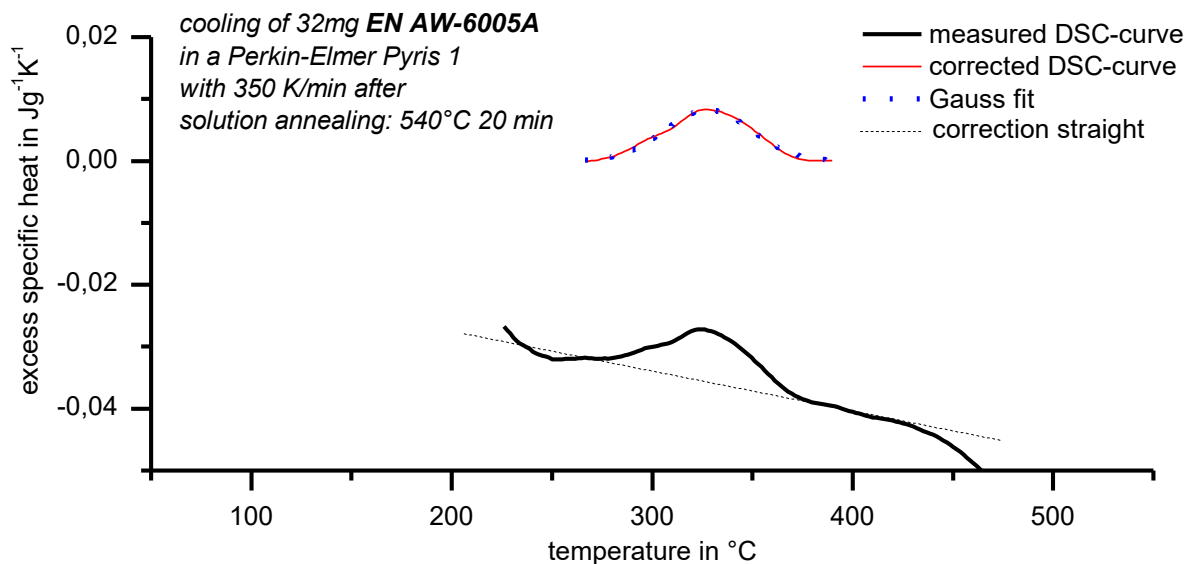


Fig. 4: Curve evaluation near critical cooling rate. T_{Start} : 371 °C; T_{End} : 285 °C; specific precipitation heat: 0.44 J/g

Results and Discussion

Fig. 5 shows the bending-corrected excess specific heat curves for the aluminium wrought alloy 6005A during cooling after solution annealing at 540 °C for 20 min. These curves were measured with three different types of DSC-devices. Cooling rate ranges from close to equilibrium conditions at 0.1 K/min to critical cooling rate, which was identified at 375 K/min in this case. Fig. 5 gives an overview of the peak-area and peak-temperature development. At the lowest cooling rate, close to equilibrium, the precipitation reaction starts at about 500 °C. Regarding the quasibinary phase-diagram Al–Mg₂Si [1], and estimating a Mg₂Si-content of 0.9 wt.-% in the investigated composition of alloy 6005A, this start-temperature is nearly consistent with the solvus-temperature. At the cooling rate of 0.1 K/min two main peaks were identified: A high-temperature peak with peak-temperature of about 470 °C and a low-temperature peak with a peak-temperature of about 250 °C. The range between the peak-values is approximately 220 K. This precipitation temperature-range shortens with increasing cooling rate. Near the critical cooling rate of the high-temperature peak (30 K/min), the difference between the peak-values is only about 80 K (approximately: 340°C to 420°C). This shows increasing precipitation suppression with increasing cooling rate. At rates faster than 30 K/min only the low-temperature peak occurs. At rates equal or faster than 375 K/min, the precipitation is suppressed completely. The shift of the lower

precipitation peak to higher temperatures with increasing cooling rate shows that thermal lag is not dominating the peak shifts observed.

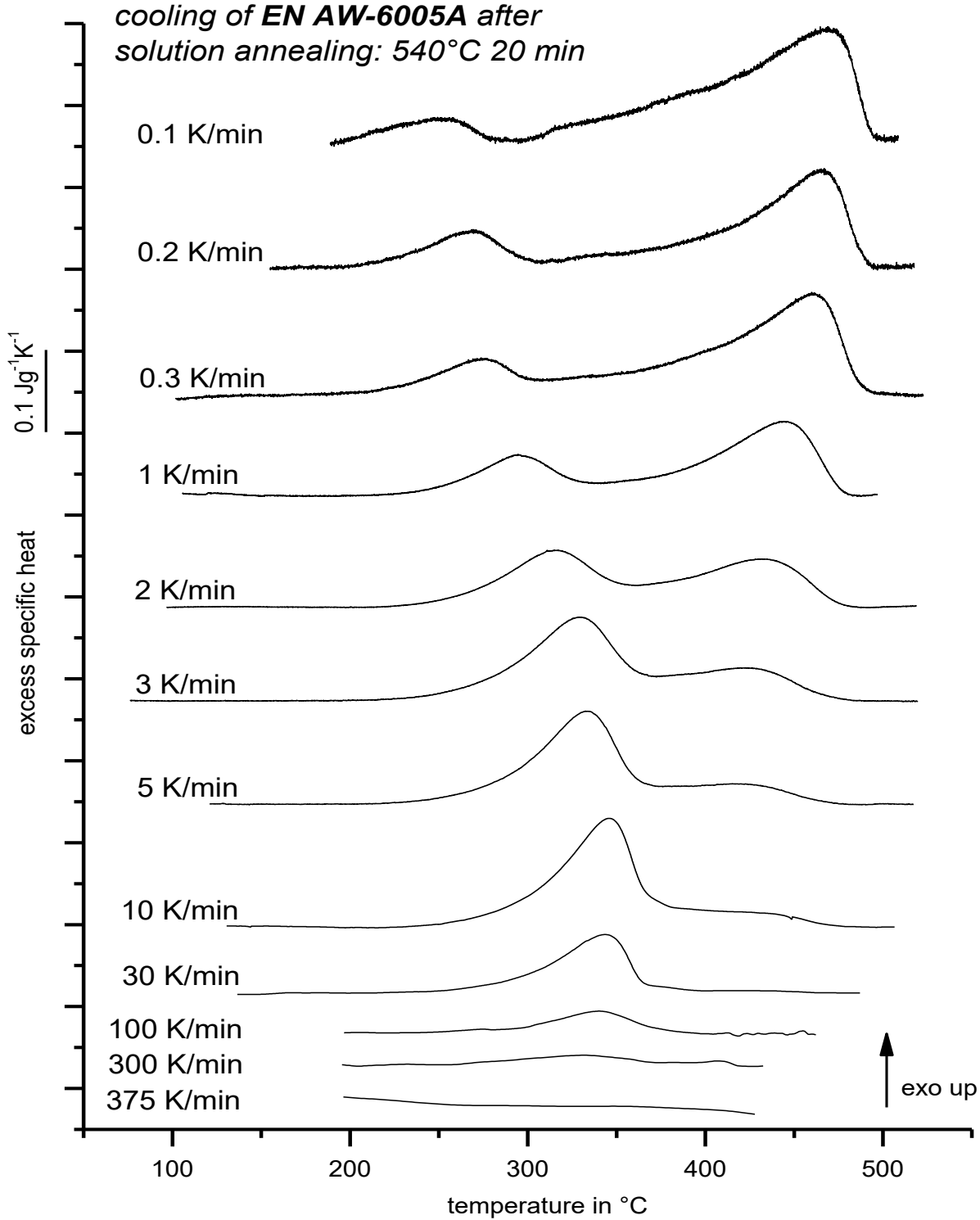


Fig. 5: Overview of bending-corrected curves from three different types of DSC-devices in a cooling rate region from 0.1 to 375 K/min (0.1 to 5 K/min: Setaram 121; 10 to 30 K/min: Mettler 823; 100 to 375 K/min: Perkin-Elmer Pyris 1

Fig. 6 presents the full range continuous cooling precipitation diagram of EN AW-6005A. This diagram displays the investigated cooling curves in a graph of temperature as a function of time. The time axis is scaled logarithmic, causing the curved traces for cooling at constant rate. At 375 K/min (fat-dotted) there is no precipitation detectable any more hence this was identified as the critical cooling rate for the aluminium wrought alloy 6005A. On the cooling curves at slower cooling the start- and end-temperatures of the Gaussian peak-fit evaluation are inserted. In the range between 30 K/min down to about 1 K/min (corresponding to cooling times between approximately 750 s to 20,000 s for the temperature range from 540 °C to 50 °C) two Gaussian peaks fit the measured curves reasonable well. In the range of even slower cooling two Gaussian curves do not fit well the measured curves. The extreme slow curves show some indication for more than two reactions, see Fig. 5.

EN AW-6005A

solution annealing 540°C 20 min

wt.-%	Si	Fe	Cu	Mn	Mg	Cr	Zn	Ti
	0.68	0.20	0.01	0.11	0.57	0.040	0.01	0.018

- ☒ start high-temperature peak
- ☒ end high-temperature peak
- ✕ start low-temperature peak
- ✚ end low-temperature peak

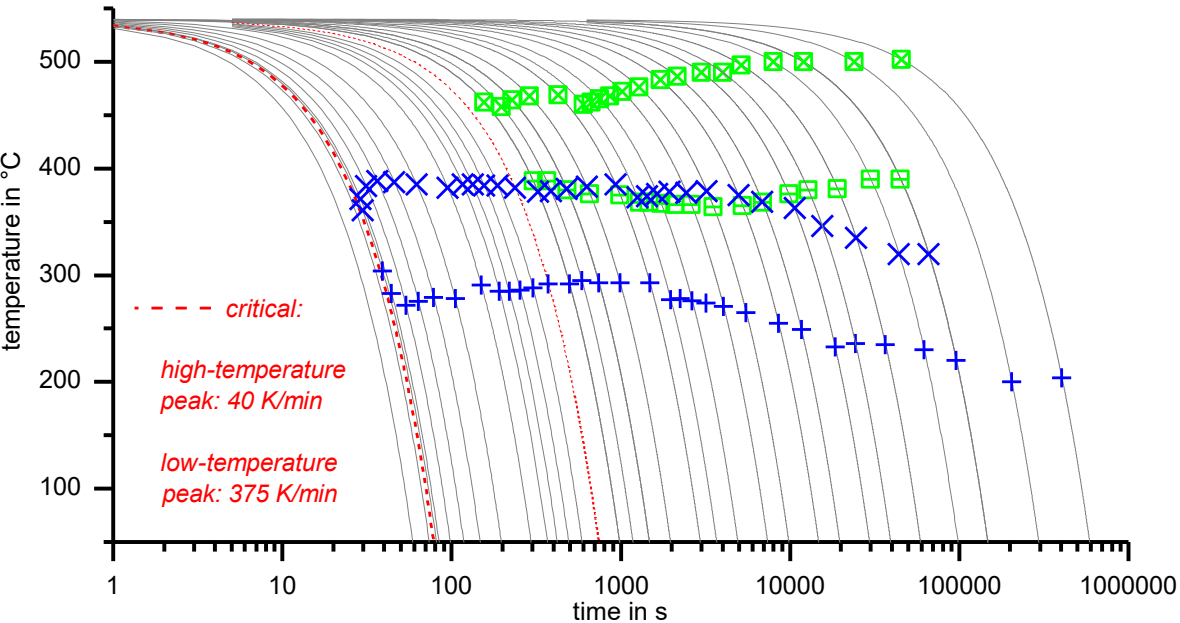


Fig. 6: Full range continuous cooling precipitation diagram of EN AW-6005A. The solid lines correspond to linear cooling in the range between 500 K/min and 0.5 K/min.

It must be mentioned, that the CCP-diagram is only valid for the investigated chemical composition, initial microstructure and solution annealing conditions. The large range between high-temperature peak and low-temperature peak indicates probably more than two reactions or at least highly asymmetric peaks. The two-peak fit is still used

because more peaks/reactions were not identifiable for sure. In those cases with less correlation between the peak fit and the measured curve, the peak fit is done like that the sum of both peak areas agrees well to the integrated area of the measured curve. At the slowest cooling rate 0.05 K/min the lower limit of the DSCs used is reached. Because of the very small effects, the released heat due to the precipitation reaction is so small per time step that it is hardly detectable. Hence, the signal to noise ratio is bad.

The CCP-diagram in Fig. 6 delivers no information about the amount of released heat or the amount of precipitates respectively. This is shown in Fig. 7, which displays the released specific precipitation heat and the Vickers-hardness after artificial aging as function of cooling rate. The cooling rate axis is scaled decreasing logarithmic. This is done to allow an easy comparison with the time scale of the CCP-diagram.

EN AW-6005A

solution annealing 540°C 20 min

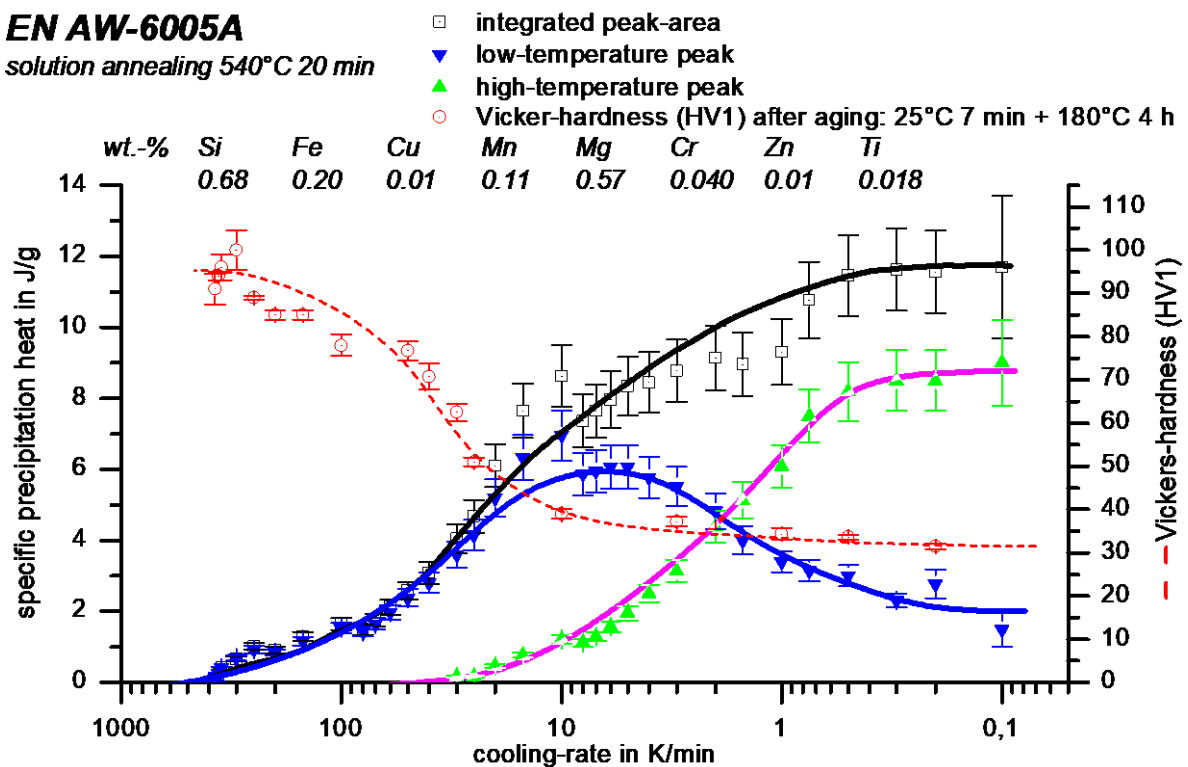


Fig. 7: Specific precipitation heat and Vickers-hardness (HV-1) after aging as a function of cooling rate. The displayed error bars shows the uncertainty, which results from evaluation.

From the peak-area determination, an uncertainty of about 10% is estimated. Additionally the single areas of the double peak from the fits are displayed. There is a strong correlation between precipitation heat and hardness. If a precipitation occurs during cooling it is hardly possible to strengthen the material during the following aging

process. At the slowest cooling the measured precipitation heat and the hardness approaches its saturation. This fact indicates that the equilibrium state is approached. Correlating the specific precipitation heat to the quasibinary phase-diagram Al-Mg₂Si, the equilibrium precipitation heat of about 11.5 J/g belongs to the amount of precipitated Mg₂Si which is nearly 0.9 wt.-percent for alloy 6005A. With this dependency the amount of precipitates can be approximated also for faster cooling. Because we do not know the (nano) size of the precipitates, which may affect the precipitation heat, we did not perform the calculation but an estimate is available from Fig. 7. At 10 K/min, for example, approximately 0.5 wt.-percent Mg₂Si are precipitated.

An additional confirmation of the DSC results is given by Fig. 8, which shows metallographic-images of samples of aluminium alloy EN AW-6005A in different cooling conditions. The left picture shows a sample, which was cooled with 362 K/min - a rate near critical cooling rate. Therefore, precipitation during cooling is suppressed nearly completely. Visible is the light-grey aluminium matrix, but also some primary precipitates, which form already during the primary shaping and which are not changed by the age-hardening process. Energy dispersive X-ray (EDX)-analysis showed that those phases mainly contain Fe, Mn and Si. Those primary precipitates can be found at each cooling condition. The most right picture of Fig. 8 shows a sample, which was cooled at 10 K/min. At this rate, the amount of precipitates during cooling is about ten times larger than at 362 K/min. The precipitates, which are formed during slow cooling, have dimensions in the µm-range. EDX-analysis showed that the phases, which are affected by the cooling rate, mainly contain Mg and Si. With X-ray diffraction (XRD) the cubic structure of Mg₂Si could be detected at the slowest cooled sample.

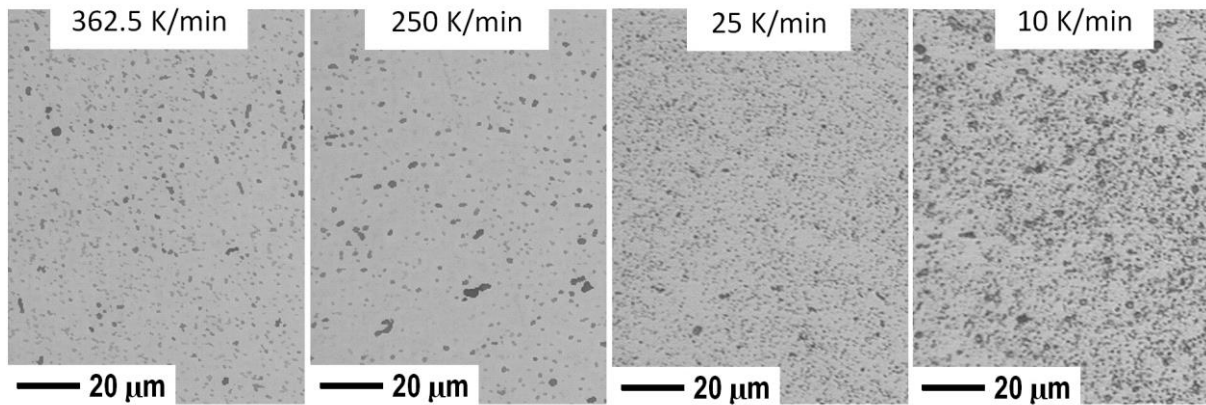


Fig. 8: Metallographic images of samples of EN AW-6005A: 540°C 20 min, quenching: 362.5 K/min; 250 K/min; 25 K/min and 10 K/min; etching: 45s with molybdenum acid (95ml distilled H₂O + 5ml HF + H₂MoO₄ supersaturated)

From the right picture to the left picture (increasing cooling rate) the amount of visible precipitates is decreasing significantly. This is also a visible expression of increasing precipitation suppression with increasing cooling rate.

Summary

For the aluminium-magnesium-silicon wrought alloy EN AW-6005A, age hardening was performed in three different types of Differential Scanning Calorimeters (DSC) whereby cooling rate varies over 3 orders of magnitude. For the used DSC devices, optimal measurement conditions were found. Unavoidable remaining bending of the measured excess specific heat capacity curves was corrected.

When an aluminium alloy is solution annealed and afterwards cooled too slowly, an exothermal precipitation reaction occurs. With increasing cooling rate, the precipitation heat is decreasing. The influence of the cooling rate on the precipitation behaviour is described by Continuous Cooling Precipitation (CCP) diagrams. With this information, the quenching step of the age hardening process can be optimized. Furthermore, simulation of precipitation processes during the quenching step of the age hardening is impossible without the material-data out of CCP- diagrams.

The complete CCP-diagram of EN AW-6005A has been recorded (Fig. 6). The critical cooling rate, which is the minimum cooling rate, at which no precipitation heat is detectable, was determined. For the investigated alloy EN AW-6005A the critical cooling rate equals 375 (± 10) K/min. The definition of precipitation start- and end-

temperatures was done by fitting the measured precipitation peaks by Gaussian peaks. Defined points of the Gauss-curves were used to evaluate the characteristic temperatures. In the cooling rate range from 375 K/min to 40K/min, only one reaction is detectable. At slower cooling rates there are at least two reactions detectable. In this region, the peak fit is done with two Gaussian peaks, which gave a good fit in the range between 30 K/min and about 1 K/min. The characteristic temperatures could be detected with an accuracy of ± 10 K. The challenge of the needed decision between thermal noise and occurrence of a reaction-peak near the critical cooling rate has been overcome by well-defined decision criteria. The amount of released heat could be determined with an uncertainty of about 10 %. The DSC results are well confirmed by hardness testing and metallographic images.

An open question is the identification of the single precipitates for overlapping peaks. Therefore, electron-microscopically analyses will be necessary to get information about the quantity of precipitates, their locations in the grain structure and their composition. First results indicate the presence of Mg_2Si .

With the used DSC devices, precipitation reactions are detectable in a range of cooling rates between 0.1 K/min and some hundred K/min. It is intended to record CCP diagrams for other aluminium alloys too. Therefore, higher cooling rates could be necessary. Scanning calorimetry is possible with cooling rates up to 1 MK/s nowadays [9, 10]. With the device used by Gao et al. [11] the gap in heating and cooling rates between ultrafast and conventional DSC is closed. Appropriate calorimeters are available, but they have to be adjusted to the specific problem.

References

- [1] I.J. Polmear, Light alloys, Butterworth-Heinemann, Oxford, 2006.
- [2] T. Herding, O. Kessler, F. Hoffmann, P. Mayr, An approach for Continuous Cooling Transformation (CCT) diagrams of aluminium alloys, Aluminum Alloys 2002: Their Physical and Mechanical Properties Pts 1-3 396-4 (2002) 869-874.
- [3] O. Kessler, R. von Bargen, F. Hoffmann, H.W. Zoch, Continuous cooling transformation (CCT) diagram of aluminum alloy Al-4.5Zn-1Mg, Aluminium Alloys 2006, Pts 1 and 2 519-521 (2006) 1467-1472.
- [4] B. Milkereit, O. Kessler, C. Schick, Continuous Cooling Precipitation Diagrams of Aluminium-Magnesium-Silicon Alloys, in: J. Hirsch, B. Skrotzki, G. Gottstein (Eds.),

- 11th International Conference on Aluminium Alloys, Deutsche Gesellschaft für Materialkunde e.V.; WILEY-VCH Weinheim, Aachen, Germany, 2008. pp. 1232-1237.
- [5] R. von Bargen, Kontinuierliche Zeit- Temperatur- Ausscheidungsdiagramme der Aluminiumlegierungen 7020 und 7050, Härterei- Technische Mitteilungen 62(6) (2007).
- [6] J.L. Cavazos, R. Colas, Quench sensitivity of a heat treatable aluminum alloy, Materials Science and Engineering a-Structural Materials Properties Microstructure and Processing 363(1-2) (2003) 171-178.
- [7] H.Y. Li, J.F. Geng, Z.Q. Zheng, C.J. Wang, Y. Su, B. Hu, Continuous cooling transformation curve of a novel Al-Cu-Li alloy, Transactions of Nonferrous Metals Society of China 16(5) (2006) 1110-1115.
- [8] E. Calvet, H. Prat, H. Skinner, Recent progress in microcalorimetry, Pergamon Press, Oxford, London, New York, Paris, 1963.
- [9] S.A. Adamovsky, A.A. Minakov, C. Schick, Scanning microcalorimetry at high cooling rate, Thermochemica Acta 403(1) (2003) 55-63.
- [10] A.A. Minakov, C. Schick, Ultrafast thermal processing and nanocalorimetry at heating and cooling rates up to 1 MK/s, Review of Scientific Instruments 78(7) (2007) -.
- [11] Y.L. Gao, E. Zhuravlev, C.D. Zou, B. Yang, Q.J. Zhai, C. Schick, Calorimetric measurements of undercooling in single micron sized SnAgCu particles in a wide range of cooling rates, Thermochemica Acta 482(1 - 7) (2008).
- [12] S. Esmaili, X. Wang, D.J. Lloyd, W.J. Poole, On the precipitation-hardening behavior of the Al-Mg-Si-Cu, Metall. Mater. Trans. A-Phys. Metall. Mater. Sci. 34A(3) (2003) 751-763.
- [13] A. Gaber, A.M. Ali, K. Matsuda, T. Kawabata, T. Yamazaki, S. Ikeno, Study of the developed precipitates in Al-0.63Mg-0.37Si-0.5Cu (wt.%) alloy by using DSC and TEM techniques, J. Alloy. Compd. 432(1-2) (2007) 149-155.
- [14] M. Vedani, G. Angella, P. Bassani, D. Ripamonti, A. Tuissi, DSC analysis of strengthening precipitates in ultrafine Al-Mg-Si alloys, Springer, 2007. pp. 277-284.
- [15] X. Wang, S. Esmaili, D.J. Lloyd, The sequence of precipitation in the Al-Mg-Si-Cu alloy AA6111, Metall. Mater. Trans. A-Phys. Metall. Mater. Sci. 37A(9) (2006) 2691-2699.
- [16] M.J. Starink, Analysis of aluminium based alloys by calorimetry: quantitative analysis of reactions and reaction kinetics, Int. Mater. Rev. 49(3-4) (2004) 191-226.
- [17] W. Hemminger, G.W.H. Höhne, Grundlagen der Kalorimetrie, Akademie-Verlag, Berlin, 1980.

**[BM2] Milkereit B, Wanderka N, Schick C, Kessler O:
*Continuous cooling precipitation diagrams of Al-Mg-Si
alloys.***

Materials Science Engineering A 550 (2012): 87–96.

Benjamin's contributions: I designed the experiments, did the DSC measurements, the analytical optical microscopy (analysis of precipitated Mg₂Si volume fractions), accompanied the SEM and TEM analysis and did the evaluation and plotting of the data. In addition, I wrote the original draft of the manuscript.

Continuous cooling precipitation diagrams of Al-Mg-Si alloys

Benjamin Milkereit^{1, 3, *}, Nelia Wanderka², Christoph Schick³, Olaf Kessler¹

¹ University of Rostock, Faculty of Mechanical Engineering and Marine Technology,
Chair of Materials Science, 18051 Rostock, Germany,

tel 0049 381 498 9486; fax 0049 381 498 9472; benjamin.milkereit@uni-rostock.de

² Helmholtz Zentrum Berlin für Materialien und Energie GmbH, Institute of Applied
Materials, 14109 Berlin, Germany

³ University of Rostock, Institute of Physics, Polymer Physics Group, 18051 Rostock,
Germany

Abstract

The temperature- and time-dependent precipitation behaviour of Al-based 6060, 6063, 6005A and 6082 alloys at different cooling rates after solution annealing has been investigated. The continuous cooling precipitation diagrams of these alloys were recorded by differential scanning calorimetry. The cooling rate was varied over five orders of magnitude (0.05 – 20,000 K/min). Cooling-rate-dependent precipitate formation was analysed by light microscopy, scanning and transmission electron microscopy. Cooling-rate-dependent hardness was tested after artificial aging. Over an appropriate range of cooling rates all alloys show similar precipitation behaviour. At least two precipitation reactions were observed in different temperature ranges. The high-temperature reactions correspond to the precipitation of the equilibrium phase β -Mg₂Si, and the low-temperature reactions correspond to the precipitation of precursor

phases such as β' and B' . The precipitation kinetics depend on the alloy composition. Maximum hardness values are to find as long as the materials were cooled faster than alloy specific critical cooling rate, which increases with increasing alloy content.

Keywords

Continuous cooling precipitation diagrams, aluminium-magnesium-silicon alloys, DSC, TEM, SEM, microstructure, precipitates

1 Introduction

The strength of metallic materials can often be adjusted by special heat treatments. The most important heat treatment used to strengthen aluminium alloys is age hardening [1], which involves solution annealing, quenching and aging. Thus, the quenching rate is an important parameter.

Continuous cooling precipitation (CCP) diagrams describe the precipitation behaviour of aluminium alloys during cooling from solution annealing as a function of temperature and time. CCP diagrams of aluminium alloys may potentially achieve the same level of importance as continuous cooling transformation diagrams have for steels; however, only a few are known to exist.

The precipitation sequence during the aging step of aluminium alloys has been frequently investigated [2-15]. These investigations often combine differential scanning calorimetry (DSC) experiments and intensive microstructure analyses [8, 11-15]. One problem is that the evaluation of the DSC data is not performed consistently in the literature, e.g., often the data is not normalised by sample mass and scanning rate. Therefore, the existing data is hard to compare.

The generally accepted precipitation sequence of Al-Mg-Si alloys after quenching can be simplified as follows: supersaturated solid solution \rightarrow Mg- / Si- (co-) cluster \rightarrow GP-zones \rightarrow β'' \rightarrow β' / B' \rightarrow β -Mg₂Si [1].

However, the precipitation behaviour during cooling from solution annealing remains relatively unknown, and very few relevant reports exist [16-21]. Zajac et al. investigated the cooling step and reported the precipitation of Mg_2Si in an fcc structure at high temperatures as well as in a hexagonal structure at lower temperatures [19-21]. Nothing about the intensity of the precipitation reactions or about the precipitated volume fractions as a function of composition and cooling rate is known. In any case, literature studies regarding the cooling rate range are insufficient. Therefore, no CCP diagrams of aluminium alloys, which are complete in terms of cooling rate range and structure information, exist. It is not known with any detail what phases precipitate at different temperatures and times during cooling from solution annealing and how these precipitates influence mechanical properties. Hence, this report proposes an approach to develop CCP diagrams of aluminium alloys.

A method to record such CCP diagrams has been developed using differential scanning calorimetry (DSC), through which the exothermal heat of precipitation is detected [18, 22-26], in combination with microstructural and hardness analysis. The purpose of this study was to compare the precipitation behaviour, microstructural and hardness evolution of Al-Mg-Si-based alloys with an excess of silicon with respect to the stoichiometric composition of the equilibrium secondary phase Mg_2Si over a wide range of cooling rates as a function of composition. Precipitation reactions were investigated by DSC. Precipitates were investigated by light microscopy, scanning and transmission electron microscopy (SEM/ TEM) at samples with different cooling states. Cooling-rate-dependent hardness was measured by Vickers hardness testing (HV1) after artificial aging.

2 Experimental

Five Al-Mg-Si-based wrought alloys with the chemical composition (mass fraction in %, obtained by optical emission spectroscopy (OES) analysis) shown in Table 1 were

investigated in the present work. Samples were machined from industrial extrusion profiles. The sample dimensions depended on the dimensions of the DSC devices used: from \varnothing 5.4 mm, length 1.4 mm to \varnothing 6.2 mm, length 21.65 mm. The solution annealing of all alloys was performed at 540 °C for 20 min.

All five alloys were investigated by DSC over the available cooling rate range (three orders of magnitude – from about 0.1 K/min to 375 K/min). The DSC signal is proportional to sample mass and scanning rate. To ensure an appropriate signal to noise ratio the sample mass should be adjusted to the scanning rate range. Therefore, three different types of DSC devices were used (0.1 – 8 K/min: Setaram 121 DSC; 10 – 30 K/min: Mettler-Tolledo 823 DSC; 30 – 375 K/min: Perkin-Elmer Pyris 1 DSC). The results of the different devices fit well at the cooling rate of intersection. The DSC experiments were performed by using the procedure described in [25]. Evaluation of the DSC data was performed like published in [27]. For microstructure analyses and hardness testing the cooling rate range was widened to about five orders of magnitude (0.05 K/min – 20,000 K/min) by using a quenching dilatometer Bähr DIL 805 A/D.

For microstructure analysis in particular, two types of cooling experiments were performed. In the first type, the samples were cooled from solution annealing with different linear cooling rates to room temperature. This treatment is called “*variation of cooling rate*” (Figure 1 A). In the other type of experiment, slow cooling rates of 0.1 K/min and 10 K/min were interrupted after discrete temperature intervals of 25 K (Figure 1 B) followed by overcritical cooling in the DSC or dilatometer in order to “freeze” the precipitation state at different temperatures during continuous cooling. This treatment is called “*variation of temperature*”. The microstructures of these different states were investigated by light microscopy as well as scanning and transmission electron microscopy (SEM and TEM).

The chemical composition of precipitates was investigated by EDX in SEM and TEM.

The crystal structures of the precipitates were analysed by selected-area electron diffraction (SAED) in TEM. Hardness tests (HV1) were carried out for samples with different cooling conditions.

Samples for light microscopy and SEM analysis were prepared by standard grinding and polishing with water-free, ethanol-based lubricants. To identify the location of precipitates within the grains or at the grain boundaries, the specimens were etched for 20 s in a solution of 4 g potassium permanganate in 100 ml distilled H₂O and 1 g sodium hydroxide. After etching an etch-skin remained on the surface, which was removed by cautious polishing.

The volume fraction of large Mg₂Si precipitates showing dark contrast in light microscopy images was determined by computerised image analysis [28]. For statistical validation, six images of each cooling condition at low magnification were evaluated. This resulted in a relatively large evaluated area of 240,000 μm² per cooling condition.

TEM samples were prepared by mechanical grinding and further by twin-jet thinning in an electrolyte (methanol to nitric acid with a ratio 3:1) at a temperature of about -30 °C and a voltage of 25 V. TEM investigations were performed in a Philips CM30 microscope operated at 300 kV and equipped with EDX spectrometer. The beam size in the EDX microanalysis measurements was typically 10 nm. The composition value was averaged over at least five measurements.

Vickers hardness test for HV1 hardness was performed at specimens after solution annealing, quenching and artificial aging for different alloys as shown below.

- solution annealing: 540 °C 20 min, quenching with different rates;
- artificial aging:
 - 6063, 6005A, 6082: 25 °C 7 min + 180 °C 4 h;
 - 6060: 25 °C 48 h + 180 °C 4 h.

Low alloyed Al-Mg-Si alloys show positive response on room temperature storage previous to artificial aging [1]. For the lowest alloyed investigated composition 6060 a room temperature storage of 48 h has been detected as the optimal storage duration in preliminary tests. For higher alloyed compositions the effect is negative. Hence, here the intermediate storage duration was kept short.

3 Results

3.1 Calorimeter and Hardness Results

Figure 2 shows seven characteristic DSC cooling curves as a function of temperature for alloy 6005A. The curves are arranged in order of increasing cooling rate, starting with the slowest rate on top. The dotted line in each DSC curve represents the zero level. Deviations exceeding this level indicate exothermal reactions. Altogether, about 200 cooling experiments with about 30 different cooling rates were performed for each alloy [25, 29-30]. All investigated alloys showed similar precipitation behaviour with high- and low-temperature precipitation reactions. There are indications for some more reactions, e.g. Figure 2, top curve 0.1 K/min, but these further reactions could not be clearly evaluated regarding start and end temperature. All five alloys have a similar precipitation behaviour.

The precipitation start and end temperatures were taken from DSC curves and plotted in a temperature/time-diagram. The resulting CCP diagram of 6005A is shown in Figure 3. The detected precipitation start and end temperatures are indicated by thick lines. Dashed lines indicate that a precipitation region was extrapolated on the basis of dilatometer results towards faster or slower cooling rates, which were not measurable by DSC. The CCP diagram provides information regarding precipitation reactions as a function of the cooling rate and temperature.

Another important piece of information is the intensity of the precipitation reactions. This intensity can be observed from the peak areas of the DSC curves like in Figure 2 and is

displayed in Figure 4 for alloy 6005A, where the specific precipitation heat during cooling to room temperature and the hardness after aging as a function of the cooling rate are presented. The cooling rate axis follows a decreasing logarithmic scale for comparison with the time scale of the CCP diagrams. Thus, Figure 3 and Figure 4 are complementary. For the precipitation heat, the error bars show an estimated error of 10 % resulting from the evaluation procedure. For the hardness values, the standard deviation calculated from six indentations is shown.

After artificial aging the hardness clearly shows maximum values as long as no precipitation heat was observed during cooling to room temperature. Maximum supersaturation after quenching ensures maximum hardness after aging. Hence, a critical quenching rate of 375 K/min for 6005A was determined.

The total precipitation heat can be divided into the high-temperature precipitation heat and the low-temperature precipitation heat. The high-temperature precipitation heat decreases with increasing cooling rate, whereas the low-temperature precipitation heat shows a maximum at about 10 K/min.

The CCP diagrams of the other investigated alloys are shown in Figures 5 to 8. For alloy 6082_{high}, the dotted line at 540 °C indicates the immediate onset of precipitation upon cooling. Generally, the precipitation processes of 6XXX Al-alloys during cooling are initiated sooner with increasing contents of the alloying elements Mg and Si.

A comparison of the total specific precipitation heat during cooling and Vickers hardness HV1 after artificial aging as functions of cooling rate for all investigated alloys is shown in Figure 9 A and B. Whereas the total specific heat of all investigated alloys decreases with increasing cooling rate, the Vickers hardness after aging increases.

The precipitation kinetics depend on the alloy composition. A lower critical cooling rate (LCCR) is defined for the highest cooling rate at which practically complete precipitation

takes place. Additionally an upper critical cooling rate (UCCR) is defined for the slowest cooling rate at which completion of supersaturation in solid solution is reached during cooling. The upper and lower critical cooling rates increased with increasing amounts of alloying elements Mg and Si (Figure 9). The same tendency was observed for the saturation level of total released heat. Generally, the precipitation heat decreases with increasing cooling rate due to the suppression of diffusion processes. Also, the saturation level of the hardness at high alloy-specific cooling rates increases with the increasing alloy content of Mg and Si. For alloys 6060, 6063 and 6005A, Figure 9 clearly shows that the maximum hardness values were reached only if no precipitation heat could be detected. Thus, it was possible to estimate the precipitation heat for both compositions of 6082 by extrapolating the precipitation heat (dotted lines in Figure 9 A). Hence, it was also possible to estimate the UCCR of both compositions of 6082.

The total precipitation heat was constant as long as the cooling rate was slower than the alloy-specific LCCR. This saturation level of specific precipitation heat values at relatively low rates could be detected for three alloys (6082_{high}, 6082_{low} and 6005A) over the investigated cooling rate range. Alloys 6060 and 6063 would require even slower cooling.

Figure 10 shows the UCCR as a function of alloy composition for the Al-Mg-Si alloys. The concentration axis shows the sum of the mass fractions of Mg and Si. The theoretical mass fraction of Mg₂Si at equilibrium and room temperature has been estimated from the alloy composition. These values are also given for each alloy. The UCCRs rose significantly with increasing alloy content. Between a Mg+Si mass fraction of about 0.8 % and 2.3 %, the UCCR increased by about two orders of magnitude. This can be explained by the higher supersaturation of the higher-alloyed materials. Even inside the allowed composition interval of 6082, UCCR differences of nearly one order of magnitude occur between low (1000 K/min) and high (8000 K/min) alloyed variants

(such high cooling rates are now also accessible to calorimetric investigations [31]). However, it must be mentioned that these results are only valid for the initial microstructures and solution annealing conditions.

3.2 Microstructure Results

The microstructural evolution of 6005A is shown in Figure 11 using micrographs obtained by light microscopy (A), SEM (B) and TEM (C). The cooling rates vary by more than three orders of magnitude between 0.05 and 100 K/min.

At least three types of precipitates were detected: primary precipitates and two main types of secondary precipitates. Primary precipitates mainly consist of high melting elements, such as Fe, Mn, Cr and Si. They can be distinguished in SEM micrographs (particles which are bright in contrast in Figure 11 B) or by EDX analysis. Such primary precipitates were not influenced by the applied heat treatment. The primary precipitates found were homogeneously distributed in the microstructure and reached up to a few micrometres in size.

Coarse secondary precipitates were observed as dark particles by light microscopy (Figure 11 A) and SEM (Figure 11 B). These dark particles precipitated inside of aluminium grains and at the grain boundaries of alloys 6060, -6063, -6005A and -6082_{low}. EBSD and XRD results for 6005A [29-30] indicate a fcc β -Mg₂Si crystal structure with lattice parameter $a = 0.635$ nm for these coarse secondary precipitates. The results of these investigations show strong indications that β -Mg₂Si particles nucleate at primary precipitates. Even for β -Mg₂Si particles located on grain boundaries, primary precipitates were observed inside the coarse β -Mg₂Si (Figure 12).

Much smaller precipitates are visible in the TEM images. Such precipitates can be observed at cooling rates of up to 100 K/min, as shown for the 6005A alloy (Figure 11 C). This second type of secondary precipitates includes rod- and lath-shaped phases. It

was found that both types of precipitates became smaller with increasing cooling rate. Though the size of Mg_2Si precipitates after cooling at 0.05 K/min, which was up to a few tens of micrometres, they could be hardly detected by light microscopy and SEM after cooling at 10 K/min. The lengths of the rod- and lath-shaped secondary precipitates were also observed to decrease from about 600 nm after cooling at 10 K/min to about 300 nm at a cooling rate of 100 K/min.

Due to the corresponding cooling rate regions it can be assumed that the precipitation of coarse Mg_2Si is a high-temperature reaction and the precipitation of fine rod- and lath-shaped precipitates is a low-temperature reaction.

Figure 13 A shows SEM images of the microstructural development of 6005A observed at a constant cooling rate of 0.1 K/min for the *variation of temperature* experiments. At 500 °C only primary precipitates are visible. The first Mg_2Si particles were detected at 475 °C, immediately before the intensity maximum of the high-temperature reactions was reached according to Figure 2.

A high fraction of Mg_2Si precipitates were observed by SEM at 450 °C after passing the intensity maximum of the high-temperature reactions. With a further decrease in temperature, the microstructure, as revealed by SEM, did not change significantly.

During the cooling of 6005A at 10 K/min, where the low-temperature reactions release the maximum amount of heat (Figure 4), first rod-/lath-shaped precipitates could be detected at 325 °C, as observed in the TEM micrographs. This temperature corresponds to the low-temperature reactions that occurred at a cooling rate of 10 K/min (Figure 2) after passing the intensity maximum. At temperatures below 325 °C, the rod-/lath-shaped precipitates grew only slightly, as illustrated in the TEM micrographs in Figure 13 B. Hence, it was concluded that the precipitation of rod-/lath-shaped precipitates corresponds to a low-temperature reaction.

Figure 14 shows a TEM bright-field micrograph of a rod-shaped precipitate embedded in an Al matrix. The corresponding SAED pattern of the [001] Al zone axis is shown in the inset. Additional superlattice reflections initiated from the rod precipitate in the SAED pattern are visible. Rod- and lath-shaped precipitates show similar diffraction patterns in the [001] Al zone axis. Because parts of the diffraction pattern initiated from the rod-/lath-shaped precipitates are located at the $\langle 100 \rangle$ positions of the aluminium matrix, these precipitates are coherent with the Al matrix along this direction. Possible crystal structures will be discussed in the next section.

The chemical composition of the rod-/lath-shaped precipitates consists of Al, Si and Mg and sometimes Cu, as measured by TEM EDX. In most cases, more Si than Mg was detected. However, the chemical composition of the elements varied between the individual precipitates.

3.3 Volume fraction of Mg_2Si

The released heat of precipitation is a measure of the converted mass fraction of alloying element atoms: if cooling is slow and all alloying element atoms are precipitated out of solid solution, the precipitation heat should reach a saturation level. Hence, it should be possible to estimate the mass and volume fractions of precipitates from the specific precipitation heat measured by DSC. This applies under certain conditions, which are discussed in detail in [29]. The results of both methods are displayed in Figure 15 for the high-temperature precipitation of Mg_2Si in alloy 6005A. The calculated values were compared with values ascertained by metallographic analysis (digital image analysis [29-30]). The error bars correspond to the standard deviation calculated from six evaluated microsections. The evolution of the volume fraction as a function of the cooling rate is shown in Figure 15. As shown, the results of both methods are in good agreement with each other. At cooling rates slower than 0.5 K/min the volume fraction of Mg_2Si reaches a saturation level of about 1.3 %. With increasing cooling rate the

volume fraction of Mg_2Si decreases, and at 10 K/min the volume fraction reaches only about 0.1 % to 0.2 %.

4 Discussion

4.1 Discussion of calorimeter results

During cooling from solution annealing the precipitation behaviour is similar for all five investigated Al-Mg-Si alloys, which feature an excess of Si. In particular, there are at least two main exothermal reactions (high temperature: coarse Mg_2Si ; low temperature: rod-/lath-shaped precipitates) that appeared over similar temperature ranges. The temperature, at which Mg_2Si precipitation is initiated, and the specific precipitation heat increase significantly with increasing amounts of alloying elements. This is expected from the quasi-binary phase diagram of Al- Mg_2Si to which the investigated alloys belong in the first approximation. Figure 16 shows the schematic quasi-binary phase diagram of Al- Mg_2Si (A) and the DSC curves measured for alloys with the highest (B, 6082_{high}) and lowest amounts of alloying elements (C, 6060) at a cooling rate of 0.3 K/min. For both alloys, the estimated Mg_2Si -concentration is marked by circles in the phase diagram. According to the phase diagram, the solvus temperature for 6060 is about 425 °C. 6082_{high} does not seem to be in the single-phase region at the applied solution annealing temperature of 540 °C. Hence, according to the DSC curve for 6082_{high} shown in Figure 16 B, precipitation is initiated immediately with the onset of cooling, this finding indicates that solution annealing was performed slightly below or at the solvus temperature. For 6060, the comparable DSC cooling curve in Figure 16 C shows that the reaction was initiated at about 430 °C. Hence, the DSC results are in good agreement with the quasi-binary phase diagram of Al- Mg_2Si .

The DSC findings of this work confirm previously reported results [24], which stated that only the high-temperature peak was detected because of a small cooling rate range. Hence, the results of this work demonstrate that it is essential to follow the entire range

of cooling rates from conditions close to equilibrium to the complete suppression of precipitation, which is of technical interest, to record CCP diagrams. The technical interest is related to the maximum values of mechanical properties like strength or hardness. Maximum Vickers hardness after artificial aging was reached as long as no precipitation reaction could be proven at DSC measurements during cooling. This is due to maximum supersaturation at the beginning of the aging process as long as no precipitates were grown during cooling.

According to our current understanding, no sharp separation between single reactions during cooling is possible. Rather, it seems that the precipitation process during cooling can be divided into at least two main overlapping regions: high temperature: coarse Mg_2Si precipitates; low temperature: rod-/lath-shaped precipitates. However, there seem to be more precipitation reactions involved. During the formation of β - Mg_2Si at least two different nucleation sites were observed: nucleation on grain boundaries and nucleation inside of aluminium solid-solution grains, both of these were likely initiated on primary precipitates [29-30]. Probably these different nucleation sites are simultaneously active, competing for alloying element atoms with different nucleation energies and diffusion paths. Hence, the asymmetric and broad DSC peak of the high-temperature reactions in the DSC curve for a rate of 0.1 K/min (Figure 2) may be due to different reactions.

4.2 Discussion of microstructure results

For the high-temperature reactions, the precipitation of Mg_2Si was observed for all alloys by SEM, EDX and XRD. A detailed proof of this observation has been published in [29] for 6005A. Because the DSC curves of all investigated alloys are similar, we conclude that the metallographic findings made for 6005A also hold for the other alloys.

Rod- or lath-shaped phases (low-temperature precipitation) were identified using electron diffraction in TEM. The diffraction pattern of the [001] zone axis of Al indicates

superlattice reflections (Figure 14), which are very similar to those found for the same kind of precipitates as reported in the literature [3, 6, 10, 32-33]. However, the interpretation of these results differs significantly between authors. While the authors of Ref. [2-3, 6, 32] suggest a hexagonal structure from the TEM diffraction pattern, the authors of Ref. [33] report a monoclinic structure determined from similar diffraction images. Furthermore, it is mentioned that both the hexagonal as well as the monoclinic crystal structure of such precipitates build upon the same Si-based structure [33]. Due to the coherence of the rod- and lath-shaped precipitates observed along the $\langle 100 \rangle$ direction of the aluminium matrix, at least one lattice parameter is known (0.405 nm), which is in agreement with the reported values of the hexagonal structure for β' ($a = 0.705$ nm, $c = 0.405$ nm) and B' ($a = 1.03$ nm, $c = 0.405$ nm) [3, 6, 10, 32]. According to [1] both types of precipitates, β' and B' , can exist concurrently; B' occurs particularly at high Si:Mg ratios. Hence, we assume the low-temperature precipitates to be β' and/or B' .

The results of this work are in accordance with the data published by Zajac et al. [19-21]. They performed continuous cooling experiments and TEM investigations on Al-Mg-Si alloys. Zajac et al. distinguish between cubic and hexagonal Mg_2Si during cooling from solution annealing for the aluminium alloys 6063, 6005 and 6082. They found that at temperatures between 500 °C and 400 °C Mg_2Si precipitates in a cubic structure as square plates along the $\langle 100 \rangle$ directions of the aluminium matrix. This finding is confirmed by our work. However, in the present work, the start and end temperatures of the precipitation reaction as well as the volume fractions can be ascertained more precisely and as a function of the cooling rate, temperature and alloy composition.

Furthermore, Zajac et al. found that at temperatures between 300 °C and 350 °C Mg_2Si precipitates in a hexagonal structure [19-21]. This structure is semi-coherent with the aluminium solid solution. Such precipitates were found to occur as plates and needles.

Zajac et al. use the designation β' for this phase. The semi-coherent phase with hexagonal structure precipitating at lower temperatures is in agreement with the results published in [19-21]. The temperature of the intensity maximum of the low-temperature reactions found in this work corresponds to the temperature range given by Zajac et al., at least over a certain cooling rate range. The exact intensities and characteristic temperatures of these low-temperature reactions can now be determined to be alloy specific, cooling rate and temperature dependent.

Compared to the alloys 6060, 6063, 6005A and 6082_{low}, the investigated alloy 6082_{high} had a significantly lower grain size after solution annealing and cooling. The UCCR of this alloy is about one order of magnitude higher than the UCCR of the alloy 6082_{low}. This result indicates that besides chemical composition the initial microstructure and solution annealing parameters strongly influence the CCT diagrams, as is known for steels as well.

5 Summary

The precipitation behaviour during cooling from solution annealing of five Al-Mg-Si-based wrought alloys featuring an excess of Si was investigated over a wide range of cooling rates (0.05 K/min - 20,000 K/min) by means of DSC, metallographic analyses, SEM, TEM and hardness testing. The results were displayed in continuous cooling precipitation (CCP) diagrams. All investigated alloys show similar precipitation behaviour, which consists of the high-temperature precipitation of at least the β -Mg₂Si phase and the low-temperature precipitation of presumably β' / B'. For all five alloys the precipitation reactions occurred in similar temperature ranges. The start temperature of β -Mg₂Si precipitation as well as the total specific precipitation heat increase with increasing amounts of alloying elements Mg and Si. The precipitation kinetics depend on the alloy composition as well. Both the lower and upper critical cooling rates (LCCR – highest cooling rate with complete precipitation / UCCR – lowest cooling rate with

complete supersaturation of solid solution) increase with increasing amounts of alloying elements Mg and Si. For example, for 6060 with the mass fractions of 0.4 % Si, 0.44 % Mg, an upper critical cooling rate of 50 K/min was determined, and for 6082 with the mass fractions of 1.23 % Si, 1.05 % Mg, an upper critical cooling rate of 8000 K/min was determined. Cooling-rate-dependent hardness reached maximum values as long as previous cooling was performed faster than the alloy specific critical cooling rate.

Acknowledgement

The authors acknowledge the assistance of the Centre for Electron Microscopy (Prof. Jonas, Dr. Laue) at Rostock University, Germany during the SEM investigations.

References

- [1] I.J. Polmear, *Ligth alloys*, 4 ed., Butterworth-Heinemann, Oxford, 2006.
- [2] C. Cayron, P.A. Buffat, *Acta Mater.*, 48 (2000) 2639-2653.
- [3] C. Cayron, L. Sagalowicz, O. Beffort, P.A. Buffat, *Phil. Mag. A - Phys. of Condens. Matter Struct. Defect. and Mech. Prop.*, 79 (1999) 2833-2851.
- [4] D.J. Chakrabarti, D.E. Laughlin, *Prog. Mater. Sci.*, 49 (2004) 389-410.
- [5] C.S.T. Chang, I. Wieler, N. Wanderka, J. Banhart, *Ultramicroscopy*, 109 (2009) 585-592.
- [6] G.A. Edwards, K. Stiller, G.L. Dunlop, M.J. Couper, *Acta Mater.*, 46 (1998) 3893-3904.
- [7] V. Massardier, T. Epicier, in: P.J. Gregson, S.J. Harris (Eds.) 8th International Conference on Aluminium Alloys, Trans Tech Publications Ltd, Cambridge, England, 2002, pp. 851-856, DOI 10.4028/www.scientific.net/MSF.396-402.851.
- [8] K. Matsuda, S. Ikeno, H. Matsui, T. Sato, K. Terayama, Y. Uetani, *Metall. Mater. Trans. A*, 36A (2005) 2007-2012.
- [9] M. Murayama, K. Hono, W.F. Miao, D.E. Laughlin, *Metall. Mater. Trans. A*, 32 (2001) 239-246.
- [10] L. Sagalowicz, G. Lapasset, G. Hug, *Philos. Mag. Lett.*, 74 (1996) 57-66.
- [11] A. Gaber, M.A. Gaffar, M.S. Mostafa, A.F. Abo Zeid, *Mater. Sci. Technol.*, 22 (2006) 1483-1488.
- [12] A.K. Gupta, D.J. Lloyd, S.A. Court, *Mater. Sci. Eng. A*, 316 (2001) 11-17.
- [13] Y. Ohmori, L.C. Doan, K. Nakai, *Mater. Trans.*, 43 (2002) 246-255.
- [14] X. Wang, S. Esmaili, D.J. Lloyd, *Metall. Mater. Trans. A*, 37A (2006) 2691-2699.
- [15] J.Y. Yao, D.A. Graham, B. Rinderer, M.J. Couper, *Micron*, 32 (2001) 865-870.
- [16] J.L. Cavazos, R. Colas, *Mater. Sci. Eng. A*, 363 (2003) 171-178.
- [17] J.L. Cavazos, R. Colas, *Mater. Charact.*, 47 (2001) 175-179.
- [18] A. Deschamps, G. Texier, S. Ringeval, L. Delfaut-Durut, *Mater. Sci. Eng. A*, 501 (2009) 133-139.
- [19] S. Zajac, B. Bengtsson, A. Johansson, L.O. Gullman, in: B.D. J.H. Driver, F. Durand, R. Fougères, P. Guyot, P. Sainfort and M. Suery (Ed.) *Aluminium Alloys - ICAA5*, 1996, pp. 397-402.
- [20] S. Zajac, B. Bengtsson, C. Jönsson, in: P.J. Gregson, S. Harris (Eds.) 8th

- International Conference on Aluminium Alloys, Trans Tech Publications Ltd., Cambridge, 2002, pp. 399-404, DOI 10.4028/www.scientific.net/MSF.396-402.399.
- [21] S. Zajac, B. Bengtsson, C. Jönsson, A. Isaksson, in: International Aluminum Extrusion Technology Seminar, Chicago, 2000, pp. 73-82.
- [22] T. Herding, O. Kessler, F. Hoffmann, P. Mayr, in: P.J. Gregson, H.S. J. (Eds.) 8 th International Conference on Aluminium Alloys, Trans Tech Publications Ltd, Cambridge, UK, 2002, pp. 869-874.
- [23] O. Kessler, R. von Bargaen, F. Hoffmann, H.W. Zoch, in: W.J. Poole, M.A. Wells, D.J. Lloyd (Eds.) 10 th International Conference on Aluminium Alloys 2006, Pts 1 and 2, Trans Tech Publications, 2006, pp. 1467-1472.
- [24] B. Milkereit, O. Kessler, C. Schick, in: J. Hirsch, B. Skrotzki, G. Gottstein (Eds.) 11th International Conference on Aluminium Alloys, DGM; WILEY-VCH Weinheim, Aachen, Germany, 2008, pp. 1232-1237.
- [25] B. Milkereit, O. Kessler, C. Schick, *Thermochim. Acta*, 492 (2009) 73-78.
- [26] R. von Bargaen, O. Kessler, H.W. Zoch, *HTM Zeitschrift für Werkstoffe, Wärmebehandlung, Fertigung*, 62 (2007) 8.
- [27] B. Milkereit, M. Beck, M. Reich, O. Kessler, C. Schick, *Thermochim. Acta*, 522 (2011) 86-95.
- [28] H. Schumann, *Metallographie*, 13 ed., Deutscher Verlag für Grundstoffindustrie, Leipzig, 1991.
- [29] B. Milkereit, in: Fakultät für Maschinenbau und Schiffstechnik, Dissertation (PhD) University of Rostock, Rostock, 2011, pp. 178, DOI 10.2370/9783832299934
- [30] B. Milkereit, L. Jonas, C. Schick, O. Kessler, *HTM J. Heat Treat. Mater.*, 65 (2010) 159 - 171.
- [31] D. Zohrabyan, B. Milkereit, O. Kessler, C. Schick, *Thermochim. Acta*, 529 (2012) 51-58.
- [32] M.H. Jacobs, *Phil. Mag.*, 26 (1972) 1-13.
- [33] C.D. Marioara, S.J. Andersen, T.N. Stene, H. Hasting, J. Walmsley, A.T.J. Van Helvoort, R. Holmestad, *Phil. Mag.*, 87 (2007) 3385-3413.

Table 1: Chemical composition of investigated alloys (mass fractions in %) obtained by optical emission spectroscopy (OES) analysis.

Alloys	Si	Fe	Cu	Mn	Mg	Cr	Zn	Ti
6060	0.4	0.2	0.01	0.02	0.44	0.001	0.01	0.009
6063	0.5	0.19	0.02	0.03	0.47	0.005	0.03	0.013
6005A	0.68	0.2	0.01	0.11	0.57	0.04	0.01	0.018
6082 _{low}	0.73	0.22	0.05	0.48	0.61	0.003	0.009	0.02
6082 _{high}	1.23	0.2	0.09	0.65	1.05	0.2	0.05	0.03

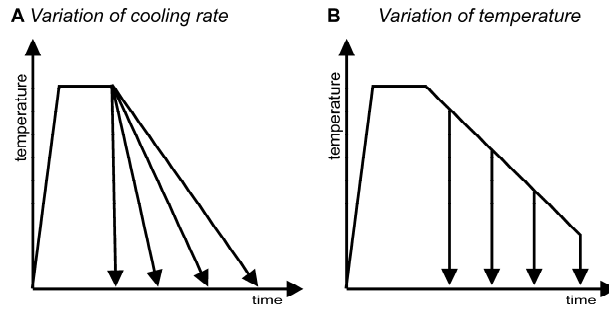


Figure 1: Schematic presentation of heat treatments applied to alloys in this work.

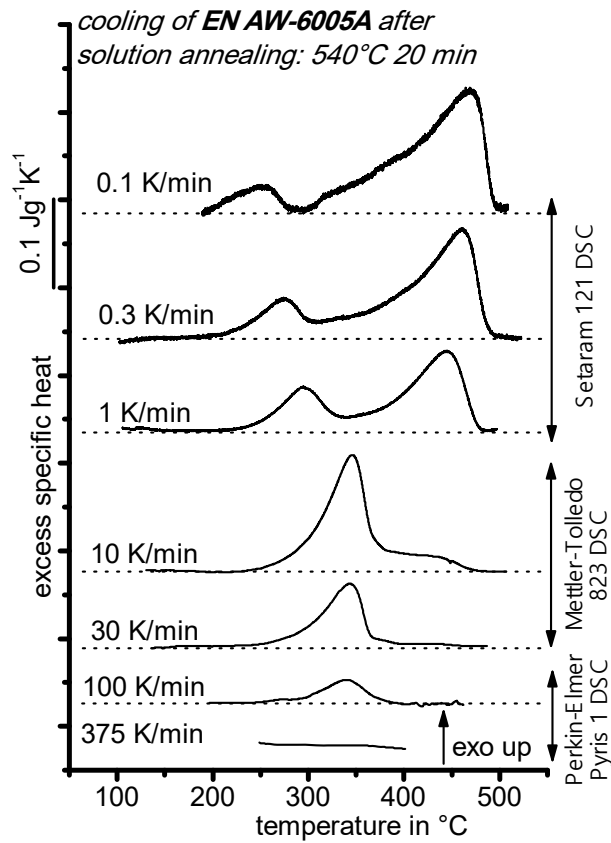


Figure 2: Selected cooling curves of the investigated composition of 6005A alloy after solution annealing at 540 °C for 20 min; curves were obtained from three different types of DSC devices corresponding to different cooling rates from 0.1 to 375 K/min.

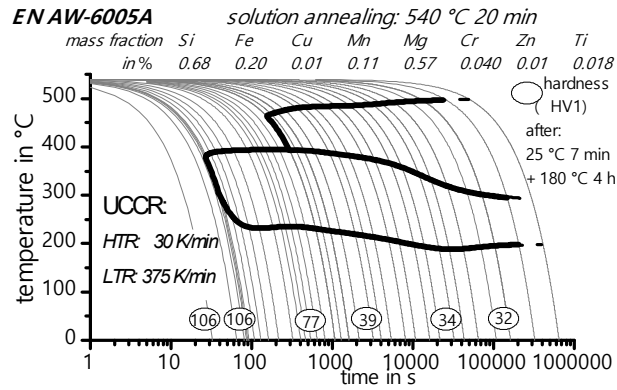


Figure 3: Continuous cooling precipitation diagram of the investigated composition of 6005A after solution annealing at 540 °C 20 min.

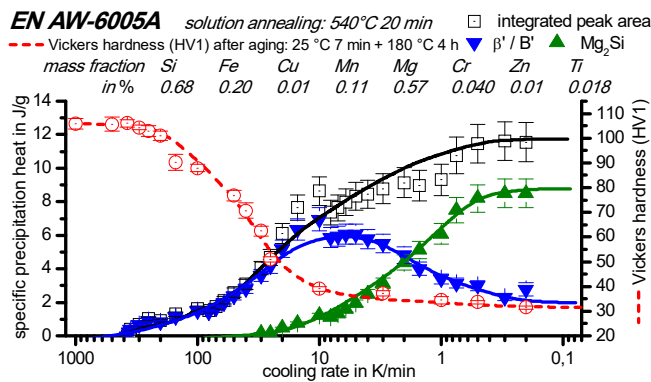


Figure 4: Specific precipitation heat after cooling to room temperature from solution annealing at 540 °C 20 min and Vickers hardness after additional artificial aging of the investigated composition of 6005A as functions of cooling rate.

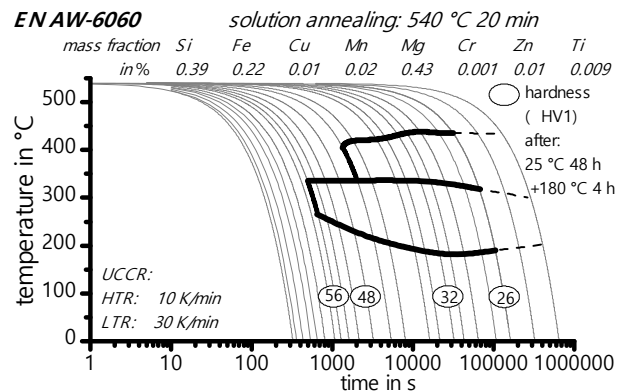


Figure 5: Continuous cooling precipitation diagram of the investigated composition of 6060 after solution annealing at 540 °C 20 min.

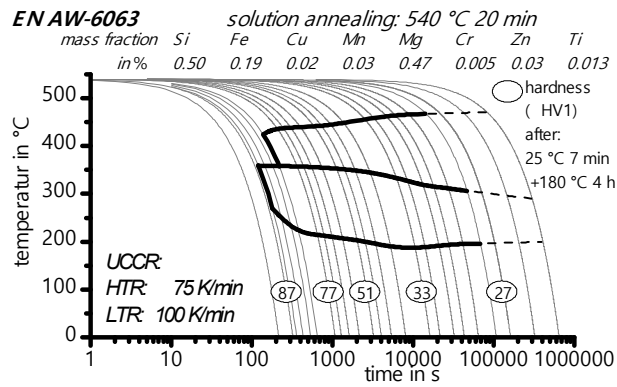


Figure 6: Continuous cooling precipitation diagram of the investigated composition of 6063 after solution annealing at 540 °C 20 min.

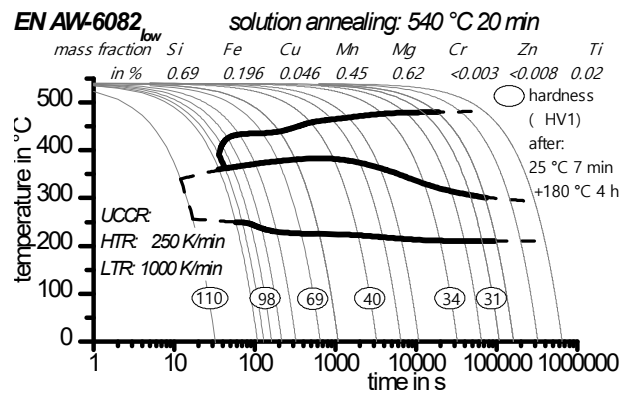


Figure 7: Continuous cooling precipitation diagram of the investigated composition of 6082_{low} after solution annealing at 540 °C 20 min.

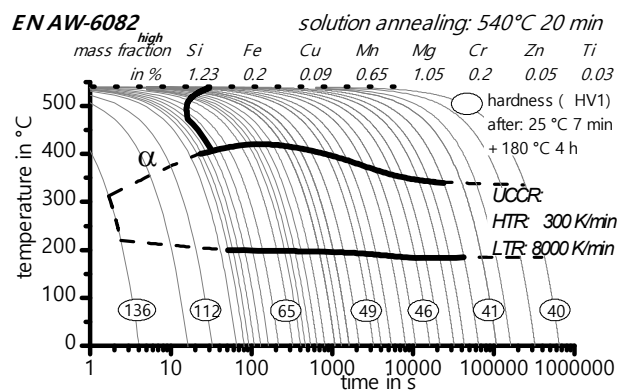


Figure 8: Continuous cooling precipitation diagram of the investigated composition of 6082_{high} after solution annealing at 540 °C 20 min.

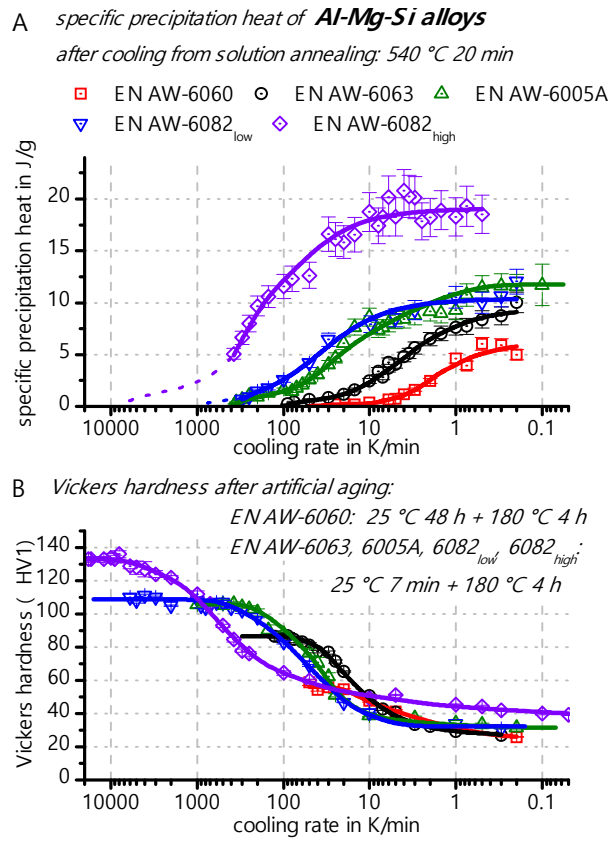


Figure 9: Specific precipitation heat after cooling following solution annealing at 540 °C 20 min (A) and Vickers microhardness after artificial aging (B) as functions of cooling rate for the investigated alloys.

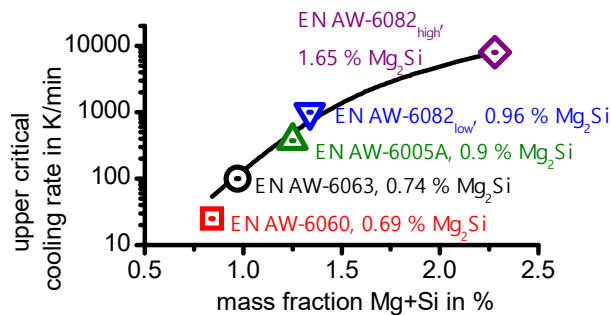


Figure 10: Upper critical cooling rate of the investigated Al-Mg-Si alloys as a function mass fraction of Mg+Si. The estimated Mg₂Si equilibrium mass fraction (at room temperature) is also given for each alloy.

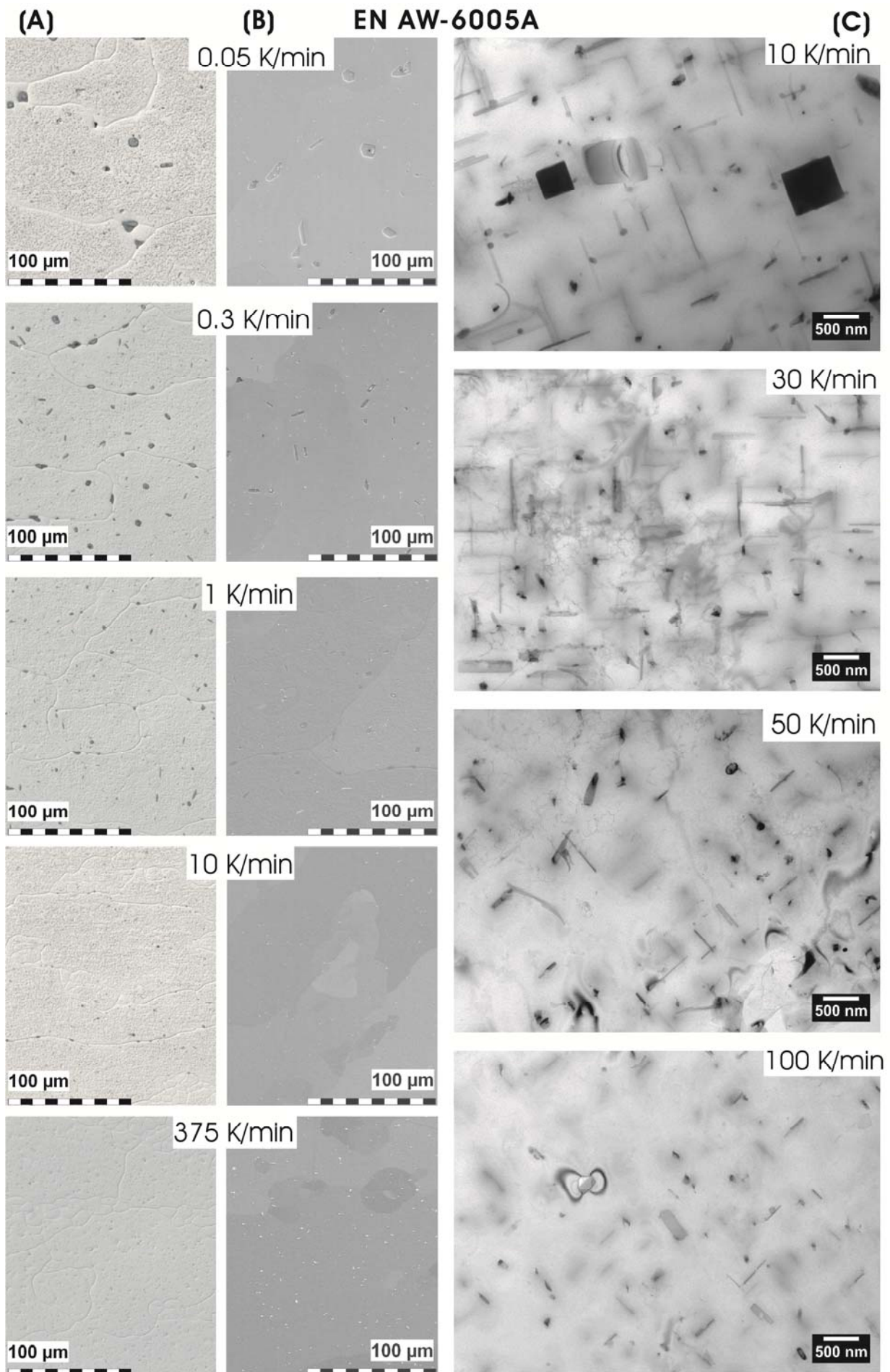


Figure 11: (A) optical microscopy, (B) bright-field SEM and (C) bright-field TEM images of 6005A samples after cooling at different rates.

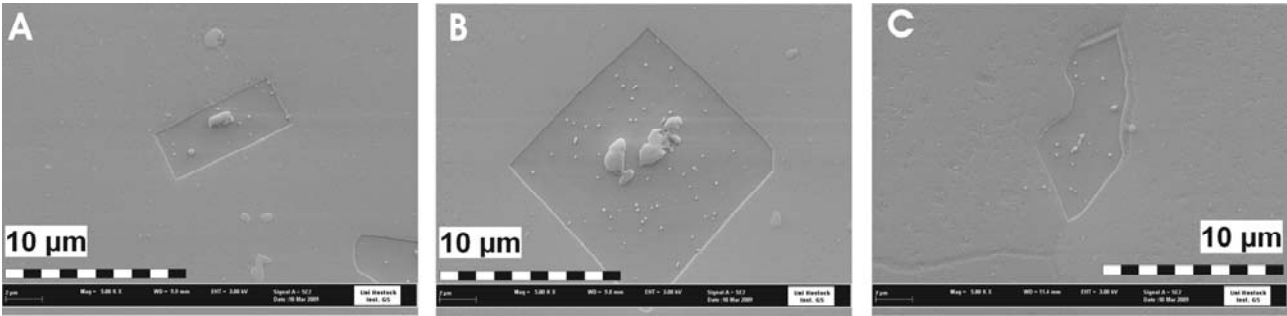


Figure 12: Bright-field SEM images of Mg₂Si precipitates (dark in contrast) found within the grains (A and B) and at the grain boundaries (C). In all investigated Mg₂Si phases, primary precipitates, (bright in contrast) were found.

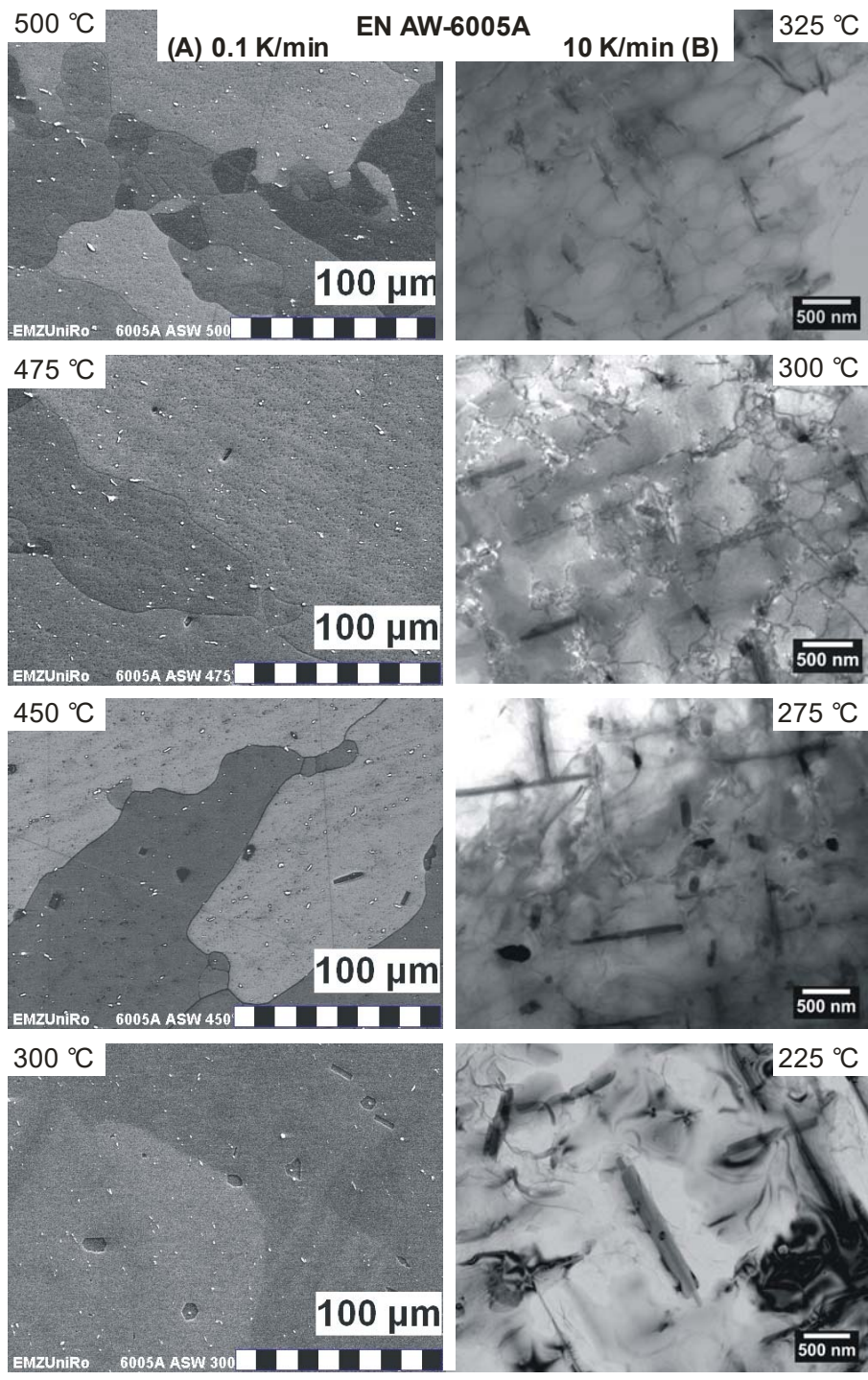


Figure 13: Microstructure of 6005A alloy samples investigated at different temperatures (A) using bright-field SEM at a cooling rate of 0.1 K/min and (B) using Bright-field TEM at a cooling rate of 10K/min.

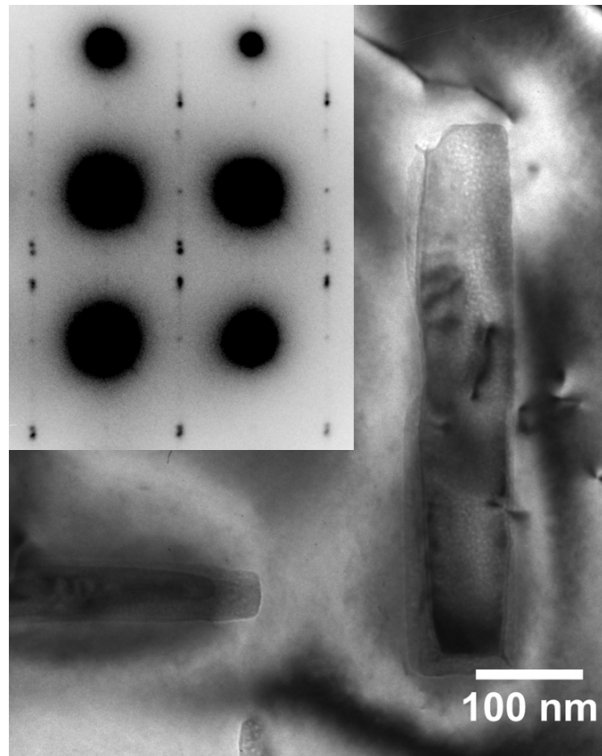


Figure 14: Bright-field TEM micrograph of a 6005A specimen after cooling at 10 K/min. The corresponding SAED pattern of [001] Al zone axis is shown in the inset.

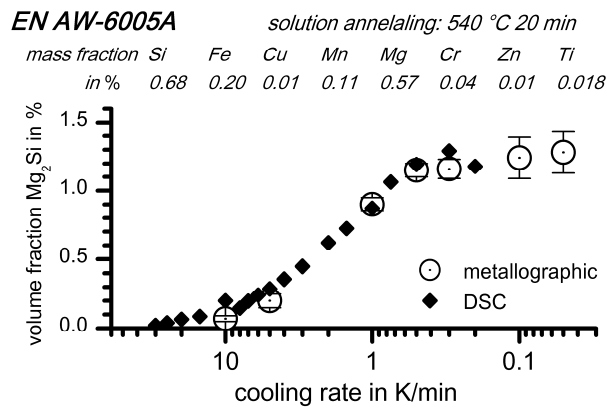
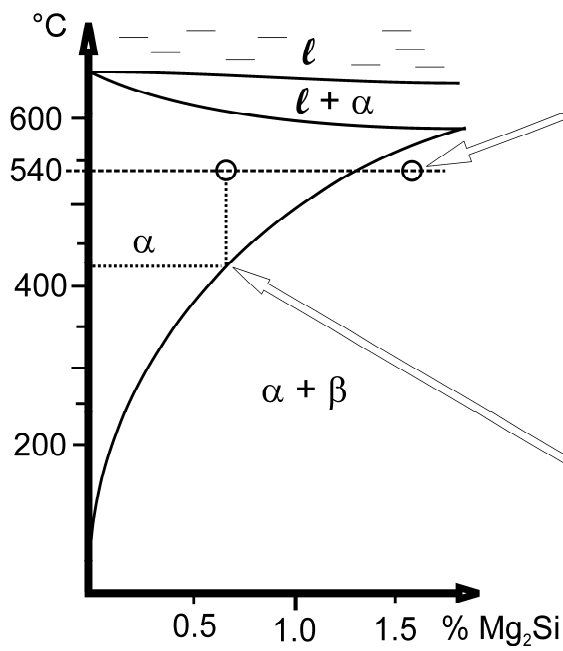
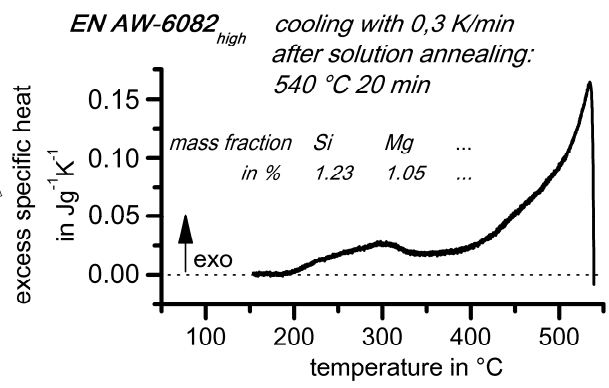


Figure 15: Volume fraction of Mg_2Si plotted as a function of cooling rate determined by metallographic method and estimated from DSC measurements as a function of cooling rate.

A Scheme of quasibinary Phasediagram **Al-Mg₂Si**



B



C

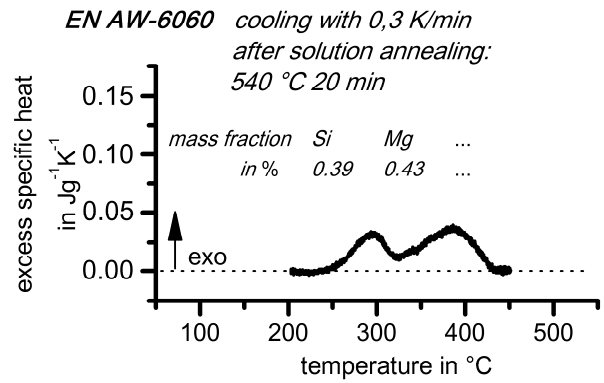


Figure 16: Schematic quasi-binary phase diagram of Al-Mg₂Si (A) [1] and DSC runs for the 6082_{high} alloy (B) and 6060 alloy (C) at a cooling rate of 0.3 K/min.

**[BM3] Zhang Y, Milkereit B, Kessler O, Schick C,
Rometsch PA:**

***Development of continuous cooling precipitation diagrams
for aluminium alloys AA7150 and AA7020.***

Journal of Alloys and Compounds 584 (2014): 581–589.

Benjamin's contributions: I managed the international collaboration, supervised the DSC measurements, partially did the DSC data evaluation and their plotting, participated in the discussion of the data and revised the manuscript.

Development of Continuous Cooling Precipitation Diagrams for Aluminium Alloys AA7150 and AA7020

Y. Zhang^a, B. Milkereit^{b,c}, O. Kessler^b, C. Schick^c, P.A. Rometsch^a

^aARC Centre of Excellence for Design in Light Metals, Department of Materials Engineering, Monash University, Clayton, VIC 3800, Australia

^bUniversity of Rostock, Faculty of Mechanical Engineering and Marine Technology, Chair of Materials Science, 18051 Rostock, Germany

^cUniversity of Rostock, Institute of Physics, Polymer Physics Group, 18051 Rostock, Germany

Abstract: Two commercial 7xxx series aluminium alloys with different solute contents and different quench-induced precipitation behaviour have been investigated by using a specialised differential scanning calorimetry (DSC) technique to record exothermal heat outputs during continuous cooling. Together with hardness testing and microstructural analysis, this DSC method was used to develop the first continuous cooling precipitation (CCP) diagrams for alloys AA7150 and AA7020. The results show that the total precipitation heat for each alloy decreases with increasing cooling rate. However, the excess specific heat at a given cooling rate in alloy AA7150 is much higher than that in alloy AA7020. It is evident that there are at least three different quench-induced reactions in different temperature regimes for alloy AA7150 cooled at various linear cooling rates, but only equilibrium MgZn_2 (η -phase) and Al_2CuMg (S-phase) particles were observed by scanning electron microscopy. There are two main precipitation peaks that can be found for alloy AA7020, which correspond to Mg_2Si and MgZn_2 (η -phase). Furthermore, a method is developed to evaluate the quench sensitivity of an alloy based on a determination of the critical cooling rate. The maximum hardness values are reached at cooling rates that are faster or similar to the critical cooling rate.

Keywords: Quench sensitivity; DSC; Al-Zn-Mg-Cu; Continuous cooling transformation; Continuous cooling precipitation diagram

Introduction:

High strength 7xxx alloys are conventionally hardened by means of a precipitation hardening treatment that includes: solution treatment, quenching and ageing [1-3]. The soluble alloying elements are dissolved into the Al matrix during solution treatment. After rapid quenching, a supersaturated solid solution is formed. In the third step, the materials are aged artificially for a certain time to obtain metastable η' precipitates [4-6]. Maximum strength is reached when the size and distribution of these precipitates are optimised to hinder the dislocations most efficiently. During extended ageing, the metastable precipitates will continue growing and transform to the

equilibrium MgZn_2 (η -phase). However, the equilibrium η -phase can also precipitate on heterogeneous nucleation sites during slow cooling, resulting in a loss of solute from solution and a reduced strength after subsequent ageing [5, 7, 8].

It is therefore important to find an optimum way of quenching the 7xxx series aluminium thick plates from the solution treatment temperature without losing excessive solute, as different cooling paths will lead to a significant variation in properties. There are two main types of transformation diagrams that are helpful in selecting the optimum cooling paths to achieve desirable properties. They are based on either (i) interrupted quenching and isothermal holding experiments, such as time-temperature transformation (TTT) or time-temperature property (TTP) diagrams, or (ii) continuous cooling experiments, such as continuous cooling precipitation (CCP) diagrams, also known as continuous cooling transformation (CCT) diagrams. It must be mentioned that in particular, the isothermal TTT diagrams are not directly suitable to design a continuous cooling process.

Fink and Willey pioneered attempts to describe the effects of quenching on the properties of aluminium alloys [9]. Using an isothermal quenching technique, they developed C-curves for the strength of 7075-T6 and the corrosion behaviour of 2024-T4[9]. Evancho and Staley successfully developed a new method called quench factor analysis, which involves an integration of cooling curves and TTP curves to allow the corrosion and/or mechanical property behaviour to be accurately determined [10]. Liu has compared C-curves for typical Al-Zn-Mg-Cu alloys 7075, 7050 and 7085 [11]. He found that the most significant change for these three different curves is that the "noses" of the curves (i.e. the critical temperatures and times) shift to lower temperatures and longer times when progressing from alloy 7075 to 7085. This means that solute can remain in solution for longer times and to relatively lower temperatures in alloy 7085. Consequently, a slower cooling rate can be tolerated in the critical temperature range for a given drop in properties. However, in order to determine the critical temperature range for a C-curve, interrupted quenching techniques are normally employed. The specimens are quenched to intermediate temperatures, held for a series of times, quenched to room temperature, and then aged using a standard practice. A large number of experiments is required to build up a complete TTT diagram by this method [12]. For real-life engineering applications, a CCT-diagram is more appropriate since industrial heat treatments tend to involve continuous cooling rather than step quenching. As a result, it is more meaningful to develop a CCP-diagram and to select an optimum cooling path from this diagram.

There are only very few CCP-diagrams that have been developed for aluminium alloys. Only recently, Kessler *et al.* provided a methodology to construct CCT-diagrams for alloy 7020 by means of a novel differential scanning calorimetry (DSC) technique [13]. Milkereit *et al.* developed this method significantly in order to record CCT-diagrams over a wide range of cooling rates from 0.1 K/min to 375 K/min by using three different types of DSC devices on alloy 6005A [14]. By recoding the exothermic heat capacity curves of the precipitation reactions during cooling, a full range of CCP-diagrams could be obtained. In addition, the hardness values

after artificial ageing were measured for the respective cooling curves. Milkereit developed CCP-diagrams for wrought aluminium alloys 6060, 6063, 6005A and two batches of 6082 by means of the same technique [15]. It was found that the critical cooling rate for 6xxx series alloys increases with an increasing concentration of alloying elements: 0.5 K/s for 6060, 1.5 K/s for 6063; 6.25 K/s for 6005A; 16.7 K/s for lean 6082; 133 K/s for concentrated 6082.

For highly alloyed 7xxx alloys, the critical cooling rate is expected to be very high. Its value can hardly be estimated by traditional DSC techniques which are limited to cooling rates of about 5 to 10 K/s. By using an indirect differential fast scanning calorimeter (DFSC) and utilising extremely small samples measuring $20\ \mu\text{m} \times 90\ \mu\text{m} \times 100\ \mu\text{m}$, Zohrabyan *et al.* found that the critical cooling rate for alloy 7049A is about 300 K/s [16]. Alloy AA7150 is nearly as highly alloyed as alloy 7049A, except that it has a lower Zn content. It is therefore reasonable to assume that the critical cooling rate for alloy AA7150 alloy is of a similar order of magnitude.

It is the purpose of this paper to construct CCP-diagrams for both alloys AA7150 and AA7020, based on a combination of DSC measurements, microstructure analysis and hardness testing. Several DSC-devices are used employing the method described by Milkereit *et al.* to record the excess specific heat curves at different cooling rates ranging from very slow cooling (~ 0.005 K/s) to as fast as possible [14]. Corresponding microstructural analysis is carried out to help interpret the results. In order to extend the range of controlled cooling rates, a quenching dilatometer is utilised to achieve cooling rates faster than 5 K/s. However no exothermal heat can be detected with the dilatometer.

Alloys AA7150 and AA7020 have been chosen due to their significant difference in quench sensitivity. Alloy AA7150 is a typical high strength aluminium alloy with a total alloying mass fraction of more than 10 wt%. The high alloying content gives a great potential for age hardening after rapid cooling. However, this alloy is so quench sensitive that its properties vary significantly with changes in the quench rate. Alloy AA7020 is known as a medium strength alloy as it only contains mass fractions of about 4 wt% Zn and 1 wt% Mg. This alloy is also regarded as a Cu-free alloy since the upper limit is only 0.2 wt% Cu. Hence this alloy is expected to be much less quench sensitive than AA7150. It is therefore of interest in this paper to quantify the quench sensitivity of both alloys by constructing novel CCP-diagrams from DSC data.

Experiments:

Samples of alloy AA7150 were cut from the center layer of a commercially produced 80 mm thick plate, supplied by the Aluminium Corporation of China Ltd (Chalco). Samples of AA7020 were cut from a 30 mm diameter extruded rod. The compositions of the studied alloys are shown in Table 1.

Table 1
Compositions of alloys under investigation.

Mass%	Si	Fe	Cu	Mn	Mg	Zn	Zr	Cr	Ti
7150	0.02	0.05	2.04	0.04	2.15	6.33	0.12	<0.01	0.01
7020	0.11	0.17	0.04	0.15	1.19	4.37	0.14	0.11	0.03

For the DSC measurements the procedure described by Milkereit *et al.* was used [14]. Therefore three different types of DSC devices were used. Solution treatment for alloy AA7150 was performed by heating up small DSC samples to 460 °C for 1 hour and then slowly heating up to 480 °C and holding for another one hour. Solution treatment for alloy AA7020 was performed by heating up samples directly to 480 °C and holding isothermally for 30 min. The solution treatment was performed in the DSC device so that it could be immediately followed by different continuous cooling treatments that were programmed into the different DSC devices. Cooling rates beyond the limit of DSC devices are carried out using a quenching dilatometer (Bähr DIL 805A/D).

For each DSC device, different conditions have been identified to reach optimal results [14]. Because the heat flow curves, measured with a DSC, are also influenced by cooling rate and sample mass, excess specific heat capacities were calculated from measurements with a pure Al sample on the reference side and subtracting baseline measurements with pure Al reference samples in both DSC-micro-furnaces. This results in an excess value of the specific heat from the exo- or endothermic reactions in the alloyed sample. Data conditioning was performed as described by Milkereit *et al.* [14]. The excess specific heat capacity can be easily calculated from the measured heat flow rate by subtracting the base-line and dividing by the sample mass and cooling rate:

$$C_p = \frac{\Phi_m - \Phi_0}{m \cdot \beta}$$

where C_p is the excess specific heat capacity, Φ_m is the measured heat flow, Φ_0 is the reference base-line, m is the sample mass and β is the cooling rate. Normally the DSC runs at constant pressure, yielding the heat capacity at constant pressure $C_p(T)$. The enthalpy is determined by integration as follows [17]:

$$\Delta H = H(T) - H(T_0) = \int_{T_0}^T C_p(T) dT$$

Due to the overlapping of the peaks, a method, described by Milkereit *et al.* [18], was used that defines the intersection points with the baseline as the initial peak temperatures and the final peak temperatures of a single reaction. A schematic of this simple evaluation is shown in Figure 1.

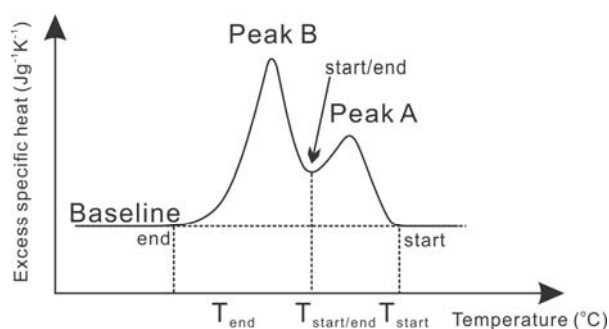


Figure 1 Schematic of data evaluation with overlapping peaks, where T_{start} is the extrapolated start temperature for peak A, $T_{start/end}$ is both the end temperature for peak A and the start temperature for peak B, and T_{end} is the extrapolated end temperature for peak B.

In addition, the cooling rate range was extended by utilising the dilatometer. The samples were heated by an induction coil and were rapidly cooled by a controlled inert gas flow. DSC samples with dimensions of about 5 mm in diameter and 1 mm in height were utilised. A thermocouple was spot welded to the sample surface, so that a desirable cooling rate could be obtained. Tests showed that the maximum cooling rate for this dilatometer instrument is about 200 K/s with the sample size that was used in this work. Vickers hardness measurements were carried out after artificial ageing for 24 h at 120 °C.

For microstructural analysis, samples were manually ground and polished with SiC paper, diamond paste and colloidal silica for examination with a JEOL JSM-7001F field emission gun scanning electron microscope (FEG-SEM), equipped with a Bruker Quantax EDS system.

Results and Discussion:

DSC curves and CCP-diagrams

Figure 2 shows the bending-corrected excess specific heat curves for alloys AA7150 and AA7020 cooled at various linear cooling rates from 0.005 K/s to 3 K/s. The original DSC-curves were obtained during cooling from solution annealing in three different types of DSC devices corresponding to different cooling rates ranges (Setaram 121 DSC: 0.005 to 0.1 K/s; Mettler-Toledo 823 DSC: 0.2 to 0.5 K/s; Perkin-Elmer Pyris 1 DSC: 0.5 to 3 K/s). In Figure 2(a) the curves are shifted and arranged in order of increasing cooling rate, starting with the slowest rate on top. The horizontal dashed lines represent the zero level. Deviations exceeding this level indicate exothermal reactions. Be aware of the different scales in the diagrams (a) and (b) in Figure 2. The same curves can be compared for both alloys without shifting and in the same scaling in diagrams (c) and (d) in Figure 2.

It can be seen that both investigated alloys showed basically similar precipitation behaviour with at least three precipitation reactions. The reactions can be subdivided into high, medium and low temperature reactions. The intensities of these three reactions differ significantly between AA7150 and AA7020.

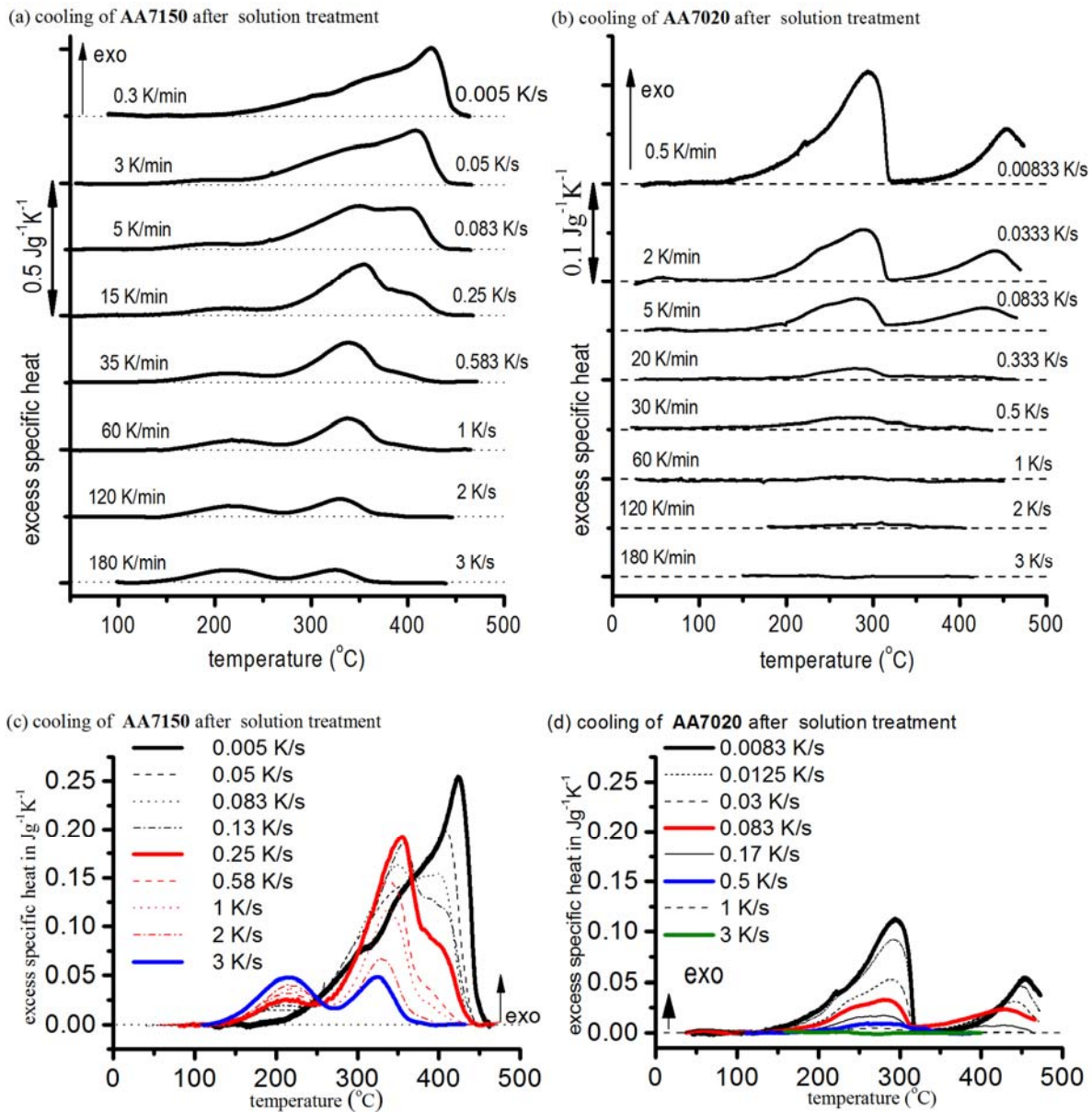


Figure 2 DSC cooling curves after solution annealing for alloys AA7150 and AA7020 with cooling rates varying from about 0.005 to 3 K/s.

For alloy AA7150, the highest temperature reaction starts at about 450 $^{\circ}\text{C}$. The peak-area decreases with increasing cooling rate, starting from about 24.7 J/g at a cooling rate of 0.005 K/s. At the cooling rate of 0.083 K/s, the second peak can be clearly distinguished at an intermediate temperature of about 350 $^{\circ}\text{C}$. It is believed that the medium temperature peak overlaps the high temperature peak so that it cannot be identified easily at slower cooling rates. With increasing cooling rate, the high temperature peak area decreases. At a cooling rate of 3 K/s the high temperature peak has disappeared, so the critical cooling rate of this reaction is about 3 K/s.

The medium temperature reaction peak area increases first, starting from about 8 J/g at a cooling rate of 0.02 K/s. The peak area values of the medium temperature reaction show a plateau value of about 12 J/g at cooling rates between 0.083 and 0.416 K/s. The peak area values of this medium temperature reaction then decrease dramatically to about 3 J/g at a cooling rate of 3 K/s, which is the fastest cooling rate achieved in these DSC experiments. It is interesting to discover that there is another low temperature reaction showing up at the faster cooling rates at a lower temperature of about 220 °C. It can be seen that the low temperature peak areas are relatively small. This indicates that the transformation amount of the low temperature reaction is quite small when compared with the high temperature and medium temperature reactions. However, this low temperature peak area increases slowly with increasing cooling rate, while the medium temperature peak area decreases in this cooling rate range. The peak areas of the medium temperature reaction and low temperature reaction are similar in size at a cooling rate of around 3 K/s.

For alloy AA7020, two distinct peaks can be found clearly at slow cooling rates. The high temperature reaction starts immediately with the onset of cooling at a temperature of about 475 °C. The peak area value decreases significantly with increasing cooling rate. It can hardly be distinguished from the baseline at a cooling rate of 1 K/s. The medium temperature reaction peak is so significant at the slower cooling rates, such as 0.0083 K/s, that it dominates the quench-induced reactions. It occurs at a relatively low temperature of about 280 °C, compared to the high temperature reaction (and compared to the medium temperature reaction in alloy AA7150). However, here the medium temperature reaction peak and low temperature reaction peak are strongly overlapping each other. As a result, the low temperature reaction peak can hardly be separated from the medium temperature peak. This changes the shape of the overall peak at temperatures of about 250 °C and less. These two peaks disappear completely at cooling rates of >1 K/s.

There are some significant differences in the results between the two alloys. In the first place, the released enthalpy at a given cooling rate in alloy AA7150 is much higher than that in alloy AA7020. As a result, the Y-axis scale in Figure 2 (a) and (b) has been adjusted to enlarge the smaller peaks of AA7020. The difference in excess specific heat is attributed to the higher alloying content in alloy AA7150. Furthermore, the onset temperatures of the high temperature reactions in the two alloys are different. The first reaction in alloy AA7150 occurs about 30 °C below the solution annealing temperature (i.e. at about 450 °C). On the other hand, the first reaction for alloy AA7020 starts immediately upon cooling. This suggests that dissolution of the soluble phases might not be fully completed within a solution treatment of 30 minutes at 480 °C for alloy AA7020.

A third significant difference is in relation to the overlapping of the peaks. For alloy AA7150, the high and medium temperature reactions strongly overlap at slower cooling rates in a temperature range of about 450 °C to 330 °C, so that at best only an approximate separation can be achieved. The low temperature reaction is well separated in alloy AA7150. For alloy AA7020,

however, the high temperature reaction is well separated while the medium and low temperature reactions are strongly overlapped in a temperature range of about 320 °C to 150 °C. For the evaluation of precipitation heats, no peak separation was performed in this case. For the medium and low temperature reactions of alloy AA7020, the precipitation heats are therefore given as a sum in the following discussion. At rates above 0.33 K/s, a separation of the peaks is impossible for these reactions by the simple separation technique used in this work. The observed differences in the overlapping of the occurring precipitation reactions are probably due to the different alloying contents and precipitation sequences during cooling, which will be discussed later together with the microstructural analysis results.

These DSC curves also lead to some questions. Figure 3 shows a detailed comparison of both alloys at a similar cooling rate. This figure suggests that there may be a fourth reaction at temperatures of around 50 °C. It should be mentioned that this temperature and cooling rate combination raise several problems for DSC measurement and evaluation. First, cooling was performed down to 25 °C and this possible very low temperature reaction ranges from about 100 °C down to about 30 °C. At the lower end of this temperature range, the actual temperature may not match the programmed temperature if the upper cooling rate limits of the different devices are reached. This loss of control might result in measurement artifacts. Due to such problems, it is difficult to perform correct evaluations, especially bending corrections [14]. Beside this, the possible very low temperature reaction has a very low intensity, amounting to a signal that is close to the detection limit. Due to these reasons, the very low temperature reaction was not evaluated any further. Further DSC investigations combined with microstructural analysis will be necessary to clarify this.

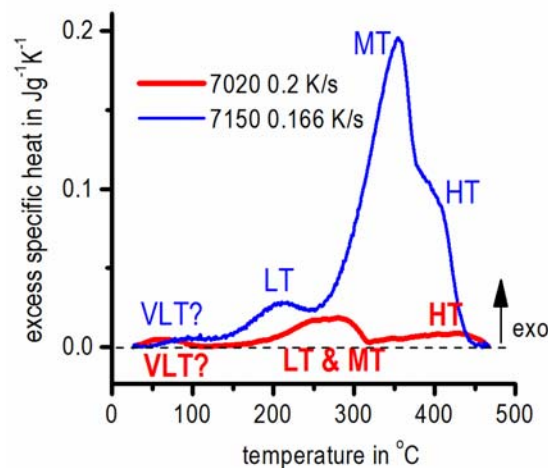


Figure 3 Comparison of DSC cooling curves at similar cooling rates for alloys AA7150 and AA7020 showing four possible reactions: a high-temperature reaction (HT), a medium-temperature reaction (MT), a low-temperature reaction (LT) and a possible very low-temperature reaction (VLT).

An important piece of information is the intensity of the precipitation reactions. The intensities of the three reactions can be calculated by integrating the precipitation enthalpy (ΔH) for the exothermic reactions at constant pressure over the cooling process. The system's change in enthalpy equals the energy released in the reaction or so called precipitation heat. This intensity can be observed from the peak areas of the DSC curves in Figure 2, and its value is displayed in Figure 4 for both alloys AA7150 and AA7020, where both the specific precipitation heats during cooling to room temperature and the hardness after ageing are presented as functions of the cooling rate. The cooling rate axis uses a decreasing logarithmic scale from left to right for ease of comparison with the time scale of the CCP diagrams presented later in this paper. For the precipitation heats, the error bars show an estimated error of 10 % for AA7150 and 15 % for AA7020 respectively, resulting from the evaluation procedure. The higher uncertainty for AA7020 originates from the above-mentioned difficulties with the bending correction. For the hardness values, standard deviations calculated from five indentations are shown.

The complete ΔH_C curves of all three reactions ($\Delta H_{HT} + \Delta H_{MT} + \Delta H_{LT}$) curves in Figure 4 show a decreasing trend with increasing cooling rate. The high temperature reactions are most clearly and increasingly suppressed with increasing cooling rate. For alloy AA7150, the intensity of the medium temperature reaction first increases with increasing cooling rate before decreasing again. For alloy AA7020, it appears that from cooling at 0.0083 K/s, the reaction intensities of all reactions are decreasing with increasing cooling rate. The suppression of a higher temperature reaction would normally enable the intensity of a lower temperature reaction to be increased due to a higher amount of alloying elements remaining in supersaturated solid solution. Hence, the low temperature reaction intensity increases with increasing cooling rate due to a combination of both the thermodynamic and kinetic factors associated with the nucleation and growth of a higher number density of smaller precipitates.

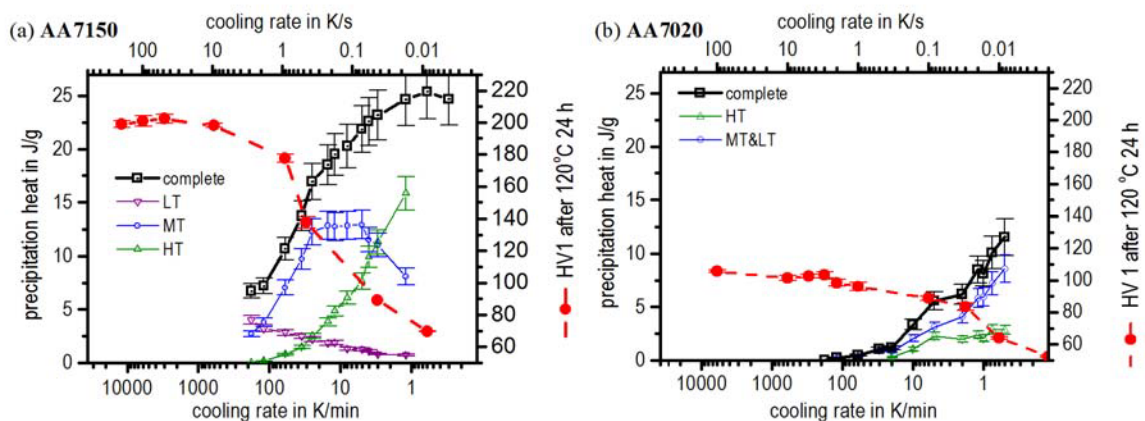


Figure 4 Specific precipitation heats for high-temperature (HT), medium-temperature (MT), low-temperature (LT) and the sum of all (complete) reactions after cooling to room temperature from solution annealing at 480 °C, for alloys AA7150 and AA7020 as a function of cooling rate. Vickers hardness values after artificial ageing for 24 h at 120 °C are also shown.

In general, the total amount transformed in these reactions tends to decrease with increasing cooling rate. The cooling rate at which ΔH_c reaches 0 is defined as the critical cooling rate (CCR). This value can be used to explain how sensitive the alloy is to cooling rate. In this case, the CCR value for alloy AA7020 is about 3 K/s. This value is consistent with the earlier results from Kessler [13]. By means of additional data analysis, an extrapolated CCR value for alloy AA7150 can be determined.

Considering that the enthalpy change of the system is caused mainly by the loss of solute from solution during the cooling process, it is reasonable to assume that the excess heat is very small at fast cooling rates since faster cooling inhibits changes in the solute concentration. The overall change of the enthalpy profile is like an S-shaped curve that changes slowly at the fast cooling end and then increases dramatically with decreasing cooling rate (Figure 5). At very slow cooling rates, the shape of the curve changes slowly as the system approaches its equilibrium state. Such behaviour has been observed previously for 6xxx alloys by Milkereit et al.[15]

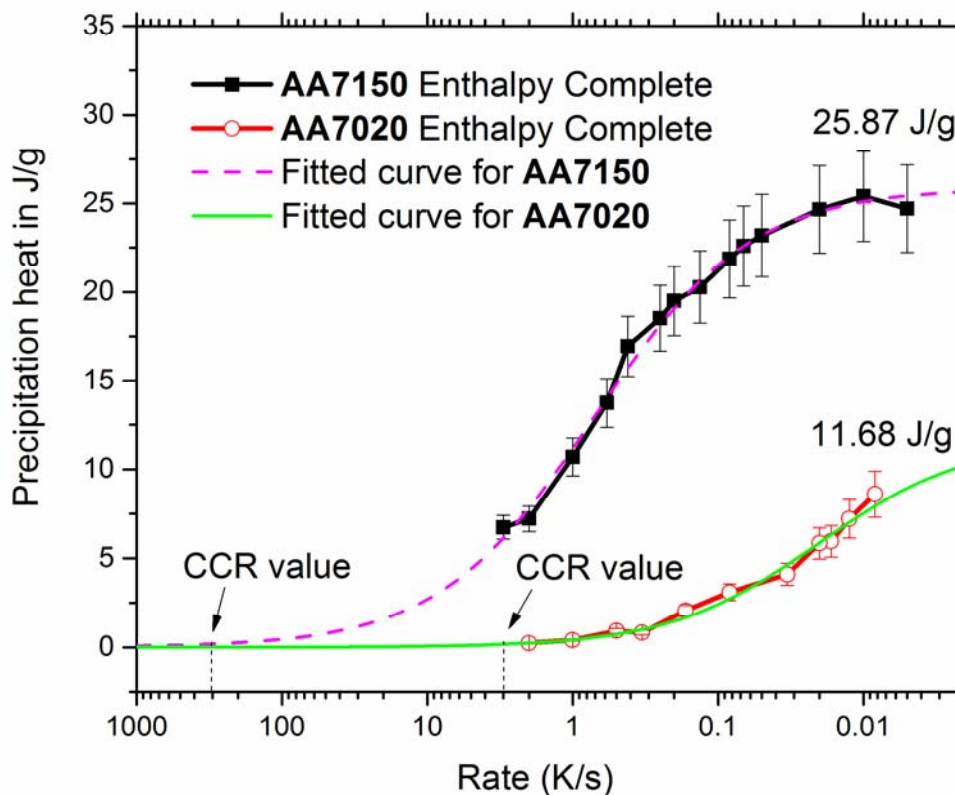


Figure 5 Determination of critical cooling rates (CCR) for both alloys by mathematical curve fitting and extrapolation.

The measured enthalpy change curves for both alloys were determined by fitting the data to the following equation:

$$\Delta H = \frac{1}{a+b(\nu)^c}$$

where a is the reciprocal of the precipitation enthalpy value in the equilibrium state where the cooling rate ν approaches zero, and b and c are model parameters. This equation is a mathematical approach with no physical basis, but describes the experimental results of several 6xxx and 7xxx alloys very well. In this case, $a_{7150}=0.039$; $a_{7020}=0.086$ since the precipitation enthalpy values in the equilibrium state are 25.87 J/g and 11.68 J/g for alloys AA7150 and AA7020 respectively. Parameters b and c ($b_{7150}=0.051$, $c_{7150}=0.814$; $b_{7020}=2.268$, $c_{7020}=0.841$) have been determined by curve fitting. By applying this equation to the current measurements, the CCR was determined by extrapolation to be 300 K/s and 3 K/s for alloys AA7150 and AA7020, respectively (i.e. the cooling rate at which the precipitation heat, ΔH , approaches zero). For AA7020 the CCR is at the upper end of the DSC experiments, while for AA7150 the CCR results from a significant extrapolation and has to be confirmed by hardness testing.

The CCR for both alloys can also be obtained using hardness testing. Figure 4 shows the Vickers hardness curves for both alloys after artificial ageing at 120 °C for 24 hours. Here it is assumed that all the remaining solute after the cooling process contributes to hardening. Thus, the hardness curves increase with increasing cooling rate as rapid cooling will preserve solute in solution for the subsequent ageing process so that the alloy has the potential to reach its maximum strength after ageing. Therefore there is no further increase in hardness if samples are cooled faster than the critical cooling rate. This hardness plateau after the CCR can be easily seen in Figure 4, where the CCR appears to be 60 K/s and 3 K/s for alloys AA7150 and AA7020, respectively. It is evident that the CCR for AA7150 from hardness testing occurs at much lower quenching rates than the CCR that was obtained by DSC with extrapolation. Possible explanations are, (i) that the hardness value is not sufficiently sensitive to reflect small changes in volume fraction of precipitates or (ii) that the extrapolation causes some uncertainty. Nevertheless, both methods result in a CCR range of 60-300 K/s, which is a relatively small range on a logarithmic scale. Both methods offer a feasible way to approximate the CCR.

Microstructural Characterisation

Figure 6 shows typical backscattered SEM images of alloy AA7150 at different cooling rates ranging from 0.005 K/s to 100 K/s. The backscattered images reflect the information of electron beam scattering interactions with different atomic species. According to phase contrast theory, phases that contain more higher atomic number elements will appear brighter in backscattered SEM images. The left column images (at a low magnification) clearly show that the total amount of precipitation increases with decreasing cooling rate, while the right column shows these phases in more detail at a higher magnification.

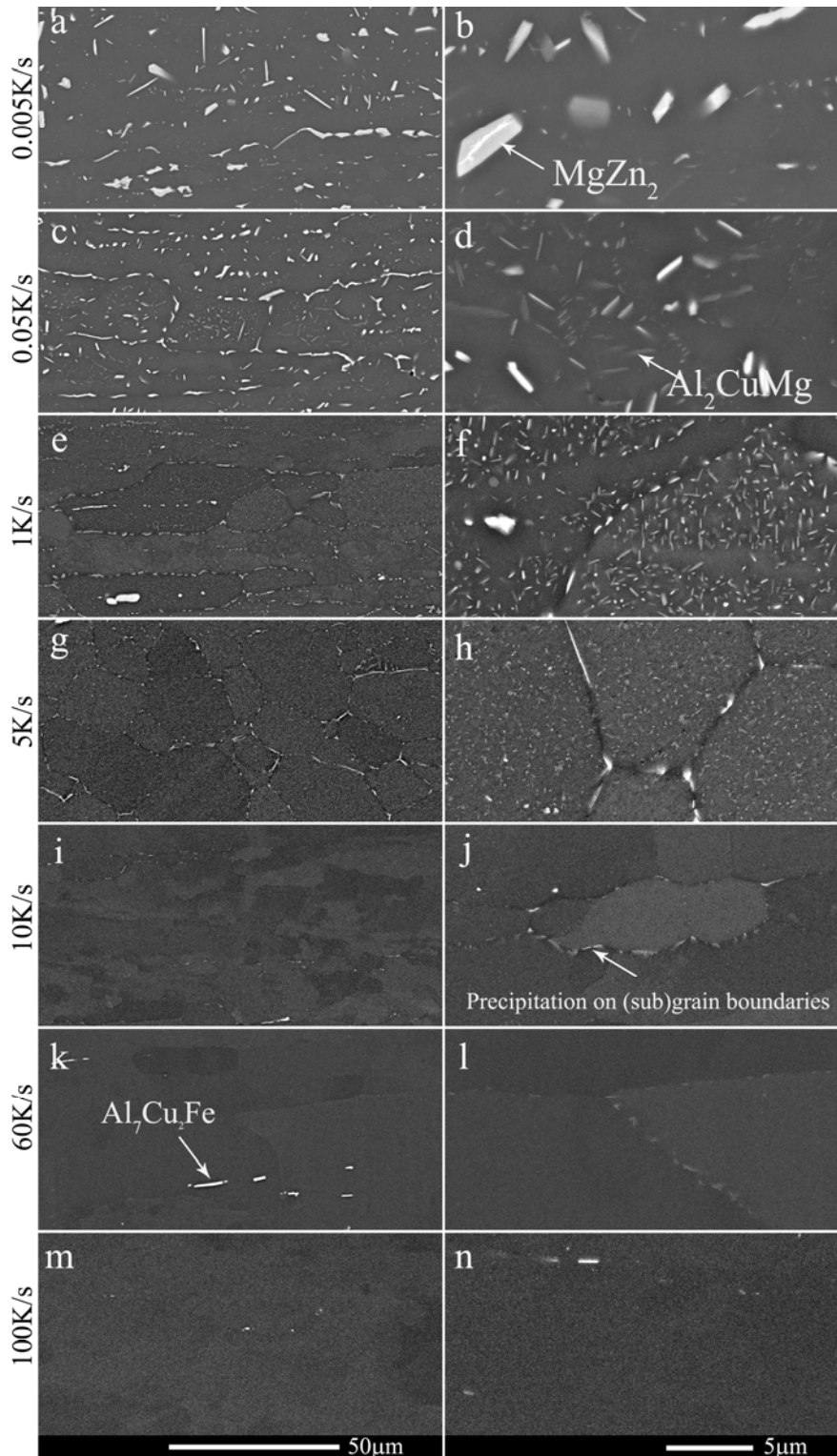


Figure 6 Backscattered SEM images of alloy AA7150 samples cooled at different rates. The two columns represent two different magnifications, as indicated by the scale bars at the bottom. The main phases are labelled.

It is evident from Figure 6(a) and (c) that at extremely slow cooling rates, quench-induced phases exhibit both a larger volume fraction and a significantly larger size than in any other conditions. This, together with the fact that it is a high temperature reaction suggests that equilibrium precipitates are formed in these slow cooling rate conditions. Based on the difference in particle size/morphology and contrast, the corresponding higher magnification images in Figure 6(b) and (d) reveal that there are at least two different phases present (identified with arrows). With reference to previous phase identifications on the same alloy, it is concluded that the brighter precipitates are equilibrium MgZn_2 (η -phase) while the grey precipitates are more likely to be Al_2CuMg (S-phase) [19]. The S-phase is difficult to be distinguished by SEM at cooling rates of more than 0.05 K/s. This corresponds with the fact that the high temperature reaction in the DSC curves can only be found in slow cooling rate conditions. Therefore it is reasonable to assume that the high temperature reaction for AA7150 corresponds to the Al_2CuMg (S-phase). In Figure 6(e) and (f) at a cooling rate of 1 K/s, the main phase appears to be MgZn_2 (η -phase), precipitated both within grains and on grain boundaries. The corresponding DSC curves in Figure 2(a) and (c) show that there are at least two peaks at the cooling rate of 1 K/s, but that the low temperature reaction peak is still relatively small at this stage. It is not expected that this low temperature phase should be observable by SEM on this scale due to their small size. Therefore the medium temperature reaction should correspond to the MgZn_2 (η -phase). At cooling rates of 10 K/s and faster, only grain- and sub-grain boundary precipitates can be observed by SEM. This is mainly due to grain- and sub-grain boundaries acting as preferential heterogeneous nucleation sites for quench-induced phases. However, at the cooling rate of 100 K/s, almost no precipitation can be found by SEM. This result is in agreement with the extrapolated critical cooling rate of about 60-300 K/s in Figure 5. There are also some coarse intermetallic phases present (highlighted in Figure 6(k)). They are identified as $\text{Al}_7\text{Cu}_2\text{Fe}$ particles that do not dissolve during solution treatment, although a small amount of rounded S-phase particles that did not dissolve completely during the solution treatment has also been observed. The precipitation of those particles will not depend on cooling rate.

According to the detected DSC curves, there are at least three different reactions that occur during linear cooling in a certain cooling rate range. The low temperature reaction was detected only at cooling rates faster than 0.05 K/s. Besides, the high temperature reaction seems to be suppressed completely at about 3 K/s. However, there is no clear evidence for the presence of low temperature precipitates at this scale of SEM. This is probably due to the small size of the low temperature precipitates at fast cooling rates. The most likely hypothesis is that the low temperature peak corresponds to homogeneously nucleated η' precipitates, although the possibility of other heterogeneous nucleation phenomena is not ruled out at this stage. More detailed microstructural analysis would be needed to clarify this.

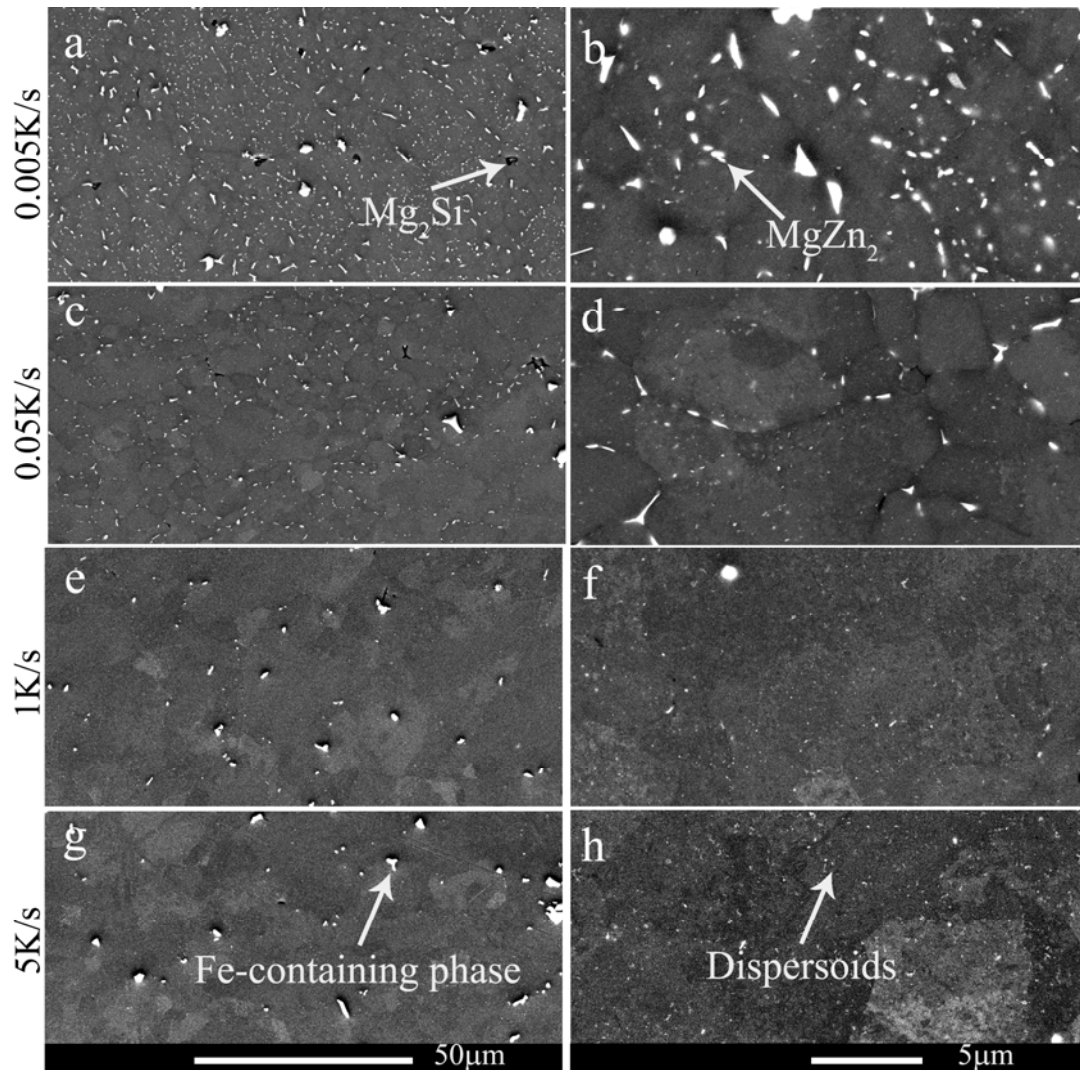


Figure 7 Backscattered SEM images of alloy AA7020 DSC and dilatometer samples cooled at different rates. The two columns represent two different magnifications, as indicated by the scale bars at the bottom. The main phases are labelled.

Figure 7 shows typical backscattered SEM images of alloy AA7020 at different cooling rates ranging from 0.005 K/s to 5 K/s. It shows the same basic trend as in Figure 6 that the quench-induced precipitates decrease in size and volume fraction with increasing cooling rate. The precipitates at a given slow cooling rate are much smaller than those in alloy AA7150, and the total volume fraction is also much smaller. This observation is in support of the results that the excess specific heat of alloy AA7020 at a given cooling rate is much smaller than that of alloy AA7150. In Figure 7(a) at a cooling rate of 0.005 K/s, there are a large amount of bright precipitates together with some coarse dark precipitates (identified with an arrow). They are identified as Mg_2Si by EDS and EBSD analysis [19]. They appear as dark particles due to the fact that Mg has a smaller atomic number than Al matrix. It is also interesting to note that the volume fraction of Mg_2Si is much smaller than that of the bright phases. Furthermore, the

amount of Mg_2Si significantly decreases with increasing cooling rate and the high temperature reaction peak in alloy AA7020 decreases dramatically with increasing cooling rate in the slower cooling rate range. It is therefore reasonable to assume that the high temperature reaction corresponds to the Mg_2Si phase. In Figure 7(c) and (d), it is evident that the coarse bright precipitates are distributed along the grain boundaries. The EDS results show that most of these coarse precipitates are equilibrium $MgZn_2$ (η -phase). When approaching and exceeding the critical cooling rate of 3 K/s for this alloy, Figure 7 (e)-(h) show that there is no further change in the microstructure and that both fine and coarse particles remain. Therefore the medium temperature reaction is believed to correspond to $MgZn_2$ (η -phase) like in AA7150. Unlike in alloy AA7150, the uniformly distributed small particles are believed to be Mn- and Cr-containing dispersoids that do not dissolve during solution treatment and therefore exist in all cooling conditions. EDS analysis of the coarse white particles in Figure 7(g) shows that they are mainly Fe-containing intermetallics. This is due to the relatively high Fe content of 0.17 wt% in this batch of alloy AA7020. These particles are insoluble phases i.e. their volume fraction did not change with increasing cooling rate.

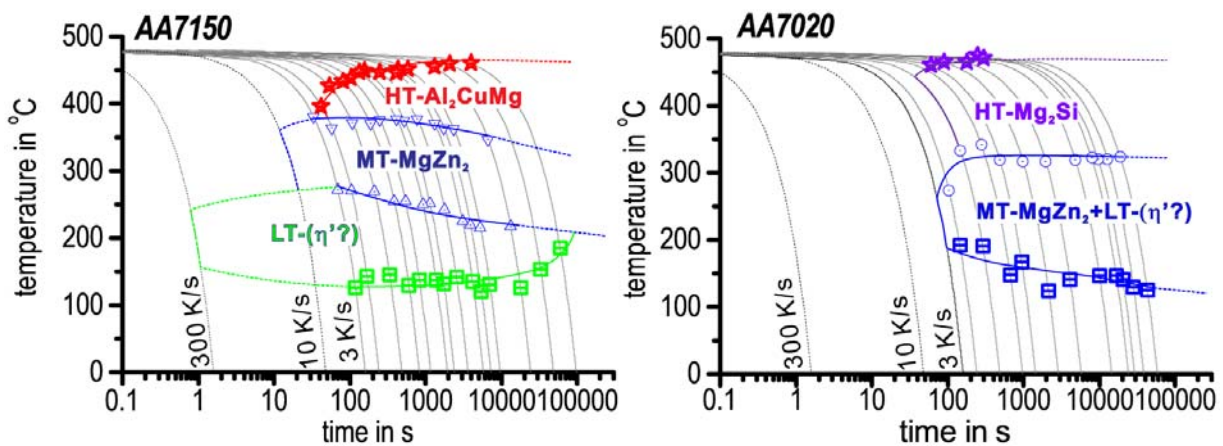


Figure 8 Developed continuous cooling precipitation (CCP) diagrams for the investigated compositions of alloys AA7150 and AA7020 after solution annealing at 480 °C for 60 and 30 min, respectively, showing linear cooling rates ranging from 300 K/s to 0.005 K/s. The dashed lines indicate regions where the precipitation reactions were extrapolated on the basis of combined evaluations of all the available DSC data, hardness curves and microstructural analysis. The main phases are labelled.

The precipitation start and end temperatures were taken from the DSC curves and plotted in a temperature/time diagram. Both diagrams are scaled in the same way, with the time-axes being scaled logarithmically. The resulting CCP diagrams of alloys AA7150 and AA7020 are shown in Figure 8. Based on the SEM results, the most likely quench-induced phases are indicated for some of the reactions. The CCP diagram provides information regarding the occurring precipitation reactions as a function of the cooling rate and temperature. The detected precipitation start and end temperatures of individual precipitation processes are indicated.

Dashed lines indicate that a precipitation region was extrapolated towards faster or slower cooling rates on the basis of microstructural and hardness results for conditions that were measurable by DSC technique. A more detailed microstructural analysis is necessary to understand more thoroughly which types of precipitates are formed and where they are nucleated for each of the different reactions.

Conclusions:

Two commercial 7xxx series alloys with different solute contents and different quench sensitivity behaviour have been studied. The exothermal heat flow from quench-induced precipitation during cooling in both alloys was investigated by means of DSC measurements.

It can be found from the evaluated DSC curves of alloy AA7150 that there are at least three quench-induced reactions while only two such clearly distinguishable reactions have been found in alloy AA7020. Due to the different alloying content, the released enthalpy at a given cooling rate in alloy AA7150 is much more than that in alloy AA7020. Nevertheless the overall ΔH_c curves for both alloys show a decreasing trend with increasing cooling rate.

The critical cooling rates (CCR) for alloys AA7150 and AA7020 were determined by extrapolation of a fitted curve to be 300 K/s and 3 K/s, respectively. The CCR for both alloys can also be obtained using hardness testing after artificial ageing, which results in the CCR apparently being 60 K/s and 3 K/s for alloys AA7150 and AA7020, respectively. Here it is assumed that all the remaining solute after the cooling process contributes to hardening after ageing. Thus, the hardness curves increase with increasing cooling rate as rapid cooling will preserve solute in solution for the subsequent ageing process so that the alloy has the potential to reach its maximum strength after ageing. Therefore there is no further increase in hardness if samples are cooled faster than the critical cooling rate. It is evident that CCR for AA7150 from hardness testing occurs at much lower quenching rates than the CCR that was obtained by DSC with extrapolation. Possible explanations are, (i) that the hardness value is not sufficiently sensitive to reflect small changes in the volume fraction of precipitates or (ii) that the extrapolation causes some uncertainty.

Based on corresponding microstructural analysis, only equilibrium $MgZn_2$ and S-phase particle precipitation was observed in alloy AA7150 by means of scanning electron microscopy. The $MgZn_2$ (η -phase) particles are clearly present at cooling rates of 5-10 K/s or less, while the S-phase appears to be present only at cooling rates of less than 1 K/s. In alloy AA7020, mainly Mg_2Si and $MgZn_2$ (η -phase) particles were observed. Further work is required to identify the three precipitation reactions more precisely in both alloys.

Continuous cooling precipitation (CCP) diagrams were developed for both alloys AA7150 and AA7020 to describe the influence of the cooling rate on the precipitation behaviour.

Acknowledgement

The authors thank the Aluminium Corporation of China Ltd (Chalco) for supporting this work financially and providing AA7150 materials as part of the Australia-China International Centre for Light Alloy Research (ICLAR). The ARC Centre of Excellence for Design in Light Metals and the Monash Centre for Electron Microscopy (MCEM) are also acknowledged.

References

- [1] I.J. Polmear, *Light Alloys: Metallurgy of the Light Metals*, 4th ed., Melbourne, 2006.
- [2] R.N. Lumley, I.J. Polmear, A.J. Morton, *Materials Science Forum*, 426-432 (2003) 303-308.
- [3] I.J. Polmear, *Materials Forum*, 28 (2004) 1-13.
- [4] A. Deschamps, M. Niewczas, F. Bley, Y. Bréchet, J.D. Embury, L.L. Sinq, F. Livet, J.P. Simon, *Philosophical Magazine A*, 79 (1998) 2485-2504.
- [5] A. Deschamps, Y. Bréchet, *Scripta Materialia*, 39 (1998) 1517-1522.
- [6] A. Deschamps, Y. Bréchet, *Acta Materialia*, 47 (1999) 281-292.
- [7] S. Liu, X. Zhang, M. Chen, J. You, X. Zhang, *Transactions of Nonferrous Metals Society of China*, 17 (2007) 787-792.
- [8] M. Conserva, P. Fiorini, *Metallurgical Transactions*, 4 (1972) 857-862.
- [9] W.L. Fink, L.A. Willey, *Transactions AIME*, 175 (1947) 414-427.
- [10] J.W. Evancho, J.T. Staley, *Metallurgical Transactions*, 5 (1974) 43-47.
- [11] J. Liu, *Materials Science Forum*, (2006) 519-521.
- [12] P. Archambault, D. Godard, *Scripta Materialia*, 42 (2000) 675-680.
- [13] O. Kessler, R.v. Bargaen, F. Hoffmann, H.-W. Zoch, *Materials Science Forum*, 519-521 (2006) 1467-1472.
- [14] B. Milkereit, O. Kessler, C. Schick, *Thermochimica Acta*, 492 (2009) 73-78.
- [15] B. Milkereit, N. Wanderka, C. Schick, O. Kessler, *Materials Science and Engineering A*, 550 (2012) 87-96.
- [16] D. Zohrabyan, B. Milkereit, O. Kessler, C. Schick, *Thermochimica Acta*, 529 (2012) 51-58.
- [17] G.W.H. Höhne, W.F. Hemminger, H.-J. Flammersheim, *Differential Scanning Calorimetry*, 2nd ed., Braunschweig, 2003.
- [18] B. Milkereit, M. Beck, M. Reich, O. Kessler, C. Schick, *Thermochimica Acta*, 522 (2011) 86-95.
- [19] D.K. Xu, P.A. Rometsch, N. Birbilis, *Materials Science and Engineering A*, 534 (2012) 234-243.

**[BM4] Schumacher P, Pogatscher S, Starink MJ,
Schick C, Mohles V, Milkereit B:
*Quench-induced precipitates in Al–Si alloys: Calorimetric
determination of solute content and characterisation of
microstructure.*
Thermochimica Acta 602 (2015): 63–73.**

Benjamin's contributions: I supervised the project, managed the international collaboration, designed the experiments, participated in the discussion of the data and revised the manuscript.

Quench-induced precipitates in Al-Si alloys: Calorimetric determination of solute content and characterisation of microstructure

Philipp Schumacher^{a,b}, Stefan Pogatscher^c, Marco J Starink^d, Christoph Schick^b,
Volker Mohles^e and Benjamin Milkereit^{a,b,d,*}

^a University of Rostock

Faculty of Mechanical Engineering and Marine Technology

Chair of Materials Science

Albert-Einstein-Str. 2, 18051 Rostock, Germany

(philipp.schumacher@uni-rostock.de, benjamin.milkereit@uni-rostock.de)

10

^b University of Rostock

Institute of Physics

Polymer Physics Group

Wismarsche Str. 43-45, 18051 Rostock, Germany

(christoph.schick@uni-rostock.de)

^c ETH Zurich

Department of Materials

Laboratory of Metal Physics and Technology

20 Vladimir-Prelog-Weg 4, 8093 Zurich, Switzerland

(stefan.pogatscher@mat.ethz.ch)

^d University of Southampton

Engineering and the Environment

Highfield, Southampton SO17 1BJ, United Kingdom

(m.j.starink@soton.ac.uk)

^e RWTH Aachen University

Institute of Physical Metallurgy and Metal Physics

30 Kopernikusstr. 14, 52056 Aachen, Germany

(mohles@imm.rwth-aachen.de)

* Corresponding author:

Benjamin Milkereit

University of Rostock

Faculty of Mechanical Engineering and Marine Technology

Chair of Materials Science

Albert Einstein-Str. 2, 18051 Rostock, Germany

E-mail address: benjamin.milkereit@uni-rostock.de

40 Tel.: +49 (0) 381 498 9486

Abstract

The present study introduces an experimental approach to investigate mechanical properties of well-defined non-equilibrium states of Al-Si alloys during cooling from solution annealing. The precipitation behaviour of binary Al-Si alloys during the cooling process has been investigated in a wide cooling rate range (2 K/s-0.0001 K/s) with differential scanning calorimetry (DSC). To access the low cooling rate range close to equilibrium an indirect DSC measurement method is introduced. Based on the enthalpy change measured by DSC a physically-based model for the calculation of remaining solute Si amount as function of temperature and cooling rate is presented. Microstructural analyses via light optical microscopy, scanning electron microscopy, atom probe tomography and X-ray diffraction have been performed to evaluate the introduced model and for information on cooling rate dependent precipitate formation. It was found that quench-induced particles of different morphology are formed during cooling. Thermomechanical analyses on clearly distinct undercooled Al-Si states show that flow stress during cooling is dependent on temperature as well as cooling rate. The mechanical behaviour is therefore influenced by solute Si content and quench-induced precipitates.

Keywords

Al-Si alloys, DSC, Precipitation enthalpy, Modelling, Microstructure control, Mechanical properties testing

1. Introduction

Age hardening is an important heat treatment to strengthen heat treatable aluminium alloys and comprises three steps - solution annealing, quenching and ageing [1]. The quenching rate is an important parameter within this treatment. If solution temperature and cooling conditions are chosen correctly, all solute elements from which strengthening particles can be precipitated during subsequent ageing are retained in the supersaturated solution. Slower cooling on the other hand may induce precipitation of coarse second-phase particles. A lower amount of solute will thus be available for precipitation of the hardening phases, resulting in a lower strength after peak ageing. Excessive cooling rates should also be avoided as they cause high thermal gradients in the treated components, which might induce residual stresses and distortion. The quenching process can therefore be considered as a critical step of the age hardening process.

Prediction of the effect of cooling conditions on residual stresses and distortion can be established by numerical heat treatment simulations using finite element methods (FEM, e.g. [2]). However, such simulations require profound knowledge about the materials' flow characteristics in dependence on temperatures, strain rates and microstructures. While empirical flow stress relations that are often implemented in FEM codes give remarkably good description of measured flow curves of defined material conditions, they are in many cases unsuitable to describe the mechanical behaviour under process-like conditions. In particular, flow behaviour is to a great extent influenced by the cooling rate as microstructural changes, including microchemical composition of the matrix

and precipitation state, can occur during the cooling step. Hence, the usual description of flow stress with macroscopic state variables (strain and overall chemical composition) is unsatisfactory in certain cases [3]. Approaches to model flow curves with more appropriate state variables have therefore been developed in the past (e.g. [4–6]). While stress-strain curves of pure aluminium and alloys with very low solute content can already be predicted over a wide range of temperatures and strain rates [7,8], influences of additional microstructural elements such as solutes and second-phase particles need further investigation.

80 It is known that flow stress of commercial age-hardenable aluminium alloys increase not only with decreasing temperature but also with increasing cooling rate, and in some works solid solution strengthening was considered to be responsible for this material behaviour (e.g. [9]). Hence, the precipitation behaviour during cooling is of great importance as it provides knowledge on the loss of solutes and on microstructural changes. The effect of single elements on solute strengthening in aluminium alloys was experimentally studied in several works (e.g. [10–14]). However, contribution on solid solution strengthening during the cooling process has not been subject to investigations so far. Furthermore, the role of quench-induced precipitates on the mechanical behaviour remains uncertain.

We aim to improve existing plasticity models with respect to microstructure evolution during quenching in the future. Therefore, reliable experimental data of well-defined material states is needed to investigate active
90 strengthening mechanisms, which have to be modelled. While strength of commercial alloys originates from a combined effect of several factors such as solid solution, grain size, aging precipitates, dispersoids or primary particles, binary alloys of high purity allow the isolation of several strength contributions [10]. Thus, binary alloys of the Al-Si system are analysed in a first step here. Al-Si is an ideal model system for the investigation of precipitation kinetics, since exothermic reactions are always due to precipitation of Si [15] and solubility of Al in the Si phase is low [16,17]. Furthermore, knowledge on influence of single alloying elements on mechanical properties is considered to be important in order to set up a new plasticity model for commercial aluminium alloys.

The present paper introduces an approach to produce well-defined microstructural states that allow a detailed study of the effect of Si solutes and quench-induced Si precipitates on mechanical properties. To control the
100 microstructure, i.e. the microchemical composition of the matrix and the corresponding precipitation state, differential scanning calorimetry (DSC) measurements are of great importance. It was shown in [18,19] that the precipitation heat (enthalpy change) is directly proportional to the volume fraction of precipitated particles, which allows in principle a calculation of remaining solute amount in dependence of cooling rate and temperature [20]. One main objective of the present work is a precise determination of formation enthalpies to provide detailed input for a physically-based model. Therefore, precipitation kinetics of low-Si binary Al-Si alloys during cooling from solution annealing are investigated in a wide cooling rate range with advanced DSC techniques (e.g. [18,21–28]). Direct DSC cooling experiments are limited to a certain slow cooling rate due to the relation between sample mass, cooling rate and heat flow. At a certain rate the signal-to-noise ratio of any DSC device will become too

small to allow signal evaluation. However, the knowledge of near equilibrium precipitation processes is the basis for the setup of any model. To access the cooling rate range close to equilibrium conditions a new indirect DSC reheating technique is introduced, which allows the quantitative evaluation of the precipitation enthalpy. Based on the enthalpy change measured by DSC, a model for the calculation of remaining solute Si amount and precipitation volume fraction as functions of temperature and cooling rate is presented, adapting an improved model for diffusion controlled reactions [29]. The microstructures of the defined states are analysed to evaluate the introduced model. Thereby, remaining solute amount and quench-induced precipitates are characterised with various methods: light optical and scanning electron microscopy (LOM / SEM), X-ray diffraction (XRD) and atom probe tomography (APT).

The mechanical behaviour of non-equilibrium microstructures is investigated by thermomechanical analysis (TMA) using a quenching and deformation dilatometer [9]. It is shown that the experimental methods can be applied for a systematic study on the correlation between microstructural states of undercooled aluminium alloys and their mechanical behaviour. With the presented experimental approach the effect of Si solutes and quench-induced Si precipitates on mechanical properties can be analysed in future, which is an essential requirement for the progression of plasticity models.

2. Experimental

2.1. Materials

Two binary Al-Si alloys of high-purity grades were studied in this work. Their chemical compositions obtained by optical emission spectroscopy (OES) analyses are shown in Table 1.

Table 1. Chemical compositions of investigated alloys obtained by optical emission spectroscopy (OES) analysis.

mass fractions	Si (ma.% / at.%)	Mg (ppm)	Fe (ppm)	Cu (ppm)	Mn (ppm)	Cr (ppm)	Zn (ppm)	Ti (ppm)
Al-0.26Si	0.26 / 0.25	< 1	< 5	4	< 3	< 3	-	20
Al-0.72Si	0.72 / 0.69	< 1	< 5	< 1	< 3	< 3	14	11

Direct chill (DC) cast ingots were made from aluminium of 99.999 % purity and high-purity alloying elements. The DC cast ingots were homogenised (12 hours at 500 °C) to obtain a uniform distribution of alloying element atoms and were subsequently hot-rolled to strips of 40 mm thickness. The hot-rolled strips were solution annealed for 24 hours at 450 °C followed by water quenching. Finally, the strips were cold-rolled to sheets of 16 mm thickness. Sampling for all experimental investigations was carried out perpendicular to the rolling direction. In the as-rolled condition both alloys had a similar grain structure with coarse, elongated grains of high aspect ratios. All subsequent investigations included a solution treatment, which resulted in a recrystallized structure with grain sizes of about 450 µm in both alloys.

2.2. Methods

A very wide range of cooling rates must be examined in order to fully understand the precipitation behaviour during cooling from solution annealing [18,22,24,26]. Three different types of DSC devices were used: Perkin-Elmer Pyris Diamond DSC (2 to 0.3 K/s), Setaram 121 DSC (0.1 to 0.01 K/s) and Setaram C600 DSC (0.005 to 0.001 K/s). The methods employed for direct DSC cooling experiments and evaluation for the fastest and intermediate cooling rate ranges are described in [22]. While six measurements with identical parameters were performed in the Pyris Diamond DSC and at least three runs under same conditions were executed in the Setaram 121 DSC, only one or two experiments for each cooling rate were carried out in the C600 DSC due to the extensive test durations. High purity aluminium (99.9995 %) was taken as reference and data evaluation was done on excess specific heat capacity curves [22]. In-situ solution annealing was performed at 540 °C for 20 min except for measurements in the C600 DSC device, which required 120 min to reach thermal equilibrium within the measuring system due to the relatively large heat capacity of sample and measuring block. A well-stabilised temperature of the system at solution annealing is needed for high quality specific heat capacity measurements.

Note that the different solution treatment times did not result in different grain sizes.

The study of slow cooling rates provides the opportunity to follow near equilibrium phase changes. This is an essential requirement for a physical approach to describe the solute state during cooling. With reference to previous work (e.g. [18,22,28]), the accessible cooling rate could be extended to very low values using the Setaram C600 DSC device with the following certain boundary conditions. Thus, cooling rates comprising four orders of magnitude could be analysed by direct cooling experiments. The Setaram C600 calorimeter is a heat flux DSC with a cylinder-type measuring system and is equipped with a high precision 3D Calvet sensor, which totally surrounds sample and reference cell. This setup provides that nearly all heat evolved is measured. Measurements comprising a temperature range from ambient temperature up to 600 °C can be realised. A closed cooling circuit was implemented using a refrigerated circulator Julabo F34-ED. Optimal results were achieved by using cylindrical samples with radiused edges. The samples had dimensions of 13.8 mm in diameter and 60.5 mm in length, which results in a sample mass of approximately 24,000 mg. The samples as well as the references were covered by conventional aluminium foil (about 110 mg) to minimize radiation losses caused by surface reactions of the samples.

A detailed analyses of alloys with very slow precipitation kinetics is hard to achieve with direct DSC cooling experiments, because an adequate statistical basis is very difficult to achieve due to extensive test durations. In order to determine the saturation value of enthalpy change for near equilibrium phase changes in such alloys, an expansion of cooling rate range to even lower rates than 0.001 K/s is necessary. This aim can hardly be established by any direct DSC cooling experiments with state of the art devices due to a low signal-to-noise ratio. Therefore, another approach based on the differential reheating method [24] was undertaken to deal with the mentioned difficulties. With implementation of the reheating method information on enthalpy changes caused by precipitation during cooling can be derived from DSC reheating experiments. Even though DSC heating curves

of aluminium alloys are often difficult to interpret in terms of quality, quantitative information can easily be obtained, provided the baseline is determined accurately. The reheating method takes as a basis that the total enthalpy change in a closed thermodynamic cycle equals zero under the premise that starting and end point are in equilibrium. The schematic temperature-time profile, indicating the enthalpy changes for the reheating method is shown in Fig. 1. For the given problem the complete solid solution at the end of the solution annealing process can be defined as such an equilibrium state with a precipitation enthalpy value of $H_0 = 0$. During slow cooling from solution annealing exothermic precipitation reactions take place causing a negative enthalpy change ΔH_{SC} . Provided that the same equilibrium state H_0 as before is achieved after a reheating cycle following the cooling process, the sum of enthalpy changes of the cooling step ΔH_{SC} and the reheating step ΔH_{RH} must be zero ($\Delta H_{SC} + \Delta H_{RH} = 0$).

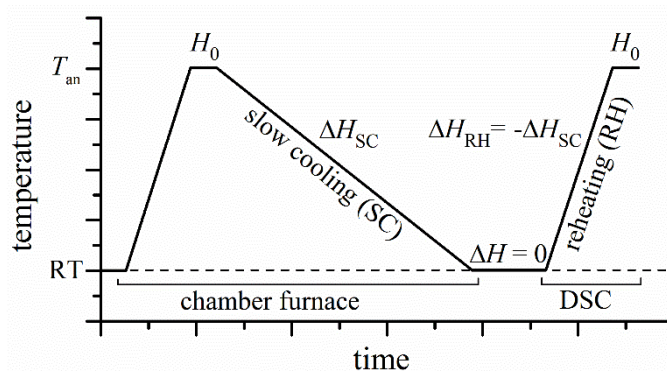


Fig. 1. Temperature-time profile for indirect determination of specific precipitation heat values during cooling with very slow rates by a DSC reheating scan.

For a sample cooled with a specific rate, a defined sequence of exothermic and endothermic reactions is detectable during the reheating cycle. Equilibrium state is achieved when all reactions are completed before the annealing temperature T_{an} is reached, i.e. the temperature exceeds the solvus temperature of the applied scanning rate. If this is the case all precipitated particles which have been formed during previous cooling and during the reheating step, respectively, are resolved and a complete solid solution with an enthalpy value H_0 is restored. On condition that equilibrium state is achieved after reheating, ΔH_{SC} can be calculated directly from the DSC curves of the heating step. For an optimal control and evaluation of the corresponding baseline, it is recommended that sample temperature exceeds the corresponding solvus temperature for some 10 K. In that case, baseline bending correction can be performed [22]. The essential benefit of this reheating method is the possibility to study characteristic physical properties for cooling rates unattainable with direct DSC measurements. Another significant advantage is the reduced duration of experiments directly performed in DSC devices because the first thermal cycle comprising the cooling process can be executed simultaneously on various samples in an appropriate furnace. In this work, solution annealing (540 °C, 20 min) and slow cooling with nearly constant rate was realised in a chamber furnace Carbolite CWF 11/13 equipped with an Invensys Eurotherm nanodac™ recorder/controller for cascade control. Prior to heat treatment samples were sealed in quartz glass under vacuum

200 in order to prevent surface reactions and thus changes in chemical composition. In addition to near equilibrium slow cooling rates, the as quenched condition after cooling in water was analysed as a reference and control measurement. After the cooling process samples were stored at -82 °C to suppress further potential precipitation reactions before they were reheated in the Setaram C600 DSC to a temperature of 570 °C. A heating rate of 0.003 K/s was chosen for those experiments as this is an optimal rate for this DSC device and also ensures the observance of the mentioned requirement for this method that is the achievement of a complete solid solution before the end of the heating step (this applies to all cooling rates down to 0.0001 K/s investigated here). At least two experiments were carried out for each material condition.

With knowledge of precipitate formation enthalpies derived from DSC measurements a model for the calculation of the solute Si content as a function of cooling rate and temperature was developed (presented in section 3.3).

210 For evaluation of this model and for the characterisation of quench-induced precipitates, metallographic investigations were carried out. Selected cooling states were investigated by LOM with a Leica DMI5000 M and SEM performed in a Zeiss Supra 25 microscope operated at 10 kV. Samples were prepared by standard grinding and polishing methods with water-free, ethanol-based lubricants. For the final polishing step an oxide polishing suspension was used. From microscopic images the volume fraction of precipitated particles was determined with stereological methods using computational image analysis [30]. For each investigated cooling condition, fifty images (analysed area per condition $> 9.5 \times 10^6 \mu\text{m}^2$) were evaluated to ensure statistical validation. It is well established in literature that only the diamond cubic Si-rich phase ($a = 0.542 \text{ nm}$) is precipitated from Al-Si supersaturated solid solution (e.g. [1]). As only coarse particles of equilibrium phase seem to form during cooling the amount of remaining solute can be calculated from metallographic results and taken for comparison with the
220 solute content derived from DSC data. For direct determination of solute contents, APT measurements were carried out. A standard two-step method [31] was used to prepare needle-shaped specimens ($0.3 \times 0.3 \text{ mm}^2$). After electropolishing the small rods with 10 % perchloric acid and 90 % methanol solution, 2 % perchloric acid in butoxyethanol was used as the second electrolyte. Prepared needle tips have been checked to only represent the Al-rich matrix and not Si precipitates via SEM. APT was performed on a LEAPTM 4000 X HR atom probe at a temperature of 30 K with a pulse fraction of 20 %, a pulse rate of 200 kHz and an evaporation rate of 0.5 % under ultra-high vacuum ($< 10^{-10} \text{ mbar}$). Three successful runs were executed for each analysed condition. For reconstruction procedure and chemical analysis the software package IVAS 3.6.6TM from Imago Scientific Instruments Corporation (Madison, WI, USA) was used. Only regions in the analysed volume free from crystallographic pole and zone lines were considered for APT analysis. XRD measurements were performed with
230 a Bruker D8 DISCOVER diffractometer (integral measurements on samples of mm-size) using Cu-K α radiation in order to confirm the crystal structures of quench-induced precipitates after cooling with different rates.

The effect of temperature and cooling conditions on flow characteristics of Al-Si was studied by TMA. The experiments were performed in accordance to Ref. [9] using a quenching and deformation dilatometer type Bähr DIL 805 A/D. At least three experiments with identical parameters were performed. True stress and

logarithmic strain were determined from measured force-displacement curves. Thereby, geometry changes due to thermal expansion were taken into account for tests at elevated temperatures. Samples were solution annealed (540 °C, 20 min), cooled with various rates to different temperatures and compressed immediately after reaching the desired temperature. A strain rate of 0.1 s^{-1} was chosen for these tests. As the precipitation behaviour is investigated dependent on cooling rate and temperature, microstructure of the samples can be taken into account for a discussion of the flow behaviour.

3. Results and discussion

3.1. DSC cooling experiments

Fig. 2 shows characteristic excess specific heat capacity curves for the investigated Al-Si alloys during cooling after solution annealing. The curves are shifted vertically and arranged in order of increasing cooling rate. DSC devices used for different cooling rate ranges are displayed. Exothermic precipitation reactions are shown by deviations exceeding the zero level, which is given by a dashed line for each curve. Note the various scaling of the excess specific heat capacity axis in Fig. 2a and Fig. 2b. It can be seen that precipitation in the investigated alloys occurs in different cooling rate ranges. Furthermore, peak temperatures and maximum excess specific heat capacities differ significantly between both alloys.

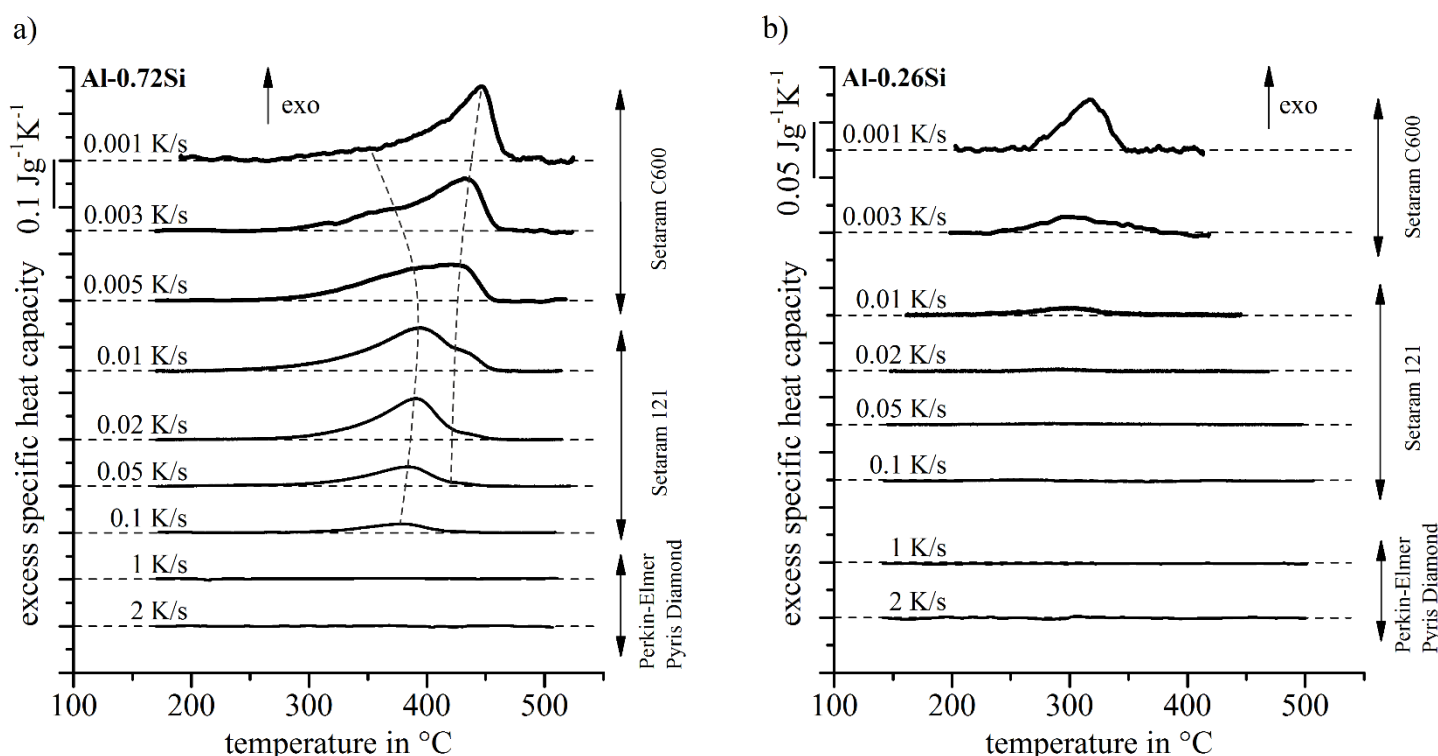


Fig. 2. DSC cooling curves of alloys Al-0.72Si (a) and Al-0.26Si (b) after solution annealing in a cooling rate range from 0.001 K/s to 2 K/s.

For both alloys, precipitation reactions decrease with increasing cooling rate. This can be explained by the suppression of diffusion processes. As only diamond cubic Si-rich phase ($a = 0.542 \text{ nm}$) is likely to occur [1,15],

the occurrence of two reaction peaks for alloy Al-0.72Si within the analysed cooling rate range may seem surprising. For the alloy containing a lower mass fraction of Si only one reaction could be detected in the same cooling rate range. For the slowest investigated cooling rate, precipitation reactions in Al-0.72Si start at about 475 °C, which is very close to the solvus temperature regarding the simple eutectic phase diagram [17] of this binary alloy system. A high temperature precipitation peak is dominating at this cooling condition, but is
260 suppressed significantly in its intensity and shifted towards lower temperatures as the cooling rate increases. While the high temperature reaction is suppressed, another peak at lower temperatures rises to a maximum and shifts to higher temperatures. Such precipitation behaviour is also shown by commercial alloys of different alloying systems (e.g. Al-Mg-Si [18], Al-Zn-Mg(-Cu) [28]).

Further increase in cooling rate results in a decrease of this low temperature peak area as well. Simultaneously, the peak of these low temperature reactions changes its shifting direction and shifts to lower temperatures as observed for commercial alloys before. In [18] “a lower critical cooling rate (LCCR) is defined for the highest cooling rate at which practically complete precipitation takes place. Additionally, an upper critical cooling rate (UCCR) is defined for the slowest cooling rate at which completion of supersaturation in solid solution is reached during cooling.” In this work, the UCCR of Al-0.72Si was found to be about 1 K/s. In Al-0.26Si only one peak
270 was observed even at relatively slow cooling rates. This reaction starts approximately 50 K below the solvus temperature presented in [17]. As a consequence, it seems probable that precipitation start may be shifted to higher temperatures for even slower cooling. The UCCR of Al-0.26Si was found to be only about 0.02 K/s.

For Al-0.26Si, reactions even in the faster (with respect to alloy kinetics) cooling rate range could therefore only be detected using relatively slow but high sensitive Calvet-type DSC devices. For cooling rates realisable with a common Perkin-Elmer Pyris Diamond DSC [22] no reactions were measurable. The great potential of Calvet-type DSC devices is demonstrated when even slower cooling curves of Al-0.72Si than recorded with the Setaram 121 DSC are investigated. While the cooling curve for 0.01 K/s already shows indications that at least two reaction peaks overlap in the temperature range around 400 °C, this precipitation behaviour can only be proven with investigation of slower cooling rates. With the extension of the cooling rate range due to high precision
280 Calvet detectors the existence of a high and a low temperature reaction peak is revealed.

For alloy Al-0.26Si, cooling with a slow rate of 0.01 K/s to RT reveals reactions causing an enthalpy change $|\Delta H_{RT}|$ of only about 0.58 J/g. Since the enthalpy characterises the heat content of a system for adiabatic reactions, $|\Delta H_{RT}|$ equals the measured specific precipitation heat (integral of excess specific heat capacity). This amount of enthalpy change is close to the detection limit for precipitation reactions of 0.1 J/g for the used DSC devices as defined in [22]. Therefore, a further decrease of cooling rate is necessary to distinguish the precipitation peak with certainty from the signals noise level. Only if measurements with the Setaram C600 DSC are taken into account the detected DSC peak can certainly be attributed to precipitation reactions.

3.2. DSC reheating experiments

In order to establish the saturation level of enthalpy change for near equilibrium phase changes DSC reheating experiments after cooling with rates down to 0.0001 K/s (60 days cooling from solution annealing) were carried out for both alloys. Fig. 3 shows DSC reheating curves of alloy Al-0.72Si in different initial conditions. The precipitation and dissolution sequence during the heating cycle is heavily dependent on the preceded cooling condition.

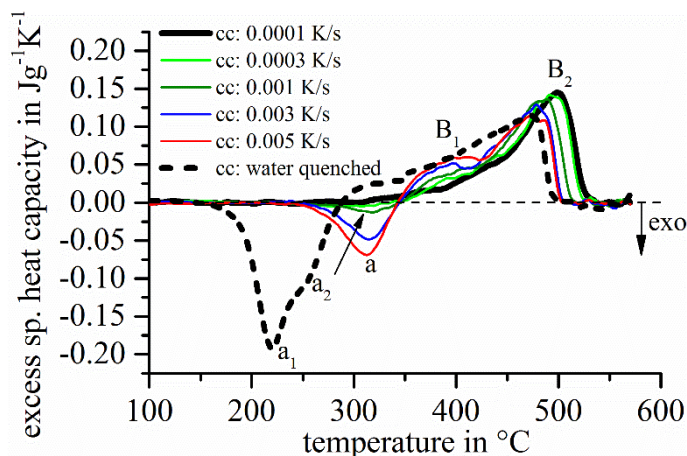


Fig. 3. DSC reheating curves (scan rate: 0.003 K/s) of alloy Al-0.72Si in different cooling conditions (cc).

In general, the sequence shown in Fig. 3 comprises exothermic precipitation reactions and endothermic reactions at higher temperature, which can be attributed to the dissolution of particles. Exothermic precipitation reactions causing two overlapping DSC peaks (a₁ and a₂) can be observed, when a water quenched sample is reheated. For samples cooled at much lower rates the exothermic peaks are suppressed significantly and also shifted towards higher temperatures. Only one main exothermic peak (a) remains, but one has to be aware of possible peak overlapping which might occur. This main peak shifts to higher temperatures as the preceding cooling rate decreases. The lower the cooling rate in the previous heat treatment was chosen, the more alloying elements are already precipitated during the cooling step. As a consequence, supersaturation of the solid solution is reduced and less Si can be precipitated upon reheating. Hence, the intensity of the exothermic peak (a) decreases with a reduction of cooling rate. Peak (a) disappears when supersaturation after cooling becomes sufficiently small for re-precipitation upon heating. The criterion for the completion of precipitation during cooling should be to maximise the integral of dissolution during heating. In that case all alloying elements insoluble in equilibrium condition at room temperature have been precipitated during previous cooling. In practise this should be quite close to the case when peak (a) disappears completely. Therefore, from the DSC reheating results a LCCR of about 0.0001 K/s can be estimated for Al-0.72Si.

Regardless of whether the previous cooling occurred fast or slow endothermic dissolution peaks (B₁ and B₂) are present at higher temperatures. These peaks are shifted to higher temperatures with decreasing cooling rate. This indicates that particles formed at low cooling rates dissolve slower than those precipitated at faster cooling

conditions. However, the DSC reheating curves show that all dissolution reactions are completed before 570 °C for all initial conditions and thus a complete solid solution is reached. As a result, the enthalpy change ΔH_{SC} evoked by the cooling step can be calculated from the DSC reheating curves.

In Fig. 4 the enthalpy change ΔH of the different conditions in Fig. 3 during reheating with a scan rate of 0.003 K/s is plotted. At high temperatures the equilibrium condition H_0 is reached and this enthalpy level is defined to be zero. As no precipitation reactions take place during water quenching the enthalpy level should be equal in both initial and reheated condition. When the water quenched condition is reheated the enthalpy evolution indeed starts at the zero level. The precipitation reactions that occur on heating lead to a decrease of enthalpy first. At higher temperatures dissolution of precipitated particles causes endothermic reactions. This results in an increase of enthalpy until the equilibrium level is reached again. Equilibrium level is also achieved after heating of all other initial conditions to 570 °C. However, in these states quench-induced precipitates exist and the initial enthalpy state is therefore negative compared to equilibrium and also differs in dependence of the cooling rate. The initial value of enthalpy change therefore equals ΔH_{SC} .

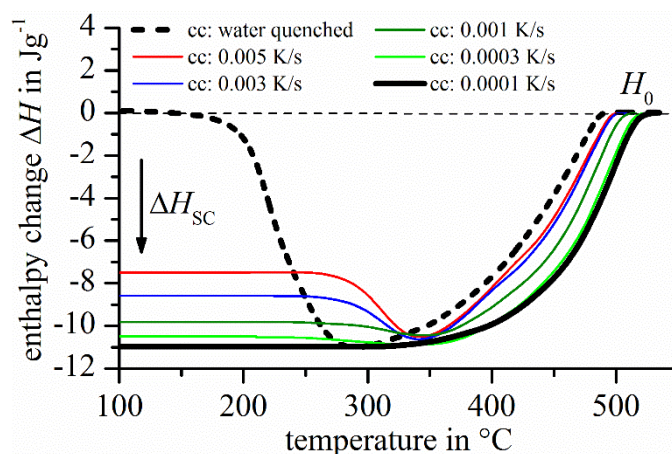


Fig. 4. Change of enthalpy state during reheating (scan rate: 0.003 K/s) of Al-0.72Si in different cooling conditions (cc).

Fig. 5 shows the enthalpy change $|\Delta H_{RT}|$, after cooling to RT from solution annealing as function of cooling rate.

Plotted are both data from direct DSC cooling experiments and values derived with the reheating method for the two investigated alloys. The error of 10 % results from the uncertainty in the determination of the peak-area from DSC data. The data obtained from both methods are in good agreement verifying the feasibility of the reheating method. With DSC reheating experiments the examinable cooling rate range could be extended covering six orders of magnitude between 2 K/s and 0.0001 K/s.

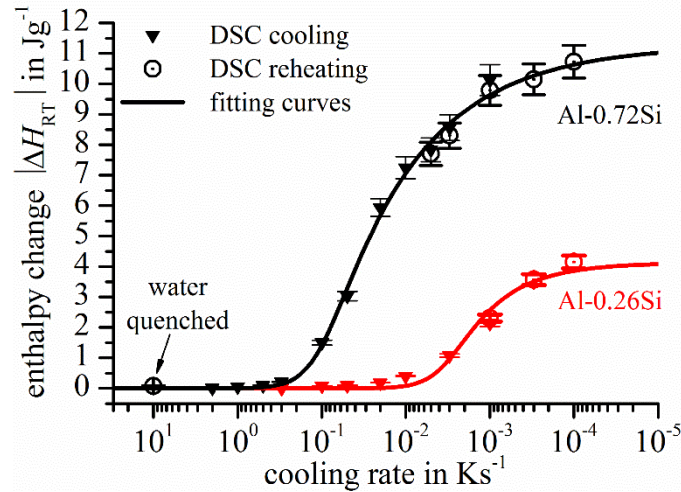


Fig. 5. Enthalpy change values $|\Delta H_{RT}|$ upon precipitation in Al-Si alloys after cooling to room temperature obtained with direct DSC cooling experiments or DSC reheating experiments and fitting results with the model presented in Eq. (3).

3.3. Model for calculation of solute content and precipitated volume fraction

For the control of the microstructure by heat treatment, i.e. the adjustment of well-defined microstructure conditions, a consistent physical description of the volume fraction of precipitates but also of remaining amount of solute in dependence of cooling rate and temperature is needed. To this end we adapt a physically-based model described in [29], which is based on models for diffusion controlled reactions in [32,33]. A prediction of the remaining solute concentration after the quench C_{AQ} is given as a function of quench factor [29]:

$$\frac{C_{AQ} - C_{\min(T)}}{C_{\max(T)} - C_{\min(T)}} = \left[\frac{(-k_1 Q)^n}{\eta_i} + 1 \right]^{-\eta_i} \quad (1)$$

where $C_{\min(T)}$ is the minimal possible and $C_{\max(T)}$ the maximal possible concentration of solutes at a certain temperature. Q represents the quench factor, while k_1 , n and η_i are model parameters. The parameter n is related to the type of nucleation mechanism active [33,34]. Q is defined as:

$$Q = \int_{t_0}^{t_f} \frac{dt}{C_t} \quad (2)$$

C_t is dependent on alloy and temperature [29]. If a constant cooling rate is employed Q is proportional to quenching duration and due to the linear relationship between quenching duration and cooling rate β , Q is also linearly proportional to $1/\beta$.

Next we replace C_{AQ} from Eq. (1) with the enthalpy change during cooling to room temperature $|\Delta H_{RT}|$. The value $C_{\min(T)}$ is replaced by the saturation level of enthalpy change at room temperature $|\Delta H_{RT_{sat}}|$, which is reached in cases where cooling is slower than the LCCR. $C_{\max(T)}$ is replaced by the minimum change in enthalpy, which is obviously zero as far as cooling is performed overcritically fast. As β is defined to be positive in this work the term in curved brackets becomes a positive sign as well. Rearranging the terms gives the fitting model:

$$|\Delta H_{RT}| = |\Delta H_{RT_{sat}}| - |\Delta H_{RT_{sat}}| \left[\frac{\left(\frac{k_M}{\beta}\right)^n}{\eta_i} + 1 \right]^{-\eta_i} \quad (3)$$

Herein, k_M is a parameter comprising k_1 and C_i , i.e. it is alloy dependent. Thus to apply this model, we need to either fit or otherwise obtain k_M , n and η_i . It has been shown [33,35,36] that if nucleation is completed early on in the reaction n should be 1.5. This would apply for heterogeneous nucleation e.g. at dispersoids or coarse intermetallic phases when the number of such sites is limited [19,37]. However, those phases are not present in the pure binary alloys investigated in this paper, and hence, n should be 2.5, which is valid for continuous nucleation during the course of the reaction [19,37]. The parameter η_i is the impingement factor and its values found in literature typically range between about 1 and 2.2 when a single process occurs [19,32,33]. However, in the present case clearly multiple processes in a wide range of temperatures are involved, and we will here fit η_i . Therefore, the values shown in Table 2 were calculated with the adapted fitting function and resultant fitting curves are shown in Fig. 5. The fit is excellent.

Table 2. Results from fitting measured DSC data to equation (3).

	$ \Delta H_{RT_{sat}} $	k_M	η_i	n
Al-0.26Si	4.1 J/g	0.002 K/s	0.315	2.5
Al-0.72Si	11.3 J/g	0.053 K/s	0.164	2.5

Saturation value $|\Delta H_{RT_{sat}}|$ should be proportional to the Si content. Due to the limited DSC data at very low cooling rates for Al-0.26Si, $|\Delta H_{RT_{sat}}|$ for this alloy was estimated from value $|\Delta H_{RT_{sat}}| = 11.3$ J/g for Al-0.72Si using the Si content proportion of both alloys. The enthalpy change of precipitation per mole Si from the Al-rich matrix was experimentally studied in [15,38] and was derived to be about 54 kJ mol⁻¹. Taking this value into account, theoretically $|\Delta H_{RT_{sat}}| \approx 13.2$ J/g for Al-0.72Si and $|\Delta H_{RT_{sat}}| \approx 4.8$ J/g for Al-0.26Si result, respectively. Therefore, within experimental error the theoretical values agree well with the data presented in this work. Accuracy of the literature values is mainly determined by the value of enthalpy change of precipitation per mole Si. Interfacial energies of precipitates formed may influence the results. Furthermore, small deviations can also be ascribed to the limited accuracy of DSC data (e.g. peak area determination) and to assumptions made in the adapted quench factor model.

As the enthalpy change is in direct proportion to the mass and volume fraction of precipitated particles [18,19], the following equation can be applied to calculate the solute content at arbitrary temperatures T_c :

$$\text{solute content}_{T_c} = (c_{el_{total}} - c_{el_{sol(RT)}}) \cdot \left(1 - \frac{|\Delta H_{T_c}(\beta)|}{|\Delta H_{RT_{sat}}|} \right) + c_{el_{sol(RT)}} \quad (4)$$

Parameter $c_{el_{total}}$ corresponds to the overall content of a specific alloying element in the material, while the soluble content of this element at RT is taken into account with value $c_{el_{sol(RT)}}$. $\Delta H_{RT_{sat}}$ again is the saturation level of

380 enthalpy change after cooling to room temperature. Value $\Delta H_{T_c}(\beta)$ represents the enthalpy change at temperature T_c to which the alloy has already been cooled with cooling rate β . $\Delta H_{T_c}(\beta)$ can thus be directly derived from integration of DSC curves taking the solution annealing temperature T_{an} as upper bound of integration:

$$\Delta H_{T_c}(\beta) = \int_{T_c}^{T_{an}} c_p(\beta) dT \quad (5)$$

While the maximum solubility of Si in the Al-rich matrix occurs at 577 °C with about 1.65 ma.%, solubility decreases to about 0.05 ma.% at 250 °C [16,39] and drops far below that value with further decrease of temperature [40]. Soluble amount of Si at RT $c_{Si_{sol}(RT)}$ therefore is negligible and equation (4) simplifies to

$$solute\ content_{T_c} = c_{Si_{total}} \cdot \left(1 - \frac{|\Delta H_{T_c}(\beta)|}{|\Delta H_{RT_{sat}}|} \right) \quad (6)$$

Solute mass fraction of Si reaches a maximum if the alloy is overcritically cooled to RT. No precipitation reactions occur ($\Delta H_{RT_{oc}} = 0$) in that case and the complete solid solution is retained. When saturation level $|\Delta H_{RT_{sat}}|$ is reached, all alloying elements should be precipitated leaving a negligible amount of Si in solid solution.

390 As only the diamond cubic Si-rich phase is assumed to be precipitated from solid solution the precipitated Si mass fraction (precipitated ma.% = overall ma.% – solute ma.%) can directly be converted into volume fraction of Si particles considering the densities of Al and Si. The precipitated volume fraction in dependence of cooling rate and temperature can also be calculated with the presented model if the maximum possible precipitated volume fraction $\Phi_{Si_{max}}$ is evaluated first:

$$precipitated\ volume\ fraction_{T_c} = \Phi_{Si_{max}} \cdot \frac{|\Delta H_{T_c}(\beta)|}{|\Delta H_{RT_{sat}}|} \quad (7)$$

The binary Al-Si alloy with a Si content of 0.72 ma.% was considered for the calculation exclusively. The computed solute mass fraction of Si (bold line) and the precipitated volume fraction of Si (thin line) after cooling to RT is shown in Fig. 6 in dependence of cooling rate.

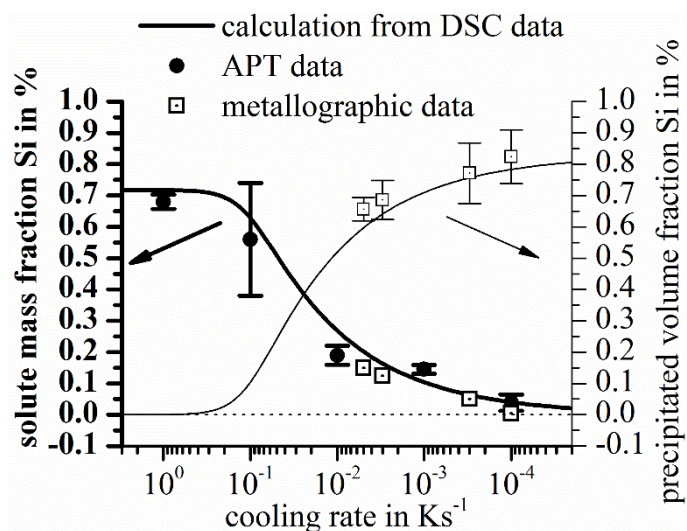


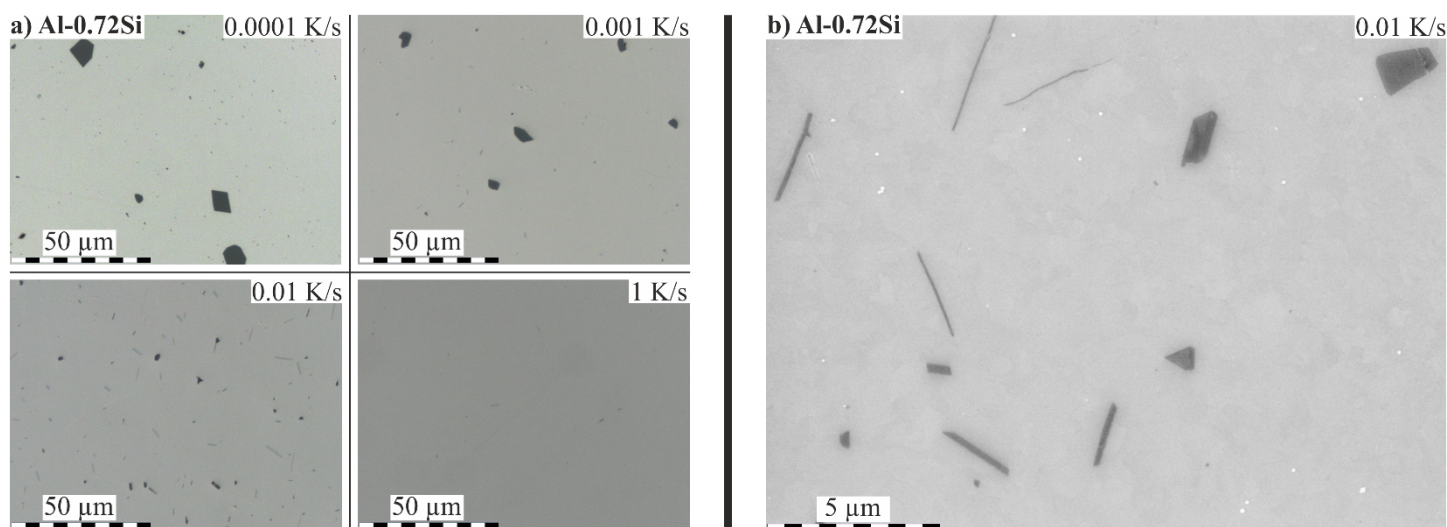
Fig. 6. Calculated solute mass fraction of Si (bold line) and calculated precipitated volume fraction (thin line) for Al 0.72Si after cooling to room temperature in comparison to APT data and results from metallographic analysis.

As the uncertainty of enthalpy values from DSC experiments are estimated to be up to 10 % (resulting from peak-area determination), the calculated solute mass fraction needs to be verified. For this, five different cooling conditions were analysed by APT. Measured data are plotted in Fig. 6 for comparison with the calculated results. Standard deviations of three runs are represented by error bars. APT data after overcritical cooling with 1 K/s (0.680 ± 0.023 ma.%) is in good agreement with the calculated solute mass fraction. It was assumed that no precipitation reactions occur in the time between quenching and APT measurements as formation of precipitates at RT is not reported in literature. Possible natural ageing processes [41,42], which would theoretically reduce the Si content in solid solution, are not considered in the measured composition. Measured values after cooling with all rates also match the calculated data well. As presumed, solute mass fraction of Si decreases with decreasing cooling rate. The value determined by APT after cooling with 0.0001 K/s (0.039 ± 0.026 ma.%) matches the calculated solute mass fraction and indicates that not all Si has been precipitated in that condition. Fig. 6 also shows the precipitated volume fraction of Si obtained from metallographic analyses in comparison to computed data. For a better comparison with APT data, the mean values of solute mass fraction Si were calculated from these results and are also given in Fig. 6. Evaluated data from metallographic analyses is in accordance to the modelled data as well. The relatively large error bars for very slow cooling conditions can be explained by the distribution of precipitates. Slow cooling rates lead to an increasingly uneven distribution of precipitated particles, which results in higher scattering of analysed volume fractions in different metallographic images. Still, the executed experiments support the data obtained from the adapted model used for the calculation of solute content.

3.4. Characterisation of quench-induced precipitates

It was demonstrated that during cooling in the DSC different reaction peaks correspond to the formation of different types of precipitates [18,28]. Coarse (dimensions some μm) incoherent equilibrium phases are

precipitated at high temperatures, while (partially) coherent precursor phases (length some 100 nm) precipitate at lower temperatures for age-hardenable aluminium alloys. However, no precipitation sequence is known for binary Al-Si alloys. Nevertheless, at least two exothermic reactions during cooling were detected for alloy Al-0.72Si (Fig. 2a). To gain additional information on the precipitated particles, metallographic studies after linear cooling from solution annealing to RT were performed on this alloy. LOM and SEM images for different cooling rates are shown in Fig. 7.



430 Fig. 7. LOM images of Al-0.72Si after cooling with different rates (a) and SEM image after cooling with 0.01 K/s (b) from solution annealing to RT.

DSC results indicated that a cooling rate of 1 K/s is overcritically fast for Al-0.72Si. After cooling with this rate no secondary precipitates were traceable with LOM and nanosized precipitates were also not detected via APT, which supports the calorimetric findings. However, it cannot be fully excluded that small precipitates untraceable with LOM form at this cooling rate as APT measurements would only reveal such particles in case of a dense spatial distribution. At slower cooling rates precipitates were observed, of which most are precipitated inside aluminium solid solution grains. Few particles on grain boundaries could be detected as well. For a cooling rate of 0.01 K/s at least two overlapping reaction peaks were detected by DSC (Fig. 2a). After cooling with this rate coarse precipitates with different morphologies were found. On the one hand rods or platelets with lengths of
 440 some μm and high aspect ratios have formed. Besides, irregular-shaped polygonal particles with low aspect ratios and few μm in size are precipitated during cooling with this rate. A more detailed view on both precipitate morphologies provides the SEM image in Fig. 7b. With a further decrease of cooling rate, the amount of rod-/platelet-shaped particles is reduced and polygonal precipitates gain in size. At a cooling rate of 0.0001 K/s very coarse polygonal particles (about 10 μm) are precipitated, while no rod-/platelet-shaped particles are visible anymore in LOM images.

It is well established in the literature that all precipitates in binary Al-Si alloys are diamond cubic Si-rich phase [15]. Our XRD experiments after cooling with 0.001 K/s and 0.01 K/s confirmed the presence of only the fcc Al-rich phase and the diamond cubic Si-rich phase. Interestingly, overlapping DSC peaks (a_1 and a_2) observed during

heating of the water quenched condition (Fig. 3) indicate that the formation of precipitates with different shapes
450 and sizes is not restricted to the cooling process. Precipitates of various shape were also found in other work after
different ageing treatments [15,43–45].

When the microstructural results are compared to the corresponding DSC cooling curves it can be assumed that
the precipitation of polygonal particles takes place at high temperatures. Rod-/platelet-shaped precipitates on the
other hand seem to be formed at lower temperatures. As the precipitation of particles with different morphologies
seem to correspond to the reaction peaks measured by DSC a more detailed microstructural analysis was carried
out to study the development of precipitate formation by a step quenching procedure introduced in [18]. The
investigated samples were cooled with 0.001 K/s and 0.01 K/s to specific temperatures before they were
overcritically cooled to maintain the precipitation state of interest.

The microstructure development of Al-0.72Si during cooling with 0.001 K/s obtained from light microscopy is
460 shown in Fig. 8a. No precipitates are visible at 490 °C, which coincides with the DSC curve for this cooling rate
as no reaction was detected at this temperature. According to Fig. 2a, the intensity maximum of the high
temperature reaction peak is reached at 440 °C. Coarse polygonal particles with low aspect ratios have already
been formed at this temperature. With a further decrease of temperature the precipitates grow and the volume
fraction increases. After cooling to room temperature a few rod-/platelet-shaped precipitates were detected. This
indicates that the low temperature reaction is also present to a certain extent at this cooling rate and supports that
these particles are formed at lower temperatures.

During cooling with 0.01 K/s the maximum amount of heat is released by low temperature reactions. However,
high temperature reactions are not fully suppressed when the alloy is cooled with this rate. At a temperature of
435 °C only polygonal-shaped precipitates with much smaller dimensions compared to the slower cooling
470 condition can be perceived, which correspond to high temperature reactions taking place in this temperature
region (Fig. 2a). When a temperature of 395 °C is reached (low temperature reaction peak maximum) these
particles have grown and first rods/platelets appear. With further decrease of temperature the polygonal-shaped
particles seem to retain their form and size. This again supports the proposition that these particles form only at
high temperatures. On the contrary, amount and size of rod-/platelet-shaped particles increases after passing the
intensity maximum of the low temperature reactions.

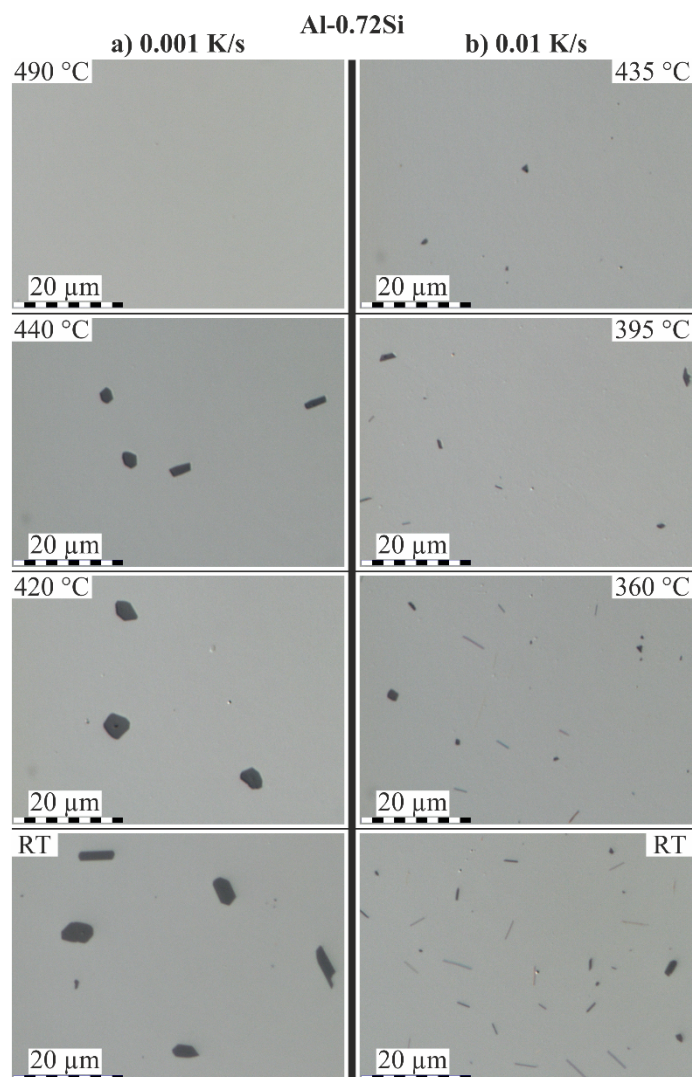


Fig. 8. LOM images of Al-0.72Si after cooling with 0.001 K/s (a) and 0.01 K/s (b) from solution annealing to specific temperatures followed by overcritical cooling.

The knowledge that precipitate morphologies are dependent on the growth temperature of particles provides an explanation for their varying shape [46]. With respect to classical nucleation theory, the driving force for solid-phase transitions such as precipitation reactions can be ascribed to three major factors. The change in the Gibbs free energy ΔG when a nucleus forms can therefore be written as:

$$\Delta G = -\Delta G_{\text{vol}} + \Delta G_{\text{sur}} + \Delta G_{\text{str}} \quad (8)$$

While ΔG_{vol} is related to the energy gain due to creation of new volume, ΔG_{sur} (surface energy) and ΔG_{str} (strain energy) represent inhibitory energies for phase transition. If nucleation is mainly arrested by creation of new interfaces, globular/polygonal nuclei and particles will form because of their small surface to volume fraction. This seems to be the case at high temperatures. Plate- or rod-shaped particles are precipitated if the strain term is the dominating factor. This can be explained with lower strain energy of particles with this shape. Vacancies in binary fcc alloys also play an important role in nucleation [44] as they increase the diffusion rate of solute atoms at moderate temperatures and thus increase the growth rate of solute clusters. Furthermore, vacancies may become part of nuclei and can reduce the barrier to precipitation.

3.5. Thermo-mechanical analyses

Flow characteristics of Al-0.72Si during the cooling process were examined by TMA dependent on cooling condition and temperature. In correlation with data from DSC cooling experiments and microstructural analyses information on the effect of Si solutes and quench-induced Si precipitates on mechanical properties can be discussed. Three cooling rates (1 K/s, 0.01 K/s, 0.001 K/s), showing very different precipitation behaviour, were studied. Compression tests after cooling with these rates were carried out at four different temperatures (500 °C, 400 °C, 300 °C, 30 °C). The results of these tests are given in Fig. 9.

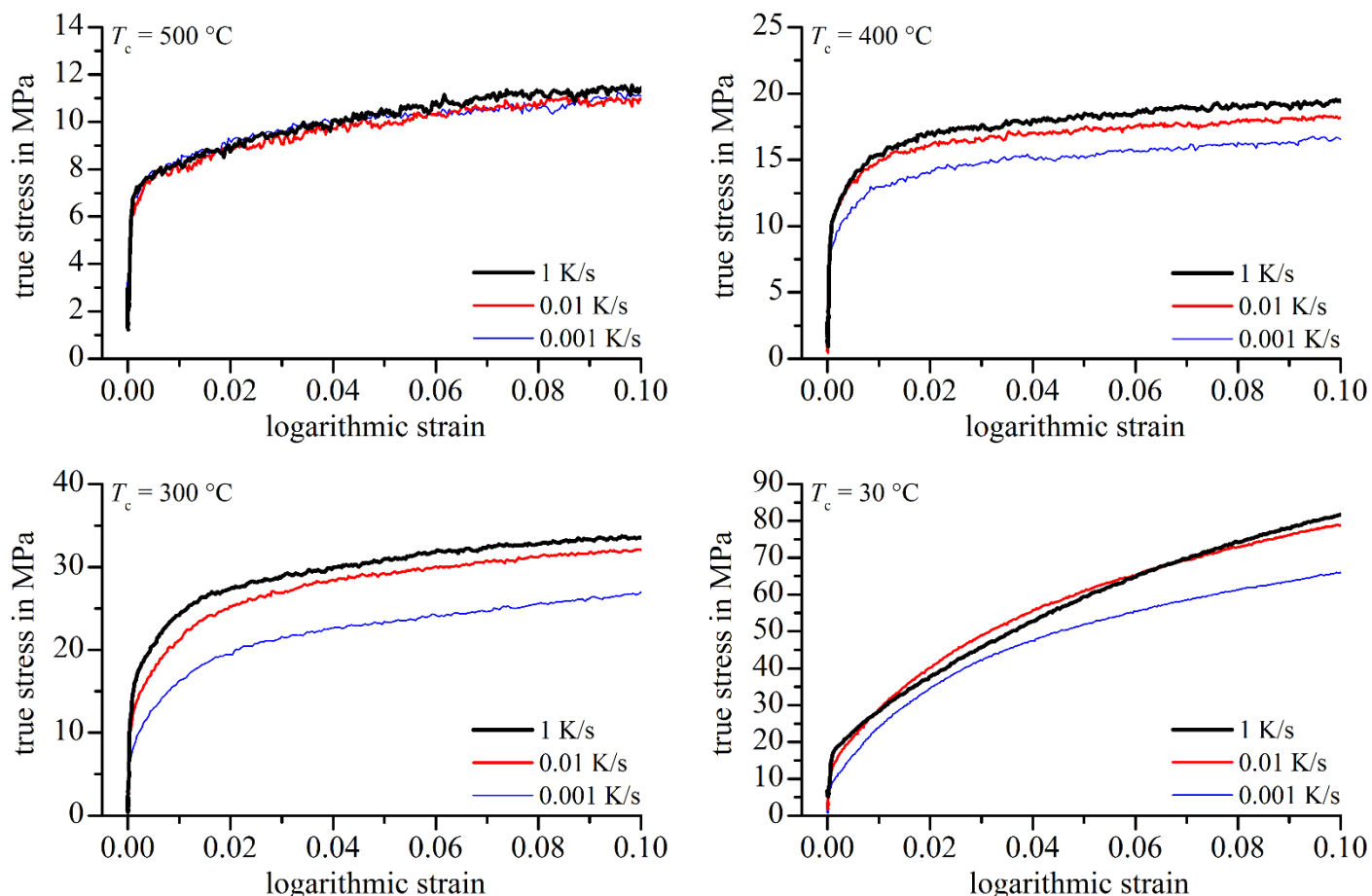


Fig. 9. Stress-strain curves of alloy Al-0.72Si from compression tests with a strain rate of 0.1 s^{-1} at different temperatures T_c after cooling with different rates from solution annealing.

Identical flow curves were recorded at a temperature of $T_c = 500 \text{ °C}$ for all cooling rates. This can be explained with the absence of precipitation reactions in this temperature range (Fig. 2a), meaning that all Si atoms remain in solution for all states. At $T_c = 400 \text{ °C}$ a decrease in strength was detected with decreasing cooling rate, which clearly results from a loss of solute Si atoms. Even greater differences in the flow stress can be observed at a temperature of $T_c = 300 \text{ °C}$ as further precipitation reactions occur in this temperature region. At both temperatures the flow stress at the initial stage of plastic deformation and at higher strains is affected nearly equally.

A main difference between cooling rates 0.01 K/s and 0.001 K/s is the morphology of the main precipitated particles as was shown in Fig. 8. Interestingly, strain hardening at high temperatures does not seem to be influenced by the quench-induced precipitates and similar work hardening rates were observed in all conditions. Work hardening is generally weak due to extensive dynamic recovery. On the other hand, work hardening rates at low temperatures seem to be affected by quench-induced precipitates formed during slow cooling. At $T_c = 30$ °C overcritically cooled samples again show the highest yield strength, implying that precipitated particles are too coarse to contribute to strength at the initial stage of plastic deformation. The yield strength hence seems to be controlled by the solute Si content. However, higher strain hardening rates up to a total strain of about 0.03 were observed for samples containing precipitates. With further increase of strain work hardening rates drop below that of precipitate-free samples. Complete solid solution thus showed a more linear hardening, while a parabolic hardening was observed for states containing quench-induced precipitates and lower solute content.

Similar observations were recently made in Al-Mn alloys containing different dispersoid densities [47,48]. A higher amount of non-shearable particles led to an increased work hardening at the initial plastic deformation, but the effect was opposite at higher strains. The more parabolic hardening, compared to a lower density of dispersoids, resulted in a crossover in the stress-strain curves similar to the results presented here. The reason for increased work hardening rates at the initial plastic deformation has been attributed to the generation of geometrically necessary dislocations (GNDs), on which Ashby [49] proposed a basic theory. It was assumed that the local dislocation density saturates at a certain amount of strain and volume fractions containing GNDs no longer contribute to further work hardening. Decreased hardening rates at higher strains therefore seems to be related to the storage and dynamic recovery of the GNDs during deformation at room temperature [48]. Although no detailed study regarding precipitate-matrix interfaces have been performed so far, most quench-induced particles in Al-Si should be incoherent with the matrix and hence non-shearable due to their sizes. Thus, work hardening characteristics of Al-Si with quench-induced precipitates might also be influenced by the generation of GNDs. A more refined discussion of this effect will require a comprehensive model that is able to consider work hardening, dynamic recovery, particle and solid solution strengthening concurrently, which is beyond the scope of the present paper.

4. Summary

In this work an approach to explore the effect of solutes and quench-induced precipitates on mechanical properties during cooling from solution annealing has been introduced on binary Al-Si alloys. Application of advanced DSC techniques for determination of precipitation enthalpies upon cooling from solution annealing (cooling rates between 2 K/s and 0.0001 K/s) allows the determination of solid solution states based on an introduced physically-based approach. Microstructural analyses by the use of light optical microscopy, scanning electron microscopy, atom probe and X-ray diffraction support the modelled solute states and it is found that quench-

induced precipitates of different morphology form dependent on cooling rate. Form and size of quench-induced particles depend on the temperature range in which they are precipitated. Coarse irregular-shaped, polygonal precipitates are formed at high temperatures, while particles precipitated at lower temperatures seem to be rods or platelets. Thermomechanical analyses showed that the strength of binary Al-Si during the cooling process is significantly influenced by temperature and cooling rate as different microstructural changes occur. Quench-induced Si precipitates appear to have no contribution to yield strength of the alloy due to their sizes. Onset of plastic deformation is therefore mostly controlled by the present amount of Si solutes. While work hardening characteristics of Al-0.72Si at elevated temperatures also seem not to be influenced by precipitated particles, increased strain hardening rates at the initial stage of plastic deformation are observed at low temperatures in samples with quench-induced precipitates. At higher strains work hardening rates are reduced. This results in a rather parabolic hardening compared to precipitate-free conditions, which show a more linear hardening.

The presented experimental approach can be used for a detailed study on the correlation between microstructural states of non-equilibrium alloy conditions and their mechanical behaviour in future work. With knowledge of microstructural changes upon cooling appropriate heat treatment parameters can be derived to control the microstructure and thereby produce well-defined material conditions. Comparison of these states by means of thermomechanical analyses will allow the investigation of strength contribution of solute Si and strengthening effects of quench-induced precipitates with different morphologies. Consequently, information on active strengthening mechanisms can be obtained to improve plasticity models.

560 Acknowledgements

The authors gratefully acknowledge funding of this work by Deutsche Forschungsgemeinschaft (MO974/4-1 and MI1731/1-1). Besides, part of this work was supported by a fellowship within the Postdoc-Program of the German Academic Exchange Service (DAAD) for Benjamin Milkereit.

References

- [1] I.J. Polmear, *Light alloys*, 4th ed., Elsevier/Butterworth-Heinemann, Oxford, 2006.
- [2] M. Reich, O. Kessler, Quenching Simulation of Aluminum Alloys Including Mechanical Properties of the Undercooled States, *Matls Perf Charact* 1 (2012) 104632. doi:10.1520/MPC104632.
- [3] M. Goerdeler, G. Gottstein, A microstructural work hardening model based on three internal state variables, *Mater Sci Eng A* 309-310 (2001) 377-381. doi:10.1016/S0921-5093(00)01728-7.
- 570 [4] U.F. Kocks, H. Mecking, Physics and phenomenology of strain hardening: The FCC case, *Prog Mater Sci* 48 (2003) 171-273. doi:10.1016/S0079-6425(02)00003-8.
- [5] E. Nes, Modelling of work hardening and stress saturation in FCC metals, *Prog Mater Sci* 41 (1998) 129-193. doi:10.1016/S0079-6425(97)00032-7.

- [6] F. Roters, D. Raabe, G. Gottstein, Work hardening in heterogeneous alloys - a microstructural approach based on three internal state variables, *Acta Mater* 48 (2000) 4181-4189. doi:10.1016/S1359-6454(00)00289-5.
- [7] G.V.S.S. Prasad, An Improved Dislocation Density Based Work Hardening Model for Al-alloys, PhD thesis, Aachen, 2007.
- [8] V. Mohles, X. Li, C. Heering, G. Hirt, S. Bhaumik, G. Gottstein, Validation of an improved dislocation density based flow stress model for Al-alloys, *Int J Mater Form* 1 (2008) 77-80. doi:10.1007/s12289-008-0040-1.
- [9] M. Reich, O. Kessler, Mechanical properties of undercooled aluminium alloys and their implementation in quenching simulation, *Mater Sci Tech* 28 (2012) 769-772. doi:10.1179/1743284711Y.00000000085.
- [10] Ø. Ryen, O. Nijs, E. Sjölander, B. Holmedal, H.-E. Ekström, E. Nes, Strengthening mechanisms in solid solution aluminum alloys, *Metall Mat Trans A Phys Metall Mat Sci* 37 (2006) 1999-2006. doi:10.1007/s11661-006-0142-7.
- [11] B. Rønning, K. Nord-Varhaug, T. Furu, E. Nes, Effect of chemical composition and microstructure on the flow stress during hot deformation of aluminum alloys, *Mater Sci Forum* 331-337 (2000) 571-576. doi:10.4028/www.scientific.net/MSF.331-337.571.
- 590 [12] Ø. Ryen, H.I. Laukli, B. Holmedal, E. Nes, Large strain work hardening of aluminum alloys and the effect of Mg in solid solution, *Metall Mat Trans A Phys Metall Mat Sci* 37 (2006) 2007-2013. doi:10.1007/s11661-006-0143-6.
- [13] Q. Zhao, B. Holmedal, The effect of silicon on the strengthening and work hardening of aluminum at room temperature, *Mater Sci Eng A* 563 (2013) 147-151. doi:10.1016/j.msea.2012.11.062.
- [14] R. Akeret, Deformation of aluminum and aluminum alloys at different temperatures, *Z Metallk* 61 (1970) 3-10.
- [15] M.J. Starink, A.-M. Zahra, Kinetics of isothermal and non-isothermal precipitation in an Al - 6 at.% Si alloy, *Philos Mag A* 77 (1998) 187-199. doi:10.1080/01418619808214237.
- [16] M. Hansen, K. Anderko, *Constitution of binary alloys*, 2nd ed., McGraw-Hill, New York, 1958.
- 600 [17] J.L. Murray, A.J. McAlister, The Al-Si (Aluminum-Silicon) system, *Bull Alloy Phase Diagr* 5 (1984) 74-84. doi:10.1007/BF02868729.
- [18] B. Milkereit, N. Wanderka, C. Schick, O. Kessler, Continuous cooling precipitation diagrams of Al-Mg-Si alloys, *Mater Sci Eng A* 550 (2012) 87-96. doi:10.1016/j.msea.2012.04.033.
- [19] M.J. Starink, Analysis of aluminium based alloys by calorimetry: Quantitative analysis of reactions and reaction kinetics, *Int Mater Rev* 49 (2004) 191-226. doi:10.1179/095066004225010532.
- [20] P. Schumacher, M. Reich, V. Mohles, S. Pogatscher, P.J. Uggowitzer, B. Milkereit, Correlation between supersaturation of solid solution and mechanical behaviour of two binary Al-Si-alloys, *Mater Sci Forum* 794-796 (2014) 508-514. doi:10.4028/www.scientific.net/MSF.794-796.508.

[21] B. Milkereit, J. Osten, C. Schick, O. Kessler, Continuous Heating Dissolution Diagrams of Aluminum Alloys, in: H. Weiland, A.D. Rollett, W.A. Cassada (Eds.), ICAA13: 13th International Conference on Aluminum Alloys, John Wiley & Sons, Inc., Hoboken, NJ, 2012, pp. 1095-1100. doi:10.1002/9781118495292.ch164.

[22] B. Milkereit, O. Kessler, C. Schick, Recording of continuous cooling precipitation diagrams of aluminium alloys, *Thermochim Acta* 492 (2009) 73-78. doi:10.1016/j.tca.2009.01.027.

[23] B. Milkereit, M. Beck, M. Reich, O. Kessler, C. Schick, Precipitation kinetics of an aluminium alloy during Newtonian cooling simulated in a differential scanning calorimeter, *Thermochim Acta* 522 (2011) 86-95. doi:10.1016/j.tca.2011.02.034.

[24] D. Zohrabyan, B. Milkereit, O. Kessler, C. Schick, Precipitation enthalpy during cooling of aluminum alloys obtained from calorimetric reheating experiments, *Thermochim Acta* 529 (2012) 51-58. doi:10.1016/j.tca.2011.11.024.

[25] M. Reich, B. Milkereit, M. Krawutschke, J. Kalich, C. Schick, O. Kessler, Advanced Dilatometry and Calorimetry for the Validation of Materials Mechanical and Transformation Models, in: M. Li, C. Campbell, K. Thornton, E. Holm, P. Gumbsch (Eds.), 2nd World Congress on Integrated Computational Materials Engineering, John Wiley & Sons, Inc., Hoboken, NJ, 2013, pp. 177-182. doi:10.1002/9781118767061.ch28.

[26] D. Zohrabyan, B. Milkereit, C. Schick, O. Kessler, Continuous Cooling Precipitation Diagram of a High Alloyed Al-Zn-Mg-Cu alloy 7049A, *T Nonferr Metal Soc* (2013) accepted manuscript.

[27] B. Milkereit, L. Giersberg, O. Kessler, C. Schick, Isothermal time-temperature-precipitation diagram for an aluminum alloy 6005A by in situ DSC experiments, *Mater* 7 (2014) 2631-2649. doi:10.3390/ma7042631.

[28] Y. Zhang, B. Milkereit, O. Kessler, C. Schick, P.A. Rometsch, Development of continuous cooling precipitation diagrams for aluminium alloys AA7150 and AA7020, *J Alloys Compd* 584 (2014) 581-589. doi:10.1016/j.jallcom.2013.09.014.

[29] P.A. Rometsch, M.J. Starink, P.J. Gregson, Improvements in quench factor modelling, *Mater Sci Eng A* 339 (2003) 255-264. doi:10.1016/S0921-5093(02)00110-7.

[30] H. Oettel, H. Schumann, *Metallografie*, 14th ed., Wiley-VCH, Weinheim, 2005.

[31] M.K. Miller, *Atom probe field ion microscopy*, Clarendon Press; Oxford University Press, Oxford, New York, 1996.

[32] M.J. Starink, A.-M. Zahra, An analysis method for nucleation and growth controlled reactions at constant heating rate, *Thermochim Acta* 292 (1997) 159-168. doi:10.1016/S0040-6031(96)03135-8.

[33] M.J. Starink, On the meaning of the impingement parameter in kinetic equations for nucleation and growth reactions, *J Mater Sci* 36 (2001) 4433-4441. doi:10.1023/A:1017974517877.

- [34] M.J. Starink, Kinetic equations for diffusion-controlled precipitation reactions, *J Mater Sci* 32 (1997) 4061-4070.
- [35] M.J. Starink, A new model for diffusion-controlled precipitation reactions using the extended volume concept, *Thermochimica Acta* 596 (2014) 109-119. doi:10.1016/j.tca.2014.09.016.
- [36] J.W. Christian, *The Theory of Transformations in Metals and Alloys, Part 1*, 2nd ed., Pergamon Press, Oxford, 1975.
- [37] F.L. Cumbreira, F. Sánchez-Bajo, The use of the JMAYK kinetic equation for the analysis of solid-state reactions: critical considerations and recent interpretations, *Thermochim Acta* 266 (1995) 315-330. doi:10.1016/0040-6031(95)02554-5.
- [38] M. van Rooyen, E.J. Mittemeijer, Precipitation of silicon in aluminum-silicon: a calorimetric analysis of liquid-quenched and solid-quenched alloys, *Metall Trans A* 20 A (1989) 1207-1214. doi:10.1007/BF02647402.
- [39] L.F. Mondolfo, *Aluminum alloys*, Butterworths, London, Boston, 1976.
- [40] K.S. Lee, Direct observations of Al-Si junction interface, *Korean J Electron Microsc* 8 (1978) 77-79.
- [41] K. Nakagawa, T. Kanadani, L. Anthony, H. Hashimoto, Microstructural changes at the initial stage of precipitation in an aluminum-silicon alloy, *Mater Trans* 46 (2005) 779-783. doi:10.2320/matertrans.46.779.
- [42] M.J. Starink, L.F. Cao, P.A. Rometsch, A model for the thermodynamics of and strengthening due to co-clusters in Al-Mg-Si-based alloys, *Acta Mater* 60 (2012) 4194-4207. doi:10.1016/j.actamat.2012.04.032.
- [43] H.S. Rosenbaum, D. Turnbull, Metallographic investigation of precipitation of silicon from aluminum, *Acta Metall* 7 (1959) 664-674. doi:10.1016/0001-6160(59)90143-9.
- [44] E. Hornbogen, A.K. Mukhopadhyay, Starke Jr. E. A., Nucleation of the diamond phase in aluminium-solid solutions, *J Mater Sci* 28 (1993) 3670-3674. doi:10.1007/BF01159852.
- [45] F. Lasagni, B. Mingler, M. Dumont, H.P. Degischer, Precipitation kinetics of Si in aluminium alloys, *Mater Sci Eng A* 480 (2008) 383-391. doi:10.1016/j.msea.2007.07.008.
- [46] D.A. Porter, K.E. Easterling, *Phase transformations in metals and alloys*, 2nd ed., Nelson Thornes Ltd, Cheltenham, 2001.
- [47] Q. Zhao, B. Holmedal, Y. Li, Influence of dispersoids on microstructure evolution and work hardening of aluminium alloys during tension and cold rolling, *Philos Mag* 93 (2013) 2995-3011. doi:10.1080/14786435.2013.794315.
- [48] Q. Zhao, B. Holmedal, Modelling work hardening of aluminium alloys containing dispersoids, *Philos Mag* 93 (2013) 3142-3153. doi:10.1080/14786435.2013.805271.
- [49] M.F. Ashby, Deformation of plastically non-homogeneous materials, *Philos Mag* 21 (1970) 399-424. doi:10.1080/14786437008238426.

List of figure captions

Fig. 1. Temperature-time profile for indirect determination of specific precipitation heat values during cooling with very slow rates by a DSC reheating scan.6

Fig. 2. DSC cooling curves of alloys Al-0.72Si (a) and Al-0.26Si (b) after solution annealing in a cooling rate range from 0.001 K/s to 2 K/s.8

Fig. 3. DSC reheating curves (scan rate: 0.003 K/s) of alloy Al-0.72Si in different cooling conditions (cc)...10

Fig. 4. Change of enthalpy state during reheating (scan rate: 0.003 K/s) of Al-0.72Si in different cooling conditions (cc).11

Fig. 5. Enthalpy change values $|\Delta H_{RT}|$ upon precipitation in Al-Si alloys after cooling to room temperature obtained with direct DSC cooling experiments or DSC reheating experiments and fitting results with the model presented in Eq. (3).12

Fig. 6. Calculated solute mass fraction of Si (bold line) and calculated precipitated volume fraction (thin line) for Al 0.72Si after cooling to room temperature in comparison to APT data and results from metallographic analysis.15

Fig. 7. LOM images of Al-0.72Si after cooling with different rates (a) and SEM image after cooling with 0.01 K/s (b) from solution annealing to RT.16

Fig. 8. LOM images of Al-0.72Si after cooling with 0.001 K/s (a) and 0.01 K/s (b) from solution annealing to specific temperatures followed by overcritical cooling.18

Fig. 9. Stress-strain curves of alloy Al-0.72Si from compression tests with a strain rate of 0.1 s^{-1} at different temperatures T_c after cooling with different rates from solution annealing.19

List of table captions

Table 1. Chemical compositions of investigated alloys obtained by optical emission spectroscopy (OES) analysis.4

Table 2. Results from fitting measured DSC data to equation (3).13

**[BM5] Osten J, Milkereit B, Schick C, Kessler O:
Dissolution and precipitation behaviour during continuous heating of Al-Mg-Si alloys in a wide range of heating rates.
Materials 8-5 (2015): 2830–2848.**

Benjamin's contributions: I designed the experiments, supervised the DSC work, participated in the discussion of the data and partially wrote and revised the manuscript.

Article

Dissolution and Precipitation Behaviour during Continuous Heating of Al–Mg–Si Alloys in a Wide Range of Heating Rates

Julia Osten ^{1,*}, Benjamin Milkereit ^{1,2}, Christoph Schick ² and Olaf Kessler ¹

¹ Chair of Materials Science, Faculty of Mechanical Engineering and Marine Technology, University of Rostock, Albert-Einstein-Str. 2, 18059 Rostock, Germany; E-Mails: benjamin.milkereit@uni-rostock.de (B.M.); olaf.kessler@uni-rostock.de (O.K.)

² Polymer Physics Group, Institute of Physics, University of Rostock, Wismarsche Str. 43-45, 18057 Rostock, Germany; E-Mail: christoph.schick@uni-rostock.de

* Author to whom correspondence should be addressed; E-Mail: julia.osten@uni-rostock.de; Tel.: +49-381-498-9486; Fax: +49-381-498-9472.

Academic Editor: Jung Ho Je

Received: 17 April 2015 / Accepted: 4 May 2015 / Published: 22 May 2015

Abstract: In the present study, the dissolution and precipitation behaviour of four different aluminium alloys (EN AW-6005A, EN AW-6082, EN AW-6016, and EN AW-6181) in four different initial heat treatment conditions (T4, T6, overaged, and soft annealed) was investigated during heating in a wide dynamic range. Differential scanning calorimetry (DSC) was used to record heating curves between 20 and 600 °C. Heating rates were studied from 0.01 K/s to 5 K/s. We paid particular attention to control baseline stability, generating flat baselines and allowing accurate quantitative evaluation of the resulting DSC curves. As the heating rate increases, the individual dissolution and precipitation reactions shift to higher temperatures. The reactions during heating are significantly superimposed and partially run simultaneously. In addition, precipitation and dissolution reactions are increasingly suppressed as the heating rate increases, whereby exothermic precipitation reactions are suppressed earlier than endothermic dissolution reactions. Integrating the heating curves allowed the enthalpy levels of the different initial microstructural conditions to be quantified. Referring to time–temperature–austenitisation diagrams for steels, continuous heating dissolution diagrams for aluminium alloys were constructed to summarise the results in graphical form. These diagrams may support process optimisation in heat treatment shops.

Keywords: continuous heating; differential scanning calorimetry (DSC); aluminium alloys; Al–Mg–Si; sheet; dissolution; precipitation; enthalpy change

1. Introduction

Al–Mg–Si alloys can be strengthened through precipitation hardening. The process consists of solution annealing, quenching, and ageing; thus, it contains heating, cooling, and isothermal steps, and thereby precipitation and dissolution reactions occur. The knowledge of the precipitation and dissolution behaviour of aluminium alloys is important for optimising heat treatment steps and acquiring information for simulation in the production chain. The necessity of investigating the heating behaviour of aluminium alloys shall be demonstrated with a few examples: aluminium sheet materials are coiled and solution annealing is performed in continuous annealing furnaces with very short solution annealing times (a few minutes, which allows production to be kept fast and cost-efficient). Knowledge of the dissolution behaviour over a wide dynamic range would help to select an appropriate heating rate, generate a full solution already during heating, and hence exhaust the full age-hardening potential. Another important field of application of dissolution is heat treatments which lead to an increase of plastic formability. This holds for forming processes such as tailored heat treated blanks (e.g., [1]), but also for joining processes such as laser-assisted clinching [2].

In recent years, the precipitation and dissolution behaviour during the ageing of Al–Mg–Si alloys has frequently been investigated through differential scanning calorimetry (DSC), occasionally in conjunction with microstructure analysis. One outcome of this has been that the highly complex precipitation sequence of Al–Mg–Si alloys is basically known (e.g., [3–5]). A simplified precipitation sequence from a saturated solid solution (sss) for Al–Mg–Si alloys could be described as: sss → cluster → GP zones → β'' → β' → β (Mg_2Si). Nevertheless, the exact sequence significantly depends on the initial microstructural condition and heat treatment respectively as well as the alloy composition (*cf.* [6–9]). It is generally accepted that an increasing heating rate shifts the reactions towards higher temperatures (e.g., [10]). This phenomenon is often used to evaluate kinetic parameters such as the activation energy for specific precipitation reactions (e.g., [11–13]). A number of different methods exist to evaluate such kinetic parameters [14,15]. All of these methods are based on the assumption that the same amount of alloying elements is transferred for varying heating rates. However, the variation of the heating rate in these methods has been limited to a relatively narrow dynamic range so far. The availability of DSC curves is limited to a typical heating rate range around 10 K/min (about 0.2 K/s). In technological applications, the heating rate will vary significantly depending on heating technique and part dimensions. Therefore, it is indispensable to investigate a multiplicity of heating rates in a wide dynamic range. Moreover, DSC data in previous studies are hard to compare because the evaluation of those curves is not consistent. Heat flow was illustrated frequently instead of excess specific heat capacity, which is normalised for scanning rate and sample mass and therefore more comparable.

The purpose of this work is to investigate the sequence of the precipitation and dissolution of Al–Mg–Si alloys in a wide dynamic range during heating by means of highly precise *in-situ* DSC analysis to make this information available for heat treatment shops as well as for heat treatment simulation.

2. Materials and Methods

2.1. Analysed Aluminium Alloys and Investigated Initial Conditions

For the experimental procedure, four wrought alloys of the alloy system Al–Mg–Si were chosen. EN AW-6005A and EN AW-6082 were supplied as extruded profiles, EN AW-6016 and EN AW-6181 instead as sheets. The chemical compositions—analysed by optical emission spectrometry (OES)—are given in Table 1. The alloy contents comply with the standard DIN EN 573-3, except aluminium alloy 6181, which has a slightly higher copper content. In addition, 99.9995% pure aluminium was used as reference material.

Table 1. Mass fraction of alloying elements of the investigated materials in %.

Aluminium Alloy	Mass fraction in %							
	Si	Fe	Cu	Mn	Mg	Cr	Zn	Ti
EN AW-6005A	0.67	0.23	0.03	0.41	0.59	0.01	0.02	0.02
DIN EN 573-3	0.5–0.9	≤0.35	≤0.3	≤0.5	0.4–0.7	≤0.3	≤0.2	≤0.1
EN AW-6082	0.73	0.22	0.05	0.48	0.61	0.003	0.01	0.02
DIN EN 573-3	0.7–1.3	≤0.5	≤0.1	0.4–1.0	0.6–1.2	≤0.25	≤0.2	≤0.1
EN AW-6016	1.15	0.24	0.07	0.07	0.40	0.022	0.007	0.04
DIN EN 573-3	1.0–1.5	≤0.5	≤0.2	≤0.2	0.25–0.6	≤0.1	≤0.2	≤0.15
EN AW-6181	0.85	0.33	0.18	0.06	0.77	0.009	0.021	0.01
DIN EN 573-3	0.8–1.2	≤0.45	≤0.1	≤0.15	0.6–1.0	≤0.1	≤0.2	≤0.1

The dissolution and precipitation behaviour strongly depends on the initial microstructural state or heat treatment state. Therefore, different heat treatment states were adjusted, naturally aged (T4), artificially aged (T6), overaged (OA), and soft annealed (SA). The corresponding time–temperature profiles are listed in Table 2. The DSC measurements of the alloys EN AW-6016 T4 and EN AW-6181 T4 were done at the same state of 7 days ageing time, since the samples were frozen at –80 °C after natural ageing prior the DSC measurements.

Table 2. Heat treatment parameters of the investigated material.

Heat treatment	Step I	Step II	Step III
T4	Solution annealing 540 °C 20 min.	Water quenching	Natural ageing 25 °C 7 days *
T6			Artificial ageing 180 °C 4 h
Overaged (OA)			Artificial ageing 200 °C 10 h
Soft annealed (SA)		98 h furnace cooling	-

* EN AW-6005A: 6–8 days; EN AW-6082: 2 months.

2.2. Thermal Analysis through DSC

The heating experiments were carried out in two different devices adapted to different heating rate ranges. For rates between 0.01 and 0.1 K/s a heat-flux DSC (Setaram DSC 121, SETARAM Instrumentation, Frankfurt am Main, Germany) and for rates between 0.3 K/s to 5 K/s a power-compensated DSC (PerkinElmer Pyris 1 DSC, PerkinElmer, Hamburg, Germany) was used.

The samples have a cylindrical geometry, with dimensions of $\text{Ø}6.1 \text{ mm} \times 21.65 \text{ mm}$ used for measurements in the Setaram DSC 121 and of $\text{Ø}6.4 \text{ mm} \times 1.0 \text{ mm}$ for measurements with the Perkin-Elmer Pyris 1 DSC. Ensuring the symmetry of the whole equipment's arrangement during the measurements is the determining factor for the quality of DSC curves. Therefore, not reacting reference samples of pure Al with the same geometries were used.

In order to obtain precisely evaluable DSC curves, as a first step the device-specific heat-flow curvature must be eliminated from the raw data. Thus, a baseline measurement is subtracted from the sample measurement. Not only does the symmetry within one measure have to be preserved, but also the symmetry of successive sample and baseline measurements. Therefore, during the sample measurement the alloyed sample is scanned against a not reacting reference sample, while the baseline measurement is made by scanning a pure Al sample against a pure Al sample. To ensure that this procedure is appropriate, it is necessary to have steady-state conditions at the beginning and at the end of the measurements. Due to thermal inertia of the devices, it is useful to start and end the measurement with an isothermal step (this is also required for the heat capacity calculation with the device software). These isothermal steps serve the equilibration of the temperature of the sample. The starting isotherm could be described as a *low temperature isotherm*, in contrast to the ending isotherm, which is a *high temperature isotherm*. In particular, the quality with which the heat-flow values are matched between the high temperature isotherms of the baseline and the sample is a quality characteristic of a DSC measurement. The values of the heat-flow differences between the sample- and the baseline measurement are device dependent. With heat-flux DSCs such as the Calvet-type Setaram DSC 121, significantly better results are generally obtained with respect to this issue.

To avoid baseline drift problems sample measurements and baseline measurements were recorded back-to-back. For slow heating rates (0.01–0.1 K/s) three sample and one baseline measurement were arranged. In contrast, six sample and three baseline measures were made for fast heating (0.3–5 K/s) rates. For measurements carried out in the PerkinElmer Pyris 1 DSC, pure nitrogen was used as a purge gas to ensure efficient heat transfer for improved sensitivity. Device-specific, no purge gas was used in the Setaram DSC 121, *i.e.*, heating was carried out in dry air.

We aim to perform a quantitative evaluation of the DSC curves. Therefore, we have to ensure that the zero level of the evaluated curve (frequently called the baseline, which should not be confused with the baseline measurement) is absolutely straight and possesses a value that is equal to zero. This is not necessarily the case, even if the measurement is performed with the best possible accuracy. Several circumstances can lead to a remaining zero-level curvature. For example, varying positions/rotations of the furnace lids or slight variations of the positions of the samples inside the furnaces can cause curve-bending effects (see e.g., [16]). In addition, the sample might have a slightly different surface colour compared with the reference sample. This will lead to a different uptake of heat radiation, which influences the heat flow particularly in heat-flux DSCs at high temperatures (see e.g., [17]). This metrological issue is reduced by covering the samples with standard aluminium crucibles, as this minimises the influence of different heat radiation behaviours of different sample surface colours on the heat flow signal and allows the reception of a good accordance of the curves of the sample measurement and the baseline [17]. Nevertheless, slight remaining bending will remain in several cases. This must be eliminated to allow accurate qualitative and quantitative evaluations. Primarily, and only if the zero level is known to within a good approximation, one can qualitatively distinguish between endo- and exothermal reactions.

Moreover, quantitative evaluation, for instance of the enthalpy transformed by the integration of the excess specific heat capacity curves, is only appropriate if the zero-level baseline is truly zero. An appropriate procedure to ensure this zero-level baseline quality will be explained below.

2.3. Specifics for Using Modified Sample Geometries during DSC Measurements

In this work a challenge was using sheet materials of EN AW-6016 (sheet thickness $t = 1.25$ mm) and EN AW-6181 ($t = 1.5$ mm) for measurements in the Setaram DSC 121. To get appropriate sample masses, several thin sheet discs needed to be stacked to arrive at the final samples. A stacked sample might be a challenge due to the significantly increased surface-to-volume ratio of the sample. In particular, this might lead to increased baseline bending as a result of heat-radiation effects. Preliminary investigations with EN AW-6005A exhibited the possibility of using common bulk samples on the one hand and stacked thin sheet samples on the other hand. Figure 1 shows a schematic and a picture of the two different sample dimensions used. Characteristics of the samples are different geometries and masses. While a common bulk sample is covered by two standard aluminium crucibles and weighs about 1,698 mg, the new stacked sheet sample fills only one crucible, weighs about 700 mg, and is capped with an aluminium lid. The reference samples were prepared in the same way to retain the symmetry of the measurements.

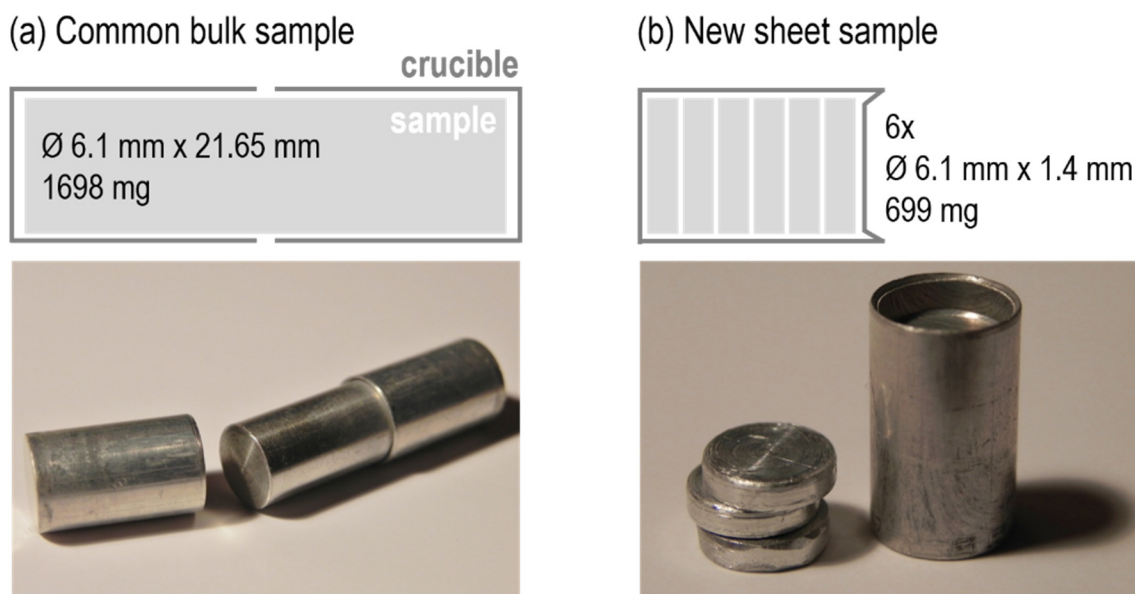


Figure 1. Schematics for the used common (a) and new sheet (b) sample with dimensions and masses as well as pictures of EN AW-6005A samples with crucibles.

The recorded heat flow curves of both sample measurements and baseline measurements as well as the normalised excess specific heat capacity curves can be seen in Figure 2. A constant heating rate of 0.02 K/s up to 540 °C was used in this example. Excess specific heat capacity curves allow a comparison of the heating curves with respect to different heating rates and mass. The curves match very well, *i.e.*, the stacked discs method has been developed successfully for DSC measurements on sheet metal.

2.4. Evaluation of Heat Flow Curves

First, as expected, it is noticeable in Figure 2a that the measured heat flows of the stacked sample are significantly lower due to the reduction in sample mass. The difference of the high temperature isotherms for the common bulk specimen is approximately 0.2 mW. In contrast, the difference for the new stacked specimen is in the region of about 0.6 mW. Although both results are quite satisfactory it can be seen that the curve values after baseline-subtraction are not necessarily zero, even if the reactions seem to be finished in the sample. In addition, the excess specific heat capacity (Figure 2b) displays a good qualitative accordance for both specimens. However, it becomes apparent that the remaining curvature of the corresponding zero levels is different.

This remaining zero-level curvature potentially can be eliminated by subtracting a polynomial (zero-level polynomial). However, for this the start and end of the measured curves should exhibit sections where no heat was exchanged by microstructural changes within the sample—*i.e.*, reaction-free zones are required to allow the fitting of a zero-level polynomial. This requirement is not fulfilled in the example in Figure 2b. Nevertheless, this problem could be overcome by heating to higher temperatures—in particular some 10 K above the solvus temperature of the equilibrium phases—which would consequently lead to curve progression with significant and expanded reaction-free sections.

EN AW-6005A T4: heating rate 0.02 K/s (up to 540 °C) | common bulk specimen vs. stacked sheet specimen

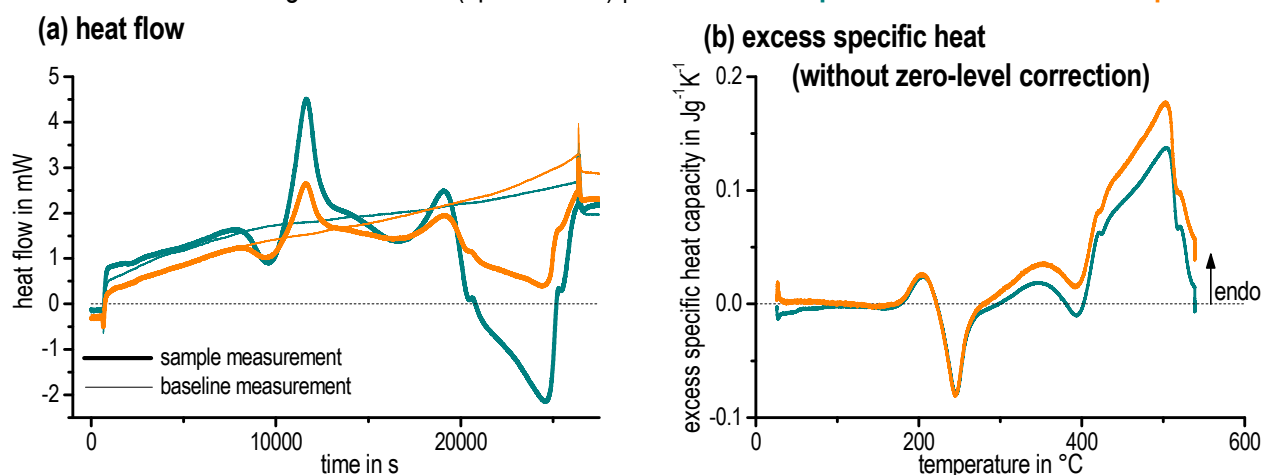


Figure 2. Comparison of different specimen types during heating of EN AW-6005A in a Setaram DSC 121: (a) heat-flow curves; and (b) excess specific heat capacity curves (normalised heating curves).

The data evaluation procedure is shown in Figure 3 with raw data from the two DSC devices measuring EN AW-6181 T4. In order to indicate the comparability of both DSC types, similar heating rates of 0.1 K/s (Figure 3a–c) and 0.3 K/s (Figure 3d–f) were chosen. The consideration of the excess specific heat capacity provides significant advantages for the characterisation of the slight dissolution and precipitation reactions in contrast to heat flow. Evaluating the excess specific heat capacity, sample heat flow (\dot{Q}_{sample}) and baseline heat flow ($\dot{Q}_{\text{baseline}}$) have to be subtracted (Figure 3a,d). The remaining zero-level curvature was corrected by subtracting a third degree polynomial (see Figure 3b,e) after

normalising through sample mass (m) and scan rate (β). This method of calculating the excess specific heat capacity is generally applied to compare different heating rates and different sample masses [18]:

$$c_p = \frac{\dot{Q}_{\text{sample}} - \dot{Q}_{\text{baseline}}}{m \cdot \beta} \quad (1)$$

The zero-level polynomial is fitted to the reaction-free zones. The curve correction should be performed on curves in the same scale. Moreover, the correction should always start on curves with the largest measuring effects due to proper estimation of the curvature. However, this procedure should only be used if it is certain that reactions and reaction-free sections can be distinguished from each other, e.g., by comparing other curves of slightly different heating rates. Nevertheless, this method is a subjective procedure and must be handled with care.

Another important fact during evaluation is shown in Figure 3a,b and 3d,e. Changing the heating rate significantly, e.g., from a constant heating rate to the isothermal soaking at high temperatures, unavoidably leads to heat-flow artefacts. A so-called overshoot peak can be seen depending on the DSC device. These artefacts must be excluded from evaluation.

Subsequently, the resulting de-bended curve can be displayed as a function of temperature (Figure 3c,f). In the course of obtaining the resulting DSC heating curves, the endothermic reactions by definition correspond to the positive number range while the exothermic reactions correspond to the negative number range [18]. The differences between the start isothermal and end isothermal for the PerkinElmer Pyris 1 DSC (Figure 3d) have a greater magnitude than for the Setaram DSC 121 due to the device. Nevertheless, both evaluated excess heat capacity curves ultimately show a similar behaviour, indicating a good comparability of the two DSC devices used.

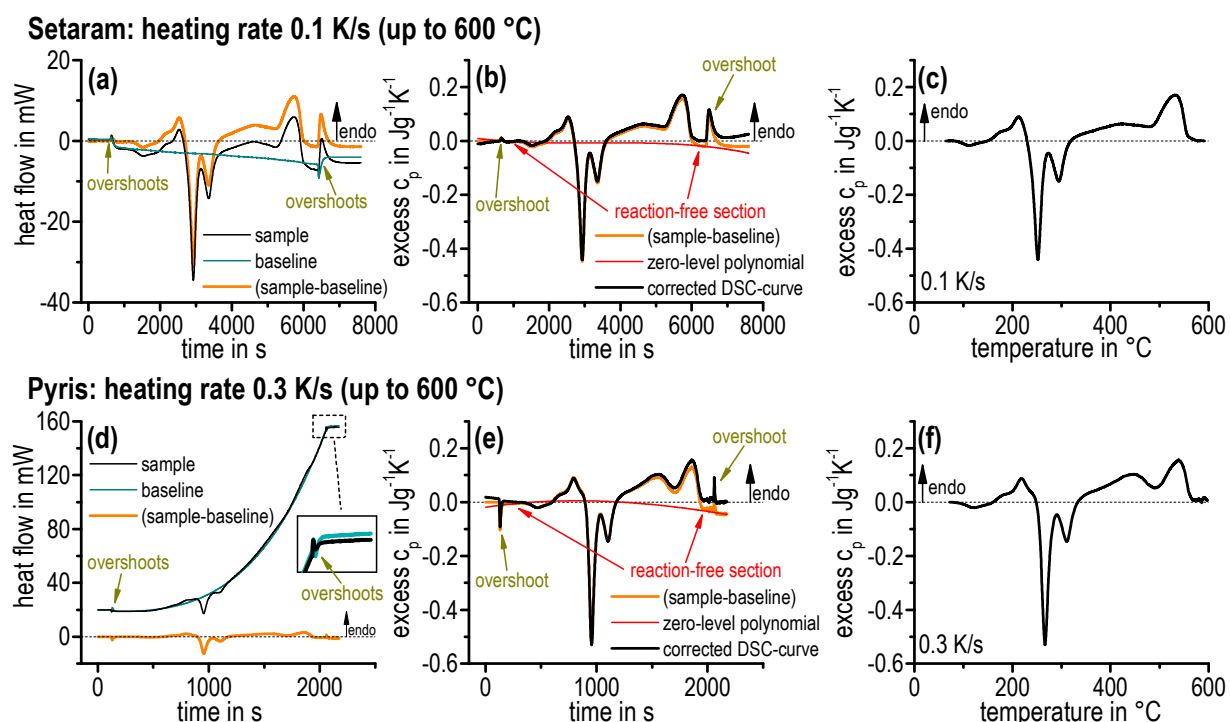


Figure 3. Data handling to obtain an undistorted normalised DSC heating curve by means of data from several devices using the example of EN AW-6181 T4. (a–c) Setaram DSC 121. (d–f) PerkinElmer Pyris 1 DSC.

The generation of continuous heating dissolution diagrams is based on the interpretation of the heating curves (excess c_p as a function of temperature). Due to the overlapping of the dissolution and precipitation reactions, a first approach has been used to determine onset and endset temperatures. The onset and endset temperatures of each precipitation and dissolution reaction respectively is defined by the zero crossing (see Figure 4). The start temperature T_{start} of the first reaction at low temperatures as well as the end temperature T_{end} of the last reaction at the highest temperature could be interpreted as the true start/end temperatures. The temperatures of the individual peaks $T_{start}^{zero\ crossing}$ are simplifications, as overlapping of the reactions is not considered. The superimposed peaks without zero crossing are a special case of evaluating onset temperatures. These temperatures $T_{start}^{low\ point}$ are defined by the minimum value between both peaks. The investigated heating curves as well as the onset and endset temperatures of the different dissolution and precipitation reactions are finally plotted in a temperature–time diagram.

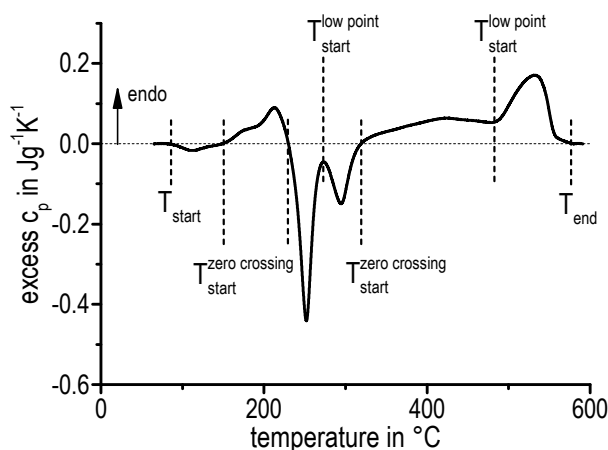


Figure 4. Separation of the individual peaks and defining onset and endset temperatures by using the example of EN AW-6181 T4 heated with 0.1 K/s employing a Setaram DSC 121.

The curve area integration over the whole temperature range provides another quantitative evaluation method for heating curves. The complete enthalpy change distinguishes the amount of existing precipitations in the initial condition just before the heating scan.

3. Results and Discussion

3.1. Excess Specific Heat Capacity Curves

In general, energy has to be supplied if chemical bonds dissociate, which refers to an endothermic reaction. However, exothermic reactions display energy release and indicate that new chemical bonds have been formed. Aluminium alloy dissolutions correspond to endothermic reactions while precipitations belong to exothermic reactions. Endothermic dissolutions are shown by deviations exceeding the zero level, which is displayed as a dashed straight line (see Figure 5). Exothermic precipitations are represented by deviations below the zero level. The interpretation of those measurements might be very difficult. This holds particularly for heating experiments on age-hardened aluminium alloys due to a sequence of alternating endothermic dissolution and precipitation exothermic

reactions. In addition, superposition of different reactions can emerge. As will be shown below, this involves the danger of significant misinterpretation during the quantitative interpretation of such DSC curves.

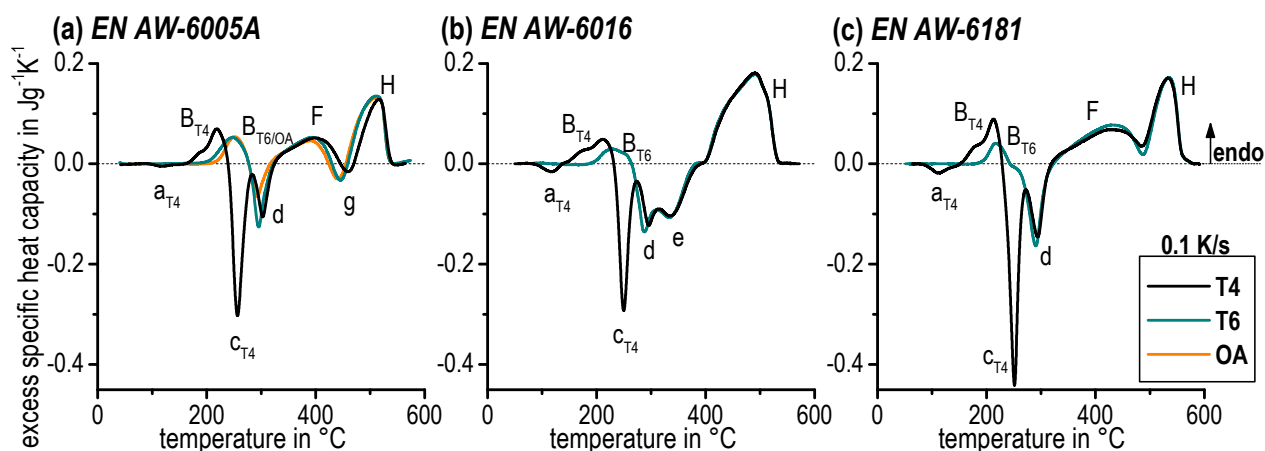


Figure 5. Continuous heating DSC curves at 0.1 K/s for various initial conditions (a) EN AW-6005A – T4, T6 and OA. (b) EN AW-6016 T4 and T6. (c) EN AW-6181 T4 and T6.

Figure 5 shows the heating DSC curves with an exemplary rate of 0.1 K/s for the alloys EN AW-6005A, EN AW-6016, and EN AW-6181 comparing the different initial conditions (T4, T6, and OA). The curves for EN AW-6082 are very similar to EN AW-6005A. The results demonstrate the complexity of the alternating endothermic and exothermic reactions caused by the precipitation sequence [3–5]. Ohmori *et al.* [10,19,20] as well as Birol [21,22] examined the heating behaviour of Al–Mg–Si alloys through DSC and showed a similar alternation of exothermic and endothermic peaks.

The excess specific heat capacity curves of all three alloys for the initial condition (T4) start with an exothermic peak a_{T4} caused by the remaining potential for the formation of clusters, which were not formed during natural ageing before. For a higher content of Mg and Si, two superimposed cluster reactions occur [23]. This could be the reason for the intense peak a_{T4} for the alloys EN AW-6016 T4 and EN AW-6181 T4. The considerably higher content of Si in those alloys causes an accelerated precipitation reaction at lower temperatures in comparison to EN AW-6005A. In addition, it should be noted that there is no exothermic reaction a_{T4} for the alloy EN AW-6082 T4 due to the fact that natural ageing lasted about 2 months, resulting in no remaining potential for cluster formation.

Endothermic reaction B_{T4} appears next and is generally interpreted as the dissolution of clusters [10] and, with respect to natural ageing, as the dissolution of GP zones [24]. The two-step shoulder in peak B_{T4} indicates such overlapping dissolution reactions.

The following exothermic peaks c_{T4} and d are frequently interpreted as precipitation of β'' and β' phases [5,25], respectively, for the T4 condition. A special case is the exothermic peak e of the alloy EN AW-6016 T4. This likely corresponds to the precipitation of B' , which is established in combination with β' as well as being related to a high Si:Mg ratio [25]. The Si:Mg ratio of the alloy EN AW-6016 is more than twice as high as the other investigated aluminium alloys.

It is obvious that the following sequence of the peaks F , g , and H could not be clearly identified for every investigated alloy. The reasons are concurrent dissolution and precipitation reactions – a first hint of the serious problem of quantitative interpretation of such DSC curves. The peaks F , g , and H detected

in EN AW-6005A correspond to the dissolution of the precursor phases such as β'' , β' and B' . The subsequent occurring peak e should correspond to the precipitation of the equilibrium phase β (Mg_2Si). The final peak H corresponds to the final dissolution of all remaining phases, predominantly β (Mg_2Si). F , g , and H heat signals overlap significantly, so that for EN AW-6181 the exothermic effect of β (Mg_2Si) precipitation only appears as a local minimum in a larger endothermic dissolution peak. Even more drastic for EN AW-6016 is the fact that the separation of those three reactions is not possible at all. Thus, for example, peak g could not be labelled for the alloys EN AW-6016 or EN AW-6181 (Figure 5b,c).

The T6 artificially aged conditions have a similar sequence of exothermic and endothermic reactions as the T4 conditions of each alloy. The specifics are non-existent peaks a and c as well as the modified peak B . This is due to the fact that GP zones and β'' had been previously precipitated in the T6 condition. These particles are dissolved at peak B_{T6} . The further sequence correlates with the development of the T4 natural aged condition.

The slightly modified curve of the OA condition of EN AW-6005A compared with the T6 condition shows a less intense reaction d . β' particles were already precipitated at overaged condition, with the result that the potential for forming new precipitations while heating was lower.

It is also conceivable that precipitation transformations occur during heating, e.g., transformation of $\beta' \rightarrow \beta$ or transformation of $pre-\beta'' \rightarrow \beta''$ might occur [25–27].

3.2. Dissolution and Precipitation Behaviour in a Wide Range of Heating Rates

Figure 6 shows selected excess specific heat capacity curves of the alloys EN AW-6005A and EN AW-6016 for the T4 and T6 initial conditions (and OA occasionally).

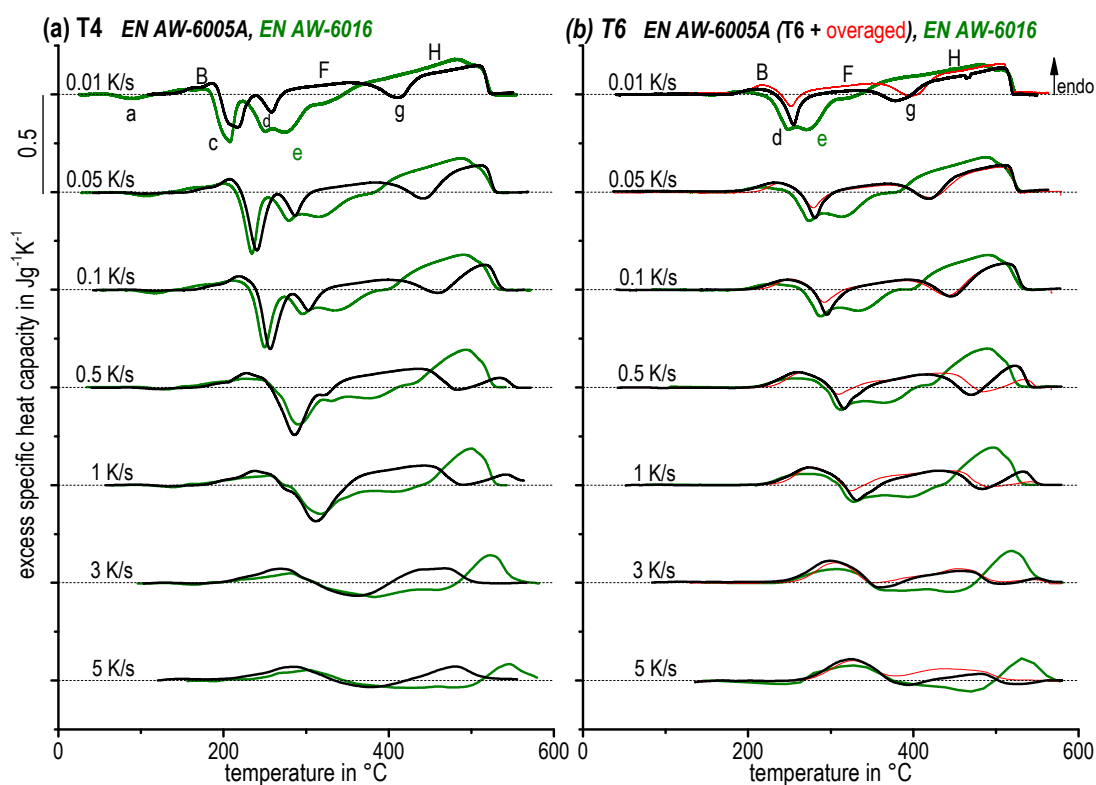


Figure 6. Selected heating curves of EN AW-6005A and EN AW-6016 for the initial conditions (a) T4. (b) T6 (and overaged).

The DSC curves are arranged in descending order of increasing heating rate. In general, the peaks shift to higher temperatures as the heating rate increases. For example, the peak temperature of the precipitation reaction c_{T4} of the alloy EN AW-6005A shifts about 160 K from 220 °C during heating at 0.01 K/s up to 380 °C during heating at 5 K/s. Further, the peak areas decrease as heating rate increases due to the suppression of diffusion processes. The precipitation of clusters (peak *a*) is suppressed completely at higher heating rates. Similar observations has been reported in Pogatscher *et al.* [28]. Higher heating rates lead to an incomplete precipitation sequence. The dissolution and precipitation reactions run earlier at slower heating rates for the alloy EN AW-6016, possibly due to its higher Si content as well as its higher Si:Mg ratio. This holds for both T4 and T6 initial conditions.

Characteristic heating curves for the alloy EN AW-6082 (T4, T6, OA, SA) could be observed in Figure 7 as well as for EN AW-6181 (T4, T6) in Figure 8.

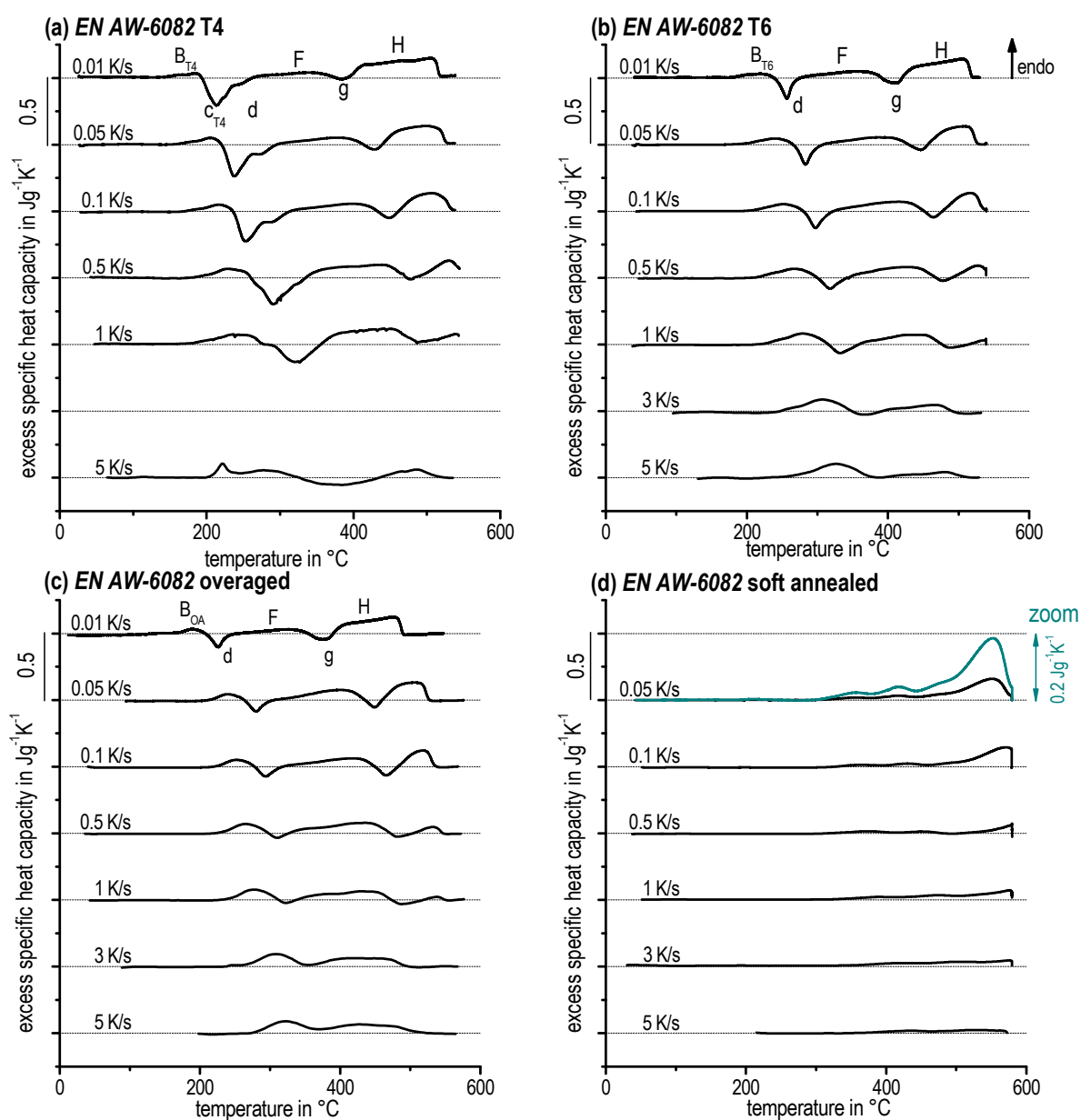


Figure 7. Continuous heating curves for EN AW-6082 with different initial conditions (a) T4. (b) T6. (c) Overaged. (d) Soft annealed.

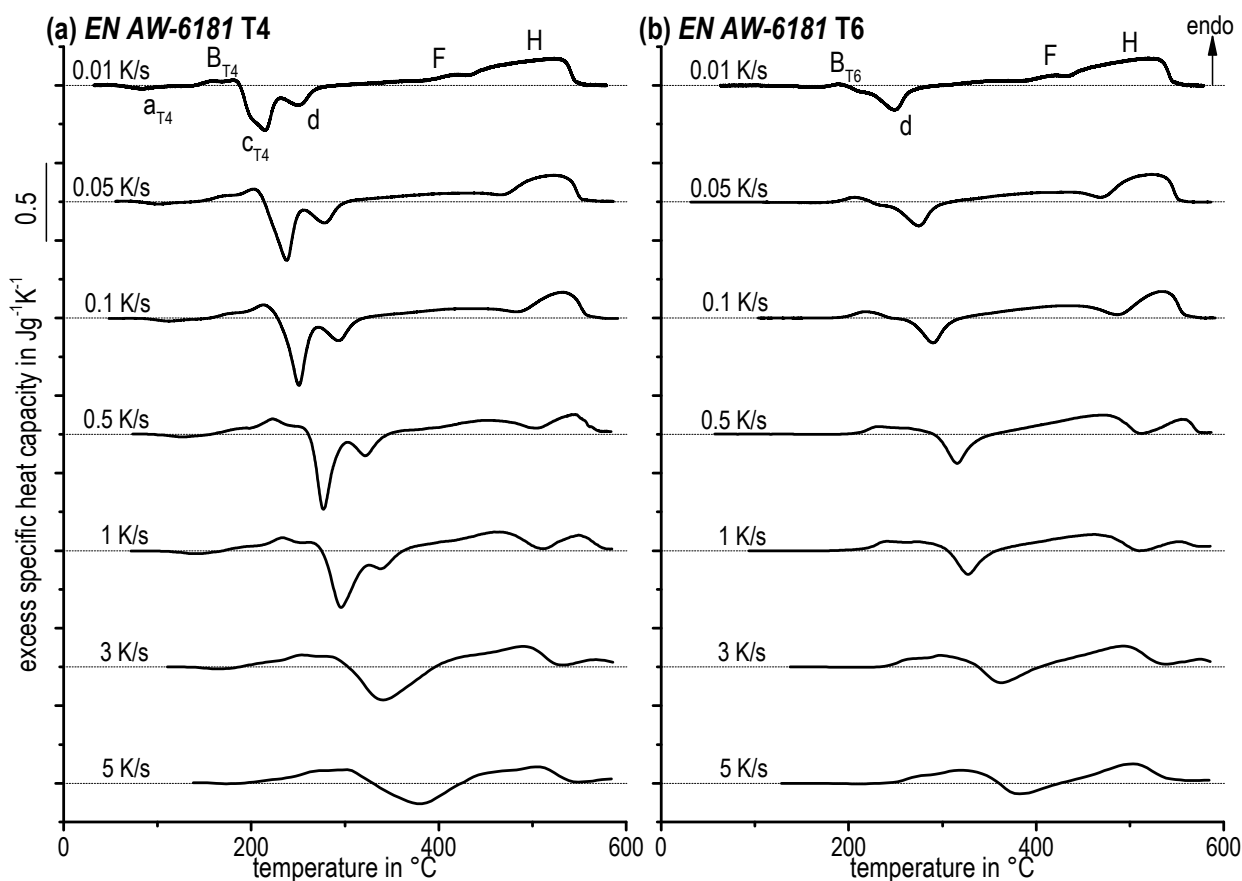


Figure 8. Continuous heating curves for EN AW-6181 with (a) T4 and (b) T6 initial condition.

Both, precipitation and dissolution are diffusion-controlled reactions and therefore it is probable that they are increasingly suppressed as heating rate increases. This can be observed, e.g., following the final dissolution peak *H* over the entire heating rate range. Peak *H* is significantly suppressed as heating rate increases. Nevertheless, e.g., the precipitation peaks *c* and *d* of the T4 initial state seem to increase their peak area as heating rate increases. However, the underlying reactions must be suppressed. The seeming increase of the related peak areas can only be ascribed to changes in the degree of overlapping by endo- and exothermic reactions. It seems possible that the kinetic shifts in temperature are different. Hence, a different shift in temperature of superimposed dissolution and precipitation will lead to different peak ratios. Another possible explanation is that the kinetics of precipitation reactions is slower compared to the kinetics of dissolution reactions. This is because precipitation requires long-range diffusion as opposed to more localised dissolution. Thereby, precipitation reactions might be suppressed more strongly than dissolution reactions. The latter seem to be the case for all investigated conditions here, as at faster heating rates endothermic dissolution reactions clearly dominate the DSC curves.

Therefore, these overlapping and superposition issues imply that evaluation of kinetic parameters, e.g., for precipitation reactions based on DSC heating curves, must be handled with care. Some of the evaluation methods for kinetic parameters, such as the Kissinger method, utilise a single peak for evaluation—which, based on the above results, obviously brings along the danger of misinterpretation. Moreover, all methods for evaluating the kinetic data from DSC heating curves are based on the assumption that the transformed fraction of alloying elements is constantly independent of the varying heating rates [14,15,29]. The basic assumption also does not hold—in particular for a variation of heating

rates in a wide dynamic range. This leads to the future task of developing new methods for the evaluation of kinetic parameters. That task might be solved by kinetic modelling. Some available models even allow the combination of both precipitation and dissolution to model the whole DSC heating curve from room temperature up to the solvus temperature (e.g., [30–34]).

In Figure 9, selected heating curves for alloy EN AW-6005A in the SA initial condition are plotted. During heating after soft annealing, only dissolution reactions occur. During soft annealing, nearly all alloying elements will precipitate predominantly to incoherent β (Mg_2Si) particles, but also to a minor fraction of semi-coherent β' and/or B' precipitates [35]. Such precipitations will dissolve during heating. For a heating rate of 0.05 K/s the dissolution is probably just completely finished at 580 °C—it can be seen in Figure 9 that the excess c_p beyond the final dissolution peak just drops back to zero. At least for the faster heating rates investigated, the dissolution reaction is incomplete. Thus, a critical heating rate applied at a certain temperature for complete dissolution exists. After faster heating to this particular temperature, additional soaking will be needed to solve all relevant alloying elements. Alloy EN AW-6082 was also investigated after soft annealing (see Figure 7d).

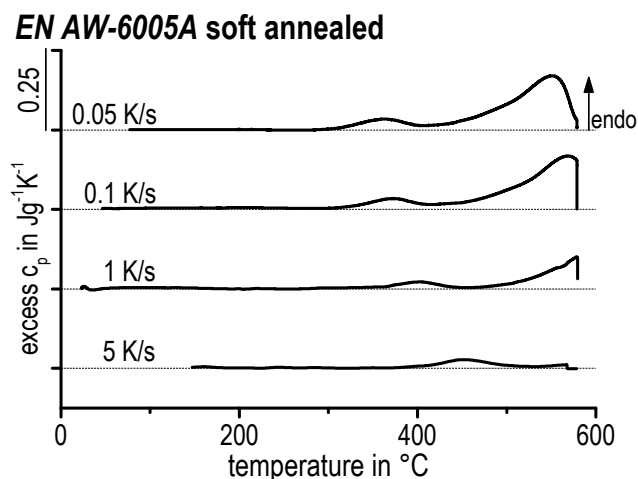


Figure 9. Selected heating curves of EN AW-6005A for the SA initial condition.

3.3. Continuous Heating Dissolution Diagrams

By entering the different start and end temperatures of the dissolution and precipitation reactions together with the varying heating curves in a temperature–time diagram, continuous heating dissolution diagrams for a wide range of heating rates could be created. Figure 10 displays the diagrams of all investigated Al–Mg–Si alloys for the T4 initial condition. These diagrams allow estimation of corresponding temperatures for dissolution or precipitation reactions during heating rates of 0.01 to 5 K/s and make these data available for heat treatment shops.

It should be mentioned again that these start temperatures were qualified by zero crossing (partial local minimum) of the DSC curves. The very first start temperature of reaction *a* and reaction *B* as well as the final end temperature of reaction *H* are physical true. The start temperatures of all other reactions are influenced by the evaluation method. The continuous heating dissolution diagrams for the T6 initial condition can be seen in Figure 11 as well as for OA and SA alloys EN AW-6005A and EN AW-6082 in Figure 12.

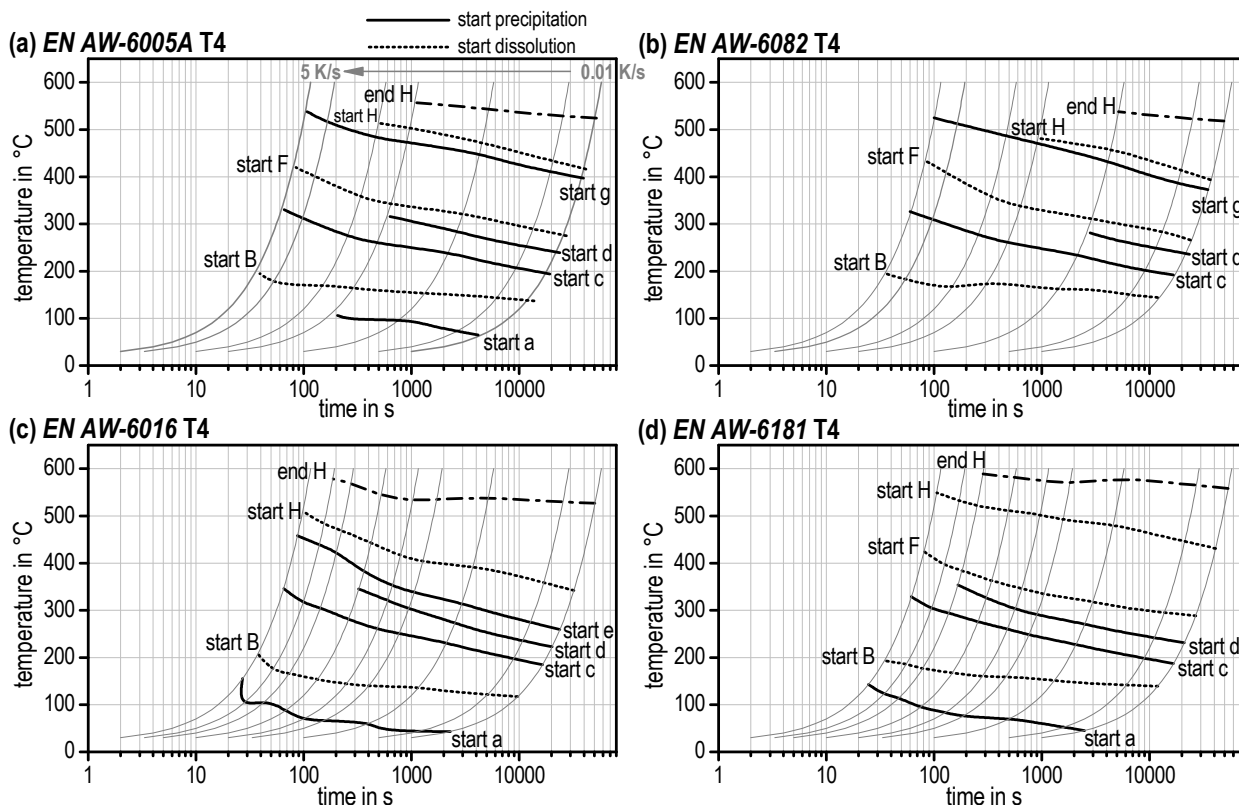


Figure 10. Continuous heating dissolution diagrams for the T4 initial condition of several aluminium alloys (a) EN AW-6005A. (b) EN AW-6082. (c) EN AW-6016. (d) EN AW-6181.

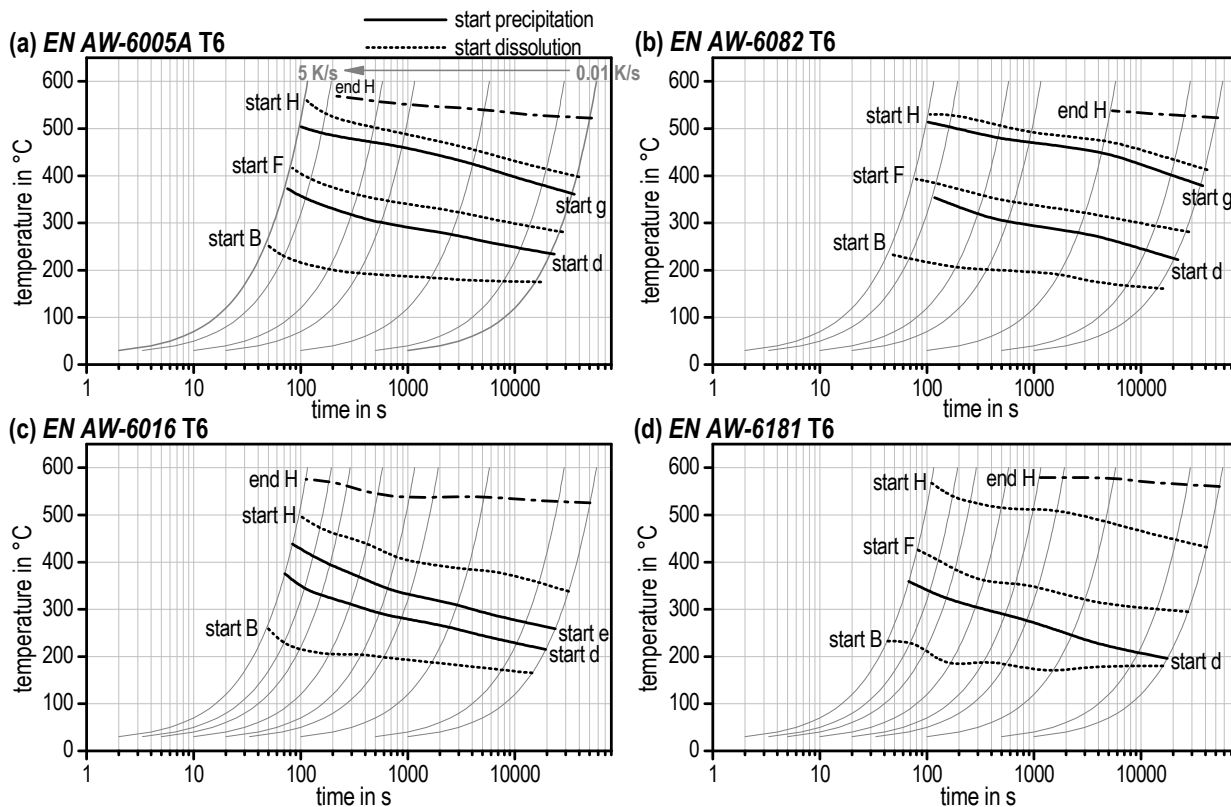


Figure 11. Continuous heating dissolution diagrams for the T6 initial condition of several aluminium alloys (a) EN AW-6005A. (b) EN AW-6082. (c) EN AW-6016. (d) EN AW-6181.

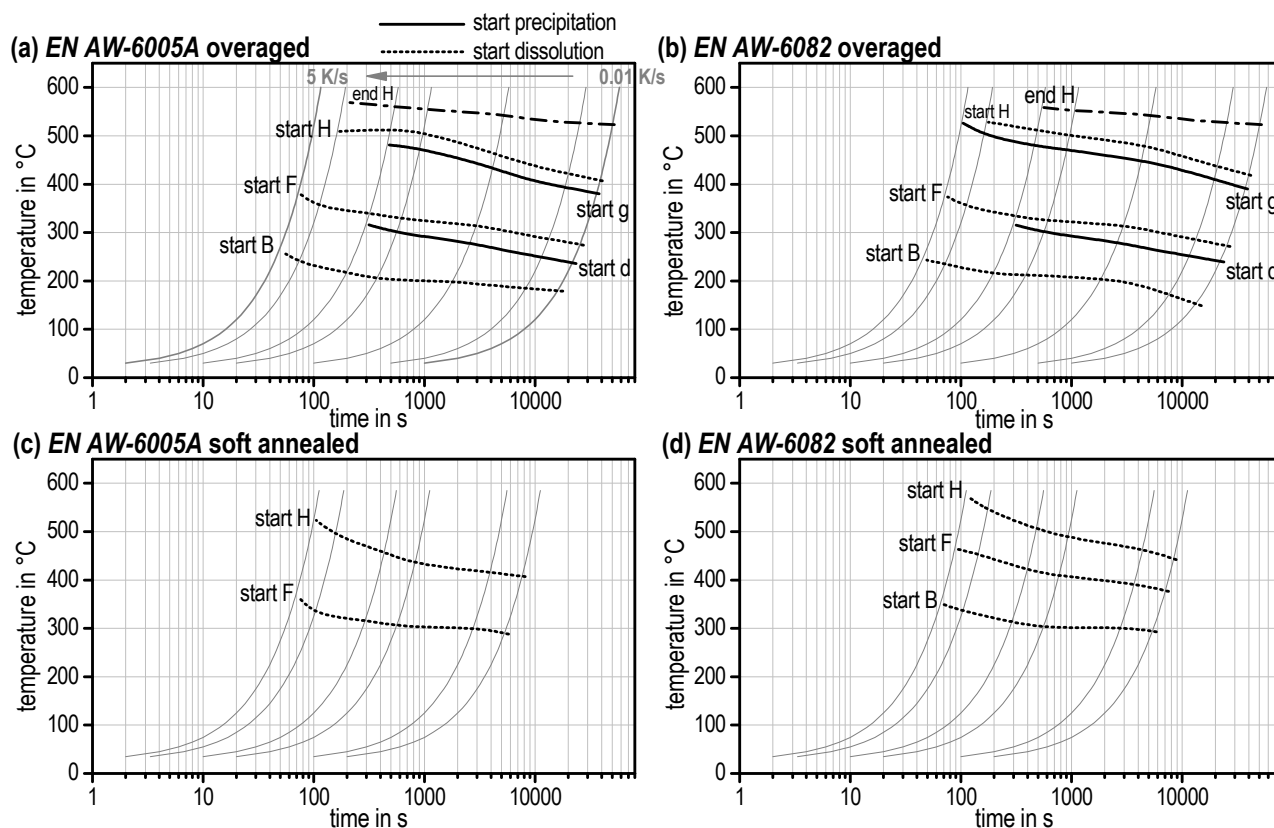


Figure 12. Continuous heating dissolution diagrams for (a) EN AW-6005A overaged; (b) EN AW-6082 overaged; (c) EN AW-6005A soft annealed; (d) EN AW-6082 soft annealed.

One important detail of those diagrams regarding solution annealing shall be explicitly mentioned. Reaction *H* describes the final dissolution of all remaining phases in the aluminium solid solution. It is obvious that the temperatures “start *H*” and “end *H*” are not reached for all alloys, initial microstructures, and heating rates (e.g., no end *H* for EN AW-6082 for T4 and T6 above approx. 0.5 K/s). Here, dissolution has not been completed at the end of the heating step and will continue in the soaking step.

3.4. Enthalpy Change

The integral of the heating curves – covering the full temperature range – gives information about the heat consumed by the dissolution of the pre-existing initial microstructural state. The course of enthalpy change indicates running dissolution and precipitation reactions. The development of enthalpy change during heating with different heating rates is displayed in Figure 13a using the example of EN AW-6005A for T4. Therein the enthalpy levels at temperatures above the solvus temperature are defined as zero. The curves start at approximately -6 J/g (grey line) and run to 0 J/g (dotted line) due to the complete dissolution of all phases. The flatter course of the curves with increasing heating rates shows that more and more precipitation reactions are suppressed. Nevertheless, the total enthalpy change is identical.

The value of the total enthalpy change can be helpful for assessing the initial condition. If heating is performed slowly enough, the initial microstructure will dissolve completely. The characteristic enthalpy change in such cases can be defined as the enthalpy level of the initial condition. The value is expected to be constant as long as all phases are dissolved completely. In this study this holds for the T4, T6, and OA initial conditions. For these conditions, precipitates with a relatively low stability form, such as clusters,

GP zones, β'' and β' . In contrast, soft annealing leads to relatively stable precipitates—predominantly coarse (up to some 10 μm) equilibrium β (Mg_2Si) plates. Those coarse precipitates cannot dissolve in short heating times. Therefore, in the investigated heating rate range of 0.01 to 5 K/s the dissolution of these coarse secondary particles is not finished even at 600 $^\circ\text{C}$ (Figure 13e).

The slower the heating the more will be dissolved and also the higher the values of enthalpy change will be. However, the enthalpy level of the SA initial state remains unknown. It is definitely larger than 15 J/g, as seen in Figure 13e.

Figure 13b–d displays the average enthalpy change of each heating rate indicated by a scatter band. Each heating rate has been repeated two to six times. Therefore, the error bars show the minimum and maximum values of all sample measurements from one heating rate. In addition, the average of the enthalpy changes of all investigated heating rates for any initial condition (T4, T6, and OA) is plotted as a straight line and an extensive scatter band indicating the standard deviation.

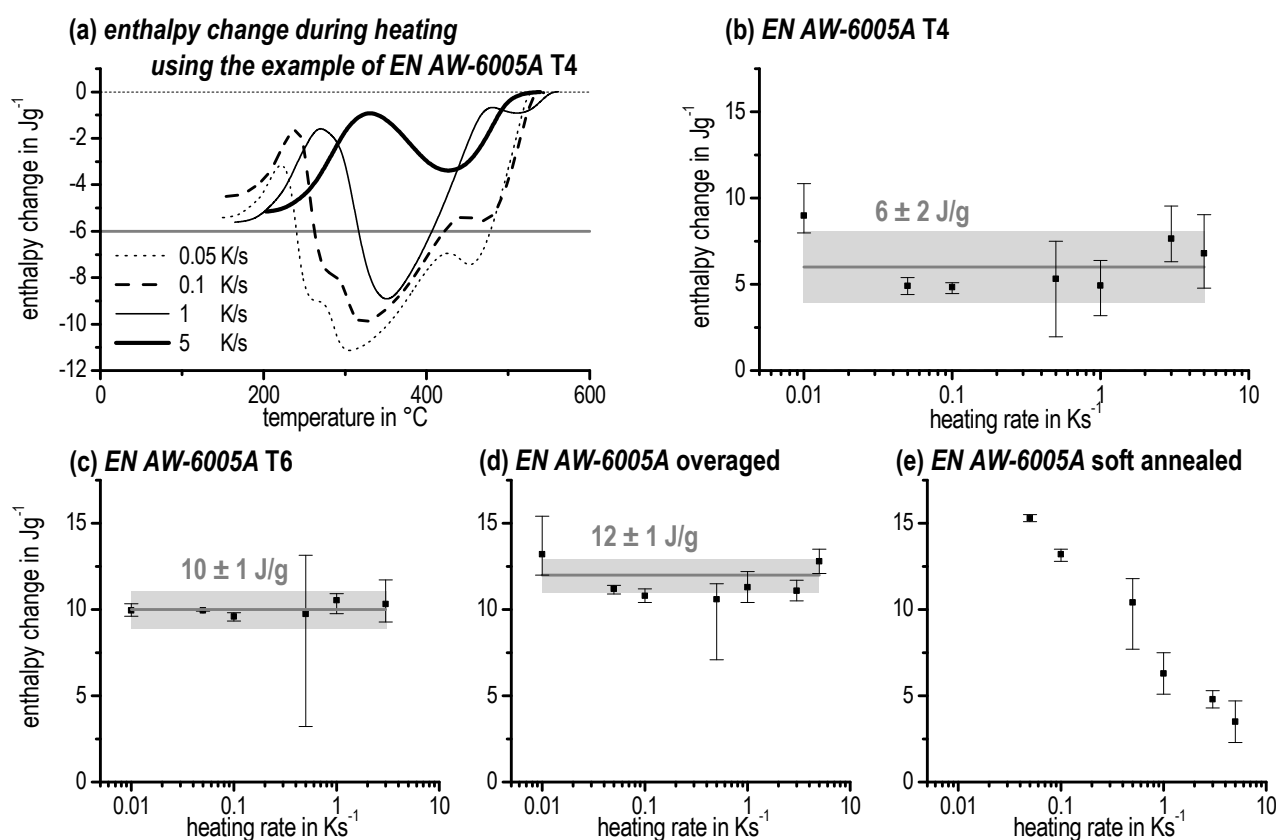


Figure 13. Enthalpy change of EN AW-6005A (a) T4, development of enthalpy change during heating with different heating rates. (b) T4. (c) T6. (d) Overaged. (e) Soft annealed.

Table 3 specifies the enthalpy change of all the investigated aluminium alloys for the T4, T6, and OA initial states: the higher the content of the alloying elements of Mg and Si, the higher the enthalpy changes. Further, the enthalpy changes increase in the order T4, T6, OA due to the fact that more stable precipitates must be dissolved.

In this context, it should also again be pointed out that the elimination of the curvature based on the heat flow curve (see Figure 3b,e) has a significant effect on the enthalpy change. Hence, it is extremely important to proceed very careful with the elimination of bending.

Table 3. Enthalpy change for the specific initial heat treatment states of the investigated aluminium alloys in J/g.

Aluminium Alloy	Enthalpy change in J/g		
	Initial condition		
	T4	T6	OA
EN AW-6005A	6 ± 2	10 ± 1	12 ± 1
EN AW-6082	7 ± 3	10 ± 1	12 ± 1
EN AW-6016	3 ± 1	7 ± 1	-
EN AW-6181	7 ± 1	13 ± 1	-

4. Summary

The dissolution and precipitation behaviour during heating was investigated for four Al–Mg–Si alloys by means of the DSC technique in a wide range of heating rates between 0.01 to 5 K/s. In general, the analysed aluminium alloys had a similar precipitation sequence during heating. The examination of heating curves is complicated, as endothermic and exothermic reactions occur simultaneously and influence each other. The evaluation of the DSC curves for several heating rates exhibits suppressed reactions as well as a shift to higher temperatures as heating rate increases. Several initial conditions were compared and their corresponding enthalpy levels were determined. The results show a strong dependence on the initial condition. Continuous heating dissolution diagrams were created by displaying the times and temperatures of both exothermic and endothermic reactions.

Acknowledgments

The authors gratefully acknowledge the partial funding of this work by the German Research Foundation (DFG), project KE616/19-1, in the framework of the Priority Program 1640 “Joining by Plastic Deformation”. Johannes Zülöw is acknowledged for his help with the DSC experiments.

Author Contributions

The measurements and evaluations were performed by Julia Osten. All authors contributed to the discussion of the results. The manuscript was written by Julia Osten, Benjamin Milkereit, Christoph Schick, and Olaf Kessler. All authors have given their approval for the final version of the manuscript.

Conflicts of Interest

The authors declare no conflict of interest.

References

1. Merklein, M.; Johannes, M.; Lechner, M.; Kuppert, A. A review on tailored blanks—Production, applications and evaluation. *J. Mater. Process. Technol.* **2014**, *214*, 151–164.
2. Osten, J.; Söllig, P.; Reich, M.; Kalich, J.; Füssel, U.; Keßler, O. Softening of high-strength steel for laser assisted clinching. *Adv. Mater. Res.* **2014**, *966–967*, 617–627.

3. Dutta, I.; Allen, S.M. A calorimetric study of precipitation in commercial aluminium alloy 6061. *J. Mater. Sci. Lett.* **1991**, *10*, 323–326.
4. Takeda, M.; Ohkubo, F.; Shirai, T.; Fukui, K. Precipitation behaviour of Al–Mg–Si ternary alloys. *Mater. Sci. Forum* **1996**, *217-222*, 815–820.
5. Edwards, G.A.; Stiller, K.; Dunlop, G.L.; Couper, M.J. The precipitation sequence in Al–Mg–Si alloys. *Acta Materialia* **1998**, *46*, 3893–3904.
6. Gupta, A.K.; Lloyd, D.J.; Court, S.A. Precipitation hardening in Al–Mg–Si alloys with and without excess Si. *Mater. Sci. Eng. A* **2001**, *316*, 11–17.
7. Bryant, J.D. The effects of preaging treatments on aging kinetics and mechanical properties in AA6111 aluminum autobody sheet. *Metall. Mater. Trans. A* **1999**, *30*, 1999–2006.
8. Matsuda, K.; Ikeno, S.; Terayama, K.; Matsui, H.; Sato, T.; Uetani, Y. Comparison of precipitates between excess Si-type and balanced-type Al–Mg–Si alloys during continuous heating. *Metall. Mater. Trans. A* **2005**, *36*, 2007–2012.
9. Afify, N.; Gaber, A.; Mostafa, M.S.; Abbady, G. Influence of Si concentration on the precipitation in Al-1 at.% Mg alloy. *J. Alloys Compd.* **2008**, *462*, 80–87.
10. Ohmori, Y.; Doan, L.C.; Nakai, K. Ageing processes in Al–Mg–Si alloys during continuous heating. *Mater. Trans.* **2002**, *43*, 246–255.
11. Gaber, A.; Ali, A.M.; Matsuda, K.; Kawabata, T.; Yamazaki, T.; Ikeno, S. Study of the developed precipitates in Al–0.63Mg–0.37Si–0.5Cu (wt.%) alloy by using DSC and TEM techniques. *J. Alloys Compd.* **2007**, *432*, 149–155.
12. Chen, S.P.; Mussert, K.M.; van der Zwaag, S. Precipitation kinetics in Al6061 and in an Al6061-alumina particle composite. *J. Mater. Sci.* **1998**, *33*, 4477–4483.
13. Ghosh, K.S.; Das, K.; Chatterjee, U.K. Kinetics of Solid-State Reactions in Al–Li–Cu–Mg–Zr Alloys from Calorimetric Studies. *Metall. Mater. Trans. A* **2007**, *38*, 1965–1975.
14. Starink, M.J. The determination of activation energy from linear heating rate experiments: A comparison of the accuracy of isoconversion methods. *Thermochim. Acta* **2003**, *404*, 163–176.
15. Starink, M.J. Analysis of aluminium based alloys by calorimetry: quantitative analysis of reactions and reaction kinetics. *Int. Mater. Rev.* **2004**, *49*, 191–226.
16. Höhne, G.W.H.; Glöggler, E. Some peculiarities of the DSC-2/-7 (Perkin-Elmer) and their influence on accuracy and precision of the measurements. *Thermochim. Acta* **1989**, *151*, 295–304.
17. Milkereit, B.; Kessler, O.; Schick, C. Recording of continuous cooling precipitation diagrams of aluminium alloys. *Thermochim. Acta* **2009**, *492*, 73–78.
18. Höhne, G.; Hemminger, W.; Flammersheim, H.-J. *Differential Scanning Calorimetry: An Introduction for Practitioners*, 2nd ed.; Springer: Berlin, Germany, 2003.
19. Doan, L.C.; Ohmori, Y.; Nakai, K. Precipitation and dissolution reactions in a 6061 aluminum alloy. *Mater. Trans.* **2000**, *41*, 300–305.
20. Ohmori, Y.; Doan, L.C.; Matsuura, Y.; Kobayashi, S.; Nakai, K. Morphology and crystallography of β -Mg₂Si precipitation in Al–Mg–Si alloys. *Mater. Trans.* **2001**, *42*, 2576–2583.
21. Birol, Y. DSC Analysis of the precipitation reactions in the alloy AA6082. *J. Therm. Anal. Calorim.* **2006**, *83*, 219–222.
22. Birol, Y. DSC analysis of the precipitation reaction in AA6005 alloy. *J. Therm. Anal. Calorim.* **2008**, *93*, 977–981.

23. Kim, S.N.; Kim, J.H.; Tezuka, H.; Kobayashi, E.; Sato, T. Formation behaviour of nanoclusters in Al–Mg–Si alloys with different Mg and Si concentration. *Mater. Trans.* **2013**, *54*, 297–303.
24. Murayama, M.; Hono, K. Pre-precipitate clusters and precipitation processes in Al–Mg–Si alloys. *Acta Mater.* **1999**, *47*, 1537–1548.
25. Polmear, I.J. *Light Alloys: From Traditional Alloys to Nanocrystals*, 4th ed.; Butterworth-Heinemann: Oxford, UK, 2005.
26. Marioara, C.D.; Andersen, S.J.; Jansen, J.; Zandbergen, H.W. The influence of temperature and storage time at RT on nucleation of the β'' phase in a 6082 Al–Mg–Si alloy. *Acta Materialia* **2003**, *51*, 789–796.
27. Tsao, C.-S.; Chen, C.-Y.; Jeng, U.-S.; Kuo, T.-Y. Precipitation kinetics and transformation of metastable phases in Al–Mg–Si alloys. *Acta Materialia* **2006**, *54*, 4621–4631.
28. Pogatscher, S.; Antrekowitsch, H.; Uggowitzner, P.J. Influence of starting temperature on differential scanning calorimetry measurements of an Al–Mg–Si alloy. *Mater. Lett.* **2013**, *100*, 163–165.
29. Starink, M.J. Activation energy determination for linear heating experiments: Deviations due to neglecting the low temperature end of the temperature integral. *J. Mater. Sci.* **2007**, *42*, 483–489.
30. Lang, P.; Povoden-Karadeniz, E.; Falahati, A.; Kozeschnik, E. Simulation of the effect of composition on the precipitation in 6xxx Al alloys during continuous-heating DSC. *J. Alloys Compd.* **2014**, *612*, 443–449.
31. Falahati, A.; Povoden-Karadeniz, E.; Lang, P.; Warczok, P.; Kozeschnik, E. Thermo-kinetic computer simulation of differential scanning calorimetry curves of AlMgSi alloys. *Int. J. Mater. Res.* **2010**, *101*, 1089–1096.
32. Falahati, A.; Wu, J.; Lang, P.; Ahmadi, M.R.; Povoden-Karadeniz, E.; Kozeschnik, E. Assessment of parameters for precipitation simulation of heat treatable aluminum alloys using differential scanning calorimetry. *Trans. Nonferr. Met. Soc.* **2014**, *24*, 2157–2167.
33. Hersent, E.; Driver, J.H.; Piot, D. Modelling differential scanning calorimetry curves of precipitation in Al–Cu–Mg. *Scripta Materialia* **2010**, *62*, 455–457.
34. Khan, I.N.; Starink, M.J. Microstructure and strength modelling of Al–Cu–Mg alloys during non-isothermal treatments Part 1—Controlled heating and cooling. *Mater. Sci. Technol.* **2008**, *24*, 1403–1410.
35. Milkereit, B.; Wanderka, N.; Schick, C.; Kessler, O. Continuous cooling precipitation diagrams of Al–Mg–Si alloys. *Mater. Sci. Eng. A* **2012**, *550*, 87–96.

[BM6] Milkereit B, Starink MJ:

Quench sensitivity of Al-Mg-Si alloys: A model for linear cooling and strengthening.

Materials & Design 76 (2015) 117–129.

Benjamin's contributions: I designed the experimental part, supervised (and partially did) the DSC work, plotted the data, participated in the results discussion and partially wrote and revised the manuscript.

Quench sensitivity of Al-Mg-Si alloys: A model for linear cooling and strengthening

B. Milkereit^{1,2,3,*}, M.J. Starink¹

benjamin.milkereit@uni-rostock.de; M.J.Starink@soton.ac.uk

¹Materials Research Group, Engineering Sciences, University of Southampton,
SO17 1BJ Southampton

²Chair of Materials Science, Faculty of Marine Technology and Mechanical Engineering, University of
Rostock, 18051 Rostock

³Polymer Physics Group, Institute of Physics, University of Rostock, 18051 Rostock

*corresponding author: Telephone: 0049-381-498-9486; Fax: 0049-381-498-9472

Abstract

This work studies the quench-induced precipitation during continuous cooling of five Al-Mg-Si alloys over a wide range of cooling rates of 0.05 - 2·10⁴ K/min using Differential Scanning Calorimetry (DSC), X-ray diffraction, optical- (OM), transmission electron- (TEM) and scanning electron microscopy (SEM) plus hardness testing. The DSC data shows that the cooling reactions are dominated by a high temperature reaction (typically 500 °C down to 380 °C) and a lower temperature reaction (380 °C down to 250 °C), and the microstructural analysis shows they are β -Mg₂Si phase formation and B' phase precipitation, respectively. A new, physically-based model is designed to model the precipitation during the quenching as well as the strength after cooling and after subsequent age hardening. After fitting of parameters, the highly efficient model allows to predict accurately the measured quench sensitivity, the volume fractions of quench induced precipitates, enthalpy changes in the quenched sample and hardness values. Thereby the model can be used to optimise alloy and/or process design by exploiting the full age hardening potential of the alloys choosing the appropriate alloy composition and/ or cooling process. Moreover, the model can be implemented in FEM tools to predict the mechanical properties of complex parts after cooling.

Keywords

Al-Mg-Si alloys; quench sensitivity; Differential Scanning Calorimetry (DSC); precipitation kinetics; Modelling

1 Introduction

In recent years substantial progress has been reported in modelling of diffusion controlled phase transformations and the modelling of the thermodynamics of commercially important complex alloy systems, including first principles modelling. In this paper we will investigate how this progress can be used to provide a computationally efficient new model for a technically important process: quench sensitivity of heat treatable aluminium alloys. In heat treatable Al-based alloys precipitation hardening is the dominant strengthening mechanism. For most commonly used alloys such as the Al-Mg-Si (6xxx) and the Al-Zn-Mg-(Cu) (7xxx) alloys, age hardening response can be seriously affected by the cooling rate from solution annealing (e. g. [1–9]; and also toughness can be reduced due to reduced cooling rate [10]. To achieve optimal mechanical properties, precipitation during quenching must be fully suppressed, and this is achieved only if the alloy is cooled with the upper critical cooling rate or faster (e. g. [4,8,7]). However, fast cooling can induce residual stresses (e. g. [11–13]), and hence, in order to obtain an optimal balance between strength and residual stresses / distortion, cooling from solution annealing should be done with the upper critical cooling rate or slightly faster. Nevertheless, in some parts with varying wall dimensions it might be difficult to realise the same cooling rate at every location. Nowadays it is relatively easy to calculate the temperature developments in such parts at every location by finite element modelling (e. g. [12]). However, for prediction of the mechanical properties at varying cooling rates, no models that incorporate reliable thermodynamic and kinetic models have hitherto been published, nor have any models been tested using extensive experimental data. The present work addresses these issues in two ways: improved models and model verification through comparison with much increased and more detailed experimental results.

Differential Scanning Calorimetry (DSC) is frequently used for investigation of diffusion-controlled precipitation reactions (e.g. [14,3,15,8,16,17]). In recent years significant improvements were obtained in the in situ investigation of the precipitation processes during cooling of Al alloys from solution annealing through the development of high sensitivity in-situ DSC techniques [18–21]. These technically and metrological sound DSC methods allow to measure the enthalpy changes over the whole cooling rate range of technical and scientific interest: from slow cooling with phase transformation close to equilibrium conditions up to cooling rates near the upper critical cooling rate. In the present work, the enthalpy change during cooling is used as basis for the modelling.

We will in this work derive a model for precipitation during quenching and subsequent ageing of Al-Mg-Si alloys and combine that with a model for precipitation hardening, to provide predictions of strength and hardness for cooling rates that stretch over 6 decades. In the model we will incorporate very recent progress in first principles modelling of the phases in the Al-Mg-Si system results [22] and very recent models for precipitation kinetics [23,24]. The model is tested against an extensive set of experimental data.

2 Experimental

2.1 Investigated alloys

In this work, five different 6xxx alloys covering a wide range of compositions were investigated. The alloys are AA6063, AA6005A, and three alloys within the composition range of AA6082, representing variants with low Mg and Si content (AA6082_{low}), typical (medium) Mg and Si content (AA6082_{typ}) and high Mg and Si content (AA6082_{high}). The chemical compositions of the investigated batches are given in **Table 1**. All alloys have been cast, homogenised and subsequently extruded. They were received as extruded profiles, from which samples were cut for further heat treatment and investigations. We combine a very large amount of new and existing experimental data (about 600 DSC experiments, about 500 hardness tests, microstructural analysis of more than 100 samples).

Table 1: Chemical composition of investigated alloys (mass fractions in %) obtained by optical emission spectroscopy (OES) analysis, with experiments performed. cDSC = cooling DSC, hDSC = heating DSC

Alloys	Si	Fe	Cu	Mn	Mg	Cr	Zn	Ti	Experiments
AA6063	0.5	0.19	0.02	0.03	0.47	0.005	0.03	0.013	TEM, cDSC, SEM, HV, OM, XRD
AA6005A	0.68	0.2	0.01	0.11	0.57	0.04	0.01	0.018	TEM, cDSC, SEM, HV, OM, XRD
AA6082 _{low}	0.73	0.22	0.05	0.48	0.61	0.003	0.009	0.02	cDSC, SEM, HV, OM, XRD
AA6082 _{typ}	1.01	0.19	0.03	0.44	0.68	0.04	0.02	0.01	TEM, hDSC, HV
AA6082 _{high}	1.23	0.2	0.09	0.65	1.05	0.2	0.05	0.03	cDSC, SEM, HV, OM, XRD

2.2 Heat treatment, Differential Scanning Calorimetry and Hardness Testing

The main focus of this work is the quenching step within the age hardening heat treatment procedure. The basic scheme of the experimental applied heat treatments is shown Fig. 1. The solution annealing at 540 °C for 20 min was followed by linear cooling with cooling rates varying in a wide range (0.05 K/min – 2·10⁴ K/min). Differential Scanning Calorimetry (DSC), covering cooling rates from 0.1 K/min to 375 K/min, are realised by employing three different types of DSC devices: Setaram 121 DSC 0.1-6 K/min; Mettler-Toledo 823 DSC 6-30 K/min; PerkinElmer Pyris 1 DSC 30-375 K/min. Samples were measured versus a thermodynamic inert reference sample of pure aluminium. The baseline measurements were performed measuring pure Al samples in both DSC-microfurnaces. For each measurement one corresponding baseline was measured, and excess specific heat capacity curves reflecting the enthalpy

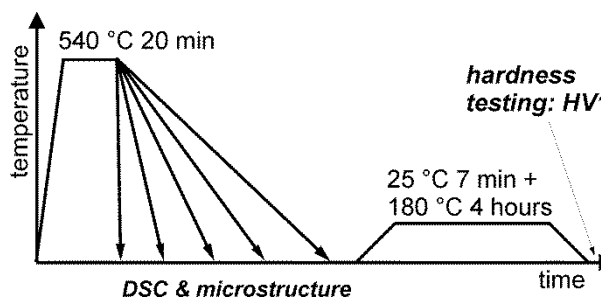


Fig. 1: Temperature-Time scheme of experiments.

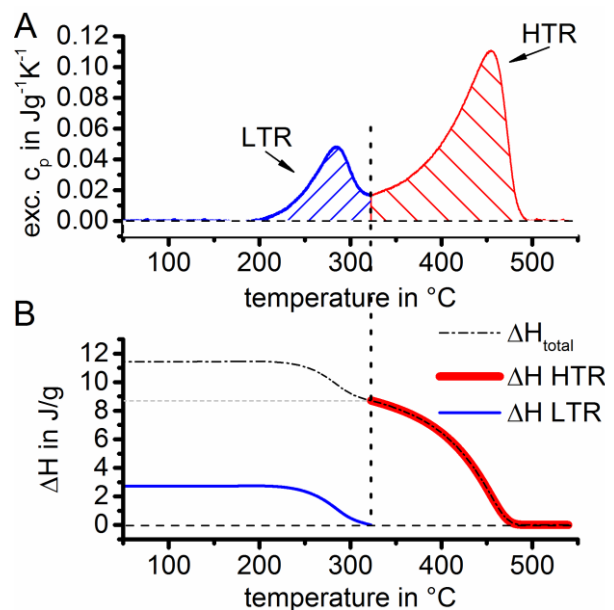


Fig. 2: Schematic evaluation of DSC cooling curves by sections wise integration. (A) DSC curve separated in high- and low-temperature-reactions (HTR / LTR). (B) Related integral curves for corresponding temperature intervals.

changes due to reactions were determined (Fig. 2A). The specific precipitation enthalpy was evaluated by integrating the excess specific heat capacity curves and precipitation enthalpies of partially overlapping precipitation peaks was evaluated using the minimum heat flow as indicated in Fig. 2B (for further details see [18]).

Samples for hardness testing were cooled to room temperature at constant rates of 0.05 K/min – $2 \cdot 10^4$ K/min, and, following a brief 7 min ageing at room temperature, they were artificial aged at 180 °C for 4 hours.

To achieve very high controlled cooling rates up to $2 \cdot 10^4$ K/min, heat treatments of additional samples were performed in a Baehr A/D 805 dilatometer. The complete heat treatments of hardness samples were performed either in DSC or dilatometer, thus ensuring a complete control of the entire temperature-time profile. Vickers hardness HV1 (load 1 kg) was tested with a Shimadzu HMV-2E small-force hardness indenter according to ISO 6507-1 applying an indentation duration of 10 s. At least six indentations per sample were performed. In addition, selected samples for microstructure investigation on AA6082_{typ} were solution annealed and subsequently cooled using procedures approximating industrial practice: quenching in room-temperature-water, cooling in slightly moving air and slow air-cooling (in still air). Cooling rates were measured, and at 370 °C the cooling rates were about 400, 3 and 1 K/min, respectively. These samples were all artificially aged after cooling (i.e. a T6 treatment) and prior to microstructure investigation.

2.3 Microstructure analysis

The microstructures of an extensive number of samples from 5 alloys were investigated through optical light microscopy (OM), scanning electron microscopy (SEM), transmission electron microscopy (TEM) and X-ray diffraction (XRD). In this work we present selected, representative results, focussing on the nucleation mechanisms of different quench induced phases as well as on the volume fraction of coarse quench-induced precipitates. Selected SEM and TEM data on one of the alloys was presented previously [7].

The alloys AA6063, AA6005A, AA6082_{low} and AA6082_{high} were analysed by X-ray diffraction (XRD) in a Siemens D5000 X-Ray Diffractometer after very slow cooling with 0.05 K/min. Cu-K α radiation (wavelength 0.15406 nm), prime-aperture gap of 2 mm and a measuring duration of 3.2 to 3.7 s per angle step were used. The angle-step-width was selected as 0.02°.

Samples for OM and SEM were prepared by standard grinding and polishing procedures. Ethanol based lubricants were used. Selected specimens were etched for 20 s in a solution of 4 g potassium permanganate in 100 ml distilled H₂O and 1 g NaHO. After etching an etch-skin remained on the surface, which was removed by careful polishing. As OM a Leica DMI 500 and for SEM a Zeiss SUPRA 25 (operated at 10 kV) were used. TEM foils were obtained by twin-jet electro-polishing (using 25 % nitric acid in methanol at about -30 °C and a voltage of 25 V). Samples were investigated in a Philips CM30 and a JEOL 2000FX TEM, both operated at 300 kV. Structure analysis of selected quench induced phases was performed in SEM with electron backscatter diffraction (EBSD) and in TEM with selected area electron diffraction (SAED). For details of those analyses see [25,7].

The volume fraction of coarse phases formed during cooling was obtained through analysis of OM images using the image analysis software by "dhs-Bilddatenbank", determining the area fractions of coarse phases (see e.g. [26]). For each investigated condition six OM micrographs with low magnification (200x) of polished samples were evaluated. This results in an evaluated area of about 240,000 μm^2 per condition. A minimum grey-scale level is adjusted to obtain areas of quench induced particles. The accuracy of this measurement is estimated to be about 0.1 vol%. Beside quench induced precipitates, a certain amount of coarse Al-Fe-Si-Mn phases are visible in the evaluated OM micrographs. Those phases are formed directly from the melt in a eutectic reaction, and they possess a very similar contrast compared to Mg₂Si (compare differences between those types of precipitates in OM and SEM micrographs in Fig. 6 in section 2.3). When cooling was performed overcritically fast, no quench-induced precipitates are present, and the determined volume fractions in those conditions possess a certain stable level and can directly be related to the fraction of coarse eutectic Al-Fe-Si-Mn precipitates. This constant level fraction may therefore be subtracted from the overall determined volume fractions in order to obtain the volume

fraction of Mg_2Si . In line with this, the amounts of these coarse eutectic Al-Fe-Si-Mn phases are consistent with Scheil Model calculations of solidification.

3 DSC cooling curves and microstructure of selected quench states

3.1 DSC cooling curves

Fig. 3 displays selected DSC cooling curves of A) AA6063, B) AA6005A, C) 6082 with low Mg and Si content (6082_{low}) and D) and 6082 with high Mg and Si content (6082_{high}). The slowest cooling rate is

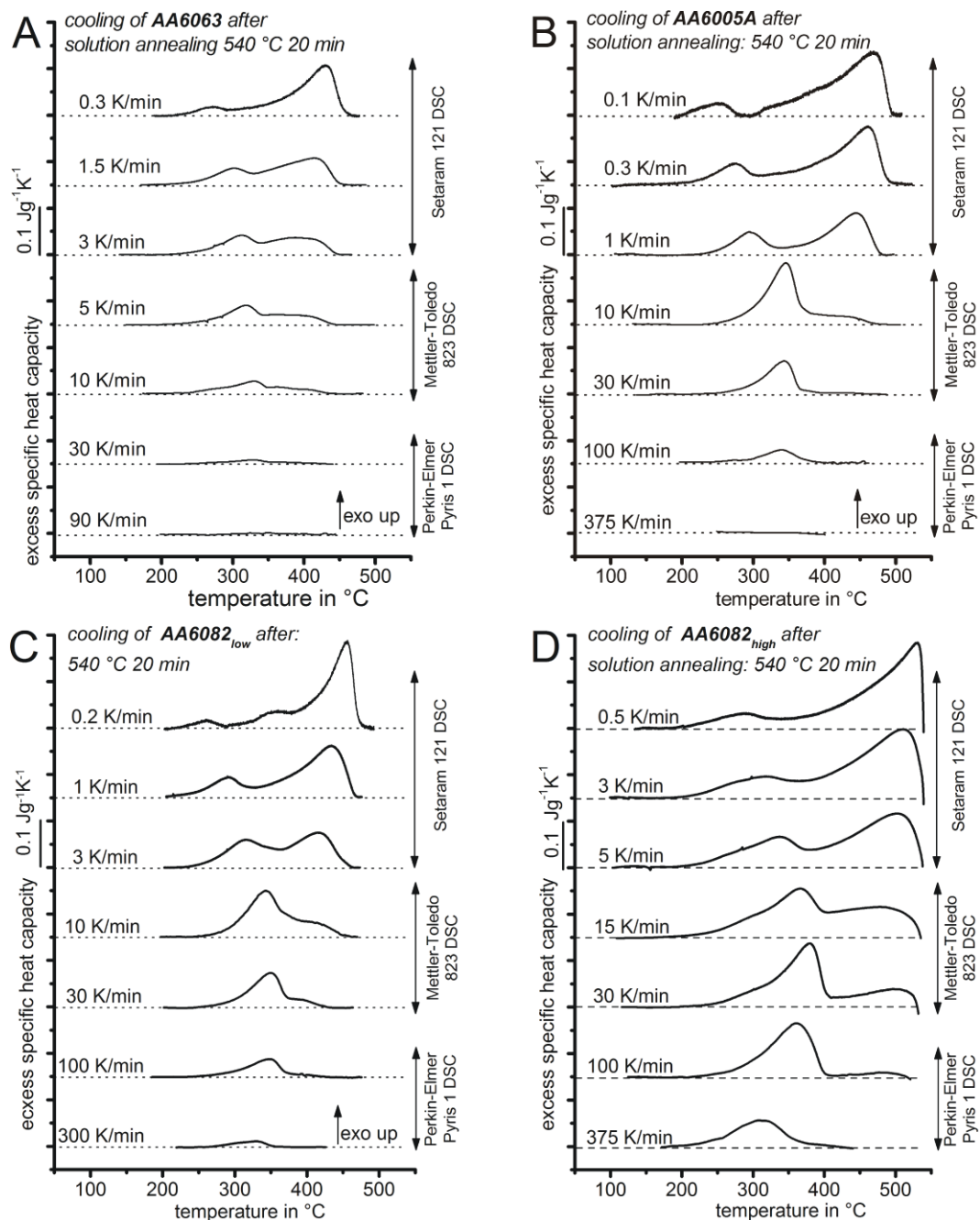


Fig. 3: Selected DSC curves during cooling after solution annealing for A) AA6063, B) AA6005A, C) AA6082_{low}, AA6082_{high}.

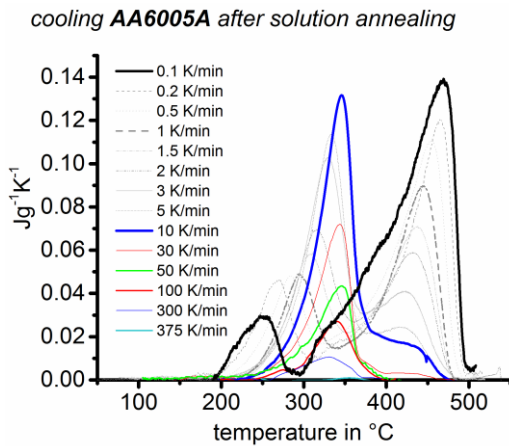


Fig. 4: DSC cooling curves of AA6005A showing the peak development.

plotted on top. For each DSC curve the corresponding zero level is given by a dashed line. As expected, all these DSC cooling curves show only exothermic reactions which are all ascribed to precipitation reactions. In all alloys precipitation during cooling from solution annealing occurs in two main temperature ranges – a high temperature reaction (HTR, typically ~500 down to 380 °C) and a lower temperature reaction (LTR, ~380 down to 250 °C). These two main reactions overlap to some degree, and these phases may also compete for the alloying element atoms in solution. From Fig. 3 and in particular from Fig. 4 one can follow the development of both main precipitation reactions areas which correspond to the specific precipitation enthalpy of the reactions. The evolution of the total enthalpy, of the HTR and the LTR is displayed in Fig. 5. The total reactions are increasingly suppressed with increasing cooling rate and at cooling rates above a certain critical rate no exothermic (precipitation) signal can be detected. Cooling then is fast enough to fully suppress all precipitation reactions. The slowest cooling rate at which precipitation is suppressed completely is alloy specific and named upper critical cooling rate (uCCR). This is the optimal cooling rate for the technological cooling process during the age hardening procedure: it ensures optimal mechanical properties whilst minimising quench-induced residual stresses.

Fig. 4 shows that at cooling rates faster than 30 °K/min, the start of the LTR for AA6005 is about constant at 400 ± 10 °C and this reaction peaks for all cooling rates faster than 10 °K/min at about 320-340 °C. For this alloy, at these cooling rates, the composition of the Al-rich phase at the start of the LTR is Al-0.61at%Si-0.63at%Mg (see section 4 for the method of evaluation), and according to the solvi determined from first principle modelling in [22] this onset temperature is about 90°C below the solvus of the β' phase. Hence this reaction cannot be due to β' phase formation. Instead, the start temperature corresponds closely (within 10 °C) to the solvi of the hexagonal Al_2MgSi_2 phase, the hexagonal $\text{Al}_4\text{Mg}_3\text{Si}_7$ phase as well as the orthorhombic Al-Mg-Si phase [22]. It has been shown that the Mg:Si ratio in the

hexagonal precipitate formed at these temperatures [27,28] is close to 1.15 [27], and hence the dominant reaction is thought to be the formation of this $\text{Al}_4\text{Mg}_6\text{Si}_7$ phase which is termed B'. (For further discussion see Section 6.)

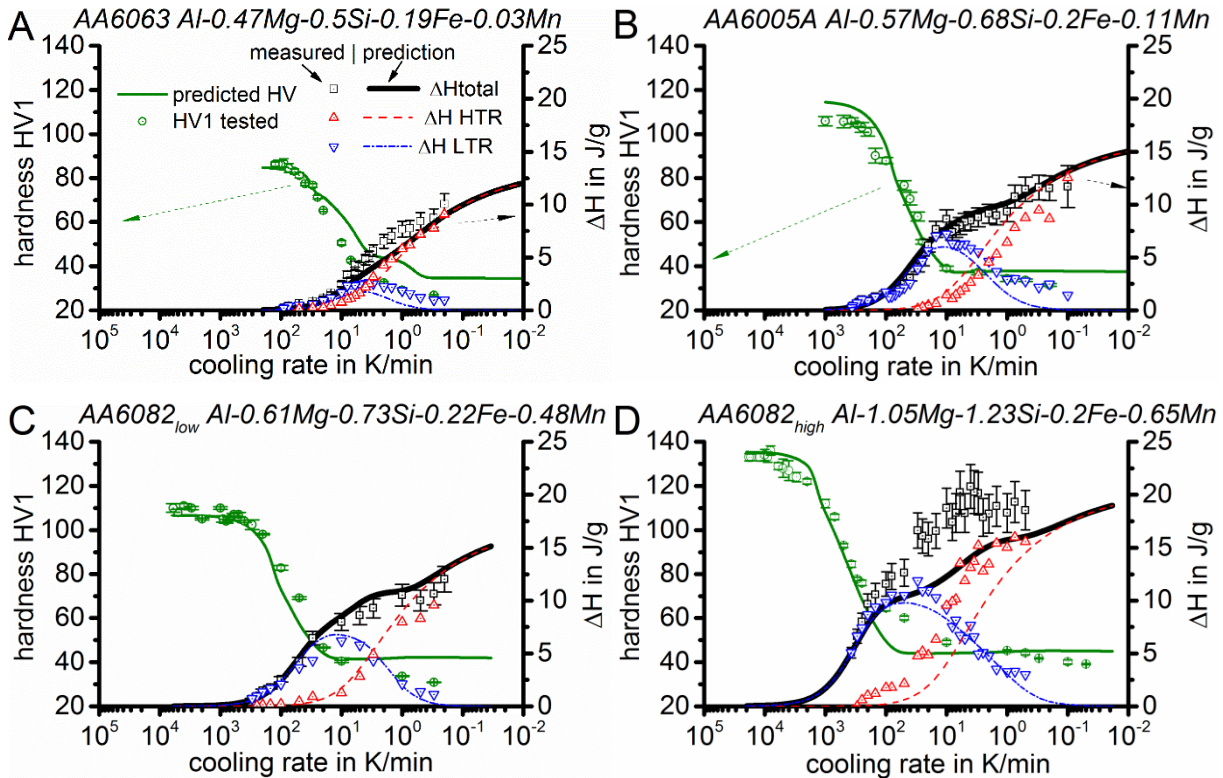


Fig. 5: Comparison of measurement and prediction for specific precipitation enthalpy and hardness after artificial ageing. The specific precipitation enthalpy values are plotted for total reactions (black squares), high-temperature reactions (red triangle tip up) and low-temperature reactions (blue triangle tip down). (A) AA6063, (B) AA6005A, (C) AA6082_{low}, (D) AA6082_{high}.

3.2 Microstructure of quenched samples

The XRD analysis (samples cooled at 0.05 K/min) showed that the diffraction peaks were due to Mg_2Si and the Al-rich phase (from [29]). (Spectra not presented.) This observation combined with the analysis in Section 3.1 shows that the precipitation during cooling of our Al-Mg-Si alloys is dominated by two different phases, Mg_2Si at high temperatures and B' at lower temperatures. The TEM and SEM studies provide further details; they reveal that Mg_2Si precipitates are square monocrystalline plates inside aluminium grains, the thickness of the Mg_2Si plates is about one third of their edge length (coarse dark precipitates in Fig. 6). The LTR are dominated by precipitation of the Mg_2Si -precursor phase B'. For a detailed discussion of phase identification see Section 6.2. TEM confirms that B' phase grows as

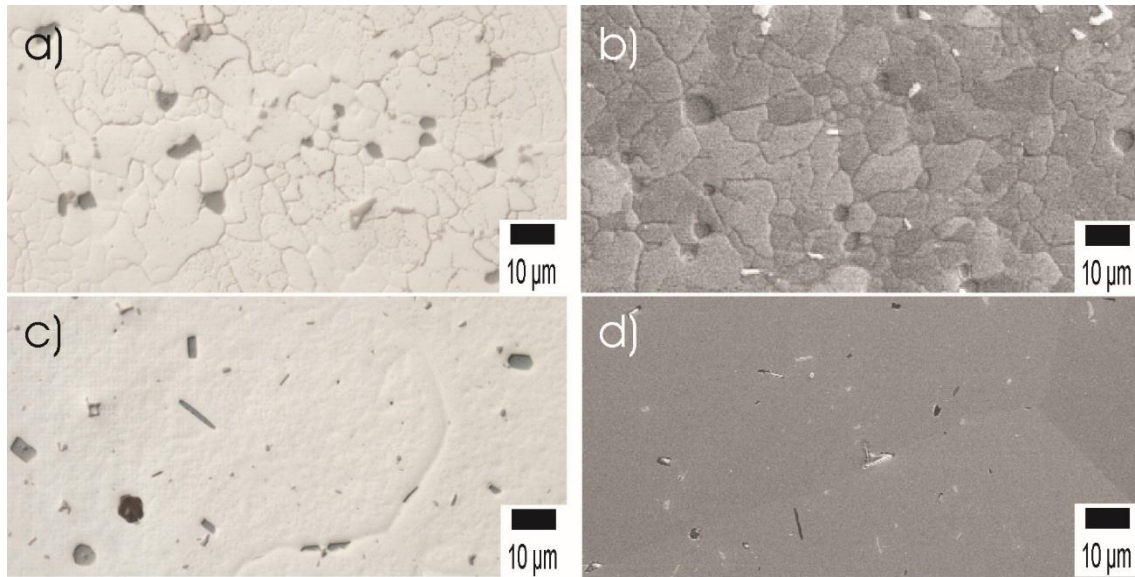


Fig. 6: (a) OM, (b) SEM image of AA6082_{high} after cooling with 0.5 K/min – dark Mg₂Si particles on the grain boundaries possess similar size like grains – no obviously visible intragranular coarse Mg₂Si precipitates. (c) OM image AA6082_{low} (d) SEM image AA6063, both cooling 0.3 K/min – Mg₂Si on grain boundaries and in particular inside the grains.

elongated rectanguloids, see Fig. 7-Fig. 9 (see also [28]). Both phases were found in every investigated sample in which the DSC cooling curves indicate the high- and also the lower temperature reaction occurred.

Selected EM micrographs are displayed in Fig. 7. Fig. 7a) shows a TEM bright field micrograph of AA6005A after slow cooling with 0.1 K/min. In this cooling condition, the HTR clearly dominate the DSC curve (see Fig. 3 and Fig. 4). Coarse Mg₂Si precipitates with dimensions of up to ~ 10 μm are observed (Fig. 6) and also some smaller Mg₂Si plates can be observed by TEM, Fig. 7a). Besides the Mg₂Si plates much finer B' precipitates are present in this cooling condition. B' precipitates formed during cooling are about 100 nm in thickness and up to several μm in length. A typical microstructure in a cooling condition, in which the LTR possess its highest intensity and dominate the DSC curve, is shown in Fig. 7d) (AA6005A after cooling with 8 K/min). In this sample, relatively small Mg₂Si plates can be found in TEM, although they are hardly detectable in OM in this condition. Beside the Mg₂Si plates, relatively large B' precipitates with diameters of some 100 nm are detected, see also Fig. 8 a). The volume fraction of these B' precipitates is higher after cooling at 8 K/min compared to 0.1 K/min.

For the setup and selection / setting of some of the parameters in the model, nucleation of the two dominating quench-induced phases are very important issues. The microstructure investigation is

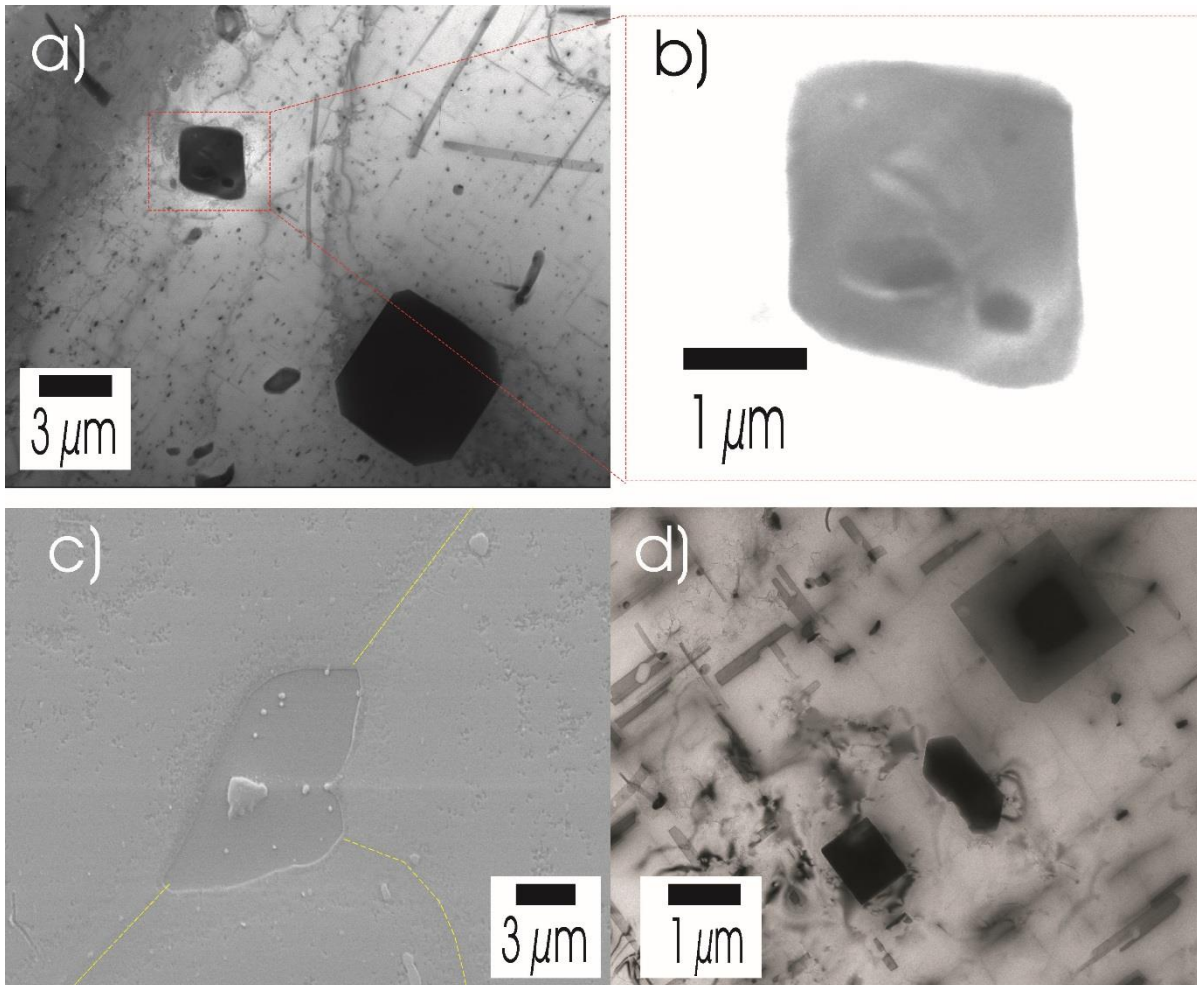


Fig. 7: (a) TEM bright-field micrograph of AA6005A after cooling with 0.1 K/min. Containing quench induced precipitates: Mg_2Si plates, Si particle (polygonal shaped precipitate, upper edge), elongated rectanguloid B' precipitates (length about 1 μm) and unidentified large rods (length several μm). (b) Magnification of Mg_2Si particle in (a) with high brightness value, showing coarse Al-Fe-Si-Mn-Cr particle as nucleation site inside the Mg_2Si plate. (c) SEM bright field image of same cooling condition like in (a, b) showing a Mg_2Si particle located at a grain boundary. Grain boundaries are highlighted. Even at grain boundaries Mg_2Si nucleation occurs on coarse Al-Fe-Si-Mn particles. (d) TEM bright-field micrograph of AA6005A after cooling with 8 K/min. Also after cooling with 8 K/min the same two main types of quench induced exist. B' in significantly coarser particles compared to slower cooling.

therefore particularly focussed on identifying nucleation sites. Fig. 6 displays OM and SEM images of AA6082_{high} (A, B), AA6082_{low} (C), and AA6063 after similar slow cooling conditions, with the grain structures being revealed due to the etching. The grain size of AA6063 and AA6082_{low} is significantly larger than that of 6082_{high}.

In all micrographs in Fig. 6 coarse, quench-induced dark Mg_2Si precipitates with dimensions of up to 10 μm are visible. Besides the dark Mg_2Si , the SEM images also show coarse eutectic Al-Fe-Si-Mn precipitates, which possess a bright contrast. Fig. 6 shows Mg_2Si nucleation occurs in many cases on grain boundaries, and for the alloy with the smallest grain size, AA6082_{high}, it occurs only on grain boundaries. In cases where the grain size is significantly larger than the dimensions of the Mg_2Si particles, Mg_2Si is located both inside the grains and on grain boundaries. The quench-induced precipitates in

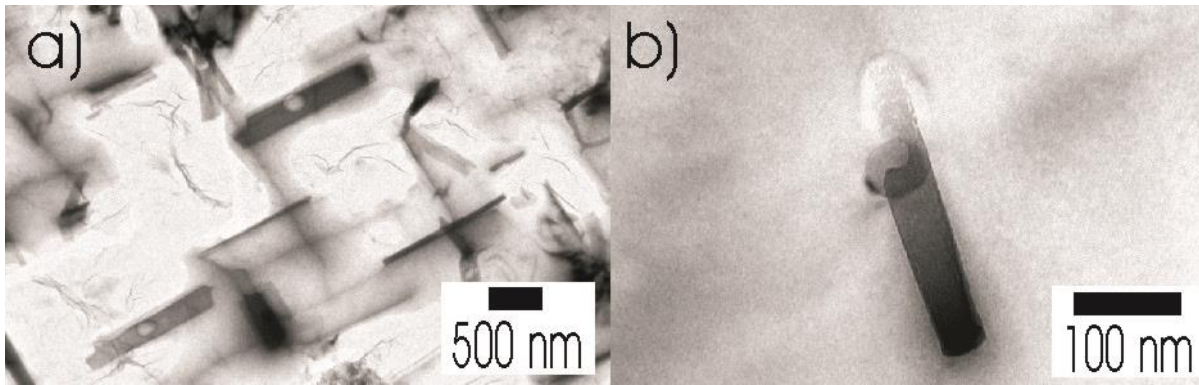


Fig. 8: TEM bright-field micrographs of (a) AA6005A after cooling with 8 K/min and (b) AA6063 after cooling with 50 K/min. In both cases quench induced B' precipitates are visible, nucleated at dispersoids.

AA6005A are very similar to AA6063 and AA6082_{low}, see OM and SEM in [25] and SEM and TEM in Fig. 6. For these alloys, nucleation of Mg₂Si starts primarily from coarse eutectic Al-Fe-Si-Mn phases. All Mg₂Si particles we investigated by SEM / TEM have such coarse Al-Fe-Si-Mn particles inside. This is independent of the Mg₂Si particle location and was found both for Mg₂Si particles inside Al grains and on grain boundaries – see Fig. 7 b) and c). We therefore conclude such coarse eutectic Al-Fe-Si-Mn particles to be the dominating and driving nucleation sites for Mg₂Si formation. Therefore, the amount of nucleation sites for Mg₂Si is limited.

Fig. 8 and Fig. 9 show that the nucleation of B' occurs on dispersoids. The amount of nucleation sites for B' therefore also is limited. In aluminium technology terminology dispersoids are particles that form during (heating to) homogenisation treatment from the as cast microstructural state. They contain Mn, Si

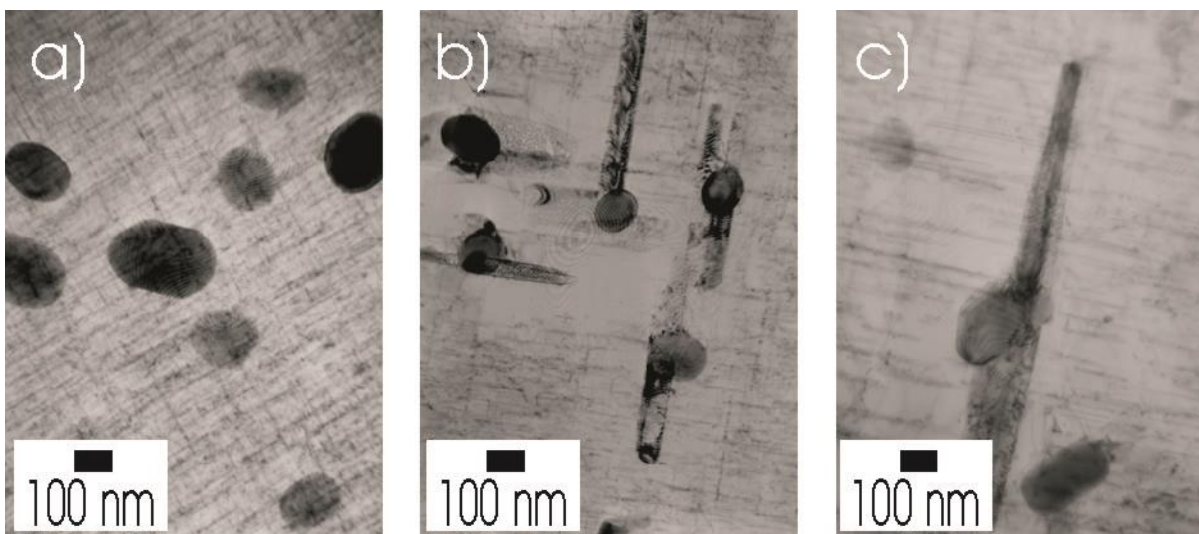


Fig. 9: TEM micrographs of AA6082_{yp} (Bright Field) of a room-temperature-water quenched (RTWQ) +T6 sample with hardness 97 HV (a), an air cooled (AC) +T6 sample with hardness 88 HV (b) and a slowly air cooled (SAC) +T6 sample with hardness 69.2 HV. In the RTWQ+T6 sample dispersoids are visible as well as a fine dispersion of hardening β'' precipitates, whilst the AC+T6 and SAC+T6 samples in addition shows non-hardening precipitates that apparently nucleated on the dispersoids during the quench.

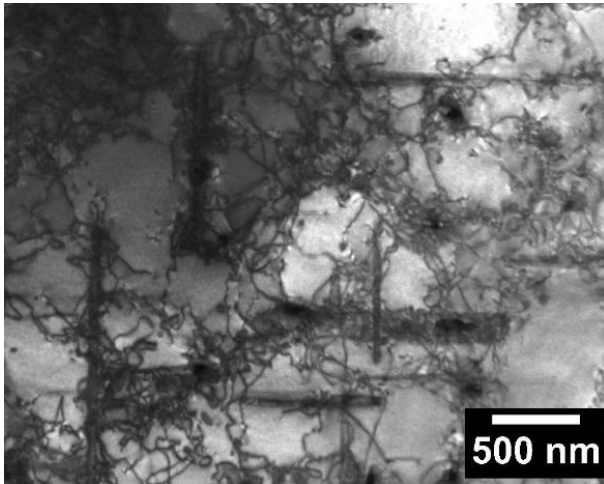


Fig. 10: TEM bright-field image of AA6005A slowly cooled with 0.1 K/min showing presence of increased dislocation density around quenched induced B' precipitates.

and Fe. Those particles formed in solid state are much finer compared to the Al-Fe-Si-Mn phases formed in eutectic reactions, which are effective as nucleation sites for Mg₂Si. Similar to those eutectic Al-Fe-Si-Mn particles, the dispersoids are not dissolved during solution annealing and are therefore available as nucleation sites during quenching.

Fig. 9 shows TEM bright field micrographs after three different cooling conditions and additional T6 ageing treatment. After water quenching and ageing (Fig. 9a) two types of particles are visible: globular dispersoids and fine needle-shaped hardening β'' precipitates, which formed during the ageing treatment. After air-cooling and slow air cooling and artificial ageing (Fig. 9 b and c), additionally B' precipitates with length of several 100 nm are present. Clearly also in AA6082_{typ} the quench-induced B' precipitates nucleated on the dispersoids during cooling. Fig. 7-Fig. 9 suggest that in all samples in which B' formation had occurred, all of the dispersoids have a B' precipitate formed on them. Comparison of Fig. 9 a, b and c shows that as the cooling rate decreases, the density of the hardening β'' precipitates decreases, and there is evidence of a zone denuded of β'' precipitates around the B' precipitates. Heating DSC experiments showed that the heat content of the β'' formation effect decreased with decreasing cooling rate, confirming the reduced β'' formation. Fig. 10 shows that in many cases a significant amount of dislocations are present around quench-induced precipitates. Therefore, in the strengthening model dislocation strengthening must be taken into account.

The hardness values of the alloys in the aged condition are presented in Fig. 5.

4 A model for precipitation during quenching and subsequent age hardening

4.1 A model for quench induced precipitation

In devising a model with general applicability we need to consider that during quenching several types of precipitates can form, including equilibrium phases at high temperatures and metastable phases at lower temperatures. Those reactions occur through a number of mechanisms, incl. precipitation on coarse intermetallics (phases that mostly are formed during solidification), precipitation on grain boundaries and precipitation in the grain, as well as, in particular for the lower temperature phases, precipitation on dispersoids (e. g. [7,8,25,30]). These reactions can occur consecutively or in overlapping time intervals. The mechanisms are potentially complicated and can lead to computationally expensive models. We will here derive a new model that is both effective as well as relatively simple, whilst it takes account of the main factors influencing kinetics. On several places in the model derivation we will use simplifications designed to provide a transparent model that can be applied in a computationally efficient manner.

As a starting point of the model, first the atomic fraction of undissolved Mn and Fe containing phases are calculated using the procedure outlined in [24]. These phases contain Si which will thus be unavailable for further precipitation reactions. The concentrations of elements in the Al-rich phase after solution treatment (i.e. just prior to start of the quench) are denoted as $X_{Mg,st}$, $X_{Si,st}$.

We consider that multiple reactions occur during the quench producing groups of particles that are distinguished by their structure and/or locations of nucleation (e.g. on grain boundaries or in the grain or on the dispersoid particles). To keep the computational complexity limited and allow a transparent model formulation, we will take the reactions to be consecutive, e.g. the interaction between the reactions occurs through taking the final state achieved after preceding reaction(s) to be the starting state of the next reaction. In the model formulation below we will present the equations for 2 reactions, but in principle the scheme can be repeated to include more consecutive reactions. As shown in Section 3, precipitation in 6xxx alloys is mainly dominated by two reactions – β (Mg_2Si) phase, followed by the formation of B' ($Mg_5Si_4Al_2$). Therefore these two reactions are incorporated in the model.

The total atomic fraction of quench induced precipitates, y_{QIP} , that forms is taken using an expansion of the quench factor model [2] which incorporates the Starink-Zahra model [31]:

$$y_{QIP} = y_{QIP}(\max) \left(1 - \left[\frac{(kQ)^n}{\eta_i} + 1 \right]^{-\eta_i} \right) \quad (1)$$

where Q is the quench factor [2], n is the reaction exponent, k is a rate constant, η_i is the impingement factor and $y_{QIP}(\max)$ is the maximum amount that can form on very slow cooling rate, which is defined by the concentrations of dissolved Mg and Si in the Al-rich phase prior to cooling (/quenching). For multiple reactions there are multiple groups i.e. there is a $y_{QIP,1}$, $y_{QIP,2}$, etc, each with a distinct set of parameters k , n , η_i , etc.

Following [2], Q is defined as:

$$Q = \int_{t=0}^t \frac{dt}{C_t} \quad (2)$$

For constant cooling rates Q is proportional to the time during the quench, which in turn is proportional to $1/\beta$. We can thus combine the latter two equations to:

$$y_{QIP} = y_{QIP}(\max) \left(1 - \left[\frac{(k_2 / \beta)^n}{\eta_i} + 1 \right]^{-\eta_i} \right) \quad (3)$$

In the latter equation the rate constant k_2 depends on a number of factors that drive the transformation rate, including density of nuclei, and diffusion rate.

A key part of the model is a functional description of the amount of precipitate phases that form during the cooling as a function of the main parameters (composition and cooling rate). We will here not attempt to provide a full ternary solution but instead determine the main factors that cause variations in k_2 and n in Eq. 3. To achieve this, we use the concept from the extended volume approach that for small $y_{QIP}/y_{QIP}(\max)$ the latter equation can be approximated as (see e.g. [32,23]):

$$y_{QIP} = y_{QIP}(\max) (k_2 / \beta)^n \propto y_{QIP}(\max) (k_2 t_c)^n \quad (4)$$

where t_c is the cooling time. This can be compared to the growth rate of spherical precipitates in a binary alloy, which is given by (see e.g. [33]):

$$\frac{dR}{dt} = \frac{\bar{c}(t) - c_m}{c_p - c_m} \frac{D}{R_p} \quad (5)$$

where D is the diffusivity, R_p is the radius of the precipitate, c_m is the concentration of the parent phase at the interphase of the nucleus, c_p is the concentration of alloying elements in the particle, $\bar{c}(t)$ is the average concentration of alloying elements in the parent phase. For the initial growth stage, $(\bar{c}(t) - c_m)$ can be considered to be constant, and the latter equation integrates to:

$$R_p^2 = A \frac{\bar{c}(t) - c_m}{c_p - c_m} Dt \quad (6)$$

From the latter equation we can see that the volume of a precipitate is proportional to $t^{3/2}$ and a number of factors as shown by:

$$V \propto R_p^3 = \left(\frac{\bar{c}(t) - c_m}{c_p - c_m} Dt \right)^{3/2} \quad (7)$$

As the temperature for the reactions will depend on composition (see e.g. Fig. 2), the magnitude of D during the reaction will be strongly alloy dependent. We can derive the composition dependency by using the following approach in which we combine the Arrhenius expression for the temperature dependency of diffusivity and the regular solution expression for the solvus to arrive at an equation providing the composition dependency of the reaction rate. Thus we firstly apply:

$$D = D_o \exp\left(-\frac{E_D}{RT}\right) \quad (8)$$

where E_D is the activation energy for diffusion of the atomic species that is rate determining, D_o is the diffusion preexponential factor. Secondly, we consider that formation of the quench-induced precipitates starts when the temperature reaches the solvus of the quench-induced precipitates. We apply a regular solution model expressions (see e.g. [34–37]), which provides:

$$c_{Mg}^q c_{Si} = C \exp\left[\frac{-\Delta H_{Mg_2Si}}{RT}\right] \quad (9)$$

where c_{Mg} and c_{Si} are the solubilities of Mg and Si as given by the solvus, q is the Mg:Si ratio in the phase, i.e. the phase is Mg_qSiAl_r , C is a constant and ΔH_{Mg_qSi} is the enthalpy change due to the formation of the

Mg_qSiAl_r phase. (The high temperature reaction is due to Mg₂Si i.e. q=2 and r=0.) The latter two equations can be combined to provide a relation between D and the alloy composition:

$$\frac{D}{D_o} = \left(\frac{c_{Mg}^q c_{Si}}{C} \right)^{\frac{E_D}{\Delta H_{MgqSi}}} \quad (10)$$

We can now combine Eqs 4, 7 and 10 to provide the functional relation between k_2 and the composition for the case that the number of growing precipitates is independent of the Mg and Si content of the alloy (this is the case for a limited number of nuclei):

$$k_2^{HTR} = k_o \left(\frac{c_{Mg}^q c_{Si}}{C} \right)^{\frac{E_D}{\Delta H_{MgqSi}}} [y_{QIP}(\max)]^p \quad (11)$$

in which p equals 1/3. The latter equation is applied for the HTR.

A further factor that influences k_2 is the density of nuclei that grow. From the investigation performed (Section 3) it is clear that for the LTR the density of nuclei is determined by the density of dispersoids. As the composition of the dispersoids are β -Al₅FeSi and α -Al₁₅(FeMn)₃Si [38–40], the Fe and Mn content of the alloys will influence the volume fraction of dispersoid phases. Formation of the various phases during solidification of 6xxx type alloys involves at least 5 phases including 3 Mn and/or Fe bearing ones; the solidification is complex and although many details are known [40,38] it is at present not fully understood. We propose to use the following simplified treatment for the k_2 for the LTR:

$$k_2^{LTR} = k_o (x_{Mn}^g + x_{Fe}^g) \left(\frac{c_{Mg}^q c_{Si}}{C} \right)^{\frac{E_D}{\Delta H_{MgqSi}}} [y_{QIP}(\max)]^p \quad (12)$$

A justification for the $(x_{Mn}+x_{Fe})$ term in the latter equation is as follows. We will consider that according to a Scheil type model of solidification in a binary eutectic system with hypoeutectic composition the amount of dispersoid-forming alloying elements dissolved in the Al-rich phase during solidification of a binary alloy increases approximately proportional to the gross alloying content of the alloy. Thus in such a simple system the volume fraction of dispersoids that form during homogenisation treatment is approximately proportional to the alloying content. We make the assumption that this proportionality holds in good approximation for the complex 6xxx alloys and that the sum of gross Fe and Mn determine the

relevant alloying content. Then, assuming that the alloying content does not influence the size of the dispersoids, the density of dispersoids is proportional to $(x_{Mn}+x_{Fe})$.

Thus after determining 3 parameters (k_o , y_{QIP} (max) and η_i), the above treatment allows determination of $y_{QIP,1}$ for a set of Al-Mg-Si based alloys. With $y_{QIP,1}$ determined, the composition of the Al-rich phase can be determined from a mass balance and $x_{Mg,st}$, $x_{Si,st}$. The composition of the matrix after reaction 1 will be denoted as $x_{Mg,q1}$, $x_{Si,q1}$. The amount of precipitates forming during reaction 2, $y_{QIP,2}$ can be determined based on the state reached after the preceding reaction. The composition of the Al-rich phase after reaction 2 will be denoted as $x_{Mg,q2}$, $x_{Si,q2}$. The final compositions achieved after completion of cooling/quenching will be denoted by $x_{Mg,q}$, $x_{Si,q}$.

4.2 A model for strength/hardness of alloys T6 aged after cooling

We will use the general approximation of the superposition of strengthening mechanisms described in [41]

$$\sigma_y = \sigma_{gb} + M(\tau_o + \tau_{sol} + \tau_d + \tau_{cl} + \tau_{pr}) \quad (13)$$

where σ_{gb} is the yield strength contribution due to grain boundaries, τ_d is the critical resolved shear stress (CRSS) increment due to stored dislocations (introduced by plastic deformation), τ_{sol} is the CRSS increment due to dissolved alloying atoms, τ_{pr} is the CRSS increment due to precipitates, τ_{cl} is the CRSS increment due to shearable clusters, τ_o is the friction resolved shear stress and M is the Taylor factor.

On artificial ageing β'' precipitates form [42], and we will consider that in the T6 condition the remaining Mg and Si in solution given by the metastable solvus of the precipitates. This metastable solvus is taken from first principles modelling of the monoclinic β'' ($Mg_5Si_4Al_2$) in [43,22], which according to the first principle models is the most stable form of a range of potential closely related monoclinic β'' structures (which include the Mg_5Si_6) [43]. From [22] we take the solvus of the monoclinic β'' ($Mg_5Si_4Al_2$) phase precipitate in the absence of interface energy effects, and from [43] we take the result that the interfacial energy terms reduce the enthalpy change by about 8 %. The latter result was obtained for precipitates with cross section of $6 \times 5 \text{ nm}^2$, which corresponds well with β'' precipitates seen in our TEM experiments

(Fig. 9). (The result is that the solubilities for a balanced Al-Mg-Si at ageing temperatures is about doubled due to the interfacial energy.)

The concentration of the main alloying elements in the Al-rich phase after the artificial ageing treatment are denoted as $x_{Mg,T6}$ and $x_{Si,T6}$. The total amount of Si and Mg in the hardening precipitates, y_{hpr} , is then given by:

$$y_{hpr} = x_{Mg,q} - x_{Mg,T6} + x_{Si,q} - x_{Si,T6} \quad (14)$$

In the literature a number of strengthening models are available which provide the relation between τ_{pr} and the volume fraction of precipitates, their sizes or average size and other parameters (see e.g. [42]. In the appendix, it is shown that the yield strength of Al-Mg-Si based alloys increases linearly with the amount of Mg and Si in the hardening precipitates and hence we take:

$$\Delta\tau_{pr,ag} = K_{\beta''} y_{hpr} \quad (15)$$

where $K_{\beta''}$ is a proportionality constant which is related to the energy required to move a dislocation through the coherent β'' ($Mg_5Si_4Al_2$) phase precipitate. Hence, we are here applying a treatment for shearable precipitates. The linear relation between strength and amount of alloying atoms in the metastable precipitates is similar to strengthening due to co-clusters in which strengthening is dominated by the bonds between the two atoms in the cluster [24] (in this case Si and Mg). Consistent with the present treatment, Midling and Grong [44] also applied a linear relation between strengthening and volume fraction of precipitates.

The B' precipitate particles precipitated during the quench will also contribute some limited strengthening, and this is treated using classical Orowan strengthening [45]. This contribution is termed $\tau_{pr,qip}$. The superposition of the total strengthening due to these 2 types of obstacles will be taken according to a quadratic superposition [46–48]:

$$\Delta\tau_{pr}^2 = \Delta\tau_{pr,ag}^2 + \Delta\tau_{pr,qip}^2 \quad (16)$$

Using the Hall-Petch relation with a Hall-Petch constant taken from [49], one can determine that for typical 6xxx alloys σ_{gb} is only about 4 MPa. As the alloys contain up to about 3 vol% intermetallic particles,

some dislocations can be generated due to the misfit caused by differences in the thermal expansion coefficients (see e.g. Fig. 10). To address this, we add a prediction of dislocation density generated by this to the model, following the work by Chawla [50]. In applying this dislocation generation model, we take the typical temperature range over which dislocations are accumulated, ΔT , and the typical difference in coefficient of thermal expansion between matrix and precipitates, $\Delta\alpha$, from an earlier analysis in [24]. The contribution to the strength is small, up to 6 MPa for 6xxx alloys with the higher Mn and Fe contents (high Mn and Fe 6xxx alloys typically contain over 0.1 at% of each element). In addition, we also add strengthening due to stress transfer to the intermetallic particles by applying the treatment in [51,52]. This contribution is also low, with typically about 1 % increase in yield strength for alloys with the higher Mn + Fe content.

We will test the model to an extensive set of data comprising both proof strength and hardness data of a range of Al-Mg-Si alloys. We will provide predictions of Vickers hardness based on modelled yield strength through a conversion which is calibrated by pairs of proof strength – hardness data from databases on commercial alloys. The presence of substantial amounts of non-shearable dispersoid particles in the commercial alloys will affect the hardness through their influence on strain hardening [53,46,54], and hence we will adopt a two-term conversion, which is given by:

$$HV = C_{\sigma-HV} \left(\sigma_{0.2} + 0.25G \sqrt{\frac{bf_{ns}}{2r_{ns}}} \sqrt{\epsilon_{eff}} \right) \quad (17)$$

where f_{ns} is the volume fraction of non shearable particles, G is the shear modulus, r_{ns} is the average radius of non shearable particles, $C_{\sigma-HV}$ is the conversion parameter (see below) and ϵ_{eff} is the effective strain reached in indentation hardness, here taken as 0.08. The second term is the strain hardening term as given in [53,46,54], which amounts to about 10 % of the hardness for our commercial 6xxx alloys. f_{ns} is taken from model predictions, r_{ns} is taken from TEM data, and $C_{\sigma-HV}$ is determined from pairs of proof strength – hardness data on commercial 6xxx alloys from databases [55,56].

Table 2: Parameters in the model.

Parameter	Value	Notes / Source
General parameters		
b	2.84×10^{-10} m	
Reaction 1: β formation		
η_i	0.4	From fit to data
k_o	1.5×10^9	From fit to data
n	$1\frac{1}{2}$	According to model for diffusion controlled reactions [23]
E_D	131 kJ/mol	Activation energy for diffusion of Mg in Al, the main component of the phases; average of two works [57,58]
ΔH_{Mg2Si}	140 kJ/mol	From solvus data in [59]
ρ_β	1.99 g/cm^3	[60]
Parameter	Value	Notes / Source
Reaction 2: B' formation		
η_i	2	From model for diffusion controlled formation of homogeneously distributed precipitates
k_o	1.4×10^{14}	From fit to data
n	$1\frac{1}{2}$	According to model for diffusion controlled reactions [23]
E_D	131 kJ/mol	Activation energy for diffusion of Mg in Al, the main component of the phases; average of two works [57,58]
Strength model		
τ_o	6 MPa	[24]
M (for tensile tests in L direction)	2.73	For tensile tests in the longitudinal direction, see [24]
M (all other tests)	2.6	For all other tensile and hardness tests; obtained from self-consistent models [61], see also [62]
K_{hpr}	15.5 GPa	Determined from literature data on strength of 6xxx alloys – see appendix
G	27 GPa	
k_{Si}	800 MPa	From [24]
k_{Mg}	590 MPa	From [47,63,64]
$\Delta\alpha$	$1.7 \cdot 10^{-5}$	Estimated from data in [65], see also [24]
ΔT	400 K	Typical temperature interval over which misfit dislocations are generated.

5 Model parameters and predictions

To apply the model, first all the model parameters need to be determined. There are 4 types of model parameters: i) parameters that are well known and well established (e.g. G , b), ii) parameters that are known to a good accuracy from a range of investigations (e.g. E_D , k_{Mg} , k_{Si}), or from models (e.g. η_i for the low temperature reaction), iii) parameters that can be determined from an analysis of literature and

handbook data (e.g. ΔH_{pr} , τ_0) and iv) parameters that are unknown and need to be determined through fitting. We have measured a total of over 1000 data points (hardness, enthalpy changes and β volume fractions for a wide range of cooling rates) and hence there are a multitude of ways in which we can attempt to determine the values of the fittable (type iv) parameters, of which there are 4 (η for the high temperature reaction, k_0 for both of the reactions, plus ΔH_B). We will here use a set of fittable parameters that provide a good balance for the range over which the model is considered to be valid. All model parameters are presented in **Table 2**.

A comparison of model predictions with measured hardness data is presented in comparisons with the ΔH values in Fig. 5. Generally an excellent correspondence is observed.

The main area where deviations occur is for ΔH at slow cooling rates for the AA6082_{high} alloy. It is thought that this is due to the higher density of nucleation sites for β precipitates due to the substantially reduced grain size and increased amount of eutectic phases for this alloy as compared to the other alloys. Nevertheless, the predictive capability of the model with regards to the quench sensitivity at the commercially important rates is not impaired, and the hardness is correctly predicted for all cooling rates down to about 1 K/min.

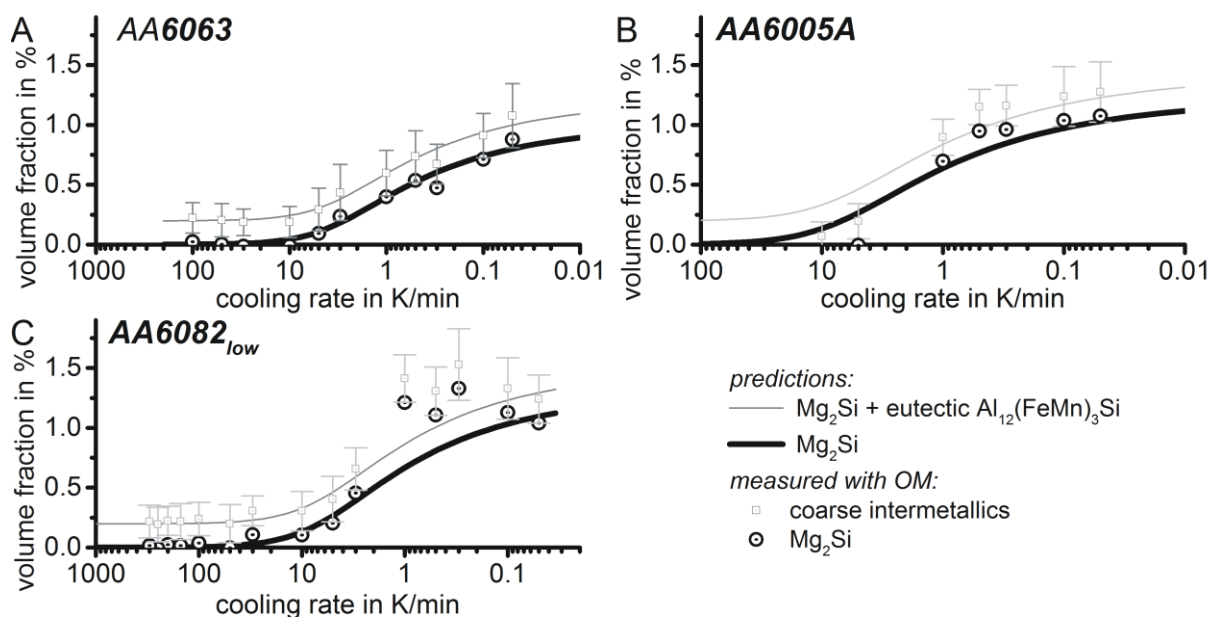


Fig. 11: Measured and predicted volume fractions.

It is worthwhile to briefly consider some of the main parameters and their values. For the LTR, the precipitates are homogeneously distributed and we can take η_i from the assessment in [23]. For the HTR the precipitates are distributed very inhomogeneously and no model assessment to determine η_i is available. The value of $\Delta H_{\text{Mg}_2\text{Si}}$ is determined from solubility data in [59] whilst $\Delta H_{\text{B}'}$, for which no data is available in the literature, is fitted. The magnitude of modelled ΔH in Fig. 5 depends strongly on these 2 values, with $\Delta H_{\text{B}'}$ determining for a large extend the ΔH where an intermediate plateau is visible, such as in AA6005 between about 1 and 10 K/min. The general good model predictions for these plateau values of ΔH , as well as for the maximum values of ΔH for the alloys in which precipitation is fastest, provides good proof that both $\Delta H_{\text{Mg}_2\text{Si}}$ and $\Delta H_{\text{B}'}$ used here are accurate. Accuracy of the values is estimated to be about $\pm 10\%$.

Fig. 11 presents a comparison of measured and predicted volume fractions of $\beta\text{-Mg}_2\text{Si}$ for AA6063, AA6005A and AA6082_{low}. The volume fraction is predicted for Mg_2Si and a sum of Mg_2Si and eutectic $\text{Al}_{12}(\text{FeMn})_3\text{Si}$ as it was measured by OM (see section 2.3 for details). The measured data is predicted well.

6 Discussion

6.1 Model efficiency and model accuracy

The present model includes integrated predictions of volume fractions of quench-induced phases and strength, through a formulation which allows evaluation with minimal computation time: all equations are closed-form and no iterations or differential time evolution computations are required. The results are very good: enthalpy changes during cooling are generally predicted well, hardness is predicted to an accuracy of about 5 HV for cooling rates faster than 2 K/min and volume fractions of $\beta\text{-Mg}_2\text{Si}$ precipitates are also predicted well. The shape of the ΔH vs cooling rate curves are predicted very well, both for the LTR and the HTR as well as the sum of the two. Small shifts along the cooling rate axis are observed for some alloys, which are thought to be mainly due to small changes in the number of nucleation sites between the various alloys caused by factors beyond the capability of the present model. In particular, for the B'

formation reaction, the density of dispersoids will determine the number of nuclei. To improve the model in this respect one would need to further refine prediction of the density of the dispersoids.

The model is further consistent with all qualitative data obtained from the present microstructural investigation as well as investigations in other work (e.g. [7,2,66–68]). Whilst the success of the model is clear, it is valuable to discuss the consequences of the approximations that are introduced, and the limitations of the model.

6.2 Phases formed during quenching/cooling

The model contains 2 reactions which are taken as formation of β -Mg₂Si phase, followed by the formation of B' (Mg₅Si₄Al₂) phase. The experimental evidence in section 3 (XRD and SEM) supports the formation of β -Mg₂Si on cooling and also other investigations have revealed the formation of this phase at temperatures above 400 °C [7,25,66–68]. The lower temperature reaction is caused by the formation of semi-coherent precipitates on the dispersoids. Zajac et al. suggested that “Mg₂Si precipitates as β' -phase” [66]. During the TEM-SAED investigation in [7] we obtained SAED patterns showing a hexagonal, semi-coherent structure of these precipitates. In the literature a range of suggestions have been provided for similar SAED patterns and both β' and B' phases are consistent with the observed SAED patterns [7,27,69–72]. Compared to these previous studies we have in this work provided a new assessment that can distinguish between these 2 phases: we have compared the start temperatures measured by highly accurate fast cooling DSC with the very recently published solvi for the β' and B' phases obtained from thermodynamic modelling incorporating first-principles calculations [22]. This comparison indicates that start of the reaction for heating rates >30 K/min is inconsistent with the solvus of β' and instead is consistent with B' phase formation. This finding is incorporated in the model.

The Si phase is thermodynamically stable in the present alloys (see [39]), and might be considered as a possible 3rd phase forming during cooling. It seems possible that a minor amount of Si phase can form in alloys with excess Si under certain conditions that have little commercial relevance such as very slow cooling (typically < 1 K/min). In such a case the excess Si in solution would be expected to precipitate as a Si rich phase. Indeed the TEM work (Fig. 7) has shown that at extremely low cooling rates (0.1 K/min)

a small fraction (less than ~5 %) of the precipitate phase is Si phase. (The XRD does not detect these small amounts of Si phase, and only the β and Al-rich phase are detected.) In line with this assessment, we can see that for selected cooling rates there is evidence in the DSC curves that more than two reactions are involved. This is seen in Fig. 3C) 6082_{low} during cooling with the extremely slow rate of 0.2 K/min. Such minor deviations from model predictions for small sections of the alloy-heat treatment space are inherent to the complexity of the multi-component, multiphase alloys treated at cooling rates over about 6 decades; and the present model is thought to provide an excellent balance of high accuracy and low computational costs, achieved through a judicious choice of modelling approaches.

6.3 Model parameters: nucleation, impingement, enthalpies of formation

The model parameters used in the model can be compared with a range of data to further elucidate the reactions and the thermodynamics. We will here consider the most relevant parameters.

An analysis of diffusion-controlled precipitation reactions in conjunction with a new model for diffusion controlled reactions [23,73] has shown that the reaction parameter n is generally $1\frac{1}{2}$, and only in cases where nucleation is continuous during the entire reaction the higher value of $2\frac{1}{2}$ is possible. In the present system it is clear from the microstructure data that nucleation is heterogeneous, occurring on defects and particles. Thus the reaction parameter n was taken as $1\frac{1}{2}$, and the excellent correspondence of the shape of the ΔH vs heating rate data to model predictions provides further proof that this part of the model and the theory on which it is based are sound.

We consider the state of the art of modelling of heterogeneous nucleation to be too limited to be able to include it in the model, and as a result we have to fit the k_0 parameter for each reaction. The results show that with just one k_0 for each reaction, we can fit the hardness, calorimetry and volume fraction data for all alloys very well. This provides confidence that the treatment is sound.

Appendix: CRSS due to age hardening precipitates

In the present model (Section 4.2) the strengthening due to age hardening is considered to be proportional to the volume fraction of precipitates formed according to Eq. 15. To determine the proportionality constant we collated yield strength data from the literature for a range of Al-Mg-Si based

alloys heat treated to T6 condition using fast quenching (i.e. with all reaction during the quench being suppressed). The data is mainly from industry handbooks [55,56,37] (the composition is taken as the median composition of the composition range), supplemented by data for very low Si Al-Mg-Si-Mn-Fe alloys from [24]. It was confirmed that with optimised proportionality constant literature data on strength has an excellent linear correlation (correlation coefficient 0.99) with predictions from the model in Section 4.2. For further confirmation we have plotted the predicted y_{hpr} vs the measured strength of the same alloys in Fig. 12, which also contains data on T4 strength (i.e. with co-cluster strengthening). The good linear correlation confirms the present treatment. (The correlation coefficient is 0.98. It is somewhat lower than that for the full model, which is primarily due to some slight variations in the minor strengthening mechanisms between the alloys.)

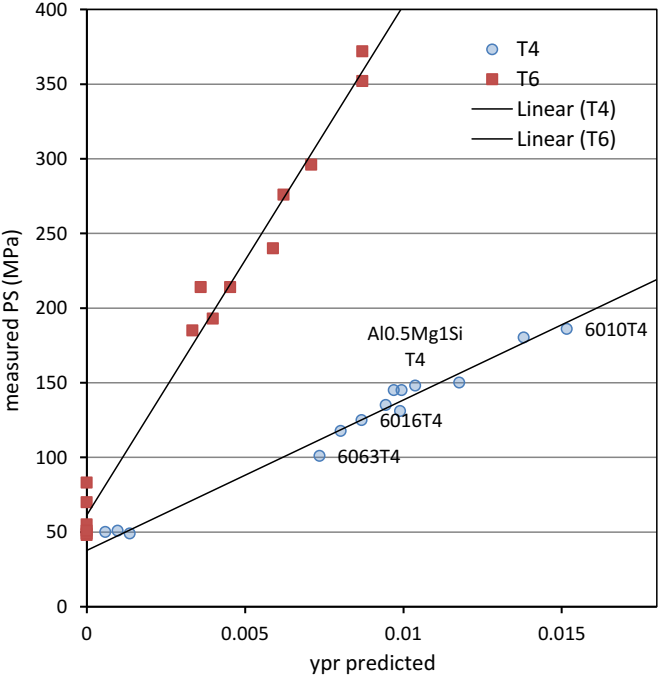


Fig. 12: Yield strength for range of Al-Mg-Si based alloys in T6 and T4 condition, as a function of the total amount of Mg plus Si in either the β'' phase (for the T6 condition) or the co-clusters (for the T4 condition, data from [24]). The alloys include AA6061, AA6063, AA6463, AA6009, AA6010, AA6066, AA6101, and Al-1Mg-0.2Si and Al-1Mg-0.2Si-0.2Cu. Also included are O temper data for AA6061 and AA6063.

7 Summary

In this work, we introduce a new physically-based model that allows to predict the quench sensitivity for the technologically important step of cooling from solution annealing during the age hardening

procedure of Al-Mg-Si alloys. The model predicts the volume fraction of precipitates formed with the corresponding enthalpy changes, and both yield strength and hardness in the quenched and in the quenched + aged condition are predicted. For its setup, the model combines the latest findings in modelling of diffusion controlled phase transformations and in modelling of the thermodynamics of technically important complex alloy systems, including first principles modelling. For the set-up and testing of the model, we considered an extensive set of experimental results from Differential Scanning Calorimetry, optical and electron microscopy as well as X-ray diffraction. All together more than 1000 data points are taken into account. The model considers two consecutive precipitation reactions during cooling: β -Mg₂Si and B'. Comparing the experimental results in a very wide dynamic range of about 0.05 to 2·10⁴ K/min for enthalpy change, Mg₂Si volume fractions and T6 hardness the model delivers generally excellent fits. Application of the model will help to optimise the exploitation of the age hardening potential of the widely used Al-Mg-Si alloys. For instance the model allows to predict the critical cooling rate of a certain alloy composition – this helps to design an appropriate cooling process for the heat treatment shop. Or, being fixed to a certain cooling method in industrial plants, one could choose the optimal alloy composition. Implementing the model in FEM tools and simulating the cooling process moreover will allow to predict the mechanical properties of complex components at every location.

Acknowledgements

Most of the experiments were performed by several experimentalists. The following persons are acknowledged for performing DSC experiments at the University of Rostock: R. Steuer, M. Beck and C. Fabry. We gratefully thank O. Kessler and C. Schick for the fruitful discussions of the DSC work. For performing SEM and TEM experiments M. Dammer, D. Hasselfeldt, M. Beck (all University of Rostock), Dr. N. Wanderka (Helmholtz Zentrum Berlin); Dr. P. Rometsch (formerly University of Southampton, now Monash University) and Dr. S. Wang (University of Southampton) are acknowledged. Aleris and British Aluminium are acknowledged for supplying selected alloys. BM is on sabbatical at the University of Southampton supported by a fellowship within the Postdoc-Program of the German Academic Exchange Service (DAAD). BM gratefully acknowledges this support.

References

- [1] Polmear IJ. Light alloys, 4th ed., Butterworth-Heinemann, Oxford, 2006.
- [2] Rometsch PA, Starink MJ, Gregson PJ. Improvements in quench factor modelling, Mater. Sci. Eng. A 339 (2003) 255-264.

- [3] Deschamps A, Texier G, Ringeval S, Delfaut-Durut L. Influence of cooling rate on the precipitation microstructure in a medium strength Al-Zn-Mg alloy, *Mater. Sci. Eng. A* 501 (2009) 133-139.
- [4] Zhang Y, Milkereit B, Kessler O, Schick C, Rometsch PA. Development of continuous cooling precipitation diagrams for aluminium alloys AA7150 and AA7020, *J. Alloy. Compd.* 584 (2014) 581-589.
- [5] Cavazos JL, Colas R. Precipitation in a heat-treatable aluminum alloy cooled at different rates, *Mater. Charact.* 47 (2001) 175-179.
- [6] Cavazos JL, Colas R. Quench sensitivity of a heat treatable aluminum alloy, *Mater. Sci. Eng. A* 363 (2003) 171-178.
- [7] Milkereit B, Wanderka N, Schick C, Kessler O. Continuous cooling precipitation diagrams of Al-Mg-Si alloys, *Mater. Sci. Eng. A* 550 (2012) 87-96.
- [8] Rometsch PA, Zhang Y, Knight S. Heat treatment of 7xxx series aluminium alloys - Some recent developments, *Trans. Nonferrous Met. Soc. China* 24 (2014) 2003-2017.
- [9] Tiryakioğlu M, Robinson JS, Eason PD. On the quench sensitivity of 7010 aluminum alloy forgings in the overaged condition, *Mater. Sci. Eng. A* 618 (2014) 22-28.
- [10] Morgener TF, Starink MJ, Wang SC, Sinclair I. Quench sensitivity of toughness in an Al alloy: Direct observation and analysis of failure initiation at the precipitate-free zone, *Acta Mater.* 56 (2008) 2872-2884.
- [11] Hoffmann F, Kessler O, Lübben T, Mayr P. "Distortion Engineering" - Distortion control during the production process, *Heat Treat. of Met.* 31 (2004) 27-30.
- [12] Reich M, Kessler O. Mechanical properties of undercooled aluminium alloys and their implementation in quenching simulation, *Mater. Sci. Technol.* 28 (2012) 769-772.
- [13] Rose A, Kessler O, Hoffmann F, Zoch HW. Quenching Distortion of Aluminium Castings – Improvement by Gas Cooling, *Materialwiss. Werkstoff.* 37 (2006) 116-121.
- [14] Starink MJ. Analysis of aluminium based alloys by calorimetry, *Int. Mater. Rev.* 49 (2004) 191-226.
- [15] Birol Y. DSC analysis of the precipitation reaction in AA6005 alloy, *Journal of Thermal Analysis and Calorimetry* 93 (2008) 977-981.
- [16] Esmaeili S, Wang X, Lloyd DJ, Poole WJ. On the precipitation-hardening behavior of the Al-Mg-Si-Cu, *Metall. Mater. Trans. A-Phys. Metall. Mater. Sci.* 34A (2003) 751-763.
- [17] Esmaeili S, Lloyd DJ. Characterization of the evolution of the volume fraction of precipitates in aged AlMgSiCu alloys using DSC technique, *Mater Charact* 55 (2005) 307-319.
- [18] Milkereit B, Kessler O, Schick C. Recording of continuous cooling precipitation diagrams of aluminium alloys, *Thermochim. Acta* 492 (2009) 73-78.
- [19] Milkereit B, Beck M, Reich M, Kessler O, Schick C. Precipitation kinetics of an aluminium alloy during Newtonian cooling simulated in a differential scanning calorimeter, *Thermochim. Acta* 522 (2011) 86-95.
- [20] Zohrabyan D, Milkereit B, Kessler O, Schick C. Precipitation enthalpy during cooling of aluminum alloys obtained from calorimetric reheating experiments, *Thermochim. Acta* 529 (2012) 51-58.
- [21] Milkereit B, Giersberg L, Kessler O, Schick C. Isothermal Time-Temperature-Precipitation Diagram for an Aluminum Alloy 6005A by In Situ DSC Experiments, *Materials* 7 (2014) 2631-2649.
- [22] Povoden-Karadeniz E, Lang P, Warczok P, Falahati A, Jun W, Kozeschnik E. CALPHAD modeling of metastable phases in the Al-Mg-Si system, *Calphad* 43 (2013) 94-104.
- [23] Starink MJ. A new model for diffusion-controlled precipitation reactions using the extended volume concept, *Thermochim. Acta* 596 (2014) 109-119.
- [24] Starink MJ, Cao LF, Rometsch PA. A model for the thermodynamics of and strengthening due to co-clusters in Al-Mg-Si-based alloys, *Acta Mater.* 60 (2012) 4194-4207.
- [25] Milkereit B, Jonas L, Schick C, Kessler O. Das kontinuierliche Zeit-Temperatur-Ausscheidungs-Diagramm einer Aluminiumlegierung EN AW-6005A, *HTM J. Heat Treat. and Mater.* 65 (2010) 159-171.
- [26] Schumann H. *Metallographie*, 13th ed., Deutscher Verlag für Grundstoffindustrie, Leipzig, 1991.

- [27] Edwards GA, Stiller K, Dunlop GL, Couper MJ. The precipitation sequence in Al-Mg-Si alloys, *Acta Mater.* 46 (1998) 3893-3904.
- [28] Dumolt SD, Laughlin DE, Williams JC. Formation of a modified beta'-phase in aluminum alloy 6061, *Scr. Metall.* 18 (1984) 1347-1350.
- [29] JCPDS. Powder diffraction file PDF-2 database sets 1-47, International Centre for Diffraction Data., 1993.
- [30] Zhang Y, Bettles C, Rometsch PA. Effect of recrystallisation on Al3Zr dispersoid behaviour in thick plates of aluminium alloy AA7150, *J Mater Sci* 49 (2014) 1709-1715.
- [31] Starink MJ, Zahra AM. Kinetics of isothermal and non-isothermal precipitation in an Al - 6 at.% Si alloy, *Philos. Mag. A-Phys. Condens. Matter Struct. Defect Mech. Prop.* 77 (1998) 187-199.
- [32] Starink MJ. On the meaning of the impingement parameter in kinetic equations for nucleation and growth reactions, *J Mater Sci* 36 (2001) 4433-4441.
- [33] Kampmann R, Wagner R. Kinetics of precipitation in metastable binary alloys -theory and application to Cu-1.9 at % Ti and Ni-14 at % Al, in: M.F. Ashby, P. Haasen, V. Gerold, R. Wagner (Eds.), *Decomposition of Alloys: Proceedings of the 2nd Acta-Scripta Metallurgica Conference*, Pergamon Press, 1984, pp. 91–103.
- [34] R. H. Brown, L. A. Willey (Eds.). *Aluminum: Properties, Physical Metallurgy and Phase Diagrams*, ASM International, Metals Park, Ohio, 1967.
- [35] Starink MJ, Wang SC. The thermodynamics of and strengthening due to co-clusters, *Acta Mater.* 57 (2009) 2376-2389.
- [36] Li X, Starink MJ. Effect of compositional variations on characteristics of coarse intermetallic particles in overaged 7000 aluminium alloys, *Mater. Sci. Technol.* 17 (2001) 1324-1328.
- [37] Hatch JE. *Aluminum*, American Society for Metals, Metals Park, Ohio, 1984.
- [38] Hsu C, O'Reilly, K. A. Q., Cantor B, Hamerton R. Non-equilibrium reactions in 6xxx series Al alloys, RQ10, Tenth International Conference on Rapidly Quenched and Metastable Materials 304–306 (2001) 119-124.
- [39] Belov NA, Eskin DG, Aksenov AA. *Multicomponent phase diagrams*, 1st ed, Elsevier, Amsterdam, Boston, 2005.
- [40] Verma A, Kumar S, Grant PS, O'Reilly, K. A. Q. Influence of cooling rate on the Fe intermetallic formation in an AA6063 Al alloy, *J. Alloy. Compd.* 555 (2013) 274-282.
- [41] Starink MJ, Deschamps A, Wang SC. The strength of friction stir welded and friction stir processed aluminium alloys, *Scr. Mater.* 58 (2008) 377-382.
- [42] Bardel D, Perez M, Nelias D, Deschamps A, Hutchinson CR, Maisonnette D et al. Coupled precipitation and yield strength modelling for non-isothermal treatments of a 6061 aluminium alloy, *Acta Materialia* 62 (2014) 129-140.
- [43] Ehlers, F. J. H., Dumoulin S, Holmestad R. 3D modelling of β' in Al - Mg - Si: Towards an atomistic level ab initio based examination of a full precipitate enclosed in a host lattice, *Comput. Mater. Sci.* 91 (2014) 200-210.
- [44] Midling OT, Grong Ø. A process model for friction welding of Al · Mg · Si alloys and Al · SiC metal matrix composites—II. Haz microstructure and strength evolution, *Acta Metall. et Mater.* 42 (1994) 1611-1622.
- [45] D. G. Morris. *Strengthening Mechanisms in Nanocrystalline Materials*, in: S.H. Whang (Ed.), *Nanostructured metals and alloys: Processing, microstructure, mechanical properties and applications*, Woodhead Pub., Cambridge, U.K., 2011.
- [46] Starink MJ, Wang P, Sinclair I, Gregson PJ. Microstructure and strengthening of Al-Li-Cu-Mg alloys and MMCS: II. Modelling of yield strength, *Acta Mater.* 47 (1999) 3855-3868.
- [47] Zhu Z, Starink MJ. Age hardening and softening in cold-rolled Al-Mg-Mn alloys with up to 0.4wt% Cu, *Mater. Sci. Eng. A* 489 (2008) 138-149.
- [48] A. Kelly, R. B. Nicholson (Eds.). *Strengthening Methods in Crystals*, Elsevier, London, 1971.
- [49] Hansen N. The effect of grain size and strain on the tensile flow stress of aluminium at room temperature, *Acta Metall.* 25 (1977) 863-869.
- [50] Chawla KK. *Composite materials*, 3rd ed., Springer, New York, London, 2009.

- [51] Ramakrishnan N. An analytical study on strengthening of particulate reinforced metal matrix composites, *Acta Mater.* 44 (1996) 69-77.
- [52] Zhang Q, Chen DL. A model for predicting the particle size dependence of the low cycle fatigue life in discontinuously reinforced MMCs, *Scr. Mater.* 51 (2004) 863-867.
- [53] Ashby MF. Work hardening of dispersion-hardened crystals, *Philos. Mag.* 14 (1966) 1157-1178.
- [54] Kamp N, Sinclair I, Starink MJ. Toughness-strength relations in the overaged 7449 Al-based alloy, *Metall. Mater. Trans. A-Phys. Metall. Mater. Sci.* 33 (2002) 1125-1136.
- [55] Kaufman JG. Introduction to aluminum alloys and tempers, ASM International, Materials Park, OH, 2000.
- [56] ASM-International (Ed.). ASM speciality handbook aluminum and aluminum alloys, Materials Park, OH, USA, 1993.
- [57] Rothman SJ, Peterson NL, Nowicki LJ, Robinson LC. Tracer Diffusion of Magnesium in Aluminum Single Crystals, *phys. stat. sol. (b)* 63 (1974) K29.
- [58] Fujikawa S. Tracer diffusion of magnesium in Pseudo-Binary Al-Mg₂Si alloys, in: *Defect and Diffusion Forum* 143-147, 1997, pp. 403-408.
- [59] Landolt-Börnstein. *Thermodynamic Properties · Ternary Alloy Systems*, Springer-Verlag, 2005.
- [60] Yaws CL. *Thermophysical properties of chemicals and hydrocarbons*, Second edition, Elsevier, Amsterdam, 2014.
- [61] Clausen B, Lorentzen T, Leffers T. Self-consistent modelling of the plastic deformation of f.c.c. polycrystals and its implications for diffraction measurements of internal stresses, *Acta Mater.* 46 (1998) 3087-3098.
- [62] Qiao XG, Starink MJ, Gao N. The influence of indenter tip rounding on the indentation size effect, *Acta Mater.* 58 (2010) 3690-3700.
- [63] Wang SC, Zhu Z, Starink MJ. Estimation of dislocation densities in cold rolled Al-Mg-Cu-Mn alloys by combination of yield strength data, EBSD and strength models, *J Microsc.* 217 (2005) 174-178.
- [64] Zhu Z, Starink MJ. Solution strengthening and age hardening capability of Al-Mg-Mn alloys with small additions of Cu, *Mater. Sci. Eng. A* 488 (2008) 125-133.
- [65] Totemeier TC, Wright RN, Swank W. FeAl and Mo-Si-B intermetallic coatings prepared by thermal spraying, *Intermetallics* 12 (2004) 1335-1344.
- [66] Zajac S, Bengtsson B, Johansson A, Gullman LO. Optimisation of Mg₂Si phase for extrudability of AA 6063 and AA 6005 alloys, *Mater. Sci. Forum* 217-222 (1996, 217-222) 397-402.
- [67] Zajac S, Bengtsson B, Jönsson C, Isaksson A. Quench sensitivity of 6063 and 6082 aluminium alloys, in: *7th International Aluminum Extrusion Technology Seminar*, Chicago, 2000, pp. 73-82.
- [68] Zajac S, Bengtsson B, Jönsson C. Influence of Cooling after Homogenisation and Reheating to Extrusion on Extrudability and Final Properties of AA 6063 and AA6082 Alloys, *Mater. Sci. Forum* 396-402 (2002) 399-404.
- [69] Cayron C, Buffat PA. Transmission electron microscopy study of the beta ' phase (Al-Mg-Si alloys) and QC phase (Al-Cu-Mg-Si alloys), *Acta Mater.* 48 (2000) 2639-2653.
- [70] Cayron C, Sagalowicz L, Beffort O, Buffat PA. Structural phase transition in Al-Cu-Mg-Si alloys by transmission electron microscopy study on an Al-4 wt% Cu-1 wt% Mg-Ag alloy reinforced by SiC particles, *Philos. Mag. A-Phys. Condens. Matter Struct. Defect Mech. Prop.* 79 (1999) 2833-2851.
- [71] Jacobs MH. Structure of metastable precipitates formed during aging of an Al-Mg-Si alloy, *Philos. Mag.* 26 (1972) 1-13.
- [72] Marioara CD, Andersen SJ, Stene TN, Hasting H, Walmsley J, Van Helvoort, A. T. J. et al. The effect of Cu on precipitation in Al-Mg-Si alloys, *Philos. Mag.* 87 (2007) 3385-3413.
- [73] Starink MJ. Analysis of nucleation and growth with the model for diffusion-controlled precipitation reactions based on the extended volume concept, *J. Alloys Comp.* 630 (2015) 250-255.

**[BM7] Starink MJ, Milkereit B, Zhang Y, Rometsch PA:
*Predicting the quench sensitivity of Al-Zn-Mg-Cu alloys: A
model for linear cooling and strengthening.*
Materials & Design 88 (2015): 958–971.**

Benjamin's contributions: I managed the international collaboration, partially designed the experimental part, supervised the DSC work, plotted the data, participated in the results discussion and partially wrote and revised the manuscript.

Predicting the quench sensitivity of Al-Zn-Mg-Cu alloys: A model for linear cooling and strengthening

Marco J. Starink¹; Benjamin Milkereit^{1,2,3,*}, Yong Zhang⁴, Paul A. Rometsch⁴

¹Materials Research Group, Faculty of Engineering and the Environment, University of Southampton, SO17 1BJ Southampton, United Kingdom

²Chair of Materials Science, Faculty of Marine Technology and Mechanical Engineering, University of Rostock, 18051 Rostock, Germany

³Polymer Physics Group, Institute of Physics, University of Rostock, 18051 Rostock, Germany

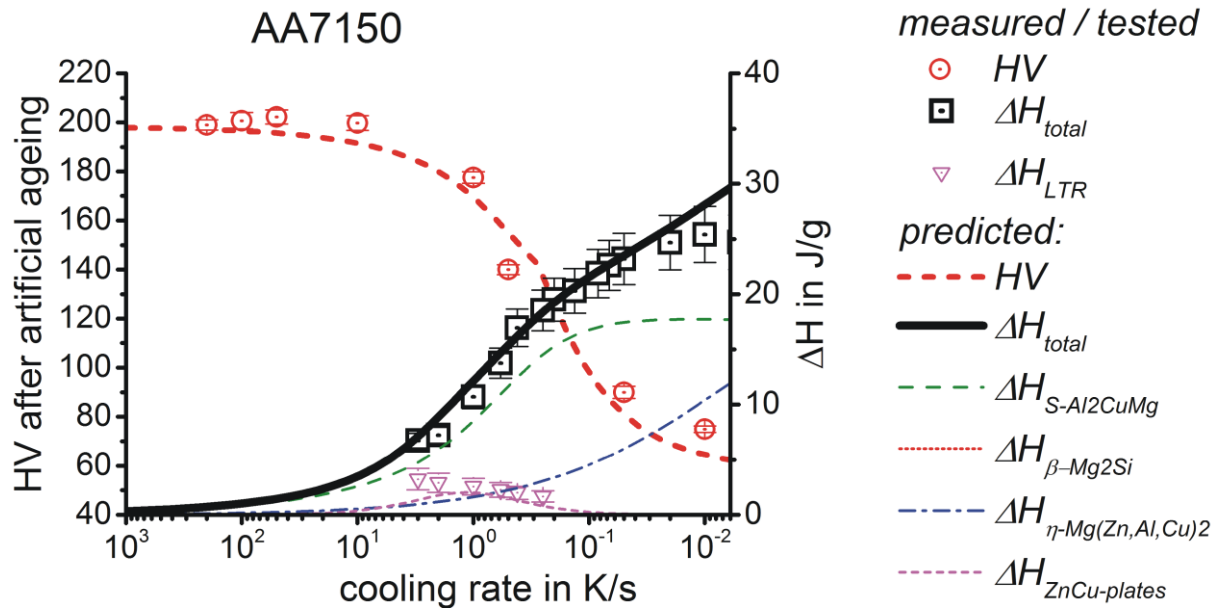
⁴Department of Materials Science and Engineering, Monash University, Clayton, VIC 3800, Australia

corresponding author: Benjamin Milkereit, benjamin.milkereit@uni-rostock.de

Abstract

In this work the quench sensitivity of Al-Zn-Mg-Cu alloys is studied through continuous cooling at constant rates of a range of alloys using differential scanning calorimetry (DSC), transmission electron microscopy (TEM), scanning electron microscopy (SEM) and hardness testing. The DSC, TEM and SEM data show that the cooling reactions are dominated by a high temperature reaction (typically ~450 °C down to ~350 °C) due mostly to S-Al₂CuMg phase formation, a medium temperature reaction (~350 °C down to ~250 °C) due predominantly to η -Mg(Al,Cu,Zn)₂ phase formation and a lower temperature reaction (~250 °C down to ~150 °C) due to a Zn-Cu rich thin plate phase. A new, physically-based model is constructed to predict rates of all reactions, enthalpy changes and resulting yield strength in the artificially aged condition. The model incorporates a recently derived model for diffusion-controlled reactions based on the extended volume fraction concept as well as recent findings from first principles modelling of enthalpies of the relevant phases. The model shows a near perfect correspondence with data on all 6 alloys studied extensively by cooling DSC and hardness testing, and allows prediction of the influence of the 3 major elements and 3 dispersoid forming elements on quench sensitivity.

Graphical abstract



Highlights

- New accurate model for continuous cooling quench sensitivity of Al-Zn-Mg-Cu alloys
- Model considers four phases: S-Al₂CuMg, β-Mg₂Si, η-Mg(Al,Cu,Zn)₂ & Zn-Cu plate phase
- Successfully tested on enthalpy changes and hardness of six alloys
- Model is verified on an extensive set of DSC, SEM, TEM and hardness experiments
- Model predicts influence of 3 major & 3 dispersoid forming elements

Keywords

Al-Zn-Mg-Cu alloys, quench sensitivity, Differential Scanning Calorimetry (DSC), precipitation kinetics, modelling

1 Introduction

In processing of high strength aluminium alloys, such as the Al-Zn-Mg and Al-Li-Cu based alloys, the quenching is a crucial stage. This is due to the formation of precipitates during (relatively) slow quenching which are generally detrimental to properties such as toughness, stress corrosion cracking resistance and yield strength (e.g. [1]). Slow quenching decreases the amount of solute that is available in the matrix for

subsequent age-hardening due to the formation of coarse, non-hardening quench-induced precipitates. This results in a reduction of the final mechanical properties, which is crucial to the application and can be the main limiting factor in application of the high strength alloy. Precipitation on defects such as grain boundaries during quenching is in practice nearly unavoidable for all high strength aluminium alloys, and the quench sensitivity generally increases with increasing content of main alloying elements. Also the minor alloying elements Zr, Mn and Cr, which form intermetallic particles of sizes typically in the range of 10-100 nm (generally termed 'dispersoids'), strongly influence the quench sensitivity as those dispersoids may act as nucleation sites for the quench-induced phase. The latter particularly holds for incoherent dispersoids, whereby the dispersoids typically lose their coherence by recrystallization (e.g. [2,3]). Hence, also the degree of recrystallisation affects the quench sensitivity. Although there are some models available, which allow fitting of multi parameter approximations to fit quenching rate data of single alloys, no model is available in the literature that predicts composition dependency.

The aim of this work is to derive and validate a model for quench induced precipitation and the resulting yield strength in age hardened condition for Al-Zn-Mg (7xxx) alloys. These 7xxx series alloys are used widely in the aerospace industry (e.g. [4]), which is still heavily reliant on these alloys due to their desirable strength-to-weight-to-cost ratios. The addition of Cu to the ternary Al-Zn-Mg system, together with small amounts of Cr, Mn and/or Zr, has resulted in the highest strength aluminium alloys available, with the yield strengths of some 7xxx alloys reaching more than 600 MPa [1].

In the new model we want to particularly include recent improved models for diffusion-controlled reactions [5,6], the advances in modelling of the thermodynamics of complex alloy systems, including first principles modelling of phases in the present alloys [7] and the computationally efficient schemes for integrating these components as recently introduced by the present authors [8]. For the validation of the model, we will use a range of experimental techniques covering the microstructure on a range of length scales, the thermodynamics of the reactions and the resulting mechanical properties. This includes transmission electron microscopy (TEM), high resolution TEM (HRTEM), scanning electron microscopy

(SEM), and high resolution fast and slow differential scanning calorimetry (DSC) covering cooling rates from 0.005 K/s to 5 K/s.

2 Experimental

2.1 Investigated alloys and their thermomechanical treatments

In total 12 Al-Zn-Mg(-Cu-Si) alloys covering a wide range of compositions were investigated from which 6 alloys were selected for extensive continuous cooling experiments. The chemical compositions of these alloys as well as an overview of the performed experiments are given in **Table 1**. (All compositions in this work are in at% and composition ratios are based on at%.)

Table 1: Chemical compositions of investigated alloys (in atomic %), with experiments performed. The alloys are termed according to the nominal or nearest AA standard of common 7xxx alloys, C refers to a commercially produced alloy, m stands for composition close to medium of alloy standard. cDSC = cooling DSC, hDSC = heating DSC

Alloys	Si	Fe	Zn	Mg	Cu	Cr	Mn	Zr	Experiments
AA7150Cm	0.02	0.03	2.74	2.51	0.91	-	0.02	0.04	TEM, cDSC, SEM, HV, OM, EBSD
AA7055m	0.03	0.02	3.56	2.36	0.90	-	-	0.04	cDSC, OM, SEM, HV
AA7085C	0.07	0.02	3.58	1.72	0.93	-	-	0.04	cDSC, OM, SEM, HV
AA7085 _{low} Cu	0.12	0.01	3.40	1.60	0.41	-	-	0.04	cDSC, OM, SEM, HV
AA7020	0.11	0.08	1.85	1.36	0.02	0.06	0.06	0.04	TEM, cDSC, SEM, OM, HV
AA7049Ac	0.26	0.18	3.60	3.43	0.86	0.12	0.10	-	cDSC, OM, SEM, HV
AA7449C	0.03	0.02	3.4	2.3	0.74	-	-	0.05	hDSC, TS, SEM, TEM, OM
AA7150m	0.03	0.02	2.61	2.65	0.84	-	-	0.04	hDSC, OM
AA7150 _{hi} Zn	0.03	0.02	2.87	2.19	0.84	-	-	0.04	hDSC
AA7150 _{lo} Cu	0.03	0.02	2.61	2.65	0.53	-	-	0.04	hDSC
AA7150 _{hi} Cu	0.03	0.02	2.61	2.65	1.1	-	-	0.04	hDSC, SEM, OM
AA7150 _{hi} ZnCu	0.03	0.02	2.91	2.2	1.1	-	-	0.04	hDSC

The AA7020 alloy is a laboratory extruded 30 mm diameter rod, whilst the AA7049Ac is a commercially extruded 50 mm diameter rod. The AA7150c and AA7449c alloys are commercially processed hot-rolled plates of 80 and 30 mm thickness, respectively. (The code c for commercial is added to distinguish them from laboratory-produced materials.) The other alloys are hot rolled plates produced in labs. The AA7020

and AA7049A extrusions have a uniform grain structure, with a grain size of $\sim 10 \mu\text{m}$; the centre of the commercially processed AA7150 plate is about 5 % recrystallized, the AA7449 alloy is about 20 % recrystallised and the lab produced plates are typically 50 % recrystallized. These differences in recrystallization are primarily due to subtly different homogenisation and thermomechanical processing [9,10]. The AA7020, AA7150C, AA7055, AA7085C, AA7085lowCu and AA7049A alloys were selected for detailed quenching studies using cooling DSC (cDSC) to record the enthalpy changes in situ during cooling at a wide range of cooling rates. The remaining 6 alloys were used for a range of additional experiments to verify the model parameters and the strengthening model in water-quenched and subsequently aged conditions. Compositions and an overview of the experiments conducted are presented in Table 1. The alloys were cooled using a range of cooling rates/procedures and subsequently aged at $120 \text{ }^\circ\text{C}$ for 24 h.

2.2 Calorimetry

In all DSC work a pure aluminium sample of mass and size comparable to the 7xxx sample is used as a reference material. A baseline using pure Al samples in both microfurnaces was determined immediately prior to or after each sample measurement. Cooling differential scanning calorimetry (cDSC), covering cooling rates from 0.005 K/s to 5 K/s, were performed employing three different devices: a Setaram 121 DSC 0.005-0.1 K/s; a Mettler-Toledo 823 DSC 0.1-0.5 K/s; a PerkinElmer Pyris 1 DSC 0.5-5 K/s. The specific precipitation enthalpy was evaluated by integrating the excess specific heat capacity curves and the relative contributions due to partially overlapping precipitation peaks were estimated using the minimum heat flow. (For further details on cDSC procedures and samples see [11,12]). Heating DSC (hDSC) experiments on solution treated and water-quenched samples of the laboratory produced AA7150 variant alloys were performed in a Shimadzu DSC-50 (cylindrical disc sample $\approx \text{Ø}5\text{x}1 \text{ mm}$; $\approx 60 \text{ mg}$) using a scanning rate of 10 K/min ($\approx 0.17 \text{ K/s}$).

2.3 Mechanical testing

Vickers hardness testing was performed on both as-quenched/cooled and artificially aged samples using a 5 kg load. Each hardness value reported is an average based on 6 indentations made on each sample. To achieve controlled cooling rates faster than 3 K/s a quenching dilatometer Baehr 805 was used. Tensile tests on the AA7449C alloy were carried out according to the ASTM standard E-8 with specimens tested in the L (longitudinal) direction.

2.4 SEM and EBSD

For SEM, samples were ground and polished with SiC paper, diamond paste and colloidal silica for examination in either a JEOL JSM-6400 or a JEOL JSM-7001F field emission gun scanning electron microscope (FEG-SEM), both equipped with an energy dispersive X-ray spectrometry (EDS) system. Unless otherwise noted, imaging was conducted in the backscattered electron imaging (BEI) mode.

Electron backscatter diffraction (EBSD) was performed on selected alloys using a JEOL JSM-7001F or a JSM 6500F SEM each equipped with an HKL-Channel 5 EBSD detector and software package (Oxford, Instruments, UK). The EBSD specimens were ground and polished and subsequently electro-polished using a solution of 33% HNO₃ and 67% methanol at a temperature of -30°C. The step size was 1 or 2 μm. The success rate of identification of Kikuchi patterns was 80-90%.

2.5 TEM and STEM

TEM foils were prepared by electro-polishing with a solution of 33% nitric acid and 67% methanol, at a temperature of -30°C. Conventional bright field (BF) TEM was carried out on a Tecnai T20, operating at 200 kV. Elemental mapping was carried out by scanning transmission electron microscopy (STEM) based EDS imaging on a JEOL 2100F operated at 200kV.

Atomic resolution HAADF-STEM was performed on a dual aberration corrected (STEM & TEM) FEI Titan3 microscope operated at 300 kV. A convergence angle of 15 mrad was employed, leading to a diffraction limited (Gaussian) probe diameter of ~0.12 nm. Images were collected on a Fischione HAADF detector.

3 DSC cooling curves and microstructure of selected quench states

In this section we will present new detailed cooling DSC studies and will give an overview about the main quench-induced precipitation reactions. To complement the microstructure data on a range of alloys available in the literature [2,9,13–17], therefore also results of microstructural studies on selected samples in different cooling conditions are presented.

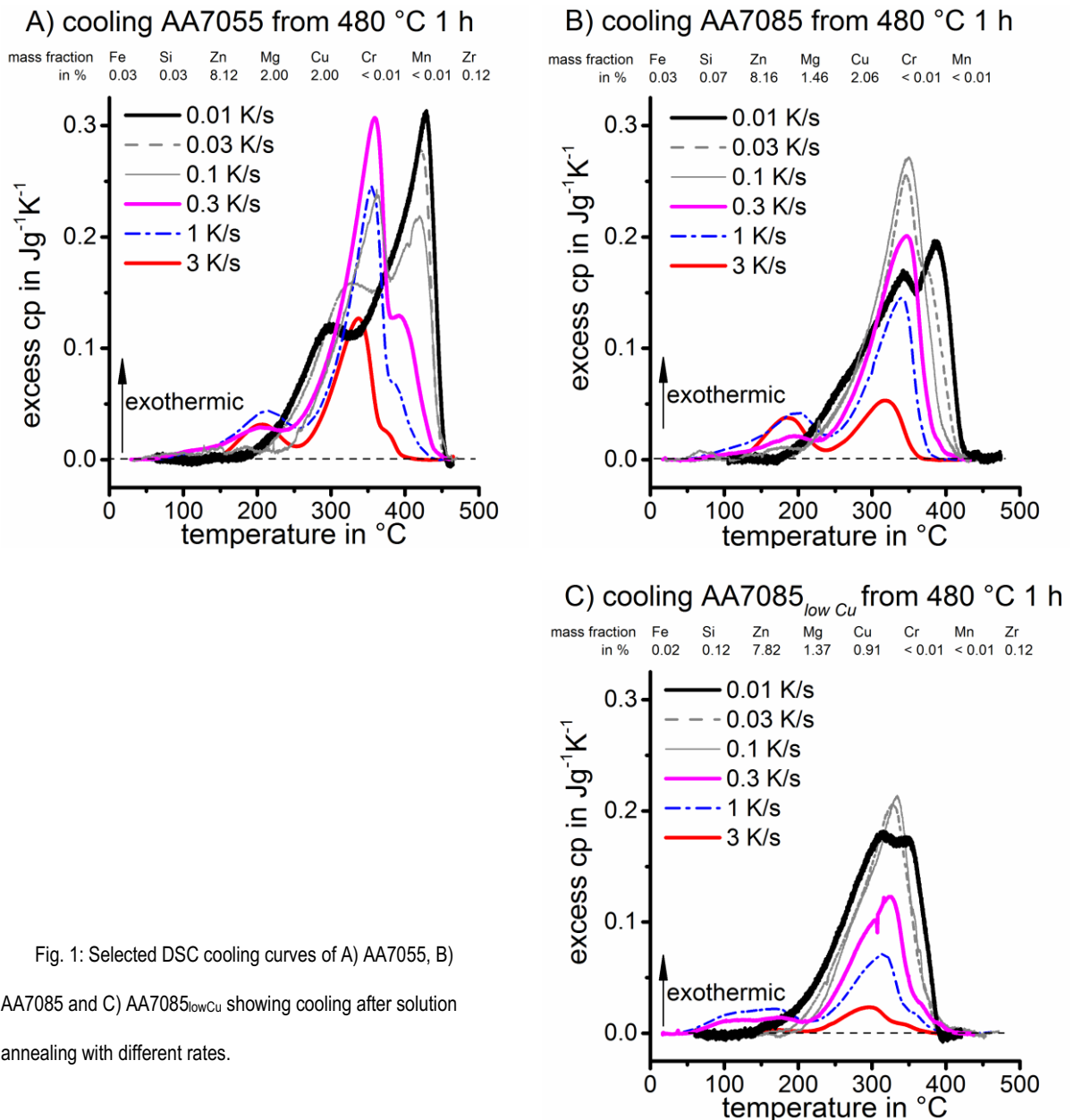


Fig. 1: Selected DSC cooling curves of A) AA7055, B) AA7085 and C) AA7085_{lowCu} showing cooling after solution annealing with different rates.

Fig. 1 displays selected cDSC curves of AA7085, AA7085_{lowCu} and AA7055; cDSC for AA7020C, AA7150C and AA7049A are presented elsewhere [11,18]. Depending on cooling rate these cDSC curves show up to 3 main reactions: a high temperature reaction (HTR, typically 450 °C down to ~350 °C), a medium temperature reaction (MTR, ~350 °C down to 250 °C) and a lower temperature reaction (LTR, ~250 °C down to ~150 °C). These reactions partially overlap, with the degree of overlap depending on alloy composition and cooling rate.

To supplement microstructure data available in the literature we performed TEM and SEM on alloy / cooling rate combinations that have hitherto not been reported on, in combination with interrupted quench experiments. The latter experiments, illustrated in Fig. 2, allowed us to identify the phases formed in the reactions seen in the cDSC curves. To determine which phase precipitates in each reaction, we cooled samples at rates for which the reaction of interest is dominating and clearly detectable (Fig. 2A) down to a temperature just below the temperature corresponding to the maximum heat flow with overcritical fast

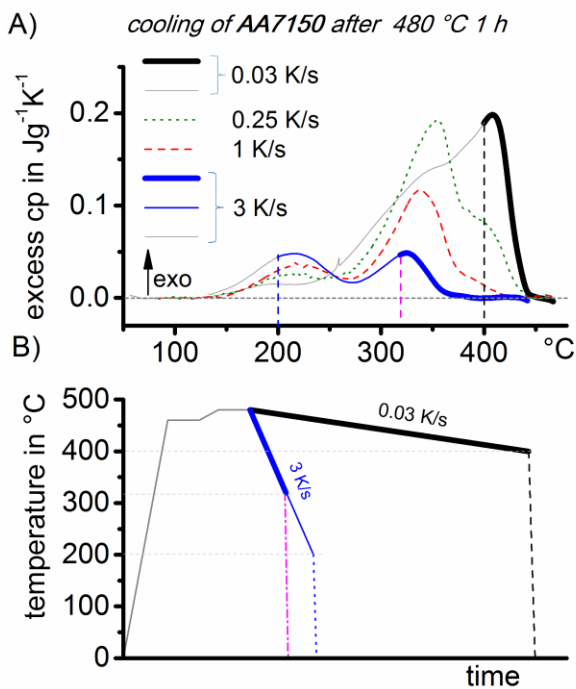


Fig. 2: Scheme of step-quench experiments. A) Selected DSC curves of relevant cooling rates of AA7150c. Exemplary cooling rates and temperatures at which the precipitation state was frozen (by overcritical quenching) are highlighted. B) Schematic temperature-time profile of the step quench experiments.

quenching rate (Fig. 2B). The cooling rate and temperature were chosen individually for each alloy. For cooling rates in which one reaction clearly dominates additional samples were investigated after cooling with a constant rate to room temperature.

To identify the reaction(s) involved in the HTR we performed TEM and SEM work. Fig. 3 shows the SEM images of an AA7150 sample cooled at 0.03 K/s to RT. TEM-SAED and EDS revealed that the large particles with irregular shapes and dimensions up to several tens of micrometres are S-Al₂CuMg precipitates. Step quench experiments confirmed that S-

Al_2CuMg precipitates form during the HTR. In SEM studies, the S- Al_2CuMg phase is also seen to have nucleated on $\text{Al}_7\text{Cu}_2\text{Fe}$ intermetallic phases (see Fig. 3). Thus the present TEM and SEM work shows the formation of S- Al_2CuMg phase is responsible for the HTR in the Cu containing alloy AA7150C and previous work has shown that S- Al_2CuMg phase formation also occurs in this high temperature range for a range of other Cu containing 7xxx alloys [19,20].

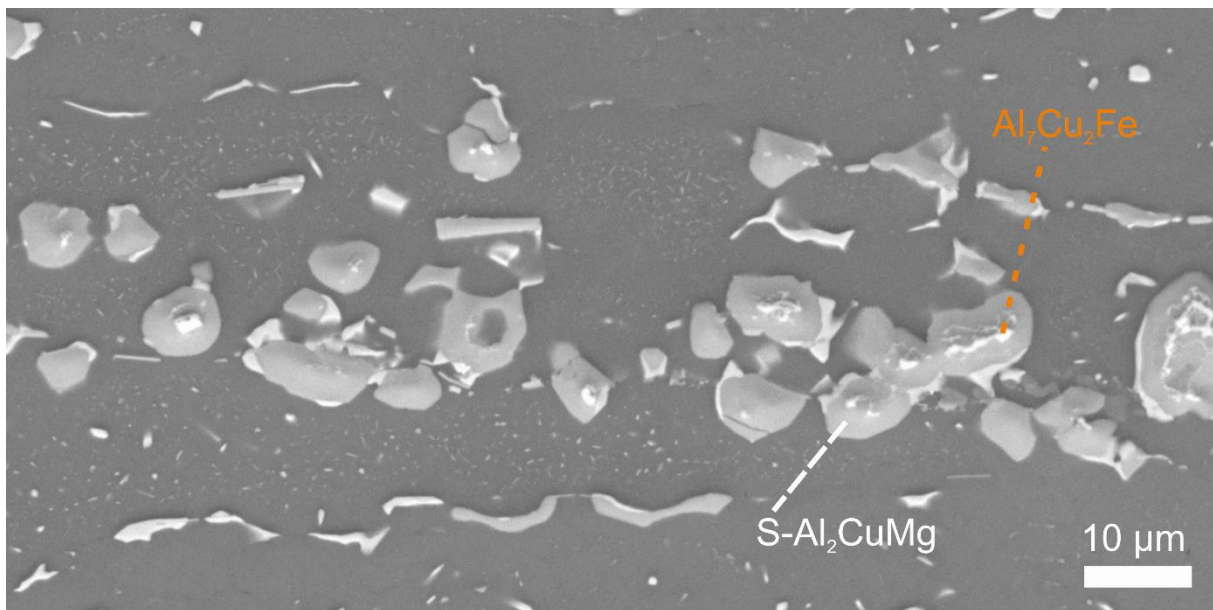


Fig. 3: SEM BEI image of an AA7150 sample cooled with 0.03 K/s to RT. Very coarse S- Al_2CuMg particles are visible (undefined shapes, dimensions up to some tens of μm). The S- Al_2CuMg precipitates appear to have nucleated at $\text{Al}_7\text{Cu}_2\text{Fe}$ particles. Besides these two precipitation species, additional much finer $\eta\text{-Mg}(\text{Zn},\text{Al},\text{Cu})_2$ precipitates are visible.

AA7020 contains no Cu and hence no S- Al_2CuMg phase forms in these samples. In this alloy, which contains about 0.1 at% Si, some limited formation of Mg_2Si is detected at very slow cooling rates – see Fig. 4. At 0.005 K/s about 0.3 vol% $\beta\text{-Mg}_2\text{Si}$ is observed, which corresponds well with expected amounts at the completion of the reaction [8]. The temperature range and cooling rate range of the HTR in the AA7020 alloy correspond well with the model for Al-Mg-Si alloys developed recently [8]. Thus in alloys which contain Cu, Mg and Si two phases may contribute to the HTR: S- Al_2CuMg and $\beta\text{-Mg}_2\text{Si}$

Fig. 5 shows two images from step-quench experiments on AA7150. The image in Fig. 5A) was recorded on a sample cooled at 3 K/s to 320 °C. According to the cDSC results (Fig. 2) in this state only precipitates of the MTR should be present as the HTR is suppressed at this high cooling rate. TEM SAED and EDS analysis revealed η -Mg(Zn,Al,Cu)₂ precipitates nucleated on Al₃Zr dispersoids and this finding is in line with published TEM and SEM work on several Al-Zn-Mg-Cu alloys [2,11,16,21–23].

The sample of Fig. 5B) was cooled at 3 K/s to 200 °C. cDSC data (Fig. 2A) shows that in this state also precipitates belonging to the LTR should be present, and Fig. 5B) reveals that besides dot-like Al₃Zr dispersoids another phase in the form of thin plates is present.

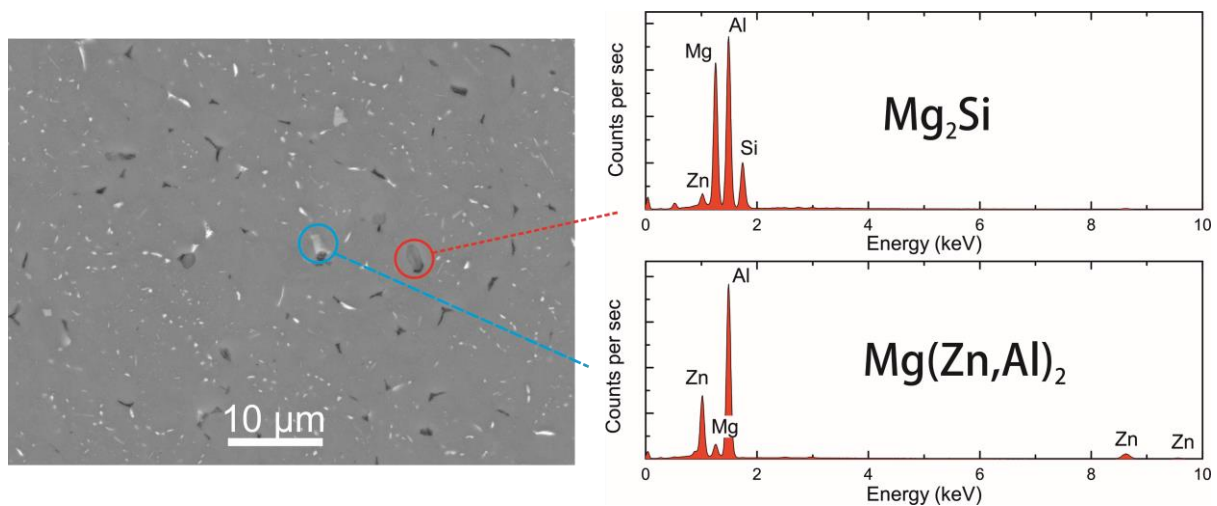


Fig. 4: Backscattered SEM image of alloy AA7020 sample cooled at 0.005 K/s and corresponding EDS analysis results for large particles with different image contrast showing that they correspond to η -phase (Mg(Zn,Al)₂) and β -phase (Mg₂Si).

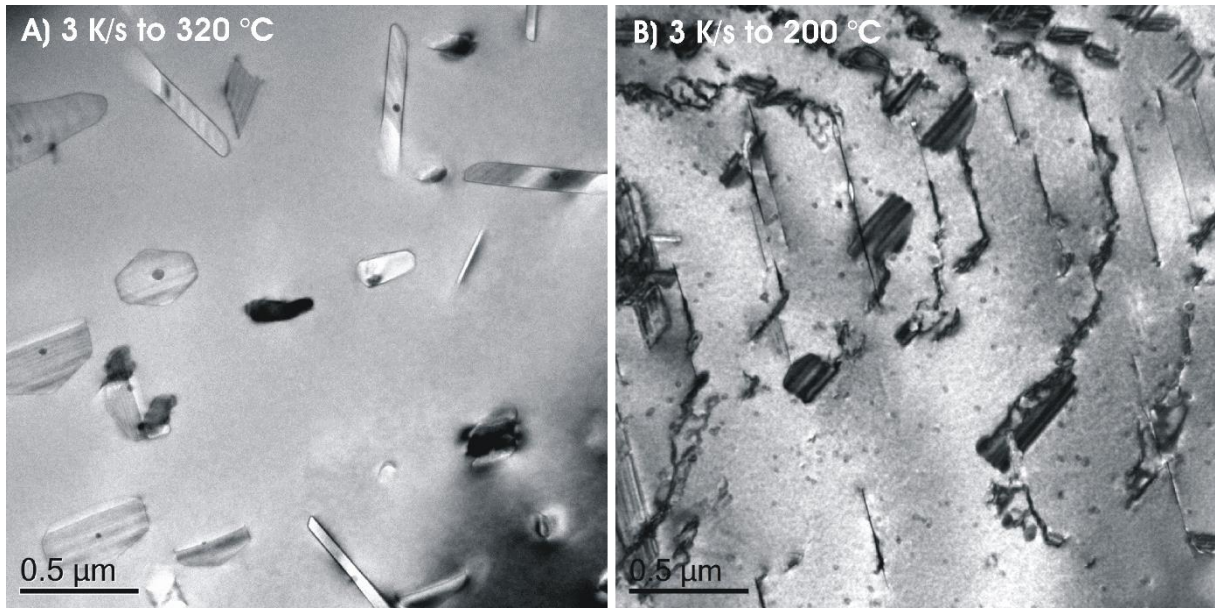


Fig. 5: TEM images (bright field) of AA7150 step quenched at a cooling rate of 3 K/s in A) to 320 °C and in B) to 200 °C. In A) two types of precipitates can be seen in a recrystallized grain. The irregular shaped precipitates with dimensions of typically 50-500 nm are η -Mg(Zn,Al,Cu)₂ and appear to have all nucleated on a spherical Al₃Zr particle (typical diameter 20-50 nm). In B) which was cooled further down to 200 °C, additionally thin plate like precipitates corresponding to the LTR can be found. Al₃Zr dispersoids are also present appearing as small dots.

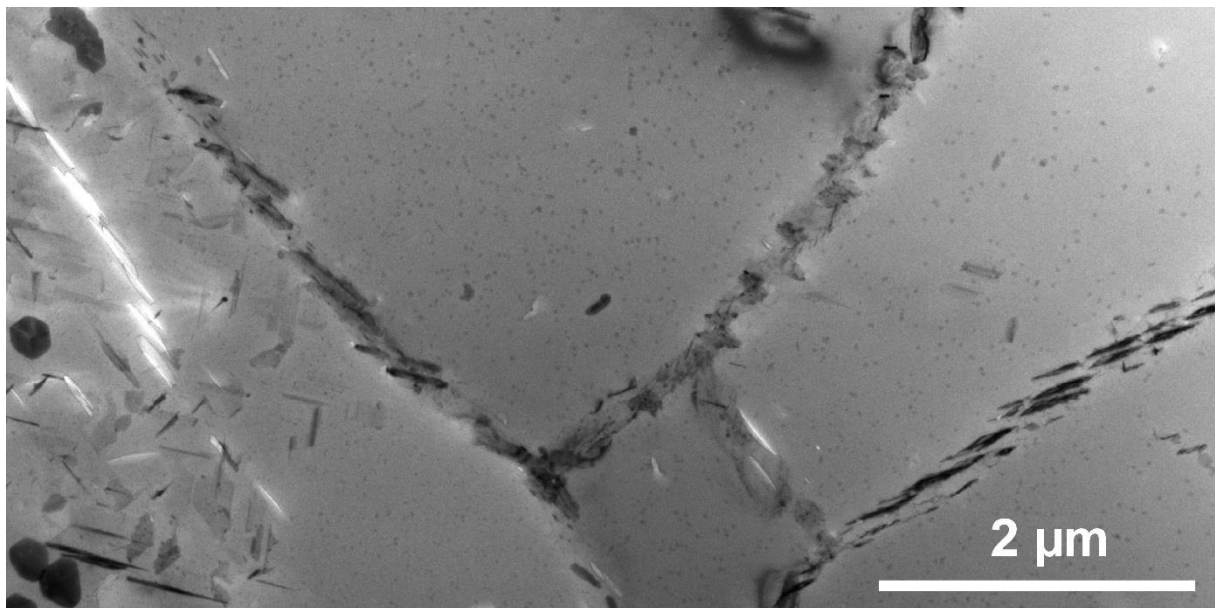


Fig. 6: TEM image of an air-cooled AA7150 sample (average cooling rate 1 K/s) showing a recrystallized grain on the left side and some subgrains on the right. It can be seen, that the quenched-induced η -Mg(Zn,Al,Cu)₂ precipitates preferentially nucleate at grain/subgrain boundaries and also appear inside the recrystallised grain nucleating at Al₃Zr dispersoids.

At a medium cooling rate (air cool, average cooling rate 1 K/s) the MTR dominates and the quench-induced phases in the AA7150 alloy precipitate preferentially within the recrystallised grains (as illustrated in Fig. 6). During cooling/quenching the η -Mg(Zn,Al,Cu)₂ precipitates nucleate preferentially on defects such as dislocations, grain boundaries and free surfaces that can reduce the activation energy barrier including dispersoids-matrix interfaces that are incoherent [3,23]. Fig. 6 shows the microstructure of an air-cooled sample (average cooling rate 1 K/s). DSC (Fig. 2A) reveals that during this type of cooling the vast majority of the precipitates will form by the MTR and Fig. 6 reveals a large number of quench-induced η -Mg(Zn,Al,Cu)₂ precipitates nucleated on Al₃Zr dispersoids in a recrystallised grain and on grain boundaries. In unrecrystallised subgrains like on the right part of Fig. 6 no quench induced η -Mg(Zn,Al,Cu)₂ precipitates can be found, as the dispersoids here are coherent with the matrix. In line with TEM analysis of a AA7055 alloy [24], no or very few η -Mg(Zn,Al,Cu)₂ precipitates are seen to nucleate on the coarser intermetallics in our alloys at cooling rates faster than 1 K/s. This is due to the fact that most of the surface area available for nucleation is provided by the dispersoids and grain and sub-grain boundaries (see Section 5). These η -Mg(Zn,Al,Cu)₂ precipitates on grain boundaries are ubiquitous in 7xxx alloys and are present even in samples cooled at relatively high rates (about 100 K/s, [2]) in Al-Zn-Mg alloys with Zn contents lower than the present alloys [2].

Fig. 7 shows an overview of precipitates nucleated in the grain and on the grain boundary for the alloys AA7085, AA7085lowCu, AA7055, AA7150c and AA7020 using SEM in BEI mode. For these samples, the cooling rates employed are such that ~50 % of the maximum ΔH of the MTR has been achieved. The left part of the figure shows a lower magnification, whilst the right part shows more details in a higher magnification. S-Al₂CuMg phase formation is suppressed (nearly) completely at the cooling rates employed for the samples in Fig. 7 and the bright precipitates visible in Fig. 7 are η -Mg(Zn,Al,Cu)₂ precipitates. The images show that in the MTR for AA7020 nearly all of the η -Mg(Zn,Al,Cu)₂ form on grain boundaries, whilst for the MTR in the other alloys the precipitation in the grains is dominant, with precipitation on grain boundaries occurring as well.

The platelet phase formed in the LTR has been studied in detail using HRTEM. Fig. 8A) shows a TEM bright field image of platelet phase precipitates in AA7150 after cooling at 10 K/s to room temperature. Fig. 8B) shows an HAADF-STEM image of one of such plates and it appears that the phase is attached to a nanometer sized void. This is suggesting it either nucleated on a void or that the solute atoms forming the precipitate were linked to vacancies which condensed to a nanovoid. Next to the platelet phase some few dispersoids free of any other precipitates can be seen, showing that the platelet phase does not form on Al_3Zr dispersoids. Fig. 8C) shows an EDS mapping of a single platelet phase revealing the segregation of predominantly Zn and Cu. The EDS results indicate a Zn/Cu ratio of about 3/2.

A range of further TEM, SEM and EDS experiments were reported elsewhere [25] and all data is consistent with the above interpretations of HTR and MTR reactions. Thus, in summary, the present results in combination with literature data show that during the quench 4 main reactions occur: formation of S-Al₂CuMg phase (HTR1), formation of Mg₂Si (HTR2), formation of η -Mg(Zn,Cu,Al)₂ phase (MTR) and formation of Zn-Cu plates (LTR). The S-Al₂CuMg phase forms predominantly on Cu containing coarse particles (S-Al₂CuMg and Al₇Cu₂Fe) and on grain boundaries. The formation of η -Mg(Zn,Cu,Al)₂ occurs in two distinct types of location: on dispersoids and on grain/subgrain boundaries, and the platelet LTR particles form in the grains apparently associated with vacancy clusters.

Our DSC experiments further show a further minor reaction in the temperature range below the LTR down to about 50 °C, which we will term very low temperature reaction (vLTR). However, due to cooling control and signal to noise limitations of the DSC devices this small reaction in this temperature range can not be consistently assessed by cDSC. Nevertheless, for AA7085 and AA7085_{lowCu} the vLTR reaction is clearly detected at rates of 0.3 and 1 K/s in Fig. 1, which are about optimal cooling rates for the DSC used for this rates and cooling was in control (at constant rate) down to about 30 °C.

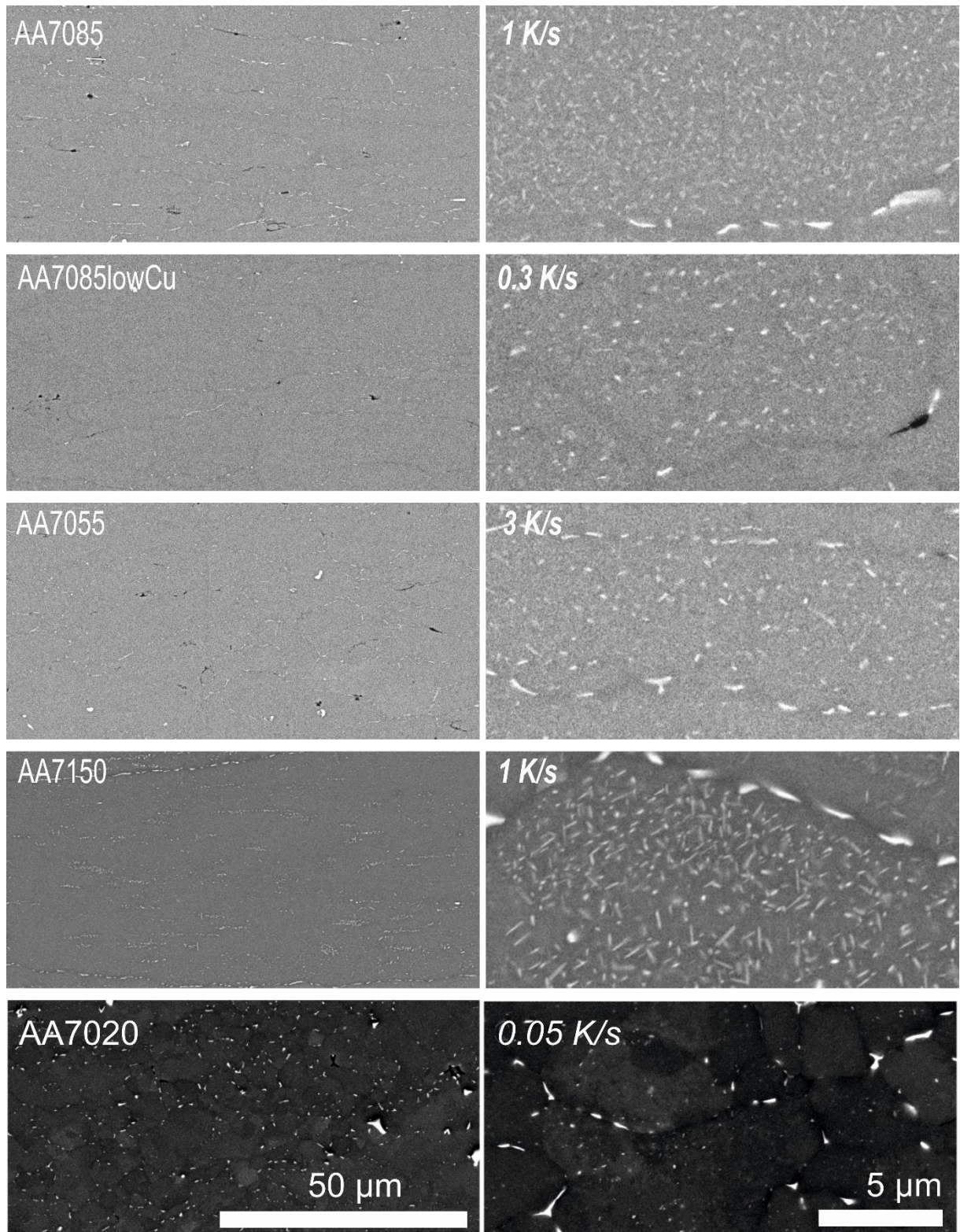


Fig. 7: SEM backscattered mode images for samples of AA7085, AA7085lowCu, AA7055, AA7150 and AA7020 cooled at the respective rates at which ~50% of the maximum ΔH of the MTR has been achieved. Left part low magnification, right part higher magnification. For all alloys nearly all quenched in precipitates visible here are η -Mg(Zn,Al,Cu)₂ precipitates.

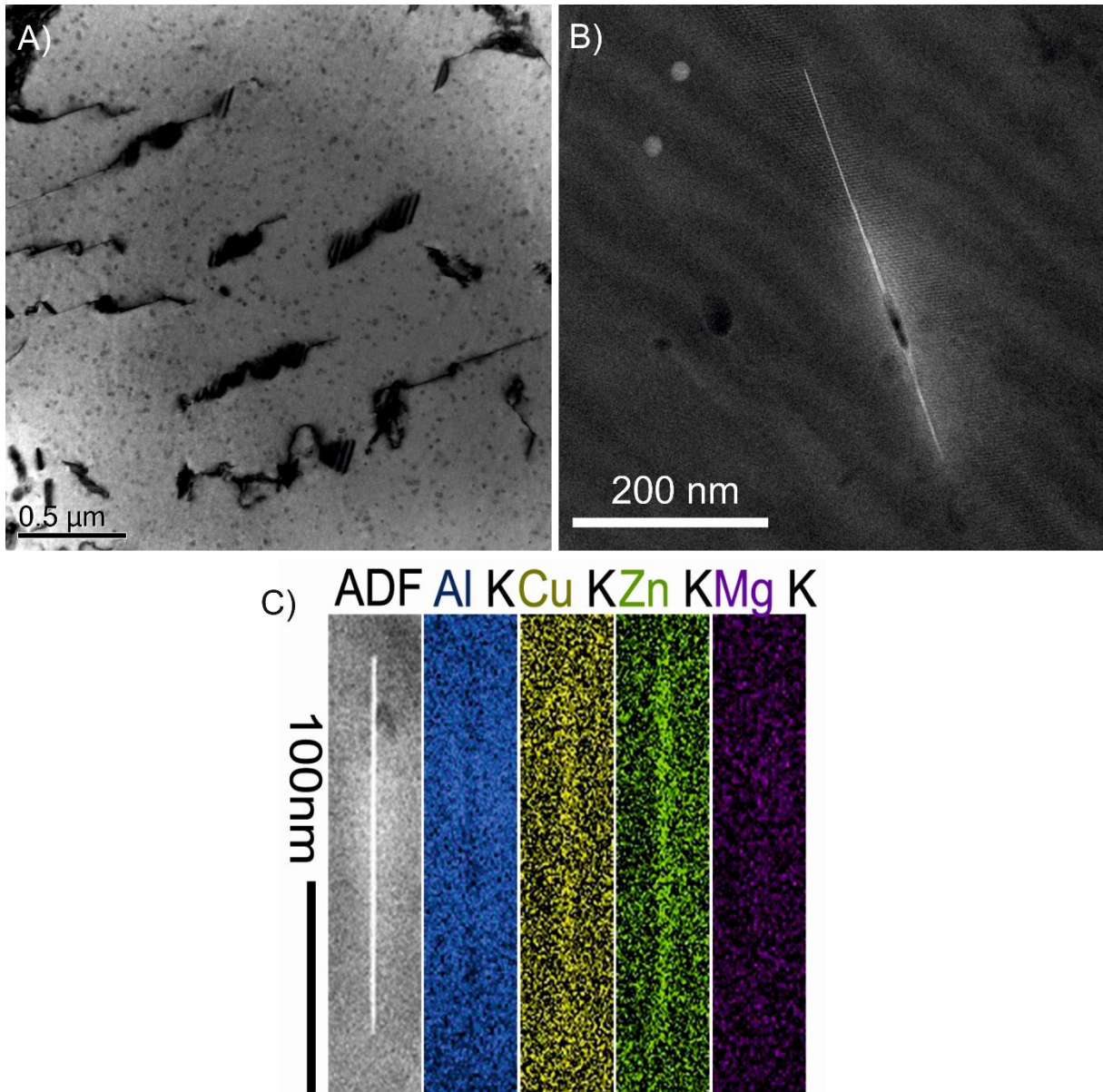


Fig. 8: HAADF-STEM figures of AA7150C A) showing several platelet structures (~200-400 nm length) together with several Al₃Zr dispersoids after cooling at 10 K/s to room temperature. B) showing the platelet structure after cooling at 3 K/s to 200 °C. The thin plate precipitate is attached to a void. C) EDS mapping (together with an ADF image left) of a single platelet phase, showing the platelet phase consists predominantly of Zn and some Cu.

We conclude that according to our HRTEM results the LTR in the temperature range of about 250-150 °C is dominated by the precipitation of a Zn-Cu rich thin plate phase. At even lower temperatures of about 150 to 50 °C additionally co-clusters may precipitate. This explains the detection of a Guinier radius decrease in SAXS experiments on continuous cooling of AA7449 below 100 °C in [26,27]. The Zn-Cu rich thin plate phase as well as clusters contribute to strength and during artificial ageing the clusters are thought to further evolve into fine η' hardening precipitates.

4 A model for precipitation during quenching and subsequent age hardening

4.1 A model for quench induced precipitation

At the start of the quench

As a starting point of the model, first the amounts of undissolved phases (coarse intermetallics and dispersoids) present at the start of the quench are predicted. The main undissolved phases present in Cu-containing 7xxx alloys are $Al_6(Mn,Fe)$ and Al_7Cu_2Fe [28,29], and if the Cu and Mg content is high, some undissolved S- Al_2CuMg phase particles will be present [30,31]. If Cr is present a Cr containing phase will form which in many alloys will be $Al_{18}Mg_3Cr_2$ [32,33]. Details of the predictions for the amounts of these phases are provided in the Appendix. This part of the model provides the concentrations of elements in the Al-rich matrix phase after solution treatment (i.e. just prior to start of the quench), which are denoted as $X_{Mg,st}$, $X_{Zn,st}$, etc.

General structure of the model for quench induced precipitation: extended volume and reaction rates in the extended volume

The present model expands the modelling strategy outlined in [8]. One simplification adopted in that model, again adopted here to drastically improve the model efficiency through reducing computational complexity, is the use of consecutive reactions, e.g. the interaction between the reactions occurs through taking the Al-rich phase composition achieved after one reaction to be the starting state of the next reaction. Following the findings in Section 3 we consider 4 consecutive reactions in the model: formation of S- Al_2CuMg phase (HTR1), formation of Mg_2Si (HTR2), formation of η - $Mg(Zn,Cu,Al)_2$ phase (MTR) and formation of Zn-Cu-rich thin plates (LTR).

A key element in the model is the use of the extended volume concept [6,34–38], the conceptual volume in which particles grow without being limited by the interaction with diffusion fields from other particles. This approach has been shown to be computationally very efficient and provide predictions for diffusion field impingement that outperform other models [5,6]. Hence we formulate the formation of precipitates in terms of the extended fraction transformed, α_{ext} , i.e. the fraction transformed that would

form in the extended volume. As provided before [39], the extended volume fraction, α_{ext} , can be represented as

$$\alpha_{ext} = (kQ)^n \quad (1)$$

where Q is the quench factor [39], k is a rate constant and n is the reaction exponent [5,38]. Following [39], Q is defined as:

$$Q = \int_{t=0}^t \frac{dt}{C_t} \quad (2)$$

For constant cooling rates, Q is proportional to the time during the quench, which in turn is proportional to the inverse of the cooling rate. Thus we find the basic expression for the extended volume fraction during cooling at constant rate:

$$\alpha_{ext} = (k/\beta)^n \quad (3)$$

where β is the cooling rate. The temperature at which the reaction occurs depends on alloy composition and the solvus of the precipitating phase. In [8] we derived that the ratio of diffusion rate, $D(T)$, where T is the temperature, and diffusion pre-exponential constant, D_o , is given by [8]:

$$\frac{D}{D_o} = \left(\frac{\prod_i c_i^{a_i}}{C} \right)^{\frac{E_D}{\Delta H}} \quad (4)$$

where c_i is the concentration of alloying element i in solution, C is a constant, ΔH is the enthalpy of formation of the phase and E_D is the activation energy for the rate-determining process of the reaction (typically the diffusion of the slowest diffusing element). The latter equation was verified through comparison of extensive cDSC data on a range of alloys with model predictions [8]. The functional relation between the formation rate of the phase, k_2 , and the composition for the case that the number of growing precipitates is independent of the solute content of the alloy (this is the case for a limited number of nuclei), is given by:

$$k_2 = k_o \frac{D}{D_o} [y_{QP}(\max)]^p \quad (5)$$

where $y_{OP}(\max)$ is the maximum amount of precipitates that can form, and p equals 1/3 [8]. The constant k_0 needs to be fitted for each reaction, whilst all the other constants in the model can, in principle, be obtained from investigation of mechanisms and thermodynamics involved. These basic elements of the model will be further expanded below, but first we will define the reactions that are to be considered in the model.

The reactions during the quench

The S-Al₂CuMg and β (Mg₂Si) phases formed in the HTR reactions are treated as stoichiometric compounds, the fixed compositions are taken as Al₂CuMg and Mg₂Si. The solvus and enthalpy of formation of Al₂CuMg is based on Refs. [30,40]. The solvus, enthalpy, activation energy and all other kinetic parameters of formation of β (Mg₂Si) are taken as described in [8].

The MTR is due to η -Mg(Zn,Cu,Al)₂ phase forming on grain and subgrain boundaries [19] and dispersoids (e.g. [3,23,41–45]); and this reaction to a large extent determines the resulting mechanical properties of the material in quench conditions that are of industrial relevance. Hence we will pay special attention to this reaction. The η -Mg(Zn,Cu,Al)₂ phase is based on the MgZn₂ topologically close-packed Laves phase and the Cu and Al contents have been discussed in several studies [7,46]. The enthalpy (and hence the stability) of topologically close-packed Laves phases such as MgZn₂ is highly dependent on the atomic size [47,48] and the electronic structure [49,50]. Cu has a valence electronic configuration that is identical to that of Zn (3d¹⁰) whilst it has a much smaller atomic radius than Mg, and thus Cu is likely to replace Zn in the η structure. First principles modelling indicates that the enthalpy of formation of the η phase increases substantially when Al and Cu replace Zn atoms in a 12 atom unit cell, and particularly the composition change from MgZn₂ to Al₁Zn₅Cu₂Mg₄ provides a much more stable composition with an enthalpy that is increased by 35% [7]. However, as the diffusion rate of Cu is an order of magnitude lower than that of Mg and Zn this composition will not be achieved when the η phase forms during the cooling. To address this, the present model considers that during nucleation and growth of the η -Mg(Zn,Cu,Al)₂ phase the Cu atoms are effectively stationary in the Al-rich phase and hence the average

Cu content of the η -Mg(Zn,Cu,Al)₂ phase particles will equal the Cu content of the alloy. Thus in the model the η -Mg(Zn,Cu,Al)₂ phase precipitates nucleated during the cooling are effectively made up of units of Mg₄Zn₈ and Al₁Zn₅Cu₂Mg₄.

The incorporation of Cu and Al in η will enhance its rate of formation through several factors:

- i. the increase in enthalpy change ΔH increases the solvus temperature of the phase and hence the precipitation rate is higher (due to the increased diffusivity);
- ii. the entropy S is increased which increases the solvus temperature of the phase;
- iii. the maximum amount of phase that can form is increased;
- iv. an enhanced number of growing nuclei;
- v. less Zn needs to diffuse to form the phase.

Factors i and iii are incorporated in the model through changing the enthalpy change ΔH , entropy S and γ , which become dependent on the Cu content, using the theory in [8]. The entropy S is incorporated by replacing the simplified expression of free energy ΔG as ΔH by its full form ($\Delta G = \Delta H - TS$), i.e.:

$$\frac{D}{D_o} = \left(\frac{\prod_i c_i^{a_i}}{C} \right)^{\frac{E_D}{\Delta G - TS}} \quad (6)$$

Homogeneous and heterogeneous nucleation depends on a range of factors, including interfacial energy, the diffusion rate and the critical particle size. Of these factors, the Cu and Al content have a strong influence on nucleation particularly through their indirect influence on the diffusion rate (via the increased solvus).

There is no data available on the interfacial energies between the η phase and matrix, or on the influence of Cu (and Al) incorporation on these interfacial energies. As there is no indication that the latter is a particularly strong effect, we will not consider this in the model. The mass density of MgZn₂ is 5.09 g/cm³ [51], which is equivalent to an atomic density that is virtually identical to that of the matrix, and thus volume misfit strains on precipitation will be minimal. (For the metastable η' phase the incorporation of Cu atoms is also considered to enhance phase stability [43,52,53].)

The initial rate of formation of η phase nuclei will be proportional to the amount of sites available, which is determined by the grain/subgrain boundary area and the particle-matrix interface area for the undissolved particles present at the start of the quench. Both are incorporated in the model. The amount of grain boundaries available is calculated on the basis on the grain and subgrain sizes reported in the literature and Section 3, and the recrystallized fractions of the alloys. The number density and total particle-matrix interface area of particles present at the start of the quench is obtained as outlined in the Appendix. We take $r_{\text{Al}_{18}\text{Mg}_3\text{Cr}_2}=30$ nm [23,54], $r_{\text{Al}_7\text{Cu}_2\text{Fe}}=2000$ nm [55], $r_S=1000$ nm [55]). Recent work on Mn containing alloys shows $\text{Al}_6(\text{Mn,Fe})$ particles in an alloy with relatively low Mn content (0.1 at%) are thin plates (average thickness about 40 nm in an alloy heat treated at 520 °C) [56]. These particles form thin plates due to very good coincidence site matching between lattice points in $(0\ 0\ 1)_p$ and $(3\ -1\ 5)_m$ planes in selected orientation relations [56]. The average thickness of the $\text{Al}_6(\text{Mn,Fe})$ for the present alloys is obtained using the latter data by Li et al. [56] and coarsening data in Kong et al. [57] (showing the activation energy for coarsening to be 200 kJ/mol) as 20 nm. Al_3Zr particles in unrecrystallised grains are coherent with the matrix and precipitates generally do not nucleate on them (e. g. [3,23]). In the recrystallized grains, which are substantially larger than subgrains, the Al_3Zr particles are incoherent and η phase does nucleate on those particles [3,23,58]. The radius of the Al_3Zr particles is typically 20-50 nm [43]. It is known that the presence of $\text{Al}_{18}\text{Mg}_3\text{Cr}_2$ causes enhanced formation of $\eta\text{-Mg}(\text{Zn,Cu,Al})_2$ during the quench, and many works have suggested that this is related to the interfacial energy, even though no data on interfacial energy is known. However, it should be noted that the $\text{Al}_{18}\text{Mg}_3\text{Cr}_2$ phase has a range of stability with variable Mg content from about $\text{Al}_{17}\text{Cr}_2\text{Mg}_4$ to $\text{Al}_{19}\text{Cr}_2\text{Mg}_2$ at 400 °C [59], whilst it can also dissolve some Zn [60,61]. Hence both Mg and Zn are available at the interface to form $\eta\text{-Mg}(\text{Zn,Cu,Al})_2$, and we can expect that its nucleation and growth rate is substantially higher as compared to formation on the dispersoids that are free of Mg and Zn. To take account of this we propose the following approach. We assume that during nucleation $\eta\text{-Mg}(\text{Zn,Cu,Al})_2$ forms through consuming Mg from the surface of the $\text{Al}_{18}\text{Mg}_3\text{Cr}_2$ involving diffusion of Mg along the interface. As diffusion along the interface is faster than bulk

diffusion and diffusion distances for Mg are small, it is likely that rather than diffusion of Mg through the Al rich matrix phase, diffusion of Zn becomes the rate limiting diffusional process in the nucleation.

S-Al₂CuMg phase nucleates on the surface of Al₇Cu₂Fe and on pre-existing/undissolved S phase particles, and hence the formation rate is taken as proportional to the surface area of these particles at the start of the quench. As growth starts from these relatively large particles, the reaction will effectively start as 1 dimensional growth and n will be $\frac{1}{2}$ for the start of the reaction [5,62]. We will adopt this value of n (and not seek to capture the later stages of the reaction, which occurs at extremely slow cooling rates).

Our HRTEM evidenced that during the heat effect associated with the LTR the formation of Zn,Cu-rich thin plate precipitates on {111} planes starting at only one atom layer thick for samples is the dominant reaction. Thin plates on {111} planes have also been identified in Al-6.0Zn-2.0 Mg-1.0Cu (wt%) (AA7012) samples aged for short times using HRTEM [63] and in an Al-11.8Zn-1.5 Mg-1.7Cu-0.16Zr-0.12Fe-0.08Si alloys aged for 2 h at RT using HRTEM [64]. Plates on {111} planes are also confirmed by first principle calculations to be energetically favourable [65,66]. In the present model we will consider these precipitates formed during quenching to contain Zn and Cu, with Zn:Cu ratio as obtained by our EDS work. The very small enthalpy changes caused by the vLTR can not be reliably measured and, therefore, we will not attempt to include them in the enthalpy predictions.

In addition to the 4 phases considered in the model, it is known [19,20] that on very slow cooling (<0.01 K/s) also T (Al₂Mg₃Zn₃) phase can form. As these very slow cooling rates have no relevance to the quench sensitivity of these alloys, we will not seek to incorporate this phase in the predictions. We will not make predictions of strength for reactions/microstructures obtained for cases where the Zn:Mg ratio in the Al rich matrix phase at any stage during the quench exceeds 8 in the model. Such conditions are thought to result from limitations introduced by approximations made in the model and occur generally for alloys with high gross Zn:Mg ratio (>1.8) at relatively low cooling rates (<0.1 K/s). These cooling rates are far removed from relevance to commercial application.

Growth and impingement of diffusion fields in the model

The diffusion-controlled growth and impingement of diffusion fields is treated with reference to the recently derived [5] model employing the extended volume concept, which was verified through comparison with a wide range of reactions in which the product phases are randomly and homogeneously distributed [5,6]. The model gives the fraction transformed, α , as [5]:

$$\alpha = \frac{\exp(-2\alpha_{ext}) - 1}{2\alpha_{ext}} + 1 \quad (7)$$

The values for the reaction exponent n relate to the mechanisms and or diffusion-controlled reactions [6,38,67,68]. We define n based on the general equation for n [6,38,67,68]:

$$n = N_{dim}g + B \quad (8)$$

where g is $\frac{1}{2}$ for diffusion-controlled (parabolic) growth, B is 0 in the case where nucleation ceases very early in the reaction, or 1 for continuous nucleation (at constant nucleation rate in the extended volume), N_{dim} is the dimensionality of the growth. Thus n is $\frac{1}{2}$ for growth for which the rate is determined by one-dimensional diffusion (e.g. growth of grain boundary precipitates for which the rate determining process is diffusion to the grain boundary) and for growth where the new product formed is a layer on an existing particle, with the layer being thin relative to that existing particle. In the extended volume concept the superposition of the two types of growing nuclei of the same phase (e.g. growing on grain/subgrain boundaries and on particles) is readily incorporated by taking [62]:

$$\alpha_{ext} = \sum_l \alpha_{ext,l} \quad (9)$$

where α_{ext} is the extended volume achieved by formation of precipitates on sites of type l . In our case l can be dispersoids and grain/subgrain boundaries, and hence $\alpha_{ext} = (k_{2,1}/\beta)^{n_1} + (k_{2,2}t)^{n_2}$, where $k_{2,1}$ and $k_{2,2}$ are the rate factors for the 2 formation processes, and n_1 and n_2 are their reaction exponents. Rather than using Eq. (7) it is more convenient to use the more flexible approximation [38,69]

$$\alpha \cong 1 - \left(\frac{\alpha_{ext}}{\eta_i} + 1 \right)^{-\eta_i} \quad (10)$$

where η_i is the impingement factor [38,62]. The latter equation has been verified to be applicable to diffusion controlled reactions in a wide range of works, incl. [70–73]. If η_i is taken as 2 then the resulting

equation closely approximates Eq (7) which is valid for randomly and homogeneously distributed nuclei, for which growth is not limited by blocking [38,74]. If nuclei are not randomly distributed, or if blocking of growth (for elongated particles) becomes involved, then η_1 will decrease [38]. (See Section 6 for further discussion.)

Illustration of model output

To illustrate the model we will at this stage provide some of the predictions using the parameters provided in Table 2. Fig 9 shows the predicted Zn and Mg contents of the Al-rich matrix phase at the start of the quench, after the MTR and after the LTR for the AA7055 alloy. The reductions in alloy content are due to the formation of the S (Al_2CuMg), η ($\text{Mg}(\text{Zn,Cu,Al})_2$) and Zn,Cu rich thin plate phases/structures. At the high cooling rates (>10 K/s) the precipitates are predominantly Zn,Cu rich thin plate precipitates and η ($\text{Mg}(\text{Zn,Cu,Al})_2$) on grain boundaries. (To aid transparency in Fig. 9, composition data after the HTR is not shown.)

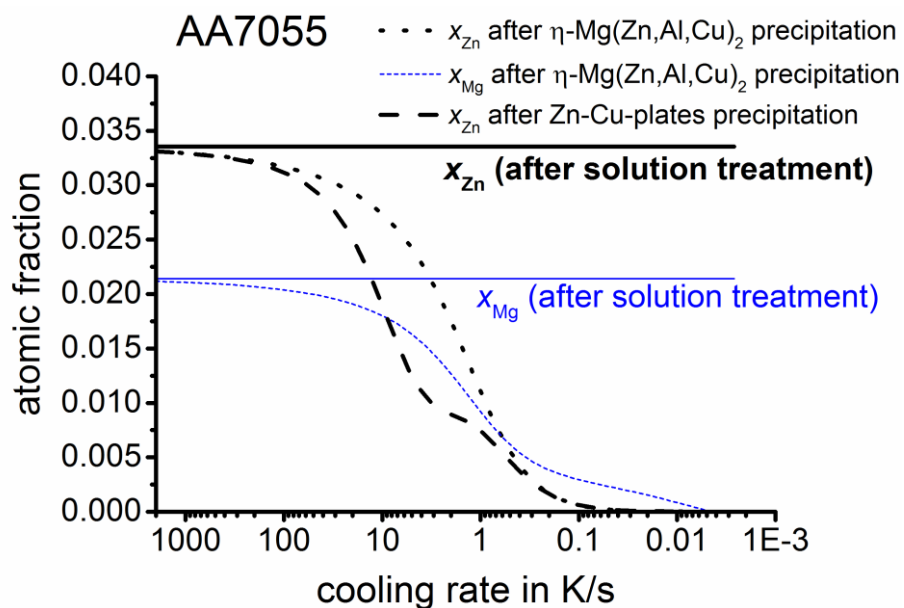


Fig. 9: Predicted Zn and Mg contents of the Al rich matrix phase at the start of the quench, after the MTR and after the LTR for the AA7055 alloy.

Thermal activation of the reactions and their activation energies

The activation energy for S-Al₂CuMg formation, which occurs at high temperature where the vacancy concentration should be close to equilibrium, is taken as the activation energy for diffusion of the slowest diffusion element, which is Cu. The activation energy is 140 kJ/mol (see eg [75]). In a first attempt the activation energy for formation of the η phase (MTR) was taken as the activation energy for Mg or Si diffusion in Al (both ~120 kJ/mol), but this produces results that are clearly inconsistent with the present data and this activation energy is also inconsistent with kinetic data on this reaction from TTT diagrams in [19] and transformation data in [76], which both indicate activation energies that are at least a factor 2 lower. It appears that the diffusion is either determined by excess vacancies which possess an activation energy for migration of 59 kJ/mol [77] or is due to diffusion occurring on subgrain boundaries and dislocations generated around misfitting particles. These defects substantially enhance diffusion [78]. We decided to obtain the activation energy for the diffusion process that governs formation of the η phase (i.e. the MTR) in a AA7150 alloy from the DSC data for the exothermic reaction in the corresponding temperature range in [79]. To this end the Type B-1.92 method for activation energy analysis [80] was applied on peak temperatures reported in [79], which produced $E_D(\text{MTR}) = 60$ kJ/mol (using only heating rates at which the reaction is clearly visible).

It is well known that at the low temperatures at which the LTR occurs, diffusion rates of alloying elements such as Zn in the presence of an equilibrium concentration of vacancies are much too low to allow any significant diffusion. TEM analysis of Zn,Cu-rich thin plate precipitates (LTR) shows that formation is associated with vacancy aggregates (nanovoids), suggesting the precipitation reaction occurs in the presence of a large supersaturation of vacancies. Thus the activation energy for this reaction should be dominated by vacancy diffusion, and it is thus taken as the activation energy for vacancy diffusion in Al: $E_D(\text{LTR}) = 60$ kJ/mol. This activation energy is comparable to the activation energy of 57kJ/mol for GP zone formation in a fast quenched Al-10Zn-0.1Mg alloy as determined in [81] from experiments performed at 0 to 40 °C.

4.2 A model for strength/hardness of alloys artificially aged after cooling

Generally a good correlation exists between yield strength and hardness for 7xxx alloys [82], but the presence of a substantial density of non-shearable dispersoid particles and grain and subgrain boundaries in commercial 7xxx alloys will cause a deviation from linearity through their influence on strain hardening [28,83,84]. Hence we will adopt a two-term strength to hardness conversion, which is given by [28,85] :

$$HV = C_{\sigma-HV} \left(\sigma_{0.2} + K \sqrt{\varepsilon_{eff}} \right) \quad (11)$$

$$K = \left(0.35 G_m \left(f_r \sqrt{\frac{b}{d_{rg}}} + (1 - f_r) \sqrt{\frac{b}{d_{sg}}} \right) + 0.25 G_m \sqrt{\frac{b f_{ns,1}}{2 r_{ns,1}} + \frac{b f_{ns,2}}{2 r_{ns,2}}} \right) \quad (12)$$

where f_r is the fraction of the material that is recrystallised, d_{rg} is the grain size in the recrystallised zones, d_{sg} is the subgrain size (in the unrecrystallised zones), $f_{ns,i}$ is the volume fraction of non-shearable particles of type i , $r_{ns,i}$ is the average radius of non shearable particles, G is the shear modulus, C_{s-HV} is the conversion parameter (see below) and ε_{eff} is the effective strain during hardness testing, taken as 0.08. C_{s-HV} is fitted using HV and $\sigma_{0.2}$ data pairs for AA7xxx alloys from the literature.

To predict the yield strength based on the microstructure, the model by Starink and Wang [86] is adopted. As that model did not incorporate the strengthening due to dislocations generated due to misfitting particles, we will add that here to the model. For strength predictions in the artificially aged state we will take the maximum yield strength predicted by the model, with the exception of the AA7020 and AA7085 alloy where the 24h/120C treatment applied will lead to a slightly underaged condition [87]. We take this into account in the predictions.

The model is designed for alloys with significant Zn and Mg content. Hence we will not produce strength predictions for cases where the ratio $x_{Mg}:x_{Zn}$ is larger than 5 or below 0.2. This is the case for alloys with excess Zn, i.e. alloys with $x_{g,Zn}:x_{g,Mg}$ ratio so high that the formation of the 4 phases considered can not remove all Zn from solid solution even at extremely low quench rates. Such issues can be resolved

by considering a fifth phase which would be a Zn-rich phase, possibly $Zn_{11}Mg_2$, but this is out of the scope of the present work.

5 Model parameters and predictions

5.1 Model parameters

The model parameters used are presented in Table 2, and they include the values identified in Section 4. Some model parameters require further discussion.

There is no prior data available on the enthalpy of formation of the Zn,Cu-rich thin plate precipitates formed in the LTR. We can estimate it from the DSC data by considering that for phases for which any differences in entropy between the phases are much smaller than the enthalpy, the ratio of solvus temperature to enthalpy of formation is approximately constant. (For instance, this holds well for the θ , θ' and Guinier-Preston structures in Al-Cu alloys [88].) We obtained the solvus temperatures for the phases involved in the LTR and the MTR, $T_{s,LTR}$ and $T_{s,MTR}$, from hDSC thermograms for 5 alloys aged at a temperature that is above the solvus for GPI zones ($\sim 150^\circ\text{C}$, see [89]). For this treatment we selected an ageing temperature of 172°C ; and we took $T_{s,LTR}$ as the maximum temperature of the first endothermic effect for alloys aged up to 16h. (Choosing the maximum for a range of treatments is appropriate because the transformation to η' and/or η during the DSC heating or during ageing will influence this measurement of $T_{s,LTR}$ and we need to have the value most representative of Zn,Mg-rich precipitates in a fully formed state.) (Selected hDSC thermograms of these alloys were present in [31]). The data presented in Table 3 confirms the present analysis through showing a consistent $T_{s,LTR} / T_{s,MTR}$ for all 5 alloys, providing $\Delta H_{LTR} = \Delta H_{\eta} T_{s,LTR} / T_{s,MTR} = 12.8 \text{ kJ/mol}$. This value is adopted in the model and is seen (see below) to provide a good correspondence with measured enthalpies from cDSC.

The grain size, sub grain size and recrystallized fractions were taken from EBSD and optical microstructure investigations of the alloys.

Table 2: Parameters in the model.

Parameter	Value	Notes / Source
General parameters		
b	2.84×10^{-10} m	
HTR 1: S formation, fixed composition Al₂CuMg		
η	2	From model for diffusion controlled formation of homogeneously distributed precipitates [5]
k_o	5×10^{20}	From fit to data
n	$\frac{1}{2}$	According to model for diffusion controlled reactions [5]
E_D	140 kJ/mol	Activation energy for diffusion of Cu in Al, the slowest diffusion element [75]
ΔH_{Al_2CuMg}	19.8 kJ/mol	From solvus data in [90]
HTR 2: β Mg₂Si formation, fixed composition Mg₂Si		
All parameters adopted from [8]		
MTR: η-Mg(Zn,Cu,Al)₂ phase, of units of Mg₄Zn₈ and Al₁Zn₅Cu₂Mg₄		
η	1.2-1.7	From model for diffusion controlled formation of inhomogeneously distributed precipitates [38]
k_o	3×10^{10}	From fit to data
n_1	$\frac{1}{2}$	For formation on grain boundaries, following the model for diffusion controlled reactions [5]
n_2	$1\frac{1}{2}$	For formation on dispersoids, following the model for diffusion controlled reactions [5]
E_D	60 kJ/mol	Activation energy for diffusion of Mg in Al in the presence of excess vacancies [91,92]
ΔH_{MgZn_2}	12.4 kJ/mol	Average of COST 507 database has (11.8 kJ/mol [93]) and value obtained by 1 st principles modelling (12.9 kJ/mol [7]).
$\Delta H_{Al_1Zn_5Cu_2Mg_4}$	$1.35x \Delta H_{MgZn_2}$	From 1 st principles modelling [7]
LTR: Zn-Cu rich platelet phase		
η	2	According to model for diffusion controlled reactions [5]
k_o	7×10^5	From fit to data
n	$1\frac{1}{2}$	Following the model for diffusion controlled reactions [5]
E_D	60 kJ/mol	Activation energy for diffusion of Mg in Al in the presence of excess vacancies [91,92]
ΔH_{LTR}	12.8 kJ/mol	See text
Strength model		
M (for tensile tests in L direction)	2.73	For tensile tests in the longitudinal direction, see [94]
M (all other tests)	2.6	For all other tensile and hardness tests; obtained from self-consistent models [95], see also [96]
G	27 GPa	

Table 3: Analysis of hDSC curves of 5 alloys.

Alloy	$T_{s,MTR}$ (°C)	$T_{s,LTR}$ (°C)	$T_{s,MTR} / T_{s,LTR}$	ΔH_{LTR} (J/mol)
AA7150m	425	240	1.42	12,725
AA7150hiZn	430	231	1.44	12,583
AA7150loCu	404	230	1.42	12,719
AA7150hiCu	400	239	1.38	13,144
AA7150hiZnCu	405	232	1.40	12,914

The impingement parameter η_i for the HTR and LTR is taken as 2 (i.e. such that impingement closely approximates the model in [5]); for the MTR η_i is predicted considering the dispersoid density using the approach in [10] and calculated using the procedure in [38]. The density of the phases was obtained from data in [51,97–99].

We also wish to consider the effect of interface energy of the dispersoid particles on the nucleation rate, however to the best of our knowledge there is no data available on the interfacial energies of the various dispersoids and the matrix. It is known however that the interfaces of Al_3Zr and $Al_6(Mn,Fe)$ are semi-coherent with the matrix, whilst the Cr containing dispersoids are generally considered to be incoherent. Typically the difference in interfacial energy between a semi coherent precipitate (misfit ~1%) and an incoherent interface is about a factor 3 to 8 [100]. In line with this we take the efficiency of Cr containing dispersoids in nucleating the η - $Mg(Zn,Al,Cu)_2$ precipitates to be a factor 5 larger than that of the semi coherent precipitates. This assumption has no effect on the accuracy of the model for the present alloys for which nucleation of quenched-in precipitates is dominated by Al_3Zr dispersoids, grain/subgrain boundaries, and, to a lesser extent, Mn containing dispersoids. It does influence the accuracy of predicting data on Cr containing alloys.

5.2 Model predictions

We first provide additional verification that the model for alloys age hardened after a fast water quench is accurate. For this we considered yield strength data on 20 alloys; including yield strength data

on peak aged and overaged conditions of our AA7449 alloy, data on our AA7150 reported previously [101] and on 18 alloys reported before in [86]. Taken together these 20 alloys cover the range 2.2-3.7 at%Zn, 2.0-3.1 at%Mg, 0.5-1.3 at%Cu, with data generated both before and after the model [86] was published. As seen in Fig. 10, the model predicts the measured yield strengths very well.

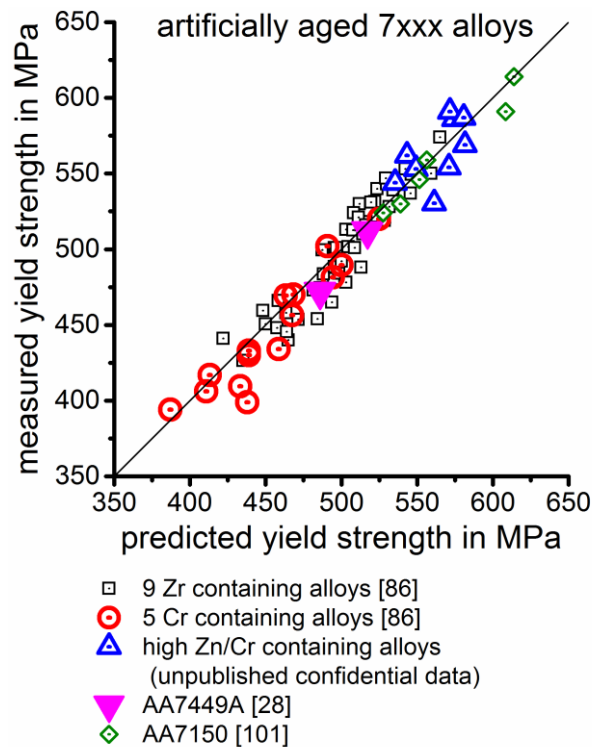


Fig. 10: Measured and predicted yield strength of 20 water quenched and subsequently artificially aged Al-Zn-Mg-Cu based alloys.

In Fig 11 the model predictions for ΔH and hardness are compared with measured data. The error bars of the measured enthalpy changes show estimated uncertainties of $\pm 10\%$ for the total enthalpy change and $\pm 30\%$ for the enthalpy change of the LTR. The uncertainty mainly is caused by the evaluation procedure and the larger value for the LTR results from an increased influence of the zero level correction at the low temperatures (compare [12]). The error bars on the hardness show the standard deviation out of six indentations. For AA7049A besides conventional cDSC also differential fast scanning chip calorimetry results are provided (see [18]). For this alloy only cooling rates larger than 3 K/s are considered, because at slower cooling rates strong overlapping of the HTR and MTR occurs [18], which cannot be captured by our model which assumes consecutive reactions. The figures show an excellent

correspondence with the data, encompassing a total of ~200 measured yield strength and ΔH values for a wide range of cooling rates and compositions. This is achieved by fitting 4 parameters, with all the other parameters determined from theory and assessment above. The 4 parameters are the initial rates of formation of the 4 types of precipitates: S-Al₂CuMg phase, η -Mg(Al,Cu,Zn)₂ formation on grain boundaries, η -Mg(Al,Cu,Zn)₂ formation on dispersoids and the Zn-Cu-rich platelets.

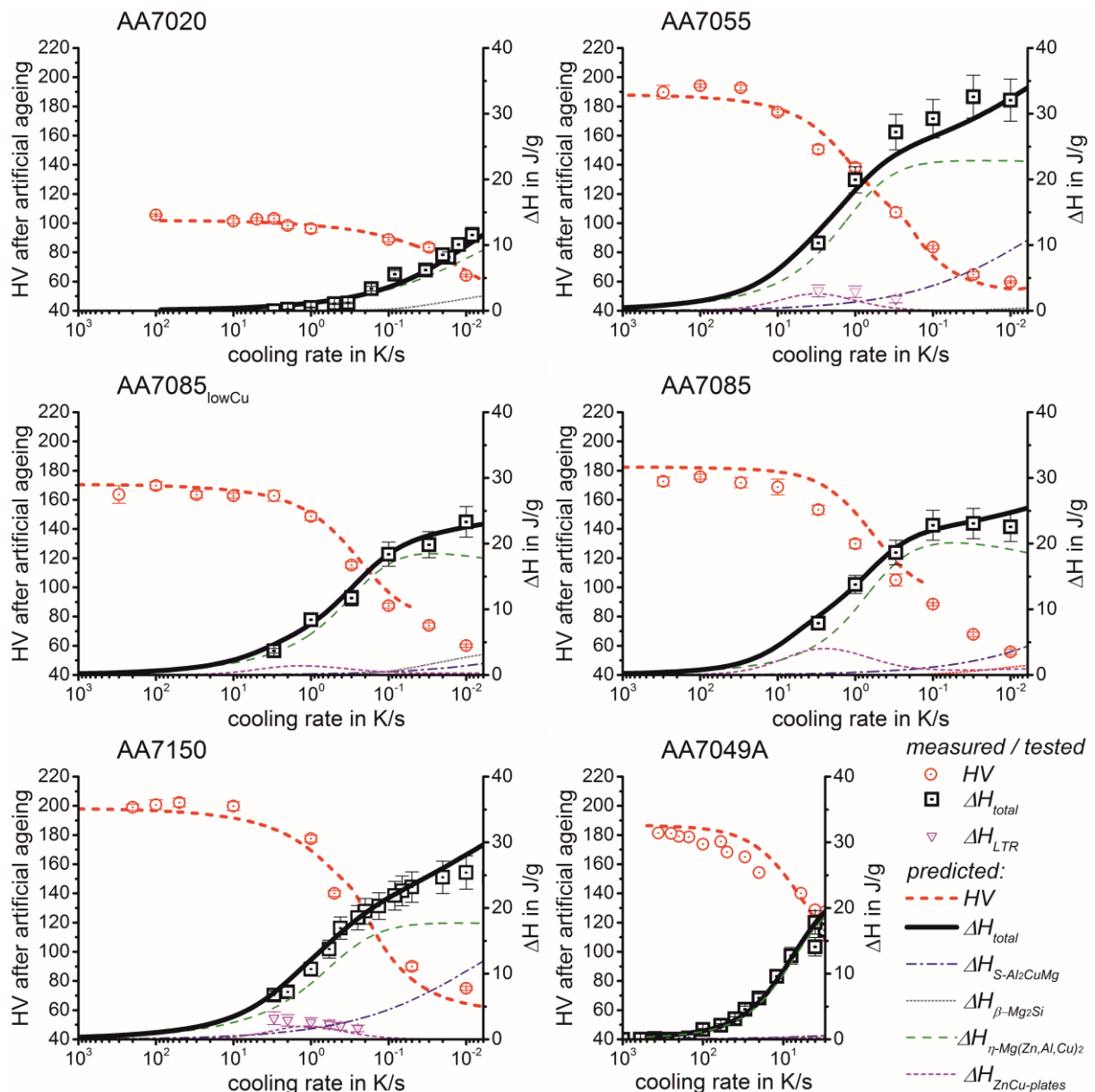


Fig. 11: ΔH and hardness as a function of the cooling rate for 6 alloys. Both, measured values (from cDSC and Vickers hardness tests) as well as model predictions (from the model in section 4) are provided.

6 Discussion

6.1 Model efficiency and model limitations

TEM data obtained in a range of works indicate that η -Mg(Zn,Al,Cu)₂ phase forms before T-Al₂Mg₃Zn₃ phase formation. This is notwithstanding the fact that various assessments of the Al-Mg-Zn phase diagram indicate that for alloys with Zn and Mg contents similar to these alloys, only T-Al₂Mg₃Zn₃ is a stable phase [46,102]. It is thought that the reason for this is that η -Mg(Zn,Al,Cu)₂ has a higher Zn:Mg ratio than T-Al₂Mg₃Zn₃ phase with Zn diffusing faster than Mg. Thus η -Mg(Zn,Al,Cu)₂ should form faster, and as the 2 reactions compete for the same alloying elements, the faster reaction suppresses the other reaction. Hence, the model includes formation of the η -Mg(Zn,Al,Cu)₂ phase, and to keep the model transparent and avoid including reactions that have no direct industrial relevance T-Al₂Mg₃Zn₃ phase is not included. The model nevertheless achieves good accuracies in predicting enthalpy changes and artificially aged hardness at medium to high cooling rates and therefore particularly in the industrially relevant cooling/quenching treatments. Apparently any limited T phase formation that might occur does generally not significantly influence the precipitation in terms of enthalpy and resulting artificially aged strength.

It was found that for the Mn containing AA7150 commercial alloy a near perfect fit to cDSC enthalpy data could be obtained by applying Eq. (7), which is valid for a random and homogeneous distribution of nuclei, whilst the overall fit of the model to all alloys including the Mn free alloys was slightly better when variation of nuclei density due to dendritic segregation of dispersoid forming elements was considered and Eq. (10) with $\gamma_1 = 1.3 \pm 0.2$ was used. This finding is consistent with the known inverse segregation behaviour of Mn and Zr: a combination of Zr and Mn will produce a more homogeneous distribution of dispersoids, which is beneficial for the mechanical properties by virtue of reducing recrystallization [103–105]. (Provided optimised Zr and Mn contents are used.) This suggest that a further improvement over the already very accurate model can be obtained by including the inhomogeneous distribution of

dispersoids in the model. To maintain the model efficiency and avoid full 3D modelling of η -Mg(Al,Zn,Cu)₂ precipitation, Eq. (10) with η determined from the assessment in [38] would then be needed.

The present model formulation is highly efficient and very successful in predicting quench sensitivity and strength of a wide range of alloys, but there is a limitation to its range of validity. The model particularly becomes invalid at the very slow cooling rates in the stage where Zn:Mg ratios in the matrix change to the extent that the reactions considered here (S, Mg₂Si, η and the Zn,Cu rich thin plate precipitates) are no longer the main precipitates that form. Thermodynamic models (Thermocalc TCAL2) in [25] show that this is particularly the case for conditions where the Zn:Mg ratio reduces to below ~0.95 at which the T-Al₂Mg₃Zn₃ phase becomes a stable phase, progressively replacing the η phase as the Zn:Mg ratio drops further. Under those conditions the model can not accurately predict the amount of Mg and Zn in the Al-rich matrix phase after cooling and we thus will not apply the strength model in those situations.

It is noted that duplex ageing or slow heating to the ageing temperature can recover some of the hardness/strength losses of Al-Zn-Mg based alloys that are quenched at rates that reduce the aged yield strength by about 20 to 60 % when a single stage artificial ageing treatment is used [22,106,107]. We hope to implement this effect in a future version of the model.

6.2 Further model predictions

With the model established we can now make predictions on quench sensitivity as a function of alloy composition. In Fig 12 predictions for the peak aged proof strength and amount of η -Mg(Zn,Al,Cu)₂ formation for 3 alloys which have an increasing Zn and Mg content and constant Zn:Mg ratio are provided. The figure shows the expected increase of strength with increasing alloying content and also shows that quench sensitivity with respect to the proof strength increases with increasing alloying content. Alloys with higher Zn and Mg content have more η -Mg(Zn,Al,Cu)₂ formed, which at the higher cooling rates will be predominantly on grain boundaries. This will also cause a lower toughness.

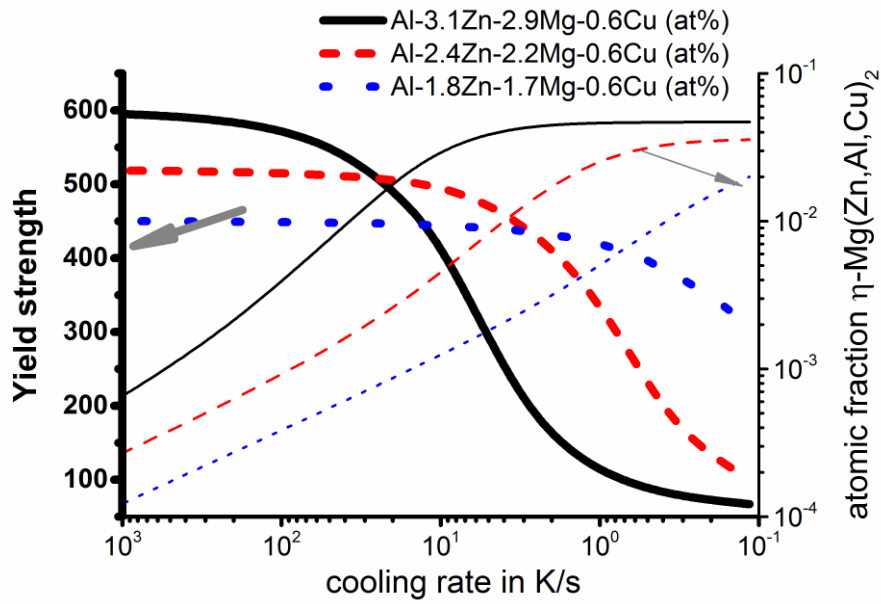


Fig. 12: Influence of quench rate on yield strength and amount of η -Mg(Zn,Al,Cu)₂ for 3 alloys with varying increasing Zn and Mg content and constant Zn:Mg ratio. ($x_{g,Cu}=0.6$ at%, $x_{g,Zr}=0.04$ at%). The proof strength throughout is predicted for the artificially aged condition, i.e. no stretching prior to ageing for 24 h at 120 °C.

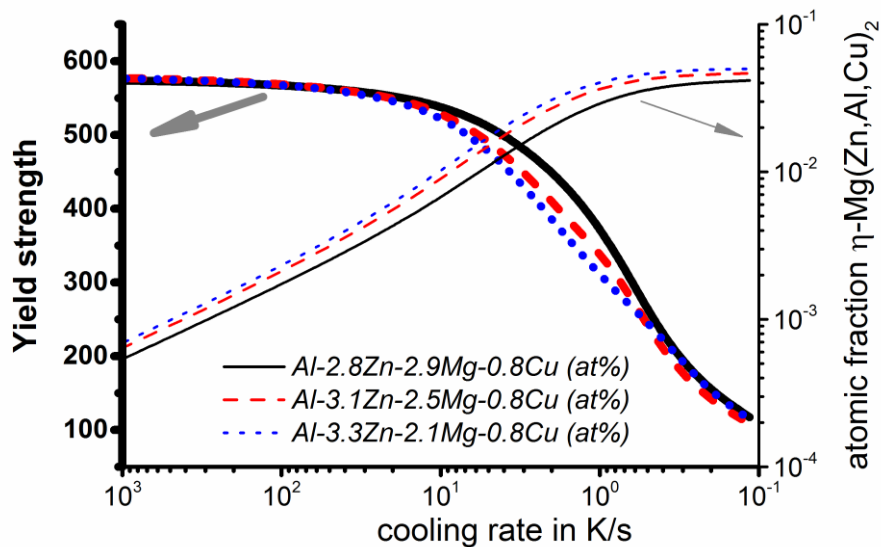


Fig. 13: Influence of quench rate on proof strength and amount of η -Mg(Zn,Al,Cu)₂ for 3 alloys with $x_{g,Cu}=0.8$ at%, $x_{g,Zr}=0.04$ at% and varying Mg and Zn contents that produce identical strength in water quenched conditions. (f_{rec} is taken as 0.1).

Fig 13 shows predictions for the peak aged proof strength and amount of η -Mg(Zn,Al,Cu)₂ formation for 3 alloys with Mg and Zn chosen such that they have a near identical strength when quenched at a cooling rate of ~40 K/s followed by artificial ageing. (A cooling rate of ~40 K/s, is typically achieved for a

25 mm plate, quenched in cold water [108]). The data indicates that the alloy with the high Zn:Mg ratio has the higher quench sensitivity due to the higher amounts of η -Mg(Zn,Al,Cu)₂ formed, although for Zn:Mg ratio > 1.2 further degradation of quench sensitivity is limited. For this cooling rate (typical of a 25 mm plate), the plate with the higher Zn:Mg ratio has more η -Mg(Zn,Al,Cu)₂ formed on grain boundaries and is thus expected to have a lower toughness.

7 Conclusions

A model for precipitation reactions during cooling of Al-Zn-Mg-Cu-Mn-Zr based alloys and their strength after an artificial ageing treatment is derived and verified through an extensive set of cooling experiments on 6 alloys (plus additional experiments on six further alloys). The DSC, TEM and SEM data shows that the reactions during quenching are dominated by four different reactions: a high temperature reaction (typically ~450 °C down to ~350 °C) due mostly to S-Al₂CuMg phase formation (alternatively Mg₂Si in the absence of Cu / presence of Si), a medium temperature reaction (~350 °C down to ~250 °C) due predominantly to η -Mg(Zn,Al,Cu)₂ phase formation and a lower temperature reaction (~250 °C down to ~150 °C) due to a Zn-Cu rich thin plate phase. The model provides accurate predictions of enthalpy changes and hardness / strength of the alloys for a wide range of cooling rates and compositions incorporating the range of commercially important alloys and cooling rates. The quench sensitivity is predicted to increase with increasing content of main alloying elements (Zn, Mg, Cu), increasing fraction recrystallised, increasing number of dispersoid particles, increasing surface: volume ratio of dispersoid particles and increasing dispersoid/matrix incoherency. The present work makes a significant contribution towards understanding the mechanisms driving quench sensitivity of Al-Zn-Mg-Cu alloys and the derived model can be used for alloy design.

Appendix

In the model the volume fractions of undissolved phases is calculated based on literature data and thermodynamic model predictions (e.g. in [30,97]), and as part of the aim of providing a computationally efficient model, some solubilities in the Al-rich phase are taken as zero and the number of phases considered is limited to the main ones observed in these alloys: $\text{Al}_6(\text{Mn,Fe})$, Al_3Zr , $\text{Al}_7\text{Cu}_2\text{Fe}$, $\text{Al}_{18}\text{Mg}_3\text{Cr}_2$ and Al_2CuMg . The Mn and Fe solubility at the solution treatment temperature are effectively zero [97], and we consider that for the present compositions all Mn is present in the $\text{Al}_6(\text{Mn,Fe})$ phase. The composition of the $\text{Al}_6(\text{Mn,Fe})$ is assessed using thermodynamic modelling software. The S- Al_2CuMg phase amount is calculated on the basis of the solubility product in [30], and the Cr solubility at the solution treatment temperature is taken as 0.04 at% [30,109]).

In the model the total particle-matrix interface area of dispersoid particles present at the start of the quench influences the nucleation of particles during the quench. For each dispersoid phase the total particle-matrix interface area is obtained by considering all particles of each phase have one typical shape, e.g. spherical for Al_3Zr , thin plate for Al_6Mn and cube for $\text{Al}_{18}\text{Mg}_3\text{Cr}_2$, and the average size is obtained from data (primarily TEM) in the literature for alloys with dispersoid forming element contents and solution heat treatments that are similar to the present alloys [25,55,56,110]. At the present stage of model development, no attempt is made to predict any potential variations of size of dispersoid particles between alloys.

Acknowledgements

We gratefully acknowledge Olaf Keßler (Materials Science, University of Rostock), Christoph Schick (Polymer Physics, University of Rostock) for discussions on the DSC results. Martin Beck (Materials Science, University of Rostock) and Davit Zohrabyan (formally University of Rostock) are acknowledged for performing some of the DSC and hardness experiments. Matthew Weyland of the Monash Centre for Electron Microscopy (Monash University) is acknowledged for his help in imaging the LTR platelet phase using the HRTEM. B.M. gratefully acknowledges the German Academic Exchange Service (DAAD) for funding his sabbatical year at the University of Southampton (DAAD-Postdoc-Program fellowship).

References

- [1] Polmear IJ. Light alloys. 4th ed. Oxford: Butterworth-Heinemann; 2006.
- [2] Morere B, Ehrström J, Gregson RJ, Sinclair I. Metall. Mater. Trans. A-Phys. Metall. Mater. Sci. 2000;31:2503–15.
- [3] Zhang Y, Bettles C, Rometsch PA. J Mater Sci 2014;49:1709–15.
- [4] Heinz A, Haszler A, Keidel C, Moldenhauer S, Benedictus R, Miller WS. Mater. Sci. Eng. A 2000;280:102–7.
- [5] Starink MJ. Thermochim Acta 2014;596:109–19.
- [6] Starink MJ. J. Alloy. Compd. 2015;630:250–5.
- [7] Fang X, Song M, Li K, Du Y, Zhao D, Jiang C, Zhang H. J Mater Sci 2012;47:5419–27.
- [8] Milkereit B, Starink MJ. Mater. Des. 2015;76:117–29.
- [9] Zhang X, Liu W, Liu S, Zhou M. Mater. Sci. Eng. A 2011;528:795–802.
- [10] Robson JD, Prangnell PB. Mater. Sci. Eng. A 2003;352:240–50.
- [11] Zhang Y, Milkereit B, Kessler O, Schick C, Rometsch PA. J. Alloy. Compd. 2014;584:581–9.
- [12] Osten J, Milkereit B, Schick C, Kessler O. Materials 2015;8:2830–48.
- [13] Song F, Zhang X, Liu S, Tan Q, Li D. Corros. Sci. 2014;78:276–86.
- [14] Robinson JS, Tanner DA, Truman CE, Paradowska AM, Wimpory RC. Mater Charact 2012;65:73–85.
- [15] Deng Y, Wan L, Zhang Y, Zhang X. J. Alloy. Compd. 2011;509:4636–42.
- [16] Park JK, Ardell AJ. MTA 1983;14:1957–65.
- [17] Shuey RT, Tiryakioğlu M, Bray GH, Staley JT. MSF 2006;519-521:1017–22.
- [18] Zohrabyan D, Milkereit B, Schick C, Kessler O. Trans. Nonferrous Met. Soc. China 2014;24:2018–24.
- [19] Tiryakioğlu M, Robinson JS, Eason PD. Mater. Sci. Eng. A 2014;618:22–8.
- [20] Lim ST, Eun IS, Nam SW. Mater. Trans. 2003;44:181–7.
- [21] Shuey RT, Tiryakioğlu M, Bray GH, Staley JT. Toughness after interrupted quench, in: 10th International Conference on Aluminium Alloys, (ICAA-10). p. 519–521.
- [22] Shuey RT, Tiryakioğlu M. Quenching of Aluminum Alloys, in: Quenching Theory and Technology, CRC Press, 2nd edition, 2011.
- [23] Rometsch PA, Zhang Y, Knight S. Trans. Nonferrous Met. Soc. China 2014;24:2003–17.
- [24] Liu S, Liu W, Zhang Y, Zhang X, Deng Y. J. Alloy. Compd. 2010;507:53–61.
- [25] Yong Zhang. Quench Sensitivity of 7xxx Series Aluminium Alloys. PhD thesis, Melbourne, Australia; 2014.
- [26] Schloth P, Wagner JN, Fife JL, Menzel A, Drezet J, van Swygenhoven H. Appl. Phys. Lett. 2014;105.
- [27] Patrick Schloth. Precipitation in the high strength AA7449 aluminium alloy: implications on internal stresses on different length scales. Lausanne; 2015 (PhD thesis, EPFL Lausanne, in press).
- [28] Kamp N, Sinclair I, Starink MJ. Metall. Mater. Trans. A-Phys. Metall. Mater. Sci. 2002;33:1125–36.
- [29] Xu DK, Rometsch PA, Birbilis N. Mater. Sci. Eng. A 2012;534:234–43.
- [30] Li X, Starink MJ. Mater. Sci. Technol. 2001;17:1324–8.

- [31] Li XM, Starink MJ. *J. Alloy. Compd.* 2011;509:471–6.
- [32] Ayer R, Koo JY, Steeds JW, Park BK. *MTA* 1985;16:1925–36.
- [33] Sharma MM. *Mater Charact* 2008;59:91–9.
- [34] Avrami M. *J Chem. Phys.* 1940;8:212–24.
- [35] Kolmogorov AN. *Izv. Akad. Nauk SSSR, Ser. Mat.* 1937:355–9.
- [36] Burbelko AA, Fraś E, Kapturkiewicz W. *Mater. Sci. Eng. A* 2005;413-414:429–34.
- [37] Tomellini M. *Thermochim Acta* 2013;566:249–56.
- [38] Starink MJ. *J Mater Sci* 2001;36:4433–41.
- [39] Rometsch PA, Starink MJ, Gregson PJ. *Mater. Sci. Eng. A* 2003;339:255–64.
- [40] Starink MJ, Gregson PJ. *Mater. Sci. Eng. A* 1996;211:54–65.
- [41] Conserva M, Fiorini P. *Metall Trans* 1973;4:857–62.
- [42] Deschamps A, Bréchet Y. *Mater. Sci. Eng. A* 1998;251:200–7.
- [43] Deschamps A, Brechet Y. *Scr. Mater.* 1998;39:1517–22.
- [44] Deschamps A, Texier G, Ringeval S, Delfaut-Durut L. *Mater. Sci. Eng. A* 2009;501:133–9.
- [45] Liu S, Zhong Q, Zhang Y, Liu W, Zhang X, Deng Y. *Mater. Des.* 2010;31:3116–20.
- [46] Liang P, Tarfa T, Robinson JA, Wagner S, Ochin P, Harmelin MG, Seifert HJ et al. *Thermochim Acta* 1998;314:87–110.
- [47] Andrae D, Paulus B, Wedig U, Jansen M. *Zeitschrift fur Anorganische und Allgemeine Chemie* 2013;639:1963–7.
- [48] Watson RE, Bennett LH. *Acta Metall.* 1982;30:1941–55.
- [49] Fritz Laves, H. Witte. *Metallwirtschaft* 1936;15:840–2.
- [50] Steurer W. *Crystal Structures of Metallic Elements and Compounds*, in: Hono, David E. Laughlin Kazuhiro (Ed.). *Physical Metallurgy (Fifth Edition)*. Oxford: Elsevier; 2014. p. 1–101.
- [51] Wandahl G, Christensen AN, Uggerud E, Songstad J, Lönnberg H, Colacio E, Mulichak AM et al. *Acta Chem. Scand.* 1989;43:296–7.
- [52] Engdahl T, Hansen V, Warren PJ, Stiller K. *Mater. Sci. Eng. A* 2002;327:59–64.
- [53] Li Y, Kovarik L, Phillips PJ, Hsu Y, Wang W, Mills MJ. *Philos Mag Lett* 2012;92:166–78.
- [54] Thompson DS, Subramanya BS, Levy SA. *MTA* 1971;2:1149–60.
- [55] Starink MJ, Li XM. *Metall. Mater. Trans. A-Phys. Metall. Mater. Sci.* 2003;34 A:899–911.
- [56] Li YJ, Zhang WZ, Marthinsen K. *Acta Mater.* 2012;60:5963–74.
- [57] Kong BO, Nam SW. *Mater Lett* 1996;28:385–91.
- [58] Kikuchi S, Yamazaki H, Otsuka T. *J Mater Process Technol* 1993;38:689–701.
- [59] Rogl P, Stiltz S, Hayes FH. *JPE* 1992;13:317–23.
- [60] Sten Samson. *Acta Cryst.* 1958;11:851–7.
- [61] K. Little, H. J. Axon, W. Humerothery. *J. Inst. Met.* 1948;75:39–50.
- [62] Starink MJ, Zahra AM. *Philos. Mag. A-Phys. Condens. Matter Struct. Defect Mech. Prop.* 1998;77:187–99.
- [63] Dlubek G, Krause R, Brümmer O, Plazaola F. *J Mater Sci* 1986;21:853–8.
- [64] Mukhopadhyay AK, Prasad KS. *Philos Mag Lett* 2011;91:214–22.
- [65] Müller S, Wang L, Zunger A, Wolverton C. *Phys. Rev. B Condens. Matter Mater. Phys.* 1999;60:16448–62.
- [66] Wolverton C. *Acta Mater.* 2001;49:3129–42.
- [67] Cumbreira FL, Sánchez-Bajo F. *Thermochim Acta* 1995;266:315–30.
- [68] Baker TA, Monti, O. L. A., Nesbitt DJ. *J. Phys. Chem. C* 2011;115:9861–70.
- [69] Starink MJ. *Int. Mater. Rev.* 2004;49:191–226.
- [70] Badji R, Kherrouba N, Mehdi B, Cheniti B, Bouabdallah M, Kahloun C, Bacroix B. *Precipitation kinetics and mechanical behavior in a solution treated and aged dual phase stainless steel*; 2014.
- [71] Gao Q, Wang C, Qu F, Wang Y, Qiao Z. *J. Alloy. Compd.* 2014;610:322–30.
- [72] Kianezhad M, Sajjadi SA. *Metall. Mater. Trans. A-Phys. Metall. Mater. Sci.* 2013;44:2053–9.
- [73] Song SJ, Liu F, Zhang ZH. *Acta Mater.* 2014;64:266–81.
- [74] Birnie III, D. P., Weinberg MC. *J Chem. Phys.* 1995;103:3742–6.
- [75] Simonovic D, Sluiter, M. H. F. *Phys. Rev. B Condens. Matter Mater. Phys.* 2009;79.
- [76] Liu S, Li C, Deng Y, Zhang X, Zhong Q. *Met. Mater. Int.* 2014;20:195–200.
- [77] Ho G, Ong MT, Caspersen KJ, Carter EA. *Phys. Chem. Chem. Phys.* 2007;9:4951–66.
- [78] Baker SP, Joo Y, Knauß MP, Arzt E. *Acta Mater.* 2000;48:2199–208.
- [79] Ghosh KS, Gao N. *Trans. Nonferrous Met. Soc. China* 2011;21:1199–209.
- [80] Starink M. *Thermochim Acta* 2003;404:163–76.
- [81] Panseri C, Federighi T. *Acta Metall.* 1963;11:575–84.
- [82] Salazar-Guapuriche MA, Zhao YY, Pitman A, Greene A. *Correlation of strength with hardness and electrical conductivity for aluminium Alloy 7010*. Vancouver; 2006.

- [83] Ashby MF. *Philos. Mag.* 1966;14:1157–78.
- [84] Starink MJ, Wang P, Sinclair I, Gregson PJ. *Acta Mater.* 1999;47:3855–68.
- [85] Ashby MF. *Strengthening Methods in Crystals* 1971:137–92.
- [86] Starink MJ, Wang SC. *Acta Mater.* 2003;51:5131–50.
- [87] Li X, Xiong B, Zhang Y, Hua C, Wang F, Zhu B, Liu H. *Sci China Ser E Technol Sci* 2009;52:67–71.
- [88] Starink MJ, van Mourik P. *Mater. Sci. Eng. A* 1992;156:183–94.
- [89] Berg L, Gjønnnes J, Hansen V, Li X, Knutson-Wedel M, Waterloo G, Schryvers D et al. *Acta Mater.* 2001;49:3443–51.
- [90] Landolt-Börnstein. *Thermodynamic Properties · Ternary Alloy Systems*: Springer-Verlag; 2005.
- [91] Rothman SJ, Peterson NL, Nowicki LJ, Robinson LC. *phys. stat. sol. (b)* 1974;63:K29.
- [92] Fujikawa S. Tracer diffusion of magnesium in Pseudo-Binary Al-Mg₂Si alloys, in: *Defect and Diffusion Forum* 143-147; 1997. p. 403–408.
- [93] Fries SG, Jantzen T. *Thermochim Acta* 1998;314:23–33.
- [94] Starink MJ, Cao LF, Rometsch PA. *Acta Mater.* 2012;60:4194–207.
- [95] Clausen B, Lorentzen T, Leffers T. *Acta Mater.* 1998;46:3087–98.
- [96] Qiao XG, Starink MJ, Gao N. *Acta Mater.* 2010;58:3690–700.
- [97] Belov NA, Eskin DG, Aksenov AA. *Multicomponent phase diagrams*. 1st ed. Amsterdam, Boston: Elsevier; 2005.
- [98] Wang SC, Starink MJ. *Acta Mater.* 2007;55:933–41.
- [99] Yaws CL. *Density of Solid – Inorganic Compounds*, in: Carl L. Yaws (Ed.). *Thermophysical Properties of Chemicals and Hydrocarbons*. Oxford: Elsevier; 2014. p. 353–365.
- [100] Martin JW, Doherty RD, Cantor B. *Stability of microstructure in metallic systems*. 2nd ed. Cambridge, New York, NY, USA: Cambridge University Press; 1997.
- [101] Xu DK, Rometsch PA, Birbilis N. *Mater. Sci. Eng. A* 2012;534:244–52.
- [102] Liang H, Chen S, Chang YA. *Metall. Mater. Trans. A-Phys. Metall. Mater. Sci.* 1997;28:1725–34.
- [103] Cheong S, Weiland H. *Understanding a microstructure using GOS (Grain Orientation Spread) and its application to recrystallization study of hot deformed Al-Cu-Mg alloys*; 2007.
- [104] Conserva M, Leoni M. *Metall Trans* 1975;6:189–95.
- [105] Tsvoulas D, Robson JD, Sigli C, Prangnell PB. *Acta Mater.* 2012;60:5245–59.
- [106] Liu SD, Zhang XM, Chen MA, You JH. *Mater Charact* 2008;59:53–60.
- [107] Lim ST, Yun SJ, Nam SW. *Mater. Sci. Eng. A* 2004;371:82–90.
- [108] Hatch JE. *Aluminum*. Metals Park, Ohio: American Society for Metals; 1984.
- [109] Mondolfo LF. *Aluminium Alloys: Structure and Properties*; 1976.
- [110] Eivani AR, Ahmed H, Zhou J, Duszczyc J, Kwakernaak C. *Mater. Sci. Technol.* 2011;27:1294–8.

[BM8] Zhang Y, Weyland M, Milkereit B, Reich M,

Rometsch PA:

Precipitation of a new platelet phase during the quenching of an Al-Zn-Mg-Cu alloy.

Scientific Reports 6 (2016): 23109

Benjamin's contributions: I managed the international collaboration, supervised the DSC work and helped with its evaluation, participated in the results discussion and revised the manuscript.

SCIENTIFIC REPORTS



OPEN

Precipitation of a new platelet phase during the quenching of an Al-Zn-Mg-Cu alloy

Yong Zhang¹, Matthew Weyland^{1,2}, Benjamin Milkereit^{3,4}, Michael Reich³ & Paul A. Rometsch¹

Received: 24 September 2014

Accepted: 29 February 2016

Published: 16 March 2016

A previously undescribed high aspect ratio strengthening platelet phase, herein named the Y-phase, has been identified in a commercial Al-Zn-Mg-Cu alloy. Differential scanning calorimetry indicates that this phase only precipitates at temperature and cooling rate of about 150–250 °C and 0.05–300 K/s, respectively. This precipitate is shown to be responsible for a noticeable improvement in mechanical properties. Aberration corrected scanning transmission electron microscopy demonstrates the minimal thickness (~1.4 nm) precipitate plates are isostructural to those of the T₁ (Al₂CuLi) phase observed in Al-Cu-Li alloys. Low voltage chemical analysis by energy dispersive X-ray spectroscopy and electron energy loss spectroscopy gives evidence of the spatial partitioning of the Al, Cu and Zn within the Y-phase, as well as demonstrating the incorporation of a small amount of Mg.

The quench sensitivity of 7xxx alloys has been extensively studied under various cooling conditions in an effort to understand the evolution of the structure-property relationship. Fink and Willey showed in the 1940s that the corrosion resistance behaviour of alloy AA7075 changes with different cooling conditions¹. Hatch demonstrated that, in the temperature range of 290–400 °C, the tensile strengths of different aluminium alloys changes vastly with average cooling rate due to the promotion of the growth of different phases². Relatively few papers have been published focusing on the nature of the quench-induced phases in 7xxx alloys. Deschamps and Bréchet demonstrated that the equilibrium M-phase nucleates on Cr- or Zr- containing dispersoids in alloy AA7010 during air-cooling³. In 2009, Deschamps *et al.* investigated the influence of cooling rate on precipitation in a medium strength 7xxx alloy without Cu (AA7020). They found that the quench-induced precipitation occurs in the temperature range between 320 to 220 °C at cooling rates ranging from 0.1 to 3 K/s⁴. Tang *et al.* proposed that the T and S phases precipitate on grain/subgrain boundaries in a 7xxx alloy during slow cooling⁵.

Recent improvements in controlled heat treatment techniques and experimental design have enabled increasingly comprehensive exploration of temperature, cooling and precipitate -growth in practical timescales. A novel differential scanning calorimetry (DSC) method was developed by Milkereit *et al.* and used to construct novel continuous cooling precipitation (CCP) diagrams for a range of 6xxx and 7xxx series alloys, including AA7020 and AA7150^{6–8}. Following this, Zhang *et al.* demonstrated that in the Al-Zn-Mg-Cu alloy AA7150 there are at least three types of quench-induced phases in different temperature ranges over a wide range of continuous cooling rates⁸. This study identified a high temperature reaction at a cooling rate range of about 0.005 to 2 K/s from about 450 °C down to 350 °C, which corresponds to the growth of S-phase (Al₂CuMg). A medium temperature reaction, corresponding to the η-phase (based on MgZn₂, but with potential variations), reaches its maximum intensity at about 0.25 K/s and occurs from about 375 °C down to 250 °C. Finally, a low temperature reaction was detected in the temperature range from ~250 °C down to 150 °C at cooling rates above 0.03 K/s. However, the nature of this phase was not unambiguously verified, due to its small volume fraction and size. The purpose of the current work is to identify this low temperature reaction phase using a combination of DSC, conventional transmission electron microscopy (TEM), and aberration corrected and analytical scanning transmission electron microscopy (STEM) techniques. It also seeks to quantify the effect of this phase on the mechanical properties.

¹Department of Materials Science and Engineering, Monash University, Clayton, VIC 3800, Australia. ²Monash Centre for Electron Microscopy, Monash University, Clayton, VIC 3800, Australia. ³Chair of Materials Science, Faculty of Marine Technology and Mechanical Engineering, University of Rostock, 18051 Rostock, Germany. ⁴CALOR – Research Competence Center Calorimetry and Thermal Analysis Rostock, Faculty for Interdisciplinary Research, Department Light, Life and Matter, University of Rostock, 18051 Rostock, Germany. Correspondence and requests for materials should be addressed to Y.Z. (email: tony.zhang@Monash.edu)

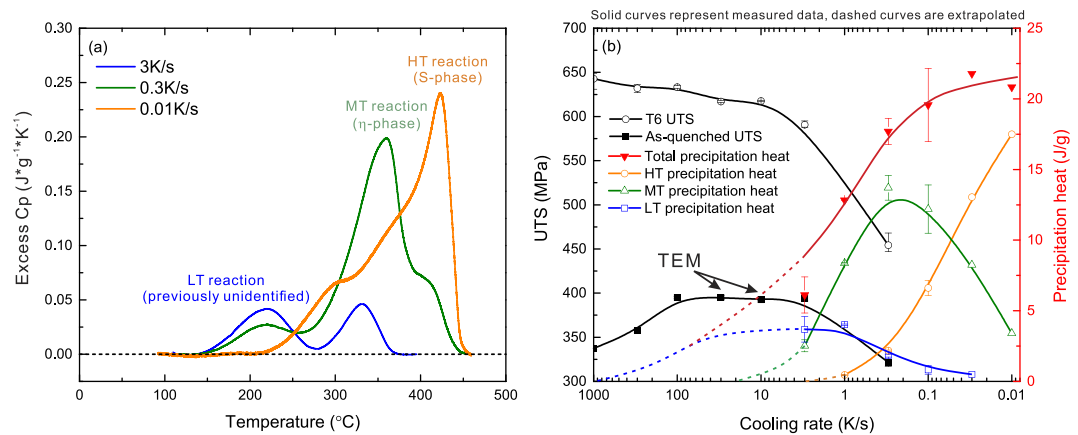


Figure 1. (a) Excess specific heat capacity curves for specimens cooled at 3, 0.3 and 0.01 K/s. (b) Precipitation heats for total precipitation, the high temperature (HT) S-phase, the medium temperature (MT) η -phase and the low temperature (LT) reaction during continuous cooling covering five orders of magnitude in cooling rate. Ultimate tensile strength (UTS) values are shown for as-quenched and T6 conditions.

Materials and Methods

Samples were cut from the centre layer of a commercially produced 80 mm thick AA7150 alloy plate (Al-0.02Si-0.05Fe-2.04Cu-2.15Mg-6.33Zn-0.12Zr in wt%), supplied by the Aluminum Corporation of China Ltd (Chalco).

Samples were solutionised at 460 °C for 1 hour and then slowly heated up to 480 °C within a differential scanning calorimeter (DSC) device and held at this temperature for another hour. Immediately after the solution treatment, the materials were continuously cooled in the same specialised DSC over a range of cooling rates from 0.005 to 3 K/s. A quenching dilatometer was used to achieve cooling rates above 3 K/s. Details of the specialised DSC devices are given elsewhere^{7,8}.

Tensile testing was carried out in a quenching and deformation dilatometer (type Bähr DIL 805 A/D) at a strain rate of 0.1 s⁻¹ immediately after quenching and/or ageing (see supplementary materials for exact geometry). An Instron 8502 servo hydraulic tensile testing machine was used to test the strength of the rapidly quenched samples (≥ 300 K/s). The tensile test samples were cut from the centre layer of the plate and all tested in the same direction. After solution annealing, the tensile test samples were cooled linearly using the quenching dilatometer. The only exceptions were the fastest two cooling rates, which were carried out by quenching in water at 50 °C and 25 °C, as these rates were not achievable in the dilatometer. As such, for these two conditions, the cooling was not strictly linear. However, based on literature², for a sample thickness of 2 mm and water temperatures of 50 °C and 25 °C, cooling rates are estimated to be about 300 and 1000 K/s respectively. As-quenched tensile strengths and T6 aged strengths (after immediate artificial ageing at 120 °C for 24 hours) were both determined with three samples per condition. Microstructural characterisation was carried out on samples continuously cooled at 10 and 30 K/s. The constructed CCP diagram⁸ (see supplementary materials) for the same alloy indicates that, these cooling rate conditions should result in near-maximum amounts of low temperature phase precipitation while being sufficiently fast to avoid the high temperature reaction completely and minimise the medium temperature reaction⁸.

Conventional bright field (BF) TEM was carried out on an FEI Tecnai T20, operating at 200 kV. High angle annular dark field scanning transmission electron microscopy (HAADF-STEM), electron energy loss spectroscopy (EELS) and energy dispersive X-ray (EDX) spectrum imaging (SI) were carried out on a dual aberration corrected (STEM and TEM) FEI Titan³ 80–300 kV microscope. For high resolution HAADF imaging the instrument was operated at 300 kV with a convergence semi-angle of 15 mrad, leading to a diffraction limited (Gaussian) probe diameter of ~ 0.12 nm. In order to minimise beam damage, analytical spectrum images were acquired at a reduced accelerating voltage of 80 kV, where a convergence semi-angle of 18 mrad was used leading to a diffraction limited probe size of ~ 0.23 nm. Images were collected on a Fischione HAADF detector with a collection angle of 57–220 mrad. Specimen thickness, and suitability for EELS, was determined by matching simulation to position averaged convergent beam electron diffraction (PACBED). All HRSTEM images are presented in unfiltered form. The EELS data were collected using a Tridiem Gatan Imaging Filter (GIF), with a collection semi-angle of 77 mrad. The EDX spectra were acquired using a Bruker Quantax 400 windowless 60 mm² SDD detector. The EELS and EDX spectra were processed via Gatan Digital Micrograph (DM) and custom routines coded in IDL. Spatial drift was compensated after acquisition by using cross correlation in the plate direction, and plate/matrix average spectra were generated using digital masks generated from simultaneously acquired STEM images.

Results and Discussion

Figure 1(a) demonstrates the DSC detected excess specific heat for specimens cooled at three selected cooling rates. Three major exothermal precipitation peaks cover different temperature ranges, with the precipitation behaviour dominated by different peaks at different cooling rates. At a cooling rate of 0.01 K/s, the high-temperature (HT) reaction at 450 to 350 °C dominates corresponding to the precipitation of the S-phase (Al₂CuMg)⁸. At cooling rate of 0.3 K/s, the medium-temperature (MT) reaction at 375 to 250 °C dominates corresponding to the η -phase (based on MgZn₂)⁸. The low temperature (LT) reaction, dominant from about 250 to 150 °C corresponds to the previously unidentified precipitates that are the focus of this work. Following Milkereit,

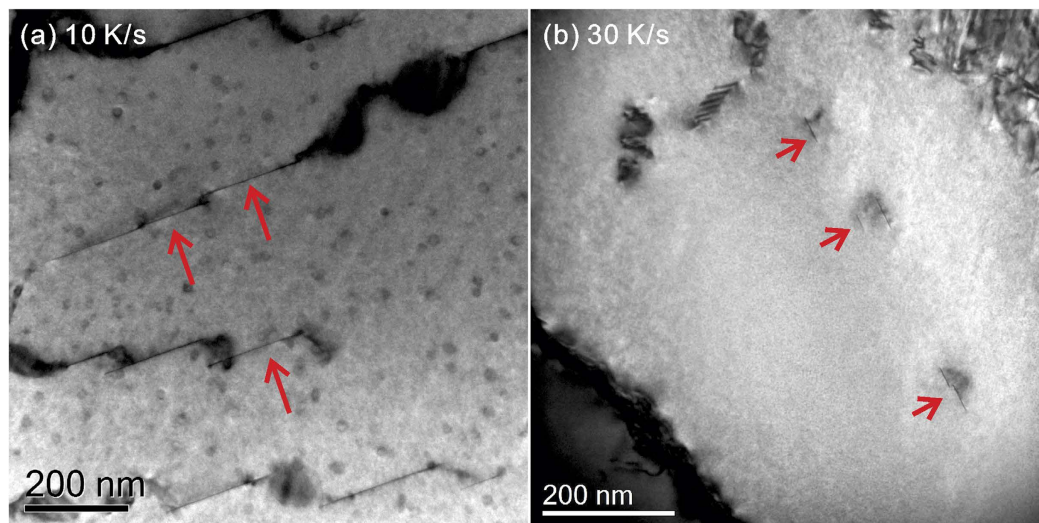


Figure 2. Bright field TEM micrographs showing the thin plate-shaped phase after cooling at (a) 10 K/s and (b) 30 K/s. The images are taken within subgrains along the $[110]_{\alpha}$ zone axis.

the area underneath the DSC peaks is the precipitation enthalpy or precipitation heat, which is directly proportional to the volume fraction of precipitation⁷. The total precipitation heat and precipitation heat values for each reaction are plotted as a function of cooling rate in Fig. 1(b). Details about the evaluation of the precipitation heat process can be found elsewhere^{8,9}.

The overall precipitation heat decreases with increasing cooling rates, suggesting that quench-induced precipitation is gradually inhibited by increasing the cooling rate. The precipitation heat values for the HT S-phase gradually decrease with increasing cooling rate. This value approaches zero at cooling rates of 1–2 K/s, suggesting negligible amounts of S-phase precipitation occur above 1 K/s. However, the detected precipitation heat values for individual quench-induced precipitation reactions are not necessarily decreasing with increasing cooling rates^{7,8}, as shown with the green MT reaction and blue LT reaction curves in Fig. 1(b). For example, the precipitation heat values for the MT precipitation of the η -phase increase over the cooling rate range from 0.01 to 0.1 K/s and then decrease at cooling rates above 0.3 K/s.

The same increasing trend can be found for the LT phase over the cooling rate range from 0.03 to 1 K/s. This behaviour can be ascribed in part to the suppression of the precipitation reactions at higher temperatures, resulting in an increased amount of solute becoming available for the LT phase precipitation. However, at a certain cooling rate, each diffusion-controlled precipitation reaction will still be suppressed by rapid cooling. It is therefore reasonable to assume that the LT phase will also be suppressed by rapid cooling at cooling rates above about 3–10 K/s (the limit of conventional DSC devices). Similar trends have been observed for 6xxx alloys at fast cooling rates^{6,7,9}.

Since the precipitation heat for the η -phase rapidly approaches zero at cooling rates above 3 K/s, it is evident that LT phase precipitation increasingly dominates the total precipitation reaction at cooling rates of ≥ 3 K/s. The extrapolation of the precipitation heat at cooling rates above 3 K/s in Fig. 1(b) is based on a combined assessment of the DSC results as well as the trends in hardness, strength and observations of microstructural evolution as discussed below.

Figure 1(b) also shows that the ultimate tensile strength (UTS) tends to increase with increasing cooling rate. The UTS value in the T6 heat treatment condition reaches a maximum value of almost 650 MPa at the maximum cooling rate of 1000 K/s (25 °C water quench after solution annealing). This is an indication that all the solutionised solute atoms have been preserved in solid solution by the rapid quenching, leading to a maximum age hardening capability. Even if there is a small amount of quench induced precipitation in that cooling rate range, its small volume fraction will lead to a negligible effect on the overall strength.

The as-quenched strength curve shows similar trends, except that the maximum as-quenched strength of about 400 MPa that can be achieved occurs over a cooling rate range of 3–100 K/s. The as-quenched strength is then seen to decrease by about 50 MPa with increasing cooling rate from 100 to 1000 K/s. At cooling rates below 3 K/s, the as-quenched strength curve also exhibits a significantly decreasing trend with decreasing cooling rate. The yield strength (YS) and hardness values show similar trends, as illustrated in the supplementary materials.

Figure 2(a,b) show bright field (BF) TEM images of samples cooled continuously to room temperature at cooling rates of 10 K/s and 30 K/s, respectively. Very few, if any, η -phase and S-phase precipitates can be detected in these cooling conditions. However, Fig. 2(a) shows that some platelet precipitates co-exist with some spherical precipitates in this cooling condition. These spherical precipitates are known to be Al_3Zr dispersoids that formed during the homogenisation process^{10–12}. The platelet precipitates are longer and present in larger amounts at the cooling rate of 10 K/s, than at the cooling rate of 30 K/s. It is therefore concluded that this platelet phase is a quench-induced phase since the growth of the platelet phase is gradually inhibited by increasing cooling rates. There are also some similar findings from DSC work on other alloys^{7,13,14}. Compared to the S-phase and

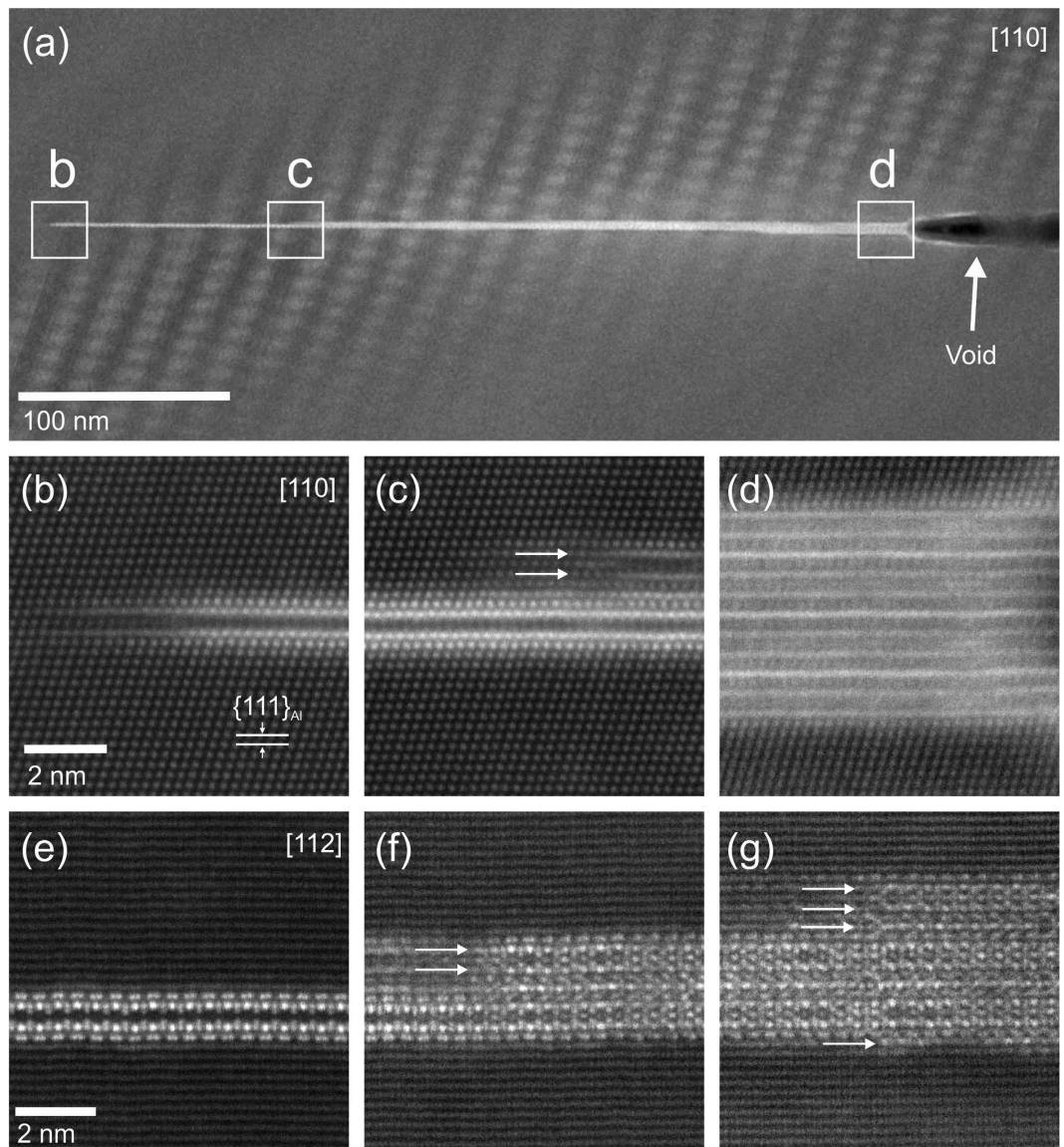


Figure 3. (a–d) HAADF-STEM images of a single platelet precipitate, viewed from the $[110]_{\alpha}$ direction, showing that the thickness varies along its length, with growth ledges indicated by arrows in (c). The regular pattern in the matrix on either side of the plate in (a) is an artifact caused by Moiré fringing between the lattice and scan frame. This plate appears to be nucleating from an attached void. Similar images in (e–g) from a second plate, but viewed from the $[112]_{\alpha}$ direction, show thickness and stacking order variations along the precipitate length.

η -phase, the inhibition of growth of the platelet precipitates happens in a relatively fast cooling rate range (i.e. >3 – 10 K/s). Therefore it is concluded that the observed platelet phase corresponds to the low temperature precipitation reaction.

To the best knowledge of the authors, this platelet phase has never previously been reported in 7xxx series alloys, despite this system being widely used in aerospace applications. We have therefore named it the Y-phase. This work shows that an appreciable amount of this Y-phase precipitation only occurs under very particular cooling conditions i.e. during continuous cooling over a relatively fast cooling rate range from about 1 to 100 K/s and in a low temperature range of about 150–250 °C⁸. The amount of Y-phase increases with increasing cooling rate over the cooling rate range from about 0.03 K/s to about 3 K/s. It is possible that this Y-phase can precipitate in very slow cooling conditions, but the amount is very limited as the precipitation heat is very low. It is expected that the precipitation of this Y-phase will be totally suppressed by very rapid cooling above about 100–1000 K/s.

The as-quenched strength is seen to reach its maximum value over the cooling rate range of 3–100 K/s. This can be ascribed in part to the precipitation of the platelet phase, as the amount of the platelet phase is close to its maximum value in these cooling conditions. With further increases of cooling rate (>100 K/s), the amount of the platelet phase decreases, causing a corresponding decrease in the strength even though the solid solution hardening increment is expected to increase. According to Nie and Muddle, platelet precipitates on the $\{111\}_{\alpha}$ planes

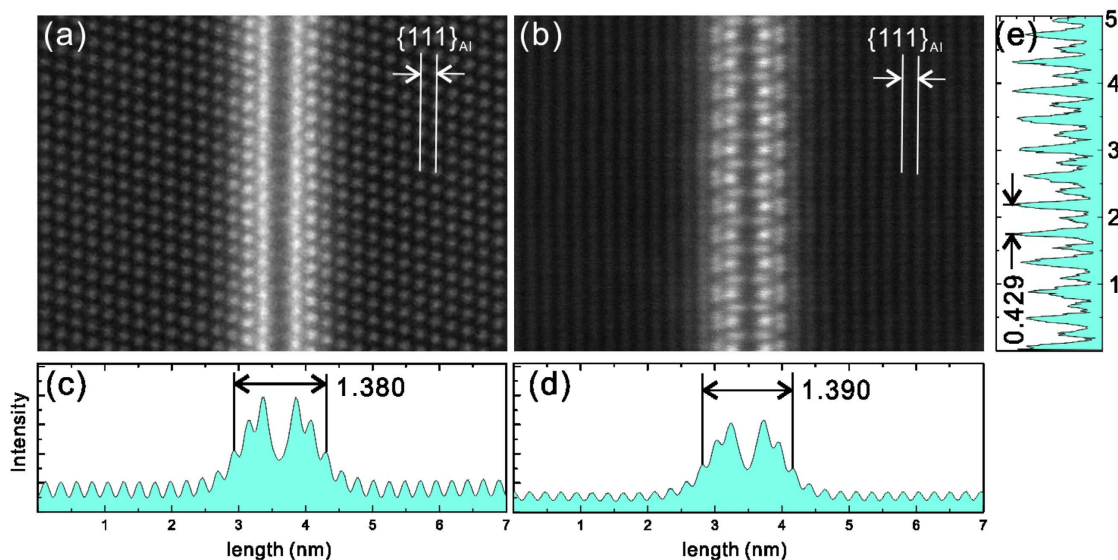


Figure 4. Atomic-resolution HAADF-STEM imaging of a single platelet precipitate viewed from (a) $[110]_{\text{Al}}$ and (b) $[112]_{\text{Al}}$ directions, with (c) and (d) showing respective plots of image intensity integrated vertically, and (e) showing the distribution of intensity along the length of the precipitate.

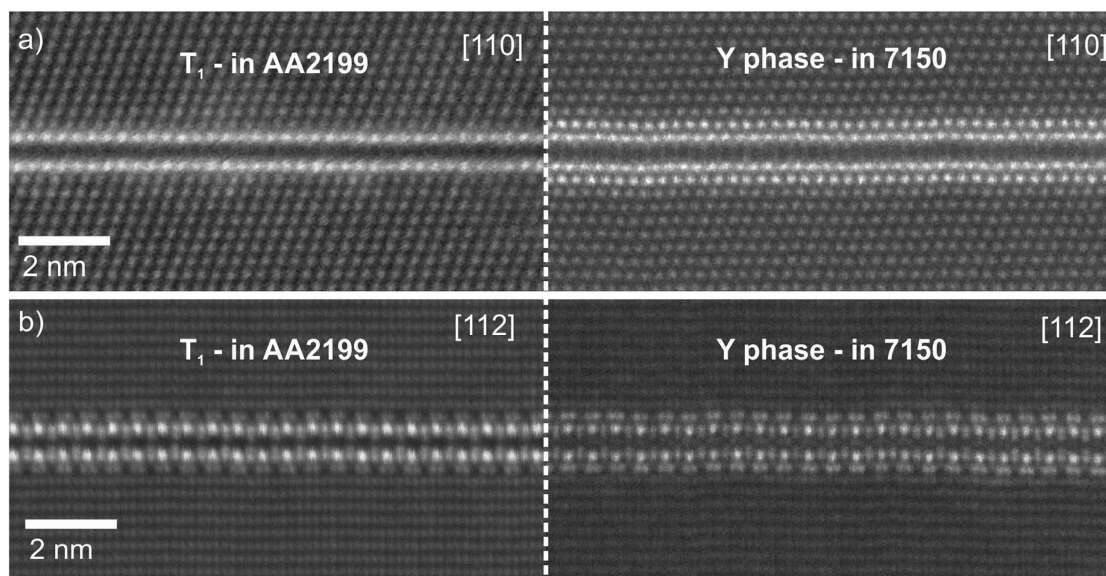


Figure 5. A direct comparison of the T_1 phase in age hardened alloy AA2199 (left) with the Y-phase from alloy AA7150 (right), viewed from both (a) 110 and (b) 112 directions.

have the highest strengthening potential in aluminium alloys¹⁵. It is therefore not unreasonable to expect a strengthening increment from this platelet phase.

Based on the conventional bright field TEM images in Fig. 2, it is interesting to see that there is only one set of edge-on plates from the $\langle 110 \rangle_{\text{Al}}$ direction (there are normally two sets of 111 plane precipitates visible in this direction) in any individual sub grain. This could be a strong indication of the nucleation route. The precipitate plates are heterogeneously distributed within subgrains. This may be due to preferential nucleated in subgrains rather than in recrystallised grains. However, the exact mechanism is as yet undetermined. The micrographs in Fig. 2 show that the Y-phase precipitates have a very low thickness and a very high aspect ratio (length/thickness ratio). This makes them clearly visible from an edge-on orientation, but almost invisible from other orientations.

Figure 3(a–d) show HAADF-STEM images of a single platelet precipitate with the electron beam parallel to the $\langle 110 \rangle_{\text{Al}}$ direction. The thickness of this platelet precipitate varies from a double-layer structure (as shown in Fig. 3(b)) to a multi-layer structure (as shown in Fig. 3(d)). Apparent growth ledges are indicated by the arrows in Fig. 3(c). Figure 3(e–g) show a second platelet with the electron beam parallel to the $\langle 112 \rangle_{\text{Al}}$ direction. The structure revealed in this direction indicates that this phase cannot be described by a regular 3D unit cell. The

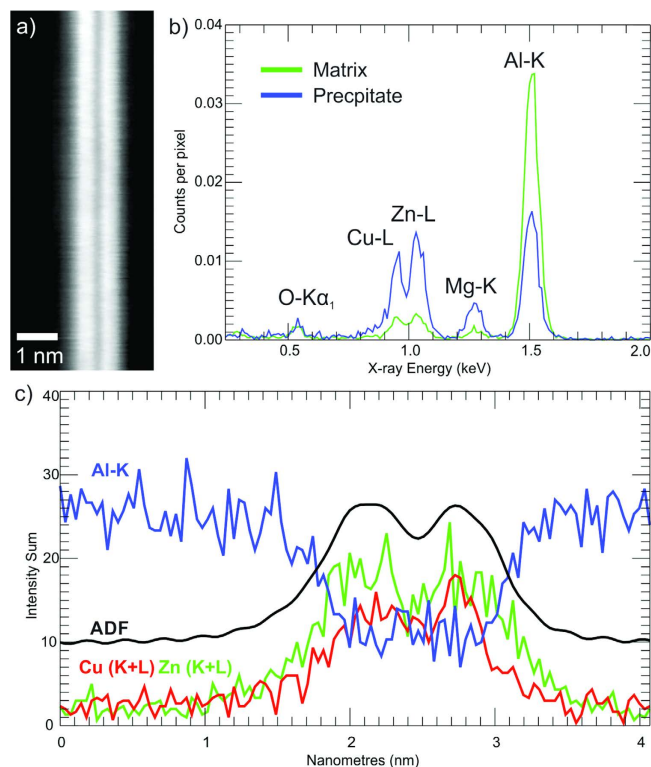


Figure 6. Results of EDX spectrum imaging (SI): (a) ADF image acquired simultaneously with EDX data; (b) Masked generated average spectra from precipitate and matrix; (c) Summed line trace across precipitate for ADF, Al-K, Cu (K + L) and Zn (K + L) signals.

structure of the minimal thickness plate in Fig. 3(e), corresponding to a double bright layer with a dark center, is not replicated when the plate thickens (Fig. 3(f,g)). The apparent replication of various layers within the thicker sections may allow them to be described as long period stacking order (LPSO) structures, such as those common in magnesium rare earth alloys. However, such a description will require the systematic characterisation of a large number of precipitates. A recent study by Marioara *et al.* on a similar alloy system (AA7449) also observed structural arrangements in a new precipitate phase showing similarities to those of the T_1 phase in Al-Cu-Li alloys¹⁶. While they did not observe any minimal thickness plates, possibly since they investigated over-aged samples, they tellingly suggested that “It may therefore be expected that in some conditions a plate isostructural to the T_1 phase could also exist in the Al-Mg-Zn system”¹⁶.

The projected atomic structure of the minimal thickness platelet bears a striking resemblance to plates of the T_1 phase that are the principal strengthening phase in 2xxx series Al-Cu-Li alloys^{15,17–23}. The images from two different observation directions in Fig. 4(a,b) strongly indicate that the Y-phase has a similar crystal structure and symmetry to the T_1 phase. The T_1 phase also shows long period stacking order in its thicker forms. On the basis of structural isomorphism with T_1 , the minimal thickness platelet has a hexagonal basis symmetry with repeat distances of $a = 0.429$ nm, $c = 1.385$ nm (T_1 is in the $P6/mmm$ space group with D_{6h} symmetry²³), with the following orientation relationship with the matrix:

$$(0001)_{\text{platelet-phase}} \parallel (111)_{\alpha} \text{ and } [11\bar{2}0]_{\text{platelet-phase}} \parallel [112]_{\alpha}$$

The measured parameters are based on HAADF-STEM images using the $\{111\}_{Al}$ plane space ($d_{111} = 0.2338$ nm) as a reference. These are subtly different to the parameters for the T_1 phase ($a = 0.496$ nm, $c = 1.391$ nm)²³. It is noted that c is very close to $6 \times d_{111} = 1.4028$ nm, so that the platelet phase is slightly mismatched with the Al matrix, as shown in Fig. 4(a). This can be attributed to the atomic positions of the different solute species within the Y-phase. A previous study of the T_1 phase showed that the T_1 phase tends to precipitate by heterogeneous nucleation on dislocations in Al-Cu-Li alloys²⁴. This may provide some clues for the nucleation mechanism of the platelet phase in alloy 7150, as the platelet precipitates are mainly found within subgrains. Based on Fig. 3(a), nucleation from voids is also a possibility.

Figure 5 shows HAADF STEM micrographs comparing the T_1 phase in an age hardened AA2199 alloy (left) with the Y-phase from alloy AA7150 (right), along both (a) 110 and (b) 112 directions. These micrographs were acquired on the same instrument using the same imaging and collection conditions (though with different, and undetermined, specimen thicknesses).

In the 112 direction there is strong similarity, with both phases showing a distinctive “zipper” appearance: bright columns separated by a dark band, with distinctive dumbbell structures on the surface and facing inwards. The appearance on 110 is similar, but the T_1 -phase lacks the extra surface layers (clearly present in 112)–in

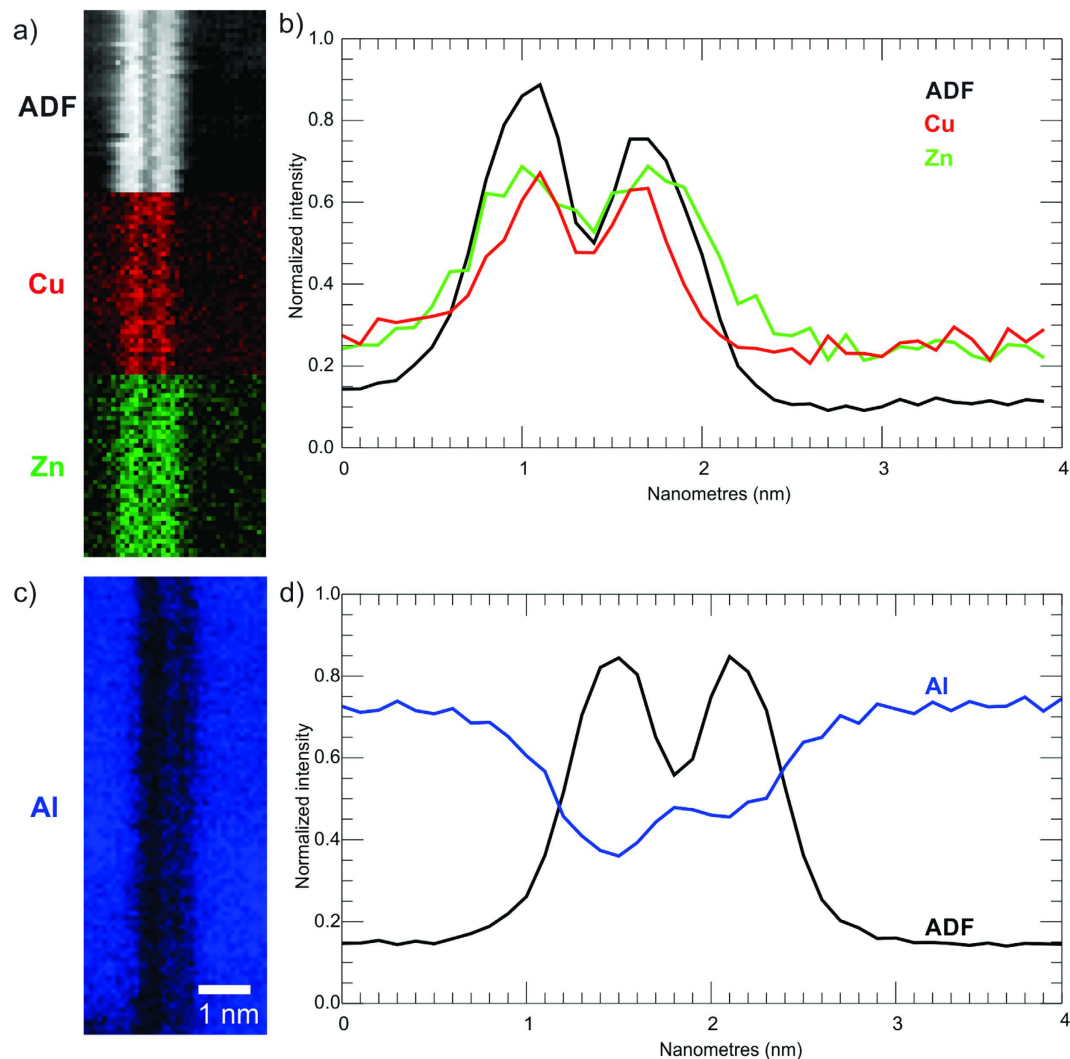


Figure 7. Results of two EELS spectrum images (SI), acquired from the same plate over different energy ranges: (a) ADF, Cu map and Zn map from first SI. (b) Summed line traces across precipitate for ADF, Cu map and Zn map; (c) Al map; (d) Summed line traces across Al map and ADF image (not shown).

projection the Li content of these layers leads to an almost complete loss of contrast. Clearly the average atomic number of the bounding layer in the new phase is higher than that of bulk Al. This is consistent with the differing relative contrast in the bounding layer of the new phase, which is significantly brighter than the matrix.

While there is clear structural similarity between the Y-phase and the T_1 phase²³, alloy 7150 contains no Li so the chemistry of this phase must be substantially different. Due to electron channelling in crystalline specimens, quantitative chemical analysis on these length scales is not possible without a full solution of the atomic structure²⁵ and precise knowledge of acquisition geometry²⁶. However, both the EDX and EELS results from the plates give a qualitative indication of the chemical makeup of, and to some extent, the partitioning within the precipitate plates.

The average EDX spectra, Fig. 6(b), taken from the precipitate shown in Fig. 6(a) confirm that the precipitates contain a significant proportion of Cu, Zn and a reduced amount of Al in comparison to the matrix. The precipitate spectra also indicate the inclusion of a small, yet significant, amount of Mg. The signal to noise ratios (SNR) of 2D maps from the EDX SI (Supplementary Fig. (4)) are low but the summed line trace from the SI across the precipitate in Fig. 6(c), indicates that the high Z contrast layers peak in both Cu and Zn content, with Al present but at a low level across the plate.

The EELS SI results, shown in Fig. 7, are consistent with the EDX data and, being of significantly higher SNR, offer insight into the chemical structure of the precipitate. The maps, Fig. 7(a,c), and average line traces, Fig. 7(b,d), indicate that Cu has a narrower distribution within the precipitate, and is strongly peaked in the two bright layers. While Zn is also peaked in the same locations, its distribution is broader and extends into the bounding layers of the precipitate. Due to the large energy difference between Al-L and Cu-L/Zn-L edge onsets (73 eV and 931 eV/1020 eV, respectively) it is not possible with the available spectrometer to map both in the same acquisition. Maps taken in a separate acquisition from the aluminium L edge from the same precipitate,

Fig. 7(c) show a small increase in Al composition in the dark (low Z) centre layer of the precipitate plate. The asymmetry of this feature is probably due to a tilt misalignment of the crystal. In the very thin area used for the acquisition (7 nm via PACBED), exact on-axis conditions are hard to achieve. The same feature is weakly indicated in the EDX trace in Fig. 6(c). Despite the Mg-K edge being included in the energy range with the Cu and Zn K edges no peak was detected above the noise level. However this can be explained by looking at the relative scattering cross sections for the three edges. The inelastic scattering cross section for the Mg-K peak, calculated via the Hartree-Slater model in Digital Micrograph, is 7 times lower than for Cu-L and 5 times lower than Zn-L over a 50 eV energy window. As such, Mg has a much lower detectability than Cu or Zn over this energy range. While the Mg-L edge is contained in the spectra with the Al-K, there is also no edge present. The large amounts of Al, and the relatively low SNR of the Al-K map in Fig. 7(c), suggests that Mg is present in very small amounts, consistent with the EDX data. The T_1 phase has also been shown to be able to incorporate small amounts of other elements, including Mg, during nucleation and growth²⁷.

Conclusions

This paper has reported the discovery of a new platelet phase that precipitates in alloy AA7150 during relatively fast continuous cooling in a relatively low temperature range of about 150–250 °C. These Y-phase precipitates with high aspect ratio grow on the aluminium $\{111\}_\alpha$ planes. The microscopy results show the Y-phase to be structurally very similar to the T_1 phase found in Al-Cu-Li alloys, and to have a hexagonal symmetry ($a = 0.429$ nm, $c = 1.385$ nm). Tensile testing indicates that this Y-phase appears to contribute up to ~50 MPa to the as-quenched strength in the investigated continuous cooling conditions. It may also precipitate in other Cu-containing 7xxx alloys.

The results of the chemical analysis are consistent with the contrast observed in the HAADF images and the chemical differences to the T_1 phase. The Y-phase is dominated by layers rich in Zn and Cu, the distinctive bright contrast in the 110 direction, with a centre plane dominated by Al and hence exhibiting darker contrast. The lack of Li in the structure compared to T_1 , results in the bounding planes being a mix of Al and Cu/Zn, with the EELS data suggesting these bounding planes are higher in Zn than Cu. The high average atomic number of these planes explains why they appear as brighter than the matrix in the 110 direction (as opposed to T_1 where the presence of Li leads to an average atomic number similar to that of the matrix, with these layers practically invisible). While the EDX results show the presence of Mg in the plate, this is at a level too low to achieve any determination of its partitioning; indeed this was too low to even be detectable via EELS. A final solution of the precipitate phase structure is ongoing, but will require construction of prospective models, and matching with extensive image simulation and *ab initio* calculation.

References

- Fink, W. L. & Willey, L. A. Quenching of 75S Aluminum Alloy. *Trans. AIME* **175**, 414–427 (1947).
- Hatch, J. E. *Aluminum: Properties and Physical Metallurgy* 157–167 (Aluminum Association Inc. and ASM International, 1984).
- Deschamps, A. & Bréchet, Y. Nature and Distribution of Quench-Induced Precipitation in an Al-Zn-Mg-Cu Alloy. *Scr. Mater.* **39**, 1517–1522 (1998).
- Deschamps, A., Texier, G., Ringeval, S. & Delfaut-Durut, L. Influence of cooling rate on the precipitation microstructure in a medium strength Al-Zn-Mg alloy. *Mater. Sci. Eng., A* **501**, 133–139 (2009).
- Tang, J. *et al.* Influence of quench-induced precipitation on aging behavior of Al-Zn-Mg-Cu alloy. *Trans. Nonferrous Met. Soc. China* **22**, 1255–1263 (2012).
- Milkereit, B., Kessler, O. & Schick, C. Recording of continuous cooling precipitation diagrams of aluminium alloys. *Thermochim. Acta* **492**, 73–78 (2009).
- Milkereit, B., Wanderka, N., Schick, C. & Kessler, O. Continuous cooling precipitation diagrams of Al-Mg-Si alloys. *Mater. Sci. Eng., A* **550**, 87–96 (2012).
- Zhang, Y., Milkereit, B., Kessler, O., Schick, C. & Rometsch, P. A. Development of continuous cooling precipitation diagrams for aluminium alloys AA7150 and AA7020. *J. Alloys Compd.* **584**, 581–589 (2014).
- Milkereit, B., Beck, M., Reich, M., Kessler, O. & Schick, C. Precipitation kinetics of an aluminium alloy during Newtonian cooling simulated in a differential scanning calorimeter. *Thermochim. Acta* **522**, 86–95 (2011).
- Robson, J. D. A new model for prediction of dispersoid precipitation in aluminium alloys containing zirconium and scandium. *Acta Mater.* **52**, 1409–1421 (2004).
- Robson, J. D. Optimizing the Homogenization of Zirconium Containing Commercial Aluminum alloys using a Novel Process Model. *Mater. Sci. Eng., A* **338**, 219–229 (2002).
- Zhang, Y., Bettles, C. & Rometsch, P. A. Effect of recrystallisation on Al_3Zr dispersoid behaviour in thick plates of aluminium alloy AA7150. *J. Mater. Sci.* **49**, 1709–1715 (2014).
- Milkereit, B., Jonas, L., Schick, C. & Keßler, O. The continuous cooling precipitation diagram of an aluminum alloy EN AW-6005A. *HTM, J. Heat Treat. Mater.* **65**, 159–171, doi: 10.3139/105.110056 (2010).
- Schumacher, P. *et al.* Correlation between supersaturation of solid solution and mechanical behaviour of two binary Al-Si-alloys. *Mater. Sci. Forum* **794–796**, 508–514 (2014).
- Nie, J. F. & Muddle, B. C. On the form of the age-hardening response in high strength aluminium alloys. *Mater. Sci. Eng., A* **A319–321**, 448–451 (2001).
- Marioara, C., Lefebvre, W., Andersen, S. & Friis, J. Atomic structure of hardening precipitates in an Al-Mg-Zn-Cu alloy determined by HAADF-STEM and first-principles calculations: relation to η -MgZn₂. *J. Mater. Sci.* **48**, 3638–3651, doi: 10.1007/s10853-013-7158-3 (2013).
- Galbraith, J. M., Toshten, M. H. & Howell, P. R. On the nucleation of θ' and T_1 on Al_3Zr precipitates in Al-Li-Cu-Zr alloys. *J. Mater. Sci.* **22**, 27–36 (1987).
- Kanno, M. & Ou, B.-L. Heterogeneous Precipitation of Intermediate Phases on Al_3Zr Particles in Al-Cu-Zr and Al-Li-Cu-Zr Alloys. *Mater. Trans. JIM* **32**, 445–450 (1991).
- Yang, J.-G. & Ou, B.-L. Hot Ductility Behavior and HAZ Hot Cracking Susceptibility of 7475-T7351 Aluminum alloy. *Scand. J. Metall.* **30**, 146–157 (2001).
- Yoshimura, R., Konno, T. J., Abe, E. & Hiraga, K. Transmission electron microscopy study of the evolution of precipitates in aged Al-Li-Cu alloys: the θ' and T_1 phases. *Acta Mater.* **51**, 4251–4266 (2003).
- Wang, S. C. & Starink, M. J. Precipitates and intermetallic phases in precipitation hardening Al-Cu-Mg-(Li) based alloys. *Int. Mater. Rev.* **50**, 193–214 (2005).

22. Donnadieu, P. *et al.* Atomic structure of T1 precipitates in Al-Li-Cu alloys revisited with HAADF-STEM imaging and small-angle X-ray scattering. *Acta Mater.* **59**, 462–472 (2011).
23. Dwyer, C., Weyland, M., Chang, L. Y. & Muddle, B. C. Combined electron beam imaging and ab initio modeling of T1 precipitates in Al-Li-Cu alloys. *Appl. Phys. Lett.* **98** (2011).
24. Cassada, W. A., Shiflet, G. J. & Starker, E. A. Mechanism of Al₂CuLi(T1) nucleation and growth. *Metall. Mater. Trans. A* **22A**, 287–297 (1991).
25. Zhu, Y. & Dwyer, C. Quantitative position-averaged k-, l-, and m-shell core-loss scattering in stem. *Microsc. Microanal.* **20**, 1070–1077 (2014).
26. Chen, Z. *et al.* Energy dispersive X-ray analysis on an absolute scale in scanning transmission electron microscopy. *Ultramicroscopy* **157**, 21–26, doi: 10.1016/j.ultramic.2015.05.010 (2015).
27. Araullo-Peters, V., Gault, B., Geuser, F. d., Deschamps, A. & Cairney, J. M. Microstructural evolution during ageing of Al-Cu-Li-x alloys. *Acta Mater.* **66**, 199–208, doi: 10.1016/j.actamat.2013.12.001 (2014).

Acknowledgements

The authors thank the Aluminium Corporation of China Ltd. (Chalco) for financial support and for providing materials. The DSC work was performed at the Polymer Physics Group at the University of Rostock. The leader of the DSC, Prof Christoph Schick, is gratefully acknowledged for helpful discussions. All the TEM work was performed on instruments within the Monash Centre for Electron Microscopy. Funding for the FEI Titan was from Australian Research Council grant number LE0454166.

Author Contributions

Y.Z. led the research, prepared specimens, carried out all preliminary microscopy and prepared the main manuscript text. M.W. carried out all aberration corrected STEM and chemical analysis, prepared Figures 3–7 and provided interpretation of microscopy results. B.M. helped with DSC measurements and data evaluations. M.R. carried out the tensile testing experiments and provided interpretations. P.R. supervised the research and corrected the manuscript text. All authors reviewed the manuscript.

Additional Information

Supplementary information accompanies this paper at <http://www.nature.com/srep>

Competing financial interests: The authors declare no competing financial interests.

How to cite this article: Zhang, Y. *et al.* Precipitation of a new platelet phase during the quenching of an Al-Zn-Mg-Cu alloy. *Sci. Rep.* **6**, 23109; doi: 10.1038/srep23109 (2016).



This work is licensed under a Creative Commons Attribution 4.0 International License. The images or other third party material in this article are included in the article's Creative Commons license, unless indicated otherwise in the credit line; if the material is not included under the Creative Commons license, users will need to obtain permission from the license holder to reproduce the material. To view a copy of this license, visit <http://creativecommons.org/licenses/by/4.0/>

[BM9] Yang B, Milkereit B, Zhang Y, Rometsch PA, Kessler O, Schick C:

Continuous cooling precipitation diagram of aluminium alloy AA7150 based on a new fast scanning calorimetry and interrupted quenching method.

Materials Characterization 120 (2016): 30–37.

Benjamin's contributions: I managed the international collaboration, participated in the design of the experiments, supervised the DSC work, partially plotted the data, participated in the results discussion and revised the manuscript.

Continuous cooling precipitation diagram of aluminium alloy AA7150 based on a new fast scanning calorimetry and interrupted quenching method

Bin Yang^{a,c*}, Benjamin Milkereit^{a,b,c*}, Yong Zhang^d, Paul A. Rometsch^d, Olaf
Kessler^{b,c}, Christoph Schick^{a,c}

^a Institute of Physics, University of Rostock, Albert-Einstein-Str. 23-24, 18051 Rostock, Germany

^b Faculty of Mechanical Engineering and Marine Technology, University of Rostock, Albert-Einstein-Str. 2, 18051 Rostock, Germany

^c Competence Centre °CALOR, Faculty of Interdisciplinary Research, University of Rostock, Albert-Einstein-Str. 25, 18051 Rostock, Germany

^d Department of Materials Science and Engineering, Monash University, Clayton, VIC3800, Melbourne, Australia

*Corresponding to: bin.yang@uni-rostock.de; benjamin.milkereit@uni-rostock.de

Abstract

Differential fast scanning calorimetry (DFSC) has been combined with a novel differential reheating method (DRM). Interrupted quenching at different temperatures followed by overcritical cooling enables both time- and temperature-dependent investigations of precipitation reactions in aluminium alloys during cooling from solution annealing at cooling rates between 1 K/s and 10⁵ K/s. Together with conventional differential scanning calorimetry

(DSC) results, for the very first time, a full continuous cooling precipitation (CCP) diagram for a highly concentrated wrought AlZnMgCu alloy has been developed. For alloy AA7150, three precipitation reactions with their respective start and end temperatures were observed by DFSC. The critical cooling rate for suppressing the high-temperature precipitation of S -Al₂CuMg was found to be ~10 K/s, whereas for the medium-temperature precipitation of η -Mg(Zn,Al,Cu)₂ it is ~100 K/s and for the low-temperature precipitation of Y -phase plates enriched in Zn and Cu it is ~300 K/s. The method can potentially be transferred to similar precipitate-forming metallic systems or related solid-state phase transformation systems also beyond the particular system analysed in the present study.

Keywords: Aluminium alloys; Differential fast scanning calorimetry; Continuous cooling precipitation diagram; Critical cooling rate; Precipitation kinetics

Introduction

The strength of precipitation hardening aluminium alloys is typically adjusted by means of a solid-state age hardening heat treatment procedure. The age hardening process contains three steps: solution annealing (in solid state), quenching and ageing. During the solution treatment all soluble phases should dissolve. During quenching, this solution should be retained and an unstable, supersaturated solid solution results. During ageing, nano-sized particles precipitate, which hinder dislocation movement by particle strengthening and thereby increase the strength of the alloy. The tendency to lose supersaturation of dissolved alloying elements during cooling from solution annealing is called quench sensitivity. The quench sensitivity or the precipitation behaviour of aluminium alloys during cooling from solution annealing is typically described in continuous cooling precipitation (CCP) diagrams. Such CCP diagrams need to cover a wide range of cooling rates from near-equilibrium slow cooling [1, 2] up to beyond the upper critical cooling rate (CCR) [1, 3, 4]. The CCR is defined

as the slowest cooling rate at which no precipitation occurs during cooling from solution annealing, which ensures maximum supersaturation after quenching and thereby maximum volume fractions of strengthening precipitates, and hence maximum strength, after subsequent artificial ageing.

During the last decade, measurement techniques to investigate the quench sensitivity of aluminium alloys were developed [1, 3-10]. For example, one of the techniques combines microstructural analysis and mechanical testing with in-situ differential scanning calorimetry (DSC) [1, 3, 4]. DSC is able to detect the enthalpy changes caused by precipitation reactions, whereby the enthalpy change gives a direct link to the thermodynamics and volume fractions of the phases. The work [1, 3, 4], which combines microstructural analysis and mechanical testing with in-situ DSC, led to the first continuous cooling precipitation diagrams of low to medium alloyed AlMgSi (6000 series) and AlZnMg(Cu) (7000 series) wrought alloys.

As a diffusion controlled process, precipitation during quenching depends on nucleation as well as on diffusion rate. Diffusion rate mainly depends on the types of diffusing atoms and matrix (e.g. Zn in Al) and temperature. Nucleation mainly depends on supersaturation (homogeneous nucleation) and intrinsic nuclei (heterogeneous nucleation). Intrinsic nuclei may be grain boundaries, primary precipitates or dispersoids. Thus, the quench sensitivity of an aluminium alloy can be influenced by its chemical composition and solution annealing parameters (supersaturation) as well as by its microstructure (intrinsic nuclei). DSC always measures the enthalpy changes due to precipitation influenced by a superposition of all above mentioned factors, i.e. diffusion rate, supersaturation and microstructure (intrinsic nuclei).

The precipitation process in AlZnMg(Cu) alloys is complex and may be divided into precipitation of different phases over different temperature and time ranges during different process steps [4, 5, 11, 12]. More specifically, there are three different classes of precipitates. Firstly, relatively coarse primary precipitates tend to grow directly from the melt (e.g. via eutectic reactions) and reach dimensions of several μm . In this particular case, the $\text{Al}_7\text{Cu}_2\text{Fe}$

intermetallic particles fall into this category. Such primary precipitates are assumed not to be influenced by the age hardening heat treatment. However, they may act as nucleation sites for coarse equilibrium phases that precipitate during slow cooling. Secondly, dispersoids occur. Dispersoids are based on minor alloying elements like Zr, Mn and Cr and form intermetallic particles of sizes typically in the range of 10-100 nm. Precipitation of dispersoids is a solid-state reaction that commonly occurs during homogenisation heat treatments. Dispersoids are also assumed not to be influenced by the age hardening heat treatment. However, they can strongly influence the quench sensitivity as dispersoids may act as nucleation sites for the quench-induced phases [12]. Thirdly, there are precipitates that form from the main alloying elements (here Zn, Mg Cu and Al) and are greatly influenced by the age hardening procedure. In an ideal case, all these last-mentioned precipitates dissolve during solution annealing, and the quenching step should suppress any precipitation during cooling. During subsequent ageing, fine metastable nano-scale hardening precipitates are nucleated and evolve along a precipitation sequence with increasing ageing. As mentioned before, the aim of quenching from solution annealing is to retain the solid solution by avoiding any quench-induced precipitation that would lower the potential for subsequent hardening. Based on recent work from the present authors [4, 12], the precipitation reactions during cooling of alloy AA7150 from solution annealing were divided into three main reactions: high-, medium- and low-temperature reactions (HTR, MTR and LTR, respectively). Nevertheless, the CCRs of MTR and LTR have so far only been inferred from ex-situ microstructure and property observations because conventional DSC is limited to cooling rates below ~ 10 K/s [13, 14]. Furthermore, their precipitation temperature ranges at cooling rates above 3 K/s are unknown [4]. However, cooling rates between 1 and 10^3 K/s are highly relevant in technological processes, because such cooling rates are reached by water quenching (depending on the material thickness and water temperature) [15]. Besides, the more concentrated higher strength Al alloys have critical cooling rates in the range from ~ 10 to 10^3 K/s [3, 4, 16-19].

Recently it was shown that the chip-sensor based differential fast scanning calorimetry (DFSC), whose heating and cooling rates can reach up to some 10^6 K/s [20, 21], could be utilised to follow precipitation reactions in Al alloy 7049A by the indirect differential reheating method (DRM) [22]. Based on this approach, the CCR of Al alloy 7049A was determined to be about 300 K/s. However, so far it was only shown that the DRM is able to detect the overall precipitation enthalpy at high cooling rates – unfortunately without any temperature-dependent information of individual precipitation reactions.

In this current work, we aim to close the former metrological gap by describing a method to obtain temperature-dependent enthalpy information of precipitation reactions in alloy AA7150 in the cooling rate range from a few up to several thousands of K/s. The DRM was developed further towards higher precision, larger cooling rate range of validity and particularly temperature dependency. Thereby, for the very first time, a full continuous cooling precipitation diagram covering all the technologically relevant cooling rates could be recorded for a highly concentrated AlZnMgCu wrought alloy (i.e. AA7150).

Materials and Methods

Bulk samples of alloy AA7150 (composition given in Table I) were cut from the centre layer of a commercially produced 80 mm thick plate, supplied by the Aluminium Corporation of China Ltd (Chalco). In order to obtain samples for DFSC measurements, a small piece of $5 \times 10 \times 20$ mm³ was cut from the centre layer of the thick plate, as shown in Fig. 1(a). Then the material was heated up to 460 °C for 1 h followed by slowly heating up to 480 °C for another 1 h and finally quenched in cold water as a pre-solutionising treatment in a furnace [4]. This pre-treatment was done to reduce local chemical inhomogeneities in the thick industrially processed plate, thereby avoiding high local solute concentrations that could result in localised melting during the DSC and DFSC heating cycles. It therefore enabled the heating times in the calorimeter to be shortened significantly without any risk of incipient

melting (which could occur if samples were heated rapidly directly to 480 °C without the prior removal of concentration gradients at a safe temperature of ~460 °C).

To obtain DFSC samples, a slice of about 300 µm thickness was cut parallel to the short transverse direction (STD) – long transverse direction (LTD) plane. Further, the slice was manually ground and polished to foils having a thickness of around 50 µm. As shown in Fig. 1(b), the foil thickness direction was aligned with rolling direction (RD) and was perpendicular to the sensor plane. The reason for this was to capture a more representative cross-section of the material, especially ensuring that sufficient grain boundaries were included in the thin foil. After that, the sample for DFSC measurements was cut into small rectangular pieces by a scalpel under an optical microscope and placed on the centre of the sensor by a thin copper wire, as shown in Fig. 1(c). In order to secure the small sample on the sensor, silicone oil was used, which would be evaporated during the first heating up to 480 °C.

DFSC is controlled by the power compensation method, which takes care of the heat losses on both sensors (loaded sample and empty reference) following the predefined temperature program very closely. Even at 10^4 K/s, the temperature difference between reference (T_R) and sample sensor (T_S) obeys the inequality, $T_R - T_S < 0.1$ K [21]. The nanocalorimeter sensor, XI-415 (Xensor Integrations, Netherlands), was used in this work. The sensor consists of an amorphous silicon-nitride membrane with a film-thermopile and a resistive film-heater placed at the centre of the membrane, as shown in Fig. 1(d). The sensor can effectively promote high heating and cooling rates up to 10^5 K/s through a preferable ratio between the added heat capacity of the sensor and sample heat capacity and applicable heating power. In a micron scale system, the most efficient cooling agents are gases because of their small heat capacity [23]. Considering these circumstances, we have chosen samples with a size of approximately $75 \mu\text{m} \times 110 \mu\text{m} \times 40 \mu\text{m}$, as shown in Fig. 1(c). The DFSC temperature was calibrated by pure In, Sn, Pb, Zn and K_2SO_4 in an Ar7.5/H₂ (volume fraction

in %) atmosphere at different heating and cooling rates up to 10^5 K/s. Further details about the temperature calibration method are given in Ref. [21].

Table I Chemical composition of the investigated AA7150 alloy (in mass fraction)

Elements	Si	Fe	Cu	Mn	Mg	Zn	Zr	Al
Mass fraction (%)	0.02	0.05	2.04	0.04	2.15	6.33	0.12	Bal

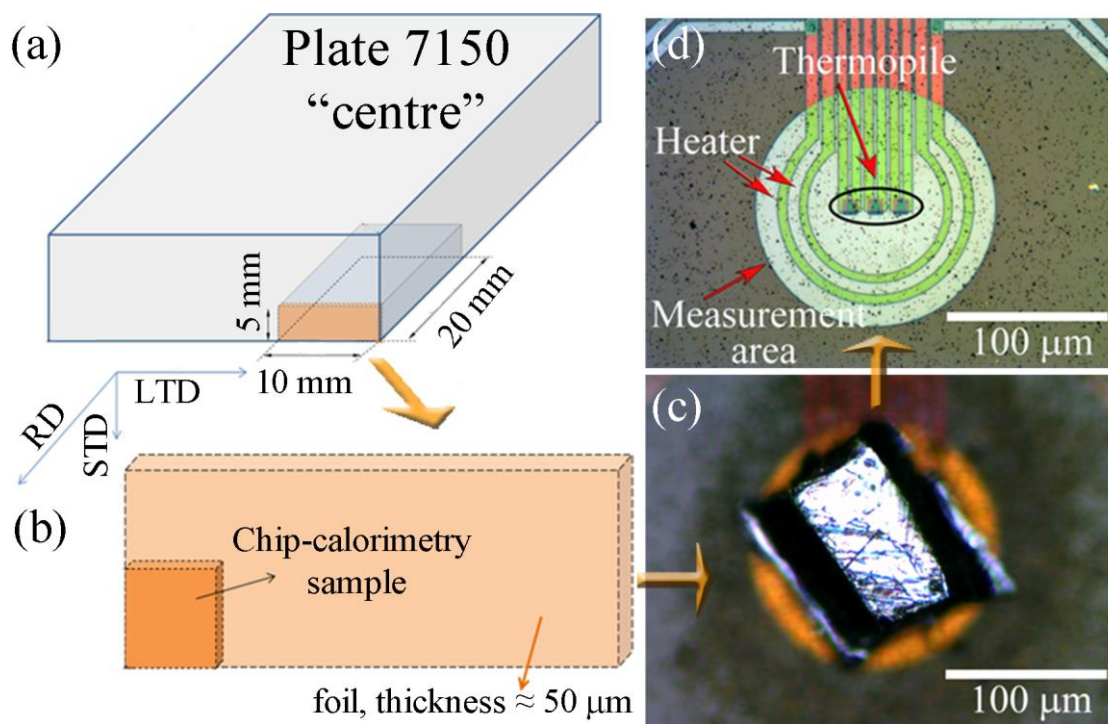


Fig. 1 Scheme of DFSC sample preparation (a)-(c) and chip-sensor (d) used for DFSC measurements.

In order to develop a complete CCP diagram, the CCR should be determined first. The CCR for alloy AA7150 is expected to be between 100 and 1000 K/s [24]. The low signal to noise ratio of the DFSC at these scanning rates, due to the very small thermal effects of precipitation reactions in the small sample, prevents direct determination of enthalpies during cooling. Considering this fact, a sophisticated DRM based on DFSC was used. This method is illustrated in Fig. 2 and is based on the assumption that precipitates formed during cooling can also be characterised by their dissolution during the following reheating process, i.e. the enthalpy change during precipitation equals the enthalpy change during dissolution. Moreover, all the precipitates that formed during slow cooling and/or reheating in the solid state could be dissolved with respect to the equilibrium condition at the solution annealing temperature. The validity of this basic assumption was verified on a quantitative basis using DRM and direct measurements during cooling by conventional DSC (see Ref. [22] for details). Conclusively, in order to use the DRM for characterisation of precipitation reactions (i.e. that the enthalpy change of precipitation can be represented by the enthalpy change of dissolution), three conditions should be fulfilled [22]. (i) At the start temperature for cooling and at the end temperature for reheating, the sample should be in the equilibrium state, i.e. during reheating and after solution annealing, the relevant precipitates fully dissolve. This excludes coarse intermetallic phases such as Al_7Cu_2Fe particles and a small amount of rounded $S-Al_2CuMg$ particles that do not dissolve during solution annealing and are not influenced by quenching [4]. (ii) The cooling after Reheating Nr. 1 (Step 8 in Fig. 2) must be done at an overcritical cooling rate. In the DFSC experiments, a cooling rate of 10^5 K/s was used, which is assumed to be about three orders of magnitude faster than the CCR for common aluminium alloys. (iii) During the isothermal holding after cooling at the lowest temperature, T_c , no precipitation should occur. To avoid precipitation at T_c , the time spent at T_c should be short. In the DFSC experiments, therefore the isothermal holding time at T_c is 0.01 s, which is also enough for temperature equilibration of the DFSC.

The temperature-time profiles used for determining the CCR are shown in Fig. 2(a). Two cycles, Steps 1-6 and 7-10, were conducted [22]. In order to fulfil the requirement (i), a compromise between full dissolution during reheating and optimum sensitivity of the DFSC must be found. A reheating rate of 10^3 K/s was selected to realise maximum sensitivity for reheating and nearly avoid any precipitation during reheating. After solution annealing at 480 °C for 5 min, cooling started (Step 4) with rates ranging from 10 to 800 K/s. Afterwards, the sample was reheated at 10^3 K/s (Reheating Nr. 1, Step 6). At high reheating rates, the temperature of full dissolution shifts to higher temperatures because of the diffusion kinetics of dissolution [25]. Particularly, the larger precipitates that have grown during the lower cooling rates in Step 4 need more time or higher temperatures to dissolve. Therefore, the maximal temperature was set to 500 °C, which is 20 K higher than the annealing temperature, T_{an} . This allowed full dissolution signals to be obtained and thereby the full dissolution enthalpy change for the previously applied wide cooling rate range. However, due to the relatively fast and short heating cycle, no melting occurs. As shown in Fig. 3(a), no melting peak upon heating (Steps 6 and 10 with previous cooling rates of 10 K/s and 10^5 K/s, respectively) was observed in the measurement curves. Particularly the second reheating, following on overcritical cooling, results in a near perfect straight, though little noisy, curve. However, reheating after undercritically slow cooling (the first reheating) clearly shows endothermic dissolution effect. Potential incipient melting would lead to a small volume fraction, causing a relatively weak melting signal, while the volume fraction of precipitates formed at cooling with 10 K/s is rather small too. Considering that transitions like precipitation and dissolution give a much smaller thermal effect compared to first-order transitions like melting, it can be clearly stated that no melting occurs during the short overheating. Subsequently, the sample was quenched at 10^5 K/s to T_{an} . Then the sample was solution annealed for the same time as before (Step 7). During the next step (Step 8), the sample was subjected to overcritical cooling to room temperature at the cooling rate of 10^5 K/s, which is much faster than the CCR of alloy AA7150. This means that the precipitation reactions were fully suppressed, which was confirmed by both DFSC and hardness

measurements. In addition, almost no precipitation can be found by scanning electron microscopy (SEM) at the cooling rate of 100 K/s (see microstructure characterisation in Ref. [4]). Later, Step 10 (Reheating Nr. 2) was conducted in the same manner as Step 6 and this measurement was used as a baseline curve.

This modified DRM method, as described above (Fig. 2 (a)), has been further improved by the addition of interrupted quenching. Interrupted quenching was conducted for the purpose of determining the start and end temperatures for the different precipitation reactions. This is illustrated in Fig. 2(b). As this new method is strongly correlated with the obtained results, further particulars are described in the subsequent Results and discussion section.

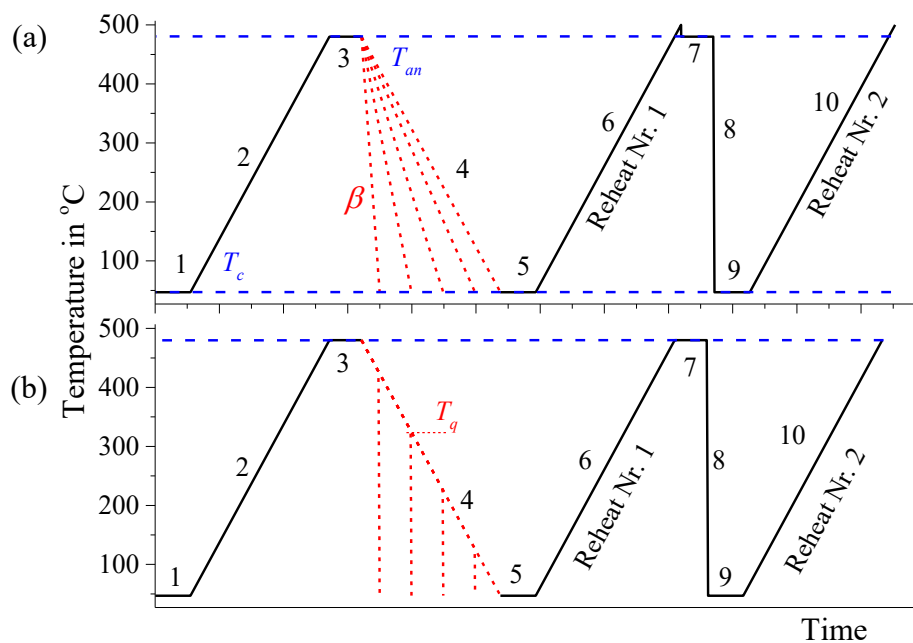


Fig. 2 (a) The temperature-time profiles for determining the CCR in DFSC measurements, consisting of two additional reheating steps after quenching. (b) The temperature-time profiles for interrupted quenching to determine the start and end temperatures for the different precipitation reactions.

Results and discussion

Based on the temperature-time profiles in Fig. 2(a), the heat flow curves from the two reheating steps (Steps 6 and 10) for different cooling rates in Step 4 were recorded (Fig. 3(a)) and subtracted from each other [22]. The subtracted measurement curves for the different cooling rates in Step 4 are shown in Fig. 3(b). Please be aware that this differential curves must not be compared with conventional DSC reheating curves as presented for instance in [25]. At slow DSC heating rates exothermic precipitation peaks occur partially superimposed with endothermic dissolution reactions, which complicates data evaluation [22]. Due to the heating rate of 1000 K/s in the DFSC experiments the endothermic dissolution peaks dominate after slow cooling. However, it can be seen, that there is an obvious signal, which decreases with increasing cooling rate. The main conclusions of this type of measurement is drawn based on the integrated enthalpy change and not on the peak position. The curve integration is based on the zero-level (often called baseline) plotted as dashed lines in Fig. 3(b). This results in the total enthalpy changes see Fig. 4. Nevertheless, it can be seen that the quench-induced precipitates are fully dissolved in this temperature range. Each subtracted curve reveals the total endothermic reaction (dissolution of precipitates formed in the cooling Step 4). Then the specific precipitation enthalpy at different cooling rates was calculated by integration. Note that the sample mass in the range of several hundred nano-grams was calculated from the sample volume, which was estimated based on the dimensions of the sample measured by optical microscopy. The edge length of the sample was estimated directly by optical micrographs, while the height was recorded according to the change of focuses on the sample surface and the sensor membrane.

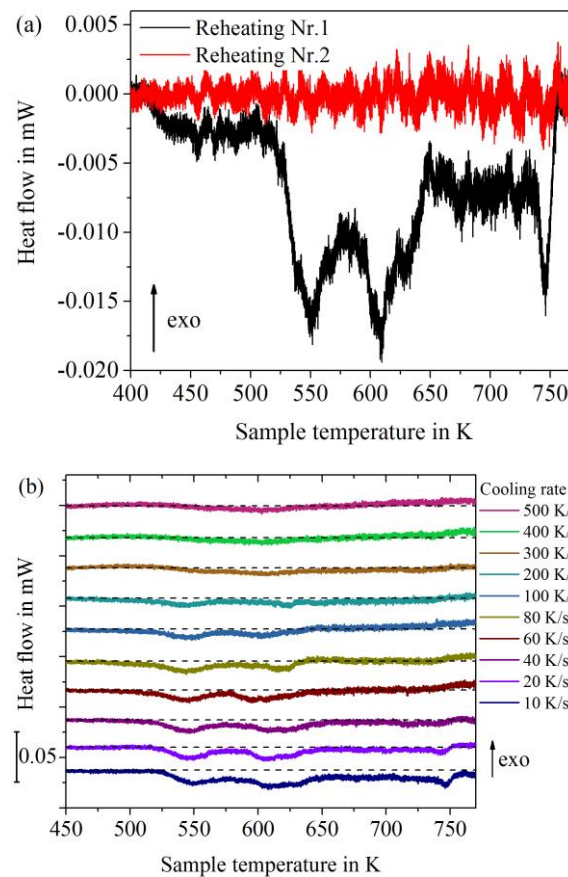


Fig. 3 (a) The curves measured in Steps 6 and 10 of Fig. 2(a) with previous cooling rates of 10 K/s and 10^5 K/s. (b) The subtracted measurement curves, i.e. the curves measured in Step 6 minus the curves measured in Step 10 for all the different cooling rates in Step 4. The baselines for integration are indicated by dashed lines.

The CCR of alloy AA7150 was determined to about 300 K/s by plotting the specific precipitation enthalpy, obtained from dissolution curves by integration, against cooling rate, as shown in Fig. 4(a). It should be mentioned here that the sample size is very small. Hence, in order to ensure that the DFSC measurements were representative of the bulk material, six different samples were measured by the same procedure and no obvious deviations were found. Typical representative curves for all the cooling rates including conventional DSC are shown in Fig. 4(b). The complete enthalpy curve shows a decreasing trend with increasing cooling rate as expected. Combining the DFSC data with conventional DSC data from Zhang

et al. [4], the CCR range at which the precipitation enthalpy reaches zero can again be determined as ~ 300 K/s (as indicated in Fig. 4). With respect to the former results in Ref. [4] it can be stated, that for the detection of the CCR the DFSC-DRM method is more sensitive compared to hardness tests, which indicate a critical cooling rate of about 100 K/s for AA7150. However, considering the logarithmic time scale this is still close to 300 K/s. Besides it should be noted that there could be a size effect on precipitation because of the smaller size of the DFSC samples compared with that of the conventional DSC samples. However, as shown in Fig. 4(b), the DFSC specific enthalpy data shows a good accordance with the data from conventional DSC and Vickers hardness tested on large samples (mm scale) after artificial ageing at 120 °C for 24 hours. It is therefore assumed that this method works well for determining the CCR. The lines shown in Fig. 4(b) are model predictions according to Ref. [12]. Except the slowest cooling rate, the model predicts the enthalpy changes nearly perfectly.

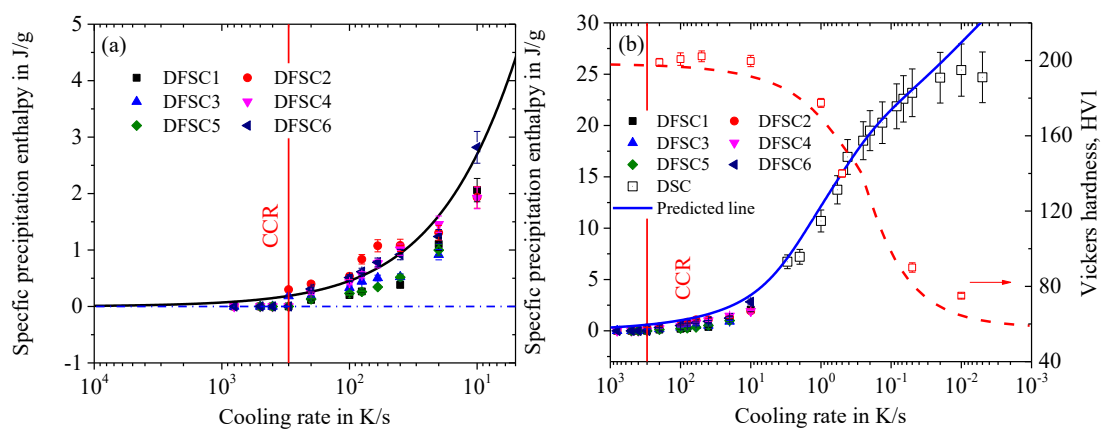


Fig. 4 (a) Specific precipitation enthalpy after solution annealing of alloy AA7150 as a function of cooling rate measured by DFSC. (b) Specific precipitation enthalpy after cooling from solution annealing and Vickers hardness after subsequent ageing (120 °C 24 hours) of alloy AA7150 as a function of cooling rate. The solid and dashed lines are model predictions from Ref. [12]. The DSC and hardness data tested on large samples were published by Zhang *et al.* [4]. Hardness has been tested on samples in the millimetre scale with the same cooling rates obtained in a quenching dilatometer.

Although now the critical cooling rate of AA7150 could be determined, the important information about which precipitation reaction happens at which temperature and at which time (or cooling rate) is still missing. Therefore, the DRM has been improved significantly by interrupted quenching. As illustrated in Fig. 2(b), interrupted quenching consists of cooling from T_{an} to the quenching temperature T_q at the cooling rate of interest and then performing subsequent interrupted cooling starting from T_q at the overcritical cooling rate of 10^5 K/s. From the differential reheating results, the precipitation enthalpy until T_q can be obtained. By varying T_q in steps of 10 K from 427 °C to 47 °C, the temperature dependence of precipitation at the studied cooling rate is now available too. Repeating this for different cooling rates allows the determination of the start and end temperatures for each precipitation reaction on cooling, as shown in Fig. 5.

The temperature-time profile for the interrupted quenching is shown in Fig. 2(b). Compared with the previous profile in Fig. 2(a), cooling rates ranging from 3 to 200 K/s and interrupted quenching at the cooling rate of 10^5 K/s were performed in Step 4. Overcritical cooling down to room temperature in the DFSC “freezes” the precipitation state at different temperatures from the previous continuous cooling (from T_{an} to T_q). In Steps 6 and 10, the sample was only heated to 480 °C instead of slightly overheating by 20 K. The reason for that is that the highest temperature should be carefully controlled in order to avoid unwanted modifications of the sample because more than 750 heating-cooling cycles were performed for one sample. Consequently, during the heating steps (Steps 6 and 10) in the DFSC experiments for determining the characteristic temperatures, high temperature precipitates may be dissolved only partly, especially for the lower cooling rates in Step 4 (i.e. a certain amount of enthalpy was always missing). The S -Al₂CuMg precipitates at the highest temperatures during relatively slow cooling [4]. Hence, during reheating, this phase will also dissolve at the highest temperatures. For this type of experiment, the slowest cooling rate was 3 K/s, which equals the critical cooling rate of this phase for this alloy according to

conventional DSC experiments [4]. Therefore, only a minor mass fraction of $S\text{-Al}_2\text{CuMg}$ may form. This fraction of $S\text{-Al}_2\text{CuMg}$ can be assumed to be dissolved during the solution annealing (480 °C, 5 min) at the latest. Accordingly, requirement (i) named above is fulfilled. However, although the total enthalpy change measured during the temperature dependent experiments (interrupted quenching) may not be used for further evaluation, the relative changes in the enthalpy change are still valid, allowing evaluation of the precipitation onset of a certain phase. Consequently, the method is still considered reliable for determining precipitation start and end temperatures.

The temperature dependence of the total precipitation enthalpy change, ΔH , at different cooling rates and interruption temperatures for one sample is shown in Fig. 5(a). It is shown that the total enthalpy change, i.e. the amount of precipitates, increases with decreasing cooling rate and decreasing interruption temperature. It means that the slower the cooling rate, the more the matrix supersaturation is reduced because the precipitated volume fraction has increased.

In Fig. 5(a) the precipitation reactions yield three steps seen in the curves for the cooling rates of 3 and 10 K/s. Further, the precipitation start and end temperatures for different cooling rates can be determined, as indicated by enlarged dots in Fig. 5(a). For example, for the cooling rate of 3 K/s, a series of slope changes on the total enthalpy change curve in Fig. 5(a) are observed at 390 °C, 360 °C, 280 °C and finally ending at 140 °C. This reveals that the precipitation process was changing, i.e. the precipitation reactions start and/or end at these temperatures, and three different precipitates were formed.

In order to verify the accuracy of the determination of characteristic temperatures from DFSC, the total enthalpy changes at different interruption temperatures at the cooling rate of 3 K/s measured by indirect DFSC and conventional in-situ DSC were compared, as shown in Fig. 5(b). It is found that the precipitation start and end temperatures from the new interrupted DRM (based on DFSC) is consistent with those from in-situ cooling DSC data at

the cooling rate of 3 K/s, as indicated by the dashed line in Fig. 5(b) and (c). This reveals that three different types of reactions occur at this cooling rate during the precipitation process.

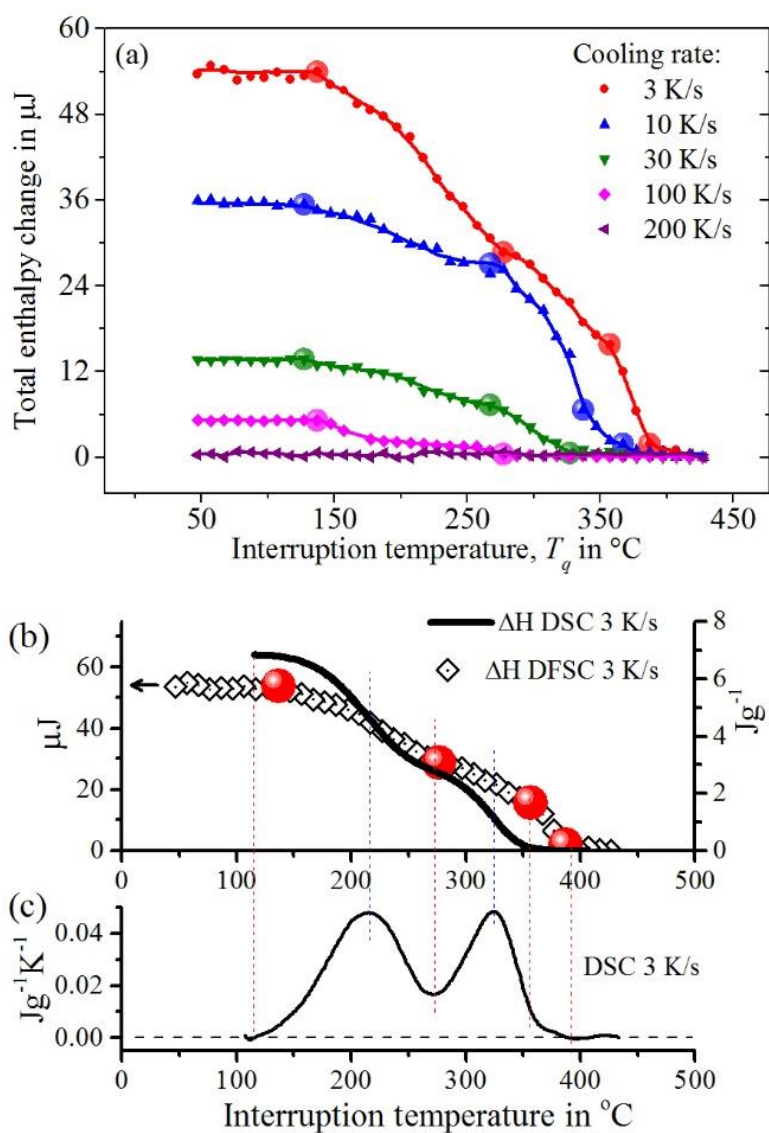


Fig. 5 (a) Total enthalpy change at different interruption temperatures and different cooling rates. The enlarged dots indicate the transition temperatures for the various precipitation reactions. (b) Total enthalpy change at the cooling rate of 3 K/s measured by DFSC and DSC. (c) DSC curve at the cooling rate of 3 K/s shown for comparison [4]. The vertical red dashed lines indicate the precipitation start and end temperatures.

Those reactions can be ascribed to the precipitation of phases determined in Refs. [4, 12, 24]. Fig. 6 summarises the types of precipitates that form in alloy AA7150 under different cooling conditions (e.g. Refs. [12, 24]). It can be shown that at high temperatures (~ 450 °C down to ~ 350 °C) and relatively slow cooling rates, the equilibrium phases S -Al₂CuMg (see Fig. 6(b)) and β -Mg₂Si can precipitate, depending on the presence of Cu, Mg and Si. Since some alloys like AA7150 contain very little Si, nearly no Mg₂Si will form. Nucleation of these equilibrium phases occurs on the most of coarse defects like primary precipitates (constituent particles). This hold for both, precipitation inside the grains and on grain boundaries [3]. At medium temperatures (~ 350 °C down to ~ 250 °C) and medium cooling rates, η -Mg(Al,Cu,Zn)₂ phase formation takes place (see Fig. 6(c)). The η -phase nucleates on dispersoids, predominantly on those which are incoherent due to recrystallization. At lower temperatures (~ 250 °C down to ~ 150 °C), the precipitation of thin Y -phase platelets rich in Zn and Cu occurs at relatively high cooling rates (see Fig. 6(d)) [12, 24]. The nucleation mechanism of the Y -phase is still under research, however, Y -phase plates have been found on voids [24] and nucleation on dislocations seems highly probable. The CCR of S -Al₂CuMg in AA7150 alloy was determined by conventional DSC to be about 3 K/s [4].

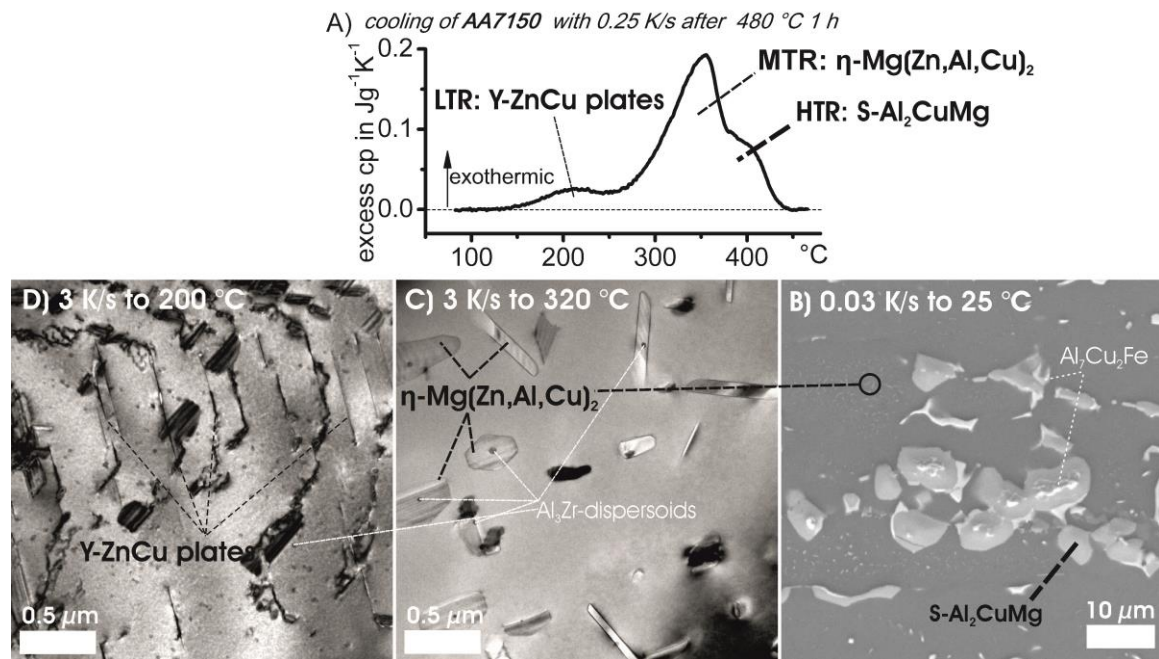


Fig. 6 Quench-induced precipitation in alloy AA7150: (a) DSC curve showing the three dominant precipitation reactions. The high temperature reaction (HTR) is dominated by the precipitation of S- Al_2CuMg , as shown in the backscattered electron image in (b). The medium temperature reaction (MTR) is dominated by the precipitation of $\eta\text{-Mg}(\text{Zn},\text{Cu},\text{Al})_2$, as shown in the bright-field transmission electron microscopy (TEM) image in (c). The low temperature reaction (LTR) is dominated by the precipitation of thin Y-phase platelets that are rich in Zn and Cu [24], as shown in the bright-field TEM image in (d). The samples corresponding to (c) and (d) were cooled relatively slowly to intermediate temperatures of 320 and 200 °C - just beyond the peak of the relevant precipitation reactions. This state was then ‘frozen’ for microstructure analysis by overcritical quenching (see Ref. [12] for further details). Figures adapted from Ref. [12].

Coming back to the discussion of the enthalpy curves in Fig. 5, it can therefore be concluded, that during cooling with 3 K/s S- Al_2CuMg , $\eta\text{-Mg}(\text{Zn},\text{Al},\text{Cu})_2$ and Y-phase platelets form with decreasing temperature [4, 12, 24]. Compared to 3 K/s the precipitation process during cooling with 30 K/s is different in that only medium- and low-temperature reactions, assigned to $\eta\text{-Mg}(\text{Zn},\text{Al},\text{Cu})_2$ and Y-phase platelets, occur. For the cooling rate of

100 K/s only the low-temperature reaction remains. For the cooling rate of 200 K/s, there is almost no precipitation detectable any more, which is consistent with the CCR of close to 300 K/s for alloy AA7150 as determined by the DRM (bearing in mind that the sensitivity of this interrupted quenching method is not expected to be as good as that of the original DRM).

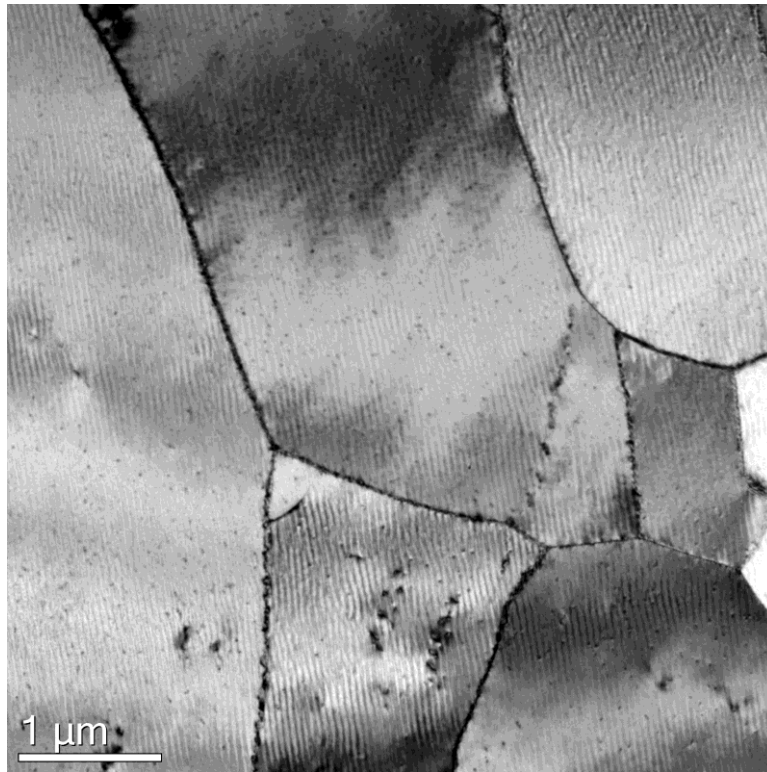


Fig. 7 TEM bright field image of an AA7150 sample cooled at 100 K/s. Quench induced precipitates can hardly be detected. Some spherical Al₃Zr dispersoids are visible.

The Vickers hardness development, as shown in Fig. 4(b), is in good agreement with tensile testing results published in Ref. [24]. The CCR found for AA7150 also is in good agreement with the CCR of Al alloy AA7049A, which was reported to be ~300 K/s [22]. To verify the CCR obtained by DFSC, samples cooled in a quenching dilatometer (Baehr 805 A/D) at 100 K/s were analysed by TEM (see Fig. 7). It is hard to find any quench induced precipitates in this cooling rate condition. The spherical particles are Al₃Zr dispersoids [26]. Although a wide area of the sample was checked by TEM, no obvious quench-induced phases

could be detected. It might be that there is a small volume fraction still present on grain- and/or sub-grain boundaries. Although there have been some indications in the literature of possible cluster formation at relatively low temperatures [12, 27, 28], such clusters were not detected in the current work. Nevertheless, in comparison to Fig. 6, the TEM results in Fig. 7 support the DFSC finding that the CCR of this alloy probably is close to 300 K/s.

Finally, the complete CCP diagram can be constructed, as shown in Fig. 8. The precipitation start and end temperatures were taken from the total enthalpy change curves (Fig. 5(a)) and plotted in a temperature-time diagram. The DSC data at different cooling rates ranging from very slow cooling (~ 0.005 K/s) to 3 K/s measured by several conventional DSC devices in Ref. [4] are also included. Therefore, the complete CCP diagram of alloy AA7150 is shown in Fig. 8 for the very first time. It provides information regarding the occurrence of precipitation reactions during cooling from solution annealing as a function of the cooling rate and temperature. Start and end temperatures of individual precipitation processes under the various specific cooling rates are indicated for the corresponding cooling curves and connected by dashed lines, respectively. The CCR is also marked. It must be mentioned that the CCP diagram is only valid for the investigated chemical composition, initial microstructure and solution annealing conditions. According to Fig. 8, quench-induced reactions take place mainly over an intermediate temperature range of 450-140 °C. It is also found that the individual critical cooling rates for the three different precipitation reactions are as follows: S -Al₂CuMg ~ 10 K/s, η -Mg(Zn,Al,Cu)₂ ~ 100 K/s and Y -phase platelets ~ 300 K/s, respectively (as listed in Table II).

This high CCR of 7150 and other highly concentrated (7000 series) wrought aluminium alloys results mainly from two reasons. 1) Their high content of age hardening alloying elements (Zn, Mg, Cu) together with a sufficient solution annealing result in a high supersaturation, being a strong driving force for nucleation of precipitates during quenching. 2) Their high content of dispersoid forming elements (Mn, Zr) results in many intrinsic nucleation sites, also promoting precipitation during quenching.

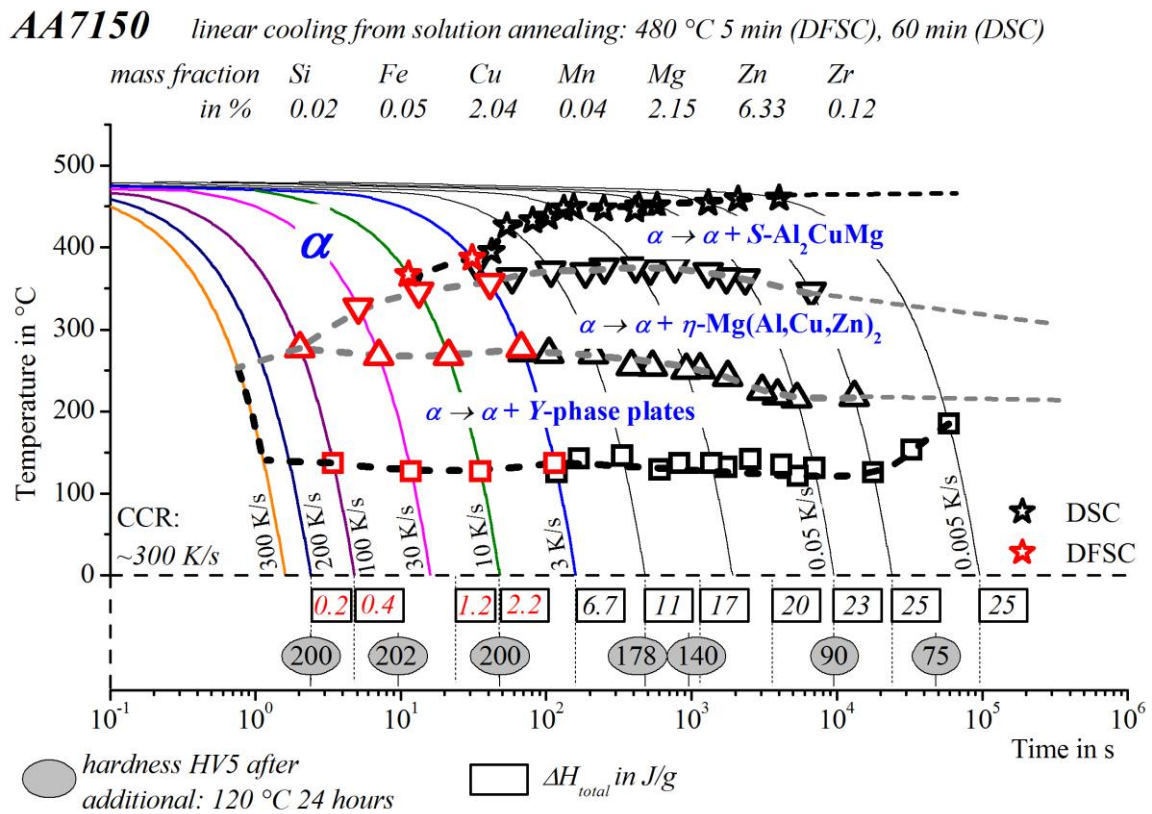


Fig. 8 Complete continuous cooling precipitation (CCP) diagram for alloy AA7150. The solid lines correspond to linear cooling in the range from 0.005 K/s to 300 K/s. The dashed lines and symbols indicate precipitation start and end temperatures. The DSC and hardness HV5 data are reproduced from Zhang et al. [4].

Table II Temperature ranges and CCRs for the three different precipitation reactions

Precipitates	S-Al ₂ CuMg,	η -Mg(Zn,Al,Cu) ₂	Y-phase platelets
Temperature range	~450 °C - ~350 °C	~350 °C - ~250 °C	~250 °C - ~140 °C
CCR	~10 K/s	~100 K/s	~300 K/s

Conclusions

In this study, we have developed a new interrupted quenching and differential reheating method by using differential fast scanning calorimetry (DFSC) to describe the influence of the cooling rate on the precipitation behaviour of high strength aluminium alloys during cooling from solution annealing. The critical cooling rate for alloy AA7150, which is the minimum cooling rate at which no precipitation heat is detectable, was determined to be close to 300 K/s. Furthermore, the interrupted quenching and differential reheating method (iqDRM) enabled determination of precipitation start and end temperatures during under-critical quenching in the cooling rate range of 3-800 K/s, which has been inaccessible before. Even higher cooling rates may be possible in future. By means of this novel method, the complete continuous cooling precipitation diagram for aluminium alloy AA7150 has been established. Based on the CCP diagram, quenching parameters in manufacturing processes can be selected properly, to decrease residual stresses and distortion while also inhibiting the decomposition of the solid solution. Further, CCP diagrams are necessary for accurate heat treatment simulation. Moreover, the method can potentially be transferred to similar precipitate-forming metallic systems or related solid-state phase transformation systems also beyond the particular system analysed in the present study.

References

- [1]. B. Milkereit, O. Kessler, and C. Schick, *Recording of continuous cooling precipitation diagrams of aluminium alloys*. *Thermochim. Acta*, 2009. **492**(1-2): 73-78.
- [2]. P. Schumacher, S. Pogatscher, M.J. Starink, C. Schick, V. Mohles, and B. Milkereit, *Quench-induced precipitates in Al–Si alloys: Calorimetric determination of solute content and characterisation of microstructure*. *Thermochim. Acta*, 2015. **602**: 63-73.
- [3]. B. Milkereit, N. Wanderka, C. Schick, and O. Kessler, *Continuous cooling precipitation diagrams of Al–Mg–Si alloys*. *Materials Science and Engineering: A*, 2012. **550**: 87-96.
- [4]. Y. Zhang, B. Milkereit, O. Kessler, C. Schick, and P.A. Rometsch, *Development of continuous cooling precipitation diagrams for aluminium alloys AA7150 and AA7020*. *J. Alloys Compd.*, 2014. **584**(0): 581-589.

- [5]. P. Archambault and D. Godard, *High temperature precipitation kinetics and ttt curve of a 7xxx alloy by in-situ electrical resistivity measurements and differential calorimetry*. *Scripta Mater.*, 2000. **42**(7): 675-680.
- [6]. J.L. Cavazos and R. Colás, *Precipitation in a heat-treatable aluminum alloy cooled at different rates*. *Mater. Charact.*, 2001. **47**(3-4): 175-179.
- [7]. J.L. Cavazos and R. Colás, *Quench sensitivity of a heat treatable aluminum alloy*. *Mater. Sci. Eng. A*, 2003. **363**(1-2): 171-178.
- [8]. S.D. Liu, X.M. Zhang, M.A. Chen, and J.H. You, *Influence of aging on quench sensitivity effect of 7055 aluminum alloy*. *Mater. Charact.*, 2008. **59**(1): 53-60.
- [9]. H.Y. Li, J.J. Liu, W.C. Yu, and D.W. Li, *Development of non-linear continuous cooling precipitation diagram for Al-Zn-Mg-Cu alloy*. *Mater. Sci. Technol.*, 2015. **31**(12): 1443-1451.
- [10]. N. Chobaut, D. Carron, and J.M. Drezet, *Characterisation of precipitation upon cooling of an AA2618 Al-Cu-Mg alloy*. *J. Alloys Compd.*, 2016. **654**: 56-62.
- [11]. D. Godard, P. Archambault, E. Aeby-Gautier, and G. Lapasset, *Precipitation sequences during quenching of the AA 7010 alloy*. *Acta Mater.*, 2002. **50**(9): 2319-2329.
- [12]. M.J. Starink, B. Milkereit, Y. Zhang, and P.A. Rometsch, *Predicting the quench sensitivity of Al-Zn-Mg-Cu alloys: A model for linear cooling and strengthening*. *Mater. Des.*, 2015. **88**: 958-971.
- [13]. T.F.J. Pijpers, V.B.F. Mathot, B. Goderis, R.L. Scherrenberg, and E.W. van der Vegte, *High-speed calorimetry for the study of the kinetics of (de)vitrification, crystallization, and melting of macromolecules*. *Macromolecules*, 2002. **35**(9): 3601-3613.
- [14]. G. Vanden Poel and V.B.F. Mathot, *High-speed/high performance differential scanning calorimetry (HPer DSC): Temperature calibration in the heating and cooling mode and minimization of thermal lag*. *Thermochim. Acta*, 2006. **446**(1-2): 41-54.
- [15]. J.E. Hatch and A. Association, *Aluminum: properties and physical metallurgy*. 1984: ASM International.
- [16]. I. Polmear and D.S. John, *Light alloys: from traditional alloys to nanocrystals*. 2005: Butterworth-Heinemann.
- [17]. B.C. Shang, Z.M. Yin, G. Wang, B. Liu, and Z.Q. Huang, *Investigation of quench sensitivity and transformation kinetics during isothermal treatment in 6082 aluminum alloy*. *Mater. Des.*, 2011. **32**(7): 3818-3822.
- [18]. D. Zohrabyan, B. Milkereit, C. Schick, and O. Kessler, *Continuous cooling precipitation diagram of high alloyed Al-Zn-Mg-Cu 7049A alloy*. *T Nonferr Metal Soc*, 2014. **24**(7): 2018-2024.
- [19]. N. Chobaut, D. Carron, S. Arsène, P. Schloth, and J.M. Drezet, *Quench induced residual stress prediction in heat treatable 7xxx aluminium alloy thick plates using Gleeble interrupted quench tests*. *J. Mater. Process. Technol.*, 2015. **222**: 373-380.
- [20]. A.A. Minakov and C. Schick, *Ultrafast thermal processing and nanocalorimetry at heating and cooling rates up to 1 MK/s*. *Rev. Sci. Instrum.*, 2007. **78**(7): 073902.
- [21]. E. Zhuravlev and C. Schick, *Fast scanning power compensated differential scanning nano-calorimeter: 1. The device*. *Thermochim. Acta*, 2010. **505**(1-2): 1-13.
- [22]. D. Zohrabyan, B. Milkereit, O. Kessler, and C. Schick, *Precipitation enthalpy during cooling of aluminum alloys obtained from calorimetric reheating experiments*. *Thermochim. Acta*, 2012. **529**: 51-58.
- [23]. A.A. Minakov, S.A. Adamovsky, and C. Schick, *Non-adiabatic thin-film (chip) nanocalorimetry*. *Thermochim. Acta*, 2005. **432**(2): 177-185.
- [24]. Y. Zhang, M. Weyland, B. Milkereit, M. Reich, and P.A. Rometsch, *Precipitation of a new platelet phase during the quenching of an Al-Zn-Mg-Cu alloy*. *Scientific reports*, 2016. **6**: 23109.
- [25]. J. Osten, B. Milkereit, C. Schick, and O. Kessler, *Dissolution and precipitation behaviour during continuous heating of Al-Mg-Si alloys in a wide range of heating rates*. *Mater.*, 2015. **8**(5): 2830-2848.

- [26]. Y. Zhang, C. Bettles, and P. Rometsch, *Effect of recrystallisation on Al₃Zr dispersoid behaviour in thick plates of aluminium alloy AA7150*. *J. Mater. Sci.*, 2014. **49**(4): 1709-1715.
- [27]. P. Schloth, J.N. Wagner, J.L. Fife, A. Menzel, J.M. Drezet, and H. Van Swygenhoven, *Early precipitation during cooling of an Al-Zn-Mg-Cu alloy revealed by in situ small angle X-ray scattering*. *Appl. Phys. Lett.*, 2014. **105**(10): 101908.
- [28]. P. Schloth, *Precipitation in the high strength AA7449 aluminium alloy: implications on internal stresses on different length scales*. 2015, École Polytechnique Fédérale de Lausanne.

[BM10] Fröck H, Milkereit B, Wiechmann P, Springer A, Sander M, Kessler O, Reich M:

Influence of Solution-Annealing Parameters on the Continuous Cooling Precipitation of Aluminum Alloy 6082. Metals 8-265 (2018): 1–16

Benjamin's contributions: I participated in the design of the experiments, supervised the DSC work, participated in the results discussion and substantially contributed to writing the manuscript.

Article

Influence of Solution-Annealing Parameters on the Continuous Cooling Precipitation of Aluminum Alloy 6082

Hannes Fröck¹, Benjamin Milkereit^{1,2,*} , Philipp Wiechmann¹, Armin Springer³,
Manuela Sander⁴, Olaf Kessler^{1,2} and Michael Reich¹

¹ Chair of Materials Science, Faculty of Mechanical Engineering and Marine Technology, University of Rostock, Albert Einstein-Str. 2, 18059 Rostock, Germany; hannes.froeck@uni-rostock.de (H.F.); philipp.wiechmann@uni-rostock.de (P.W.); olaf.kessler@uni-rostock.de (O.K.); michael.reich@uni-rostock.de (M.R.)

² Competence Centre °CALOR, Department Life, Light & Matter, Faculty of Interdisciplinary Research, University of Rostock, Albert-Einstein-Str. 25, 18059 Rostock, Germany

³ Medical Biology and Electron Microscopy Centre, University Medical Center Rostock, Strepelstraße 14, 18057 Rostock, Germany; armin.springer@med.uni-rostock.de

⁴ Chair of Structural Mechanics, Faculty of Mechanical Engineering and Marine Technology, University of Rostock, Albert Einstein-Str. 2, 18059 Rostock, Germany; manuela.sander@uni-rostock.de

* Correspondence: benjamin.milkereit@uni-rostock.de; Tel.: +49-381-498-6887

Received: 26 February 2018; Accepted: 3 April 2018; Published: 13 April 2018



Abstract: We use a systematic approach to investigate the influence of the specific solution condition on quench-induced precipitation of coarse secondary phase particles during subsequent cooling for a wide range of cooling rates. Commercially produced plate material of aluminum alloy EN AW-6082 was investigated and the applied solution treatment conditions were chosen based on heating differential scanning calorimetry experiments of the initial T651 condition. The kinetics of the quench-induced precipitation were investigated by in situ cooling differential scanning calorimetry for a wide range of cooling rates. The nature of those quench-induced precipitates was analyzed by electron microscopy. The experimental data was evaluated with respect to the detrimental effect of incomplete dissolution on the age-hardening potential. We show that if the chosen solution temperature and soaking duration are too low or short, the solution treatment results in an incomplete dissolution of secondary phase particles. This involves precipitation during subsequent cooling to start concurrently with the onset of cooling, which increases the quench sensitivity. However, if the solution conditions allow the formation of a complete solid solution, precipitation will start after a certain degree of undercooling, thus keeping the upper critical cooling rate at the usual alloy-specific level.

Keywords: EN AW-6082; AlMgSi alloy; solution treatment; solution temperature; differential scanning calorimetry (DSC); scanning electron microscopy (SEM); continuous cooling precipitation; quench sensitivity; complete solution; incomplete dissolution

1. Introduction

The most important heat treatment which allows to increase the strength of several aluminum alloys is the age-hardening heat treatment [1]. Within this heat treatment, solution annealing, which is the generation of a solid solution, establishes the basis for the potential decomposition of solid solutions by quench-induced precipitation and/or supersaturation of the solid solution during subsequent cooling. A fully supersaturated solid solution is the precondition to obtain maximum strength after

the final process “aging” step [1–3]. If a full solution is obtained during the solution treatment, a complete supersaturation can be achieved by overcritical cooling. If cooling is done “to slow”, “quench-induced” precipitation will occur. Quench-induced precipitation reduces the age-hardening potential by lowering the amount of solutes after cooling (prior to aging). This phenomenon is commonly called quench sensitivity. The upper critical cooling rates (uCCR) required to completely suppress quench-induced precipitation, depend on several aspects, for instance, alloy composition. Thereby, higher concentrations of alloying elements cause higher uCCRs [4,5]. In practical applications, the cooling rates can be adapted by choosing a suitable cooling media [6].

For the solution treatment, lower temperatures and shorter soaking durations are preferable for economic reasons, such as the continuous annealing in sheet and plate production or quenching from extrusion heat. Another example of a very short “solution treatment” occurs in the heat-affected zone of welding processes [7] or in the production of tailored heat-treated pre-products [8–11]. These short-solution treatments, particularly if they are performed at relatively low temperatures, might end with an incomplete solution. However, incomplete dissolution of the secondary phase particles might lead to reduced time spent for nucleation of the quench-induced precipitation. Thereby incomplete dissolution has the potential to influence quench sensitivity. The solution treatment was kept constant in most quench sensitivity studies. Thus, to the best knowledge of the authors, no recent study exists that systematically varies the solution temperature and soaking duration for investigations of Al-alloy quench sensitivity.

The quench sensitivity, and thus the precipitation behavior during cooling from solution treatment and its kinetics, have been investigated to a great extent in recent years (e.g., in AlMgSi alloys [4,5,12–14]). Differential scanning calorimetry (DSC) has proven to be a very helpful method in these investigations, particularly if combined with micro- and nanostructure analyses [4,5,15].

The main objective of this work is to investigate the detrimental effect of incomplete dissolution during the solution treatment within the age-hardening heat treatment of Al alloys with respect to the kinetics of quench-induced precipitation. Therefore, the solution-annealing temperature, as well as the soaking duration, was systematically varied. The solution conditions were chosen based on DSC heating experiments of the initial T651 condition. The precipitation behavior during the cooling of the EN AW-6082 alloy was analyzed by DSC for a wide range of cooling rates. The DSC findings are discussed in comparison with hardness after artificial aging, previous studies, and the observed microstructures, which are analyzed by scanning electron microscopy (SEM) and transmission electron microscopy (TEM).

2. Materials and Methods

2.1. Investigated Aluminum Alloys

The samples were prepared from a 10-mm-thick plate of commercially supplied aluminum alloy, EN AW-6082, in the initial T651 delivery condition. Aluminum wrought alloy EN AW-6082 has been chosen as it is a very widely used age-hardening aluminum alloy. This condition comprises solution treatment, quenching, stress reduction by stretching a controlled amount (1.5–3 % of the plate), and final artificial aging. The chemical composition was analyzed by optical emission spectroscopy (OES). The mass fractions of alloying elements are shown in Table 1.

Table 1. Mass fractions of the alloying elements in the investigated EN AW-6082 alloy, in %.

EN AW-6082	Mass Fraction, in %							
	Si	Fe	Cu	Mn	Mg	Cr	Zn	Ti
OES	0.83	0.38	0.06	0.48	0.92	0.03	0.01	0.02
DIN EN 573-3	0.7–1.3	≤0.5	≤0.1	0.4–1.0	0.6–1.2	≤0.25	≤0.2	≤0.1

2.2. Differential Scanning Calorimetry (DSC)

Here, heating and cooling rates in the 0.01–5 K/s range were investigated using two different types of DSC devices. The slower scanning rates (up to 0.1 K/s) were performed in a CALVET-type heat-flux DSC (Setaram DSC 121, Caluire-et-Cuire, France), whereas the faster rates (0.1–5 K/s) were examined in power-compensated DSCs (PerkinElmer Pyris Diamond DSC, PerkinElmer DSC 8500, Waltham, MA, USA). The two DSC device types required different sample geometries. Cylindrical samples with a diameter of 6 mm, a length of 21.65 mm, and a mass of about 1600 mg were used for the measurements in the heat-flux DSC. The samples for the power-compensated DSCs also have a cylindrical shape, but with a diameter of 6.4 mm, a height of 1 mm, and a mass of about 80 mg. The samples were packed in pure aluminum crucibles and then placed in the micro-ovens of the calorimeter. The heating rate to reach the solution-annealing temperature is 0.1 K/s in the heat-flux DSC and 2 K/s in the power-compensated DSCs.

2.3. Data Processing of Raw Measured Heat Flow Curves

It is necessary to eliminate the device-specific curvature to obtain high-quality DSC raw data. This curvature can be determined by recording a baseline measurement. Pure aluminum references are placed in both micro-ovens (the two DSC sensors) for the baseline measurement, and the identical temperature program to the one performed during a sample measurement is performed. Pure aluminum (99.9995% purity) was used as the reference material for DSC. The device-specific curvature of the measured curves can change slightly, especially for the power-compensated calorimeters, within a few hours. The following scheme of first acquiring a sample measurement, followed by a baseline measurement, and then another sample measurement, was performed. The aim is to have a fresh baseline for each sample measurement. However, to keep experimental effort small, we use one baseline run for two sample measurements—one before and one directly after the baseline run. By subtracting the baseline from the sample measurement, the device-specific curvature can be removed from the raw data.

The heating experiments consisted of four sample measurements and two baselines in the heat-flux DSC, and eight single-sample measurements were recorded with four related baseline measurements in the power-compensated DSCs for each heating rate. The cooling experiments for each cooling rate in the heat-flux DSC consisted of two–four sample measurements with one or two associated baseline measurements in the heat-flux DSC, and six sample measurements with three related baseline measurements in the power-compensated DSCs.

Comparison of the measurements with different heating or cooling rates (β) and different sample masses (m_S) requires the normalization of the measured heat flow to the value of excess specific heat capacity ($C_{p_{excess}}$) according to Equation (1) [16], where \dot{Q}_S and \dot{Q}_{Bl} are the sample and baseline heat flows, respectively, and β is the scan (heating or cooling) rate.

$$C_{p_{excess}} = \frac{\dot{Q}_S - \dot{Q}_{Bl}}{m_S \cdot \beta} \text{ (in J g}^{-1} \text{ K}^{-1}\text{)}, \quad (1)$$

Figure 1 shows the evaluation of the DSC curves for a heating curve produced from a heating rate of 0.5 K/s that was recorded with a power-compensated DSC. Figure 1A shows the recorded raw data. The device-specific curvature is eliminated by subtracting the baseline measurement from the sample measurement, as shown in Figure 1B. Figure 1C shows the data normalized by scanning rate and sample mass, which still contains overshoot artefacts [15] that have to be excluded from further evaluations. Figure 1D shows two resulting heating curves of the EN AW-6082 alloy from the initial state T651, with a heating rate of 0.5 K/s depending on temperature. As shown in Figure 1D, the dissolution of precipitates is not complete even at high temperatures up to 580 °C. This can be seen by the fact, that the DSC signal is not dropping back to zero at high temperatures. Thus, a zero-level correction by subtraction of a polynomial, as suggested in Osten et al. [11] and Milkereit et al. [15,17], was not applicable. Experiment specific curve fluctuations (e.g., caused by slight position differences of

the sensor-lid or sample [17]) are definitely minimized by averaging the curves measured for a single set of parameters. This data treatment was recently introduced by our group, and discussed in detail in Kemsies et al. [18]. As the reproducibility of the DSC measurements was found to be high, with small fluctuations, as shown in Figure 1D, we do not plot the curve fluctuation ranges here to maximize the readability of the plots, which also allows for the easy comparison of multiple DSC curves.

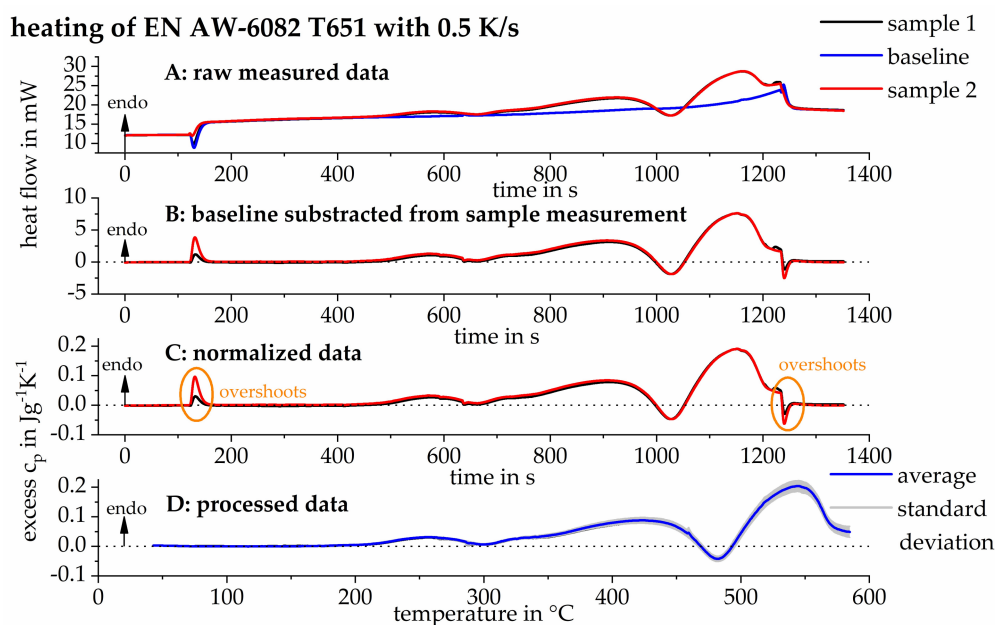


Figure 1. Evaluation procedure of the heating experiments. (A) Raw data measurements; (B) subtraction of baseline measurements from the sample measurements; (C) normalization of the data; (D) processed data.

A dotted straight line is additionally plotted on all the DSC heating and cooling curves, thus indicating the related zero level. A deviation of the measurement curve from this zero level signifies either an endothermic dissolution reaction or an exothermic precipitation reaction. Both the heating and cooling curves are shown here. In terms of the specific heat capacity, the endothermic area is shown upwards in the heating experiments [15,19], whereas the exothermic area is shown upwards in the cooling experiments [5]. Any figures presented in the results and discussion section below that consist of DSC curves from different scanning rates are arranged and shifted in order of the scanning rate used, starting with the lowest rate on top.

2.4. Microscopy

The samples for the microstructure investigations were heat-treated in a DSC, as well as in a quenching dilatometer (Bähr 805 A/D), based on the DSC results presented below. After thermal preparation, the samples for SEM analysis were cold-embedded in epoxy resin and then mechanically ground and polished with water-free lubricants. The final polishing was done with 0.05 μm oxide polishing suspension. The polished samples were rinsed after polishing and were analyzed in the polished condition.

The SEM samples were analyzed by a field emission SEM (MERLIN®VP Compact, Co. Zeiss, Oberkochen, Germany), equipped with an energy-dispersive X-ray (EDX) detector (XFlash 6/30) and analysis software (Quantax400, Co. Bruker, Berlin, Germany). Representative areas of the samples were analyzed and mapped to determine the elemental distribution on basis of the EDX-spectra data by the QUANTAX ESPRIT Microanalysis software (version 2.0).

The embedded and polished samples were mounted on the SEM carrier with adhesive conductive carbon and aluminum tape (Co. PLANO, Wetzlar, Germany). SEM-secondary electron (SEM-SE)

images were obtained using high efficiency Everhart-Thornley-type HE-SE detector at 5 kV acceleration voltage. The acceleration voltage for the EDX analysis was varied between 5 and 15 kV.

Samples for transmission electron microscopy (TEM) were prepared by mechanical grinding, polishing up to a thickness of 100–150 μm , and further treatment by twin jet electro-polishing in methanol and nitric acid (2:1 ratio). The electrolytic thinning occurs at a temperature of about $-20\text{ }^{\circ}\text{C}$, with a voltage of 12 V. TEM analysis was done by a Zeiss LIBRA 120 (Oberkochen, Germany), equipped with a LaB_6 cathode and an in-column omega spectrometer. Representative areas of the samples were analyzed with 120 kV accelerating voltage and digital images were acquired using a bottom-mount 2×2 k slow scan digital camera system (Proscan, Co. TRS, Moorenweis, Germany). Image processing was done with the iTEM software (Olympus Soft Imaging Solutions GmbH, Münster, Germany).

2.5. Hardness Tests

The hardness was examined for different solution-annealing conditions and cooling rates to correlate the results of the thermal analysis with a characteristic mechanical value, after a subsequent artificial aging at $180\text{ }^{\circ}\text{C}$ for 4 h. Hardness tests were chosen as the hardness can be tested directly on the DSC samples. The heat treatments, with cooling up to 5 K/s , were carried out in the DSC. However, faster cooling rates of 10 to 300 K/s were also realized in the quenching dilatometer Bähr 805 A/D. The hardness (HV1) was determined with a micro-hardness tester, HMV-2, from Shimadzu, Japan. Six hardness indentations were recorded per parameter set. The results plot the average, hardness values. Additionally, the minimum and maximum values are given as error bars.

3. Results and Discussion

3.1. Continuous Heating of the T651 Initial Condition

The solution-annealing temperature was chosen as $540\text{ }^{\circ}\text{C}$ in several previous investigations of the quench sensitivity of AlMgSi alloys [4,5,12]. However, the DSC heating experiments on the particular alloy batch and the initial T651 condition used here (shown in Figure 2), even for slow heating at 0.01 K/s , indicate that dissolution of the secondary precipitates of interest is just completed at about $560\text{ }^{\circ}\text{C}$. Furthermore, Figure 2 shows that the temperature at which the dissolution of the secondary phases is completed strongly depends on the heating rate. An increase in the heating rate shifts this dissolution completion to higher temperatures. As derived from findings in Schumacher et al. [20], it can be expected that the specific solvus temperature will be reduced by up to a few tens of Kelvin at even lower heating rates or under isothermal solution-annealing conditions. One solution-annealing temperature was thus chosen as $560\text{ }^{\circ}\text{C}$, which, according to the heating experiments, should be above the equilibrium solvus temperature in any case. As mentioned above, $540\text{ }^{\circ}\text{C}$ is a typical solution-annealing temperature that has been used in previous works, and $550\text{ }^{\circ}\text{C}$ was chosen as the temperature in between these values. Two different solution-annealing soaking durations of 1 and 20 min were also examined. Since the slower CALVET-type DSC required at least 5 min to achieve thermal equilibration [13], a soaking duration of 1 min is only investigated in the faster DSCs ($0.3\text{--}5\text{ K/s}$). Therefore, a systematic investigation of the quench sensitivity or quench-induced precipitation behavior after different solution-annealing conditions was conducted, and the DSC experiments were performed with three significant parameters varied, as follows:

- Solution-annealing temperatures: 540, 550, and $560\text{ }^{\circ}\text{C}$;
- Solution-annealing soaking durations: 1 and 20 min;
- cooling rates: $0.01\text{--}5\text{ K/s}$.

This corresponds to 33 sets of parameters and more than 200 single DSC experiments.

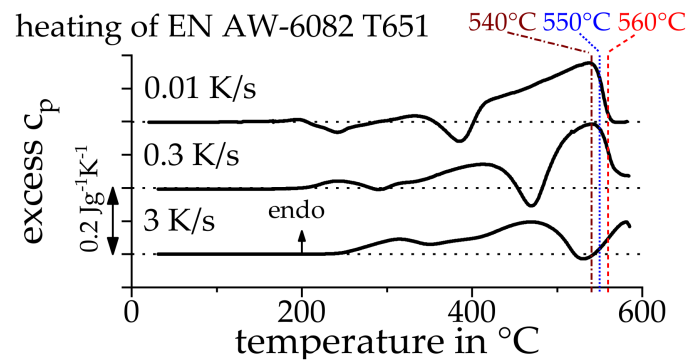


Figure 2. Differential scanning calorimetry (DSC) heating curves of EN AW-6082 initially T651 as a function of temperature. The solution temperatures chosen for later experiments are indicated.

3.2. Continuous Cooling Experiments, Starting from Different Solution Treatment Conditions

Figure 3 highlights one parameter set of the cooling experiments, plotted according to the 540, 550, and 560 °C solution-annealing temperatures. The DSC cooling curves of the two different soaking durations are plotted in two colors. The area between a DSC curve peak and its corresponding zero level is proportional to the precipitation enthalpy, and thus the volume fraction, of the precipitates grown during a certain reaction/peak [4].

Figure 3A shows that the DSC curves/reactions are insensitive to the soaking time at 540 °C. Furthermore, a broad high-temperature reactions (HTRs) peak dominates, even at high cooling rates. A similar pattern is observed if cooling started from 560 °C regarding the insensitivity to soaking time (Figure 3C). However, the shape of the cooling curves varies significantly when comparing soaking at these two temperatures. Two main exothermic precipitation reaction peaks are observed for the soaking at 560 °C. The low temperature reactions (LTRs) peak begins to dominate the precipitation behavior during faster cooling from 560 °C. The medium solution-annealing temperature at 550 °C highlights that the soaking duration significantly impacts the curvature of the observed DSC curves, as shown in Figure 3B. Here, the shorter soaking times (1 min) yield DSC curves that are similar to those at 540 °C, whereas the longer soaking times (20 min) yield DSC curves that are similar to those at 560 °C.

The same DSC data are rearranged in Figure 4 to highlight the role of the solution-annealing temperature. Two major arguments can be derived from these data: (1) only minor differences in the DSC curve curvatures are observed at the slower cooling rates (up to 0.1 K/s, resulting in cooling durations of 1.4 to 14 h) and 20 min of soaking. However, (2) for faster cooling rates of 0.3 to 5 K/s those differences are more significant while those cooling rates additionally are considered to be much more technologically relevant, covering cooling durations ranging from 30 s to a few minutes. Considerably different DSC curves are produced at these fast cooling rates, the two different soaking times, and the range of solution-annealing temperatures, which exhibit the largest differences for the medium cooling rates of 0.3 and 1 K/s.

The findings from Figures 3 and 4 thus suggest that there are two major types of DSC curvatures for a given cooling rate. The resultant DSC curvature obviously depends on the specific solution condition applied prior to cooling. Therefore, the DSC data are arranged into these two types of DSC curves, as shown in Figure 5. The DSC curves in Figure 5A are dominated by HTRs, while the DSC curves in Figure 5B are dominated by LTRs. This leads one to ask what the cause of these different DSC curves and their quench-induced precipitation behavior is. We thus postulate that the two different types of precipitation behavior depend on whether the cooling started from an incomplete solution (as seen in Figure 5A) or if a (largely, if not fully) complete solution precedes the cooling (as seen in Figure 5B).

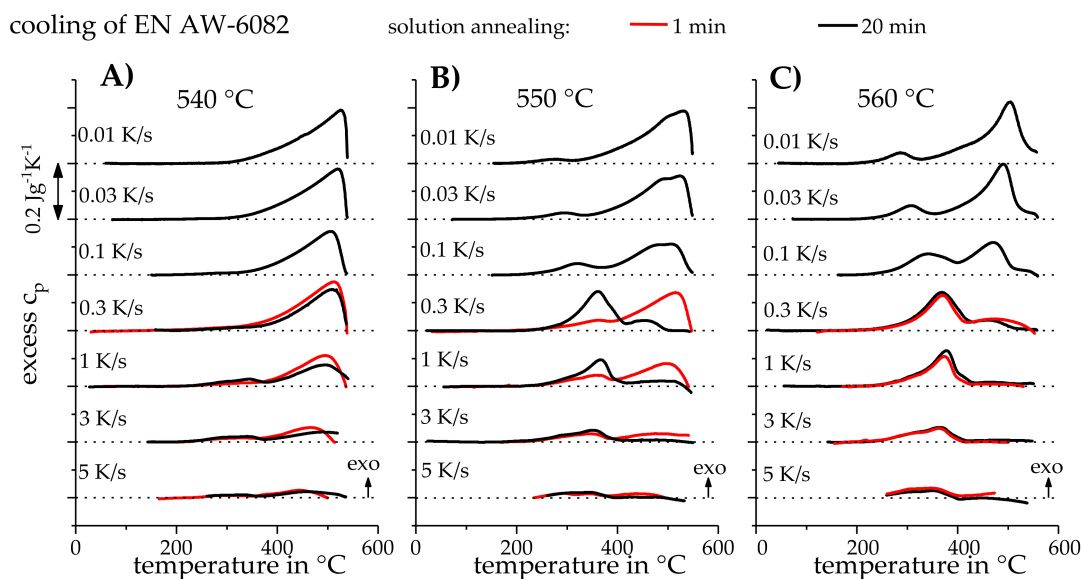


Figure 3. DSC cooling curves of EN AW-6082 (initially T651) with cooling rates from 0.01 up to 5 K/s after solution-annealing at (A) 540 °C, (B) 550 °C and (C) 560 °C for 1 min (red) and 20 min (black).

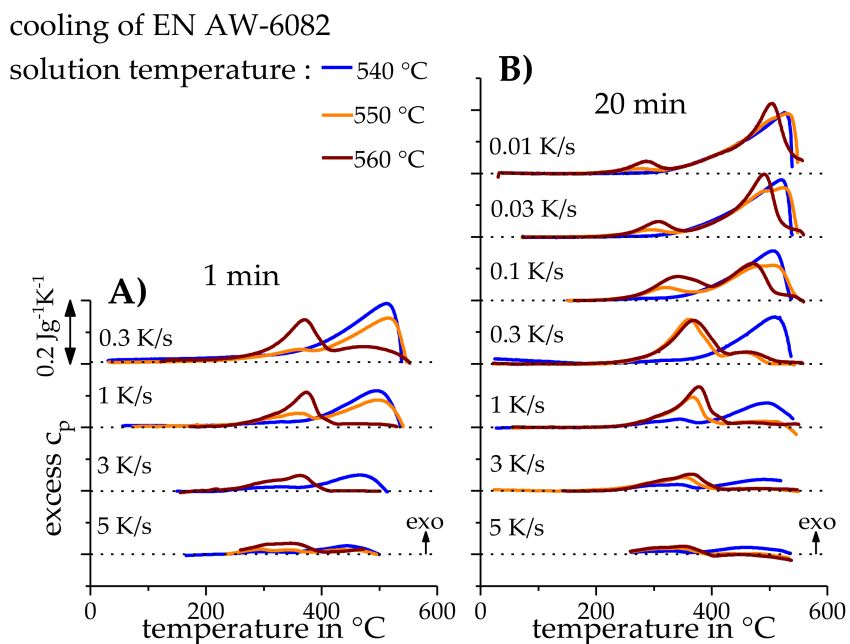


Figure 4. DSC cooling curves of EN AW-6082 (initially T651), with cooling rates ranging from 0.01 to 5 K/s and after solution-annealing at various conditions. (A) Soaking duration of 1 min and (B) 20 min. The three different applied temperatures are color-coded to highlight the degree of variability with soaking time and cooling rate.

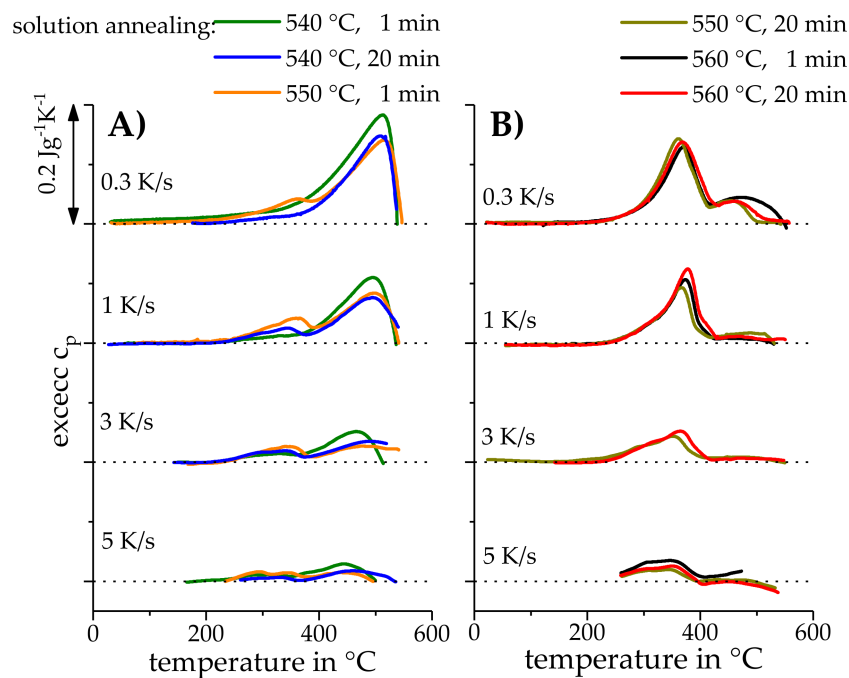


Figure 5. DSC cooling curves of EN AW-6082, with cooling rates from 0.3 to 5 K/s after solution-annealing, resulting in: (A) an incomplete solution and (B) a complete solution.

This postulation is derived from three arguments:

- i. According to Figure 2 (and the related discussion), the solvus temperature of the initial T651 condition of this particular batch of EN AW-6082 for slow heating is below 560 °C.
- ii. If cooling is starting from a more-or-less complete solution (e.g., 560 °C solution-annealing temperature and 20 min soaking time), the main precipitation begins after a certain degree of undercooling.
- iii. The quasi-binary phase diagram Al-Mg₂Si (Figure 6) indicates that the Mg₂Si equilibrium solvus temperature for this alloy is near or slightly above 540 °C.

Our reasoning for these three arguments is as follows:

- i.: The heating rate-specific solvus temperature can drop below 560 °C during very slow heating, as demonstrated in Figure 2. The cooling experiments in Figure 5 were conducted after relatively fast heating (2 K/s). Therefore, according to Figure 2, the dissolution remained incomplete at the end of the heating process. A complete solution can still be obtained with the switch to isothermal soaking, as seen in Figure 5B. Here 20 min of soaking at 550 and 560 °C results in precipitation beginning after a certain degree of undercooling, while a short soaking of 1 min at 560 °C still causes the direct onset of precipitation.
- ii.: Taking the cooling rate of 0.3 K/s as an example, cooling from 560 °C and 20 min of soaking causes the precipitation to start at about 500 °C, after a certain degree of undercooling. However, starting from a condition that we claim to be an incomplete solution (e.g., 540 °C solution-annealing temperature), the same cooling rate of 0.3 K/s causes the immediate onset of precipitation when the temperature drops below 540 °C, with precipitation thus starting 40 K higher than that in the complete solution. Two different types of precipitation onset (1: immediate precipitation onset with the onset of cooling; and 2: onset of precipitation after a certain degree of undercooling) were attributed to the observations from the quasi-binary Al-Mg₂Si phase diagram, which depended on whether the cooling starts from the α -Al solid-solution single-phase region or from the α -Al + β -Mg₂Si two-phase region [21].

→ iii.: The three applied solution temperatures are indicated in the quasi-binary phase diagram Al-Mg₂Si and shown in Figure 6, as well as the estimated maximum amount of Mg₂Si for the particular batch of EN AW-6082 that was used in the experiments. While the comparison of EN AW-6082 with this phase diagram is a simplification, the precipitation of the β-Mg₂Si phase from the α-Al solid solution is dominating the HTRs during cooling from the solution treatment of AlMgSi alloys [5], including two batches of EN AW-6082. It is thus inferred that the most likely phase to be considered in terms of complete solution is β-Mg₂Si. The equilibrium solvus of the estimated β-Mg₂Si mass fraction is close to 540 °C, which is additionally supported by the DSC experiments shown in Figure 7. The latter used soaking durations ranging from 1 to 120 min at 540 °C that preceded a cooling rate of 1 K/s. A complete solution was still not attained after two hours of soaking at 540 °C, with the Mg₂Si precipitation starting concurrently with the onset of cooling. Therefore, it is reasonable to assume that the alloy batch-specific equilibrium β-Mg₂Si solvus temperature is close to 540 °C (very likely a few Kelvin above 540 °C).

It can thus be concluded that a relatively short soaking at a high enough temperature (some 10 K above the alloy specific solvus) can result in the intended complete solution. The formation of a complete solution requires both an appropriate solution temperature and soaking duration to be chosen. As seen from the above results, a complete solution as the initial condition for subsequent cooling results in the initiation of precipitation temperatures that are some 10 Kelvin lower than the initial condition of an incomplete solution. This aspect can be quite important in an industrial/production context. For instance, the transportation of the solution-treated part from the furnace to the quenching media is unavoidably going to experience some cooling before quenching. Ensuring a complete solution during the technological application of the solution treatment can thus help to avoid quench-induced precipitation. This aspect might be of even more relevance, because the general quench sensitivity is also increased if the dissolution remains incomplete during the solution treatment (see the discussion on hardness below).

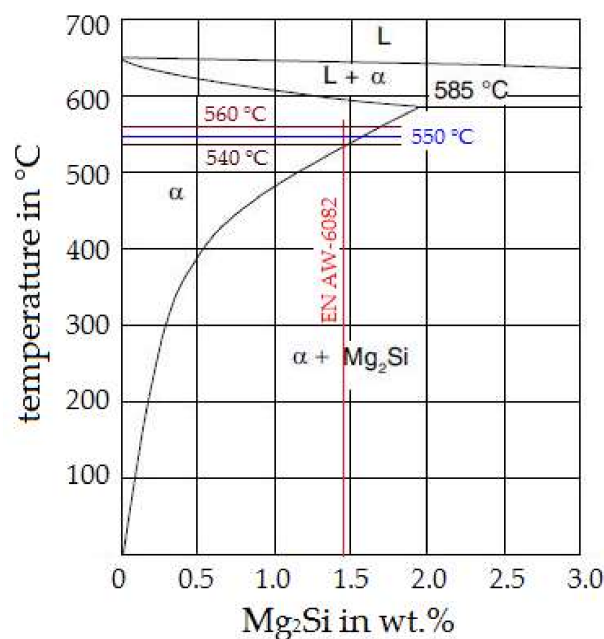


Figure 6. Section from the quasi-binary phase diagram Al-Mg₂Si (adopted from Polmear [1]). The theoretical maximum amount of β-Mg₂Si in this batch of EN AW-6082 (vertical red line), as well as the applied solution temperatures (horizontal lines), is highlighted.

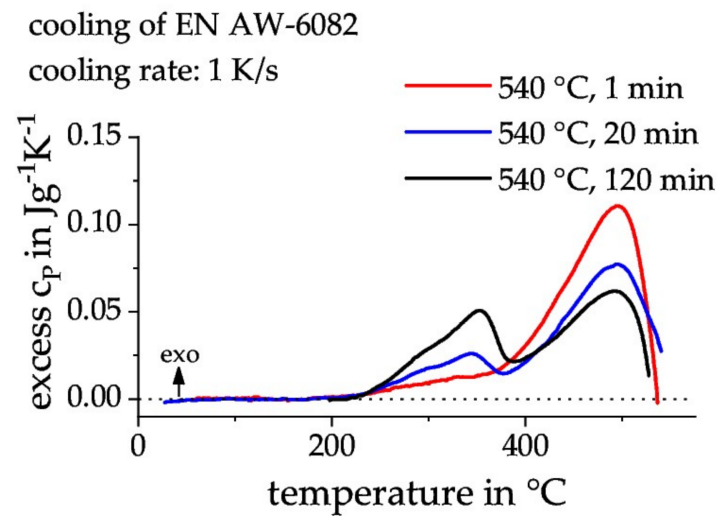


Figure 7. DSC cooling experiments on EN AW-6082 after solution treatment at 540 $^{\circ}C$, soaking times of 1, 20, and 120 min, and a cooling rate of 1 K/s.

3.3. Analysis of the Quench-Induced Microstructure

The schematic temperature-time profile applied for the heat treatment of samples used for the microstructure analysis is shown in Figure 8. The parameters were chosen based on the cooling DSC results. For clarity, the corresponding DSC curves are plotted next to the microstructure images in Figures 9A and 10A. Figures 9 and 10 show the DSC curves and representative SEM-SE images from 540 $^{\circ}C$ and 560 $^{\circ}C$, respectively, with 20 min of soaking and a cooling rate of 0.3 K/s. The cooling was continued at this low rate down room temperature in Figure 9B,D and Figure 10B,D. Alternatively, the low cooling rate of 0.3 K/s was applied until 425 $^{\circ}C$, and subsequently overcritically gas-quenched (~ 400 K/s) to room temperature (see Figure 8) in Figure 9C,E and Figure 10C,E.

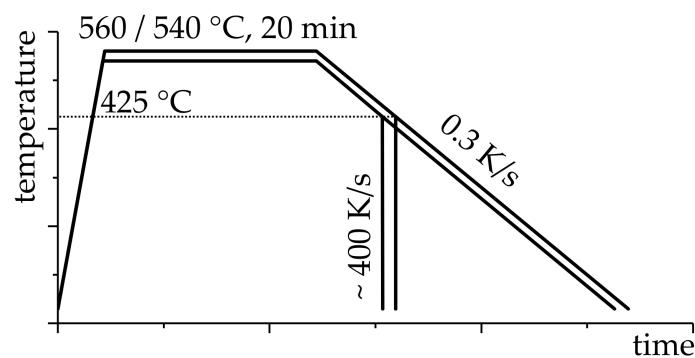


Figure 8. Schematic time-temperature profile of the heat treatments for the microstructure analysis.

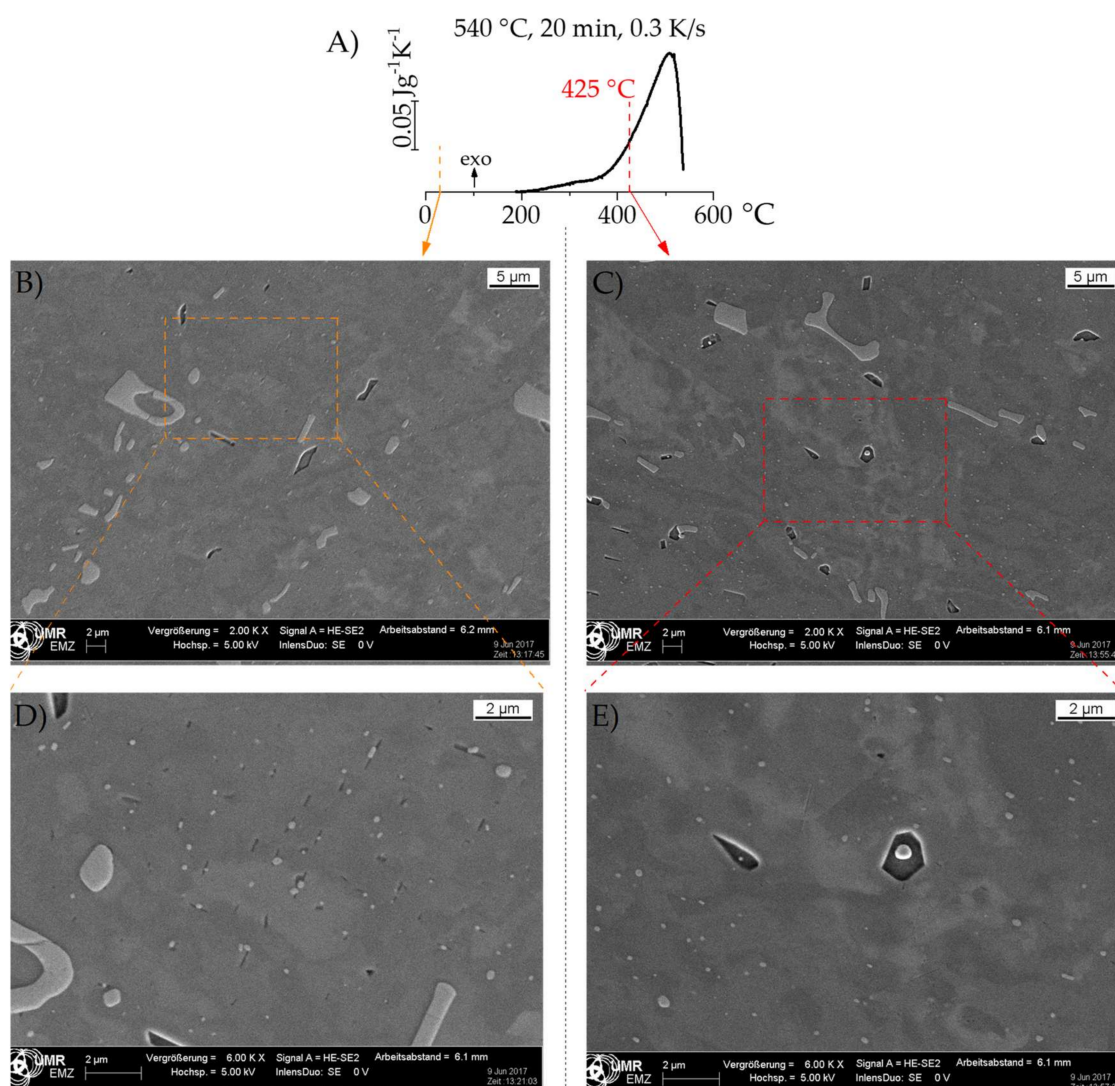


Figure 9. (A) DSC cooling curve after solution-annealing at 540 °C, a 20 min soaking time, and a cooling rate of 0.3 K/s, and (B–E) associated scanning electron microscopy (SEM) images at different magnifications.

Some similar microstructural components are observed in the SEM-SE images under both conditions. This is exemplified through the coarse primary, intermetallic, mostly irregularly shaped particles in a variety of dimensions in the μm range. These primary particles appear bright in the SEM-SE images. EDX revealed them to be enriched in Fe, Mn, and Si. Those primary particles most likely precipitated from the melt.

Coarse dark particles are also seen in Figure 9. EDX showed an enrichment of Mg and Si for these particles. Based on both our experience and the published literature, these are $\beta\text{-Mg}_2\text{Si}$ -phase particles [4,5]. Nucleation of Mg_2Si is reported to occur on primary Fe, Mn, and Si rich intermetallic particles. Such primary particles are also often found within the Mg_2Si particles (e.g., see Figure 9E). Figure 10 contains fewer and smaller Mg_2Si particles, corresponding to the weaker HTR. As seen from Figure 9C,E, as well as Figure 10C,E, Mg_2Si is already present when the HTRs are nearly finished, as detected by DSC. This is in perfect agreement with previous studies that report the HTRs in AlMgSi alloys were predominantly caused by the precipitation of $\beta\text{-Mg}_2\text{Si}$ -phase particles [5].

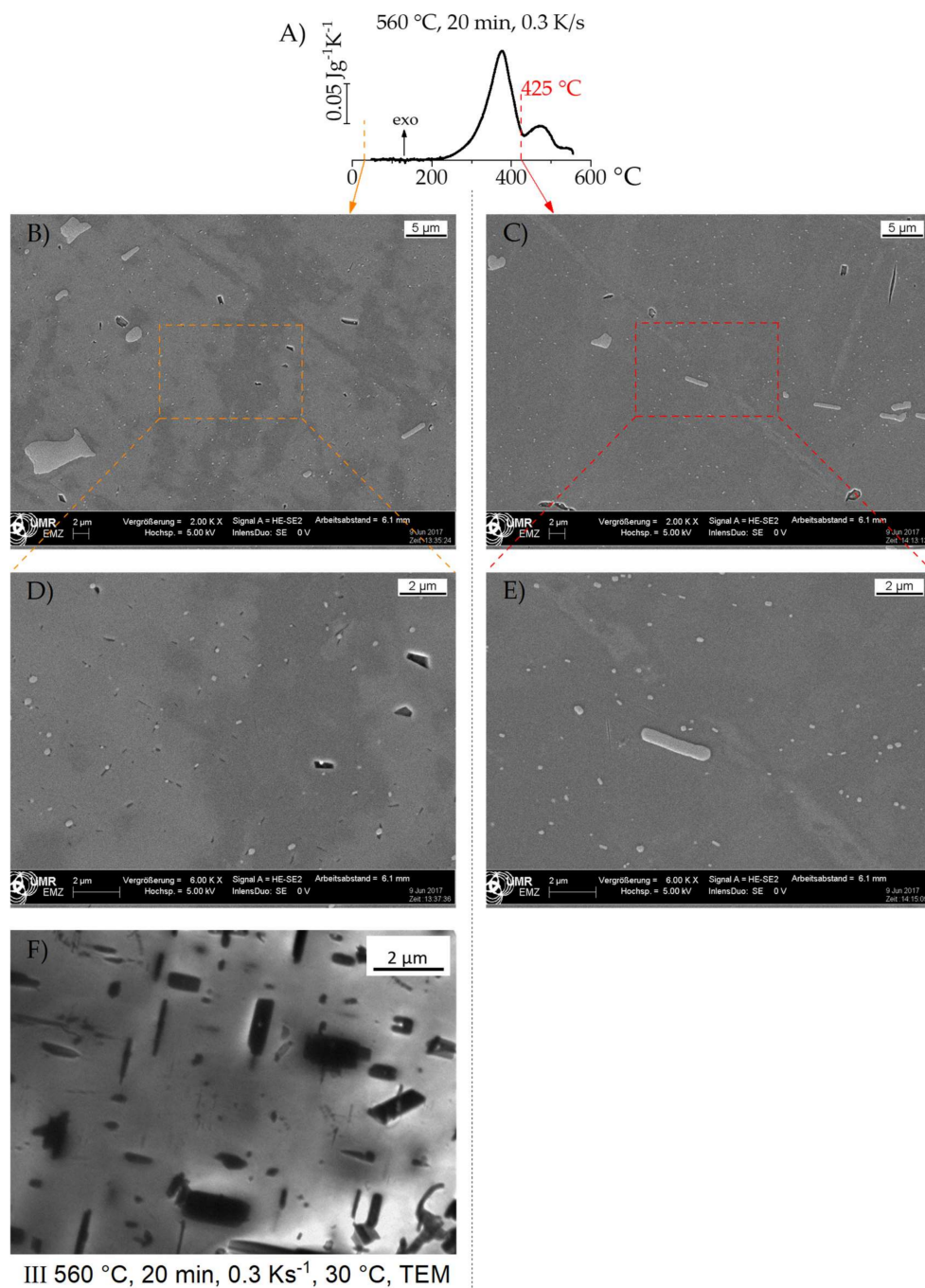


Figure 10. (A) DSC cooling curve after solution-annealing at 560°C , a 20 min soaking time, and a cooling rate of 0.3 K/s , and associated (B–E) SEM and (F) transmission electron microscopy (TEM) images at different magnifications.

These Mg_2Si particles are found almost unchanged if there is continuous cooling down to room temperature. Another population of smaller, dark, regularly shaped, elongated particles is also precipitated during the LTRs, as seen from the SEM-SE images (Figures 9D and 10D). Plate- or rod-shaped, elongated particles can even better be detected via TEM (see Figure 10F). Their sizes range from a few hundreds of nm to a few μm in length, and some tens to a few hundreds of nm in diameter. Previous studies suggest that these particles likely belong to the $\text{B}'\text{-Mg}_5\text{Si}_4\text{Al}_2$ phase [5]. Nucleation of the quench-induced B' -particles is reported to occur on dispersoids [5], and thus forms a much smaller

and finer distribution of nucleation sites compared to the nucleation sites of the HTRs precipitation of β -Mg₂Si.

The following inferences can be made with regard to the onset condition of cooling, which largely depend on whether the solution is a complete or incomplete solution. The HTRs dominate the quench-induced precipitation behavior, and thus the DSC curve, if the cooling starts from an incomplete solution. As discussed above, the HTRs are predominantly related to the precipitation of the β -Mg₂Si phase. Although it is difficult to statistically conclude this possibility from the two SEM images plotted here, a comparison of the microstructures after cooling from 540 °C (Figure 9C) and 560 °C (Figure 10C) shows that there is a higher number of even larger Mg₂Si particles if the cooling started with an incomplete solution (Figure 9C). This is also supported by a number of additionally recorded SEM images that are not shown here. Furthermore, the DSC peak areas, which are proportional to the volume fraction precipitated [2], suggest that the precipitated volume fraction of Mg₂Si is much higher if the same cooling rate is applied to an initially incomplete solution. However, if the cooling is starting from a complete solution (with respect to Mg₂Si), the quench-induced precipitation is dominated by the LTRs, which are related to the precipitation of B'-Mg₅Si₄Al₂. The latter considerations particularly hold if one specific (medium to fast) cooling rate is considered to start from the different initial conditions of an incomplete or complete solution. We interpret this to be related to the following: if the dissolution of the remaining Mg₂Si is incomplete, there is no need for new nucleation of that phase, and the existing Mg₂Si particles are immediately able to grow again with the onset of cooling. The Mg₂Si-precipitation out of a complete solution, though, requires a certain amount of time to initiate the precipitation by nucleation. Thus, dynamic suppression of the precipitation of this equilibrium phase is much easier, which substantially reduces the precipitated volume fraction at the specific cooling rate. In general, it can be stated, that quench-induced precipitates reduce the atomic fraction of alloying elements in solid solution which are available for final aging. This reduced amount of solutes is reducing the age hardening potential as the amount of strength increasing precipitates will be lowered.

3.4. Hardness Development after Cooling at Various Rates and Additional Artificial Aging

Incomplete dissolution accelerates the kinetics of quench-induced precipitation due to a reduced effort for nucleation, particularly for coarse high-temperature precipitates. The influence of an incomplete versus complete solution, with respect to the quench sensitivity of EN AW-6082, is also obvious from the hardness values after cooling and subsequent aging. Figure 11 compares the hardness after cooling from the 540 and 560 °C solution-annealing temperatures for 1 min and subsequent artificial aging as functions of cooling rate.

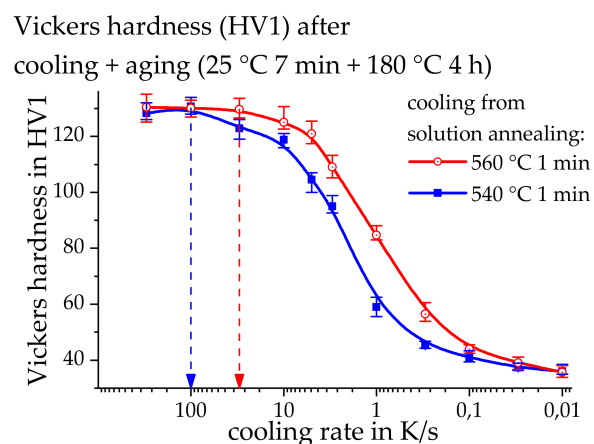


Figure 11. Hardness values (HV1) after cooling and artificial aging, as function of cooling rate, for the following solution-annealing conditions: 540 °C and 560 °C, both with a 1 min soaking time. The upper critical cooling rates (uCCRs) for the two temperatures are indicated by arrows.

These two cases show a sigmoidal increase in hardness values from slow to fast cooling. The upper critical cooling rate (uCCR) is defined as the slowest cooling rate at which precipitation is completely inhibited. The hardness after aging thus reaches a saturation level at this and faster cooling rates. The uCCR for the complete dissolution of EN AW-6082, with solution-annealing at 560 °C and 1 min of soaking, is found to be about 30 K/s, whereas the uCCR for incomplete dissolution is about 100 K/s, with solution-annealing at 540 °C and 1 min of soaking. The uCCR for EN AW-6082 may thus increase by a factor of three if the solution treatment is terminated leaving an incomplete dissolution.

A hardness of about 85 HV1 is obtained after a cooling rate of 1 K/s is applied from the solution-annealing temperature of 560 °C and 1 min of soaking (initially complete dissolution, with quench-induced precipitation dominated by B'), and aging. The same cooling rate, starting from 540 °C and 1 min of soaking (initially incomplete dissolution, with quench-induced precipitation dominated by β -Mg₂Si) leads to only about 60 HV1 after aging. This suggests that at medium cooling rates, incomplete dissolution may reduce the hardness by up to 30 % compared to complete dissolution as the onset condition. It is thus seen that, particularly for technologically relevant cooling, the danger of a substantial hardness reduction is present in the case of incomplete dissolution during solution treatment.

It still remains unclear as to why similar hardness values are achieved for both solution conditions at the highest cooling rates. The expectation is that the undissolved Mg₂Si should lead to a reduced saturation level for hardness after aging. It might be that the hardness testing is not sufficient to detect this difference, thus requiring tensile testing to potentially detect these differences in the future.

These results are also especially important for welding with rapid heating and almost no soaking in the heat-affected zones (HAZ), particularly since the HAZ microstructures of aluminum alloys cannot be predicted with conventional continuous cooling precipitation (CCP) diagrams. For steels special welding-time-temperature-transformation diagrams are available [22]. However, such special welding CCP diagrams do not exist for aluminum alloys and thus need to be developed in future.

4. Conclusions

This work, for the first time, quantifies the difference between complete and incomplete dissolution with respect to quench sensitivity in terms of critical cooling rate and potential loss in aging/hardening potential. The above considerations on the AlMgSi wrought alloy EN AW-6082 have led to the following conclusions:

1. The precipitation behavior during cooling after solution-annealing is significantly dependent upon whether complete or incomplete dissolution occurred during the solution treatment, particularly for medium to faster cooling rates (which are technologically relevant).
2. The undissolved Mg₂Si particles can instantly begin to grow within the solution at the onset of cooling when there is incomplete dissolution. Thus, undissolved particles allow for the immediate start of quench-induced precipitation.
3. Quench-induced precipitation requires nucleation when there is complete dissolution. The required nucleation, in combination with dynamic suppression due to cooling, causes a certain degree of undercooling before the onset of precipitation.
4. Incomplete dissolution increases the quench sensitivity. The upper critical cooling rate may increase by a factor of three. At medium cooling rates, the hardness is reduced by up to 30 %.
5. Complete dissolution is highly recommended to ensure optimal alloy performance that exploits its full age-hardening potential. This can be achieved by using an appropriately high-solution temperature while maintaining a short soaking duration (a few minutes).

Acknowledgments: The authors acknowledge funding of this work from the German Research Foundation (DFG), within the scope of the research project "Materials Based Simulation of Limit Load Behaviour for Welded Aluminium Structures" (DFG RE3808/2-1 and DFG SA 960/7-1).

Author Contributions: The DSC measurements, hardness tests and evaluations were performed by Philipp Wiechmann and Hannes Fröck. The SEM and TEM analyses were performed by Armin Springer. All authors contributed to the discussion of the results. The manuscript was written by Hannes Fröck and Benjamin Milkereit. All authors have revised the text and given their approval for the final version of the manuscript.

Conflicts of Interest: The authors declare no conflict of interest.

References

1. Polmear, I.J. *Light Alloys. From Traditional Alloys to Nanocrystals*, 4th ed.; Elsevier Butterworth-Heinemann: Amsterdam, The Netherlands, 2006.
2. Milkereit, B.; Kessler, O.; Schick, C. Recording of continuous cooling precipitation diagrams of aluminium alloys. *Thermochim. Acta* **2009**, *492*, 73–78. [[CrossRef](#)]
3. Kammer, C. *Aluminium Taschenbuch Band 1*; Aluminium-Verlag, Aluminium-Zentrale Düsseldorf: Düsseldorf, Germany, 1998.
4. Milkereit, B.; Wanderka, N.; Schick, C.; Kessler, O. Continuous cooling precipitation diagrams of Al-Mg-Si alloys. *Mater. Sci. Eng. A* **2012**, *550*, 87–96. [[CrossRef](#)]
5. Milkereit, B.; Starink, M.J. Quench sensitivity of Al-Mg-Si alloys: A model for linear cooling and strengthening. *Mater. Des.* **2015**, *76*, 117–129. [[CrossRef](#)]
6. Ostermann, F. *Anwendungstechnologie Aluminium*, 3rd ed.; Springer Berlin Heidelberg: Berlin/Heidelberg, Germany, 2014.
7. Sarmast, A.; Serajzadeh, S.; Kokabi, A.H. A study on thermal responses, microstructural issues, and natural aging in gas tungsten arc welding of AA2024-T4. *Proc. Inst. Mech. Eng. B J. Eng. Manuf.* **2013**, *228*, 413–421. [[CrossRef](#)]
8. Merklein, M.; Maren, J.; Lechner, M.; Kuppert, A. A review on tailored blanks—Production, applications and evaluation. *J. Mater. Process. Technol.* **2014**, *214*, 151–164. [[CrossRef](#)]
9. Fröck, H.; Graser, M.; Milkereit, B.; Reich, M.; Lechner, M.; Merklein, M.; Kessler, O. Precipitation Behaviour and Mechanical Properties during Short-Term Heat Treatment for Tailor Heat Treated Profiles (THTP) of Aluminium Alloy 6060 T4. *MSF* **2016**, *877*, 400–406. [[CrossRef](#)]
10. Geiger, M.; Merklein, M.; Vogt, U. Aluminum tailored heat treated blanks. *Prod. Eng. Res. Dev.* **2009**, *3*, 401–410. [[CrossRef](#)]
11. Kerausch, M.; Merklein, M.; Geiger, M. Improved material flow for deep drawing of aluminium blanks by local laser heat treatment. In Proceedings of the 10th International Conference on Sheet Metal, SheMet 2003; Kals, H.J.J., Shirvani, B., Sing, U.P., Geiger, M., Eds.; University of Ulster: Jordanstown, UK, 2003; pp. 73–80.
12. Strobel, K.; Lay, M.D.H.; Easton, M.A.; Sweet, L.; Zhu, S.; Parson, N.C.; Hill, A.J. Effects of quench rate and natural ageing on the age hardening behaviour of aluminium alloy AA6060. *Mater. Charact.* **2016**, *111*, 43–52. [[CrossRef](#)]
13. Saito, T.; Marioara, C.D.; Røyset, J.; Marthinsen, K.; Holmestad, R. The effects of quench rate and pre-deformation on precipitation hardening in Al-Mg-Si alloys with different Cu amounts. *Mater. Sci. Eng. A* **2014**, *609*, 72–79. [[CrossRef](#)]
14. Kim, J.; Hayashi, M.; Kobayashi, E.; Sato, T. Influence of Si addition on quenching sensitivity and formation of nano-precipitate in Al-Mg-Si alloys. *J. Nanosci. Nanotechnol.* **2016**, *16*, 1814–1817. [[CrossRef](#)] [[PubMed](#)]
15. Osten, J.; Milkereit, B.; Schick, C.; Kessler, O. Dissolution and precipitation behaviour during continuous heating of Al-Mg-Si alloys in a wide range of heating rates. *Materials* **2015**, *8*, 2830–2848. [[CrossRef](#)]
16. Sarge, S.M.; Höhne, G.W.H.; Hemminger, W.F. *Calorimetry. Fundamentals Instrumentation and Applications*; Wiley-VCH Verlag GmbH & Co. KGaA: Weinheim, Germany, 2014.
17. Milkereit, B.; Kessler, O.; Schick, C. Precipitation and Dissolution Kinetics in Metallic Alloys with Focus on Aluminium Alloys by Calorimetry in a Wide Scanning Rate Range. In *Fast Scanning Calorimetry*; Schick, C., Mathot, V., Eds.; Springer International Publishing: Cham, Switzerland, 2016; pp. 723–773.
18. Kemsies, R.H.; Milkereit, B.; Wenner, S.; Holmestad, R.; Kessler, O. In situ DSC investigation into the kinetics and microstructure of dispersoid formation in Al-Mn-Fe-Si(-Mg) alloys. *Mater. Des.* **2018**, *146C*, 96–107. [[CrossRef](#)]

19. Fröck, H.; Graser, M.; Reich, M.; Lechner, M.; Merklein, M.; Kessler, O. Influence of short-term heat treatment on the microstructure and mechanical properties of EN AW-6060 T4 extrusion profiles: Part A. *Prod. Eng. Res. Dev.* **2016**, *10*, 383–389. [[CrossRef](#)]
20. Schumacher, P.; Pogatscher, S.; Starink, M.J.; Schick, C.; Mohles, V.; Milkereit, B. Quench-induced precipitates in Al–Si alloys: Calorimetric determination of solute content and characterisation of microstructure. *Thermochim. Acta* **2015**, *602*, 63–73. [[CrossRef](#)]
21. Milkereit, B. Kontinuierliche Zeit-Temperatur-Ausscheidungs-Diagramme von Al-Mg-Si-Legierungen. Ph.D. Thesis, University of Rostock, Rostock, Germany, 2011.
22. Zhang, Z.; Farrar, R.A. *An Atlas of Continuous Cooling Transformation (CCT) Diagrams Applicable to Low Carbon Low Alloy Weld Metals*; Bourne Press Ltd.: Southampton, UK, 1995.



© 2018 by the authors. Licensee MDPI, Basel, Switzerland. This article is an open access article distributed under the terms and conditions of the Creative Commons Attribution (CC BY) license (<http://creativecommons.org/licenses/by/4.0/>).

9 Appendix

Table 4: Atomic fractions (bold) and mass fractions of alloying elements for the considered alloys

		Mass fraction in %					Atomic fraction in %				
Wrought alloys											
Product type		Si	Fe	Cu	Mn	Mg	Cr	Zn	Ti	Zr	Al
6xxx - AlMgSi											
6060	Commercial extrusion, thin-walled profile	0.4 0.38	0.2 0.10	0.01 0.00	0.02 0.01	0.44 0.49	0.001 0.00	0.01 0.00	0.009 0.01		98.9 99.0
6063	Commercial extrusion, closed profile	0.5 0.48	0.19 0.09	0.02 0.01	0.03 0.01	0.47 0.52	0.005 0.00	0.03 0.01	0.013 0.01		98.7 98.9
6005A	Commercial extrusion, open profile	0.68 0.65	0.2 0.10	0.01 0.00	0.11 0.05	0.57 0.63	0.04 0.02	0.01 0.00	0.018 0.01		98.4 98.5
Al0.6Mg0.8Si	Laboratory extrusion, rectangular bar 20 x 50 mm	0.79 0.76	<0.001	<5 ppm	<5 ppm	0.59 0.65	<5 ppm	<10 ppm	<2 ppm		98.6 98.6
Al0.8Mg0.6Si	Laboratory extrusion, rectangular bar 20 x 50 mm	0.61 0.59	<0.001	<5 ppm	<5 ppm	0.8 0.89	<5 ppm	<10 ppm	<2 ppm		98.6 98.5
6082 I	Commercial extrusion, rod ø30 mm	0.733 0.71	0.22 0.11	0.05 0.02	0.48 0.24	0.609 0.68	0.003 0.00	<0.01 0.00	0.008 0.00		97.9 98.2
6082 II	Commercial extrusion, thin-walled open profile	0.94 0.91	0.19 0.09	0.045 2 0.019	0.575 0.28	0.757 0.84	0.0803 0.042	0.198 0.082	0.024 5 0.014		97.2 97.7
6082 III	Commercial 10 mm sheet	0.83 0.80	0.38 0.18	0.06 0.03	0.48 0.24	0.92 1.03	0.03 0.02	0.01 0.00	0.02 0.01		97.3 97.7
6082 IV	Commercial extrusion, rod ø30 mm	1.19 1.15	0.435 0.21	0.106 0.05	0.476 0.24	0.64 0.71	0.04 0.02	0.096 0.04	0.034 0.02		97.0 97.6
6082 V	Commercial extrusion, rod ø70 mm	1.23 1.19	0.2 0.1	0.09 0.038	0.65 0.32	1.05 1.17	0.2 0.104	0.05 0.021	0.03 0.017		96.5 97.0
7xxx - AlZnMg(Cu)		Si	Fe	Cu	Mn	Mg	Cr	Zn	Ti	Zr	Al
7020	Laboratory extrusion, rod ø30 mm	0.11 0.11	0.17 0.08	0.04 0.02	0.15 0.06	1.19 1.36	0.11 0.06	4.37 1.85	0.03	0.14 0.04	93.69 96.42
7021	Commercial 2 mm sheet	<0.25	<0.4	<0.16	<0.1	1.6-2.1	<0.05	6.0-6.8	<0.1	<0.1 8	
7055	Laboratory hot-rolled plate	0.03 0.03	0.03 0.02	2 0.9	<0.01	2 2.36	<0.01	8.12 3.56		0.12 0.04	87.7 93.09
7150	Commercial thick plate, centre layer	0.02 0.02	0.05 0.03	2.04 0.91	0.04 0.02	2.15 2.51	<0.01	6.33 2.74	0.01	0.12 0.04	89.24 93.73
7150	Commercial thick plate, surface layer	0.02 0.02	0.05 0.03	2.04 0.91	0.04 0.02	2.15 2.51	<0.01	6.33 2.74	0.01	0.12 0.04	89.24 93.73
7085	Laboratory hot-rolled plate	0.07 0.07	0.03 0.02	2.06 0.93	<0.01	1.46 1.72	<0.01	8.16 3.58		0.12 0.04	88.1 93.64
7085 _{lowCu}	Laboratory hot-rolled plate	0.12 0.12	0.02 0.01	0.91 0.41	<0.01	1.37 1.6	<0.01	7.82 3.4		0.12 0.04	89.64 94.42
7075 I	Commercial extrusion, rod ø35 mm	0.17 0.17	0.22 0.11	1.57 0.698	0.11 0.06	2.08 2.42	0.22 0.12	5.95 2.57	0.05 0.029		89.63 93.83
7075 II	Commercial 2 mm sheet	0.19 0.19	0.11 0.06	1.5 0.67	0.04 0.02	2.64 3.06	0.18 0.10	6.06 2.61	0.04 0.024		89.24 93.27
7049A	Commercial extrusion, rod ø50 mm	0.25 0.26	0.35 0.18	1.9 0.86	0.2 0.1	2.9 3.43	0.22 0.12	8.2 3.6	-	-	86.0 91.45

2xxx - AlCu(Mg)		Si	Fe	Cu	Mn	Mg	Cr	Zn	Ti	Zr	Al
2219	Commercial 9 mm sheet	0.041 0.04	0.089 0.045	6.41 2.83	0.301 0.15	0.005 7 0.007	<0.001 <0.001	0.031 0.013	0.034 0.020		93.1 96.9
2024	Commercial extrusion, rod ø30 mm	0.138 0.14	0.209 0.10	4.64 2.03	0.58 0.29	1.5 1.72	0.007 0.00	0.066 0.03	0.05 0.03		92.8 95.7
Al-Si binary		Si	Fe	Cu	Mn	Mg	Cr	Zn	Ti	Zr	Al
Al0.26Si	Laboratory 20 mm plate	0.26 0.25	<5 ppm	4 ppm	<3 ppm	<1 ppm	<3 ppm	-	20 ppm		99.74 99.75
Al0.72Si	Laboratory 20 mm plate	0.72 0.69	<5 ppm	<1 ppm	<3 ppm	<1 ppm	<3 ppm	14 ppm	11 ppm		99.28 99.31
Cast alloys											
AlSiMg cast		Si	Fe	Cu	Mn	Mg	Cr	Zn	Ti	Zr	Al
Al7Si0.3Mg	Mould cast	7.31 7.05	0.092 0.04	0.005 0.002	0.005 0.002	0.31 0.35			0.13 0.07		92.1 92.5
Al10Si0.3Mg	High-pressure die cast	10.92 10.56	0.16 0.08	0.02 0.01	0.39 0.19	0.23 0.26		0.02 0.01	0.04 0.02		88.2 88.9
Al10Si0.3Mg	Laser beam molten bar	9.46 9.13	0.16 0.08	0.01 0.004	0.003 0.001	0.30 0.33		0.02 0.01	0.01 0.00		90.0 90.4

Statement of authorship

Herewith I affirm that I have written the cumulative habilitation thesis in hand by myself. No other references and resources than those declared have been incorporated. The contents or passages used from the external literature are properly marked.

Benjamin Milkereit

Rostock, the 2nd of October.2019

List of abbreviations

DSC	Differential scanning calorimetry
DFSC	Chip sensor-based fast scanning calorimetry
OES	Optical emission spectroscopy
OM	Optical microscopy
RT	Room temperature
SEM	Scanning electron microscopy
SEM-SE	SEM secondary electron imaging
SEM-BSE	SEM backscattered electron imaging
TEM	Transmission electron microscopy
HR-TEM	High-resolution TEM
STEM	Scanning TEM
HAADF-STEM	High angle annular dark field-STEM
SAED	Selected area electron diffraction in TEM
NBD	Nano beam diffraction
EBDS	Electron backscatter diffraction in SEM
EDS	Energy-dispersive X-ray spectroscopy
HTR	High-temperature reaction
LTR	Low-temperature reaction
CCP diagram	Continuous cooling precipitation diagram
UCCR	Upper critical cooling rate
LCCR	Lower critical cooling rate
UCHR	Upper critical heating rate
LCHR	Lower critical heating rate

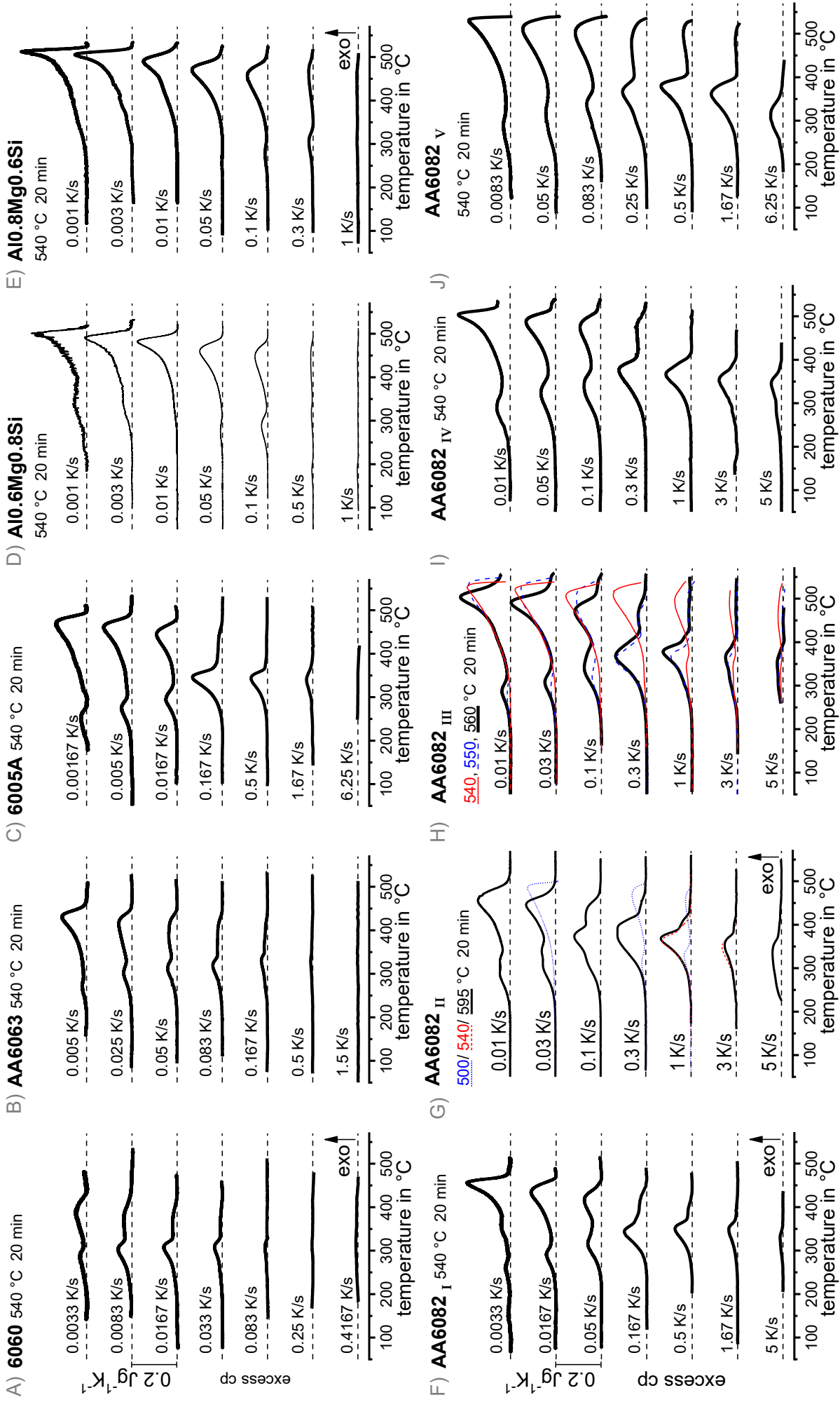


Figure A1: Comparison of DSC cooling curves for 10 different AlMgSi alloys.

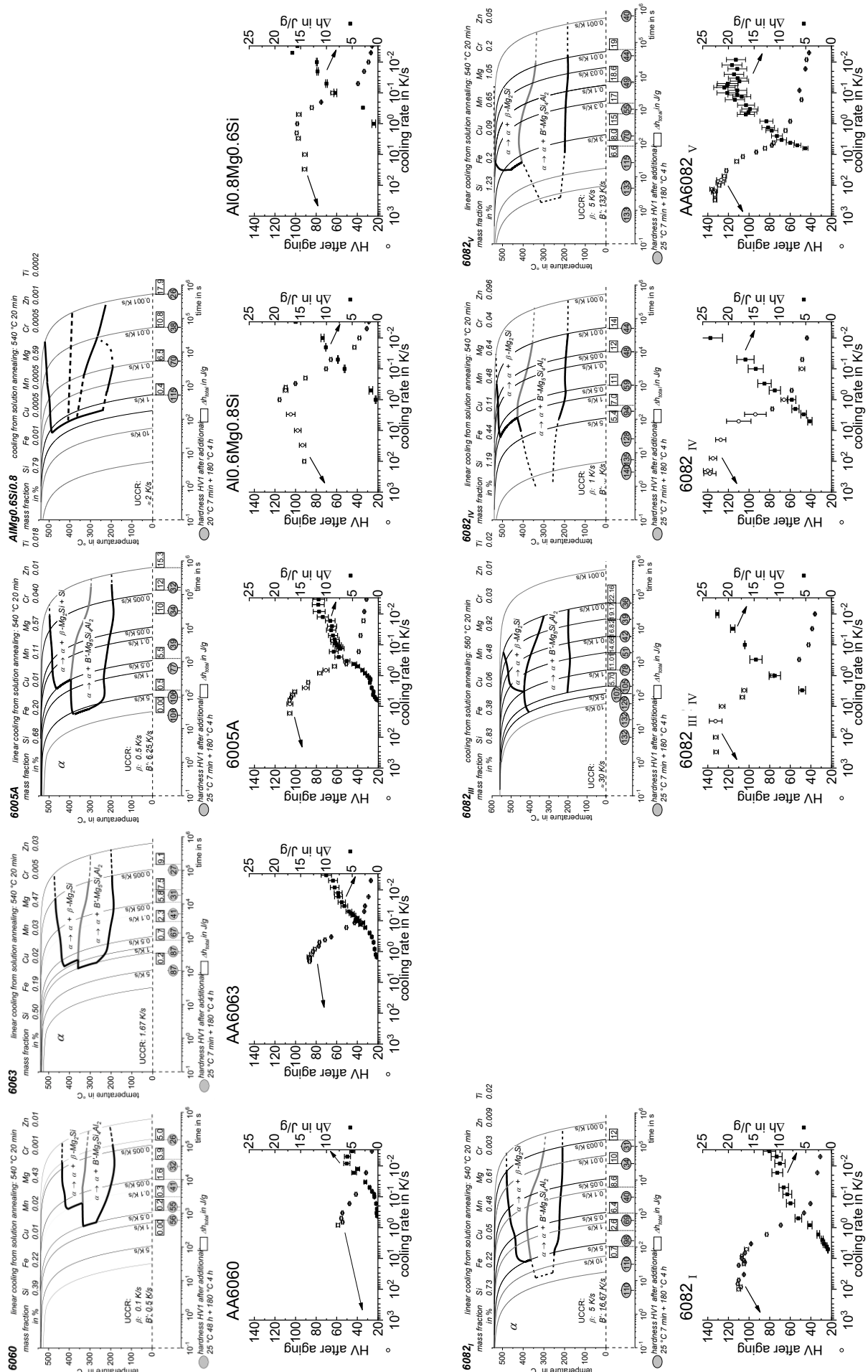


Figure A2: Comparison of the continuous cooling precipitation diagrams, the total specific precipitation enthalpies after cooling and hardness after additional artificial ageing, for 9 different AlMgSi alloys.

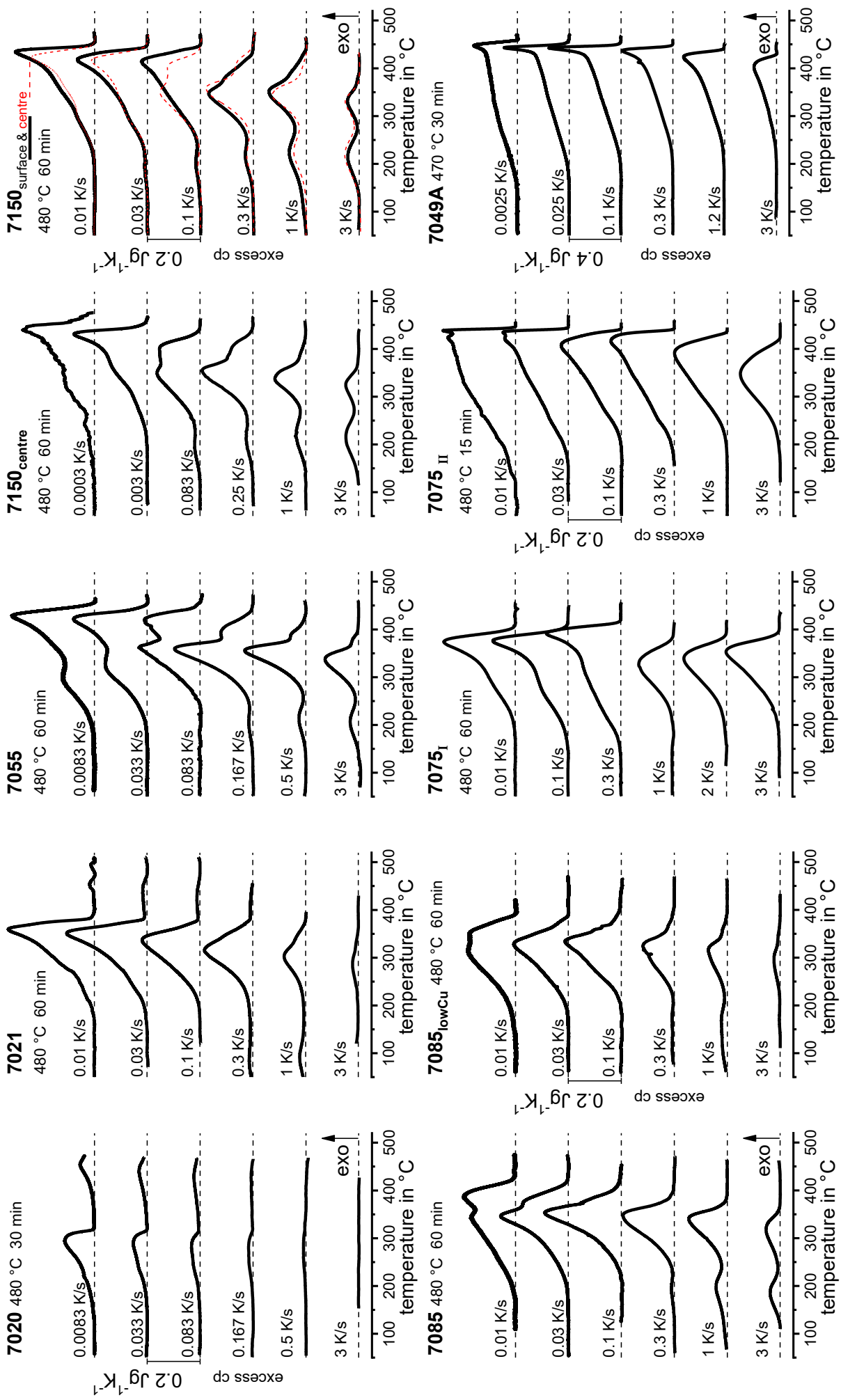


Figure A3: Comparison of DSC cooling curves for 10 different AlZnMg(Cu) alloys. The ordinate scaling is identical for all alloys except 7049A, for which the distance of the shifted zero-levels is doubled.

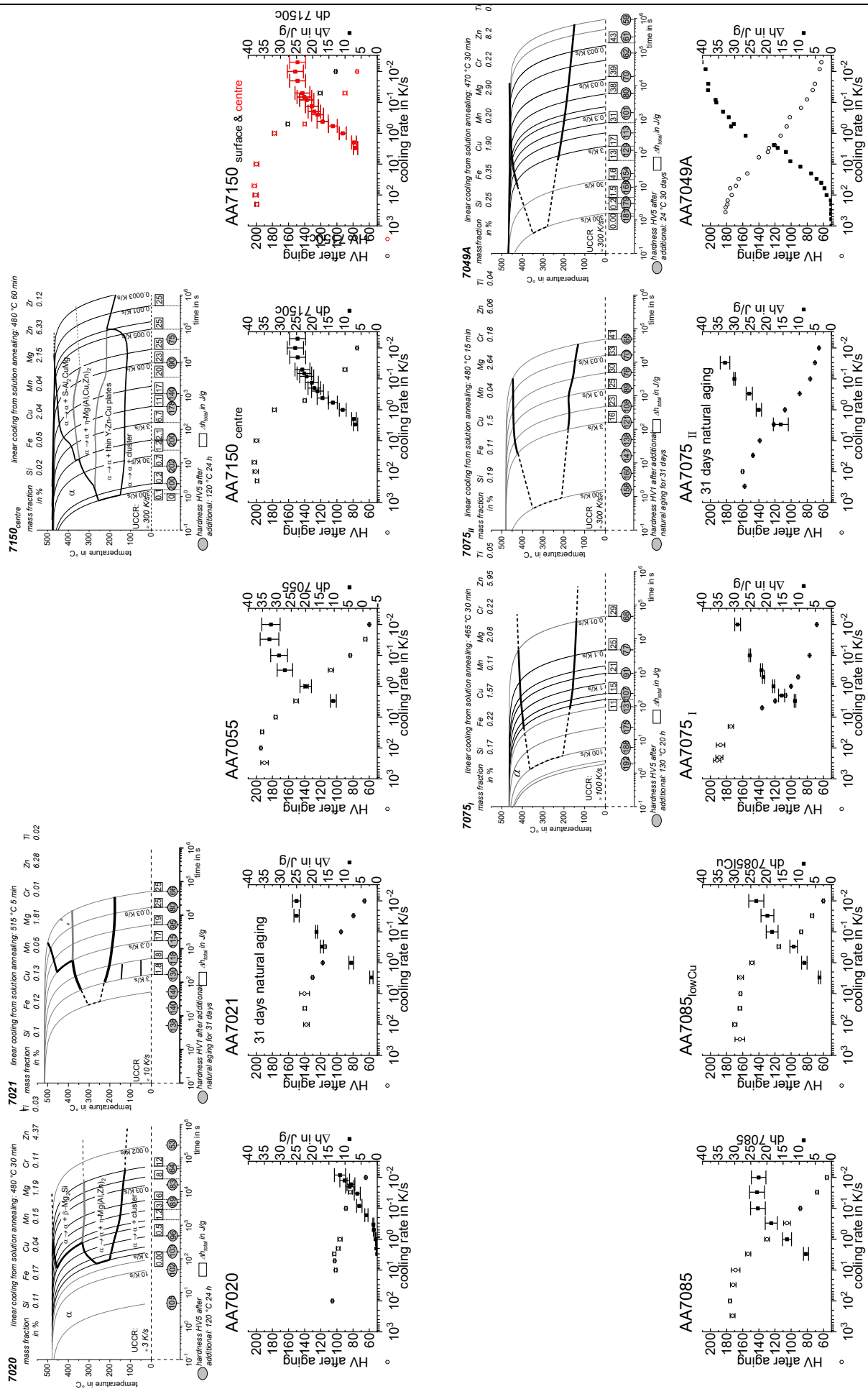


Figure A4: Comparison of the continuous cooling precipitation diagrams, the total specific precipitation enthalpies after cooling and hardness after additional artificial ageing, for 10 different AlZnMg(Cu) alloys.